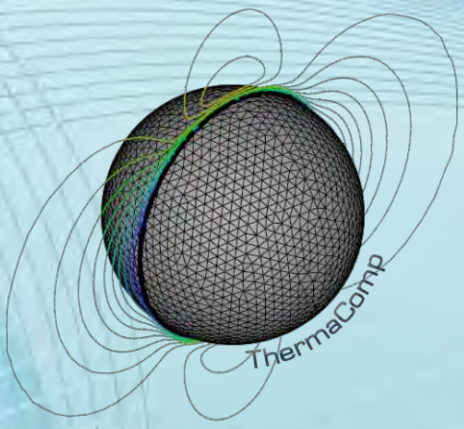

ThermaComp2016

Fourth International Conference on

COMPUTATIONAL METHODS FOR THERMAL PROBLEMS

Edited by
Nicola Massarotti
Perumal Nithiarasu
Yogendra Joshi

JULY
6-8, 2016
ATLANTA,
USA

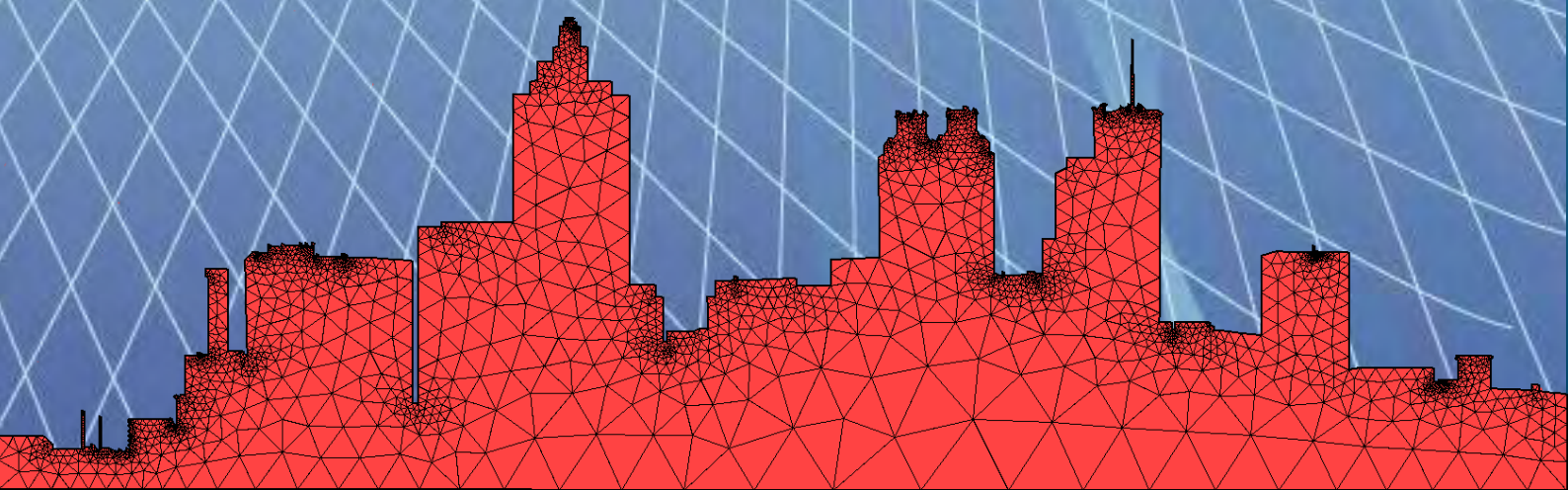

THERMACOMP2016

FOURTH INTERNATIONAL CONFERENCE ON COMPUTATIONAL METHODS FOR THERMAL PROBLEMS

JULY 6-8, 2016, GEORGIA TECH, ATLANTA, USA

EDITED BY:

NICOLA MASSAROTTI
DIPARTIMENTO DI INGEGNERIA
UNIVERSITÀ DEGLI STUDI DI NAPOLI "PARTHENOPE"
NAPOLI, ITALY

PERUMAL NITHIARASU
CIVIL AND COMPUTATIONAL ENGINEERING CENTRE
SCHOOL OF ENGINEERING, SWANSEA UNIVERSITY
SWANSEA, UNITED KINGDOM

YOGENDRA JOSHI
G.W. WOODRUFF SCHOOL OF MECHANICAL ENGINEERING
GEORGIA INSTITUTE OF TECHNOLOGY
ATLANTA, GEORGIA

WITH THE SUPPORT FROM:
ALESSANDRO MAURO AND SIMONA DI FRAIA
UNIVERSITÀ DEGLI STUDI DI NAPOLI "PARTHENOPE"

4th International Conference on Computational Methods for Thermal Problems, 2016, Georgia Tech, Atlanta, USA

Fourth Edition, July 2016

ISBN 13: 978-88-7431-828-5

Publisher: Giannini Editore
Via Cisterna dell'Olio 6/b, 80134 Napoli
www.gianninispa.it

PREFACE

It is our pleasure to welcome all participants in Atlanta for the *Fourth International Conference on Computational Methods for Thermal Problems* (THERMACOMP2016). Computational and mathematical methods have a profound impact on the understanding and advancement of engineering science and technology. When this series of Conferences was started back in Naples Italy in 2009, we thought that even though there were many conferences in the area of computational methods serving the community, a focused conference in the area of computational methods for thermal problems had been long overdue. This Conference aims to convene a diverse scientific audience of mathematicians, physicists and computational scientists that have a communal interest in modelling thermal problems. It is encouraging to learn that this conference represents an interdisciplinary forum of scientists with expertise ranging from heat conduction, convection and radiation to CFD and micro and nano heat transfer. We hope that the interaction between scientists during the conference leads to new topics of research, new collaborations, and new friends.

THERMACOMP2016 consists of three plenary lectures, six keynote lectures, five organized mini-symposia and nine parallel sessions. We are grateful to all invited speakers for accepting our invitation.

We would also like to take this opportunity to thank THERMACOMP2016 sponsors, mini-symposium organizers, executive and advisory committee members, as well as everyone who has been involved in the organization for their support.

Nicola Massarotti
Università di Napoli Parthenope
Italy

Perumal Nithiarasu
Swansea University
United Kingdom

Yogendra Joshi
Georgia Institute Of Technology
USA

SPONSORS

UNIVERSITÀ DEGLI STUDI DI NAPOLI "PARTHENOPE"

SWANSEA UNIVERSITY

GEORGIA INSTITUTE OF TECHNOLOGY

SUPPORTING ORGANIZATIONS

DIPARTIMENTO DI INGEGNERIA

CONSORZIO DI RICERCA PER L'AMBIENTE I VEICOLI L'ENERGIA E I BIOCOMBUSTIBILI

UNIVERSITÀ DEGLI STUDI DI CASSINO E DEL LAZIO MERIDIONALE

COMMITTEES

HONORARY CHAIR
R.W. Lewis, Swansea University, UK

CO-CHAIRS
N. Massarotti, University of Naples "Parthenope", Italy
P. Nithiarasu, Swansea University, UK
Y. Joshi, Georgia Institute of Technology, USA

INTERNATIONAL EXECUTIVE COMMITTEE
P. Cheng, Shanghai Jiao Tong University, China
G. Comini, CISM, Italy
M: Ishizuka, Toyama Prefecture University, Japan
Y. Jaluria, Rutgers, The State University of New Jersey, USA
X. K. Li, Dalian University of Technology, China
J. Murthy, University of California, Los Angeles, USA
J. Nurthy, University of Texas, Austin, USA
V. Naso, Università di Napoli Federico II, Italy
B. Sarler, University of Nova Gorica & Institute of Metals and Technology, Slovenia
K.N. Seetharamu,PES Institute of Technology, India
B. Sunden, Lund University, Sweden
W.Q. Tao, X'ian Jiatong University, China
K. Vafai, University of California, Riverside, USA

INTERNATIONAL ADVISORY COMMITTEE
S. Acharya, Memphis State University, USA
F. Arpino, Università degli Studi di Cassino e del Lazio Meridionale, Italy
B.R. Baliga, McGill University, Canada
S.W. Baek, Korea Advanced Institute of Science & Technology, South Korea
G. Biswas, Indian Institute of Technology Kanpur, India
A. Carotenuto, Università di Napoli "Parthenope", Italy
A.J. Chamkha, Public Authority for Applied Education and Training, Kuwait
S. Chang, National University of Singapore, Singapore
F. Chinesta, Ecole Centrale de Nantes, France
R. Codina, Universitat Politècnica de Catalunya, Spain
R.M. Cotta, Universidade Federal do Rio de Janeiro, Brazil
D. Drikakis, University of Strathclyde, UK
G. Dulikravich, Florida International University, USA
T. Fushinobu, Tokyo Institute of Technology, Japan
D. Givoli, Technion - Israel Institute of Technology, Israel
D. Gobin, CNRS, France
S. Idelsohn, CIMNE - International Center for Numerical Methods in Engineering, Spain
A. Kassab, University of Central Florida, USA
M. Li, Taiyuan University of Technology, China
R. Lohner, George Mason University, USA
A.G. Malan, Council for Scientific and Industrial Research, South Africa
O. Manca, Seconda Università di Napoli, Italy
J.C. Mandal, Indian Institute of Technology Bombay, India
A. Mauro, Università di Napoli "Parthenope", Italy
C. Nonino, Università di Udine, Italy
A.J. Nowak, Silesian Polytechnic University, Poland
J. Patterson, University of Sydney, Australia
I. Pop, University of Cluj, Romania
D. Pradip, Indian Institute of Science, Bangalore, India
J. Reese, University of Strathclyde Glasgow, UK
W. Shyy, Hong Kong University of Science and Technology, Hong Kong
Siraj-ul-Islam, University of Engineering and Technology Peshawar, Pakistan
J. Summers, Leeds University, UK
K. Sungjin, Korea Advanced Institute of Science and Technology, South Korea
V.R. Voller, University of Minnesota, USA
I. Vusanovic, University of Montenegro, Montenegro
W. Wall, Technische Universität München, Germany
L. Xiaobing, Huazong University of Science and Technology, China

ORGANISING COMMITTEE
S. Di Fraia, Università di Napoli "Parthenope", Italy
S. Kumar, Georgia Institute of Technology, USA
A. Mauro, Università di Napoli "Parthenope", Italy

CONTENTS

PLENARY LECTURES

KEYNOTE LECTURES

MINI-SYMPOSIA

ELECTRONICS COOLING MODELING

MINI SYMPOSIUM ORGANISED BY KRISHNA KOTA

Three computational methods for analysing thermal airflow distributions in the cooling of data centers
de Boer Greg, Delbosc Nicolas, Johns Adam, Burdett Daniel, Summers Jon, Tatchell-Evans Morgan

Rack Level Transient CFD Modeling of Data Center
Fulpagare Yogesh, Joshi Yogendra, Bhargav Atul

CFD Study of Variable Pin Fin Density Microgap Heat Sinks for 3D-Stacked ICs
Lorenzini Daniel, Joshi Yogendra

Assessment of Flow Distribution Features in Microgaps for 3D Stacking of ICs
Lorenzini Daniel, Asrar Pouya, Woodrum Casey, Kottke Peter, Fedorov Andrei, Sitaraman Suresh, Joshi Yogendra

Numerical Modeling of Energy-Efficient Liquid Cooling Using Conducting-Lubricating (CO-LUB) Surfaces
Reyes Jessica, Kota Krishna

Liquid Jet Impingement with an Angled Confining Wall
Maddox John F., Knight Roy W., Bhavnani Sushil H.

MICRO-NANO SCALE HEAT TRANSFER IN NANOSTRUCTURES AND DEVICES

MINI SYMPOSIUM ORGANISED BY SATISH KUMAR

Sensitivity of Thermal Conductivity Calculations to Errors in Interatomic Forces
Brock Casey N., Gerboth Matthew D., Walker D. Greg

Investigation of Phonon Transport and Thermal Boundary Conductance at Interface of Functionalized SWCNT and Poly (Ether-Ketone)
Huang Haoxiang, Kumar Satish, Varshney Vikas, Roy Ajit

Interface Conductance Modal Analysis Across Si-Ge Interfaces
Kiarash Gordiz, Asegun Henry

Thermal transport analysis of mini-channel heat sink partially filled with metal foam sandwiched on the fin sides
YongTong Li, MingHai, Xu Liang Gong

Conjugated Heat Transfer in Complex Geometries via Total Integral Transformation and Single Domain Formulation
Zotin José Luiz Zanon, Knupp Diego Campos, Cotta Renato Machado

Perfect Absorption in Hbn/Metal Grating Hybrid Anisotropic Structures
Zhao Bo, Zhang Zhuomin M.

MULTISCALE METHODS IN THERMAL SIMULATIONS

MINI-SYMPOSIUM ORGANISED BY PRATAP VANKA AND YOGENDRA JOSHI

Multi-Length Scale Electro-Thermal Simulations of GaN High Electron Mobility Transistors
Hao Qing, Zhao Hongbo, Xiao Yue

A Comparison Between Different Lifting Relations from Macroscopic Variables to Lattice Boltzmann Distribution Functions
Tong Zi-Xiang, Ming-Jia Li, Ya-Ling He, Wen-Quan Tao

Multi Scale Thermal Modeling In GaN HEMTs
Vallabhaneni Ajit K, Kumar Satish

Hierarchical Multiscale Simulations for Data Center Cooling
Vanka S. P., Athavale Jayati, Yoda Minami, Joshi Yogendra

COMPUTATIONAL BIOHEAT TRANSFER

MINI-SYMPOSIUM ORGANISED BY PERUMAL NITHIARASU

The role of stress-dependent permeability in enhanced geothermal systems modelling
Coccarelli Alberto, Parthimos Dimitris, Hasan Hayder, Nithiarasu Perumal

Investigation of Thermofluid Dynamics in a Human Eye: Numerical Modeling of Aqueous Humor Flow in Porous Tissues
Mauro A., Massarotti N., Salahudeen M., Romano M.R., Romano V., Nithiarasu P.

Numerical Simulation of Suprachoroidal Shunts for Treatment of Glaucoma
Mauro A., Massarotti N., Romano M.R., Romano V., Nithiarasu P.

Modelling Energy Transport in a Human Respiratory System
Nithiarasu Perumal

State Estimation Problems In PRF-Shift Magnetic Resonance Thermometry
Pacheco César C., Orlande Helcio R. B., Colaço Marcelo J., Dulikravich George S.

VALIDATION, VERIFICATION AND EXPERIMENTAL UNCERTAINTY QUANTIFICATION FOR HEAT AND FLUID FLOW PROBLEMS

MINI-SYMPOSIUM ORGANISED BY F. ARPINO, G. CORTELLESSA,F. IANNETTA, N. MASSAROTTI, A. MAURO, F. SCARANO AND A.SCIACCHITANO

Schlieren And Mie Scattering Techniques for the ECN "Spray G" Characterization and 3D CFD Model Validation
Allocca L., Costa M., Lee S.Y., Montanaro A., Piazzullo D., Rocco V.

Numerical and experimental comparison of velocity derived quantities in rectangular cavity flows
Iannetta F., Sciacchitano A., Arpino F., Scarano F.

Numerical and Experimental Investigation of the Performance of a Car Prototype for the Shell Eco Marathon
Scungio M., Arpino F., Iannetta F., Frattolillo A., Cortellessa G., Fuoco L.

Validation of Thermal Models of Single Phase Thermal Management Flow Loops
Spector Mark S., Joshi Yogendra, Doty John, Eussen Bart, Cerza Martin

PARALLEL SESSIONS

CONDUCTION, CONVECTION AND RADIATION

Operating Rooms: Numerical Modeling of Heat and Mass Transport Phenomena
Carotenuto Alberto, Massarotti Nicola, Mauro Alessandro, Sainas Domenico

A one-dimensional numerical model to determine thermal and optical performance of a PCM-filled double glazing unit
Dong Li, Yumeng Zheng, Changyu Liu, Xiaoyan Liu, Hanbing Qi, Guozhong Wu

Inhomogeneities inside thermal bridges: effects on heat and vapor transport
Iodice Paola, Massarotti Nicola, Mauro Alessandro

Heat transfer enhancement in PCM storage tanks through topology optimization of finning material distribution
Pizzolato Alberto, Verda Vittorio, Sciacovelli Adriano

Heatline and Entropy Generation Based Analysis of Natural Convection in Porous Cavities with Curved Walls Subjected To Rayleigh-Benard Heating
Pratibha Biswal, Tanmay Basak

A Numerical Investigation on Aero-Thermodynamic Characteristics of a Nose Cone in Wind Tunnel and Near Space Flight Environment
Lin Shen, Jianhua Wang, Wenjie Dong

Influence of Temperature Dependent Properties on Dusty Fluid
Sadia Siddiqa, Naheed Begum, Md. Anwar Hossain

Thermal Radiation Effects on Two-Phase Dusty Fluid Past a Vertical Wavy Surface
Sadia Siddiqa, Naheed Begum, Md. Anwar Hossain

Numerical Investigation of Laminar Rayleigh-Bénard Convection of Power-Law Fluids in Square Cross-sectional Cylindirical Annular Cavity
Sahin Yigit, Nilanjan Chakraborty

Numerical Modeling of Convective Flows Structured at Isothermal Diffusion in Vertical Cylindrical Channels at Different Pressures
Zhakebayev D.B., Kosov V.N., Kosov Y.V.

REACTIVE HEAT AND MASS TRANSPORT

Non-equilibrium Framework Applicable at all Spatial and Temporal Scales Using Steepest-Entropy-Ascent Quantum Thermodynamics
Li Guanchen, von Spakovsky Michael R.

Non-equilibrium Predictions of Diffusion in Closed and Open Systems at Atomistic Levels Using Steepest-Entropy-Ascent Quantum Thermodynamics
Younis Aimen M., von Spakovsky Michael R.

HEAT AND MASS TRANSFER IN POROUS MEDIA

Two-Phase Explicit CBS Procedure For Compressible Viscous Flow Transport in Porous Materials
Arpino Fausto, Cortellessa Gino, Fernicola Vito

Macro-Scale Modelling of Heat Sinks with Highly Conductive Periodically Arranged Fins
Buckinx G., Baelmans M.

Linear stability analysis of natural convection in partially porous tall annuli
Ciccolella Michela, Massarotti Nicola, Mauro Alessandro, Cortellessa Gino

Examination of Two Approaches for Determining Interfacial Conduction Coefficient in Porous Media
Cimmino Massimo, Baliga Bantwal R. (Rabi)

NUMERICAL METHODS

HIGH PERFORMANCE COMPUTING

HEAT EXCHANGERS AND FUEL CELLS

Experimental Set-Up And Thermo Hydro Mechanical Model For An Energy Pile
Adinolfi M., Mauro A., Maiorano R.M.S., Massarotti N., Aversa S., Normino G., Marotta P.

Transitional Fluid Flow Numerical Modelling in Sinusoidal Heat Exchanger Channels
Greiciunas Evaldas, Borman Duncan, Summers Jon

Molecular dynamics simulation of oxygen transport characteristics in the MEA of PEMFC
Kato Mahiro, Henry Asegun, Graham Samuel, Hong Duc Doan, Fushinobu Kazuysohi

Experimental Validation Of Quasy-3d CVFEM Model Of Borehole Heat Exchangers
Tombarevic Esad, Vušanović Igor

BOILING AND CONDENSATION

CFD Modeling of High-Speed Condensation in Supersonic Nozzles, Part II: R134a
Biferi Giulio, Mazzelli Federico, Little Adrienne B., Garimella Srinivas, Bartosiewicz Yann

CFD Modeling of High-Speed Condensation in Supersonic Nozzles, Part I: Steam
Giacomelli Francesco, Mazzelli Federico, Milazzo Adriano

Saturated Film Boiling in Reduced Gravity with Applied Electric Field
Pandey Vinod, Biswas Gautam and Dalal Amaresh

Nucleate Boiling Performance Evaluation of Different Cavities at Mesoscale Level
Yutong Mu, Li Chen, Qinjun Kang, Ya-Ling He and Wen-Quan Tao

POWER PLANTS AND EQUIPMENT

Finite volume model of a flat plate cogenerative collector: thermodynamic and experimental analysis
Calise Francesco, Figaj Rafal Damain, Vanoli Laura

Heat Transfer Analysis of a Fluidized Bed Stripper Ash Cooler
Ravi Inder Singh, Karan Ghule

ENERGY CONVERSION

PLENARY LECTURES

Fourth International Conference on Computational Methods for Thermal Problems
THERMACOMP2016, July 6-8, 2016, Georgia Tech, Atlanta, USA
N. Massarotti, P. Nithiarasu and Y. Joshi (Eds.)

Lattice Boltzmann Simulations of Boiling Heat Transfer Phenomena: A New Research Frontier for Numerical Heat Transfer

P. Cheng, S. Gong and C.Y. Zhang
School of Mechanical Engineering, Shanghai Jiao Tong University, Shanghai 200240, P. R. China,
pingcheng@sjtu.edu.cn

ABSTRACT

Effects of wettability, roughness, heater size and subcooling on pool boiling from horizontal superheated surfaces are investigated numerically based on a newly developed lattice Boltzmann method. Complete pool boiling curves from onset of convection through nucleate boiling to critical heat flux, and from transition boiling to film boiling under constant wall temperature and constant heat flux are obtained for the first time. Boiling patterns under different conditions are illustrated. Accuracy of this newly developed LB phase-change method is compared with exact analytical solutions. It is shown that this newly developed lattice Boltzmann phase-change method provides a promising tool for investigation of boiling heat transfer phenomena.

Key Words: *Boiling Curves, Lattice Boltzmann Method, Wettability, Roughness, Subcooling, Heater size.*

1. INTRODUCTION

Boiling heat transfer is one of the most effective heat transfer modes with a wide range of applications in energy conversion and cooling technologies. In 1934, Nukiyama [1] performed a well-known experiment on pool boiling from a horizontal wire under controlled heat flux conditions. He presented his boiling heat flux data versus degree of superheat, and found the maximum heat flux which has been called the critical heat flux. Subsequently, many investigators have obtained boiling curves under controlled wall temperature and controlled heat flux conditions [2], and the shape of boiling curves were different under these two different thermal conditions. During the past century, research work on boiling heat transfer has been mostly experimental in nature with results often expressed in the form of correlation equations in terms of relevant dimensionless variables with empirical constants. In the past, most commonly used numerical simulation tools for boiling heat transfer are based on interface tracking models such as level set or VOF method [3, 4]. The major drawback of these numerical methods is that the initial condition of a bubble must be specified artificially at a specific location, independent of conditions on the heating surface. Thus, onset of bubble nucleation and critical heat flux could not be simulated, and therefore it was impossible to simulate complete boiling curves using these macroscopic numerical methods [4].

In 2012, Gong and Cheng proposed a phase-change lattice Boltzmann method [5, 6] which is capable of simulating the entire boiling process including bubble nucleation. The method is based on modifications of Shan-Chen's multiphase lattice Boltzmann model for isothermal flow [7] and Hazi-Markus's phase-change lattice Boltzmann model [8]. In this paper, we will summarize simulated results for boiling heat transfer phenomena based on this newly developed model. Near field effects of wettability/roughness/size of heated horizontal surfaces as well as far field effects of subcooled environment on pool boiling from horizontal superheated surfaces are investigated numerically [9-11]. Based on 2D simulations, complete saturated pool boiling curves from onset of nucleation to critical heat flux, and from transition boiling to stable film boiling on smooth/rough superheated surfaces under controlled wall temperature [9, 10] and controlled wall heat flux [11] are obtained for the first time. Near field and far field effects on onset of nucleation, bubble

departure diameter, bubble departure frequency, and critical heat flux are shown. These effects on boiling patterns in the nucleate boiling, transition boiling and stable boiling regimes are illustrated.

2. THE GONG-CHENG PHASE-CHANGE LB MODEL

The modified pseudo-potential lattice Boltzmann model for multiphase flows

The evolution equation for the density distribution function is given by

$$f_i(\mathbf{x}+\mathbf{e}_i\delta_t, t+\delta_t) - f_i(\mathbf{x},t) = -\frac{1}{\tau}\left(f_i(\mathbf{x},t) - f_i^{(eq)}(\mathbf{x},t)\right) + \Delta f_i(\mathbf{x},t) \tag{1}$$

where $f_i(\mathbf{x}, t)$ is the particle distribution function with velocity $\mathbf{e}_i$ at position $\mathbf{x}$ and time t, τ is the relaxation time and $f_i^{(eq)}(\mathbf{x}, t)$ is the corresponding equilibrium distribution function which is given by

$$f_i^{(eq)} = \omega_i \rho\left[1 + \frac{\mathbf{e}_i \cdot \mathbf{u}}{c_s^2} + \frac{(\mathbf{e}_i \cdot \mathbf{u})^2}{2c_s^4} - \frac{\mathbf{u}^2}{2c_s^2}\right] \tag{2}$$

where ω_i is the weighting coefficients and c_s is the lattice sound speed.

The exact difference method [12] was adopted to incorporate the body force term $\Delta f_i(\mathbf{x}, t)$ in Eq. (1), which is given by

$$\Delta f_i(\mathbf{x},t) = f_i^{(eq)}\left(\rho(\mathbf{x},t), \mathbf{u}+\Delta\mathbf{u}\right) - f_i^{(eq)}\left(\rho(\mathbf{x},t), \mathbf{u}\right) \tag{3}$$

with $\Delta\mathbf{u} = \mathbf{F}\delta_t/\rho$ being the velocity change under the action of body force during time step δ_t, where $\mathbf{F}$ is given by

$$\mathbf{F} = \mathbf{F}_s(\mathbf{x}) + \mathbf{F}_g(\mathbf{x}) + \mathbf{F}_{int}(\mathbf{x}) \tag{4}$$

with $\mathbf{F}_s$ being the fluid-solid interaction force, $\mathbf{F}_g$ being the gravitational force and $\mathbf{F}_{int}$ the interparticle interaction force responsible for phase separation which is given by

$$\mathbf{F}_{int}(\mathbf{x}) = -\beta\psi(\mathbf{x})\sum_{\mathbf{x}'} G(\mathbf{x},\mathbf{x}')\psi(\mathbf{x}')(\mathbf{x}'-\mathbf{x}) - \frac{1-\beta}{2}\sum_{\mathbf{x}'} G(\mathbf{x},\mathbf{x}')\psi^2(\mathbf{x}')(\mathbf{x}'-\mathbf{x}) \tag{5}$$

where β is the weighting factor depending on the equation of state adopted, and $\psi(\mathbf{x})$ is the "effective mass", which is a function of the local density and determined by the equation of state used in the simulation:

$$\psi(\rho) = \sqrt{\frac{2(p-\rho c_s^2)}{c_0 g}} \tag{6}$$

with c_0 = 6.0. The Peng-Robinson (P-R) equation of state is adopted in this simulation, which is given by

$$p = \frac{\rho RT}{1-b\rho} - \frac{a\rho^2\phi_0(T)}{1+2b\rho-b^2\rho^2} \tag{7}$$

where $\phi_0(T) = [1+(0.37464+1.54226\omega-0.26992\omega^2)(1-\sqrt{T/T_c})]^2$, with ω being the acentric factor.

The wettability of the heating surface is incorporated by the fluid-solid interaction force $\mathbf{F}_s$, which is given by

$$\mathbf{F}_s(\mathbf{x}) = -\psi(\mathbf{x})\sum_i g_s \omega_i s(\mathbf{x}+\mathbf{e}_i\delta_t)\cdot\mathbf{e}_i\delta_t \tag{8}$$

where g_s is the fluid-solid interaction strength for adjusting the contact angles, and $s(\mathbf{x})$ is the indicator function which is equal to 1 when $\mathbf{x}$ is a solid node and equal to 0 when $\mathbf{x}$ is a fluid node.

The gravity is incorporated by

$$\mathbf{F}_g(\mathbf{x}) = (\rho(\mathbf{x}) - \rho_{ave})\mathbf{g} \tag{9}$$

with $\boldsymbol{g}$ being the gravitational acceleration and ρ_{ave} the average density of the whole computation domain at each time step.

The density and velocity are obtained by

$$\rho = \sum_i f_i \tag{10a}$$

$$\rho\mathbf{u} = \sum_i \mathbf{e}_i f_i \tag{10b}$$

Note that $\mathbf{u}$ is not the real fluid velocity. The real fluid velocity $\mathbf{U}$ is obtained by

$$\rho\mathbf{U} = \sum_i \mathbf{e}_i f_i + \frac{\delta t}{2}\mathbf{F} \tag{11}$$

Energy equation model

The evolution equation for the temperature distribution function is given by

$$g_i(\mathbf{x}+\mathbf{e}_i\delta_t, t+\delta_t) - g_i(\mathbf{x},t) = -\frac{1}{\tau_T}\left(g_i(\mathbf{x},t) - g_i^{(eq)}(\mathbf{x},t)\right) + \delta_t\omega_i\phi \tag{12}$$

where τ_T is the relaxation time for temperature and $g_i^{(eq)}(\mathbf{x}, t)$ is the equilibrium distribution function for temperature which is given by

$$g_i^{(eq)} = \omega_i T\left[1 + \frac{\mathbf{e}_i\cdot\mathbf{U}}{c_s^2} + \frac{(\mathbf{e}_i\cdot\mathbf{U})^2}{2c_s^4} - \frac{\mathbf{U}^2}{2c_s^2}\right] \tag{13}$$

The source term ϕ in Eq. (12), which is responsible for liquid-vapor phase change, is derived as

$$\phi = T\left[1 - \frac{1}{\rho c_v}\left(\frac{\partial p}{\partial T}\right)_\rho\right]\nabla\cdot\mathbf{U} \tag{14}$$

Note that at the liquid-vapor interface, fluid properties χ (such as thermal diffusivity and viscosity) are given by

$$\chi = \chi_{liquid}\cdot\frac{\rho-\rho_{vapor}}{\rho_{liquid}-\rho_{vapor}} + \chi_{vapor}\cdot\frac{\rho_{liquid}-\rho}{\rho_{liquid}-\rho_{vapor}} \tag{15}$$

The temperature is obtained by

$$T = \sum_i g_i \tag{16}$$

Detailed discussion of this newly developed model can be found in our previous work [5, 6].

3. 2D LB SIMULATIONS FOR POOL BOILING FROM SUPERHEATED HORIZONTAL SURFACES

2D LB simulations, based on the Gong-Cheng model presented in Section 2, on effects of wettability, roughness, heater size (with different lengths L_H) and subcooling on pool boiling have been carried out. The results of these simulation are presented in Figs. 1-4, where the boiling heat flux q versus the Jakob number Ja where $Ja = c_{p,l}(T_w-T_s)/h_{fg}$, with T_w being the wall temperature. For the controlled wall temperature case, T_w is given and q is computed from the numerical simulation, while for the controlled heat flux case, q is given and T_w is the average wall temperature obtained from numerical simulation.

Wettability effects

LB simulation for saturated pool boiling from horizontal smooth hydrophilic/hydrophobic surfaces under *controlled wall temperature* has been carried out by Gong and Cheng [9]. Simulated saturated boiling curves on a hydrophilic heater with $\theta = 53°$ with a length of $L_H = 11.3l_0$ (where l_0 is the capillary length defined as $l_0 = [\sigma/g(\rho_l-\rho_v)]^{0.5}$), a thickness of $H = 1.1l_0$ and a hydrophobic heater with $\theta = 103°$ with the same size are presented in Fig. 1. As shown, these two curves almost collapse into one in the natural convection regime as well as in the film boiling regime, indicating that the surface wettability has little effect on single-phase convective heat transfer. It is also observed that the hydrophobic heating surface exhibits a lower ONB temperature than on the hydrophilic heating surface. In addtion, the hydrophobic heating surface exhibits higher boiling heat transfer rates in nucleate boiling regime but a lower critical heat flux than the hydrophilic heating surface. Three small inserts for boiling patterns in nucleate boiling regime, critical heat flux and film boiling regime are also presented in this figure. As shown, bubbles on the surface seem to be relatively isolated in nucleate boiling regime. When CHF occurs, strong interaction between adjacent bubbles and the coalescence of adjacent bubbles on the surface causes formation of vapor columns and partial dryout of the heating surface. In film boiling regime, a stable vapor film is formed to cover the entire heating surface. It is interesting to note the two simulated boiling curves have the same characteristics as the experimental data, namely, as the wall temperature is increased, heat flux increases from ONB to critical heat flux, after which heat flux decreases as the wall temperature is increased until the end of the transition boiling regime, and it increases again in the stable film boiling regime.

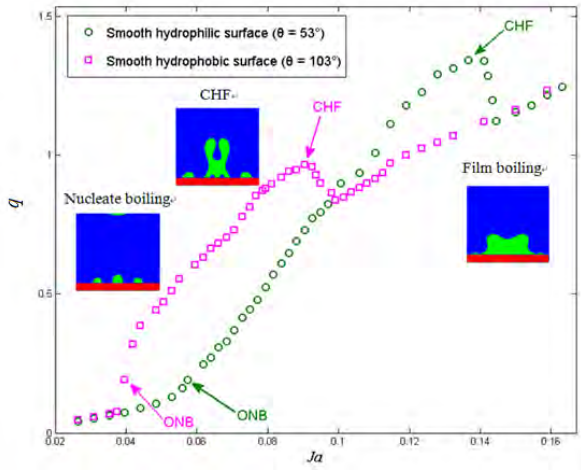

FIGURE 1. Wettability effects on saturated boiling curves for pool boiling from horizontal superheated smooth surfaces under constant wall temperature conditions with $L_H = 11.3l_0$ and $H = 1.1l_0$ [9]

Roughness effects

Fig. 2(a) is a comparison of saturated boiling curves for a smooth hydrophilic surface (θ = 53°) and a rough hydrophilic surface with the same contact angle having 7 rectangular cavities under *controlled wall temperature* conditions. Fig. 2 (b) shows a similar comparison of saturated boiling curves for a smooth and rough hydrophobic surfaces (θ = 103°) having the same seven rectangular cavities. It can be seen from these two graphs that (i) all of the simulated boiling curves on rough surfaces have the same classical shape for controlled wall temperature as discussed in connection with Fig. 1. (ii) ONB occurs at a lower superheat on a rough surface than that on the corresponding smooth surface, indicating that presence of the roughness on the heating surface promotes boiling incipience. (iii) Boiling curves on the hydrophilic/hydrophobic rough surface move to the left of the corresponding smooth surface, i.e, nucleate boiling heat flux is higher on a rough surface than that on a smooth surface at the same degree of superheat. (iv) Critical heat flux occurs at a lower wall temperature on the rough surface than on a smooth surface. To show the wettability effects on rough surfaces, the boiling curve for rough hydrophilic surface (θ = 53°) from Fig. 2(a) and the boiling curve for rough hydrophobic surface (θ = 103°) from Fig. 2(b) are replotted together in Fig. 2(c) for comparison. As shown, the boiling curve on the hydrophobic rough surface moves to the left of the hydrophilic rough surface, and CHF on the hydrophobic rough surface is lower than that on the hydrophilic rough surface.

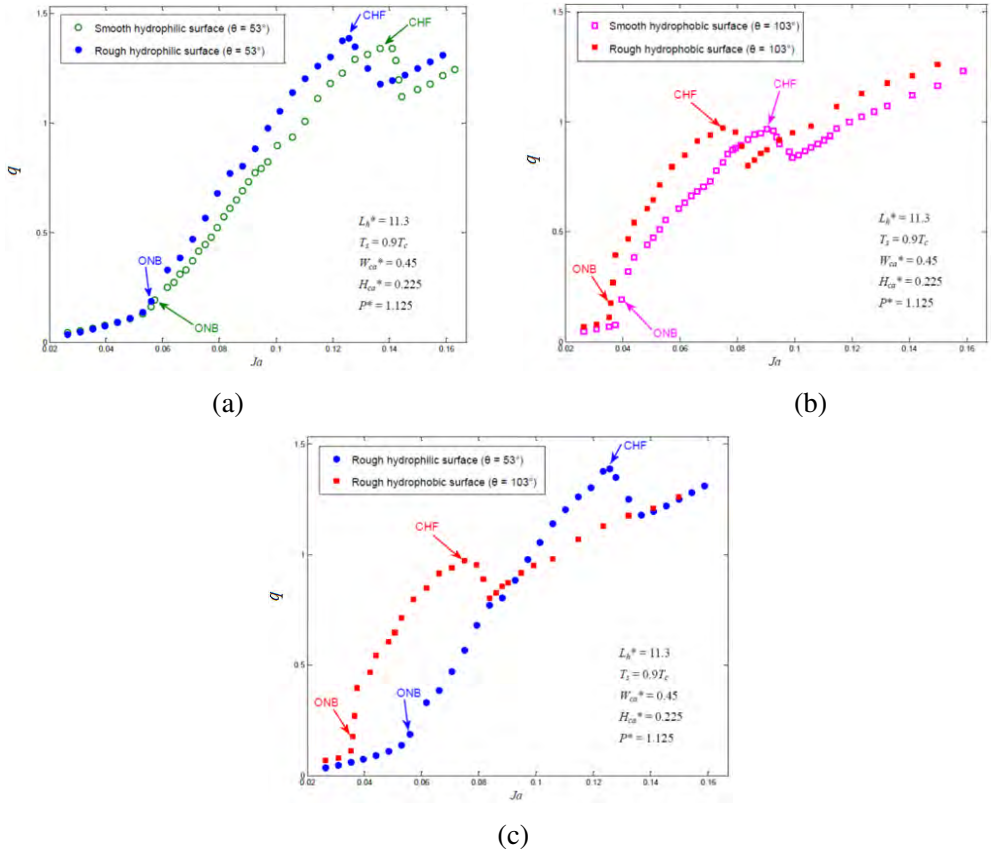

FIGURE 2. Roughness and wettability effects on saturated boiling curves for pool boiling from horizontal superheated surfaces (with a length of $L_H = 11.3l_0$ and thickness $H = 1.1l_0$) under constant wall temperature conditions. (a) Roughness effects on saturated boiling curves of hydrophilic surfaces (θ = 53°); (b) Roughness effects on saturated boiling curves of hydrophobic surfaces (θ = 103°); (c) Wettability effects on saturated boiling curves of rough surfaces [10]

Heater size effects

LB simulation on heater size effects in saturated pool boiling from horizontal smooth surfaces under *controlled heat flux conditions* has been carried out by Zhang and Cheng [11]. Computations are carried out for a heater with length L_H/l_0 = 1 to 16. Fig. 3 shows saturated boiling curves for heaters with L_H/l_0 = 1 to 16, where the imposed boiling heat flux is plotted versus the Jacob number where the averaged wall temperature is obtained from the numerical simulation. It is interesting to note that heater size has only small effects on the nucleate boiling regime, especially for large heaters with $L_H/l_0 \geq 12$, whose boiling curves in the nucleate boiling regime (*b-d*) almost collapse into one. This indicates that heater size has no effect in nucleate boiling regime for large heaters with $L_H/l_0 \geq 12$. For medium heater size with L_H/l_0 = 6 ~ 12, CHF (point *d*) is enhanced with decreasing heater size. And the CHF on a hydrophilic surface occurs at a higher value of *Ja* than that on a hydrophobic surface. After the CHF points, transition boiling regime appears (*d-e*) with temperature jump under controlled wall heat flux conditions. With decreasing heater size, we can see that both the CHF and the transition temperature increase while the film boiling (*e-f*) regime moves to the left, making the temperature jumps (i.e., the transition boiling regime) shorter. It should be noted that shapes of boiling curves under *controlled heat flux* conditions differ from those under *controlled wall temperautre* conditions during the transition boiling regime. With heater size's further decrease, the transition boiling regime finally disappears when $L_H/l_0 \leq 4$. Thus, boiling curves for small heaters with $L_H/l_0 \leq 4$ have only nature convection and boiling regime which differ greatly from the classical shape. After the nature convection regime, nucleate boiling and film boiling cannot be divided on the boiling curve, and there is no critical heat flux nor temperature jump up on the hydrophilic surface or on the hydrophobic surface on the boiling curve.

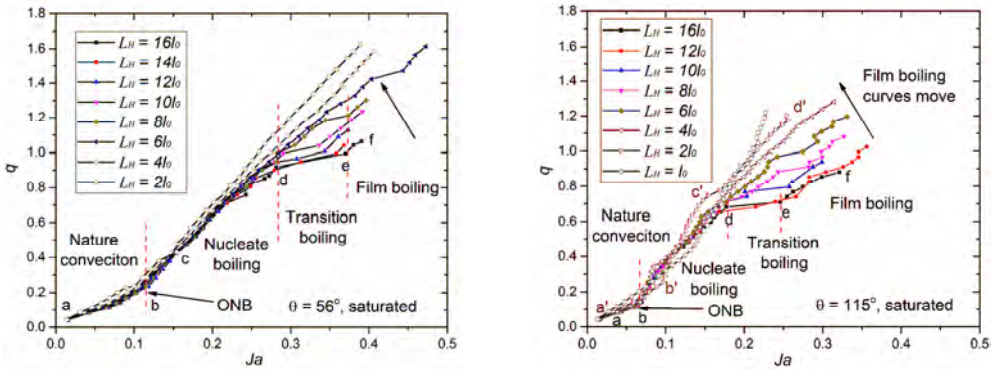

(a) hydrophilic surfaces (b) hydrophobic surfaces

FIGURE 3. Heater size effects on saturated boiling curves for pool boiling from horizontal superheated smooth surfaces (with a thickness $H = 1.6l_0$) under constant wall heat flux conditions. (a) Heater size effects on saturated boiling curves of hydrophilic surfaces ($\theta = 56°$); (b) Heater size effects on saturated boiling curves of hydrophobic surfaces ($\theta = 115°$) [11]

Subcooling effects

LB simulations of boiling curves for a hydrophilic (θ = 56°) and a hydrophobic (θ = 115°) larger heater with $L_H = 12l_0$ (i.e., an infinite plate) at different subcooling from $0.02T_{sat}$ to $0.08T_{sat}$ as well as at the saturated state under *controlled heat flux q* are presented in Figs. 4(a) and 4(b) respectively. From these figures we can see that subcooling increases the heat transfer coefficient in the nature convection (*a-b*) and incipient nucleate boiling regimes (*b-d*), but it has little influence on the ONB (*b*) temperature, the fully-developed nucleate boiling (*c-d*) and film boiling regime (*e-f*). But subcooling has significant effects on CHF and the transition boiling regime. The CHF (*d*) value increases with subcooling for the same heater under the same pressure. After the CHF point, the heat flux during the transition boiling regime (*d-e*) increases only slightly and jumped to a higher temperature gradient during film boiling regime (*e-f*) on both hydrophilic and hydrophobic surfaces. With a larger subcooling, the temperature jump during transition boiling regime becomes shorter.

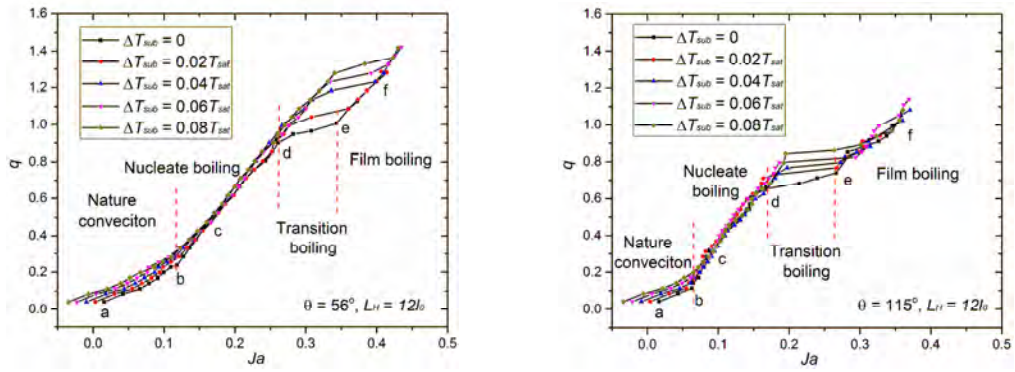

(a) hydrophilic surfaces (b) hydrophobic surfaces

FIGURE 4. Subcooling effects on pool boiling curves for a large heater (with a thickness $H = 1.6l_0$) under different constant wall heat flux conditions. (a) hydrophilic surfaces ($\theta = 56°$); (b) hydrophilic surfaces ($\theta = 115°$) [11]

REFERENCES

[1] S. Nukiyama, The maximum and minimum values of the heat Q transmitted from metal to boiling water under atmospheric pressure, J. JaN. Soc. Mech. Eng. 37 (1934) 367-374 (also, translated in International Journal of Heat and Mass Transfer 9 (1966) 1419-1433.).

[2] V.P. Carey, Liquid–Vapor Phase-Change Phenomena, Hemisphere, Washington, 1992.

[3] G. Son, V.K. Dhir, N. Ramanujapu, Dynamics and heat transfer associated with a single bubble during nucleate boiling on a horizontal surface, *Journal of Heat Transfer*, 121(3) (1999) 623-631.

[4] P. Cheng, X. Quan, S. Gong, X. Liu, L. Yang, Recent Analytical and Numerical Studies on Phase-Change Heat Transfer, Chapter Four - in: *Advances in Heat Transfer*, Elsevier, 2014, pp. 187-248.

[5] S. Gong, P. Cheng, A lattice Boltzmann method for simulation of liquid-vapor phase-change heat transfer, *International Journal of Heat and Mass Transfer*, 55(17-18) (2012) 4923-4927.

[6] S. Gong, P. Cheng, Lattice Boltzmann simulation of periodic bubble nucleation, growth and departure from a heated surface in pool boiling, *International Journal of Heat and Mass Transfer*, 64 (2013) 122-132.

[7] X. Shan, H. Chen, Lattice Boltzmann model for simulating flows with multiple phases and components, *Physical Review E*, 47 (1993) 1815-1819.

[8] G. Hazi, A. Markus, On the bubble departure diameter and release frequency based on numerical simulation results, *International Journal of Heat and Mass Transfer*, 52(5–6) (2009) 1472-1480.

[9] S. Gong, P. Cheng, Lattice Boltzmann simulations for surface wettability effects in saturated pool boiling heat transfer, *International Journal of Heat and Mass Transfer*, 85 (2015) 635-646.

[10] S. Gong, P. Cheng, Two-dimensional mesoscale simulations of saturated pool boiling from rough surfaces. Part II: bubble interactions above multi-cavities, *International Journal of Heat and Mass Transfer* (2016), http://dx.doi.org/10.1016/j.ijheatmasstransfer.2016.04.082.

[11] C. Zhang, P. Cheng, F. Hong, Mesoscale simulation of heater size and subcooling effects on pool boiling under controlled wall heat flux conditions, *International Journal of Heat and Mass Transfer* (2016), http://dx.doi.org/10.1016/j.ijheatmasstransfer.2016.05.036.

[12] A. Kupershtokh, Calculations of the action of electric forces in the lattice Boltzmann equation method using the difference of equilibrium distribution functions. in *Proc. 7th Int. Conf. on Modern Problems of Electrophysics and Electrohydrodynamics of Liquids*, St. Petersburg State University, St. Petersburg, Russia, 2003.

Fourth International Conference on Computational Methods for Thermal Problems
THERMACOMP2016, July 6-8, 2016, Georgia Tech, Atlanta, USA
N. Massarotti, P. Nithiarasu and Y. Joshi (Eds.)

NUMERICAL MODELLING OF MULTIPLE LENGTH AND TIME SCALES IN THERMAL TRANSPORT PROCESSES

Yogesh Jaluria
Board of Governors Professor
Mechanical and Aerospace Engineering Department
Rutgers University, Piscataway, NJ 08854, USA
Email: jaluria@jove.rutgers.edu

ABSTRACT

In a wide range of thermal processes and systems, multiple length and time scales are encountered, making it imperative to model the different scales accurately and couple these to simulate the entire system. In forest and building fires, for instance, the transport processes near the source involve much smaller length scales than far from the source, resulting in different mechanisms, behaviour and concerns. Similarly, in materials processing, the transformations in the material occur at micro and nanometer scales, whereas the system is at engineering scale. This paper presents the major considerations that arise and the approaches that may be used to model and couple different scales. Several examples are presented to illustrate different aspects, approaches and results in multiscale modelling.

Key Words: *Multiple Scales, Numerical Modelling, Thermal Transport, Thermal Systems, Multiscale Problems*

1. INTRODUCTION

A particularly important aspect in many thermal processes and systems is that of mathematical and numerical modeling of different length and time scales that arise. For example, numerical simulation of environmental flows, such as buoyant flows generated by large fires and thermal energy discharges from power plants and industries into the ambient medium, involve very different length scales close to the source and those far downstream. Similarly, cooling of electronic components, which are generally at engineering length scales, is often efficiently achieved by the use of microchannel flows. Data centers involve servers and racks that are much larger in length scales as compared to individual components. Thus, different length scales and, correspondingly, different time scales are encountered. In manufacturing processes, these considerations are particularly critical.

In all these cases, our interest from the simulation lies in the overall behavior of the system and the characteristics of the results obtained. These outputs may, for instance, be the quality and quantity of the resulting product, efficiency of heat removal, environmental effect, energy consumption, and fire spread. However, depending on the dimensions, different flow regimes arise with different underlying mechanisms, which demand different analyses and pose different challenges to experimentation. It is thus critical to model the different scales accurately and then couple these to obtain the overall model for the system or the process to obtain the inputs needed for design, prediction and optimization.

This paper presents a range of fundamental and practical problems where multiple length and time scales are of interest. It considers the modelling at different scales and then addresses the coupling of the different models to obtain the overall model and simulation for the system or process. Both numerical and experimental methods to obtain results at the small scales are considered. The

challenges posed by model validation, different transport mechanisms and different governing equations and parameters are outlined. Several examples, from materials processing, environmental flows and electronic systems, are given to present the different approaches that may be adopted to achieve the desired level of accuracy, control and predictability.

2. MODELLING AND SIMULATION

In multiscale problems involved with thermal processes, the following two main circumstances may be considered:

1. Multiple scales in separate regions
2. Multiple scales within a given region

The first one is a fairly common situation and is easier to model. Each region, which may involve different governing mechanisms, is treated separately and the solutions are coupled at the boundaries. Figure 1 (a) shows such a circumstance, where the region near the fire involves combustion and a resulting energy release rate. The region away from the fire is a convective flow driven by buoyancy, with heat transfer to the walls and inflow and outflow at the opening [1]. The energy release rate and the starting flow are provided as inputs to the outer region for simulating the transport processes in the entire room. The second approach is more complicated and applies in thermal systems where the regions with different scales are not distinct. This is the case in most material processing applications since micro/nanoscale material changes occur within the macroscopic thermal transport. Figure 1 (b) shows a chemical vapour deposition (CVD) reactor for the fabrication of thin films, which result from deposition on a heated susceptor. Chemical reactions in the gases and at the susceptor are intrinsically linked with the bulk flow and have to be considered concurrently [2, 3].

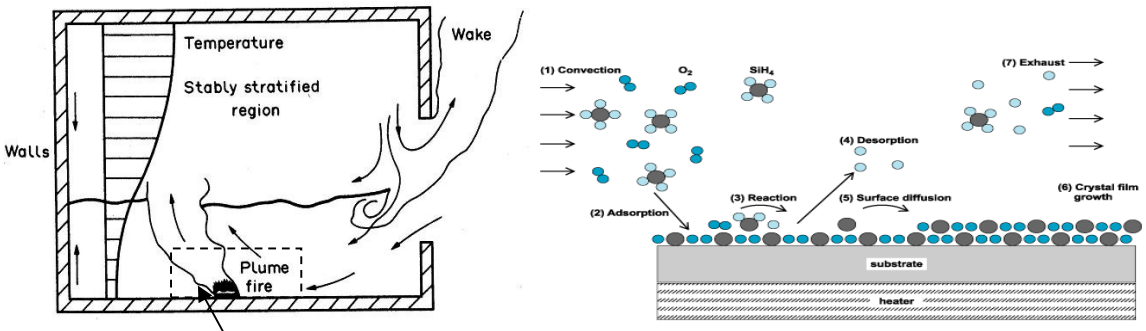

Figure 1. (a) Sketch of a room fire; (b) A horizontal chemical vapour deposition reactor.

In the cooling of electronic systems, multiscale problems are frequently encountered. For electronic device cooling, microchannel flows may be used to remove high heat fluxes that are of particular interest today, see Fig. 2 (a). The modelling of microchannel flows, which could involve high pressures and viscous dissipation as well as rarefaction and slip for gases, is quite different from the conjugate conduction-convection problem that arises in the heat sink [4]. Data centres, for which a simple sketch is shown in Fig. 2 (b), involve wide variations in length and time scales, as one goes from electronic chips, through circuit boards, to servers, racks and rooms [5]. Each scale would generally require separate modelling and linking of all these would yield the simulation of the overall system. In most cases, approximations are needed to make the problem tractable. For instance, the heat input from the devices and servers may be employed, along with a porous

medium approximation to model the flow through racks with different configurations and arrangements. Such a model may then be used to study the thermal behaviour of the data centre.

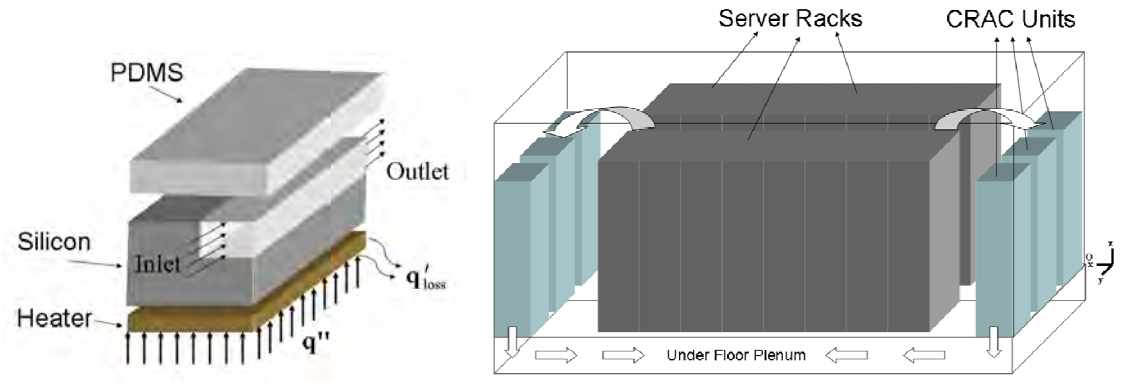

Figure 2. (a) A sketch of the cooling arrangement for a localized heat source such as an electronic chip by microchannel flow; (b) A sketch of a simple data centre.

3. TYPICAL RESULTS

Figure 3 shows some characteristic results from the modeling of a simple data center and from the simulation of a vertical CVD reactor. At high air flow rates, the temperatures are lower, as expected. At low flow rates, the temperatures increase and could violate the constraints for satisfac-

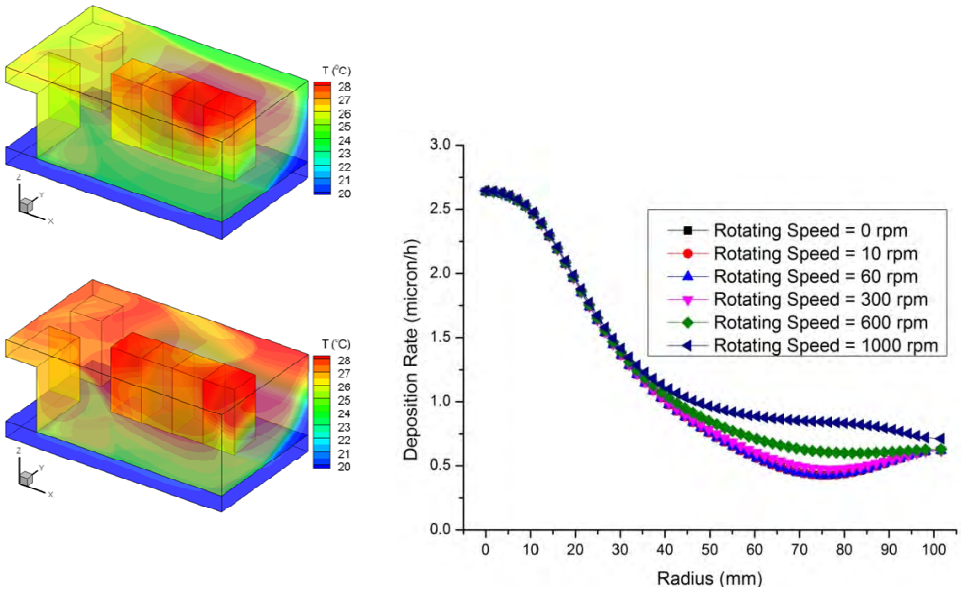

(a) **(b)**

Figure 3. (a) Numerical results from the simulation of the simple data centre shown in Fig. 2 (b) at high and low air flow rates; (b) Effect of rotational speed on the deposition rate in a vertical CVD reactor with a rotating susceptor.

tory operation. The model can be used for optimizing the geometry and the operating conditions to obtain the desired characteristics in transient and steady operation [6] The CVD results indicate the deposition becomes more uniform as the rotational speed increases. Calculations and experiments have shown that rotation stabilizes the flow and curbs recirculating flow, giving rise to greater uniformity in deposition [7].

Similarly, many other multiscale problems can be considered and modelled following the approaches outlined here. In the batch annealing system for the heat treatment of steel sheets that have been rolled up into coils, different components have different length and time scales. The furnace has a total height of around 8 m, whereas several components are only millimetres in thickness. The thick walls heat up slowly, with large response times, whereas the gases typically respond within seconds. Thus, different scales have to be considered in various regions and components and modelled with appropriate governing mechanisms, simplifications, and assumptions. These are finally coupled to obtain the model for the thermal process undergone by the steel coils as well as by the system. Comparisons with experimental data have validated these models, which may then be used for prediction, control and optimization.

The small scales are often investigated experimentally to obtain, for instance, defect generation, microstructure in the material or material conversion. Depending on the phenomenon under consideration, different experimental techniques can be used,. For chemical conversion, for instance, a Differential Scanning Calorimeter (DSC) is used to determine the degree of conversion in biopolymers like food materials. Micro PIV may be used to explore the meniscus in coating. The measured chemical kinetics as function of temperature, shear, concentration, etc., or the shape and dimensions of the meniscus can then be provided as an input to the analytical/numerical modeling of the transport processes at discrete locations on the numerical grid. Numerical methods such as molecular dynamics can also be used to model the changes occurring at small scales, for instance, at the susceptor surface in CVD. These results at the small scale are incorporated in the simulation of the system [8, 9]. The results from the overall simulation can then be used for prediction, design and optimization of the process.

3. CONCLUSIONS

This paper considers multiscale problems that are frequently encountered in many thermal processes and systems, ranging from environmental and energy systems to manufacturing and electronic systems. The main aspects that arise and the approaches that may be adopted for the modelling and simulation of the overall system are discussed. Two main approaches are discussed. The first one obtains solutions separately in regions with different scales and then couples these for the complete process. The other approach solves the different scales concurrently and uses the results from the small scales to link with the solution for the larger scales as the numerical simulation proceeds. Experimental as well as analytical/numerical treatments of smaller scales are outlined. A few important examples are chosen by way of illustration and characteristic results are presented. The critical importance of multiscale modelling in obtaining accurate and dependable results for system prediction, control, and optimization is stressed.

REFERENCES

[1] J.G. Quintiere, Fire behavior in building compartments, *Proc. Combust. Inst.*, 29, 181–193, 2002.

[2] B. Wu, R. Ma and H. Zhang, Epitaxy growth kinetics of GaN films. *Journal of Crystal Growth*, 250, 14-21, 2003.

[3] L. Kadinski, V. Merai, A. Parekh, J. Ramer, E.A. Armour, R. Stall, A. Gurary, A. Galyukov and Y. Makarov, Computational analysis of GaN/InGaN deposition in MOCVD vertical rotating disk reactors, *Journal of Crystal Growth*, 261, 175-181, 2004.

[4] J. Zhang, T. Zhang, S. Prakash and Y. Jaluria, Experimental and numerical study of the transient electronic chip cooling by liquid flow in microchannel heat sink, *Numerical Heat Transfer*, 65, 627-643, 2014.

[5] S.V. Patankar, Airflow and cooling in a data center, *J. Heat Transfer*, 132, 073001-1 to 17, 2010.

[6] K. Le, J. Zhang, J. Meng, R. Bianchini, Y. Jaluria and T.D. Nguyen, Reducing electricity cost through virtual machine placement in high performance computing clouds, *SC 11 Int. Conf. High Perf. Comput.*, Networking, Storage & Anal., Seattle, WA, November 2011.

[7] J. Meng and Y. Jaluria, Numerical simulation of GaN growth in a metalorganic chemical vapor deposition process, *Journal of Manufacturing Science and Engineering*, 135, 061013-1 to 7, 2013.

[8] D. Poulikakos, Ed., Transport phenomena in materials processing, *Adv. Heat Transfer*, 18, 1996.

[9] Y. Jaluria, Microscale Transport phenomena in materials processing, *J. Heat Transfer*, 131, 033111-1 to 17, 2009.

Fourth International Conference on Computational Methods for Thermal Problems
THERMACOMP2016, July 6-8, 2016, Georgia Tech, Atlanta, USA
N. Massarotti, P. Nithiarasu and Y. Joshi (Eds.)

TOPOLOGY OPTIMIZATION FOR HEAT CONDUCTION APPLICATIONS WITH EFFICIENT AUTOMATIC PARTIAL DIFFERENTIATOR

Ajay Vadakkepatt, Sanjay R. Mathur, Jayathi Y. Murthy
Mechanical Engineering, The University of Texas at Austin, TX, ajay.sudhamani@utexas.edu

ABSTRACT

In this paper, we develop an automatic code differentiation technique by employing our RAPID (Residual Automatic Partial Differentiator) infrastructure for calculating sensitivities efficiently and accurately for use in Topology optimization. We demonstrate the application of our technique to perform topology optimization for heat conduction applications within an unstructured co-located finite volume framework. Realistic test cases in realistic geometries for practical heat conduction applications are presented.

Key Words: *Heat Conduction, Finite Volume Method, Automatic Differentiation, Adjoint Method, RAPID*

1. INTRODUCTION

Topology optimization is a method for developing optimized geometric designs that maximize a quantity of interest (QoI) subject to constraints. The algorithm builds the geometry iteratively by placing material pixels in a specified background domain aiming to maximize the QoI. Topology optimization is formulated generally as a material distribution problem [1]. In a typical problem, a design space is specified and discretized using cells. The optimal placement of a material in the cells is determined in order to maximize or minimize an objective function, subject to constraints. Typical objective functions for conduction heat transfer may maximize the heat transfer rate on a boundary, minimize the maximum temperature in the domain or minimize the average energy of domain. Constraints typically require the total volume fraction of a particular material to be held below a specified value. In this paper, we present conjugate conduction problems that require filling the design space with two materials of finite conductivity.

2. MAIN BODY

The governing equation is the steady state heat conduction equation given by $\nabla \cdot (k\nabla T) + S = 0$, where k represents thermal conductivity, T the temperature field (also called the state variable), and S the heat source in the domain. Dirichlet, Neumann or mixed boundary conditions may be considered. We employ a conservative cell-centered finite volume scheme [2] for solving the governing pde. The design domain is discretized with n arbitrary convex polyhedral cells. The governing equations are discretized by enforcing conservation on each cell, which yields a system of linear equations for the state variable. The linear system is set up in the residual formulation $\boldsymbol{R}(\boldsymbol{T}, \boldsymbol{k}, \boldsymbol{S}) = \boldsymbol{0}$, the solution of which yields the temperature $\boldsymbol{T}$. The residual of each cell R_i is the sum of heat transfer rates across all its faces and the integrated source term $S\Delta V$, ΔV being the volume of cell. The flux across the particular face of the cell is given by the sum of the primary flux $\mathcal{P}_f$ and secondary flux $\mathcal{S}_f$ (details in [2]). Calculation of $\mathcal{S}_f$, which is more complex than $\mathcal{P}_f$, requires the temperature gradients of cells calculated using a least squares approximation (details in Ref. [2]) and requires the temperature values at neighbor cell centroids.

Topology optimization is formulated as a pde-constrained optimization where a cost function c is minimized. The goal of topology optimization here is to distribute two materials with conductivity k_1 and k_2 $(k_1 > k_2)$ with specified volume fractions ε and $1 - \varepsilon$ respectively within a specified design space of volume V_0. Each cell is associated with a design variable $\boldsymbol{\beta} \in [0,1]$ that physically represents microscopic volume fraction of material 1 (with conductivity k_1). The effective

conductivity in the pde is interpolated as $\boldsymbol{k}(\boldsymbol{\beta}) = k_2 + (k_1 - k_2)\boldsymbol{\beta}^p$, where p is the penalization factor. This formulation, called single isotropic material interpolation (SIMP), helps the optimization algorithm to steer β to either 0 or 1 and to steer k to either k_1 or k_2 in tandem. This effectively assigns a particular material to a cell. Thus, we seek to find the distribution of $\boldsymbol{\beta}$ over V_0 that minimizes the functional c by satisfying all the constraints of the problem.

$$\begin{aligned} &\text{Step1:} && \boldsymbol{R}(\boldsymbol{T}, \boldsymbol{k}(\boldsymbol{\beta}), \boldsymbol{S}(\boldsymbol{\beta})) = \boldsymbol{0} \\ &\text{Step2:} && \begin{cases} \text{minimize } c = c(\boldsymbol{T}, \boldsymbol{\beta}) \\ \text{subject to } \sum_i^n \beta_i - \varepsilon \leq 0 \text{ and } \; 0 \leq \boldsymbol{\beta} \leq 1 \end{cases} \end{aligned} \tag{1}$$

In practice, the problem is generally solved using the nested formulation shown in Eq. 2. Given an initial distribution of $\boldsymbol{\beta}$, followed by SIMP interpolation to obtain material properties, the discretized pde is solved for $\boldsymbol{T}$ and the desired cost function c is calculated in step 1. Using a non-linear optimization program, $\boldsymbol{\beta}$ is updated so as to minimize the cost function c in Step 2. The iteration continues until the difference in the values of $\boldsymbol{\beta}$ satisfies a prescribed tolerance. We use the Method of Moving Asymptotes (MMA) algorithm developed by Svanberg [3] as the non-linear optimizer. The sensitivity of the cost function with respect to design variables $dc/d\boldsymbol{\beta}$ is an important constituent for gradient based optimizer.

An adjoint method is used to calculate sensitivity derivatives $dc/d\boldsymbol{\beta}$. Once the partial derivatives $\partial\boldsymbol{R}/\partial\boldsymbol{T}$, $\partial\boldsymbol{R}/\partial\boldsymbol{\beta}$, $\partial c/\partial\boldsymbol{\beta}$ and $\partial c/\partial\boldsymbol{T}$ are calculated, the sensitivity is calculated in two steps as given by Eq. 5. First an adjoint field $\boldsymbol{\psi}$ is calculated by solving adjoint linear system given by Eq. (3a). Then the sensitivity is calculated using Eq. (3b).

$$\left[\frac{\partial \boldsymbol{R}}{\partial \boldsymbol{T}}\right]^{\mathrm{T}} \boldsymbol{\psi} = \left[\frac{\partial c}{\partial \boldsymbol{T}}\right]; \tag{3a}$$

$$\frac{dc}{d\boldsymbol{\beta}} = \left(\left[\frac{\partial c}{\partial \boldsymbol{\beta}}\right] - \left[\frac{\partial \boldsymbol{R}}{\partial \boldsymbol{\beta}}\right]^{\mathrm{T}} \boldsymbol{\psi}\right) \tag{2b}$$

The biggest challenge in calculation of sensitivities lies in the calculation of these partial derivatives. As can be seen from Eq. (2), the formula for the residual is quite complicated and derivative calculations for the secondary gradient term S_f can be quite laborious. Each time a new QoI is specified, a new implementation of the calculation of $\partial c/\partial \boldsymbol{T}$ must be coded. A method that performs these differentiation operations automatically, without reference to particular problems or cost functions is desirable.

We have developed a novel technique for calculating partial derivatives through automatic differentiation called Residual Automatic Partial Differentiator (RAPID) [4]. Automatic differentiation (AD) may be used to obtain derivatives accurately. However, computational complexity and storage can increase significantly in conventional AD codes when the number of independent variables is large. Thus these conventional approaches are infeasible for topology optimization applications.

The RAPID infrastructure was developed to obtain partial derivatives for such situations efficiently and accurately. It exploits the feature that each dependent variable in a discretized residual formulation depends only on a few independent variables, i.e., R_i depends only on variables in neighbor cells and in next-near-neighbor cells. The method is implemented through the 'map' standard template library and operator overloading functionalities available in the C++ compiler. The RAPID data type is shown in Figure 1a. The first floating point variable stores the function value of the variable. Next it has a collection of associated pairs, each containing a key of type integer and a floating point variable. The key serves as an identifier of the independent variable with respect to which the partial derivative is required. The associated floating point variable stores this derivative value. The number of pairs can grow dynamically depending on the number of independent variables that a variable depends on. Figure 1a shows two such pairs. A RAPID data type is used generically to represent both independent and dependent variables.

Let us assume that we are calculating the residual R_i of a cell i. Assume that R_i depends on $\boldsymbol{T}$ and $\boldsymbol{\beta}$ of two adjacent cells $c0$ and $c1$. Therefore $T_{c0}, T_{c1}, \beta_{c0}$ and β_{c1} form the independent variables. RAPID facilitates setting up of *independent variables* as is depicted in Figure 1(b). The first floating point variable stores its value. Every independent variable has only a single pair. The four indices l, m, u and v corresponding to $T_{c0}, T_{c1}, \beta_{c0}$ and β_{c1}, are the keys of these independent variables. In each case, the corresponding floating point variable, representing the derivative, is set to a value 1, indicating the derivative of a variable with respect to itself is 1. We next consider the *dependent variable* R_i in RAPID mode. The first floating point variable stores its value. For this example R_i has four pairs. As shown in Figure 1c each pair stores the corresponding partial derivative of R_i with each independent variable identified by the key. Similarly the variable c in RAPID mode has it function value and again, four derivatives as shown. The 'map' standard template library allows the number of pairs associated with each dependent variable to vary dynamically, depending on how many independent variables it depends on. This feature is critical in minimizing the storage associate with computing Jacobians, for example; here, the number of independent variables depends on the local connectivity of the mesh.

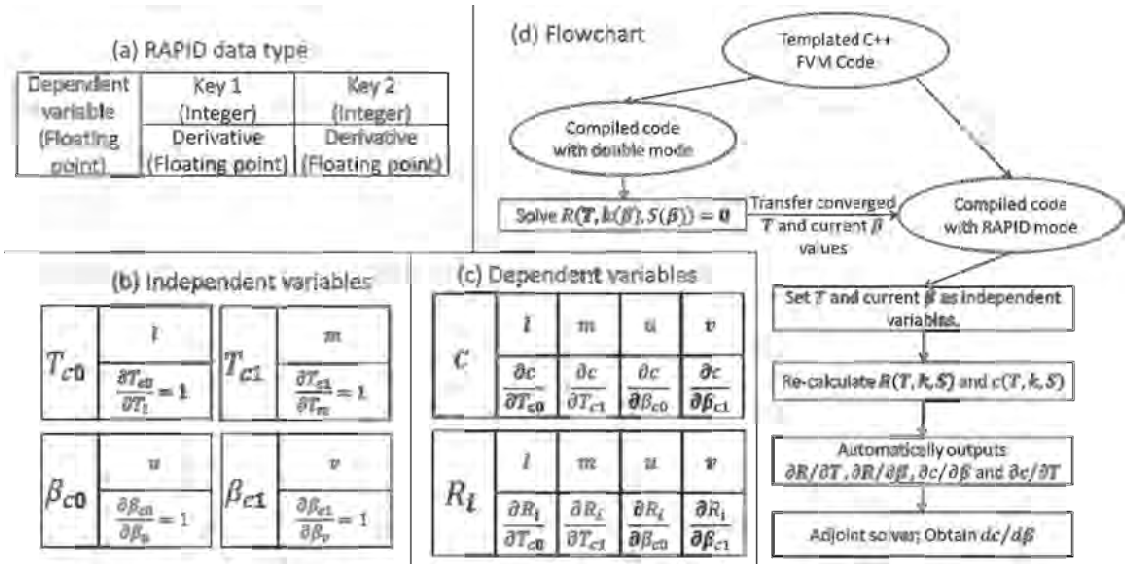

FIGURE 1: Illustration of the RAPID infrastructure

C++ allows the variable type to be templated and suitably type-cast at compile time. Figure 1d shows such a C++ finite volume templated code. Two compiled versions of the code are generated, one type-cast in the basic type – 'double' and the other one in the 'RAPID' user defined type. For a given $\boldsymbol{\beta}$, the residual equations are solved for $\boldsymbol{T}$ using the code in 'double' mode. The converged $\boldsymbol{T}$ and $\boldsymbol{\beta}$ are transferred to the code compiled in RAPID mode and then set as independent variables. Residuals and cost function are re-calculated in RAPID mode, which automatically generates all the required derivatives for sensitivity calculation as shown in Figure 1d. This automation is critical in making the code independent of cost function definition, and also independent of the underlying physics. If a new governing equation is added to the parent code, the RAPID infrastructure will automatically generate all necessary derivatives without any new coding.

3. RESULTS

Here we present some representative results of performing topology optimization with RAPID infrastructure. Figure 2 depicts the validation of the RAPID technique for performing topology optimization. A rectangular design space specified with temperature boundary conditions T_1 and T_2 on two opposite faces, and adiabatic condition on other faces. The objective is to fill the design space with two materials of conductivity k_1 and k_2 $(k_1 > k_2)$ to maximize the heat transfer rate on the face as shown in Figure 2(a).The maximum heat flow

occurs in a scenario where the thermal conductive resistance is the least. Therefore the geometry with minimum path length and maximum cross-sectional area is the optimal solution. Such an optimal geometry is presented in Figure 2(d).

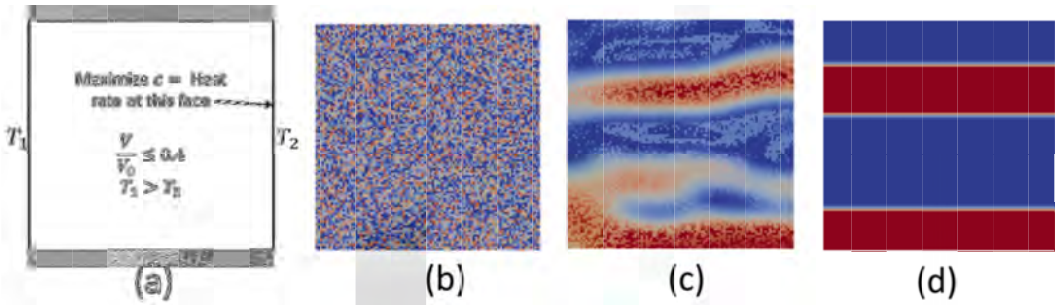

FIGURE 2. Validation of RAPID technique. (a) Initial design space with boundary conditions and objective function. Here we use Cartesian mesh; therefore S_f is absent. (b) shows the initial random distribution of materials which is subjected topology optimization. (d) shows the final distribution of materials. Red region represents k_1 while blue k_2. (c) shows one of the intermediate steps leading to optimized geometry.

Figure 3 shows a non-rectangular geometry which is meshed with triangular elements. Since the mesh is non-cartesian, the secondary gradient flux term S_f is existent. The objective of the problem is provided in Figure 3(a). Figure 3(b) shows the final topology where the high-conducting material is seen to be deployed in a continuous band connecting the hot and cold boundaries, as expected.

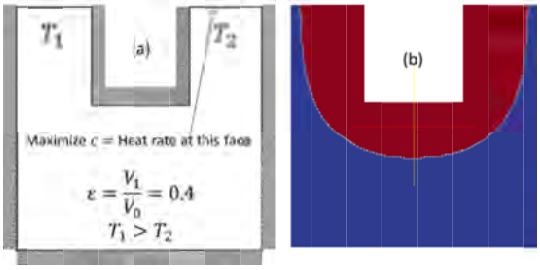

FIGURE 3. Performing topology optimization on non-rectangular geometry with unstructured mesh.

4. CONCLUSIONS

In this paper, we demonstrated the application of a novel automatic partial differentiation infrastructure that we developed to perform topology optimization for heat conduction applications within an unstructured co-located finite volume framework. The infrastructure enables calculation of sensitivities, needed for gradient based topology optimization, with computational efficiency, reusability of existing codes and generality to extend to new problems.

REFERENCES

[1] M. P. Bendsoe and O. Sigmund, *Topology optimization: theory, methods and applications*. Springer Science & Business Media, 2003.

[2] S. Mathur and J. Murthy, A pressure-based method for unstructured meshes, *Numerical Heat Transfer*, 31(2), 195-215, 1997.

[3] K. Svanberg, The method of moving asymptotes-a new method for structural optimization, *International journal for numerical methods in engineering*, 24(2), 359-373, 1987.

[4] A. Vadakkepatt, J. Mathur, and M. Sanjay, An efficient automatic partial differentiation library - RAPID, *In preparation,* 2016.

KEYNOTE LECTURES

Fourth International Conference on Computational Methods for Thermal Problems
THERMACOMP2016, July 6-8, 2016, Georgia Tech, Atlanta, USA
N. Massarotti, P. Nithiarasu and Y. Joshi (Eds.)

Slot film cooling – Effect of upstream turbulence

Yousef Kanani, Sumanta Acharya*
University of Memphis, 312 Engineering Science, Memphis, USA
ykanani@memphis.edu
s.acharya@memphis.edu
*corresponding author

ABSTRACT

Jet in crossflow are encountered in a variety of applications including turbine cooling, electronic cooling, VSTOL aircrafts, and plume discharges. As an example, in modern gas turbine engines components are subject to gas temperatures in excess of 3000° F that are well above the material limits for reliable operation. The engine components have to be therefore actively cooled to prevent engine failure. One of the more common cooling strategies is injecting a coolant jet onto or from the surface into the crossflow. The mixing of the coolant jet dictates the effectiveness of the cooling. In this report, the physics of slot-film-cooling-jet of is analyzed based on Large Eddy Simulation (LES) results. In particular, the role of external disturbances originating upstream of the crossflow (i.e., freestream turbulence) are examined in detail. Results show the inverse relationship of turbulence intensity and thermal effectiveness as expected. Detail analysis of turbulence statistics is performed in order to better understanding of flow physics.

Key Words: *Slot film cooling, Turbulence intensity, Large Eddy Simulation.*

1. INTRODUCTION

Film cooling on the turbine blade surface has been extensively studied during last 60 years; however, the majority of the studies are mostly dedicated to discrete hole film cooling since this has been the primary configuration implemented by turbine manufacturers. Slot film cooling can provide higher cooling effectiveness, but has not been considered in practice due to structural and manufacturing considerations. Recent advances in manufacturing technologies that enable double walled structures to be fabricated have sparked an interest in slot-cooling[1,2]. Hartnett [3] has reviewed the early literature on slot film cooling that typically include parallel (wall-jet) and normal-injection slot geometries[4–7]. As an example of one of the earlier studies, Hartnett et al [8] performed a study on slot film cooling over a flat plate and have proposed a correlation for thermal effectiveness for x/MS of higher than 80. Their experiments were performed with very low free stream turbulence. Due to a large number of parameters affecting the slot film cooling performance such as the slot geometry, upstream turbulence in the crossflow and that exiting the slot, crossflow pressure gradients etc., correlations for cooling effectiveness presented by Hartnett [8] are not broadly applicable. Most of the available correlations only hold for regions far from the slot and none of these studies have accounted for upstream and slot turbulence that can potentially play an important role [3,8,9] . Marek and Tacina [5] have studied the effect of free stream turbulence on slot film cooling. However, their effort for correlating the thermal effectiveness to the turbulent intensity was not successful due to the complexity of the flow (e.g. anisotropic turbulence at the free stream, slot turbulence, length scales). Recently, Busche and Ames [2] studied the effect of turbulence intensity on the film cooling effectiveness on a curved surface with a cylindrical leading edge which mimics the vane geometry. Their case study involved both free stream and slot turbulence in an accelerating flow which have a negative effect on the thermal effectiveness[4].

The goal of the present study is to explore the role of freestream turbulence on slot-cooling and to provide a greater understanding of the flow physics and heat transfer in slot film cooling. The

baseline configuration of Hartnett et. al. [8] is selected and numerical simulations are performed for different freestream turbulence intensities. The role of turbulence intensity on cooling effectiveness and the flow structures are analysed and presented.

2. NUMERICAL DOMAIN AND PARAMETERS

The geometry and cases setup in this study is identical to the Hartnett et al experiments [8]. They performed an extensive study of the flow and temperature field of air injection into the free stream with a turbulent boundary layer upstream of the slot. In the experiments, a fully turbulent boundary layer was established by installing a sandpaper trip in the front of the tunnel. Although the boundary layer was fully turbulent, all tests were conducted under low freestream turbulence. Their measurements include velocity and temperature profiles along with the adiabatic thermal effectiveness. A free stream velocity of 52.2 m/s and a blowing ratio of 0.28 was used.

Air injection slot is constructed from a horizontal channel which merges to the mainstream by a curved ramp on the bottom side. The upstream corner of the slot has a razor-sharp edge (see FIGURE 1). The slot is 3.124 mm in height which will be denoted with s. Inlet boundary has been placed 20 slot height upstream of the origin and the domain extended downstream to x/Ms of about 178 where M is the blowing ratio. The domain extends 5 slot height in the lateral direction, and 81 slot height normal to the wall to diminish the effect of the top boundary on the film cooling. The spanwise dimension of the numerical domain is 5s and is equivalent to approximately 3.2δ upstream of the slot and 2δ at the exit plane where δ is the boundary layer thickness. As the length scales are smaller than δ, this size should be suitable [10].

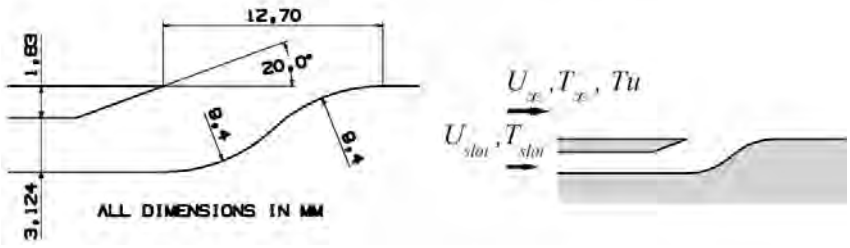

FIGURE 1. Shape of air injection slot used by Hartnett et al [8]

As the upstream boundary layer is fully turbulent, a proper turbulent inflow boundary condition needs to be utilized. The Synthetic Eddy Method by Jarrin [11] is used to generate the inflow turbulence intensity with specific intensity and length scale. This method is capable of generating non-isotropic turbulence by providing the known Reynolds stress tensor. However, in this study, we chose to provide isotropic turbulence at the inlet and let the wall force anisotropicity to the velocity signal near the wall. The upstream flat plate is about 11.6 times of the initial boundary layer thickness which is enough for the development of turbulence statistics of a fully turbulent boundary layer. Slip boundary condition is imposed on the top plane by the assumption that flow field far from the injection point will not be affected by the injection through the slot. Remaining boundary conditions are non-reflecting at the outflow, no-slip adiabatic at wall boundaries and periodic in the lateral direction.

Numerical simulations with several turbulence intensities are performed to evaluate the effect of turbulence on the thermal effectiveness and to study the flow physics to understand the underlying mechanism and their importance on the thermal effectiveness. Turbulence statistics is measured in all cases at 3.2s upstream of the slot leading edge. Peak and freestream streamwise turbulence intensity values are reported in Table 1.

For the first case, an estimated turbulence intensity for the reference experimental data [12] is imposed at the inflow to validate the numerical simulation results and to evaluate grid independence. Unfortunately, there is no available measured data on the turbulence intensity upstream of the slot. We have simulated the validation case numerically with three different grid sizes (4.2 million, 6.4 million and 10 million) to evaluate the grid independence. Turbulence intensity of 8% with the length scale of a quarter of boundary layer thickness is used in this case (not shown here). Thermal effectiveness results were nearly identical between 6.4 million and 10 million grid points. Therefore, the intermediate grid (6.4 million) is selected for all other simulations.

Case	Length scale(mm)	$Tu_{x,peak}$	$Tu_{x,fs}$	Legend
A1	1.72	7.5	0.1	□
A2	1.72	11.3	2.6	Δ
A3	1.72	13.6	4.4	○
B1	1.72	1.7	0.1	■
B2	1.72	5.1	2.6	▲
B3	1.72	11.2	4.4	●
Hartnett et al	N/A	N/A	N/A	+

TABLE 1. Simulation parameters

2. RESULTS

Figure 2 shows the mean velocity profile for the different cases. The velocity profiles from the experiment results are also included. Calculated velocity profiles are in good agreement with the experimental data. Mean velocity profile varies slightly with the change in the upstream turbulence intensity. Note that upstream mean velocity profile is compared with the velocity profile measured with no injection in the experiments. This could explain the lower wall shear stress in our simulations as flow faces a deceleration approaching the slot.

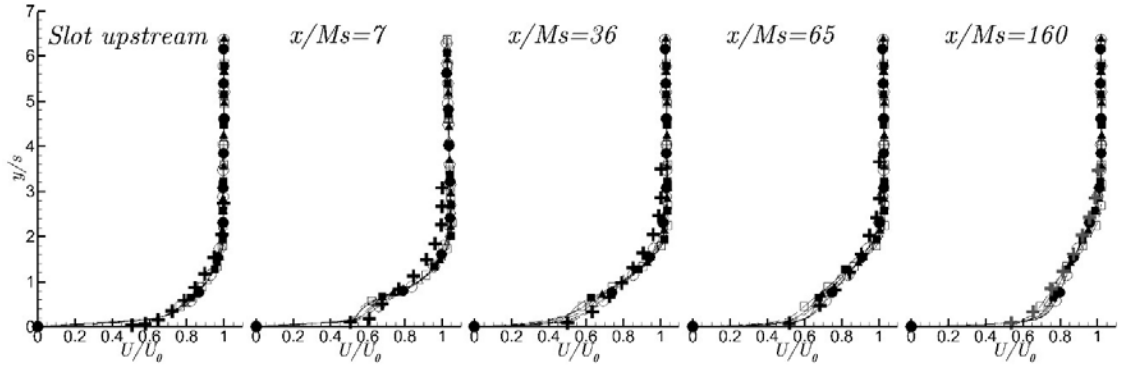

FIGURE 2. Mean velocity profiles nondimensionalized by free stream velocity. For legends see Table 1.

Figure 3 shows the turbulence intensity profiles upstream of the slot for the simulated cases. Peak and freestream streamwise turbulence intensities are provided in Table 1. Wall-normal and spanwise turbulence intensities at the free stream for different case setups are %0.1, %1.9 and 3.4%. For each freestream turbulence intensity, there are two cases with high and low turbulent intensity near the wall which will result in different profiles. Turbulence intensity profiles at x/Ms = 3.5 are shown in Figure 4. Except for the low freestream Case B1, other cases show similar behaviour

downstream of the slot. Turbulence intensity downstream of the slot is typically higher for the higher upstream turbulence intensity cases. The peak of the turbulence intensity profiles is placed at the shear layer between the jet and the free stream. Also, streamwise turbulence intensity profiles show a peak very close to the wall which is due to the formation of a turbulent boundary layer after the slot exit. Other than this, the turbulence intensity profiles downstream of the slot are mostly influenced by the upstream turbulence and the mixing layer. For the Case B1, where the turbulence in the freestream and boundary layer are both low, strong Kelvin-Helmholtz vortices are generated and will affect the flow physics and thermal effectiveness significantly. This case will be discussed individually later.

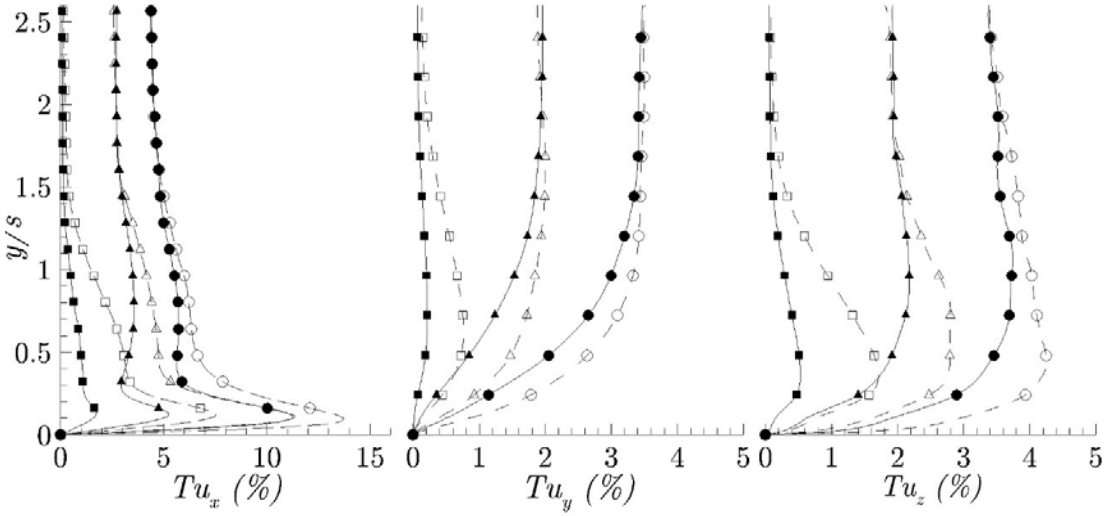

FIGURE 3. Turbulence intensity profiles upstream of the slot. For legends see Table 1.

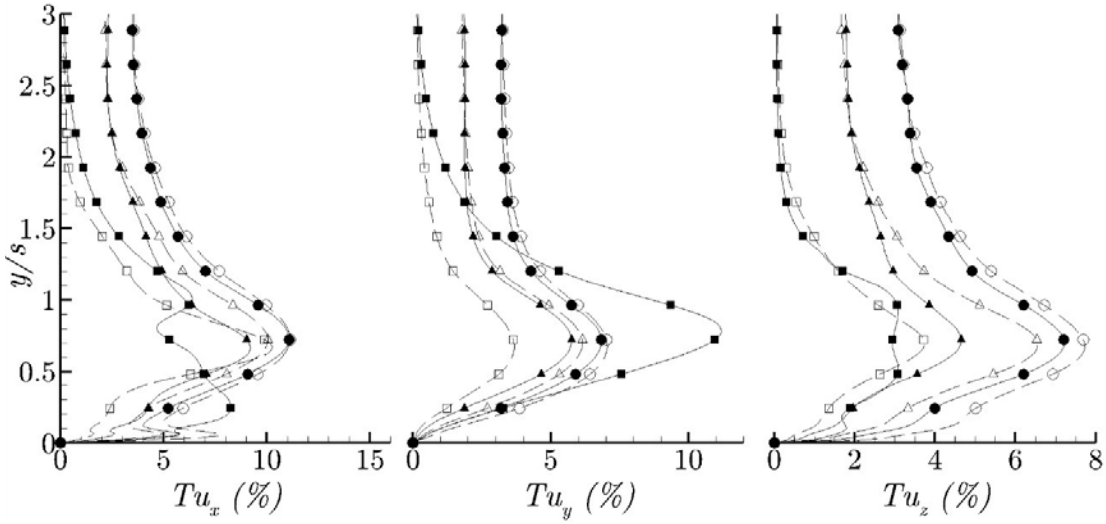

FIGURE 4. Turbulence intensity profiles at x/Ms=3.5. For legends see Table 1.

Due to the small blowing ratio, the coolant jet experiences strong acceleration before merging with the free stream (see FIGURE 5). Streamlines show two separation bubbles on the both top and bottom of the slot. The upstream separation bubble and the interface between the coolant jet and the crossflow both play an important role in the mixing downstream (Figure 8) and cooling effectiveness.

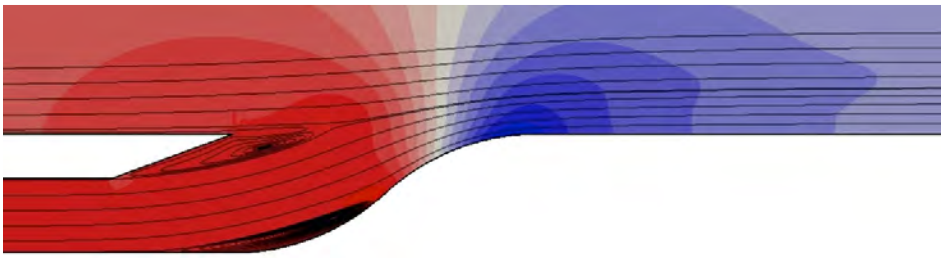

FIGURE 5. Mean pressure distribution in the vicinity of the slot exit (Case A1). Red colors indicate high and Blue indicates low pressure.

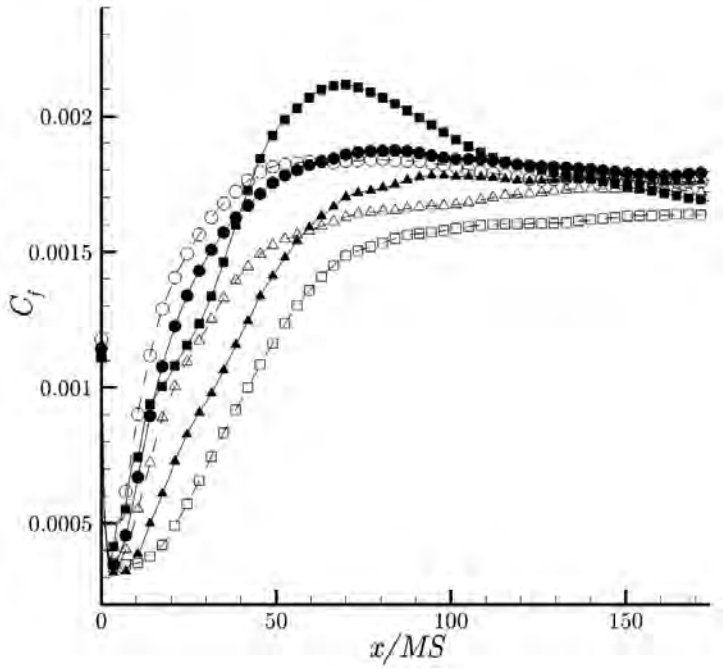

FIGURE 6. Skin friction coefficient over the plate. For legends see Table 1.

The effect of the upstream turbulence is evident in the skin friction coefficient distributions (see FIGURE 6). In all cases, the skin friction asymptotes to a constant C_f, with shorter lengths for the asymptotic development at the higher turbulence levels. The profiles show an initial sharp increase in C_f followed by a transition to the asymptotic value. Case A2 (open triangle) and Case B3 (solid circle) have almost the same peak streamwise turbulence intensity (see Figure 3). Other than this similarity, turbulence intensity profiles of these two cases are not similar. However, the skin friction coefficient distribution downstream of the slot are different. This suggests that the peak streamwise turbulence intensity (i.e. near the wall) may not be directly correlated to the skin friction coefficient. Turbulence intensity profiles upstream of the slot are similar in the wall-normal and spanwise directions just near the wall ($y < 1.5$ mm) for Case A1 (open square) and B2 (solid triangle) (see Figure 3). Profiles deviate from each other for further distances from the wall. These two cases also show different behaviour in the skin friction downstream of the slot (see Figure 6). Hence, it

appears that turbulence very close to the wall does not play an important role on the skin friction coefficient downstream of the slot. Rather, the mixing of the coolant jet with the crossflow is the strongest correlating factor, and a stronger correlation can be found between the turbulence levels in the upper portions of the coolant jet (Figures 3 and 4) and the skin friction coefficient (Figure 6). The only exception is case B1 which shows anomalous behavior.

Slot film cooling thermal effectiveness predictions are shown in FIGURE 7. A direct correlation between the thermal effectiveness and skin friction coefficient can be observed. Hence, it can be concluded based on the previous arguments regarding skin friction that the thermal effectiveness distribution downstream of the slot cannot be directly correlated to the upstream turbulence intensities very close to the wall, and that the free stream turbulence plays a more important role in the cooling effectiveness distribution. Also, it can be noted that thermal effectiveness has a higher decay rate in the transition region between x/Ms of 30-70. For example, the rate of decrease of effectiveness for Case A1 (open square) is higher than Case A3 (open circle) at x/Ms of 50 where the skin friction for the Case A1 (lower turbulence) is still increasing, but for case A3 (higher turbulence), it has reached its maximum values (see Figure 6). From the thermal effectiveness distribution over the surface downstream of the slot, it can be concluded that the turbulence intensity profile upstream of the slot has a significant effect on the effectiveness profile especially for x/Ms smaller than 100. Hence, a proper knowledge of upstream turbulence profile (not just the peak or freestream turbulence intensities) would be required for the prediction of thermal effectiveness numerically.

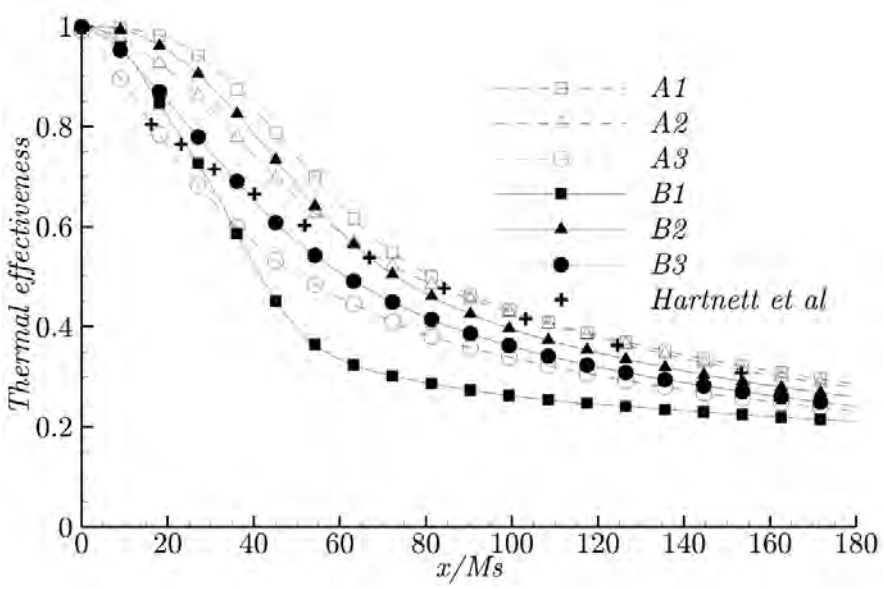

FIGURE 7. Laterally averaged thermal effectiveness over the surface

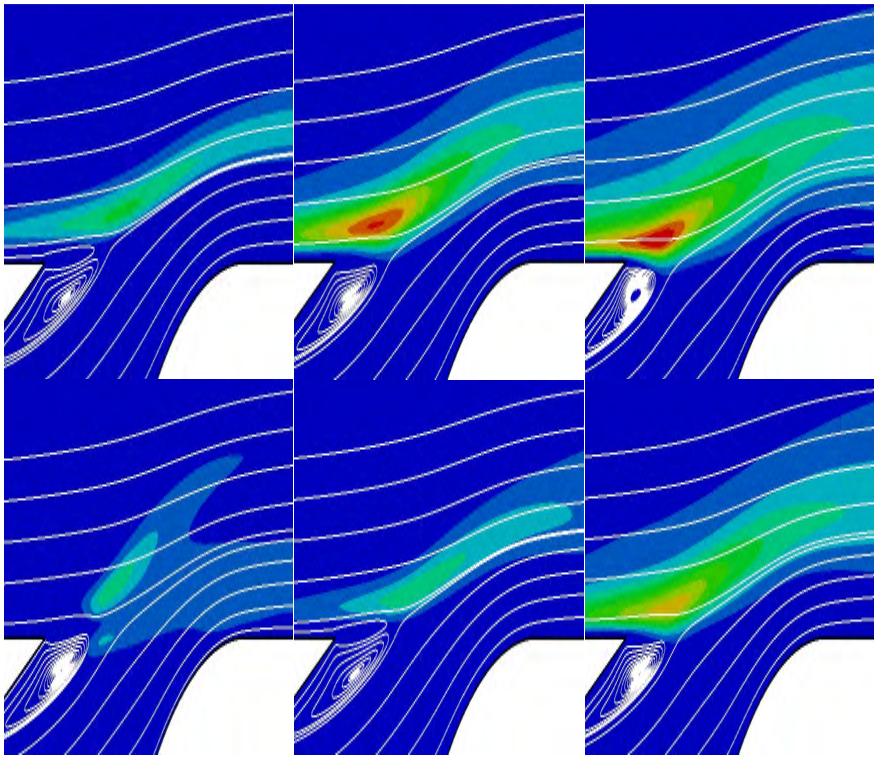

FIGURE 8. Streamwise turbulence intensity contour and mean velocity streamlines. Top row from left to right: Case A1,A2,A3. Bottom row from left to right: B1,B2,B3. Red and blue indicate higher and small values respectively. Plots are made 4 times larger in the vertical direction for clarity.

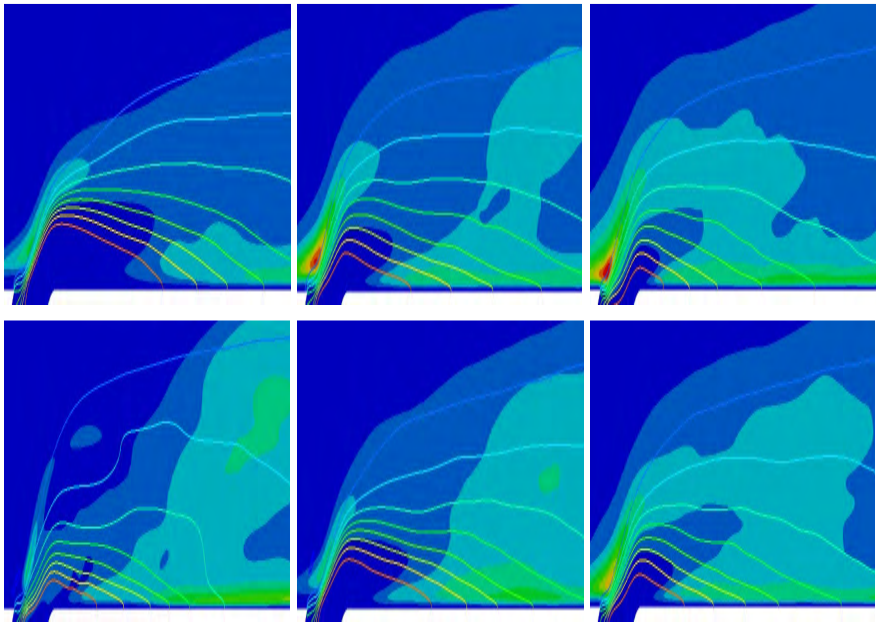

FIGURE 9. Contours of mean temperature (lines) and streamwise turbulence intensity. Red and blue indicate higher and small values respectively. Plots are made 16 times larger in the vertical direction for clarity.

Streamwise turbulence intensity contours and mean streamlines are shown in FIGURE 8. Upstream turbulence levels have a significant effect on the peak of turbulence intensity which occurs just ahead of where the mainstream and the slot jet meet. The turbulence level in the mainstream-jet interaction region increases in magnitude and spatial extent with higher freestream turbulence. This is expected due to the presence of the shear layer between the two flow streams which acts as a source of turbulence generation.

In Figure 9, the temperature contours are overlaid on the turbulence intensity contours; the red line represents the coolant temperature. It can be seen that as turbulence increases, the region enclosed by the red line decreases indicative of greater mixing.

We will now consider case B1 where both the freestream and boundary layer turbulence levels are low, and this case exhibits unique behaviour. Iso-surfaces of vorticity for case B1 is shown in Figure 10. Low turbulence upstream of the slot allows the formation of Kelvin-Helmholtz and streamwise vortices in the braids. These structures have been observed previously in plane mixing layers [13–15]. Formation of these structures and their dominant behavior is the main reason for the different behaviour of the statistical values for this case.

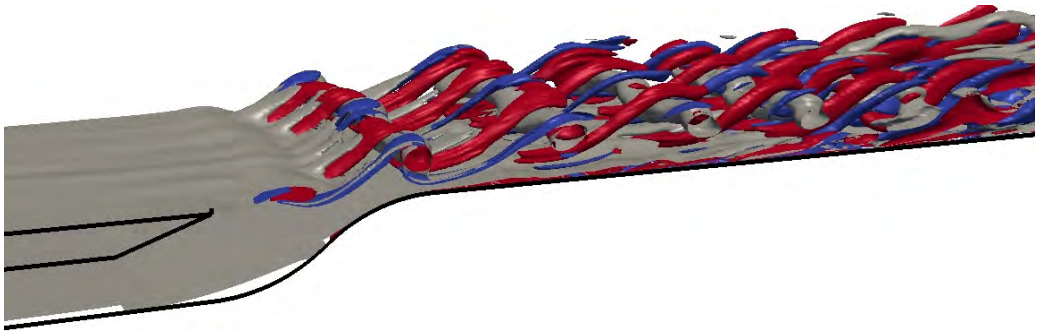

FIGURE 10. Iso-surfaces of spanwise (gray) and streamwise vorticity (colored) for case B1. Red and blue indicate positive and negative values respectively.

The spectral power density of the streamwise velocity signal is shown in Figure 11. The dominant frequency of 4028 Hz is related to the Kelvin-Helmholtz structure. It is interesting that we are able to capture up to 15^{th} harmonics of Kelvin-Helmholtz frequency at the shear layer. Further downstream of the slot, dissipation becomes more dominant as the -7 slope starts from lower frequencies. Streamwise vortices have a significant effect on the surface temperature. Signature of those effects can be seen in the mean temperature contours at the surface (see Figure 12).

Maximum skin friction, in this case, lies near x/Ms=60 (Figure 6). It can be seen in Figure 13 that this location is where Kelvin-Helmholtz vortices completely break down and forms three-dimensional turbulent structures.

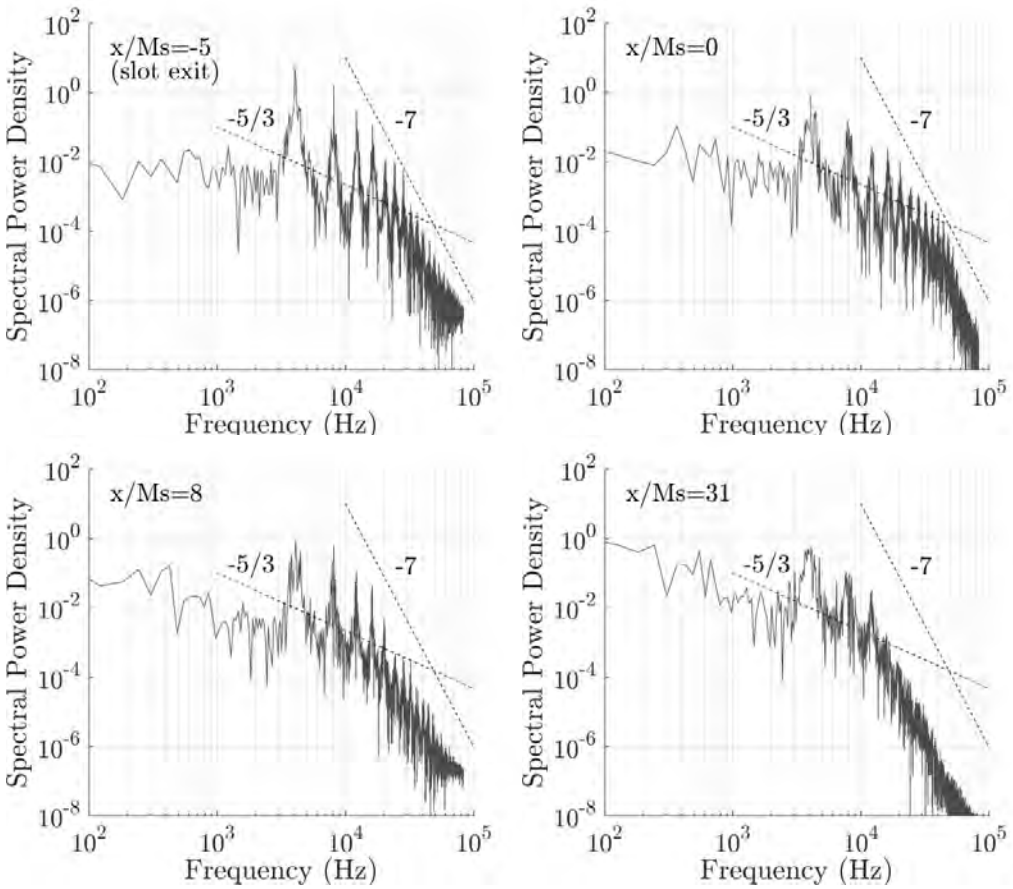

FIGURE 11. The spectral power density of streamwise velocity at different locations.

FIGURE 12. The mean temperature at the surface. Left side is slot exit and flow is from left to right.

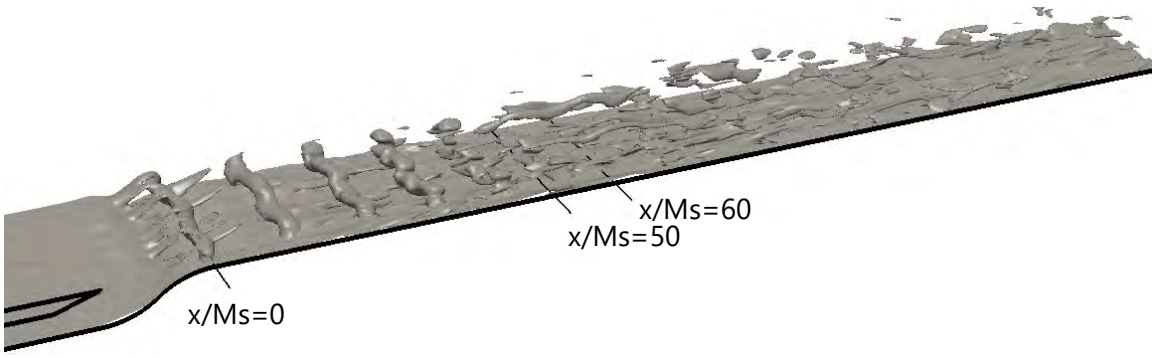

FIGURE 12. Iso-surfaces of spanwise vorticity.

4. CONCLUSIONS

In this paper, the effect of upstream turbulence on slot film cooling at a blowing ratio of 0.28 is evaluated based on large eddy simulations. It is shown that the upstream free stream and boundary-layer turbulence alters the thermal effectiveness. Results suggest that the turbulence very close to the wall has a lower impact on the wall-thermal behaviour downstream of the slot compared to the turbulence in the outer coolant-jet regions. Contrary to expectations, very low turbulence upstream of the slot led to the smallest values of the thermal effectiveness. Further analysis revealed that this behaviour relates to the formation of Kelvin-Helmholtz and secondary streamwise vortices. By increasing the freestream or boundary layer turbulence these distinct structures transition to three dimensional turbulence and the strong K-H structures breaks up which leads to higher effectiveness. Further increasment of the turbulence intensity decreases the effectiveness possibly due to enhanced mixing.

REFERENCES

[1] Bunker, R. S., 2011, "A Study of Mesh-Fed Slot Film," J. Turbomach., **133**(1), pp. 011022,1–8.

[2] Busche, M. L., and Ames, F. E., 2014, "Slot Film Cooling Measurements on an Accelerating Test Surface Subjected a Range of Turbulence Conditions," Proceedings of ASME Turbo Expo 2014.

[3] Rohsenow, Hartnett, and Ganic, 1985, Handbook of Heat Transfer Applications, McGraw-Hill, NewYork.

[4] Carlson, L. W., and Talmor, E., 1968, "Gaseous film cooling at various degrees of hot-gas acceleration and turbulence levels," Int. J. Heat Mass Transf., **11**(11), pp. 1695–1713.

[5] Marek, C. J., and Tacina, R. R., 1975, "Effect of free-stream turbulence on film cooling."

[6] Cruz, C. a., and Marshall, A. W., 2007, "Surface and Gas Measurements Along a Film-Cooled Wall," J. Thermophys. Heat Transf., **21**(1), pp. 181–189.

[7] Teekaram, A. J. H., Forth, C. J. P., and Jones, T. V., 1991, "Film Cooling in the Presence of Mainstream Pressure Gradients," J. Turbomach., **113**(3), pp. 484–492.

[8] Hartnett, J. P., Birkebak, R. C., and Eckert, E. R. G., 1961, "Velocity Distributions , Temperature Distributions , Effectiveness and Heat Transfer for Air Injected Through a

Tangential Slot Into a Turbulent Boundary Layer," J. Heat Transfer, **83**(3), pp. 293–305.

[9] Bogard, D. G., and Thole, K. A., 2006, "Gas Turbine Film Cooling," J. Propuls. Power, **22**(2), pp. 249–270.

[10] Wu, X., and Moin, P., 2009, "Direct numerical simulation of turbulence in a nominally zero-pressure-gradient flat-plate boundary layer," J. Fluid Mech., **630**, p. 5.

[11] Jarrin, N., Benhamadouche, S., Laurence, D., and Prosser, R., 2006, "A synthetic-eddy-method for generating inflow conditions for large-eddy simulations," Int. J. Heat Fluid Flow, **27**(4), pp. 585–593.

[12] Klebanoff, P. S., and Diehl, Z. W., 1952, "Some features of artificially theickened fully developed turbulent boundary layers with zero pressure gradient," NACA Tech. Memo.

[13] Neu, J. C., 1984, "The dynamics of stretched vortices," J. Fluid Mech., **143**, pp. 253–276.

[14] Comte, P., Silvestrini, J. H., and Bégou, P., 1998, "Streamwise vortices in Large-Eddy simulations of mixing layers," Eur. J. Mech. - B/Fluids, **17**(4), pp. 615–637.

[15] Bernal, L. P., and Roshko, A., 1986, "Streamwise vortex structure in plane mixing layers," J. Fluid Mech., **170**, pp. 499–525.

Fourth International Conference on Computational Methods for Thermal Problems
THERMACOMP2016, July 6-8, 2016, Georgia Tech, Atlanta, USA
N. Massarotti, P. Nithiarasu and Y. Joshi (Eds.)

MACRO-SCALE HEAT TRANSFER MODELLING IN DEVICES WITH REPETITIVE FIN STRUCTURES

Martine Baelmans (keynote speaker) & Geert Buckinx
KU Leuven, Department of Mechanical Engineering, Celestijnenlaan 300A, 3001 Leuven, Belgium

ABSTRACT

Detailed flow and heat transfer simulations for devices with repetitive fin structures easily become computationally very costly. Appropriate filtering of the governing equations, involving well-chosen macro-scale temperature and pressure definitions allows to extract "natural" macro-scale equations for such geometries, i.e. similar to the ones governing developed channel flow. A detailed flow simulation can then be limited to a unit cell around a single solid structure. This unit cell information serves as an input for the macro-scale equations in the sense that it provides spatially constant interaction terms. Moreover, it allows to reconstruct the full flow field and accompanying temperature field in the device in a simple way, while retaining at the macro-scale level the analogy with simpler flows where no periodic solid structures are involved. This way both model and data reduction is achieved.

Key Words: *Macro-Scale, Volume-Averaging, Periodically Developed Flow*

1. INTRODUCTION

Compact heat exchanger and heat sink design often employs periodically corrugated geometries or periodically finned structures to enhance heat transfer. In these designs, local separation and reattachment flow features as well as increased surface area are employed to improve their overall characteristics with respect to heat transfer, while keeping the pressure drop below design limits. In order to enable optimal trade-offs and novel design evaluations, numerical simulations are indispensable. However, a full numerical simulation, including all flow and heat transfer details, comes at a huge – often unaffordable – computational cost.

Essentially two alternative approaches are presently used to enable these computations within an affordable computational cost. At the one hand the cost can be reduced by focusing on a representation of the detailed structure for a part of the geometry only. Developed flow is assumed to cover most of the region of interest. The question then arises how these simulations need to be set up in order to be representative for the larger domain of interest. In this context, Patankar et al. [1] and Stalio and Piller [2], performed pioneering work by developing respectively a mathematical model and associated reference temperature for developed flows through isothermal channels with streamwise-periodic variations of cross-sectional area. We have shown that it is possible to adapt this model towards fin structured geometries [3-5]. On the other hand many authors, e.g. [6-11], start from the experimental observation that overall characteristics in periodic structures seem to follow a similar behaviour as encountered in porous media, the latter being governed by statistically randomized distributions of pores. In this case global properties such as permeability, interphase heat transfer coefficients, etc. for the structure need to be determined. These properties can then be determined using either a real or a numerical experiment. In this context Whitaker [12] and Quintard et al. [13] showed how to derive these properties for momentum and energy equations respectively when applied to flows through homogeneous porous media.

It should be noted that Quintard [14,15] showed that when using volume averaging for periodically developed Stokes flow additional, so-called geometric tensors, arise in the averaged equations. These terms vanish when using double volume averaging. Furthermore, Teruel and Díaz [16], proposed double volume averaging to extract heat transfer coefficients from DNS simulation, though without providing a theoretical reason for doing so. Thus, some hints to use more advanced averaging procedures, can be found in literature.

In the context of heat exchangers and heat sinks simulations, above mentioned approaches are very often (inconsistently) combined over the last decades by studying small periodic subdomains as a representative elementary volume (REV) within the porous medium approach. Thus, neither the underlying theory as elaborated by Whitaker and Quintard was fully exploited, nor advantage was taken from the specific features of periodically developed flows. In this work we review how both approaches can be combined in a fully consistent way when using appropriate weighting functions. The latter is in essence a further elaboration of the pioneering work of Quintard for porous media [14,15]. Thus, we arrive at a set of equations, similar to the ones governing the developed flow regimes for momentum and temperature, for describing the overall flow and solid quantities. We will refer to them as "natural" flow equations. The developed equations for fully developed flow are then derived in a fully consistent way, making use of an appropriate weighting function. It is shown that spatially constant closure terms arise to account for the interaction between solid structures and fluid flow. A dedicated simulation on a unit cell only is needed to assess the local flow phenomena and to derive the interaction terms between solid structures and the flow at a global level. It should be noted that this approach can cope with flows that are not in-line with the periodic structure and is suited for isothermal surfaces as well as for periodically heated ones, while it remains relatively simple (i.e. simpler than the ones used in [15] for porous media) and computationally cost effective.

The developed theory is at present rigorously elaborated for the case of heat transfer in periodically developed laminar flows [3-5]. This flow regime is often encountered in the core of compact heat exchangers and small-sized heat sinks. This makes it readily applicable for practical heat transfer simulations in these devices. In order to arrive at a "natural" flow description at the global level, a careful choice for the assessment of global flow quantities for pressure, velocity and temperature are crucial. Therefore these proper global flow quantities will be discussed in the next section. Subsequently, the application of the developed method will be discussed at a global level followed by a unit cell simulation description.

2. THE QUEST FOR CONVENIENT MACRO-SCALE FLOW QUANTITIES

An essential part in the approach to periodic flow through periodic structures is to define global or macro-scale quantities for the overall evolution of the developed flow. Therefore, we now first elaborate on their definition. With **macro-scale quantities** we refer to averaged or overall values. As the noun quantity suggests, every macro-scale quantity is intrinsically linked to a specific physical quantity. As such, the macro-scale temperature is derived from some physically measurable temperature field that is of interest. This physical temperature field can be measured, at least in principle, by placing a sufficient number of temperature sensors within the fluid and the solid device. We assume that this temperature field can equally well be quantified by solving the temperature equations according to classical continuum mechanics. Similarly, we define the global flow velocity and pressure in terms of the velocity and pressure fields as obtained from the Navier-Stokes flow equations for incompressible fluids. Most importantly, the exact definition of these macro-scale quantities needs to serve the purpose for which they are introduced, i.e. the need for data and model reduction. Moreover, a macro-scale quantity needs to comply with a "simple" or "natural" macro-scale model.

The need for **data reduction** stems from the fact that temperature, velocity and pressure in a flow through a heat exchanger with periodically arranged fins vary from point to point. Consequently, a complete description of one of these physical quantities without loss of information comprises a huge amount of data. However, such detailed information is not always directly of interest, nor easy to interpret. Often, we are more interested in the overall or integral changes of a physical quantity. For example, we want to know the overall temperature difference between the inlet and the outlet of a heat sink or we want to know how the temperature varies globally over the heat sink. The quantity that we call the macro-scale temperature represents this overall or average impression of the temperature data that we do have interest in and does not contain all the point-wise variations in the values of the original quantity. Therefore, the macro-scale quantity itself can be described entirely by a smaller amount of values.

The need for **model reduction** points at the desire to reduce the efforts involved for measuring a physically quantity, be it through a numerical simulation or a real-word experiment. Because a physical quantity in a device typically changes from point to point, it is clear that for a complete description of the quantity, a lot of point-wise measurements would need to be collected, either via physical experiments or direct numerical simulation (DNS). Obviously, such a detailed analysis is mostly not desired, as it is a time-consuming task which requires a lot of measuring equipment or computational resources. On the contrary, for a complete description of the corresponding macroscale quantity, a reduced model is required. In our case we need a macro-scale flow and heat transfer model which can be solved to obtain the macro-scale temperature, macro-scale velocity and macro-scale pressure in a heat transfer device with periodically arranged solid structures. It should comprise a reduced model for the Navier-Stokes flow and temperature equations.

To comply with the quest for macro-scale or averaged quantities that are governed by "natural" flow equations, the link between the physical quantities Φ and the macro-scale property $\langle\Phi\rangle_m$ is generalised by using a weighted spatial average over the volume $\mathrm{d}\Omega$:

$$\langle\Phi\rangle_{m|_{(x,t)}} \triangleq \int_{\boldsymbol{r}\in\bar{\Omega}(\boldsymbol{x})} m(\boldsymbol{x}-\boldsymbol{r})\Phi(\mathbf{r},\mathrm{t})\mathrm{d}\Omega(\mathbf{r}). \tag{1}$$

It should be noted that in this context we use the so-called superficial spatial average, which incorporates both averaging over the fluid and solid regions. This is in contrast to the intrinsic spatial averages $\langle\Phi\rangle_m^f$ and $\langle\Phi\rangle_m^s$ that consider respectively averaging over the solid or over the fluid region only [3]. Now, the proper choice of the weighting function should cope with the need for a natural data reduction (i.e. such that it refers to the "natural" evolution in channel flows) and the need for model and data reduction (i.e. the use of a unit cell simulation to cope with all flow details). Therefore proper choices for the weighting function will be discussed for hydraulic and thermal fully developed flows in the next section. The additional volumetric source terms arising, after weighted-volume averaging the original equations, in the global (macro-scale) equations will turn out to provide a valuable tool to cope with the above listed goals.

3. MODELING MACRO-SCALE FLOW AND HEAT TRANSFER

In the core of compact heat transfer devices, laminar flow is often encountered due to its small dimensions. Even though we restrict ourselves to laminar flow conditions here, it is readily applicable to a set of applications. Like in channel flow without fins, **pressure and velocity profiles** in flows with periodically placed fins will develop to repetitive profiles. Similar to fully developed channel flows, we expect the global velocity constant along the streamwise direction, while the global pressure is expected to decrease linearly in streamwise direction and remains constant over the cross-sectional area. However, due to the presence of periodically positioned fins, velocities will now exhibit repetitive profiles throughout the developed region, while variations in pressure are superposed on a steadily decreasing pressure evolution along the streamwise direction.

These repetitive profiles will typically settle after the flow passed a couple of fins only (see Fig. 1 for the repetitive feature in normalized streamwise velocity). The flow is then called periodically developed. It is clear that, given mass continuity, the averaged velocity in the streamwise direction – i.e. averaged over the full cross-sectional channel area including the area filled with solid structures –through a cross-sectional plane will be constant, while its exact profile might differ from cross-section to cross-section in the streamwise direction.

Let us now examine the link between the physical flow quantities (velocity $\boldsymbol{u}$ and pressure p in this case) and the global ones ($\langle \boldsymbol{u} \rangle_m$ and $\langle p \rangle_m$). To obtain an (averaged) macro-scale velocity several possibilities exist. These macro-scale quantities are usually obtained either by averaging over the cross-section or by volume-averaging over a periodic unit cell. It is clear that cross-sectional averaging is inappropriate to meet our goals as they lead to quantities that vary from cross-section to cross-section and therefore do not allow any model or data reduction. Essentially, for the geometries under investigation, it is clear that all local quantity information is captured in a unit cell volume. This excludes area-averaging as well as volume-averaging over domains smaller than the unit cell. Therefore, we use volume-averaged over a unit cell to obtain the macro-scale velocity components. In contrast, this volume-averaging procedure does not lead to the expected linearly decreasing macro-scale pressure profile (see Fig. 2 left). Indeed, volume averaging of the pressure over the periodic unit cell induces a periodically oscillating deviation on top of a linear streamwise pressure decrease. In order to get an appropriate macro-scale pressure a weighted volume averaging procedure is needed. Here, we propose to use **double volume averaging**. Similarly, for periodically heated surfaces, macro-scale temperatures should linearly increase and can be obtained with the same type of filtering. In section 4 we will discuss how a periodic unit cell simulation using periodic boundary conditions as in [1] can provide information on the closure terms that arise in the macro-scale equations. Furthermore, it is remarkable that, by opting for this "natural" choice for macro-scale properties, the closure terms will turn out to be spatially constant and local quantities are easily reconstructed. This in turn allows for model and data reduction.

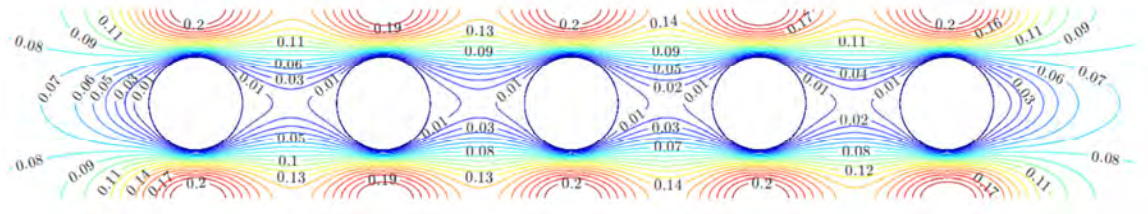

FIGURE 1. Dimensionless streamwise velocity for a 2D flow around cylindrical tubes [4]

For a **flow through isothermal finned surfaces**, the macro-scale temperature is expected to develop exponentially in the streamwise direction. This expectation is again based on a fully developed channel flow, this time with constant wall temperature. The macro-scale temperature is now defined by an exponential envelope of the detailed temperature profile, using a matched weighting function

$$m(\boldsymbol{x}-\boldsymbol{r}) = \frac{\beta}{V}\exp((\boldsymbol{x}-\boldsymbol{r})\cdot\boldsymbol{\lambda}, \tag{2}$$

with β a normalization factor and λ the overall decay rate which can be determined from an eigenvalue problem governed by macro-scale conduction, convection, thermal dispersion and heat transfer at the fluid-solid interface [5]. It was already shown in [1] that the use of the bulk temperature, i.e. the cross-sectional averaged temperature that would be obtained after adiabatic mixing of the flow, as a reference will lead to a periodically varying λ. In Fig.2 right, it can be seen that this periodically varying feature is indeed retrieved in the non-dimensional bulk temperature T_b^+. The non-dimensional temperature is defined as $T^+ \triangleq$

$\frac{T-T_s}{T_{ref}-T_s}$, with T_{ref} taken to be the inlet temperature. Also, the volume-averaged non-dimensional temperature $\langle T^+ \rangle^f$ displays a deviation from the expected "natural" exponential decay. In contrast, the matched **exponentially-weighted volume averaging** results in an exponential decaying macro-scale temperature $\langle T^+ \rangle_m^f$. Again it should be noted that, using this macro-scale temperature, the closure terms in the temperature equation, governing a.o. the heat transfer coefficients, are constant values in the fully developed flow region. This will be further elaborated in the next section.

It is clear that the determination of these spatially constant closure terms are in turn crucial in enabling the macro-scale temperature equation to be solved for the full heat exchanger of heat sink device. This can be done using a unit cell approach. Moreover, the detailed solution of this unit cell simulation allow for a full reconstruction of the physical flow quantities. Thus, in addition, it can serve for data reduction. Therefore, the unit cell simulation will be discussed in the next section.

4. CLOSURE TERMS AND DATA REDUCTION

For all above cases, the defined macro-scale quantities are now governed by macro-scale equations that contain closure terms. For a more comprehensive elaboration of the equations the reader is referred to [3-5]. E.g., for an incompressible steady flow, the following equations holding over the entire computational domain, irrespective of the presence of solid material, can be derived [4]:

$$\nabla \cdot \langle \boldsymbol{u} \rangle_{\boldsymbol{m}} = 0, \tag{3}$$

$$\rho_f \nabla \cdot \left(\epsilon_{fm}^{-1} \langle \boldsymbol{u} \rangle_m \langle \boldsymbol{u} \rangle_m \right) + \rho_f \nabla \cdot \boldsymbol{M} = -\nabla \langle p \rangle_m + \nabla \cdot \langle \boldsymbol{\tau} \rangle_m + \boldsymbol{b}_{fs} + \rho_f \mathbf{g} \epsilon_{fm}, \tag{4}$$

with ρ_f the fluid density, ϵ_{fm} the weighted porosity of the solid structure, and $\langle \boldsymbol{\tau} \rangle_m = \mu \nabla \langle \boldsymbol{u} \rangle_m + \mu (\nabla \langle \boldsymbol{u} \rangle_m)^T$ the smoothed viscous stress tensor. The closure terms arise from the solid structure interaction on the flow: $\boldsymbol{b}_{fs} \triangleq \langle \boldsymbol{n}_{fs} \cdot (-p\boldsymbol{I} + \boldsymbol{\tau}) \delta_{fs} \rangle_m$ is the smoothed interfacial force and arises due to the drag the flow exerts on the solid structures, while $\boldsymbol{M} \triangleq \langle \boldsymbol{u}\boldsymbol{u} \rangle_m - \epsilon_{fm}^{-1} \langle \boldsymbol{u} \rangle_m \langle \boldsymbol{u} \rangle_m$ is the weighted momentum dispersion source and represents the momentum exchange by local flow variations induced by the presence of the fins.

The equations for the macro-scale temperature of the fluid (f) and solid structures (s) for a given heat source $\dot{q}$ and viscous dissipation $\dot{q}_{visc}$ are respectively

$$\begin{aligned} \rho_f \nabla \cdot \left(c_f \langle \boldsymbol{u} \rangle_m \langle T \rangle_m^f \right) = \nabla \cdot k_f \nabla \cdot \left(\epsilon_{fm} \langle T \rangle_m^f \right) + \nabla \cdot k_f \langle \boldsymbol{n}_{fs} T_f \delta_{fs} \rangle_m + \langle \boldsymbol{n}_{fs} \cdot k_f \nabla T_f \delta_{fs} \rangle_m \\ - \rho_f \nabla \cdot c_f \boldsymbol{D} + \epsilon_{fm} \langle \dot{q} \rangle_m^f + \epsilon_{fm} \langle \dot{q}_{visc} \rangle_m^f , \end{aligned} \tag{5}$$

$$0 = \nabla \cdot k_s \nabla \cdot (\epsilon_{sm} \langle T \rangle_m^s) - \nabla \cdot k_s \langle \boldsymbol{n}_{fs} T_s \delta_{fs} \rangle_m + \langle \boldsymbol{n}_{fs} \cdot k_s \nabla T_s \delta_{fs} \rangle_m + \epsilon_{sm} \langle \dot{q} \rangle_m^s , \tag{6}$$

with c the specific heat and k the thermal conductivity. Several closure terms in the temperature equation appear, governing a.o. the heat transfer coefficient $h_{fs} \triangleq \frac{\langle \boldsymbol{n}_{fs} \cdot k_f \nabla T_f \delta_{fs} \rangle_m}{\langle T \rangle_m^f - \langle T \rangle_m^s} = \frac{\langle \boldsymbol{n}_{fs} \cdot k_s \nabla T_s \delta_{fs} \rangle_m}{\langle T \rangle_m^f - \langle T \rangle_m^s}$, the thermal dispersion source $\boldsymbol{D} \triangleq \langle \boldsymbol{u} T \rangle_m - \langle \boldsymbol{u} \rangle_m \langle T \rangle_m^f$ and the tortuosity $\langle \boldsymbol{n}_{fs} T_s \delta_{fs} \rangle_m = \langle \boldsymbol{n}_{fs} T_f \delta_{fs} \rangle_m$.

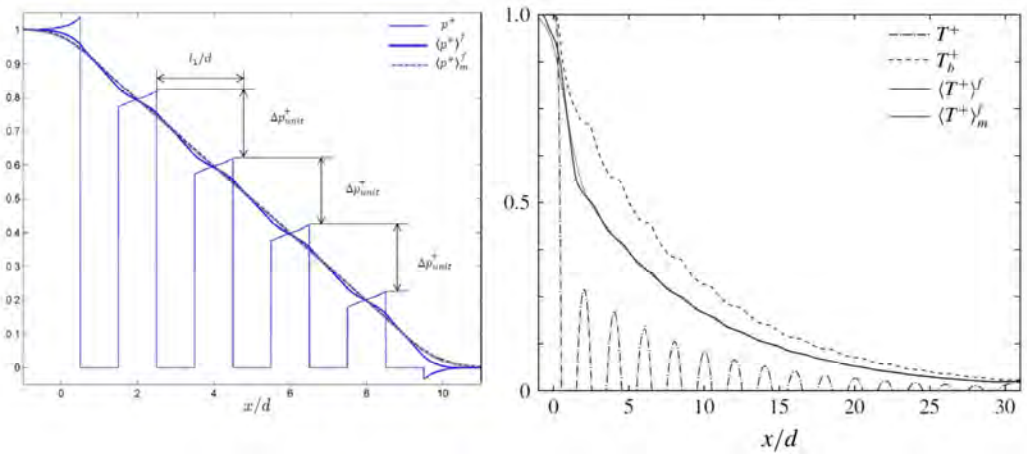

FIGURE 2. Pressure (left) [4] and temperature (right) [5] in the centreline of a cylindrical array

The closure terms now need to be derived from a dedicated (numerical) experiment. To this end we consider a unit cell of the periodic structure. As an example consider the 2-D configuration as shown in Fig. 3. The unit cell consists of a single fin surrounded by the fluid flow. The local flow quantities are governed by

$$\nabla \cdot \boldsymbol{u} = 0 \tag{5}$$

$$\rho_f \nabla \cdot (\boldsymbol{u}\boldsymbol{u}) = -\nabla \mathrm{p} + \nabla \cdot \boldsymbol{\tau} + \rho_f \mathbf{g} \tag{6}$$

Supplemented with periodic boundary conditions, though accounting for a prescribed constant pressure gradient, i.e. $p(\boldsymbol{x}+\boldsymbol{l}) = p(\boldsymbol{x}) + \nabla \mathrm{p} \cdot \boldsymbol{l}$ and $\boldsymbol{u}(\boldsymbol{x}+\boldsymbol{l}) = \boldsymbol{u}(\boldsymbol{x})$. When the fins are at a constant temperature T_s, the local temperature T in the unit cell is retrieved from the rescaled temperature $\theta \triangleq (T - T_s)/(\langle T \rangle_m - T_s)$, which is now governed by the following two coupled equations:

$$\rho_f \nabla \cdot \left(\boldsymbol{u} c_f \theta\right) = \nabla \cdot k \nabla \theta + \left(2 k_f \nabla \theta - \rho_f \boldsymbol{u} c_f \theta + k_f \theta \boldsymbol{\lambda}\right) \cdot \boldsymbol{\lambda} \,, \tag{7}$$

$$\langle n_{fs} \cdot k_f \nabla \theta \delta_{fs} \rangle - \rho_f c_f \langle \boldsymbol{u} \theta \rangle \cdot \boldsymbol{\lambda} + k_f \theta \boldsymbol{\lambda} \cdot \boldsymbol{\lambda} = 0 \,, \tag{8}$$

with periodic boundary conditions for θ over the unit cell and $\theta = 0$ at the fin boundary.

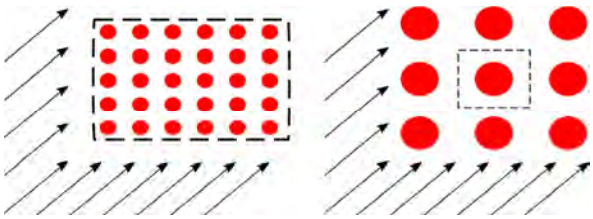

FIGURE 3. Unit cell configuration

The closure terms (such as $\boldsymbol{b}_{fs}$ and $\boldsymbol{M}$) can then be calculated from the local flow quantities, while the closure terms for the temperature equation (such as the interfacial heat transfer coefficient $h_{fs} = \langle n_{fs} \cdot k_f \nabla\theta\delta_{fs}\rangle$) can be calculated from the local temperature quantities. A similar procedure can be followed for a conjugate heat transfer problem or a periodic heat transfer problem. It is important to note that, by taking the "natural" definition for the macro-scale quantities, all closure terms turn out to be spatially constant for the hydraulic and thermal cases discussed above. This provides a way to drastically reduce the local or detailed information on flow and solid quantities. Moreover, complementing the global flow quantities with the physical ones (the latter being established for a unit cell only) enables to fully reconstruct the physical quantities all over the device. As an example the reconstruction of the normalized velocity $\boldsymbol{u}^+$ and pressure p^+ around the third fin in a row of five is shown in Fig. 4 (left and middle, resp.) for the hydraulic case [3]. Similarly the reconstruction of the non-dimensional flow temperature T^+ in the vicinity of the eighth cylinder in a row of 15 for an isothermal heat transfer problem is displayed in Fig. 4 (right) [5].

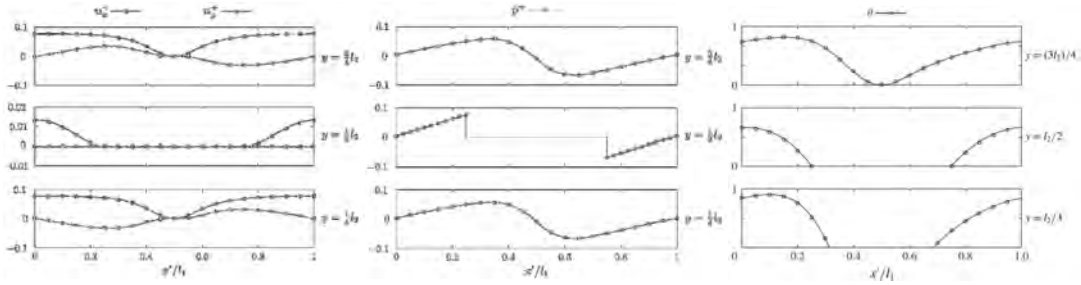

FIGURE 4. Reconstruction of velocity, pressure in a hydraulic case [3] and temperature in an isothermal heat transfer problem [5] for flows around a row of cylinders (lines represent the solution obtained from a simulation over the full geometry, while markers are used for the reconstructed profile)

5. CONCLUSIONS AND OUTLOOK

A concise definition of macro-scale velocity, pressure and temperature, referred to as "natural" global quantities, enables a fully consistent approach to integral properties and models for periodically developed laminar flows through periodically fin geometries. A weighted volume approach for pressure and a matched weighted volume approach for temperatures provides the link between physical and macro-scale properties. In this way a macro-scale model is retrieved that includes constant solid-fluid interaction terms. The latter can be deduced from a single unit cell simulation and allow to fully reconstruct the physical flow quantities at a local scale. Thus, both model and data reduction is achieved. The approach is at present further elaborated for conjugate 3-D heat transfer problems and can be extended to include unsteady or turbulent flows.

ACKNOWLEDGEMENTS

The work of G. Buckinx is sponsored by the Flanders Innovation and Entrepreneurship Agency. Numerical results in this paper were obtained using FVMLab, a C++/Matlab-based finite volume solver package developed by Frederik Rogiers and Geert Buckinx. For all numerical results we used the infrastructure of the VSC - Flemish Supercomputer Center, funded by the Hercules foundation and the Flemish Government - department EWI.

REFERENCES

[1]. S.V. Patankar, C.H. Liu, and E.M. Sparrow, "Fully Developed Flow and Heat Transfer in Ducts Having Streamwise-Periodic Variations of Cross-Sectional Area," J. Heat Transf., vol. 99, no. 2, p. 180, 1977.

[2]. E. Stalio and M. Piller, "Direct numerical simulation of heat transfer in converging-diverging wavy channels," J. Heat Transf., vol. 129, no. 7, pp. 769–777, 2006.

[3]. G. Buckinx and M. Baelmans, "Multi-scale modelling of flow in periodic solid structures through spatial averaging," J. Comp. Phys., vol. 291, pp. 34–51, 2015.

[4]. G. Buckinx and M. Baelmans, "Towards a general spatial averaging procedure for multi-scale flow modelling in heat transfer devices with repetitive fin structures, Proc. of the 15th International Heat Transfer Conference,IHTC-15. Kyoto, 10-15 August 2014 (art.nr. 1234)

[5]. G. Buckinx and M. Baelmans, "Macro-scale heat transfer in periodically developed flow through isothermal solids," J. Fluid Mech., vol. 780, pp. 274–298, 2015.

[6]. A. Horvat and I. Catton, "Numerical technique for modeling conjugate heat transfer in an electronic device heat sink. Int. J. Heat Mass Transf., vol. 46, no. 12, pp. 2155–2168, 2003.

[7]. A. Horvat and B. Mavko, "Hierarchic modeling of heat transfer processes in heat exchangers," Int. J. Heat Mass Transf., vol. 48, no. 2, pp. 361–371, 2005.

[8]. F. Zhou and I Catton, "Obtaining closure for a plane fin heat sink with elliptic scale-roughened surfaces for Volume Averaging Theory (VAT) based modeling," Int. J. Therm. Sci., vol. 71, pp. 264–273, 2013.

[9]. F. Zhou, N.E. Hansen, D.J. Geb, and I. Catton, "Obtaining Closure for Fin-and-Tube Heat Exchanger Modeling Based on Volume Averaging Theory (VAT)". J. Heat Transfer, vol. 133, no. 11, 111802, 2011.

[10]. A.A. Alshare, P.J. Strykowski, and T.W. Simon, "Modeling of unsteady and steady fluid flow, heat transfer and dispersion in porous media using unit cell scale," Int. J. Heat Mass Transf., vol. 53, no. 9-10, pp. 2294–2310, 2010.

[11]. A.A. Alshare, P.J. Strykowski, and T.W. Simon, "Simulations of flow and heat transfer in a serpentine heat exchanger having dispersed resistance with porous-continuum and continuum models", Int. J. Heat Mass Transf., vol. 53, pp. 1088–1099, 2010.

[12]. S. Whitaker, "The Forchheimer equation: a theoretical development", Transp. Porous Media 25, 27–61, 1996.

[13]. M. Quintard, M. Kaviany, and S. Whitaker, "Two-medium treatment of heat transfer in porous media: numerical results for eeffective properties", Adv. Water Resour., 20(2-3), 77-94, 1997.

[14]. M. Quintard and S. Whitaker, "Transport in ordered and disordered porous media I: The cellular average and the use of weighting functions," Transp. Porous Media, vol. 14, no. 2, pp. 163–177, 1994.

[15]. M. Quintard and S. Whitaker, "Transport in ordered and disordered porous media II: Generalized volume averaging," Transp. Porous Media, vol. 14, no. 2, pp. 179–206, 1994.

[16]. F.E. Teruel and L. Díaz, "Calculation of the interfacial heat transfer coefficient in porous media employing numerical simulations", Int. J. Heat Mass Transf. 60, 406–412, 2013.

Fourth International Conference on Computational Methods for Thermal Problems
THERMACOMP2016, July 6-8, 2016, Georgia Tech, Atlanta, USA
N. Massarotti, P. Nithiarasu and Y. Joshi (Eds.)

THERMAL TRANSPORT BY PHONONS AND ELECTRONS FROM FIRST PRINCIPLES CALCULATIONS

Alan J. H. McGaughey, Ankit Jain
Department of Mechanical Engineering, Carnegie Mellon University, Pittsburgh PA 15213
mcgaughey@cmu.edu, ankitjain.me.iitk@gmail.com

ABSTRACT

A computational framework for predicting phonon properties, electron properties, and thermal conductivity from first principles is presented. The effect of the pseudopotential and exchange-correlation in the density functional theory calculations on the thermal conductivity of silicon is predicted and discussed. The thermal conductivity of the two-dimensional material black phosphorene is shown to have an anisotropy ratio of three. The phonon mean free paths that dominate thermal transport in aluminum, silver, and gold are found to be an order to magnitude smaller than the dominant electron mean free paths.

Key Words: *Density Functional Theory, Lattice Dynamics Calculations, Boltzmann Transport Equation, Silicon, Phosphorene, Metals.*

1. INTRODUCTION

The integration of density functional theory (DFT) calculations, lattice dynamics calculations, and the Boltzmann transport equation (BTE) has enabled thermal conductivity predictions for bulk crystalline materials that agree with experimental measurements [1-3]. This agreement points to the fidelity of the computational framework and to its power to elucidate fundamentals details about the carrier-level (i.e., phonon and electron) transport. Access to phonon and electron mode-level properties enables nanostructure thermal conductivity prediction, interpretation of cutting-edge experiments, and screening of large material design spaces for optimized transport properties.

The first part of this talk will describe a first-principles-based computational framework for predicting phonon properties and thermal conductivity using silicon as a test case. The second part will present two applications: (i) phonon transport in the two-dimensional material black phosphorene, and (ii) phonon and electron transport in the metals aluminum, silver, and gold.

2. FIRST-PRINCIPLES COMPUTATIONAL FRAMWORK

For a given material, the first step is to specify the lattice constant, which can be obtained through energy minimization in a DFT calculation. Harmonic force constants are obtained from density functional perturbation theory (DFPT) calculations, which are used to build the dynamical matrix. Solution of an eigenvalue problem gives the phonon frequencies and polarization vectors, and from these, heat capacities, dispersion curves, group velocities, and phonon-point defect (e.g., isotope) scattering rates. Cubic force constants are obtained from DFT calculations. Along with harmonic-level properties, the cubic force constants are the input to solutions of the BTE for determining three-phonon scattering rates. Both the relaxation time approximation to the BTE and a full solution can be considered. The heat capacities, group velocities, and scattering rates are then combined to predict thermal conductivity.

We use the Quantum Espresso for the DFT and DFPT calculations and in-house codes for the lattice dynamics and Boltzmann transport equation. Careful convergence tests are required in performing these calculations, including [2,4]:

- Electron wave vector grid, plane wave energy cutoff, and phonon wave vector grid for the DFT and DFPT calculations.
- DFT supercell size and cutoff distance for the cubic force constants (for which translational invariance must be enforced).
- The vacuum space for low-dimensional materials.
- Phonon wave vector grid for the thermal conductivity.

We recommend performing these convergence tests, which may require iteration, on the full thermal conductivity at the lowest temperature considered.

When performing the DFT and DFPT calculations, two important choices are the selection of the pseudopotential (PP) and the exchange-correlation (XC). The PP is a model that simplifies the description of the nucleus and the core electrons. The XC is a model for quantum effects that do not have an exact solution.

With isotopically-pure silicon as a test case, we investigated how thermal conductivity is affected by the choice of PP and XC [4]. At a temperature of 300 K, for ultrasoft, norm-conserving, and PAW PPs, the LDA, PBE, and PBEsol XCs predict thermal conductivities between 137 and 148 W/m-K. This range is 3-10% lower than the experimental value of 153 W/m-K.

The thermal conductivity accumulations as a function of the phonon mean free path for all cases considered are plotted in Fig. 1. Other than for the BLYP XC (norm-conserving PP) and the PW91 XC (ultrasoft PP), the behaviors are very similar, with phonons covering mean free paths between 10 nm and 10 μm contributing to thermal conductivity. We interpret the predicted thermal conductivities by considering the sound velocity extracted from the phonon dispersion, the three-phonon phase space, and the Gruneisen parameters.

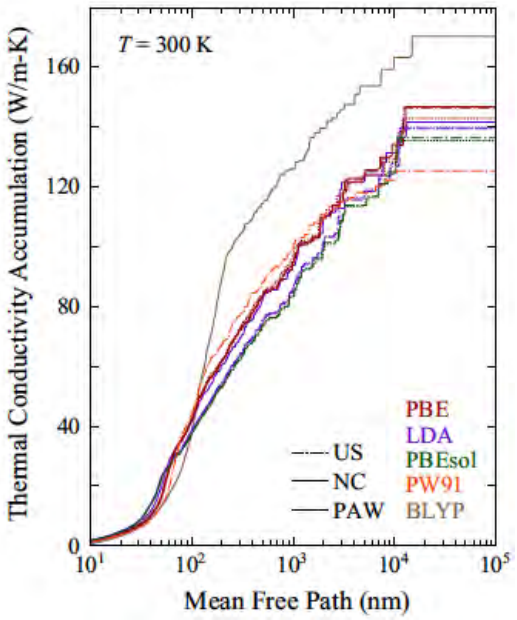

FIGURE 1. Thermal conductivity accumulation of silicon with respect to mean free path from different PPs and XCs [4].

3. PHOSPHORENE

Black phosphorene is an anisotropic two-dimensional material with a direct band gap that shows promise for applications in next-generation electronic devices [5,6]. Using the first principles calculation framework, we predicted the phonon properties and thermal conductivity of black phosphorene, along with that of another allotrope, blue phosphorene, which is isotropic [7]. The structures are shown in Figs. 2(a) and 2(b).

We predict black phosphorene to have a thermal conductivity anisotropy ratio of three, with values of 110 and 36 W/m-K along its armchair and zigzag directions at a temperature of 300 K. For blue phosphorene, which is isotropic with a zigzag structure, the predicted value is 78 W/m-K. As shown in Fig. 2(b), the two allotropes show strikingly different thermal conductivity accumulation, with phonons of mean free paths between 10 nm and 1 μm dominating in black phosphorene, while a much narrower band of mean free paths (50–200 nm) dominate in blue phosphorene.

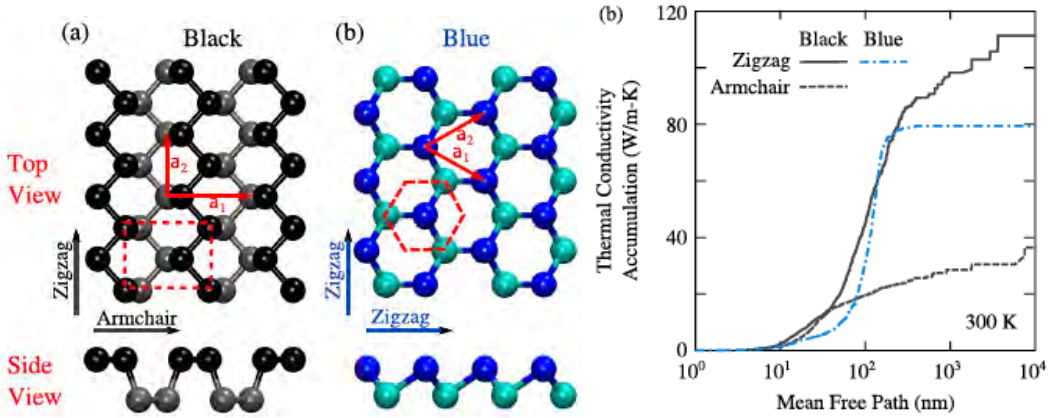

FIGURE 2. Structures of (a) black phosphorene and (b) blue phospherene. (c) Thermal conductivity accumulation functions. [7]

4. METALS

Phonon transport in metals is mostly untouched because of the small contribution of phonons to bulk thermal conductivity and the computational complexity of rigorously modeling electron-phonon (e-p) interactions. Even though electrons dominate thermal and electrical transport in metals, phonons play a critical role in that the electron transport is limited by e-p scattering at intermediate and high temperatures (i.e., above one-tenth of the Debye temperature). Furthermore, e-p interactions are important in superconductivity, hot-carrier mobility, the response of a material abruptly heated by ion bombardment or laser irradiation, and thermal transport across metal-dielectric interfaces in thermoelectric and plasmonic devices.

We predicted mode-dependent phonon and electron transport properties in aluminum, silver, and gold [8]. Beyond the computational framework described in Section 1, electron-phonon scattering rates are obtained on a coarse grid using DFPT calculations and then interpolated to a finer grid using the

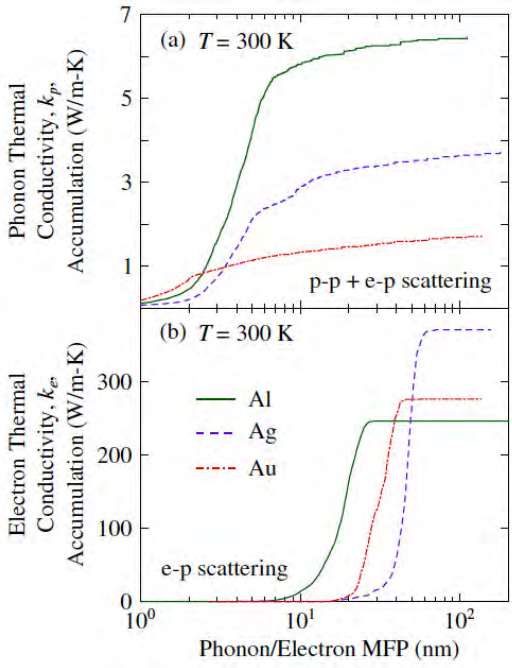

FIGURE 3. (a) Phonon and (b) electron thermal conductivity accumulation with respect to phonon/electron mean free path at a temperature of 300 K [8].

Electron-Phonon Wannier package [9]. These calculations necessitate additional convergence tests.

The predicted thermal conductivities, electrical conductivities, electron-phonon coupling coefficients, and electron-phonon mass enhancement parameters are in agreement with experimental measurements. As shown in Figs. 3(a) and 3(b), phonons with mean free paths between 1 and 10 nm are the dominate contributors to the thermal conductivity at a temperature of 300 K, while the relevant electron mean free paths are 10-100 nm. Despite similar atomic masses, the phonon thermal conductivity of aluminum is an order of magnitude smaller than that of silicon due to a larger three-phonon phase space and stronger anharmonicity.

REFERENCES

[1] D. A. Broido, M. Maloney, G. Birner, N. Mingo, and D. Stewart, Intrinsic lattice thermal conductivity of semiconductors from first principles, *Appled Physics Letters*, 91, 231922, 2007.

[2] L. Lindsay, D. A. Broido, and T. L. Reinecke, *Ab initio* thermal transport in compound semiconductors, *Physical Review B*, 87, 165201, 2013.

[3] B. Liao, B. Qiu, J. Zhou, S. Huberman, K. Esfarjani, and G. Chen, Significant reduction of lattice thermal conductivity by the electron-phonon interaction in silicon with high carrier concentrations: A first principles study, *Physical Review Letters*, 114, 115901, 2015.

[4] A. Jain and A. J. H. McGaughey, Effect of exchange-correlation on first-principles-driven lattice thermal conductivity predictions of crystalline silicon, *Computational Materials Science*, 110, 115-120, 2015.

[5] H. Liu, A. T. Neal, Z. Zhu, Z. Luo, X. Xu, D. Tomanek, and P. D. Ye, Phosphorene: An unexplored 2D semiconductor with a high hole mobility, ACS Nano, 8, 4033-4041, 2014.

[6] L. Li, Y. Yu, G. J. Ye, A. Ge, X. Ou, H. Wu, D. Feng, X. H. Chen, and Y. Zhang, Black phosphorun field effect transistors, Nanture Nanotechnology, 9, 372-377, 2014.

[7] A. Jain and A. J. H. McGaughey, Strongly anisoptropic in-plane thermal conductivity in single-layer black phosphorene, Scientific Reports, 5, 8501, 2015.

[8] A. Jain and A. J. H. McGaughey, submitted.

[9] F. Guistino, M. L. Cohen, and S. G. Louie, Electron-phonon interaction using Wannier functions, Physical Review B, 76, 165108, 2007.

Fourth International Conference on Computational Methods for Thermal Problems
THERMACOMP2016, July 6-8, 2016, Georgia Tech, Atlanta, USA
N. Massarotti, P. Nithiarasu and Y. Joshi (Eds.)

NUMERICAL ANALYSIS OF COMPACT PLATE-FIN HEAT EXCHANGERS FOR AEROSPACE APPLICATIONS

C. Ranganayakulu
P.B. 1718, Vimanapura Post. Aeronautical Development Agency, Bangalore – 560017, India.
Email: chennu_r@rediffmail.com

ABSTRACT

Thermo-hydraulic performances of Compact Heat Exchangers (CHE's) is strongly depending upon the prediction of performance of various types of heat transfer surfaces such as Offset Strip fins, Wavy fins, Rectangular fins, Triangular fins, Triangular and Rectangular perforated fins in terms of Colburn '*j*' and Fanning friction '*f*' factors. Numerical methods plays major role for anlysis of compact plate-fin heat exchangers, which are cost effective and fast. This paper presents the on-going research and work carried out earlier for single-phase steady state heat transfer and pressure drop analysis on CHE passages and fins. An analysis of a crossflow plate-fin compact heat exchanger, accounting for the individual effects of two-dimensional longitudinal heat conduction through the exchanger wall, inlet fluid flow mal-distribution and inlet temperature non-uniformtity are carried out using a Finite Element Method (FEM).

The performance deteriorations of high-efficiency cross flow plate-fin compact heat exchangers have been reviewed with the combined effects of wall longitudinal heat conduction and inlet fluid flow/temperature non-uniformity using a dedicated FEM analysis. It was found that the performance deteriorations are quite significant in some typical applications due to the effects of wall longitudinal heat conduction and inlet fluid flow nonuniformity on crossflow plate-fin heat exchangers. A mathematical equation is developed to generate different types of fluid flow/temperature maldistribution models considering the possible deviations in fluid flow. A Computational Fluid Dynamics (CFD) program FLUENT has been used to predict the design data in terms of '*j*' & '*f*' factors for plate-fin heat exchanger fins. The suitable design data is generated using CFD analysis covering the laminar, transition and turbulent flow regimes for various types of fins.

Key Words: *Heat Transfer Coefficient, FEM/ CFD Analysis, Compact Heat Exchanger fins, Colburn 'j' and friction 'f' factors, Single phase steady state numerical analysis, Longitudinal Heat Conduction effects, inlet flow and temperature non-uniformity effects.*

1. INTRODUCTION

Thermo-hydraulic design of a compact heat exchanger is strongly dependent upon the performance of heat transfer surfaces (in terms of Colburn factor *j* and Fanning friction factor *f* vs. Reynolds number Re characteristics). The orientation of inlet and outlet headers plays a major role in performance especially in aerospace applications, where the orientation of headers and nozzles are not straight and uniform due to space limitations. The accurate prediction of the thermal performance of a compact heat exchanger in the design stage is highly desirable for aerospace applications. The longitudinal heat conduction (LHC) through the heat exchanger wall structure in the direction of fluid flows has the effect of decreasing the exchanger performance for a specified NTU, and this reduction may be quite serious in exchangers with short flow length designed for high effectiveness (> 80%) [1]. These effects have been well recognized and the numerical data are available in [2,3] for periodic-flow heat exchangers and in [4-6] for the direct transfer type heat exchangers. The flow mal-distribution effects have been well recognized for heat exchangers. The

flow non uniformity (FN) effects have been well recognized and presented for heat exchangers[7-9]. Similarly, the fluid inlet temperature non uniformity (TN) effects have also been investigated for cross flow heat exchangers [10,11]. In actual practice, heat exchangers may be subjected to wall LHC, inlet FN and TN together. Literature on the investigation of combined effects of LHC, TN and FN for a cross flow plate-fin heat exchanger is limited [10,14].

2. MAIN BODY

2.1 FEM ANALYSIS:

A discretized model of a cross flow plate-fin heat exchanger is shown in Fig.1-(a). It is divided into a number of equal strips. The strip 1 is isolated and shown in Fig.1-(b). The exchanger may be visualized as a wall separating the two fluid streams flowing at right angles with plate-fins on both sides as shown in Fig.1-(c). Each strip consists of a number of pairs of stacks which carry hot and cold fluids. A pair of stacks is separated and shown in Fig.1-(d). It is the basic element for which the element matrices are derived. In the cross flow plate-fin exchanger wall, a 4-noded element has been considered for studying the two-dimensional longitudinal wall heat conduction effects. Two-nodded linear elements have been considered for both hot and cold fluids in the present analysis. Thus a 16-noded box element has been obtained as shown in Fig.1-(d). Similarly, the discretized exchanger for counter flow plate-fin and parallel-flow plate-fin type heat exchangers are shown in Figs.1-(e)-(f) respectively. The wall temperature distribution in counter flow plate-fin and parallel-flow plate-fin heat exchangers are one-dimensional and hence 2-noded elements have been considered in the exchanger plate for longitudinal wall heat conduction effects. Thus a 10-noded element has been obtained for counter flow and parallel-flow plate-fin heat exchanger as shown in Figs.1-(e)-(f) respectively. Here, the possible inlet fluid flow non uniformity models are generated by distorting the velocity profile and keeping the average fluid velocity as unity [6-7]. One of this model named as Model A1 is tabulated in Table 1. Also, a typical fluid flow mal-distribution model is shown in Fig. 2. The velocity at the wall of inlet duct is zero. The non-zero velocity values in the proposed models are at the points away from the wall of transition duct. In each model, there are 10 x 10 local flow non uniformity dimensionless parameters (α's), which correspond to the 10 x 10 subdivisions on the x-z plane perpendicular to the direction of non-uniform fluid flow.

Model – A1

J = 1 ; 10	0.500	0.500	0.500	0.500	0.500
2 ; 9	0.500	0.639	0.776	0.899	0.998
3 ; 8	0.500	0.776	1.045	1.291	1.489
4 ; 7	0.500	0.899	1.291	1.655	1.956
5 ; 6	0.500	0.998	1.489	1.956	2.356

Table 1- Flow Non-uniformity Parameters (α's)

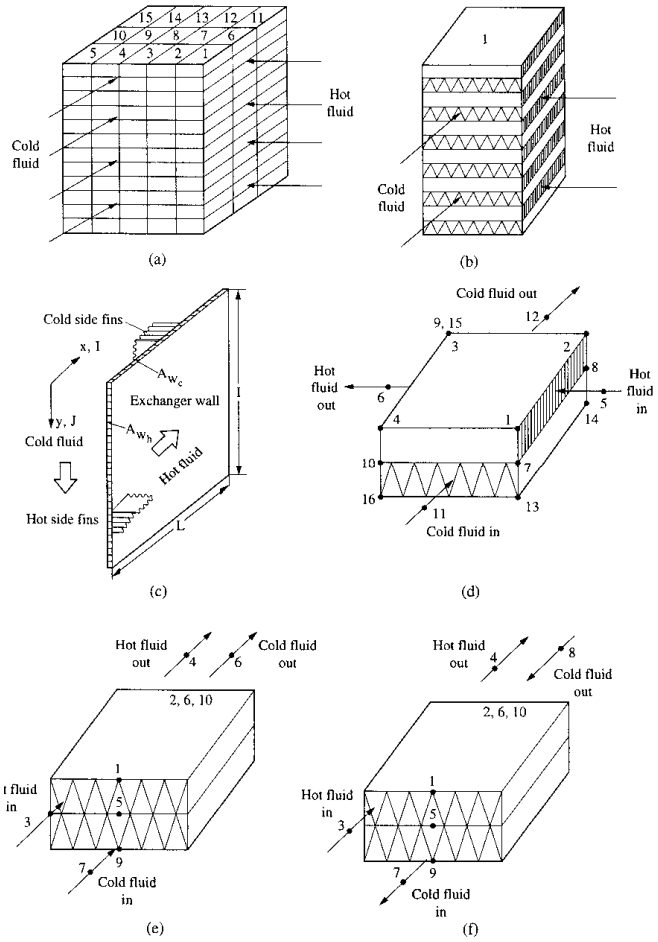

Fig. 1 Single pass Pate-fin Heat Exchanger

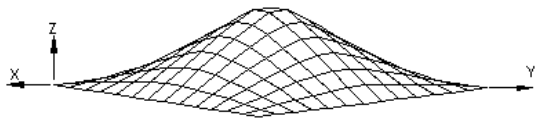

Fig. 2 Flow non-uniformity model

2.2 CFD ANALYSIS:

In this paper, the following geometries of various types of fins are considered for CFD analysis for estimation of j and f data: Fig. 3(a) shows the isometric view of a Wavy fin, Fig 3(b) shows Wavy fin dimensional notations, Fig. 3(c) shows the schematic of Offset fins, Fig. 3(d) shows the geometry of Rectangular plain fin, Fig. 3(e) shows the Model of Rectangular perforated fin, Fig. 3(f) shows the Fin geometry of Triangular plain fin and Fig 3(g) shows the model of Triangular perforated fin. The dimensionless representations of these variables are given by ratios of s/h, 2A/s and L/2A. In the fin designation as denoted by Kays and London [1], the first number indicates the fin density (fins/inch), the second number indicates the fin wavy length (L) in inches and the third number indicates the fin thickness in inches as 11.44-3/8W-0.006.

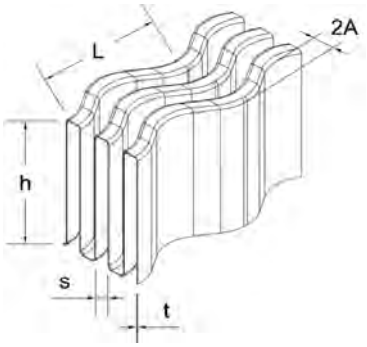

(a) Schematic of Wavy fin

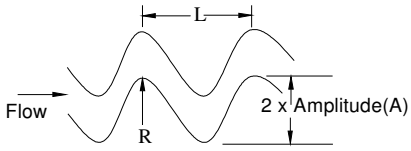

(b) Wavy fin dimensional notations

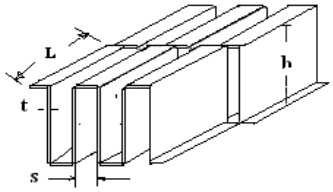

(c) Offset fin dimensional notations

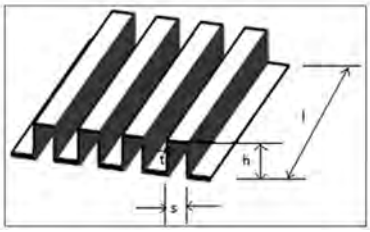

(d) Rectangular Plain fin geometry

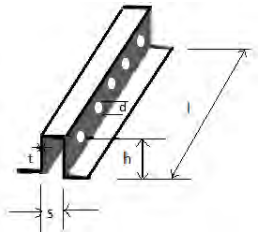

(e) Model of Rectangular perforated fin

(f) Fin geometry of Triangular plain fin

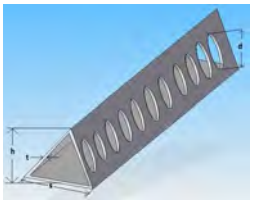

(g) Model of triangular perforated fin

Fig. 3 Geometries of different types of Fins

3. RESULTS

3.1 FEM RESULTS:

The performance evaluation with the combined effects of wall LHC and inlet fluid FN on cross flow heat exchanger is presented for balanced flow, $C_{min}/C_{max} = 1$, as well as for unbalanced flow, C_{min}/C_{max} not equal to one. Detailed results for all cases can be found in earlier paper [10-14]. However, a sample case is shown here. The relation between the ratio of C_{min}/C_{max} and λ with correction factor (τ) is shown in Fig. 4.

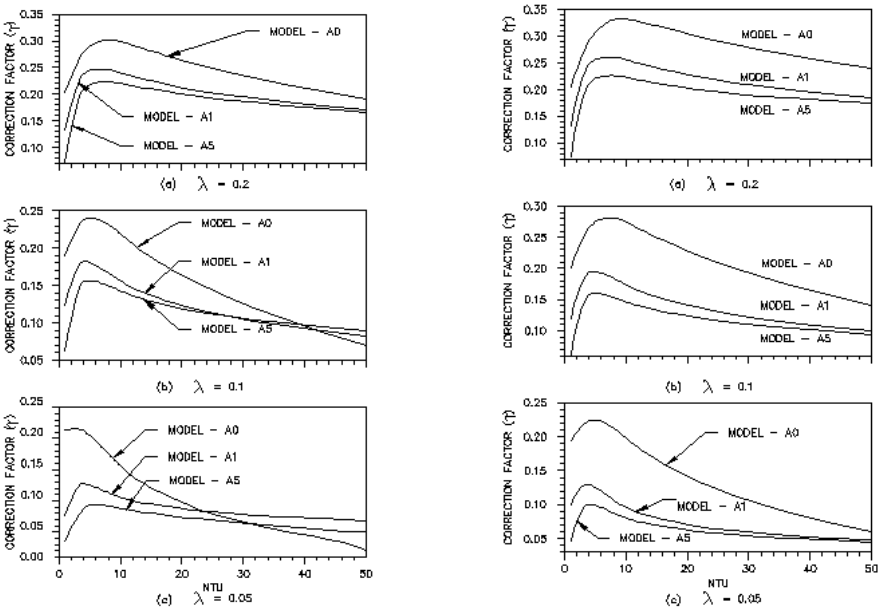

Fig. 4 Combined effects of LHC and Flow non-uniformity–Plate-fin Heat Exchanger, (i) C_{max} fluid side (ii) both fluid side : C_{min}/C_{max}=1.0

3.2 CFD RESULTS:

The *f* and *j* values are generated using CFD technique for different types of offset strip fins and wavy fins. The complete results can be seen in earlier papers [15-21]. However, the correlations generated using CFD are listed below for various types of fins in Table 2 for ready reference:

S. No	Type of fin surface	Design data	Correlations	Range of Applicability
1	Wavy fins	*f*	$9.827Re^{-0.705}\left(\frac{h}{s}\right)^{0.322}\left(\frac{2A}{s}\right)^{-0.394}\left(\frac{L}{2A}\right)^{-0.603}$	$100 \le Re \le 800$
		f	$10.628\,Re^{-0.359}\left(\frac{h}{s}\right)^{0.264}\left(\frac{2A}{s}\right)^{-0.848}\left(\frac{L}{2A}\right)^{-1.931}$	$1000 \le Re \le 15000$
		j	$2.348\,Re^{-0.786}\left(\frac{h}{s}\right)^{0.312}\left(\frac{2A}{s}\right)^{-0.192}\left(\frac{L}{2A}\right)^{-0.432}$	$100 \le Re \le 800$
		j	$0.242\,Re^{-0.375}\left(\frac{h}{s}\right)^{0.235}\left(\frac{2A}{s}\right)^{-0.288}\left(\frac{L}{2A}\right)^{-0.553}$	$1000 \le Re \le 5000$
2	*Wavy fin R134a*	*j*	$2.989Re^{-0.54241}\frac{h}{s}^{-0.72276}\frac{2A}{s}^{-0.83914}\frac{L}{2A}^{-0.7588}$	$100 \le Re \le 1000$
3	*Wavy fin Water*	*j*	$1.154Re^{-0.65938}\frac{h}{s}^{-0.96698}\frac{2A}{s}^{0.176702}\frac{L}{2A}^{0.288785}$	$100 \le Re \le 1000$
4	*Wavy fin Water & R134a*	*f*	$18.607Re^{-0.59381}\frac{h}{s}^{-0.088954}\frac{2A}{s}^{-0.46976}\frac{L}{2A}^{-0.926}$	$100 \le Re \le 1000$
5	Offset fins	*f*	$10.882(Re)^{-0.79}(s/h)^{-0.359}(t/s)^{-0.187}(t/l)^{0.284}$	$300 \le Re \le 800$
		f	$2.237(Re)^{-0.236}(s/h)^{-0.347}(t/s)^{0.151}(t/l)^{0.639}$	$1000 \le Re 15000$
		j	$0.661(Re)^{-0.651}(s/h)^{-0.343}(t/s)^{-0.538}(t/l)^{0.305}$	$300 \le Re \le 800$

		j	$0.185(Re)^{-0.396}(s/h)^{-0.178}(t/s)^{-0.403}(t/l)^{0.29}$	$1000 \leq R_e \leq 15000$
6	Rectangular plain	*f*	$12.892(Re)^{-1.229}(h/s)^{0.452}(t/s)^{-0.198}$	$100 \leq Re \leq 1000$
		f	$3.133\ (Re)^{-1.285}(h/s)^{0.247}(t/s)^{-0.181}$	$1000 < Re \leq 7500$
		j	$0.454\ (Re)^{-0.977}(h/s)^{0.435}(t/s)^{-0.227}$	$100 \leq Re \leq 1000$
		j	$0.166\ (Re)^{-1.011}(h/s)^{0.228}(t/s)^{-0..366}$	$1000 < Re \leq 7500$
7	Rectangular perforated fin	*f*	$0.7127(Re)^{-1.8858}(h/s)^{0.4196}(t/s)^{-1.4826}$	$100 \leq Re \leq 1000$
		f	$0.4345(Re)^{-1.3029}(h/s)^{0.3725}(t/s)^{-1.3178}$	$1000 < Re \leq 7500$
		j	$0.121\ (Re)^{-2.2920}(h/s)^{2.75}(t/s)^{-1.830}$	$100 \leq Re \leq 1000$
		j	$11.71\ (Re)^{-2.3111}(h/s)^{2.144}(t/s)^{-1.9237}$	$1000 < Re \leq 7500$
8	Triangular Plain fin	*f*	$3.12(Re)^{-0.852}(h/s)^{0.156}(t/s)^{-0.184}$	$100 \leq Re \leq 1000$
		f	$2.69(Re)^{-0.918}(h/s)^{0.355}(t/s)^{-0.175}$	$1000 < Re \leq 10000$
		j	$0.718\ (Re)^{-0.625}(h/s)^{0.765}(t/s)^{0.765}$	$100 \leq Re \leq 1000$
		j	$0.789\ (Re)^{-1.1218}(h/s)^{1.235}(t/s)^{-0.764}$	$1000 < Re \leq 10000$
9	Triangular Perforated fin	*f*	$10.127\ (Re)^{-1.588}(h/s)^{0.778}(t/s)^{-0.868}$	$300 \leq Re \leq 1000$
		f	$1.685\ (Re)^{-0.798}(h/s)^{0.447}(t/s)^{-0.276}$	$1000 < Re \leq 7500$
		j	$0.544\ (Re)^{-1.673}(h/s)^{2.278}(t/s)^{-1.589}$	$300 \leq Re \leq 1000$
		j	$7.579\ (Re)^{-1.626}(h/s)^{1.185}(t/s)^{-1.689}$	$1000 < Re \leq 7500$

Table 2: *f* and *j* correlations for various types of CHE fins.

4. CONCLUSIONS

This paper presents both Finite Element Method Analysis and Computational Fluid Dynamic analysis of Compact Heat Exchangers are presented for Aerospace applications. Using FEM the Flow Non-uniformity, Temperature Non-uniformity and Longitudinal Heat Conduction effects have been analysed. The thermal performance deterioration of cross flow compact heat exchanger due to the combined effects LHC and FN is not always negligible, especially when the fluid capacity rate ratio of both fluids is equal to 1.0 and when the longitudinal heat conduction parameter(λ) is greater than 0.005. Using CFD, the various types of fins such as Offset Strip fins, Wavy fins, Rectangular fins, Triangular fins, Triangular and Rectangular perforated fins, which are widely used in aerospace industry, are analysed. The expressions provided for the heat transfer coefficient in terms of Colburn *j* factor and frication factor *f* allows the computation for all values of Reynolds number, including the laminar and turbulent regions for CHE design ranges. The above FEM results and CFD correlations can be used by heat exchanger designers and can reduce the number of tests and modification of the prototype to a minimum for similar applications.

NOMENCLATURE

A_w total solid elemental area available for longitudinal heat conduction, m^2
C $= mC_p$ fluid heat capacity rate, J/s K
c_p specific heat of the fluid at constant pressure, J/kg K
FN Flow Non uniformity case
f Fanning friction factor, dimensionless
h fin height, mm
I divisions in the x-direction (1,2,3 .....n)
j Colburn factor ($StPr^{2/3}$), dimensionless
J divisions in the y-direction (1,2,3 .....n)

l	offset strip/fin length, mm
L	pitch of fin waviness, mm
LHC	Longitudinal Heat Conduction case
m	mass flow rate, kg/s
Pr	Prandtl number, dimensionless
Re	Reynolds number, dimensionless
R	wavy fin curvature radius, mm
S_t	Stanton number, dimensionless
s	fin spacing, mm
TN	Temperature Non-uniformity
t	fin thickness, mm

GREEK SYMBOLS:

λ	longitudinal heat conduction parameter,, dimensionless
τ	conduction effect factor or correction factor, dimensionless

SUBSCRIPTS:
min – minimum
max - maximum

REFERENCES

[1] W.M. Kays and A.L. London, *Compact Heat Exchangers*, 3rd ed, McGraw-Hill, New York, 1984.
[2] G.D. Bahnke and C.P. Howard, The effect of longitudinal heat conduction on periodic-flow heat exchanger performance, *ASME J. of Engineering for Power*, vol. 86, pp. 105-121, 1964.
[3] R.K. Shah, A correlation for longitudinal heat conduction effects in periodic-flow heat exchangers, *ASME Journal of Engineering for Power*, vol. 97, Sec. A, pp 453-454, 1975
[4] R.K. Shah, A review of longitudinal wall heat conduction in recuperates, *J. of Energy, Heat and Mass Transfer*, vol.16, pp 15-25, 1994.
[5] J.P. Chiou, The effect of longitudinal heat conduction on cross flow heat exchanger, *ASME Journal of Heat Transfer*, vol.100, pp 346-351, 1978.
[6] Ch. Ranganayakulu, K.N. Seetharamu and K.V. Sreevatsan, The effects of longitudinal heat conduction in compact plate-fin and tube-fin heat exchangers using a finite element method, *Int. J. Heat Mass Transfer*, vol. 40, no. 6, pp 1261-1277, 1997.
[7] Ch. Ranganayakulu, K.N. Seetharamu and K.V. Sreevatsan, The effects of inlet fluid flow non-uniformity on thermal performance and pressure drops in cross flow plate-fin compact heat exchangers, *Int. J. of Heat Mass Transfer*, vol. 40, no. 1, pp 27-38, 1997.
[8] J.P. Chiou, Thermal performance deterioration in a cross flow heat exchanger due to the flow non uniformity, *ASME Journal of Heat Transfer*, vol.100, pp 580-587, 1978.
[9] S.C. Kranc, The effect of non-uniform water distribution on cooling tower performance, *J. Energy,* no.7, pp 636-639, 1983.
[10] Ch. Ranganayakulu and K.N. Seetharamu, The combined effects of inlet fluid flow non uniformity and temperature non uniformity on thermal performance of cross flow plate-fin heat exchanger, *Journal of Heat Mass Transfer (Warme und Stoffubertragung*), no. 32, pp 375-383, 1997.
[11] Ch. Ranganayakulu, K.N. Seetharamu, The combined effects of longitudinal heat conduction, flow non uniformity and temperature non uniformity in cross-flow plate-fin heat exchangers, *International journal of Comm. Heat Mass Transfer* 26, 669-678, 1999.
[12] J.P. Chiou, The advancement of compact heat exchanger theory considering the effects of longitudinal heat conduction and flow non uniformity effects, In 'Compact Heat Exchangers -

History, Technological Advancement and Mechanical Design Problems, Edited by Shah. R.K et al, *ASME*, New York, pp 101- 121, 1980.

[13] Ch. Ranganayakulu and K.N. Seetharamu, The combined effects of longitudinal Heat Conduction and inlet fluid flow maldistribution in cross flow plate-fin heat exchangers, *Journal of Heat Mass Transfer*, No. 36, pp 247-256, 2000.

[14] Ranganayakulu C., Seetharamu K.N., The Combined Effects of Inlet Flow Non-uniformity and Temperature Non-uniformity on Thermal Performance of Cross Flow Plate-Fin Heat Exchanger, *International Journal of Warme und Stoffubertragung*, 32, 375-383, 1997.

[15] Sheik Ismail L, Ranganayakulu C, Shah Ramesh K, Numerical study of flow patterns of compact plate-fin heat exchangers and generation of design data for offset and wavy fins, *International Journal of Heat and Mass Transfer*, 52, pp. 3972-3983, 2009.

[16] Pallavi P, Ranganayakulu C., Development of Heat Transfer coefficient and Friction factor correlations for Offset fins using CFD, *Int. Journal of Numerical Methods for Heat and Fluid Flow,* Volume 21, No. 8, pp. 935-951, 2011.

[17] C. Ranganayakulu, "Steady state and transient analysis of Compact plate fin heat exchanger fins for generation of design data using CFD", *International J of Numerical Methods for Heat & Fluid Flow,* vol. 26, Iss:2, pp:440-460, 2016.

[18] Bala Sundar Rao R, Ranganath G, Ranganayakulu C, Development of Colburn 'j' factor and fanning friction factor 'f' correlations for compact heat exchangers plain fins by using CFD, *Journal of Heat Mass Transfer*, Volume 49(7), pp. 991-1000, 2013.

[19] R. Bala Sundar Rao, G. Ranganath, C. Ranganaykulu, Development of Colburn 'j' factor and fanning friction factor 'f' correlations for compact surfaces of the triangular perforated fins using CFD, *International Journal of Heat Transfer Engineering*, Volume 37, Issue 2, pp 150-161, 2016.

[20] K V Ramana Murthy, C. Ranganayakulu, T P Ashok Babu, Development of Heat Transfer Coefficient and Friction Factor Correlations for Serrated Fins in Water Medium using CFD, *International Journal of Physical Science and Application,* 5(3), 238-248, doi:10.17265/2159-5348/2015/03.006, 2015.

[21] Amaranatha Raju. Muppala, Ashok Babu T.P, Ranganayakulu C., Development of single phase heat transfer correlations for water and R134a in rectangular channel with smooth wavy fin, *International Journal of Physical Science and Application*, 5(3), 199-208, doi:10.17265/2159-5348/2015/03.006, 2015.

Fourth International Conference on Computational Methods for Thermal Problems
THERMACOMP2016, July 6-8, 2016, Georgia Tech, Atlanta, USA
N. Massarotti, P. Nithiarasu and Y. Joshi (Eds.)

SIMULATION OF GAS FOCUSED LIQUID JETS BY THE METHOD OF REGULARIZED SOURCES

Božidar Šarler
Institute of Metals and Technology, Lepi pot 11, SI-1000 Ljubljana, Slovenia; University of Nova Gorica, Vipavska 13, 5000 Nova Gorica, Slovenia, bozidar.sarler@imt.si

Rizwan Zahoor
University of Nova Gorica, Vipavska 13, 5000 Nova Gorica, Slovenia, rizwan.zahoor@imt.si

Ming Li
College of Mathematics, Taiyuan University of Technology, Yingze West Street 79, 030024, Taiyuan, China, liming04@gmail.com

Kenneth R. Beyerlein
Center for Free Electron Laser Sciences, Deutsches Elektronen-Synchrotron, Notkestraβe 85, 22607, Hamburg, Germany, kenneth.beyerlein@desy.de

Henry N. Chapman
Center for Free Electron Laser Sciences, Deutsches Elektronen-Synchrotron, Notkestraβe 85, 22607, Hamburg, Germany; Department of Physics, University of Hamburg, Lurper Chaussee 149, 22607, Hamburg, Germany; Center for Ultrafast Imaging, Notkestraβe 85, 22607, Hamburg, Germany, henry.chapman@desy.de

Saša Bajt
Photon Science, Deutsches Elektronen-Synchrotron, Notkestraβe 85, 22607, Hamburg, Germany, sasa.bajt@desy.de

ABSTRACT

The paper describes basic elements of a novel boundary meshless simulation approach for designing nozzles for gas-focused micro-jets [1], used for delivering samples in femtosecond crystallography experiments [2]. The recently developed axisymmetric version of the method of regularized sources (MRS) [3] is used for solving incompressible free boundary Stokes flow problem, associated with the gas focusing of micro-jets. The nodes are put on the boundary of the gas and liquid and the solution is sought as a linear combination of the fields due to the regularized axisymmetric sources in the boundary nodes. The intensity of the regularized sources in the nodes is adjusted to comply with the flow magnitude as prescribed by the boundary conditions. Artificial boundary as encountered in the classical method of fundamental solutions (MFS) in not needed. The flow fields are calculated coupled for the gas and for the liquid regions. The interphase between the gas and the liquid is parametrised with its length. The shape of the free boundary is adjusted based on the normal stress balance equilibrium which takes into account the surface tension and the curvature. The redistribution of the boundary nodes and smoothing of the boundary shape [4] is needed during this procedure. The procedure allows for efficient calculation of the jet shape as a function of the nozzle geometry, gas and liquid process parameters and material properties.

Key Words: *Stokes Flow, Method of Regularized Sources, Gas Focused Micro Jets, Femtosecond Crystallography.*

1. INTRODUCTION

Serial femtosecond crystallography (SFX) using X-ray Free-Electron Lasers (XFELs) allows for room temperature protein structure determination without evidence of conventional radiation damage. In this method, a liquid suspension of protein microcrystals can be delivered to the X-ray beam in vacuum as a micro-jet, which replenishes the crystals at a rate that exceeds the current XFEL pulse repetition rate. Gas dynamic virtual nozzles (see Fig. 1) produce the required micrometer-sized streams by the focusing action of a coaxial sheath gas and have been

shown to be effective for SFX experiments. Here, we describe a boundary meshless numerical approach for design and characterization of such nozzles.

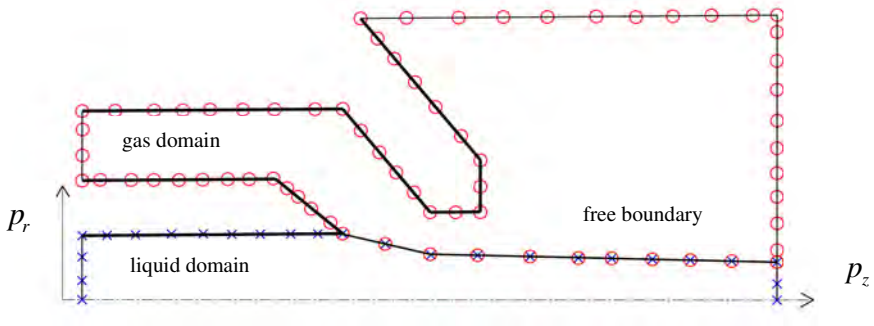

FIGURE 1. Scheme of the gas focused nozzle with the boundary meshless discretisation schematics. o – gas noides, x – liquid nodes.

2. GOVERNING EQUATIONS

Consider a fixed domain Ω with a boundary Γ filled with liquid ($\wp = l$) and gas ($\wp = g$) in contact over a not necessary connected free boundary Γ_{lg}. Both phases are considered to exhibit steady incompressible Stokes flow with constant viscosities μ_l and μ_g. The boundary value problem with a free liquid-gas surface is governed by the following set of equations for mass and momentum conservation, and the boundary conditions on the fixed boundary

$$\nabla \cdot \mathbf{v}_\wp(\mathbf{p}) = 0, \quad -\nabla P_\wp(\mathbf{p}) + \mu_\wp \nabla^2 \mathbf{v}(\mathbf{p}) + \mathbf{f}_\wp(\mathbf{p}) = 0, \ \wp = l, g, \tag{1,2}$$

$$v_{\wp\varsigma}(\mathbf{p}) = \overline{v}_{\wp\varsigma}(\mathbf{p}); \mathbf{p} \in \Gamma^D_{\wp\varsigma}, \qquad \partial v_{\wp\varsigma} / \partial p_\xi(\mathbf{p}) = \overline{v}_{\wp\varsigma\xi}(\mathbf{p}); \mathbf{p} \in \Gamma^N_{\wp\xi\varsigma}, \ \wp = l, g. \tag{3,4}$$

where $\mathbf{p}$ represents the position vector, $\mathbf{v}$ is the velocity, P is the pressure, μ is the viscosity, $\mathbf{f}$ is the body force, Γ^D_ς is the Dirichlet part of the boundary for the coordinate ς, $\Gamma^N_{\varsigma\xi}$ is the Neumann part of the boundary for the coordinate ς and the derivative over the coordinate ξ. $\overline{v}_\varsigma$ and $\overline{v}_{\varsigma\xi}$ stand for the known boundary conditions forcing functions. The interphase boundary conditions for the free surface between immiscible fluids at $\mathbf{p} \in \Gamma_{lg}$ with normal $\mathbf{n}_l$ and tangent $\mathbf{t}_l$ on the liquid phase are

$$\mathbf{v}_l(\mathbf{p}) - \mathbf{v}_g(\mathbf{p}) = 0, \quad \mathbf{t}_l \cdot \left[\mu_l \nabla^2 \mathbf{v}_l(\mathbf{p}) - \mu_g \nabla^2 \mathbf{v}_g(\mathbf{p})\right] \cdot \mathbf{n}_l = 0, \tag{5,6}$$

$$-P_l(\mathbf{p}) + P_g(\mathbf{p}) + \mathbf{n}_l \cdot \left[\mu_l \nabla^2 \mathbf{v}_l(\mathbf{p}) - \mu_g \nabla^2 \mathbf{v}_g(\mathbf{p})\right] \cdot \mathbf{n}_l = \sigma\kappa, \tag{7}$$

with σ and κ standing for the surface tension and curvature, respectively. We seek the solution of the pressure and the velocity fields of the liquid and the gas in Ω and unknown parts of Γ as well as the position of the free boundary Γ_{lg}. Let us introduce the axisymmetric coordinate system $\mathbf{p} = p_r \mathbf{i}_r + p_z \mathbf{i}_z$ with the basis vectors $\mathbf{i}_\varsigma; \varsigma = r, z$ and the coordinates $p_\varsigma; \varsigma = r, z$. The axisymmetric coordinates and basis vectors are expressed by using the three dimensional Cartesian coordinate system $\mathbf{p} = p_x \mathbf{i}_x + p_y \mathbf{i}_y + p_z \mathbf{i}_z$ with the basis vectors $\mathbf{i}_\varsigma; \varsigma = x, y, z$ and the coordinates $p_\varsigma; \varsigma = x, y, z$ as $p_r = \left(p_x^2 + p_y^2\right)^{1/2}$, $p_z \equiv p_z$, $\varsigma, \xi = r, z$, $\mathbf{i}_r = \mathbf{i}_x \cos p_\varphi + \mathbf{i}_y \sin p_\varphi$; $p_\varphi = \arctan\left(p_y / p_x\right)$ $\mathbf{i}_z \equiv \mathbf{i}_z$. The governing equations are thus

$$\frac{v_{\wp r}}{p_r}+\frac{\partial v_{\wp r}}{\partial p_r}+\frac{\partial v_{\wp z}}{\partial p_z}=0\,,-\frac{\partial P}{\partial p_\varsigma}+\mu_\wp\left(\frac{1}{p_r}\frac{\partial v_{\wp\varsigma}}{\partial p_r}+\frac{\partial^2 v_{\wp\varsigma}}{\partial p_r^2}-\frac{v_{\wp\varsigma}}{p_r^2}+\frac{\partial^2 v_{\wp\varsigma}}{\partial p_z^2}\right)+f_{\wp\varsigma}=0;\wp=l,z,\ \varsigma=r,z,\ (8,9)$$

with $P_\wp=P_\wp(p_r,p_z)$, $\mathbf{v}_\wp(p_r,p_z)=v_{\wp r}\mathbf{i}_r+v_{\wp z}\mathbf{i}_z$, and in the b.c. (3,4,5,6,7) stand with $\varsigma,\xi=r,z$.

3. SOLUTION PROCEDURE

The Stokes flow solution at the point $\mathbf{p}$ around the source of the type $\mathbf{f}(\mathbf{p},\mathbf{s})=\mathbf{f}_{\,\varepsilon}\phi(\mathbf{p}-\mathbf{s})$ is at the point $\mathbf{s}$ given by $P(\mathbf{p},\mathbf{s})=\mathbf{f}\cdot\nabla_\varepsilon\hat{\phi}(\mathbf{p}-\mathbf{s})$, $\mathbf{v}(\mathbf{p},\mathbf{s})=\left[(\mathbf{f}\cdot\nabla)\nabla_\varepsilon\hat{\hat{\phi}}(\mathbf{p}-\mathbf{s})-\mathbf{f}_{\,\varepsilon}\hat{\phi}(\mathbf{p}-\mathbf{s})\right]/\mu$, with $\nabla_\varepsilon\hat{\phi}={}_\varepsilon\phi$, and $\nabla_\varepsilon\hat{\hat{\phi}}={}_\varepsilon\hat{\phi}$. In the case that the Dirac delta function $\delta(\mathbf{p}-\mathbf{s})$ is selected for the function ${}_\varepsilon\phi(\mathbf{p}-\mathbf{s})$ these equations reduce to the well-known Stokes fundamental velocity and pressure. Consider a three-dimensional situation. Instead of selecting Dirac delta function for the source shape, a function, called the rational blob is introduced ${}_\varepsilon\phi(\mathbf{p}-\mathbf{s})=15\varepsilon^4\left(|\mathbf{p}-\mathbf{s}|^2+\varepsilon^2\right)^{-7/2}/8\pi$, $|\mathbf{p}-\mathbf{s}|^2=r^2=(p_x-s_x)^2+(p_y-s_y)^2+(p_z-s_z)^2$, where ε stands for the shape parameter. The function has the same strength as the Dirac delta function δ, i.e. $\int_\Omega\delta d\Omega=1$, $\int_0^\infty{}_\varepsilon\phi[r(\mathbf{p}-\mathbf{s})]4\pi r^2dr=1;\ r\in 3D$, and approaches the Dirac delta function when $\varepsilon\to 0$. The derivation of formulas for axisymmetry and rational blob is given in [3]. The related equations in axisymmetry read as

$$P_\wp(\mathbf{p})=c_{\wp r}(\mathbf{p},\mathbf{s})f_{\wp r}(\mathbf{s})+c_{\wp z}(\mathbf{p},\mathbf{s})f_{\wp z}(\mathbf{s}),\qquad v_{\wp\varsigma}(\mathbf{p})=c_{\wp\varsigma r}(\mathbf{p},\mathbf{s})f_{\wp r}(\mathbf{s})+c_{\wp\varsigma z}(\mathbf{p},\mathbf{s})f_{\wp z}(\mathbf{s});\varsigma=r,z,\ (10,11)$$

with the expressions for $c_{\wp rr}$, $c_{\wp rz}$, $c_{\wp zr}$, $c_{\wp zr}$, $c_{\wp r}$ and $c_{\wp z}$ explicitly given in [3]. The boundary of the liquid and gas domains is discretized with the collocation points $\mathbf{p}_{\wp n};n=1,2,...,N_\wp$, where the de-singularized sources with $\mathbf{s}_{\wp n}=\mathbf{p}_{\wp n}$ and $\varepsilon=\varepsilon(\mathbf{s}_{\wp n})$ are positioned. N_{lg} points of the liquid and of the gas are positioned on the free interface. The unknown forces $f_{\wp r}(\mathbf{s})$ and $f_{\wp z}(\mathbf{s})$ in the source points in phase $\wp$ are determined from $2N_\wp\times 2N_\wp$ system of linear equations in such a way that the boundary conditions are satisfied. The systems of equations for the gas and the liquid are

$$\mathbf{A}_\wp\mathbf{x}_\wp=\mathbf{b}_\wp,\ A_{\wp jn}x_{\wp n}=b_{\wp j};\ j=1,2,...,2N,n=1,2,...,2N,\qquad x_{\wp 2n-1}=f_{\wp r}(\mathbf{s}_n),\ x_{\wp 2n}=f_{\wp z}(\mathbf{s}_n)\ (12,13)$$

$$\begin{aligned}
A_{\wp(2j-1)(2n-1)}&=\Upsilon^D_{\wp r}(\mathbf{p}_j)c_{\wp rr}(\mathbf{p}_j,\mathbf{s}_n)+\Upsilon^N_{\wp rr}(\mathbf{p}_j)c_{\wp rr,r}(\mathbf{p}_j,\mathbf{s}_n)+\Upsilon^N_{\wp rz}(\mathbf{p}_j)c_{\wp rr,z}(\mathbf{p}_j,\mathbf{s}_n),\\
A_{\wp(2j-1)(2n)}&=\Upsilon^D_{\wp r}(\mathbf{p}_j)c_{\wp rz}(\mathbf{p}_j,\mathbf{s}_n)+\Upsilon^N_{\wp rr}(\mathbf{p}_j)c_{\wp rz,r}(\mathbf{p}_j,\mathbf{s}_n)+\Upsilon^N_{\wp rz}(\mathbf{p}_j)c_{\wp rz,z}(\mathbf{p}_j,\mathbf{s}_n),\\
A_{\wp(2j)(2n-1)}&=\Upsilon^D_{\wp z}(\mathbf{p}_j)c_{\wp zr}(\mathbf{p}_j,\mathbf{s}_n)+\Upsilon^N_{\wp zr}(\mathbf{p}_j)c_{\wp zr,r}(\mathbf{p}_j,\mathbf{s}_n)+\Upsilon^N_{\wp zz}(\mathbf{p}_j)c_{\wp zr,z}(\mathbf{p}_j,\mathbf{s}_n),\\
A_{\wp(2j)(2n)}&=\Upsilon^D_{\wp z}(\mathbf{p}_j)c_{\wp zz}(\mathbf{p}_j,\mathbf{s}_n)+\Upsilon^N_{\wp zr}(\mathbf{p}_j)c_{\wp zz,r}(\mathbf{p}_j,\mathbf{s}_n)+\Upsilon^N_{\wp zz}(\mathbf{p}_j)c_{\wp zz,z}(\mathbf{p}_j,\mathbf{s}_n),
\end{aligned}\ (14)$$

$$\begin{aligned}
b_{\wp 2j-1}&=\Upsilon^D_{\wp r}(\mathbf{p}_j)\overline{v}_{\wp r}(\mathbf{p}_j)+\Upsilon^N_{\wp rr}(\mathbf{p}_j)\overline{v}_{\wp rr}(\mathbf{p}_j)+\Upsilon^N_{\wp rz}(\mathbf{p}_j)\overline{v}_{\wp rz}(\mathbf{p}_j),\\
b_{\wp 2j}&=\Upsilon^D_{\wp z}(\mathbf{p}_j)\overline{v}_{\wp z}(\mathbf{p}_j)+\Upsilon^N_{\wp zr}(\mathbf{p}_j)\overline{v}_{\wp zr}(\mathbf{p}_j)+\Upsilon^N_{\wp zz}(\mathbf{p}_j)\overline{v}_{\wp zz}(\mathbf{p}_j).
\end{aligned}\ (15)$$

The following b.c. indicators were introduced for expressing the system (12) in a compact form

$$\Upsilon^{D}_{\wp\varsigma}(\mathbf{p})=\begin{cases}1;\mathbf{p}\in\Gamma^{D}_{\wp\varsigma}\\0;\mathbf{p}\notin\Gamma^{D}_{\wp\varsigma}\end{cases};\varsigma=r,z,\ \Upsilon^{N}_{\wp\varsigma\xi}(\mathbf{p})=\begin{cases}1;\mathbf{p}\in\Gamma^{N}_{\wp\varsigma\xi}\\0;\mathbf{p}\notin\Gamma^{N}_{\wp\varsigma\xi}\end{cases};\varsigma,\xi=r,z\,.$$

(16)

The two systems of equations are joined together in one system $\mathbf{A}\mathbf{x}=\mathbf{b}$ of the dimension $\left(2N_l+2N_g-2N_{\mathrm{lg}}\right)\times\left(2N_l+2N_g-2N_{\mathrm{lg}}\right)$, by equating the gas velocity on the interphase boundary with the liquid velocity. The solution of the joined system of equations gives an exact fulfillment of the boundary conditions and interphase conditions (5,6), however not interphase condition (7). Respectively, an iterative solution procedure for adjustment of the position of the free boundary position is needed. The description of the procedure is elaborated in [4], and involves representation of the position of the interphase boundary by the radial basis functions, parametrisation of its shape and equidistant repositioning of the nodes as well as smoothing of the interphase boundary during iterations. The iterations are stopped after the condition (7) is reasonably fulfilled. The final discrete approximate solution to the problem in both phases is

$$P_{\wp}(\mathbf{p})=\sum_{n=1}^{N_{\wp}}\left[c_{\wp r}(\mathbf{p},\mathbf{s}_n)f_{\wp r}(\mathbf{s}_n)+c_{\wp z}(\mathbf{p},\mathbf{s}_n)f_{\wp z}(\mathbf{s}_n)\right],$$

(17)

$$v_{\wp\varsigma}(\mathbf{p})=\sum_{n=1}^{N_{\wp}}\left[c_{\wp\varsigma r}(\mathbf{p},\mathbf{s}_n)f_{\wp r}(\mathbf{s}_n)+c_{\wp\varsigma z}(\mathbf{p},\mathbf{s}_n)f_{\wp z}(\mathbf{s}_n)\right];\wp=s,l;\varsigma=r,z\,.$$

(18)

4. CONCLUSIONS

The represented axisymmetric MRS for Stokes flow problems is a very simple, integration-free and efficient, boundary meshless method of the MFS type without artificial boundary. The solution is constructed through the superposition of the exact solutions due to the regularized sources placed on the physical boundary as well as the free boundary of the problem. The method is in this paper for the first time formulated for solving free boundary problems. A detailed assessment of the method and the related gas focused liquid jet simulations will be shown at the conference.

REFERENCES

[1] K.R. Beyerlein, L. Adriano, M. Heymann, R. Kirian, J. Knoška, F. Wilde, H.N. Chapman and S. Bajt, Ceramic micro-injection molded nozzles for serial femtosecond crystallography sample delivery, *Review of Scientific Instruments*, 86, 125104, 2015.

[2] H.N. Chapman, P. Fromme, A. Barty, T. White, R.A. Kirian, A. Aquila, M. Hunter, J. Schulz, D.P. DePonte, U. Weierstall, B. Doak, F.R.N.C. Maia, A. Martin, I. Schlichting, L. Lomb, N. Coppola, R.L. Shoeman, S. Epp, R. Hartmann, D. Rolles, A. Rudenko, L. Foucar, N. Kimmel, G. Weidenspointner, P. Holl, M. Liang, M. Barthelmess, C. Caleman, S. Boutet, M.J. Bogan, J. Krzywinski, C. Bostedt, S. Bajt, L. Gumprecht, B. Rudek, B. Erk, C. Schmidt, A. Hömke, C. Reich, D. Pietschner, L. Strüder, G. Hauser, H. Gorke, J. Ullrich, S. Herrmann, G. Schaller, F. Schopper, H. Soltau, K.U. Kühnel, M. Meserschmidt, J. Bozek, S.P. Hau-Riege, M. Frank, C. Y. Hampton, R. Sierra, D. Starodub, G. Williams, J. Hajdu, N. Timneanu, M.M. Seibert, J. Andreasson, A. Rocker, O. Jönsson, S. Stern, K. Nass, R. Andritschke, C.-D. Schröter, F. Krasniqi, M. Bott, K. Schmidt, X. Wang, I. Grotjohann, J. Holton, S. Marchesini, S. Schrob, D. Rupp, M. Adolph, T. Gorkhover, H. Hirsemann, G. Potdevin, H. Graafsma, B. Nilsson, and J. C. H. Spence, Femtosecond x-ray protein nanocrystallography, *Nature*, 470, 78-81, 2011.

[3] W. Kai, S. Wen, R. Zahoor, M. Li and B. Šarler, Method of regularized sources for axisymmetric Stokes flow problems, *International Journal for Numerical Methods in Heat & Fluid Flow*, 26, 1226-1239, 2016.

[4] B. Šarler, Solution of a two dimensional bubble shape in potential flow by the method of fundamental solutions, *Engineering Analysis with Boundary Elements,* 30, 227-235, 2006.

Fourth International Conference on Computational Methods for Thermal Problems
THERMACOMP2016, July 6-8, 2016, Georgia Tech, Atlanta, USA
N. Massarotti, P. Nithiarasu and Y. Joshi (Eds.)

NUMERICAL SIMULATION OF NEAR-FIELD RADIATIVE HEAT TRANSFER BETWEEN NANOSTRUCTURES

Zhuomin Zhang,* Xianglei Liu
George W. Woodruff School of Mechanical Engineering
Georgia Institute of Technology, Atlanta, GA 30332, USA
*zhuomin.zhang@me.gatech.edu

ABSTRACT

When two or more bodies at different temperatures are brought sufficiently close to each other with vacuum gap spacing smaller than the characteristic thermal wavelength, near-field radiative heat flux can exceed the far-field blackbody limit, governed by the well-known Stefan-Boltzmann law, by orders of magnitude. As a result, new routes for efficient thermal management and energy harvesting are opened. Artificial nanostructures have attracted much attention in the field of both photonics and phononics due to their unprecedented radiative and thermal properties beyond the capabilities of bulks. Advanced theoretical developments for nanostructures are critically presented, such as analytical effective medium theory and its quantitative application condition, semi-analytical scattering theory based on rigorous coupled wave analysis, and exact numerical methods for calculating near-field radiative transfer between arbitrary particles or periodic nanostructures based on Langevin approach, fictitious surface current, and discrete dipoles approximations. Some recent results from our group are also discussed.

Key Words: *Near-field thermal radiation, thermal fluctuation, nanostructures*

1. INTRODUCTION

Thermal emission of macroscale objects is governed by the Stefan-Boltzmann law for the total emissive power and by Planck's law for spectral emission, modified by the corresponding surface emissivity. At the micro- and nanoscales, when the geometric dimension is comparable to the characteristic wavelength of thermal radiation ($\lambda_{\mathrm{Th}} = \hbar c / k_{\mathrm{B}} T$), wave interference and photon tunneling must be considered and the resulting radiative energy exchange can greatly exceed the limit set by blackbodies [1-4]. The fluctuation-dissipation theorem (FDT) attributes the origin of thermal emission to the random motion of charges, which in turn, produces a fluctuating current [5]. While the time average of the electromagnetic field due to the randomly fluctuating current is zero, the energy density can be very high near the surface and the Poynting vector depends on the correlation of the fluctuating currents. When two objects are placed in close proximity, evanescent waves with large wavevectors can tunnel through the space that separates the objects. This provides additional modes or heat transfer channels beyond what are available between objects placed far apart. Here, we give a brief survey and update of the recent theoretical and computational progress of near-field thermal radiation between nanostructures and discuss some interesesting results obtained from our group.

2. NUMERICAL METHODS

2.1. Radiation Formula between Anisotropic Materials of Arbitrary Shapes

Thermal radiation is originated from fluctuating currents due to thermal motion of charge carriers as shown in Fig. 1. Fortunately, these chaos like fluctuating currents can be quantified in

terms of the optical response of emitters . For an anisotropic, local, and nonmagnetic medium with time-reversal symmetry at local thermal equilibrium, the correlation function of fluctuating currents can be expressed as [5]

$$\left\langle J_i(\mathbf{r},\omega)J_k^*(\mathbf{r}',\omega')\right\rangle = \frac{4\omega\varepsilon_0\Theta(\omega,T)\varepsilon_{ik}''(\mathbf{r},\omega)}{\pi}\delta(\mathbf{r}-\mathbf{r}')\delta(\omega-\omega') \tag{1}$$

where subscripts *i* or *k* refer to the vector component, Θ is the mean energy of a Planck oscillator, ε_0 is the vacuum permittivity, ε_{ik}'' is the imaginary part of the dimensionless dielectric tensor component, and $\delta(\mathbf{r}-\mathbf{r}')$ or $\delta(\omega-\omega')$ is the Dirac delta function indicating spatial or temporal incoherence, respectively. The electric and magnetic fields are related to the fluctuating currents by corresponding dyadic Green function $G^{E,H}$ .The near-field radiative heat flux between two anisotropic media, at temperatures of T_1 and T_2, respectively, separated by a vacuum spacing as illustrated in Fig. 1 is given as [3]

$$q = \frac{2k_0^2}{\pi}\int_0^\infty\left[\Theta(\omega,T_1)-\Theta(\omega,T_2)\right]d\omega\int_{V'}\mathrm{Re}\left[j\sum_{i,k=x,y,z}\varepsilon_{ik}''(\omega)(G_{xi}^E G_{yk}^{H*}-G_{yi}^E G_{xk}^{H*})\right]dV' \tag{2}$$

Note that Eq. (2) is generic and can be applied to metamaterials with arbitrary non-magnetic dielectric functions and shapes. For more general anisotropic materials with a non-unity permeability tensor, an extra term similar to Eq. (1) but with permittivity tensor changed to be corresponding permeability without correlations between electric and magnetic currents should be added into the right side of Eq. (1). As a result, magnetic metamaterials will provide an extra channel taking into account magnetic surface plasmon resonance associated with transverse electric waves for radiative energy exchange. Nevertheless, the calculation of the dyadic Green function for arbitrary geometry though possible with available numerical methods is usually nontrivial and time prohibitive. Different methods including analytical, semi-analytical, and numerical techniques are critically discussed.

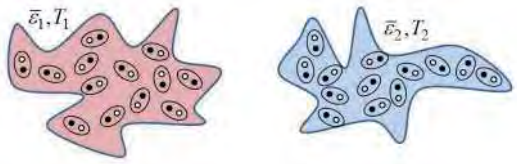

Fig. 1 Near-field thermal radiation between anisotropic materials with arbitrary shapes.

2.2. Effective Medium Theory and Its Quatitative Application Condition

Artificial metamaterials can be effectively treated as anisotropic and homogeneous in the long-wavelength limit. This homogenization method combined with fluctuational electrodynamics has been widely used to predict the near-field heat flux between subwavelength metamaterials due to its simplicity and low computational demand . For effectively anisotropic materials, *q* can be expressed analytically based on *k*-space integration according to the scattering theory

$$q = \frac{1}{8\pi^3}\int_0^\infty\left[\Theta(\omega,T_1)-\Theta(\omega,T_2)\right]d\omega\int_0^\infty\int_0^\infty\xi(\omega,k_x,k_y)dk_x dk_y \tag{3}$$

where k_x and k_y are the transverse wavevector in *x* and *y* direction, respectively, and $\xi(\omega,k_x,k_y)$ is called the energy transmission coefficient or photon tunneling probability, and is given as

$$\xi(\omega,k_x,k_y) = \begin{cases}\mathrm{Tr}\left[(\mathbf{I}-\mathbf{R}_2^*\mathbf{R}_2)\mathbf{D}(\mathbf{I}-\mathbf{R}_1\mathbf{R}_1^*)\mathbf{D}^*\right], & \beta < k_0\\ \mathrm{Tr}\left[(\mathbf{R}_2^*-\mathbf{R}_2)\mathbf{D}(\mathbf{R}_1-\mathbf{R}_1^*)\mathbf{D}^*\right]e^{-2|k_{z0}|d}, & \beta > k_0\end{cases} \tag{4}$$

where $\beta = \sqrt{k_x^2 + k_y^2}$ is the magnitude of the lateral wavevector, d is the vacuum gap between the two semi-infinite media, and $k_{z0} = \sqrt{k_0^2 - \beta^2}$ is the z-component wavevector in the vacuum. When $\beta > k_0$, k_{z0} is purely imaginary and photon tunneling can occur at close proximity, resulting in significant enhancement of radiative transfer especially when surface modes or hyperbolic modes exist. $\mathbf{R}_1$ and $\mathbf{R}_2$ are the 2 × 2 Fresnel's reflection matrix for incidence from the vacuum to medium i = 1 or 2.

Although EMT has been extensively used to obtain the first-hand near-field heat flux predictions, it is still unclear that under what conditions the results are reliable. Liu et al. [6] based on 90% confidence gave explicit formulas of the cutoff wavevectors for surface and hyperbolic modes described as $2.55/(\varepsilon''^{0.21}d)$ and $1.94/d$, respectively. Combined with Bloch theory, they provided a quantitative validity criterion of applying EMT for predicting near-field heat flux between multilayered metamaterials. Similar derivations might be extended to other 2D or 3D nanostructures.

2.3. Scattering Theory Based on Rigorous Coupled-Wave Analysis (RCWA)

Bimonte and Santamato [7] related the fluctuating electromagnetic fields outside a hot surface at thermal equilibrium to only its scattering properties such as reflection coefficients. As a result, the heat transfer between two nonequilibrium objects can be predicted based only on their scattering coefficients since objects radiate independently. The formula for near-field heat transfer between two 1D gratings is given as [8]

$$q = \frac{1}{2\pi^3}\int_0^\infty \left[\Theta(\omega,T_1) - \Theta(\omega,T_2)\right] d\omega \int_0^{\pi/p}\int_0^\infty \xi\left(\omega,k_x,k_y\right) dk_x dk_y \tag{5}$$

where p is the period in the x direction, and the k_x is folded into the first Brillouin zone. The energy transmission coefficient $\xi\left(\omega,k_x,k_y\right)$ is given as

$$\xi\left(\omega,k_x,k_y\right) = \mathrm{Tr}\left(\mathbf{D}\mathbf{W}_1\mathbf{D}^\dagger\mathbf{W}_2\right) \tag{6a}$$

$$\mathbf{D} = \left(\mathbf{I} - \mathbf{S}_1\mathbf{S}_2\right)^{-1} \tag{6b}$$

$$\mathbf{W}_1 = \sum\nolimits_{-1}^{\mathrm{pw}} - \mathbf{S}_1 \sum\nolimits_{-1}^{\mathrm{pw}} \mathbf{S}_1^\dagger + \mathbf{S}_1 \sum\nolimits_{-1}^{\mathrm{ew}} - \sum\nolimits_{-1}^{\mathrm{ew}} \mathbf{S}_1^\dagger \tag{6c}$$

$$\mathbf{W}_2 = \sum\nolimits_{1}^{\mathrm{pw}} - \mathbf{S}_2^\dagger \sum\nolimits_{1}^{\mathrm{pw}} \mathbf{S}_2 + \mathbf{S}_2^\dagger \sum\nolimits_{1}^{\mathrm{ew}} - \sum\nolimits_{1}^{\mathrm{ew}} \mathbf{S}_2 \tag{6d}$$

where $\mathbf{S}_1 = \mathbf{R}_1$ and $\mathbf{S}_2 = e^{ik_{z0}d}\mathbf{R}_2 e^{ik_{z0}d}$. Here, $\mathbf{R}_1$ and $\mathbf{R}_2$ are the reflection matrices for medium 1 and medium 2 that are obtained by using the rigorous coupled-wave analysis (RCWA). The basic idea is that the fields for homogenous layer and grating region are written as Rayleigh expansions and Fourier series, respectively. Employing boundary conditions by making tangential fields equal will help to obtain every unknown Rayleigh term which constitutes $\mathbf{R}_1$ and $\mathbf{R}_2$. Operators $\sum_{-1(1)}^{\mathrm{pw(ew)}}$ identify propagating and evanescent modes. This is a k-space method based on the scattering theory, and is mainly for 1D periodic photonic crystals. It can be extended for arbitrary 2D periodic or aperiodic metamaterials though the memory requirement will arise tremendously.

2.4. Langevin Approach based on Monte Carlo or Wiener Chaos expansion

Based on Langevin approach, a fluctuating term is added to Newton's equation of motion, which can be solved directly to get the radiative heat flux [9]. Treating charge carriers as damped harmonic oscillators driven by an external field **E** and a random force representing uncorrelated thermal fluctuations, the polarization equation can be expressed as [9].

$$\frac{d^2\mathbf{P}}{dt^2}+\gamma\frac{d\mathbf{P}}{dt}+\omega_0^2\mathbf{P}=\sigma\mathbf{E}+\mathbf{K}(t) \tag{7}$$

where **P** is the polarization, γ is the frictional coefficient, ω_0 is the resonance frequency, σ is the strength related to conductivity, and **K** is the random force term. The correlation function of **K** can be found by combining Eq. (1) with Fourier transform into time-domain. Though volume integration is circumvented, this is a statistical method (Monte Carlo) using randomly generated current distributions, and the obtained heat flux should be ensemble averaged over many (such 50) independent simulations until the solution converges [10]. Alternatively, based on Wiener chaos expansion theory, the fluctuation current can be decomposed as $J(\mathbf{r},\omega)=\sqrt{4\omega\Theta\varepsilon_0(\omega,T)\varepsilon''(\omega)/\pi}\,dW(r)$, where $dW(r)$ is the frequency-independent white noise function satisfying $\langle dW(r)\rangle=0$ and $\langle dW(r)dW(r')\rangle=\delta(r-r')$ [11, 12]. Further, $dW(r)$ can be expressed as linear combination of orthogonal eigenmodes: $dW(r)=\sum_{n=1}^{\infty}j_n(\mathbf{r},\omega)$, where $j_n(\mathbf{r},\omega)$ can be found in Refs. [11, 12]. The correlation of fluctuating currents can thus be rearranged in the following:

$$\left\langle J_i(\mathbf{r},\omega)J_k^*(\mathbf{r}',\omega')\right\rangle=\frac{4\omega\varepsilon_0\Theta(\omega,T)\varepsilon''(\omega)}{\pi}\sum_{n=1}^{\infty}j_n(\mathbf{r},\omega)j_n^*(\mathbf{r}',\omega')\delta(\omega-\omega')\delta_{ik} \tag{8}$$

After adding $J(\mathbf{r},\omega)$ governed by Eq. (8) in the Maxwell equations, the original stochastic radiative heat transfer problem becomes a set of deterministic Maxwell equations. Many of the established numerical methods such as FDTD can be used to solve these partial differential equations. Liu and Shen [11] demonstrated that the convergence is rather fast for nanowires with the number of simulation times considering different modes much less than that based on the previously discussed FDTD method. Nevertheless, the number of modes required for convergence might rise quickly for irregular structures, metamaterials with large unit size, or composite metamaterials consisting of different materials as thermal sources.

2.5. Fictious Surface Current Method

Fictious surface current method is another approach mainly for 3D arbitrary particles which are characterized as surface meshes. Scattered fields are expressed using fictitious electric and magnetic currents determined by boundary conditions of continuous tangential fields crossing interfaces [13]. As a result, the volume integral generally needed can be replaced by surface integral of fictitious surface currents. The radiative heat flux finally can be written in an elegant basis-independent trace formula involving only standard matrixes which could be obtained by using boundary element method directly. Since incoming and outgoing waves don't need to be separated as the scattering theory does, this surface current based method can be well applied to interleaved bodies such as interlocked rings. The detailed introduction can be referred to Refs. [14-16].

2.6. Thermal Discrete Dipole Approximation

Edalatpour and Francoeur [17] reported a thermal discrete dipole approximation (TDDA) to predict the radiative heat transfer between 3D arbitrary particles. Both the receiver and emitter are discretized as cubic sub-volumes treated as electric dipoles with the effective moment obtained using Clausius-Mossotti model. This method is essentially an exact Green function method, and the accuracy depends on the number of dipoles used to approximate the particles. Though TDDA is a simple method to use, the requirement of memory will be high for metallic particles or particles with large aspect ratios. Besides, it is mainly for 3D particles, and how to extend it to periodic nanostructures has not been presented yet.

3. SELECTED RESULTS

3.1. Near-field Thermal Radiation between Metasurfaces

Metasurfaces, planar metamaterials with subwavelength thicknesses, have some peculiar advantages over conventional metamaterials, such as less volumetric propagation loss, relative easy fabrication, and compatible integration with other nanodevices. As shown in Fig. 2, patterning the film into 1D metasurface can enhance thermal radiation for all practical volume filling ratios. The gap distance is 100 nm, the thickness of metasurface is 400 nm, and T_1 = 310 K and T_2 = 290 K. Interestingly, while the 2D metasurface yields a radiative heat flux higher than that of thin films at moderate filling ratios, it does not support a heat flux as high as that of the 1D metasurface. The underlying mechanism of enhanced thermal radiation of metasurfaces lies in the support of hyperbolic dispersions leading to broadband high local density of states.

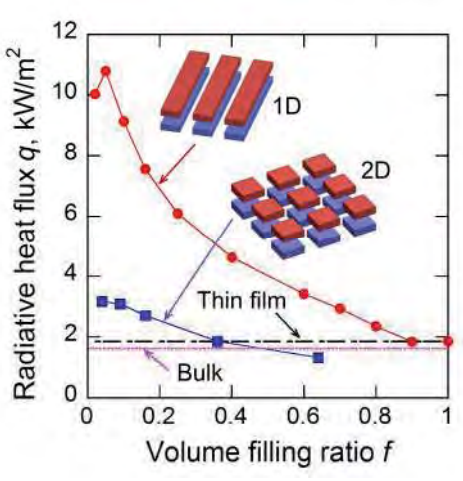

Fig. 2 Radiative heat flux between metasurfaces.

3.2. Giant Ehnacement of Thermal Radiation Based on Hyperbolic Graphene Plasmons

As shown in Fig. 3, the heat flux between graphene ribbons can be 15.3 times that between suspended graphene sheets at d = 15 nm and is more than 3 folds when d increases to 100 nm. This giant enhancement may offer possible benefits to energy harvesting of thermal radiation by increased heating rate capability, potential thermal management enhancements, and augmented noncontact temperature measurement. The underlying mechanism is due to the excitation of hyperbolic graphene plasmons featured with open dispersion relations and thus infinite density of states. The agreement between the numerically exact calculations with EMT is good especially for large gap spacings.

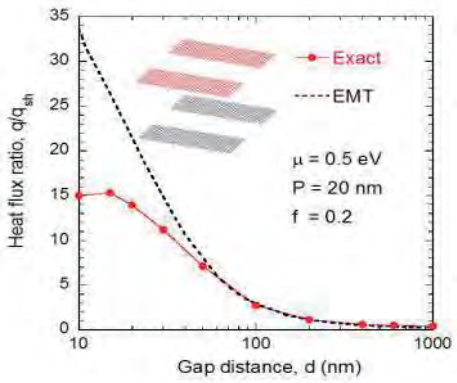

Fig. 3 Enhancement of radiative heat flux of graphene ribbon over graphene sheets. Here, T_1 = 310 K and T_2 = 290 K.

4. CONCLUSIONS

The recent theoretical and computational progress in near-field thermal radiation between nanostructures is briefly critically reviewed. Currently, the exact prediction of near-field radiative heat flux is attainable for general anisotropic materials, spheres, periodic metamaterials, and 3D arbitrary particles. Each method has its own advantages and limitations. The theoretical calculation for complex nanostructures is very time consuming considering that near-field heat flux is a broadband phenomenon and the radiation of each sub-volume needs to be considered separately. Therefore, faster and exact methods applicable to general metamaterials for predicting near-field heat flux are always desirable. High-performance computing techniques would be implemented for facilitating the numerical simulation of near-field thermal radiation. Exciting recent results from our group, such as 1D metasurface outperforming 2D metasurface and giant enhancement enabled by hyperbolic graphene plasmons, are discussed.

REFERENCES

[1] Zhang, Z. M., 2007, Nano/Microscale Heat Transfer. New York: McGraw-Hill.

[2] Joulain, K., Mulet, J. P., Marquier, F., Carminati, R., and Greffet, J. J., 2005, "Surface Electromagnetic Waves Thermally Excited: Radiative Heat Transfer, Coherence Properties and Casimir Forces Revisited in the Near Field," Surf. Sci. Rep., **57**, pp. 59-112.

[3] Liu, X. L., Wang, L. P., and Zhang, Z. M., 2015, "Near-Field Thermal Radiation: Recent Progress and Outlook," Nanoscale Microscale Thermophys. Eng., **19**, pp. 98-126.

[4] Xuan, Y., 2014, "An Overview of Micro/Nanoscaled Thermal Radiation and Its Applications," Photon. Nanostr. Fundam. Appl., **12**, pp. 93-113.

[5] Rytov, S. M., Kravtsov, Y. A., and Tatarskii, V. I., 1989, Principles of Statistical Radiophysics. New York: Springer.

[6] Liu, X. L., Bright, T. J., and Zhang, Z. M., 2014, "Application Conditions of Effective Medium Theory in Near-Field Radiative Heat Transfer between Multilayered Metamaterials," J. Heat Transfer, **136**, p. 092703.

[7] Bimonte, G. and Santamato, E., 2007, "General Theory of Electromagnetic Fluctuations near a Homogeneous Surface in Terms of Its Reflection Amplitudes," Phys. Rev. A, **76**, p. 013810.

[8] Guérout, R., Lussange, J., Rosa, F. S. S., Hugonin, J. P., Dalvit, D. a. R., Greffet, J. J., Lambrecht, A., and Reynaud, S., 2012, "Enhanced Radiative Heat Transfer between Nanostructured Gold Plates," Phys. Rev. B, **85**, p. 180301.

[9] Luo, C., Narayanaswamy, A., Chen, G., and Joannopoulos, J. D., 2004, "Thermal Radiation from Photonic Crystals: A Direct Calculation," Phys. Rev. Lett., **93**, p. 213905.

[10] Rodriguez, A. W., Ilic, O., Bermel, P., Celanovic, I., Joannopoulos, J. D., Soljačić, M., and Johnson, S. G., 2011, "Frequency-Selective Near-Field Radiative Heat Transfer between Photonic Crystal Slabs: A Computational Approach for Arbitrary Geometries and Materials," Phys. Rev. Lett., **107**, p. 114302.

[11] Liu, B. and Shen, S., 2013, "Broadband Near-Field Radiative Thermal Emitter/Absorber Based on Hyperbolic Metamaterials: Direct Numerical Simulation by the Wiener Chaos Expansion Method," Phys. Rev. B, **87**, p. 115403.

[12] Wen, S.-B., 2010, "Direct Numerical Simulation of Near Field Thermal Radiation Based on Wiener Chaos Expansion of Thermal Fluctuating Current," J. Heat Transfer, **132**, p. 072704.

[13] Reid, M. T. H., Rodriguez, A. W., and Johnson, S. G., 2013, "Fluctuation-Induced Phenomena in Nanoscale Systems: Harnessing the Power of Noise," Proceedings of the IEEE, **101**, pp. 531-545.

[14] Rodriguez, A. W., Reid, M. T. H., and Johnson, S. G., 2013, "Fluctuating-Surface-Current Formulation of Radiative Heat Transfer: Theory and Applications," Phys. Rev. B, **88**, p. 054305.

[15] Mccauley, A. P., Reid, M. T. H., Krüger, M., and Johnson, S. G., 2012, "Modeling Near-Field Radiative Heat Transfer from Sharp Objects Using a General Three-Dimensional Numerical Scattering Technique," Phys. Rev. B, **85**, p. 165104.

[16] Krüger, M., Bimonte, G., Emig, T., and Kardar, M., 2012, "Trace Formulas for Nonequilibrium Casimir Interactions, Heat Radiation, and Heat Transfer for Arbitrary Objects," Phys. Rev. B, **86**, p. 115423.

[17] Edalatpour, S. and Francoeur, M., 2014, "The Thermal Discrete Dipole Approximation (T-DDA) for near-Field Radiative Heat Transfer Simulations in Three-Dimensional Arbitrary Geometries," J. Quant. Spectrosc. Radiat. Transf., **133**, pp. 364-373.

MINI SYMPOSIA

MINI SYMPOSIUM

ELECTRONICS COOLING MODELING

MINI SYMPOSIUM ORGANISED BY KRISHNA KOTA

Fourth International Conference on Computational Methods for Thermal Problems
THERMACOMP2016, July 6-8, 2016, Georgia Tech, Atlanta, USA
N. Massarotti, P. Nithiarasu and Y. Joshi (Eds.)

Three computational methods for analysing thermal airflow distributions in the cooling of data centers.

Greg de Boer
Department of Aeronautics, Imperial College London, London, SW7 2AZ, UK,
g.de-boer@imperial.ac.uk

Nicolas Delbosc, Adam Johns, Daniel Burdett, Jon Summers
School of Mechanical Engineering, University of Leeds, LS2 9JT, UK,
{mnnd;A.Johns;mn09d3b;J.L.Summers}@leeds.ac.uk

Morgan Tatchell-Evans
School of Chemical and Process Engineering, University of Leeds, LS2 9JT, UK,
pm08mrte@leeds.ac.uk

ABSTRACT

This paper develops computational models to study thermal airflow distribution when cooling a data center. The thermal airflow distribution study employs three computational approaches, namely finite element, finite volume and lattice Boltzmann methods, which are respectively implemented via commercial Multiphysics software, opensource CFD code and home grown GPU based code. The results focus on comparison of the three methods, all of which include models for turbulence, when applied to 2 rows of racks with cool air supplied by a plenum. Advantages and disadvantages of the three computational methods are addressed in terms of application to thermal management of data centers.

Key Words: *Data center cooling, Lattice Boltzmann, Finite Elements, Finite Volume.*

1. INTRODUCTION

A data center hosts a large number of datacom systems, usually laid out in 2m tall racks. The expansive layout of datacom systems in a data center results in a distributed and dynamic generation of heat that needs to be transported by the air and rejected to the outside environment using heat exchangers and chillers. The global growth in the number and size of data centers means that they account for more than 1.5% of global electricity consumption and approximately 45% of this energy is used to remove the heat from the datacom systems [1]. Improvements in energy efficiency are now becoming important to reduce costs and environmental impact based on good practice [2].

Managing air distributions in data centers is one way to help reduce inefficiencies, and this can be aided by the application of Computational Fluid Dynamics (CFD) models, in which it is possible to predict the presence of hot spots for both new and upgraded data center layouts [3]. This in turn enables the air distribution to be optimised to minimise energy consumption whilst ensuring a suitable thermal environment is provided. CFD has been used successfully to investigate the impact of floor grilles [4], optimise placement of IT equipment [5] and study the effect of aisle containment [6]. The major challenges in producing accurate models are the multiple length-scales [3], from the chip to the room level, and the various modes of thermal transport and flow regimes [7].

CFD is an increasingly being applied to analyse air distributions in data centers as it offers a much greater resolution of data compared to most experimental approaches. However, there exist a range of modelling methods and software packages available for this task, each with individual advantages and disadvantages. This paper analyses the air flow through an simplified datacentre for

several different modelling strategies to identify the trade-offs between methodologies. The methods applied in this work are; i) a developed lattice Boltzmann method (LBM) GPU based program, ii) an opensource CFD finite volume method (FVM) based package OpenFOAM[1], and the commercial CFD finite element method (FEM) based software Comsol[2]. Previous studies have demonstrated through experimental validation that CFD models can accurately predict data centre air flows and thermal environments [4-7]; this work aims to demonstrate the range of numerical methods available which produce similar results to tried and tested methods.

2. MAIN BODY

The geometry of the data center is designed to allow for a simple implementation in each of the numerical methods considered while keeping most of the characteristics of a typical data center.

The data center floor space has a surface area of 28.8m^2, comprised of ten racks that are organised in two rows. The datacom units in the racks have the fronts facing each other making up the cold aisle in the center. Each rack is separated into two datacom units along the height, so that the digital workload between the top half and bottom half of the rack can differ. This is a simplification as a rack would normally be composed of many more datacom systems. A computer room air conditioner (CRAC) unit is placed in line with the cold aisle at one end of the data center, and feeds cool air into the plenum under the floor as depicted in Figure 1.

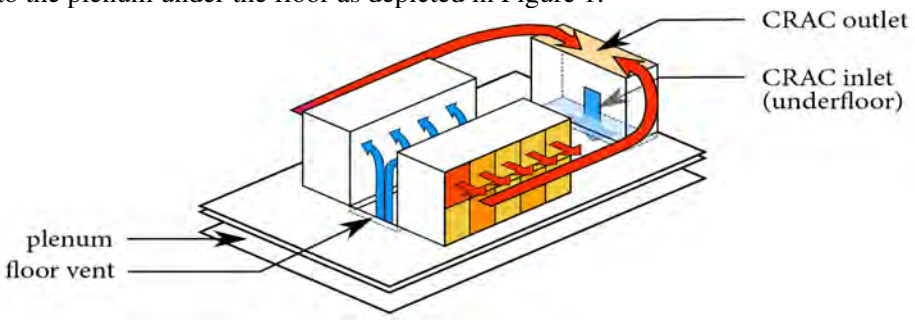

FIGURE 1. Schematic of the data center racks and the air flows.

The cold air is supplied to the room at a constant temperature of 289K and a constant flow rate of 1.134 m^3/s through the bottom of the CRAC unit, which coincides with the top of the plenum as indicated in the schematic of Figure 1. Cold air travels in the plenum and then enters the room through the floor vents, modelled here as open holes and located equidistant between the two rows of racks. This is a simplified model, as in reality the plenum is supported by an array of legs to support the floor of the data center, but also there will be cables and/or pipes that would noticeably affect the distribution of velocities arriving at the floor vent. Floor grilles are used and contain detailed features that straighten the flow and affect its momentum, and they can sometimes be oriented to change the angle of the flow to provide the cool air where it is required.

The air enters each datacom unit through their front-faces and exits from their back-faces after an increase in momentum and a rise in temperature. The volume flow rate through each datacom system, $Q_{datacom}$, as well as the temperature rise, $\Delta T_{datacom}$, are dependent on the datacom unit's

[1] www.openfoam.org

[2] www.comsol.com

power draw, $P_{datacom}$, since $P_{datacom} = \rho c_p Q_{datacom} \Delta T_{datacom}$. Therefore knowing the datacom unit's power demand and air flowrate yields a value of temperature difference between the front and the back of the unit. The inlet to each datacom system is an outlet of the data center domain and the outlet from each datacom system is an inlet to the data center domain. The boundary conditions on each datacom unit for both air flowrate and temperature are linked as described by Summers et al [8]. All other boundary conditions are set as no-slip for the flow and insulating for the temperature field. The air flowrates are such that a turbulence model is required in the simulations. For the FEM and FVM the flows are solved under steady state conditions and the Reynolds Averaged Navier-Stokes (RANS) is employed. Whereas the LBM is inherently transient and the turbulence is accounted for by the adoption of a Large Eddy Simulation (LES) approach.

3. RESULTS

To enable the comparison of the results between the three computational methods, the LBM results are required to be averaged over time, since these results are transient. This is achieved by averaging for 3 minutes (of physical time), starting after 2 minutes from an initial state of zero air velocity and a constant temperature everywhere in the room of 293K. Figure 2 demonstrates the temperature and velocity fields for all three methods: the temperature at the back of the datacom systems shows similar distributions, the cold air coming up through the floor vents rises to approximately 1.6m in height. The full paper will show that the hot air is projected out of the back of the datacom systems with similar angles and strengths, all of which indicate similar treatment of the buoyancy effects in each of the three computational approaches.

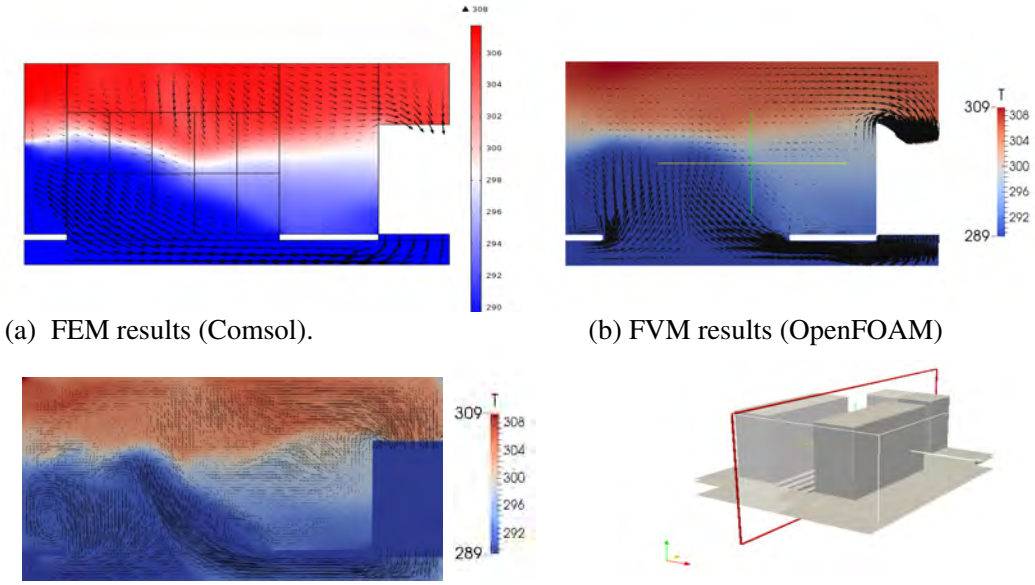

(a) FEM results (Comsol). (b) FVM results (OpenFOAM)

(b) LBM results (d) Geometrical position of cross section.

FIGURE 2.Velocity and temperature fields at the cross section depicted in (d) for the three methods.

A trend is confirmed by comparing the average temperature at each of the datacom inlets across the three computational approaches. For some datacom inlets all three methods give the same temperature within 1K, but for inlets of some datacom systems towards the center of the aisle, there is up to a 4K difference between the hottest and coldest prediction. Overall, the predicted

temperature at the datacom inlets agree well, but the LBM appears to give consistently a slightly higher temperature (by about 1 degree) than the other methods, this may be a side effect of using an LES turbulence model as opposed to the RANS model used for the FEM and FVM but is likely a result of the choice of the initial temperature. Each computational approach has its own performance constraints, levels of accuracy, stability and convergence conditions. The FEM solution required 403825 elements to meet a convergence criterion of 10^{-5} and took 52814 seconds to compute, the FVM solution required 1303093 cells to meet a convergence criterion of 10^{-5} and took 19996 seconds to compute. The LBM solution was computed on a regular grid composed of 753984 lattice points with a time-step of $5x10^{-3}$s and took 300 seconds to compute (i.e. real-time). While being the fastest method for the given resolution and time-step, the LBM displays spurious thermal fluctuations that appear as a chequerboard pattern and are due to numerical instabilities. This work is also able to highlight the computational performance of both the FVM and FEM as well as identifying further aspects of the modelling approach and assumptions that position these computational techniques as valuable tools for analysing thermal air management of data centers. The full paper discusses the trade-offs of each of the computational methods, time required to develop the model (or technical knowledge required to apply the software) and additional challenges of modelling data center airflows.

4. CONCLUSIONS

The simulation results of thermal air flows in data centers obtained with three computational methods demonstrate good agreement in terms of the overall flow structures and the average temperatures at each datacom inlet. The level of accuracy achieved by the FVM, the FEM and the LBM are similar. There are clear advantages of using the LBM in respect to computational performance and applicability for transient flows, which also offers the potential to inform on the dynamic nature of real thermal air management of data centers.

REFERENCES

[1] Koomey, J., 2011. Growth in data center electricity use 2005 to 2010. *A report by Analytical Press, completed at the request of The New York Times*, p.9.

[2] Liam Newcombe, Mark Acton, John Booth, Sophia Flucker, Paul Latham, Steve Strutt, and Robert Tozer. 2012 Best Practices for the EU Code of Conduct on Data Centres. European Commission, Joint Research Centre, 2012.

[3] Yogendra Joshi and Pramod Kumar. Introduction to Data Center Energy Flow and Thermal Management. In Yogendra Joshi and Pramod Kumar, editors, Energy Efficient Thermal Management of Data Centers, pages 1–38. Springer US, 2012.

[4] Emad Samadiani, Jeffrey Rambo, and Yogendra Joshi. Numerical modeling of perforated tile flow distribution in a raised-floor data center. Journal of Electronic Packaging, 132(2):021002, 2010.

[5] Jayantha Siriwardana, Saman K Halgamuge, Thomas Scherer, and Wolfgang Schott. Minimizing the thermal impact of computing equipment upgrades in data centers. Energy and Buildings, 50:81–92, 2012.

[6] Kyosung Choo, Renan Manozzo Galante, and Michael M. Ohadi. Energy consumption analysis of a medium-size primary data center in an academic campus. Energy and Buildings, 76(0):414 – 421, 2014.

[7] S.K. Shrivastava, B.G. Sammakia, R. Schmidt, M. Iyengar, and J.W. VanGilder. Experimental-Numerical Comparison for a High-Density Data Center: Hot Spot Heat Fluxes in Excess of 500 W/FT2. In Thermal and Thermomechanical Phenomena in Electronics Systems, *2006* ITHERM '*06*. The Tenth Intersociety Conference on, pages 402–411, May 2006.

[8] Summers, J., Kapur, N. and Thompson, H., 2013, March. Design of data centre rack arrangements using open source software. In *Semiconductor Thermal Measurement and Management Symposium (SEMI-THERM), 2013 29th Annual IEEE* (pp. 45-51). IEEE.

Fourth International Conference on Computational Methods for Thermal Problems
THERMACOMP2016, July 6-8, 2016, Georgia Tech, Atlanta, USA
N. Massarotti, P. Nithiarasu and Y. Joshi (Eds.)

RACK LEVEL TRANSIENT CFD MODELING OF DATA CENTER

Yogesh Fulpagare[1*], Yogendra Joshi[2], Atul Bhargav[1]
[1]Indian Institute of Technology Gandhinagar, Palaj, Gujarat – 382355, India
[2]Georgia Institute of Technology, CEETHERM Laboratory, Atlanta, USA
[1*]fulpagare_yogesh@iitgn.ac.in

ABSTRACT

The high computing devices and faster internet demands have led to major thermal management concerns for data center operators. To tackle this issue, capturing the system thermal dynamics is imperative. This paper deals with the rack level transient CFD study using commercial tool STAR CCM+. A single sever simulator rack with its cold and hot aisle containment has been modelled with known cold air supply temperature and flow-rate. The detailed server thermal mass and porous boundary conditions were implemented through literatures. The significant transient effects on the streamlines and thermal profile has been observed due to variation of heat source.

Key Words: *CFD, Data Center, Heat Transfer, Transient.*

1. INTRODUCTION

About 2% of the total electricity generated is consumed by data centers in the USA [1]. The power consumption in data center is dominated by cooling units [2]. These units provide adequate airflow to the servers based on the system requirement. Therefore, data center environment involves the circulation of hot and cold air flows which is highly dynamic. An efficient way to understand this dynamics of the data center is Computational Fluid Dynamics (CFD) modelling. Various parameters such as rack inlet-outlet temperatures, tile flow rates, CRAC air supply temperature and flow rates have been studied for different data center configurations using steady state CFD analysis [3]–[5]. Thermal conditions within a data center are highly dynamic due to rack power, CRAC supply air temperature and flow-rates and hence cannot be captured through steady state analysis [6]. The first transient numerical analysis was performed by Beitelmal et al. [7] to study the impact of CRAC failure on the temperature variations within the data center. The thermal mass characteristics with detailed transient boundary conditions for data center system level simulations were highlighted by Ibrahim et al. & Gondipalli et al. [8], [9], [10]. However, system level transient CFD study on data center is difficult and computationally expensive. Therefore, the rack level transient study was focused in this paper to gain more insight for understanding the dynamic nature of the system. The main contribution of this paper are: 1) Transient CFD model of a server simulator rack inside raised floor plenum data center and 2) transient effects on thermal and flow field due to variation in server load and airflow configuration.

2. NUMERICAL MODELING

Server simulator rack from the raised floor plenum data center room was considered for the analysis (FIGURE 1 [11]). The 42U (1U = 4.45 cm) rack houses four server simulators each having height

of 10U. Each server simulator has four fans mounted on a plate and dial settings to set desired flow rates through the rack [11]. One down-flow Computer Room Air Conditioning (CRAC 2) was operational during the experiments and other two CRAC were switched off. The similar rack has been used for the analysis previousely by Arghode et al. [12].

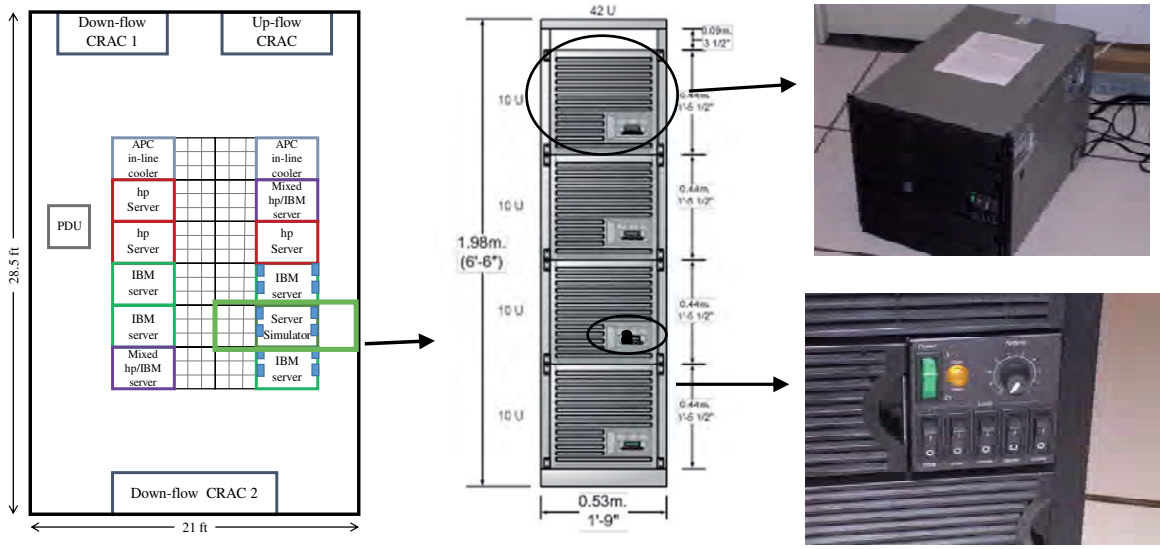

FIGURE 1. The overall system layout with highlighted area of interest for modeling & details of rack with server simulator used for computational domain

3. BOUNDARY CONDITIONS

This section highlights the meshing and boundary conditions details of the the computational domain. The rack walls were assumed to have no slip boundary condition. The tile flow rate was specified by using average velocity inlet as 1.53 m/s and the top surface of the domain is modeled to be exhaust with zero gauge pressure. All four server simulators were modelled as having 75% porosity. The method for determining the inertial and viscous resistance for the porous media which exactly replicates the flow conditions as that of actual flow inside the servers was adopted from [13]. Each server simulator was assigned total heat source of 2500 W that contributes 10 kW total heat on the rack. The rear side of the rack was modelled with fan curve provided by manufacturer [11] and the thermal mass of the servers were defined from [14]. The flow was assumed to be incompressible and to account turbulence the k-epsilon model was used. Three dimensional, transient CFD analysis of current model involves momentum forces coupled with complex thermo-fluid interaction [15]. The commercial software STAR CCM+ from CD-adapco used for this analysis [16]. The hexahedral mesh with cell count around 0.8 million was used.

4. RESULTS & CONCLUSIONS

The flow and thermal dynamics of the system were captured for 16 hour with step variation of heat source input to 2nd simulator after first 3 hours of steady state, within the domain and on horizontal planes at different time steps as shown in FIGURE 2. The transient run was carried out for 16 hours to test various heat source inputs and it was found that

initially system takes around three hours to stabilize. The total solution time for this transient simulation was about 30 hours on i5, 2.5 GHz processor desktop. It is observed that temperature increases with height from bottom to ceiling and the maximum temperature difference between the top and bottom section was found 4°C & 15°C in cold aisle and hot aisle respectively. The hottest temperature zone was observed in hot aisle at the exit of bottom simulator. While finding the reason behind this unnatural observed phenomenon, three distinct zones were highlighted in streamline figure. In the velocity streamline, the cold air flow is passing through servers from tiles and then to ceiling. The high temperature zone in the outlet aisle is due to low air velocity zone at the exit of bottom simulator.

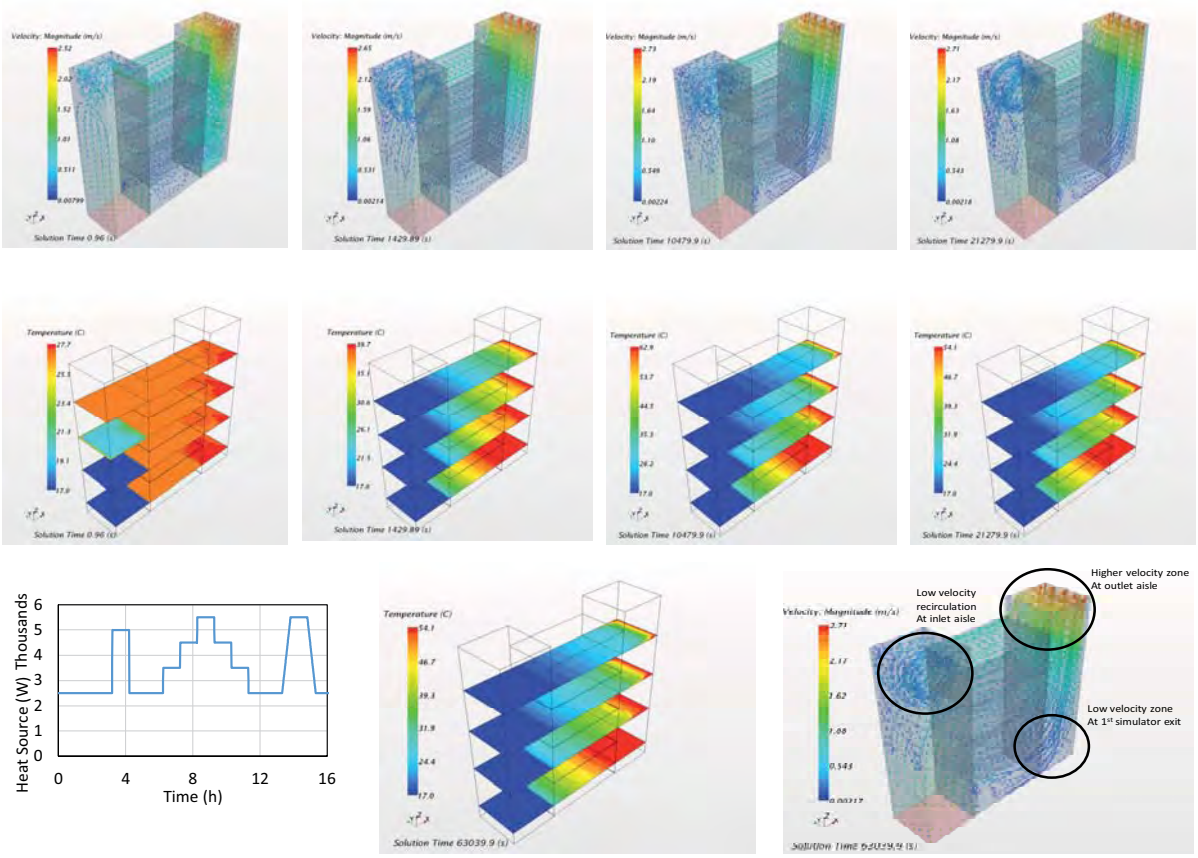

FIGURE 2. Velocity streamlines and Temperature contours at different time steps within the domain and on horizontal planes. Each horizontal plane is a mid section of each server simulator. Third column shows the same countours at the end of the simulation and the input heat source to 2nd simulator.

Velocity of air increases as it flows through the server due to the pressure differential of server fans and enhances the convective heat transfer at the rear end of the rack. The dynamics of the data center depends on the server workload (heat released due to workload) and cold air flow rate through CRAC units. These two parameter affects the server inlet and outlet temperatures. Overall the purpose of transient rack level CFD analysis was successfully accomplished. The further analysis includes the response study of server racks with respect to changes in input. This response study will be more helpful to understand the effect of changes in

inputs on rack inlet-outlet temperatures. The charactrsitcs between these variables will form the base for data driven modeling.

REFERENCES

[1] R. Brown, E. Masanet, B. Nordman, A. Shehabi, J. Stanley, D. Sartor, and P. Chan, "Report to Congress on Server and Data Center Energy Efficiency : Public Law 109-431 Environmental Energy Technologies Division Alliance to Save Energy ICF Incorporated," 2007.

[2] J. G. Koomey, "Growth in data center electricity use 2005 to 2010 . Oakland, CA: Analytics Press."

[3] Y. Fulpagare and A. Bhargav, "Advances in data center thermal management," *Renew. Sustain. Energy Rev.*, vol. 43, pp. 981–996, 2015.

[4] Y. Fulpagare, G. Mahamuni, and A. Bhargav, "Effect of Plenum Chamber Obstructions on Data Center Performance," *Appl. Therm. Eng.*, vol. 80, pp. 187–195, 2015.

[5] J. Rambo and Y. Joshi, "Multi-scale modeling of high power density data centers," in *IPACK'03, Kauai, HI*, 2003, pp. 1–7.

[6] M. Jonas, R. R. Gilbert, J. Ferguson, G. Varsamopoulos, and S. K. S. Gupta, "A transient model for data center thermal prediction," *2012 Int. Green Comput. Conf.*, pp. 1–10, Jun. 2012.

[7] A. H. Beitelmal and C. D. Patel, "Thermo-fluids provisioning of a high performance high density data center," *Distrib. Parallel Databases*, vol. 21, no. 2–3, pp. 227–238, 2007.

[8] M. Ibrahim, S. Bhopte, B. Sammakia, B. Murray, M. Iyengar, and R. Schmidt, "Effect of transient boundary conditions and detailed thermal modeling of data center rooms," *IEEE Trans. Components, Packag. Manuf. Technol.*, vol. 2, no. 2, pp. 300–310, 2012.

[9] M. Ibrahim, S. Bhopte, B. Sammakia, B. Murray, M. Iyengar, and R. Schmidt, "Effect of Thermal Characteristics of Electronic Enclosures on Dynamic Data Center Performance," in *IMECE2010 November 12-18, Vancouver, British, Columbia, Canada*, 2010, pp. 1–10.

[10] S. Gondipalli, M. Ibrahim, S. Bhopte, B. Sammakia, B. Murray, K. Ghose, M. K. Iyengar, and R. Schmidt, "Numerical Modeling of Data Center With Transient Boundary Conditions," in *InterSociety Conference on Thermal and Thermomechanical Phenomena in Electronic Systems, ITHERM*, 2010, pp. 1–7.

[11] G. Nelsonpartial, "Development of an experimentally-validated compact model of a server rack: Master Thesis," Georgia Institute of Technology, 2007.

[12] V. K. Arghode, P. Kumar, Y. Joshi, T. Weiss, and G. Meyer, "Rack Level Modeling of Air Flow Through Perforated Tile in a Data Center," *J. Electron. Packag.*, vol. 135, no. 3, p. 030902, 2013.

[13] A. Almoli, "Air flow management inside data centers," University of Leeds, 2013.

[14] Z. M. Pardey, D. W. Demetriou, J. W. Vangilder, H. E. Khalifa, and R. R. Schmidt, "Proposal for Standard Compact Server Model for Transient Data Center Simulations," vol. 121, pp. 413–422, 2015.

[15] K. Karki, A. Radmehr, and S. Patankar, "Use of Computational Fluid Dynamics for Calculating Flow Rates Through Perforated Tiles in Raised-Floor Data Centers," *HVAC&R Res.*, vol. 9, no. 2, pp. 153–166, Apr. 2003.

[16] CD-adapco Company, "STAR CCM+: Commercial CFD software." .

Fourth International Conference on Computational Methods for Thermal Problems
THERMACOMP2016, July 6-8, 2016, Georgia Tech, Atlanta, USA
N. Massarotti, P. Nithiarasu and Y. Joshi (Eds.)

CFD STUDY OF VARIABLE PIN FIN DENSITY MICROGAP HEAT SINKS FOR 3D-STACKED ICs

Daniel Lorenzini, Yogendra Joshi
George W. Woodruff School of Mechanical Engineering
Georgia Institute of Technology, Atlanta, Georgia, USA, 30332
lorenzini@gatech.edu , yogendra.joshi@me.gatech.edu

ABSTRACT

Single-phase liquid cooling of microelectronics has the capability of removing high heat fluxes in relatively low profile heat sinks. The use of microgaps with pin fins is an option for both cooling of 3D integrated circuit (IC) architectures and transversal interconnection (through silicon vias, TSV). Although surface area enhancement with pin fins is a key feature to remove target heat fluxes on the order of 100-1000 W/cm^2, large temperature gradients within the device may arise as a result of the increase of the fluid temperature downstream. Thermal stresses are intimately related with device temperature differences, and may lead to a reduction of the electrical performance and/or structural failure; hence a cooling method capable to homogenize the temperature distribution within the device is desired. In the present work, the use of variable surface area enhancement features is proposed and investigated. The hydraulic and thermal characteristics of such arrays is assessed and compared for circular pin fins with the main objective of reducing the device temperature gradients (hence also reduce thermal stresses) and required pumping requirements (reduced pressure drops).

Key Words: *Electronics Cooling, Single Phase, CFD, Microgap, Variable Pin Fin Density.*

1. INTRODUCTION

Liquid cooling has been actively studied as an effective option for thermal management of high-power microelectronics. The first demonstration of the promising capabilities of such cooling technique was presented in the multi-cited work of Tuckerman and Pease [1], where it was experimentally reported the dissipation of 790 W/cm^2 in a silicon microchannel heat sink. Despite these encouraging results, several issues were also associated, such as a relatively large pressure drop (> 200 kPa) and a highly non-uniform temperature distribution with a difference larger than 70 ºC between the inlet and outlet sections. The presence of relatively high temperature gradients across the device leads to thermal stresses, which have a negative impact in the system and may lead to a reduction of the electrical performance and/or structural failure.

A number of publications assessing the use of liquid cooling have been presented [2-10], where the use of silicon microchannels or micro-features has been proposed in order to alleviate/balance the critical issues of pressure drop and temperature gradients. Three-dimensional (3D) integration of ICs has been proposed as an alternative way to reduce system size, to increase processing speeds by employing short vertical interconnects, and also to improve power consumption and signal transmission [11]. However, there are critical issues associated to this so-called 3D-integration. Thermal management is a fundamental part for enabling such technologies, since conventional heat sinks cannot be escalated for these devices, constrained by the short interconnects. Inter-tier microfluidic cooling has been actively investigated as an alternative for obtaining high heat transfer coefficients in relatively short microgaps [10-11].

Single-phase cooling is in general an effective option for the thermal management of ICs through the use of microchannels or micro pin fin heat sinks. However, one of the main issues of using such internal flow forced convection mechanism is that as the mean fluid temperature increases, the wall surface temperature also increases in a similar fashion (fully developed condition), leading to the non-desirable temperature gradients discussed before. In order to maintain a more uniform surface temperature, a few options exist: 1) increase the heat transfer coefficient, 2) increase the heat transfer area. From basic theory, it is expected that the heat transfer increases as the hydraulic diameter decreases at the expense of a higher pressure drop. In the present study, the idea of using a

microgap from the cooling layer of 3D IC with a variable density of pin fins is explored in an effort to homogenize the device temperature.

2. DESCRIPTION OF THE PIN FIN LAYOUTS

The microgap cooling layer is designed based on a square surface with the standard dimensions of 10 mm × 10 mm used for ICs, resulting in a heated area of 1 cm^2 used for the present simulations. This microgap is constrained in height by the transversal interconnection length of the TSVs, which is fixed in the present study to 175 μm. Cylindrical pin fins in a staggered array were chosen for the present study; a baseline configuration with uniform fin distribution is defined in order to compare with the proposed designs with a variable density of pin fins. For the baseline configuration (BL), a constant pin fin diameter of D = 150 μm was defined with equal longitudinal and transversal pitches of $S_L = S_T$ = 225 μm. For the proposed designs, the heated length of 10 mm was equally divided into three sections for the allocation of pin fin arrays with different pitches and/or diameters. The main idea is to increase the heat transfer coefficient and surface area in downstream regions in order to compensate for the increase in mean fluid temperature. Four designs with variable fin density (VFD) are proposed, whose layouts are depicted in Figure 1, with the flow defined in the positive x-direction; it is clearly noted how the density of fins increases downstream. The geometric features of each design are summarized in Table 1.

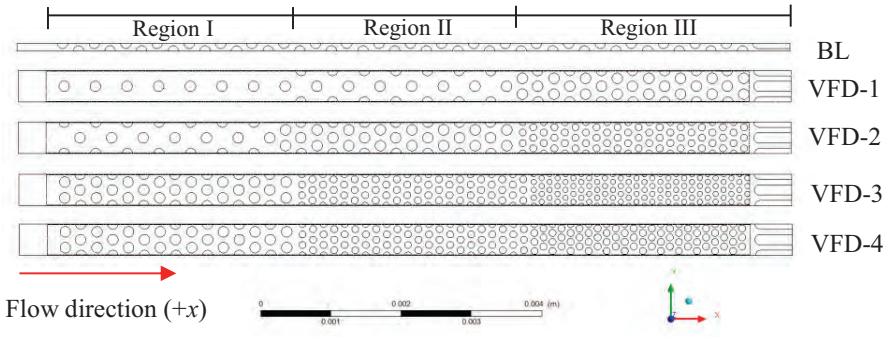

FIGURE 1. Layout of the baseline and proposed designs with variable pin fin density

TABLE 1. Summary of geometric dimensions for the different analyzed configurations

	Region I			Region II			Region III		
Design	D	S_L	S_T	D	S_L	S_T	D	S_L	S_T
BL	150	225	225	150	225	225	150	225	225
VFD-1	150	450	450	150	225	450	150	225	225
VFD-2	150	225	450	150	225	225	100	150	150
VFD-3	150	225	225	100	150	150	75	112.5	112.5
VFD-4	150	225	225	100	150	150	100	128.5	128.5

* All dimensions in μm

3. COMPUTATIONAL MODEL

The CFD analysis of the conjugate heat transfer problem relies on the following assumptions: 1) Steady state, laminar and incompressible flow, 2) Constant and uniform heat flux, 3) Radiation effects are negligible, 4) Constant fluid and solid thermophysical properties except fluid dynamic viscosity, which has a high variation with temperature. The governing equations that are discretized for the numerical solution are the mass and momentum conservation equations for the fluid domain, while for the solid regions the Laplace equation is solved under the assumptions of isotropic and constant thermal properties. The coolant fluid used for all the simulations is water, while the solid domain is silicon. A constant mass flux condition is specified at the inlet section with values ranging from 1000 to 2000 kg/m^2s. The depicted configurations in Figure 1 represent the minimum computational domain that can be analyzed for each configuration in order to save computational time, defining symmetry boundary conditions at each side of the analyzed domains. The walls where the fluid and solid domains meet are set as interfaces while the walls adjacent to both inlet

and outlet are considered as adiabatic. A constant and uniform heat flux is specified at the bottom surface of the heat sink with values ranging from q''=200 W/cm^2 to 500 W/cm^2. Zero mass flux and no-slip boundary conditions were prescribed at the channel internal walls (fluid-solid interface).
The computational fluid dynamics (CFD) software ANSYS® FLUENT® 16.2 was used to solve numerically the governing equations through the finite volume method. After a mesh independence analysis to find a mean element size (fluid) between 10 and 15 μm, the solution was initially approached using the first-order upwind scheme for discretizing the momentum equation and, after a certain level of convergence was attained, the solution was refined by using the second-order upwind scheme. The SIMPLE algorithm was employed for the coupling of velocity and pressure. Residuals for convergence were set to 10^{-4} for all of the equations except for the energy, set at 10^{-7}.

4. RESULTS

The first set of simulations were run for the case with an inlet mass flux of liquid water of G =1000 kg/m^{2}s at a uniform inlet temperature of T_{in} = 20 ºC, and background heat flux of q'' = 200 W/cm^2, which is a representative value for high-power IC architectures. Figure 2 depicts the resulting temperature contours for the analyzed cases, where interesting and significantly different results may be noted even though the operating conditions are the same for every case.

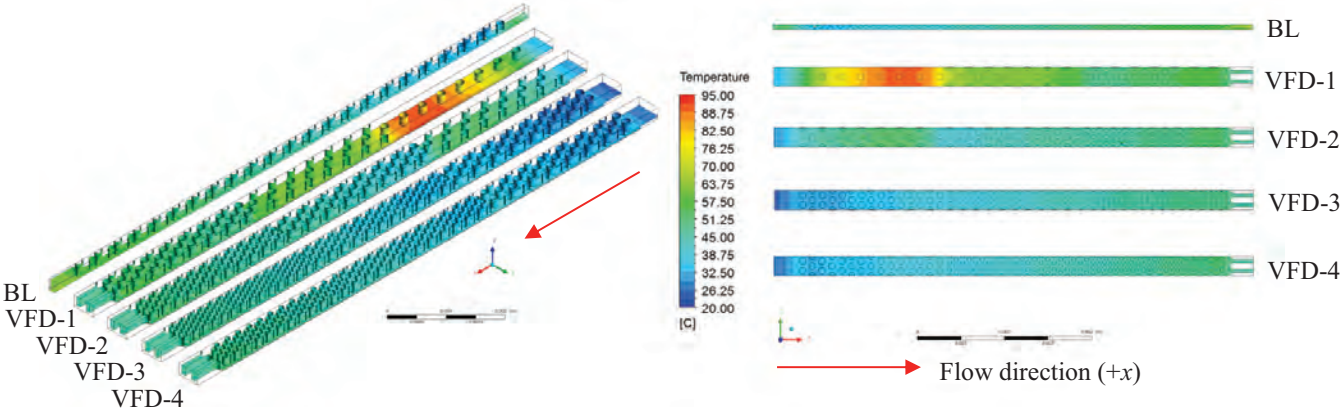

FIGURE 2. Temperature fields of the analyzed designs at G = 1000 kg/m^{2}s and q'' = 200 W/cm^2

Table 2 presents a summary of the computed cooling performance parameters which includes the average temperature, maximum temperature gradient, thermal resistance, and pressure drop. Due to the variety of performance parameters and the well-known tradeoff between thermal resistance and pressure drop for single-phase-cooled devices, it is difficult to determine which configuration offers the best overall cooling performance. According to Table 2, design VFD-2 offers the most uniform temperature uniformity with a maximum gradient across the device of ΔT_s = 15.76 ºC, nearly one-third of the gradient for the baseline case, which is the highest of the analyzed cases at 41.98 ºC. VFD-2 design also reduces the thermal resistance and the pressure drop when compared to the BL configuration. According to these results, VFD-2 certainly represents a significantly better option than the conventional uniform pin fin distribution, both thermally and hydraulically.

TABLE 2. Cooling performance comparison for the different designs

	G = 1000 kg/m^{2}s and q'' = 200 W/cm^2				G = 2000 kg/m^{2}s and q'' = 500 W/cm^2			
Design	$T_{s,avg}$ (ºC)	ΔT_s (ºC)	R (K/W)	ΔP (kPa)	$T_{s,avg}$ (ºC)	ΔT_s (ºC)	R (K/W)	ΔP (kPa)
BL	47.70	29.46	0.1385	150.22	53.28	41.98	0.0865	405.48
VFD-1	64.63	48.40	0.2231	71.25	80.17	96.42	0.1403	192.42
VFD-2	47.56	15.76	0.1375	141.35	51.36	14.84	0.0827	377.76
VFD-3	40.97	20.34	0.1049	229.44	42.52	24.99	0.0650	551.36
VFD-4	40.71	19.91	0.1035	281.26	42.34	22.98	0.0647	778.31

Designs VFD-3 and VFD-4 represent a more aggressive cooling scheme by increasing the fin density with respect to the previous cases at the expense of higher flow restriction. The thermal

resistances for both cases are remarkably low at values of 0.065 - 0.104 K/W, hence offering the lowest surface temperatures among the analyzed cases with a reasonably good temperature uniformity across the device with a maximum gradient of approximately 20 ºC for both cases. The pressure drop is increased to higher values than that of the baseline case; however, it is important to consider that these designs should outperform both thermally and hydraulically a configuration with uniform pin fin distribution in a dense array to obtain similar thermal resistance.

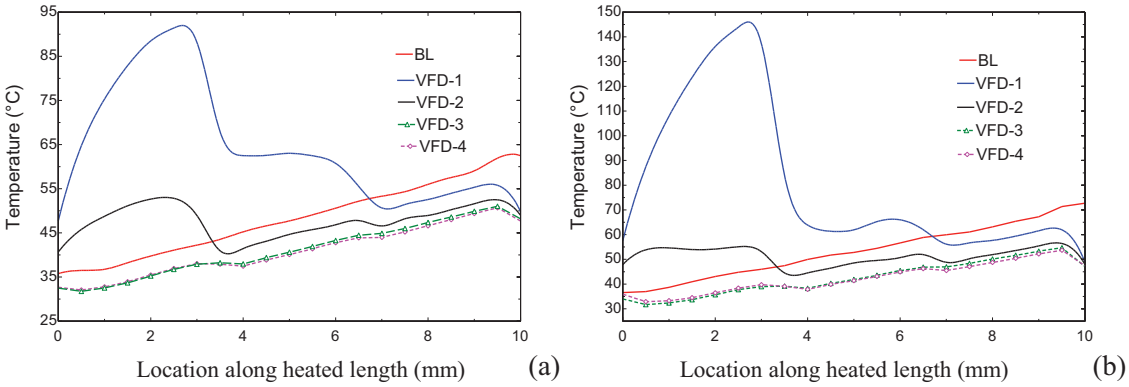

FIGURE 3. Axial temperature variation for the different designs: a) G = 1000 kg/m^{2}s and q'' = 200 W/cm^2, b) G = 2000 kg/m^{2}s and q'' = 500 W/cm^2

5. CONCLUSIONS

The present study has demonstrated the capability of variable pin fin density arrays to dissipate very high heat fluxes with a relatively low pressure drop when compared to uniform arrays. Temperature uniformity was shown to be an attractive feature of the present designs, allowing to reduce the negative effects of the accumulative mean fluid temperature in single-phase cooling by increasing both the heat transfer coefficient and the surface area in the flow direction. Design VFD-2 was proven to achieve the design targets and significantly outperform the baseline case with a uniform fin distribution in all of the parameters of performance, such as thermal resistance, temperature uniformity and even pressure drop. Design VFD-3 offered the lowest thermal resistance and an alternative option to VFD-2 for higher heat transfer rates at the expense of increased flow restriction.

REFERENCES

[1] D. B. Tuckerman and R. F. W. Pease, “High-performance heat sinking for VLSI,” IEEE Trans. Electron Dev., vol. 2, no. 5, pp. 126–129, May 1981.
[2] Y. Peles, A. Ko¸sar, C. Mishra, C. J. Kuo, and B. Schneider, “Forced convective heat transfer across a pin fin micro heat sink,” Int. J. Heat Mass Trans., vol. 48, no. 17, pp. 3615–3627, 2005.
[3] Kosar, A., Mishra, C., and Peles, Y., 2005, “Laminar Flow Across a Bank of Low Aspect Ratio Micro Pin Fins,” Journal of Fluids Engineering-Transactions of the ASME, Vol. 127(3), pp. 419-430, DOI: 10.1115/1.1900139.
[4] Kosar, A., and Peles, Y., 2006, “Thermal-Hydraulic Performance of MEMS-Based Pin Fin Heat Sink,” Journal of Heat Transfer-Transactions of the ASME, Vol. 128(2), pp. 121-131.
[5] Kosar, A., and Peles, Y., 2007, “Micro Scale Pin Fin Heat Sinks – Parametric Performance Evaluation Study,” IEEE Transactions on Components and Packaging Technologies, Vol. 30(4), pp. 855-865.
[6] E. G. Colgan, B. Furman, M. Gaynes, N. LaBianca, J. H. Magerlein, R. Polastre, R. Bezama, K. Marston, and R. Schmidt, “High performance and subambient silicon microchannel cooling,” J. Heat Mass Trans., vol. 129, no. 8, pp. 1046–1051, 2007.
[7] E. G. Colgan, B. Furman, M. Gaynes, W. S. Graham, N. LaBianca, J. H. Magerlein, R. Polastre, M. B. Rothwell, R. J. Benzema, R. Choudhary, K. C. Marston, H. Toy, J. Walkil, J. A. Zitz, and R. R. Schmidt, “A practical implementation of silicon microchannel coolers for high power chips,” IEEE Compon. Packag. Technol., vol. 30, no. 2, pp. 218–225.
[8] W. Escher, B. Michel, and D. Poulikakos, “A novel high performance, ultrathin, heat sink for electronics,” Int. J. Heat Fluid Flow, vol. 31, no. 4, pp. 586–598, Aug. 2010.
[9] Yogendra Joshi. “Microfludic Cooling to Enable 3D Mycrosystems”. ME6779 W15.2 notes.
[10]. Zhang, Y., Dembla, A., Joshi, Y., and Bakir, M.S., 2012, “3D Stacked Microfluidic Cooling for High-Performance 3D ICs,” Proceedings of the 62nd IEEE Electronic Components and Technology Conference (ECTC), May 29-June 1, San Diego, CA, pp. 1644-1650.
[11]. Zhang, Y., and Bakir, M.S., 2013, “Independent Interlayer Microfluidic Cooling for Heterogeneous 3D IC Applications,” Electronic Letters, Vol. 49(6), pp. 404-406.

Fourth International Conference on Computational Methods for Thermal Problems
THERMACOMP2016, July 6-8, 2016, Georgia Tech, Atlanta, USA
N. Massarotti, P. Nithiarasu and Y. Joshi (Eds.)

ASSESSMENT OF FLOW DISTRIBUTION FEATURES IN MICROGAPS FOR 3D STACKING OF ICs

Daniel Lorenzini, Pouya Asrar, Casey Woodrum, Peter Kottke, Andrei Fedorov, Suresh Sitaraman, Yogendra Joshi*
George W. Woodruff School of Mechanical Engineering
Georgia Institute of Technology, Atlanta, Georgia, USA, 30332
lorenzini@gatech.edu , pouya@gatech.edu , dwoodrum3@gatech.edu , peter.kottke@me.gatech.edu , agf@gatech.edu , suresh.sitaraman@me.gatech.edu , yogendra.joshi@me.gatech.edu

ABSTRACT

The three-dimensional (3D) stacking of integrated circuit (IC) chips requires low profile heat sinks for the removal of high heat fluxes (>100 W/cm^2); the use of microgaps with surface enhancement features for both single and two-phase cooling has shown to be an effective solution. However, flow maldistribution effects associated with the inlet/outlet plenum design can significantly affect the temperature distribution and stress concentration across the device. In the present study, the hydrodynamic behavior for two different chip designs is assessed through computational fluid dynamics (CFD) methods. The flow behavior is quantified in terms of the mass flow rate uniformity and pressure drop for devices that are designed to withstand relatively high fluid pressures (~1 MPa) for flow boiling of dielectric refrigerants. Results indicate the strong effect of the plenum shape and mechanical support structures on the hydrodynamic characteristics of the analyzed chips, providing useful design guidelines and considerations for the practical implementation of such cooling layers.

Key Words: *Electronics Cooling, Flow Distribution, CFD, Microgap.*

1. INTRODUCTION

The miniaturization and vertical integration of microelectronics have resulted in the need for more effective and compact cooling approaches. Forced convection cooling through single phase flow, or boiling in silicon microgaps have demonstrated remarkable capabilities for removing heat fluxes of 100 W/cm^2 and beyond. Several geometric parameters play an important role in the design of these microgaps, such as the height, shape and dimensions of plenum and pin fins, among others. The use of dielectric refrigerants has been actively explored for inter-tier cooling configurations due to the close proximity of the coolant to electrical connections. The low thermal conductivity and specific heat of these fluids requires higher mass flow rates, as well as operating in flow boiling to exploit the latent heat of vaporization; this also results in higher operating pressures. A critical issue related to the use of high pressure refrigerants in flow boiling is the device reliability; since the microgap itself requires being thin enough to reduce the vertical interconnection length, it becomes a major issue leaving structurally unconstrained areas within the microgap. Green et al. [1] suggested the use of support structures in the inlet and outlet plenums of the microgap to withstand high-pressure dielectric fluids, such as R245fa and R134a. However, the use of such support structures to avoid mechanical fracture has a strong effect on the resulting flow field and its uniformity throughout the device. In the present investigation, computational fluid dynamics (CFD) techniques are used to provide guidelines for the hydraulic design of microgaps intended to operate in flow boiling regimes at high pressure. Two designs will be compared, emphasizing on important aspects such as flow uniformity and pressure drop, as well as its direct relation to the inlet/outlet plenum layout.

2. DESCRIPTION OF THE MICROGAPS AND CHALLENGES

The analyzed devices are designed based on several constraints imposed by the ultimate application (3D STAECOOL concept [1]) in which the cooling layer must comply with electrical, structural, hydraulic, and thermal specifications. For the present designs, the heated section of the device has an area of 1 cm^2, distributed on a square geometry of 10 mm × 10 mm. The microgap height is fixed at 200 μm, while the heated area is populated with a staggered array of cylindrical pin fins of 150 μm diameter, which share the same height with the microgap. The array has equal longitudinal and transversal pitches of 200 μm. Although the previous specifications for the heated zone are in

general well defined by the application and its constraints, a non-trivial part of the combined design are the flow distribution, and inlet/outlet plenum configurations. In the present investigation, two microgap designs are compared. The first design corresponds to an already microfabricated and tested device; the Georgia Tech 3rd generation test device vehicle (TDV) for the DARPA's ICECool Program [2]. This design derives from a learning curve in efforts to reconcile the multiphysics problem involving structural reliability, two phase-pressure drop, flow and temperature uniformity, clogging, erosion, among others. Fig. 1 shows this 3rd generation TDV, where the relevant zones are indicated. Starting from the inlet port and plenum, it can be noticed that there is an array of cylindrical pins (500 µm diameter), whose main purpose is to provide the required structural support to operate with high pressure dielectrics (~1 MPa and beyond). The pin fin constriction, or flow redistribution line, was incorporated in an effort to reduce two-phase flow instabilities, where the flow gap between pins is as low as 20 µm. Two pressure measurement ports are included in the design to experimentally quantify the pressure drop across different sections of the device.

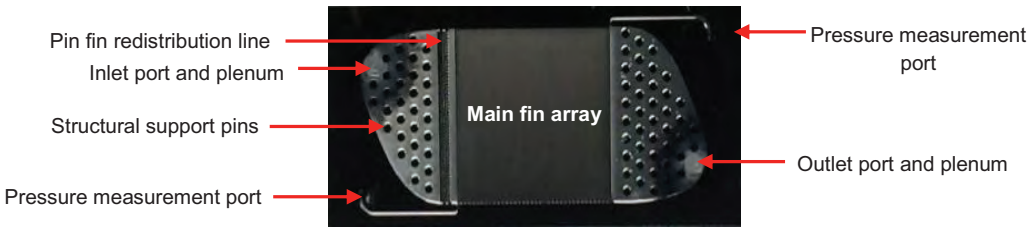

FIGURE 1. Georgia Tech 3rd generation TDV and its main zones

Experimental results for the 3rd generation (Gen 3) TDV have indicated relatively large pressure drops at the inlet constriction, which have been associated with the presence of clogging. In addition, asymmetric two-phase flow at relatively large heat fluxes (~300 W/cm^2) has also been observed. Although this type of devices are designed for operation in flow boiling, and the most appropriate comparison using CFD should account for such phase-change phenomena, this area is still in its early development and demands large computational cost [3-5]. A cost-effective CFD design approach in which the different size features of the TDV are included is proposed here by only focusing on the single-phase, adiabatic flow field features. Hence, the hydrodynamic behavior for a given design may be quantified and provide insightful results for the ultimate goals.

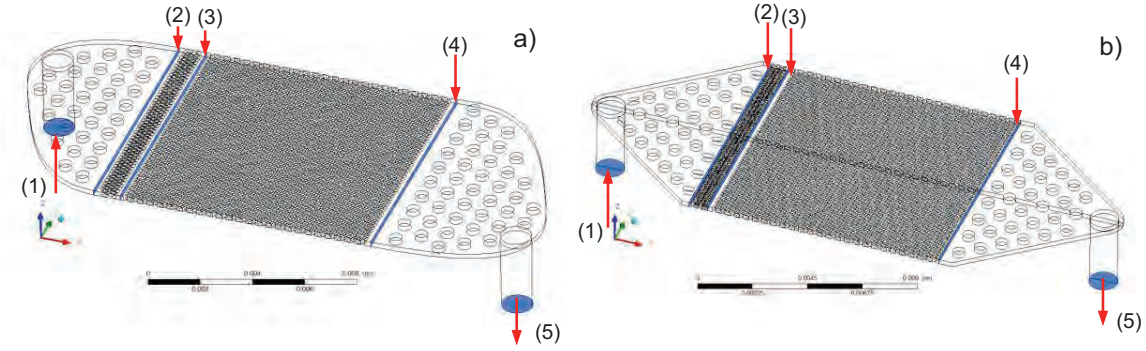

FIGURE 2. Schematic of the analyzed microgap designs: a) Gen 3, b) Proposed Gen 4

The second analyzed design in this work, and a potential candidate for the 4th generation (Gen 4) of TDVs, represents an effort to reduce/mitigate the aforementioned issues with clogging and pressure drop. It is important to note that the proposed design keeps successful features of its predecessors, such as the structural support fins. Relevant modifications for this design are: 1) Increase of the minimum gap at the flow redistribution line from 20 to 50 µm, 2) Redesign of the inlet/outlet plenums to a symmetric distributor. Recognizing that the structural pins at the plenum zones affect the resulting flow field in the device, Gen 4 design is aimed to provide a balance between mechanical reliability specifications and flow distribution. Fig. 2 depicts a schematic of these designs, indicating zones of interest for the post-processing of CFD results.

3. COMPUTATIONAL MODEL

The governing equations of mass and momentum conservation are solved for the fluid domain and considering the solid interface boundaries as zero-thickness walls. ANSYS® FLUENT® 16.2 was used as the solver with the SIMPLE algorithm for steady, incompressible, turbulent flow simulation employing the $k-\varepsilon$ formulation. A constant mass flow rate of R245fa 100 mL/min is specified at the inlet section (1), with a density of 1250 kg/m^3 and viscosity of 2.685×10^{-4} kg/m-s.

4. RESULTS

Experimental results from the hydraulic, adiabatic tests of Gen 3 have been compared to those predicted by the CFD simulation, which are listed in Table 1 for similar operating conditions at a flow rate of 100 mL/min, and temperature (constant) of 19.14 °C. It can be noted a relatively large mismatch between the measured and predicted pressure drop, where the sub-indexes denote the region between which it is computed. The pressure drop across the main fin array ($\Delta P_{3\text{-}4}$) is somewhat larger in the experiment, possibly attributed to clogging and microfabrication defects in the TDV. However, the largest difference is for the pressure drop across the inlet constriction ($\Delta P_{1\text{-}3}$), suggesting that clogging in this zone has a strong negative effect. An extra simulation with a reduced gap between pins at the inlet constriction from 20 to 10 µm was run in an effort to reconcile results. Although pressure drop was significantly increased across points 1 to 3, the experimental measurement is still larger, suggesting an even larger constriction effect due to clogging.

Table 1. Comparison between measured and predicted pressure drops for Gen 3 device

Case	$\Delta P_{1\text{-}3}$ (kPa)	$\Delta P_{3\text{-}4}$ (kPa)
Gen 3 experimental	485.67	276.57
Gen 3 simulation (20 µm gap)	92.36	208.54
Gen 3 simulation (10 µm gap)	265.51	205.84

Fig. 3 depicts the simulation results for Gen 3 and Gen 4 devices, where the velocity contours on the top are displayed at a mid-section plane across the entire device, providing some qualitative insight about the effect of the structural support fins on the flow distribution. For Gen 4, such structural supports have been relocated in such a way that the preferred flow lanes provide a symmetric flow field in an effort to homogenize the flow before entering the main fin array.

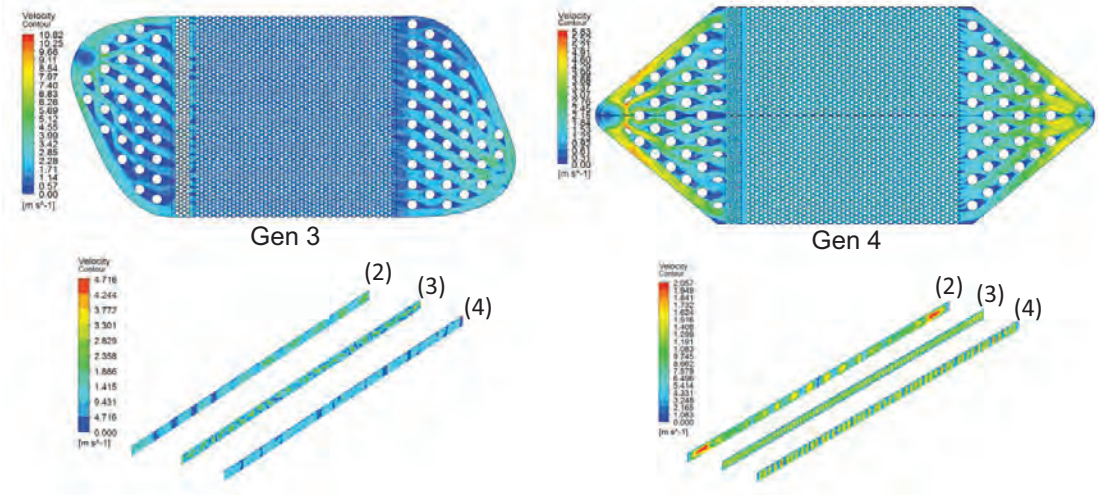

FIGURE 3. Velocity contours (m/s) across different sections of the analyzed designs

The contours on the lower part of Fig. 3 indicate the velocity magnitude for the cross-sections at points (2), (3), and (4). When comparing both designs after the flow redistribution line (3), it can be observed that Gen 4 offers a significantly more uniform velocity profile, which is desirable for both single and two-phase flow in the main fin array. In order to quantify the foregoing statements, 10 zones of equal area were defined along the cross-section surface at (3), and the flow rate crossing

each one was tracked and plotted. For the ideal case, the flow rate across each of these surfaces should be 1/10 of the total input. This is used as the line of reference and the flow deviation percentage is depicted in Fig. 4 for both designs. The symmetric and uniform flow advantages of Gen 4 over Gen 3 are clearly noted. The Gen 3 design exhibits a highly variable behavior, as a result of the array of structural pins and flow redistribution line.

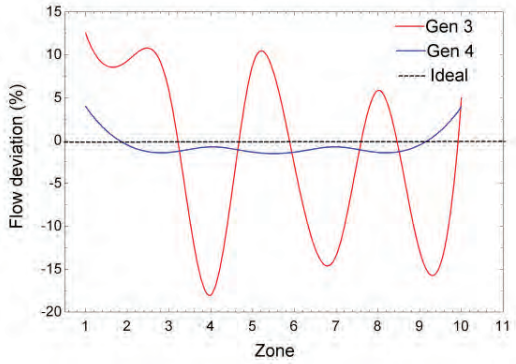

FIGURE 4. Flow uniformity simulation results for the analyzed designs

In addition to offering a more uniform flow distribution, Gen 4 design reduces the restrictive pressure drop across the redistribution line by increasing the minimum gap to 50 µm. This is also expected to reduce clogging issues during experimentation. Pressure drop results across different sections are listed in Table 2.

Table 2. Pressure drop from the simulation results at 100 mL/min for the different TDVs

Design	$\Delta P_{1\text{-}2}$ (kPa)	$\Delta P_{2\text{-}3}$ (kPa)	$\Delta P_{3\text{-}4}$ (kPa)	$\Delta P_{4\text{-}5}$ (kPa)	ΔP_{total} (kPa)
Gen 3	11.81	72.10	189.11	14.53	284.59
Gen 4	14.97	3.46	188.65	14.68	211.77

5. CONCLUSIONS

The proposed symmetric design for Gen 4 offers significantly better flow uniformity and lower pressure drop when compared with Gen 3, resulting from a careful redesign of the inlet/outlet plenums, strategic relocation of the mechanical support fins, and by redefining the minimum gap between structures to avoid clogging issues.

ACKNOWLEDGEMENT

The Defense Advanced Research Projects Agency (DARPA) IceCool Fundamentals Program (Award No. HR0011-13-2-0008) provided financial support for this work.

REFERENCES

[1] Green, C., Kottke, P., Han, X., et al., 2015, "A Review of Two-Phase Forced Cooling in Three-Dimensional Stacked Electronics: Technology Integration", J. Electron. Packg., Vol. (137), pp. 040802-1-9.
[2] Bar-Cohen, A., Maurer, J.J., Felbinger, J.G., 2013, "DARPA's Intra/Interchip Enhanced Cooling (ICECool) Program", CS MANTECH Conference, New Orleans, Louisiana, USA, pp. 171-174.
[3] Matin, K., Bar-Cohen, A., Maurer, J.J., 2015, "Modeling and Simulation Challenges in Embedded Two Phase Cooling – DARPA's ICECool Program", ASME 2015 13th International Conference on Nanochannels, Microchannels, and Minichannels, InterPACK & ICNMM, San Francisco, California, USA.
[4] Lorenzini, D., Joshi, Y.K., 2015, "CFD Analysis of Flow Boiling in a Silicon Microchannel with Non-Uniform Heat Flux", ASME 2015 13th International Conference on Nanochannels, Microchannels, and Minichannels, InterPACK & ICNMM, July 6-9, San Francisco, California, USA.
[5] Lorenzini, D., Joshi, Y.K., 2016, "CFD Study of Flow Boling in Silicon Microgaps with Staggered Pin Fins", Accepted to IEE ITHERM Conference 2016, Las Vegas, NV, USA.

Fourth International Conference on Computational Methods for Thermal Problems
THERMACOMP2016, July 6-8, 2016, Georgia Tech, Atlanta, USA
N. Massarotti, P. Nithiarasu and Y. Joshi (Eds.)

NUMERICAL MODELING OF ENERGY-EFFICIENT LIQUID COOLING USING CONDUCTING-LUBRICATING (CO-LUB) SURFACES

Jessica Reyes, Krishna Kota
New Mexico State University, 3055 Williams Avenue, Las Cruces, NM 88003
jessy7@nmsu.edu, kkota@nmsu.edu

ABSTRACT

In electronics cooling applications employing liquid cold plates, addressing the problem of obtaining considerable pressure drop reduction without negatively impacting heat transfer as much is an arduous challenge. In this paper, numerical simulation is used to pursue the viability of Conducting-Lubricating (CO-LUB) surfaces in addressing this challenge for single phase liquid cooling. CO-LUB surfaces can be prepared using various fabrication techniques published in the literature and designed to have exceptionally high wetting characteristics. These surfaces, when saturated with a liquid microlayer, provide remarkable lubrication to bulk liquid flow and simultaneously facilitate heat transfer through the microlayer. In the simulations, the side walls of a high aspect ratio rectangular channel were assumed as CO-LUB surfaces, and convective heat transfer of bulk liquid flow was modeled using ANSYS FLUENT 14.5. Volume-of-Fluid (VOF) method was used to model the two liquids with a free surface interface, with water as the microlayer liquid and oil (coolant) as the bulk liquid, in a narrow channel of 5 mm width and 50 mm length under laminar flow, constant wall heat flux conditions. The results were compared with a regular channel of the same dimensions (without CO-LUB surfaces) and it was found that the CO-LUB walls would help in a substantial pressure drop decrease but with improved heat transfer performance, which will lead to highly energy-efficient cooling. The paper also focused on a parametric study of the microlayer thickness on the overall performance of the CO-LUB surfaces.

Key Words: *Liquid Cooling, Forced Convection, Energy Efficiency, Cold Plates.*

1. INTRODUCTION

With a recent surge in embedded liquid cooling in applications such as in 3D stacked electronics and high heat density data center servers, exploring ways to enhance heat transfer in liquid cooling of electronics without the negative impact of increased pressure drop (or vice versa) has been of significant interest. Prior efforts on improving heat transfer focused essentially on surface modification techniques for inhibiting thermal boundary layer development and promoting flow mixing including slots, bumps, delta wings, dimples, wavy walls, and helical inserts to name a few. While research in heat transfer augmentation has been the focus for many decades, research in pressure drop reduction gained momentum comparatively recently with relatively far less amount of published work especially for bulk liquid flows.

In this paper, numerical simulation of single phase forced convective transport in a channel with conducting-lubricating (CO-LUB) surfaces for achieving decreasing the pressure drop without any heat transfer attenuation is pursued. On CO-LUB surfaces, the bulk liquid flows on a microlayer of the wetting liquid constrained in the micro-/nanoporous media of the surfaces. The micro-/nanoporous surface with exceptionally high wetting characteristics (similar to a paper towel) would hold the wetting liquid with help of strong capillary forces [1]. The surface along with its wetting liquid is termed as the *Conducting-Lubricating* (CO-LUB) surface as it provides lubrication to the bulk liquid and simultaneously transfers heat through the microlayer.

2. NUMERICAL MODEL

ANSYS FLUENT 14.5 was used to model two-dimensional flow of bulk liquid in a high aspect ratio channel (1 mm width for bulk liquid flow and 300 mm length) with CO-LUB surfaces as the side walls. The free surface between the bulk liquid and the microlayer liquid was resolved using volume-of-fluid (VOF) technique. Water was assumed as the microlayer liquid under laminar flow, constant wall heat flux conditions. Thermal XP was considered as the bulk liquid. In the simulations, the microlayer liquid thickness was varied from 0.1 mm to 1 mm and its impact on the overall performance was studied. A no-slip boundary condition was assumed at the walls to which a heat flux of 10,000 W/m^2 was specified. A shear-free condition was assumed at the free surface interface between the two liquids. For thermal transport across the interface, a no-temperature-jump condition was assumed. An inlet velocity of 1 m/s (corresponding to a Reynolds number, *Re*, of 64) and an inlet temperature of 300 K were specified for the bulk fluid at the channel entrance.

Properties of Thermal XP at 308 K (average of inlet and outlet temperatures for most cases considered in this paper) were used with density= 868.9 kg/m^3, dynamic viscosity=0.027 Pa·s, specific heat=1886 J/Kg·K, and thermal conductivity=0.141 W/m·K. Properties of water at 311 K (average of inlet and outlet temperatures for most cases considered in this paper) were used with density= 993 kg/m^3, dynamic viscosity=$7X10^{-4}$ Pa·s, specific heat=4180 J/Kg·K, and thermal conductivity=0.591 W/m·K. Antonow's rule [2] was used for implementing the interfacial tension.

Grid independence checks were performed and it was found that a $3X10^{-5}$ m mesh with 389,922 elements, a $3.75X10^{-5}$ m mesh with 403,875 elements, and a $4X10^{-5}$ m mesh with 438,287 elements were able to reasonably resolve the flow field for 0.1 mm, 0.5 mm, and 1 mm microlayer thickness respectively. A structured meshing scheme was employed. SIMPLEC and PRESTO schemes were used for continuity and pressure discretization respectively. Second order upwinding was used to discretize momentum and energy equations. Low under-relaxation factors (~0.3-0.5) were used to obtain convergence. The solution was assumed converged if the residuals for continuity, volume fraction, momentum and energy reached below 10^{-3}.

The developed model was verified with the experimental data published by Salim et al. [3] on pressure drops for flow of oil and water in a microchannel of 700 μm height, 780 μm width and 120 mm length. From the results reported in the paper, a water inlet velocity of 0.1143 m/s was chosen and two oil inlet velocities of 0.1143 m/s and 0.18 m/s were chosen. It was observed that the current model captured the flow regimes as well as the measured drops very well (matched within 1.1%).

3. RESULTS

Results of the simulations were compared for flow through a plain-walled channel to estimate the performance improvements, which were found to strongly depend on the microlayer thickness that has a limiting value of zero when the CO-LUB surface behaves as a plain surface. Increasing the thickness of the microlayer from 0.1 mm to 1 mm was found to aid in decreasing the pressure drop by an increasing factor compared to flow through a plain-walled channel with a maximum decrease at 1 mm. Therefore, the following results were presented for this best case scenario.

In Fig. 1, a portion of the observed velocity field is shown in comparison with the flow field in a channel without CO-LUB surfaces for which the velocity contours followed the traditional Poiseuille flow profile (with zero velocity at the walls), while with CO-LUB surfaces, significant apparent slip can be observed (with ~1 *m/s* velocity at the apparent wall i.e., the CO-LUB surface and the bulk liquid interface). Volume fraction of oil obtained from the simulations is shown Fig. 2, where a flow pattern similar to core annular flow in pipes can be observed. From Fig. 3, it can be observed that there is a remarkable decrease (by ~16 to 280 times) in the pressure drop in the case of channel with CO-LUB surfaces compared to a channel with plain walls.

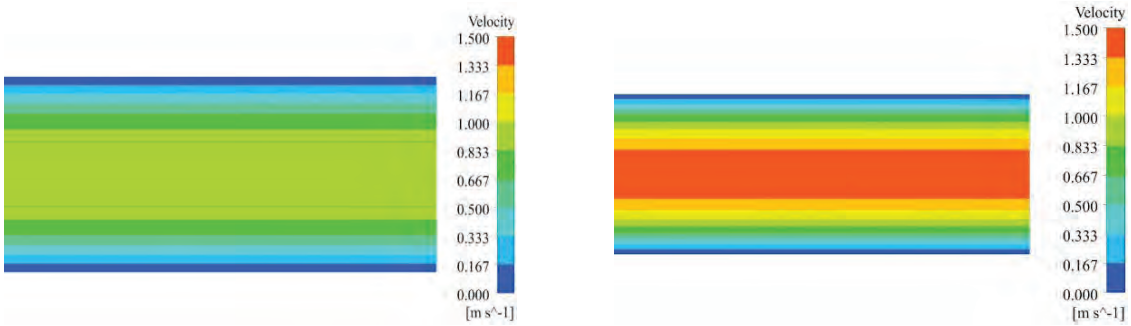

FIGURE 1. Apparent velocity slip on CO-LUB surfaces (left) vs. no slip in a plain channel (right)

FIGURE 2. Volume fraction (0 – water and 1 – oil) of Thermal XP oil with CO-LUB surface walls

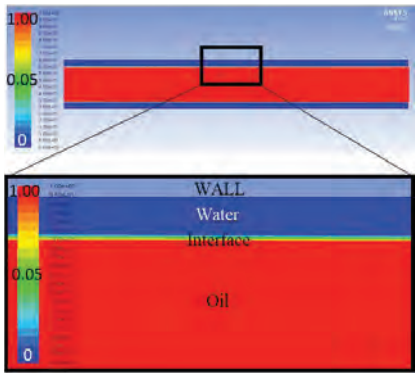

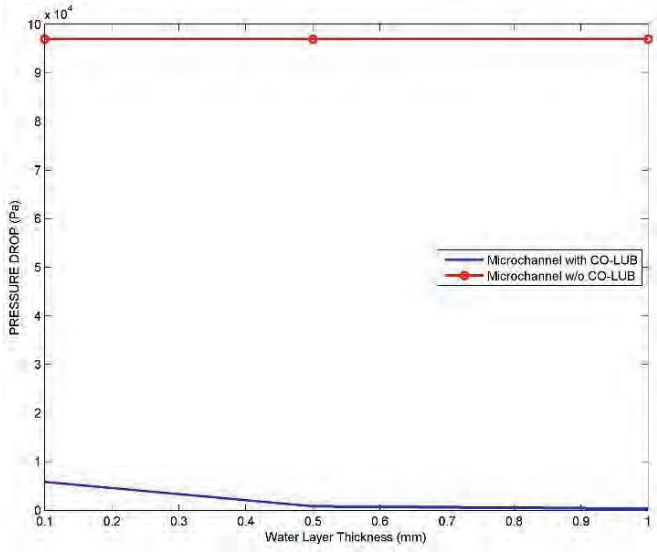

FIGURE 3. Pressure drop vs. microlayer thickness

Heat transfer coefficient was estimated from the simulation results using the specified wall heat flux, average wall temperature and average bulk liquid temperature. The results are plotted in Fig. 4 from which it can be seen that CO-LUB surfaces show an improvement in the heat transfer, which showed a increase by ~2 to 3 times compared to the channel without CO-LUB surfaces. CO-LUB surfaces with a thin conducting liquid microlayer next to the wall were found to provide scope for excellent heat transfer to the bulk liquid. The increased heat transfer coefficient can be attributed to the apparent velocity slip.

A *Performance Factor* (*PF*) [4] was evaluated as a measure of energy efficiency. It captures the relative heat transfer augmentation in forced convection of a fluid due to an enhancement mechanism for the same pumping power (through the same flow area) without the enhancement mechanism. *PF* showed an increase by ~14 times.

4. CONCLUSIONS

In this paper, the effectiveness of Conducting-Lubricating (CO-LUB) surfaces in enhancing liquid cooling of electronics is numerically pursued in a high aspect ratio channel (of 1 mm width and 300 mm length) with water as the microlayer liquid and Thermal XP oil as bulk liquid under low *Re* (=64) laminar flow, constant wall heat flux (10^4 W/m^2) conditions. The results were compared with a plain-walled channel of the same dimensions. The performance improvements of the CO-LUB surfaces were found to be strongly dependent on the microlayer thickness with 1 mm case exhibiting significantly better performance than the 0.1 mm case. For a microlayer thickness of 1

mm, the pressure drop decreased remarkably by more than ~280 times associated with a simultaneous increase of heat transfer coefficient by ~2 times leading to highly energy-efficient liquid cooling. The energy-efficiency as measured by a performance factor, *PF*, showed enhancement by up to ~14 times with CO-LUB surfaces. Further, it was observed that, in the presence of apparent slip due to the presence of a constrained liquid microlayer near the walls, it is possible to achieve a flow configuration similar to core annular flow in pipes, which is highly conducive to slip for the core/bulk liquid. Development of more advanced numerical models is necessary to capture the thermal-fluid dynamics of the microlayer and the effect of its thickness on performance improvements.

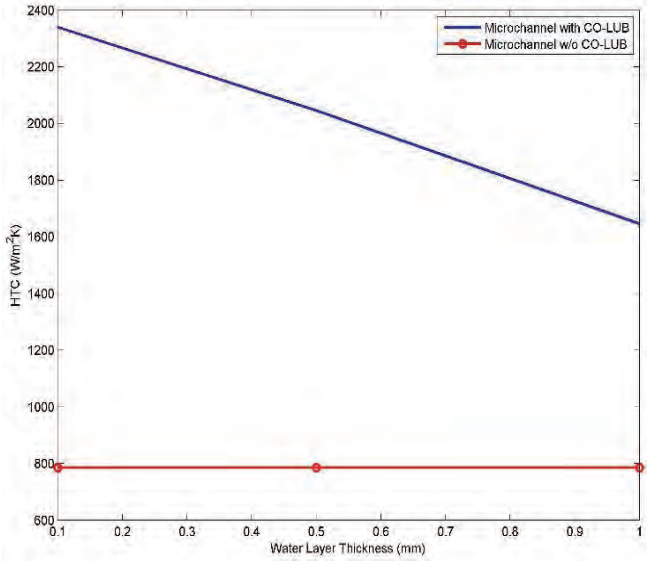

FIGURE 4. Heat transfer coefficient vs. microlayer thickness

REFERENCES

[1] https://www.youtube.com/watch?v=Gd5Z9If6XUg

[2] G.N. Antonow, Sur la tension superficielle à la limite de deux couches, *Journal de Chimie Physique (Journal of Physical Chemistry)*, 5, 371, 1907.

[3] A. Salim, M. Fourar, J. Pironon, and J. Sausse, Oil-water two-phase flow in microchannels: flow patterns and pressure drop measurements, *Canadian Journal of Chemical Engineering*, 86, 978-988, 2008.

[4] D.L. Gee, R.L. Webb, Forced convection heat transfer in helically rib-roughened tubes, *International Journal of Heat and Mass Transfer*, 23, 1127–1136, 1980.

Fourth International Conference on Computational Methods for Thermal Problems
THERMACOMP2016, July 6-8, 2016, Georgia Tech, Atlanta, USA
N. Massarotti, P. Nithiarasu and Y. Joshi (Eds.)

Liquid Jet Impingement with an Angled Confining Wall

John F. Maddox
University of Kentucky, Paducah, KY, john.maddox@uky.edu

Roy W. Knight, Sushil H. Bhavnani
Auburn University, Auburn, AL, roy.w.knight@auburn.edu, bhavnsh@auburn.edu

ABSTRACT

A model was developed to investigate the effects of an angled confining wall on the spent flow behaviour and surface transfer characteristics of an array of circular, normal, single-phase liquid water, impinging jets. An angled confining wall was found to be an effective method of spent flow management, allowing the jets to be placed closer to each other and to the surface without interfering with the performance of the neighbouring jets.

Key Words: *Heat Transfer, Jet Impingement, Spent Flow Management, Angled Confining Wall.*

1. INTRODUCTION

Impinging liquid jets offer the highest single-phase heat transfer coefficient at the stagnation point of currently available cooling techniques. Additionally, the relatively low pressure drop and high volumetric flow rate of jet impingement systems makes them well suited for incorporation into automotive and power electronics applications, such as hybrid electric vehicles.

When arrays of jets are used to cool large surfaces, the spent fluid from upstream jets can become entrained in and divert incoming downstream jets as the spent fluid moves toward the system exit, as shown in Figure 1. For a jet array with a parallel confining wall, the spent fluid causes a successive degradation in performance of each subsequent downstream jet as each row of jets introduces more spent fluid into the crossflow, causing an increase in the momentum of the spent fluid stream.

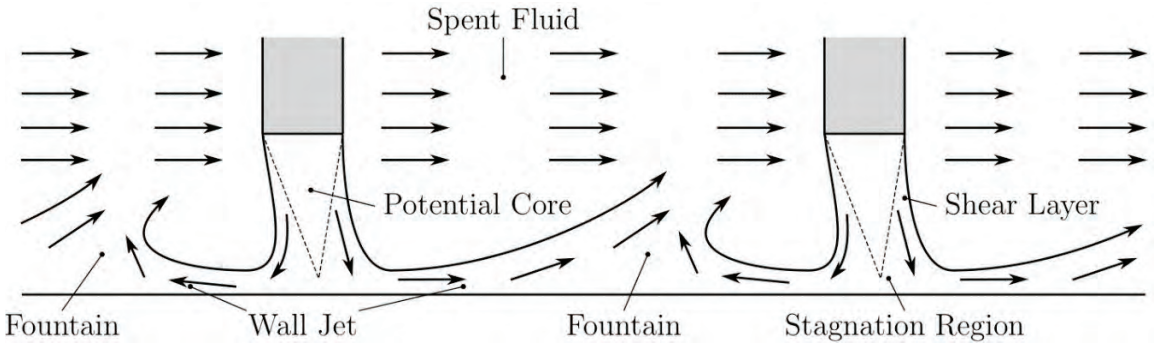

FIGURE 1. The effects of crossflow on an array of impinging jets

The impact of the spent fluid on downstream jets is driven by the ratio of the spent fluid momentum to the incoming fluid momentum. The jet momentum is relatively constant for nominally uniform flow distribution amongst the jets. However, the crossflow momentum increases with downstream position due to the accumulation of spent fluid for a channel with a constant cross-sectional area. In order maintain a more consistent jet to crossflow momentum ratio, this study will investigate the effects of implementing an angled confining wall on the spent flow behaviour and the surface heat transfer characteristics.

2. MAIN BODY

A model was developed in ANSYS® Fluent, Academic Research, Release 14.5.7, to characterize the flow patterns and surface transport characteristics for a half-symmetry geometry of circular, normal, inline, single-phase liquid water jets impinging on a copper surface with confining wall angles of 0°, 5°, and 10° relative to the impingement surface. The geometry and flow properties were chosen to enable comparison to the experimental results presented by Maddox et al. [1].

A uniform velocity boundary condition was applied to a plenum upstream of the nozzles to capture the effects of non-uniform flow distribution amongst the nozzles. The magnitude of the uniform velocity was chosen to result in an average jet Reynolds number of 5,000 for each case to enable direct comparison to experimental data,

$$Re_D = \frac{UD}{\nu} = 5{,}000$$

where U is the average jet velocity, D is the jet diameter, and ν is the kinematic viscosity. In order to capture the effects of conductive spreading within the copper block, a uniform heat flux was applied to the bottom of the copper block and a no-slip conjugate heat transfer condition was applied at the interface between the fluid and the copper block. A pressure outlet boundary condition was applied at the exit of the impingement region. All other surfaces were treated as adiabatic.

Three Reynolds-averaged Navier-Stokes (RANS) turbulence models were considered for this study: the traditional k-ε model, Menter's shear stress transport (SST) model [2], and Durbin's v^2f model [3]. Both the SST and v^2f models provided significant improvements in accuracy over the traditional k-ε model. A grid independence study showed that for one geometry, the SST model required 5 million nodes to reach grid independence, whereas the v^2f model required 9 million nodes. Due to this, it was determined that the small improvements in accuracy of the v^2f model over the SST model did not justify the added computational costs, and the SST model was used for the rest of the study.

3. RESULTS

The pressure contours for the 0° and 5° cases are shown in Figure 2, where the fluid enters from the top surface, flows through the plenum and nozzles, impinges on the surface and exits the impingement to the right. For each case, the majority of the pressure drop occurs at the sharp edged inlet to the nozzle from the plenum and there is an adverse pressure gradient in the stagnation region. Additionally, the pressure drop experienced by the spent fluid decreases with increasing confining wall angle.

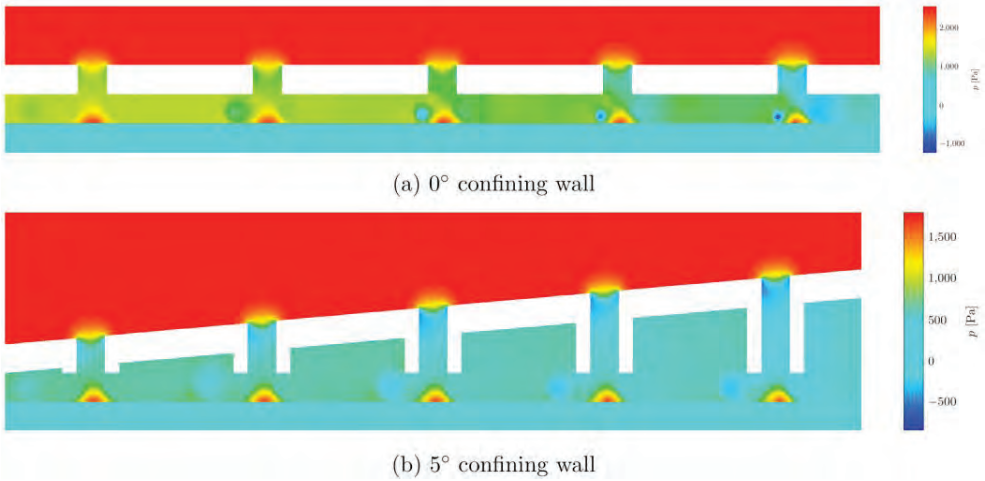

FIGURE 2. Pressure contours for $Re_D = 5{,}000$

The resulting flow distributions for the 0° and 5° cases are illustrated as pathlines colored by the magnitude of the velocity in Figure 3. The pressure drop in the spent flow channel causes a non-uniform flow distribution between the nozzles with higher flowrates in the downstream nozzles. This effect is more pronounced for the 0° case than for the 5° case. The fountain region where the neighbouring wall jets meet and the fluid leaves the surface is clearly visible on the upstream side of the nozzles. For the 0° case, the momentum of the spent fluid increases with each downstream jet, causing the fountain region to shift successively further downstream for each jet. However, the fountain region for the 5° case does not shift as far downstream because the relief provided by the increasing channel area minimizes the increase in momentum of the spent fluid.

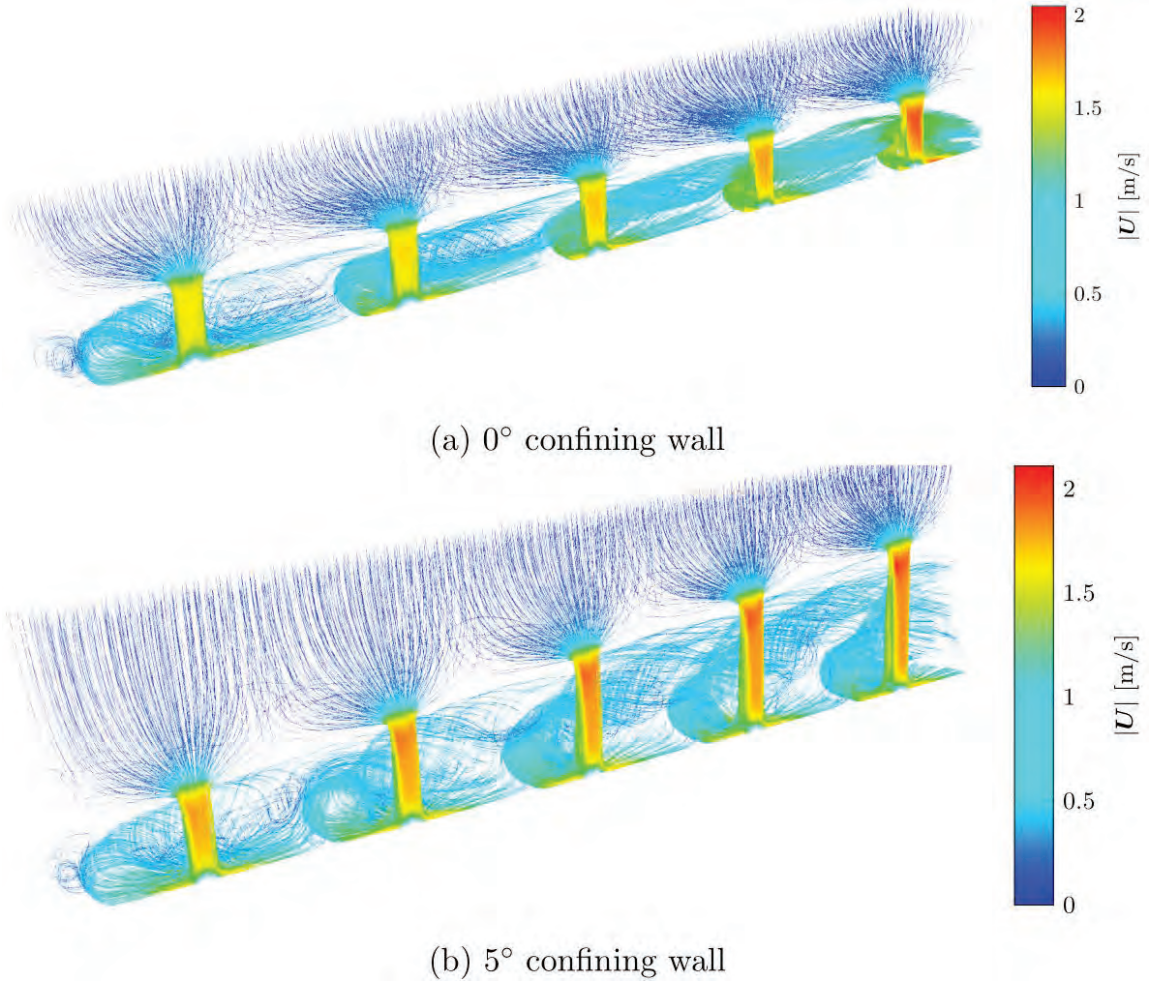

FIGURE 3. Pathlines for the flow field colored by the velocity magnitude for $Re_D = 5{,}000$

The variation in heat transfer coefficient at the impingement surface is illustrated as a surface contour map in Figure 4. For both the 0° and 5° cases, a secondary peak in heat transfer is seen at the location of the fountain region where the neighbouring wall jets interact and the flow separates from the surface. The thermal performance of the jets in the 0° case decreases with downstream position because the accumulation of spent fluid momentum causes the area of elevated heat transfer in the stagnation and wall jet regions to get successively smaller with each downstream jet. However, the 5° confining wall maintains a consistent momentum for the spent fluid, and the area of elevated heat

transfer for each nozzle stays constant with downstream position, thus providing more uniform cooling of the surface.

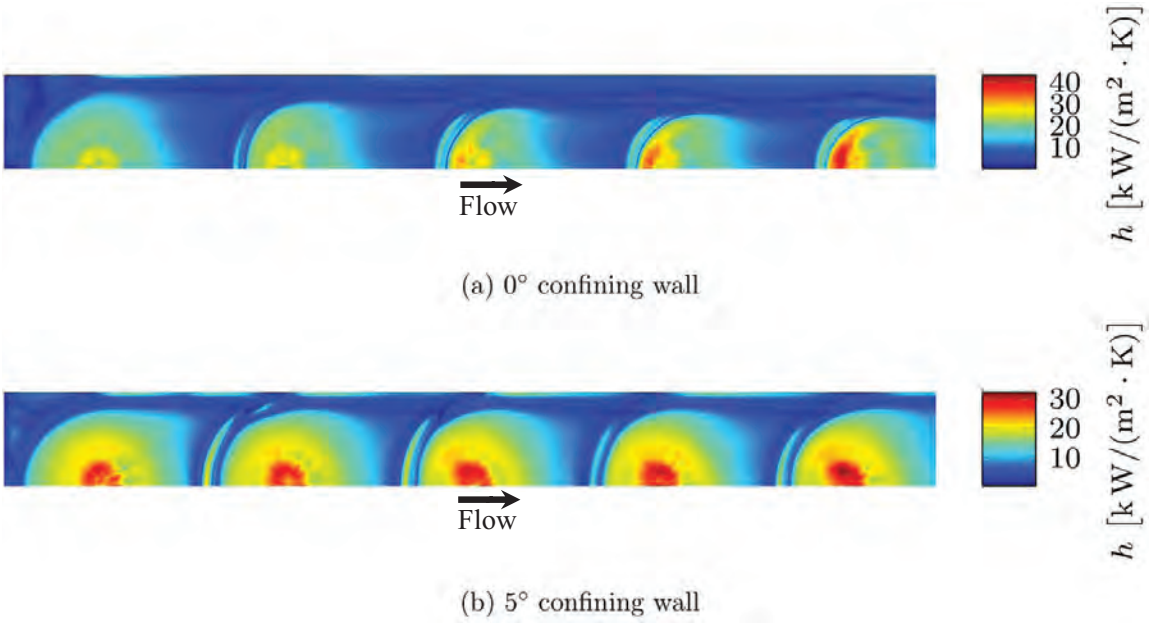

FIGURE 4. Heat transfer coefficient contours for $Re_D = 5{,}000$

4. CONCLUSIONS

A model of an array of circular, normal, single-phase liquid water jets was developed in ANSYS® Fluent using the transition SST turbulence model to investigate the effects of varying the confining wall angle on the jet-to-jet interactions and surface transport characteristics. It was found that for the 0° confining wall, the build-up of spent fluid momentum caused the fountain regions between the jets to shift downstream and caused a successive degradation in performance for each subsequent downstream jet. In contrast, the 5° confining wall provided relief for the spent fluid to be diverted away from the incoming downstream jets, which prevented the momentum of the spent fluid from increasing and degrading the performance of downstream jets. As a result, the 5° confining wall maintains a consistent rate of heat transfer for each jet regardless of its downstream position.

REFERENCES

[1] J.F. Maddox, R.W. Knight, and S.H. Bhavnani, "Liquid Jet Impingement with an Angled Confining Wall for Spent Flow Management for Power Electronics Cooling with Local Thermal Measurements", *Journal of Electronic Packaging*, 137.3, 031015, 2015.

[2] F.R. Menter, "Zonal Two Equation *k*-ω Turbulence Models for Aerodynamic Flows", In the *24th Fluid Dynamics Conference*, volume 93-2906, 1993.

[3] P.A. Durbin, "Separated Flow Computation with the *k*-ε-v^2 Model", *AIAA Journal*, 33(4), 659-664, 1995.

MINI SYMPOSIUM

MICRO-NANO SCALE HEAT TRANSFER IN NANO-STRUCTURES AND DEVICES

MINI SYMPOSIUM ORGANISED BY SATISH KUMAR

Fourth International Conference on Computational Methods for Thermal Problems
THERMACOMP2016, July 6-8, 2016, Georgia Tech, Atlanta, USA
N. Massarotti, P. Nithiarasu and Y. Joshi (Eds.)

SENSITIVITY OF THERMAL CONDUCTIVITY CALCULATIONS TO ERRORS IN INTERATOMIC FORCES

Casey N. Brock, Matthew D. Gerboth
Materials Science Program, Vanderbilt University
2201 West End Ave, Nashville, TN 37235
casey.brock@vanderbilt.edu, matthew.d.gerboth@vanderbilt.edu

D. Greg Walker
Mechanical Engineering, Vanderbilt University
2201 West End Ave, Nashville, TN 37235
greg.walker@vanderbilt.edu

ABSTRACT

The quality of results from a molecular dynamics (MD) simulation is determined by the accuracy of calculated interatomic forces. Often interatomic forces are determined using quantum mechanical methods such as density functional theory (DFT). However, we have previously shown that DFT will not always produce accurate forces. Presumably errors in the forces from DFT will cause errors in MD results, but the sensitivity has not been quantified. In this work, we focus on one property that can be calculated using molecular dynamics, the thermal conductivity (k). Ultimately we want the change in thermal conductivity with respect to the interatomic forces. Direct exploration of changes in k by varying parameters for the DFT calculations (and thus the forces) would be very expensive, but we can extract this sensitivity indirectly using classical MD with the Lennard-Jones potential for solid argon. Then we can quantitatively evaluate the effects of changes in interatomic forces on thermal conductivity calculations. Using this method, we have found that the percent change in thermal conductivity of argon is 1.17 times the percent change in average force magnitude, which provides a useful metric for estimating errors in thermal conductivity of argon that result from errors in interatomic forces. Although we expect the result to generalize to other materials and potentials, we have not performed sufficient studies to verify such a claim.

Key Words: *molecular dynamics, thermal conductivity, sensitivity analysis, interatomic forces.*

1. INTRODUCTION

Molecular dynamics (MD) results are only as good as the models used to calculate forces between atoms. Therefore, we are interested in improving the accuracy of interatomic force calculations through electronic structure calculations. In contrast to classical MD, where interatomic forces are modeled with empirical potentials, one can use ab-initio molecular dynamics, which uses electronic structure calculations to generate forces as the simulation progresses. This approach has the advantage of using quantum theory so that it is based on fundamental physical parameters and not empirical fits. However, even using density functional theory (DFT), electronic structure calculations are very expensive meaning ab-initio MD can only address problems a small fraction of the size of classical MD problems.

Through optimization of DFT simulation parameters [1], we have seen speedup in DFT calculations. Furthermore, we have shown that DFT calculations can be optimized to produce accurate forces [2]. Through this force-based optimization, drastic speedup is achievable with only small sacrifices in force accuracy. These speed gains would be a huge advantage for users of ab-initio MD and other electronic structure based research. However, we don't know how much force

accuracy we can sacrifice while still maintaining the overall accuracy advantages of using ab-initio methods.

While errors in forces between different simulations are easy to evaluate, researchers are generally more interested in actual measurable properties. Errors in forces will cause errors in MD results, but this effect has not yet been quantified. We have decided to explore a single measurable property, the thermal conductivity. In this work, we determine how changes in interatomic forces affect thermal conductivity calculated from MD. On one hand, it's possible that the thermal conductivity is very sensitive to changes in forces. In this case, force-based optimizations of DFT calculations are very important for accurately predicting properties. On the other hand, it may be that small changes in forces have negligible effects on thermal conductivity, and thus forces do not need to be accurate to a high precision. In this case, requirements of force accuracy could be relaxed, allowing significant speedup of force calculations using DFT. Ultimately, we would like to quantify how far off the forces can be.

Other groups have performed sensitivity analysis of measurable properties with interatomic potential parameters [3]. The parameters are coefficients to interatomic potentials that govern the shape of the potentials, similar to σ and ε in the Lennard-Jones potential. They studied graphene and aluminum and looked at many measurable propertied such as thermal conductivity. Their approach is useful for knowing how sensitive observables are to individual parameters in a given potential. However, we are interested in the effect of actual forces, not parameters in an empirical potential. Also, we are studying a different material. Because we are interested in this problem for ab-initio MD, the most direct way to achieve this would be to run ab-initio simulations where forces are calculated by DFT. Using different parameters for DFT that produce different forces, the sensitivity of the observables to the forces would be apparent. However, calculations like this are prohibitively expensive, especially for the system sizes necessary for accurate thermal conductivity calculations. To address this problem, we have developed a two-step sensitivity analysis process that result in sensitivities of observables to changes in forces using only classical MD and no ab-initio calculations.

2. METHODS

We calculate thermal conductivity using non-equilibrium molecular dynamics (NEMD). Simulations were performed using LAMMPS [4] and Lennard-Jones argon in the FCC structure. The Lennard-Jones potential is defined as $V = 4\varepsilon\left[\left(\frac{\sigma}{r}\right)^{12} - \left(\frac{\sigma}{r}\right)^{6}\right]$ where σ and ε are parameters adjusted to reproduce experimental bulk data. We used $\sigma = 3.405$ Å which has been fit for argon [5]. Because we are varying the parameter ε, we chose $\varepsilon_0 = 0.0103$ eV as the nominal value [5] and varied it by ±20%. For each value of ε investigated, 16 initial configurations were prepared and the thermal conductivity results were averaged over the 16 different configurations. We use systems with 512 unit cells between the heat baths, and with a cross section of 2x2 unit cells; heat baths and walls 2 unit cells thick are added to each side (Figure 1). Periodic boundaries were applied normal to the direction of transport. Prior to calculating thermal conductivity, each simulation was equilibrated at 40 K for 4.67 ns (10^6 time steps). A 10 K temperature difference was then applied across the heat baths, and the system reached steady state after 2.34 ns. Heat fluxes were then averaged over the next 4.67ns, and thermal conductivity was found from Fourier's law.

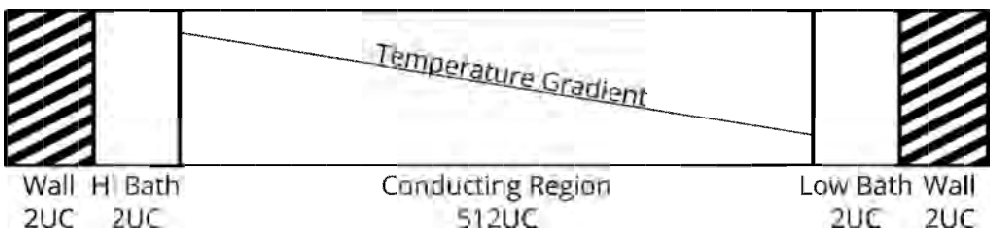

FIGURE 1. Schematic of MD setup for calculating thermal conductivity. UC = unit cells.

To find the sensitivity of thermal conductivity to forces, we first calculate the sensitivity of thermal conductivity to interatomic potential parameters, and then sensitivity of forces to the potential parameter ε. We can refer to these sensitivities as $\frac{\partial k}{\partial \varepsilon}$ and $\frac{\partial F}{\partial \varepsilon}$, where k is thermal conductivity and F is related to forces. From this we derive $\frac{\partial k}{\partial F} = \frac{\partial k}{\partial \varepsilon}\frac{\partial \varepsilon}{\partial F}$. Each of these steps is discussed below.

For $\frac{\partial k}{\partial \varepsilon}$, we are looking for changes in the observable property thermal conductivity as the parameters of an interatomic potential change. We chose this system because the potential is simple and easy to work with, although this method could be used with other materials and potentials. The Lennard-Jones potential has two parameters, σ and ε. We vary the parameter ε to change our potential, and observe the outcome of these changes on calculated thermal conductivity.

The second step of our method is finding $\frac{\partial F}{\partial \varepsilon}$. This step does not require any additional MD runs once we have $\frac{\partial k}{\partial \varepsilon}$. Given a single snapshot of all atomic positions in the crystal, we can calculate the net forces on all atoms using the LJ potential. Changing the potential parameter ε will alter the potential resulting in different net forces. These changes in forces effectively give us $\frac{\partial F}{\partial \varepsilon}$. We chose this method so we can compare forces from different potentials on the *same* atomic configuration, giving us an unbiased estimate of how the forces change when the potential changes. The snapshot we will use is the last time step of one of the 16 MD runs for $\varepsilon = \varepsilon_0$, which was already run when finding $\frac{\partial k}{\partial \varepsilon}$. We use this snapshot because it represents a realistic configuration of atoms, which is the product of an equilibrated MD run. Because many forces are present in this system, we define the force metric as $F = \frac{1}{N}\sum_{i=1}^{N}|\boldsymbol{w_i}|$, where $N = 8192$ is the number of atoms in the system and $\boldsymbol{w}_i$ is the force vector on the ith atom. F, then, is the change in force magnitude for all atoms. This metric neglects any changes in the direction of forces, but in practice the directions only change by a small fraction of a degree for this problem.

With $\frac{\partial k}{\partial \varepsilon}$ as well as $\frac{\partial F}{\partial \varepsilon}$ we can derive our final sensitivity, $\frac{\partial k}{\partial F} = \frac{\partial k}{\partial \varepsilon}\frac{\partial \varepsilon}{\partial F}$.

3. RESULTS

We calculated the thermal conductivity for different values of ε, as shown in Figure 2a. As a general trend, the thermal conductivity increases as ε increases. We determined $\frac{\partial k}{\partial \varepsilon} = 139.3$ W/(m·K·eV) by using regression to determine the slope of a linear fit. Similarly, we calculated the average magnitude of the forces on the atoms for different values of ε. The results are shown in Figure 2b. We determined $\frac{\partial F}{\partial \varepsilon} = 4.548$ Å^{-1} by estimating the slope of a linear fit. We assume linear relationships because changes from ε_0 are small, and the derivative of the Lennard-Jones potential with respect to ε is constant. From these derivatives, we have $\frac{\partial k}{\partial F} = \frac{\partial k}{\partial \varepsilon}\frac{\partial \varepsilon}{\partial F} = 30.63$ W·Å/(m·K·eV).

Using this we can now see how small changes in forces will affect thermal conductivity results. Let

$$k = k_0 + \frac{\partial k}{\partial F}\Delta F$$

where k is thermal conductivity, $k_0 = 1.212$ W/(m·K) is the thermal conductivity derived from the linear fit in Figure 2a at $\varepsilon = \varepsilon_0$, and $\Delta F = F - F_0$ is the absolute change in F where $F_0 = 0.04648$ eV/Å is derived from the linear fit in Figure 2b at $\varepsilon = \varepsilon_0$. Then the relative change in thermal

conductivity, $\eta_k = \frac{k-k_0}{k_0}$, is $\eta_k = \frac{\partial k}{\partial F}\frac{\Delta F}{k_0} = \frac{\partial k}{\partial F}\frac{F_0}{k_0}\eta_F = 1.17\eta_F$ where $\eta_F = \frac{\Delta F}{F_0}$ is the relative change in F. Therefore a 1% error in the average force magnitude produces a 1.17% error in the thermal conductivity, or a 10% error in forces produces an 11.7% error in thermal conductivity.

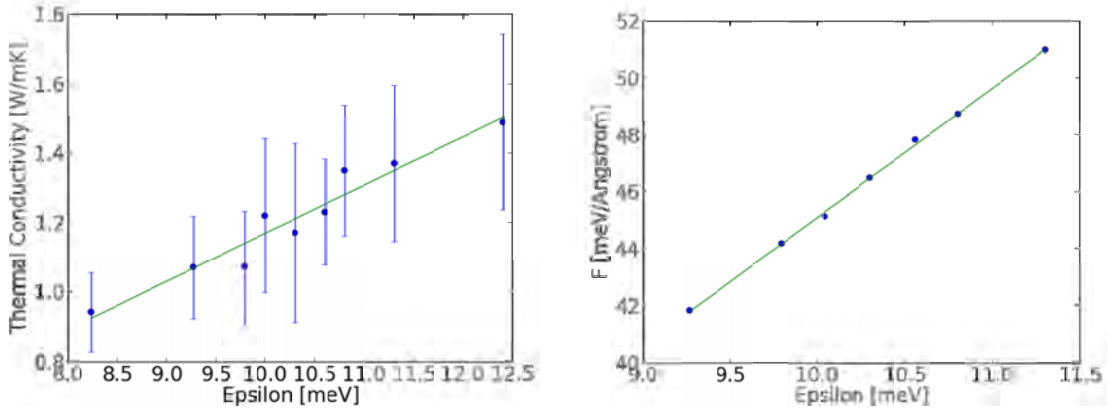

(a) (b)

FIGURE 2. (a) Change in thermal conductivity as the Lennard-Jones parameter ε is varied. The slope of the linear fit is $\partial k/\partial \varepsilon$.(b) Change in average force magnitude in the atoms as the Lennard-Jones parameter ε is varied. The slope of the linear fit is $\partial F/\partial \varepsilon$.

4. CONCLUSIONS

We have shown that the effects of force errors on thermal conductivity can be quantified using a simple sensitivity analysis. This quantification is useful for optimization of parameters in different types of force calculation methods such as empirical interatomic potentials and DFT. We have found that the percent change in thermal conductivity is 1.17 times the percent change in average force magnitude for this problem. A useful rule of thumb is that the percent change in thermal conductivity is about the same as the percent change in forces. This method could easily be extended to other systems interatomic potentials, and measurable properties to give useful insight into how force errors affect MD results.

REFERENCES

[1] R.A. Hansel, C.N. Brock, B.C. Paikoff, A.R. Tackett, and D.G. Walker, Automated generation of highly accurate, efficient and transferable pseudopotentials, *Computer Physics Communications,* 196, 267-275, 2015.

[2] C.N. Brock, B.C. Paikoff, M.I.M. Sallih, A.R. Tackett, and D.G. Walker, Force-based optimization of pseudopotentials for non-equilibrium configurations, *Computer Physics Communications*, 201, 106–118, 2016.

[3] T. Mawyin, Sensitivity Analysis of Material Property Predictions in Molecular Dynamics with Interatomic Potentials under Uncertainty, Thesis, University of Toronto, 2015.

[4] S. Plimpton, Fast Parallel Algorithms for Short-Range Molecular Dynamics, *Journal of computational physics*, 117, 1-19, 1995.

[5] A. Michels, H. Wijker, and H.K. Wijker, Isotherms of argon between 0°C and 150°C and pressures up to 2900 atmospheres, *Physica*, 15(7), 627-633, 1949.

Third International Conference on Computational Methods for Thermal Problems
THERMACOMP2016, July 6-8, 2016, Atlanta, USA
N. Massarotti, P. Nithiarasu and Y. Joshi (Eds.)

Investigation of Phonon Transport and Thermal Boundary Conductance at Interface of Functionalized SWCNT and Poly (Ether-Ketone)

Haoxiang Huang, Satish Kumar
G. W. Woodruff School of Mechanical Engineering, Georgia Institute of Technology, Atlanta, GA, 30332-0405

Vikas Varshney, Ajit Roy
Materials and Manufacturing Directorate, Air Force Research Laboratory, WPAFB, Dayton, OH, 45433

ABSTRACT

The thermal and electrical applications of many polymers commonly used in commercial and defense applications are scarce due to their low conductivities. The addition of carbon nano-structures such as carbon nanotubes (CNTs) in the polymer matrix can lead to significant improvement in the thermal and electrical properties of the resulting nano-composite. An exceptional improvement in the electrical and thermal conductivity of fibers made by poly (ether) ketone (PEK) grafted few walled carbon nanotube has been observed in the experiments. However, the thermal interaction of functionalized CNT and PEK molecules has not been understood yet. In this study, the interface thermal boundary conductance between functionalized SWCNT and PEK were estimated using transient relaxation method. The energy transport across the interface were investigated through the decay of spectral temperature in different frequency bands of CNT.

Key Words: *Heat Transfer, Molecular Dynamics, Nanoscale Heat Transfer, Polymer Science.*

1. INTRODUCTION

In past ten years, energy transport at the interface between crystalline material and amorphous material has interested scientists and engineers leading to a large number of experimental and numerical studies [1, 2]. In nano-composites, significant enhancement in heat dissipation capability and related performance is achieved using high-conductivity constituents as filler in low-conductive matrix. The most commonly studied fillers in this context are CNTs and graphene [3-6]. Even though fillers can improve the properties of polymeric matrix, the enhancement of performance is far away from the expectations. Several studies have found that functionalization can enhance the thermal properties of composite significantly, such as thermal conductivity and thermal boundary conductance (TBC) [7-9]. In this study, the thermal boundary conductance (TBC) at the interface between CNT and PEK has been computed by transient relaxation method via molecular dynamics (MD) simulations. The spectral temperature decay of CNT subjected to pulsed heating and subsequent relaxation has been used to understand phonon coupling between CNT and PEK and complex thermal interactions of CNT with the PEK matrix.

2. MAIN BODY

Motivated by previous experimental work that report high thermal conductivity of PEK grafted CNT fibers, we analyse the effect of functionalization on interfacial thermal transport between PEK and SWCNT [2]. The model of polymeric composite in this simulation consists of a (20, 20) double-wall CNT embedded in PEK matrix, (see FIGURE 1a)). In order to functionalize (20, 20) SWCNT, we follow a similar process that is reported in Varshney et al. [7], i.e., the reactive sites of the PEK chains within certain distance ($\leq$ 5Å) to (20, 20) CNT are chosen for forming bonded with carbon atoms of (20,

20) SWCNT. To form a chemical bond between the PEK chain and CNT, hydroxyl group (-OH) of the PEK is removed from the carboxylic acid groups and the carbon atom of carbonyl group is covalently bonded to a C atom of CNT. The partial charges of (-OH) are removed and they are changed to non-participated atoms in simulations. The charges are redistributed to the activated carbon atoms on SWCNT to maintain the charge neutrality of the system. The aforementioned procedure is iterated for every new bond created and the coefficients of new bond, angle, dihedral and improper created in functionalized system are updated following the consistent valence force field (CVFF). Finally, the system is equilibrated for 50 ps in NPT, 100 ps NVT and 50 ps NVE simulations processes.

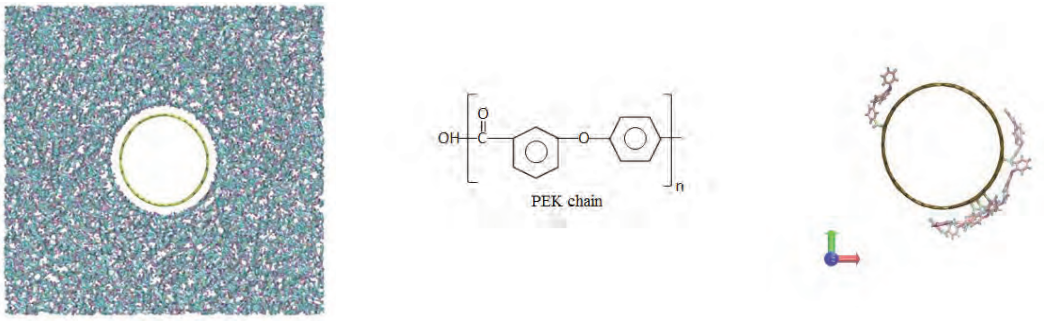

FIGURE 1. a) The CNT/PEK composite structure prepared using MD simulations. The (-OH) of b) PEK chain is deleted, and C atom of COOH group is bonded with a nearest carbon atom on CNT. The sample corresponding to 5-bond case is shown in c).

The thermal properties of polymers has been accurately modelled in the previous studies [8, 9] using the CVFF force field. In this study, the TBC in samples with different number of covalent bonds is calculated by transient relaxation method [10], which can be expressed as:

$$G = \frac{k_B}{\tau_T A} \cdot \frac{N_{CNT} N_{PEK}}{N_{CNT} + N_{PEK}} \tag{1}$$

where k_B is the Boltzmann constant, N is the number of degrees of freedom for (20, 20) CNT or PEK, A is the interfacial contact area , and τ_T is the time constant fitted with exponential function for time history of the temperature difference between CNT and PEK.

Next, the spectral temperature analysis is performed to understand the physics of thermal interactions in different regimes of frequency by bonded crosslinks. The transient and equilibrium phonon spectra, $g^{neq}(\omega)$ and $g^{eq}(\omega)$, are calculated by Fourier transform of velocity profiles of SWCNT [3, 11]. While the equilibrium temperature T_{eq} is specified as 300K, the change of spectral temperature T_{sp} of different frequency bands of CNT with time is calculated for samples with different number of bonds in order to analyze the thermal coupling between SWCNT and PEK in different frequency regimes. T_{sp} can be given as:

$$T_{sp}(t) = \frac{T_{eq}}{\omega_1 - \omega_2} \int_{\omega_1}^{\omega_2} \frac{g^{neq}(\omega)}{g^{eq}(\omega)} d\omega \tag{2}$$

where ω_1 is lower limit of the frequency and ω_2 is the upper limit for the band.

3. RESULTS

We first analyse the TBC at CNT-PEK interface for different samples prepared using MD. The temperature difference between the CNT and substrate is fitted with an exponential function for all prepared samples which lead to calculation of time constant of 79.10 ps, 75.23 ps, and 58.21 ps for samples with no-bonds, 1 bond and 5-bond at the interface (see TABLE 1). This corresponds to TBC of 16.71 MW/m^2-K, 17.57 MW/m^2-K and 22.70 MW/m^2-K, repectively. As expected, the calculated TBC is increasing as number of bonds increases. So the physical process of making bonds at interface result in better thermal coupling [8, 9]. The covalent bonds enhance energy transfer from SWCNT to polymeric matrix and even though the defects created by bonds on the surface of SWCNT impede the phonon transport along the axis of SWCNT and increase phonon scattering, the functionalization may lead to enahnced thermal conductivity of CNT-PEK matrix due to enhanced TBC.

Next, we compute the spectral temperature of CNTs for 4 frequency bands- (a) Band 1: 0-9 THz, (b) Band 2: 9-20 THz, (c) Band 3: 20-40 THz, (d) Band 4: 40-68 THz. The spectral temperatures explain the energy decay for different frequency bands of the CNT. The difference between the spectral temperature, T_{sp}, of SWCNT of different band and the temperature of PEK is shown in FIGURE 3. This temperature difference is fitted with an exponential function to find the relaxation time of spectral temperature decay for each frequncy band. The 1st frequency band decay fastest compared with the other frequncy bands, which indicates that the low frequency band phonons play an important role in the energy transfer at the interface. When the number of bonded crosslinks increase at the interface, the relaxation time of all bands decreases with increasing number of bonds (see Table 1). This suggests that the covalent bond strongly affect the energy transfer in both low and high frequency regime.

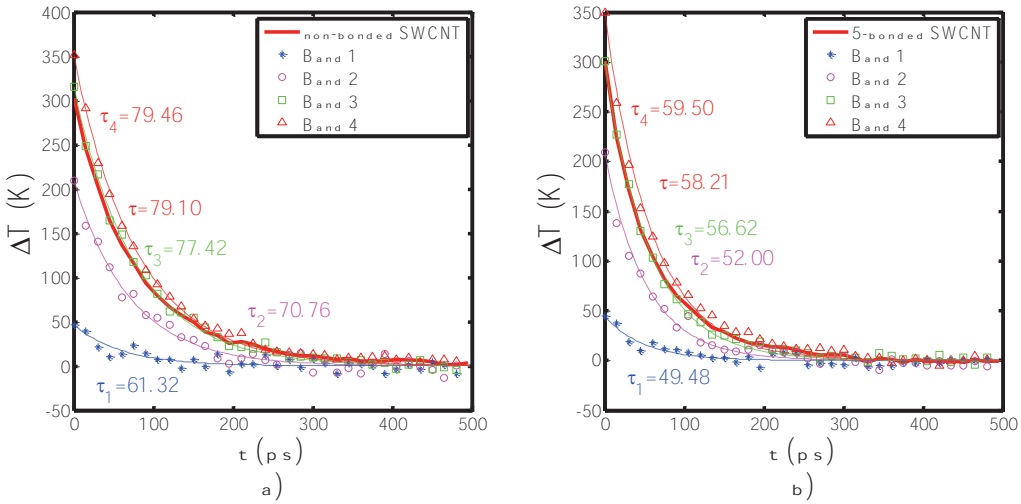

FIGURE 3. Spectral temperatue decay of CNT's frequency bands for a) non-bonded case, and b) 5-bond case.

Bonding	τ (ps)	τ_1 (ps)	τ_2 (ps)	τ_3 (ps)	τ_4 (ps)
Non-bonded	79.10	61.32	70.76	77.42	79.46
1-bonded	75.23	62.85	69.05	74.75	75.95
5-bonded	58.21	49.48	52.00	56.62	59.50

TABLE 1. Relaxation Time of Spectral Temperature with Different Number of Bonds at Interface.

4. CONCLUSIONS

The computations for TBC and spectral temperature elucidate the phonon transport at the interface between functionalized CNT and PEK. When CNT was functionalized with higher number of bonds, the thermal coupling at the interface between CNT and polymeric matrix is stronger. TBC increases as the number of bonds at the PEK-CNT interface increases. Meanwhile, the spectral temperature analysis confirms that the bonds provides channels for enhanced interfacial thermal transport and increases the efficiency of energy transfer in different frequency regions. The low frequency bands play an important role in energy transfer as relaxation of these modes are much faster.

REFERENCES

1. Jain, R., et al., *Processing, structure and properties of poly(ether ketone) grafted few wall carbon nanotube composite fibers.* Polymer, 2010. **51**(17): p. 3940-3947.
2. Moon, J., et al., *Note: Thermal conductivity measurement of individual poly(ether ketone)/carbon nanotube fibers using a steady-state dc thermal bridge method.* Review of Scientific Instruments, 2012. **83**(1).
3. Carlborg, C.F., J. Shiomi, and S. Maruyama, *Thermal boundary resistance between single-walled carbon nanotubes and surrounding matrices.* Physical Review B, 2008. **78**(20).
4. Luo, T.F. and J.R. Lloyd, *Enhancement of Thermal Energy Transport Across Graphene/Graphite and Polymer Interfaces: A Molecular Dynamics Study.* Advanced Functional Materials, 2012. **22**(12): p. 2495-2502.
5. Ong, Z.Y. and E. Pop, *Molecular dynamics simulation of thermal boundary conductance between carbon nanotubes and SiO2.* Physical Review B, 2010. **81**(15).
6. Hida, S., et al., *Thermal resistance and phonon scattering at the interface between carbon nanotube and amorphous polyethylene.* International Journal of Heat and Mass Transfer, 2013. **67**: p. 1024-1029.
7. Varshney, V., et al., *A molecular dynamics study of epoxy-based networks: Cross-linking procedure and prediction of molecular and material properties.* Macromolecules, 2008. **41**(18): p. 6837-6842.
8. Roy, A.K., et al., *Importance of Interfaces in Governing Thermal Transport in Composite Materials: Modeling and Experimental Perspectives.* Acs Applied Materials & Interfaces, 2012. **4**(2): p. 545-563.
9. Varshney, V., et al., *Effect of Curing and Functionalization on the Interface Thermal Conductance in Carbon Nanotube-Epoxy Composites.* Jom, 2013. **65**(2): p. 140-146.
10. Rajabpour, A. and S. Volz, *Thermal boundary resistance from mode energy relaxation times: Case study of argon-like crystals by molecular dynamics.* Journal of Applied Physics, 2010. **108**(9).
11. Chen, L. and S. Kumar, *Heat Dissipation Mechanism at Carbon Nanotube Junctions on Silicon Oxide Substrate.* Journal of Heat Transfer-Transactions of the Asme, 2014. **136**(5): 052401.

Fourth International Conference on Computational Methods for Thermal Problems
THERMACOMP2016, July 6-8, 2016, Georgia Tech, Atlanta, USA
N. Massarotti, P. Nithiarasu and Y. Joshi (Eds.)

INTERFACE CONDUCTANCE MODAL ANALYSIS ACROSS Si-Ge INTERFACES

Kiarash Gordiz, Asegun Henry*
George W. Woodruff School of Mechanical Engineering, Georgia Institute of Technology, Atlanta GA, 30332, USA, *email: ase@gatech.edu

ABSTRACT

Using non-equilibrium molecular dynamics simulations we show that introducing amorphous sides to the interface of Si/Ge structures increases thermal interface conductance compared to the case of having crystalline materials at both sides of the interface. In addition, we calculate the modal contributions to thermal interface conductance by using the recently proposed interface conductance modal analysis formalism. Results show dramatic changes from the case that both sides are crystalline to the cases where at least one side is amorphous. Our study shows that although amorphous materials have lower thermal conductivities, they have the potential to transfer heat faster at interfaces, which potentially can introduce a new perspective on interfacial thermal transport.

Key Words: *Interfacial Heat Transfer, Interface Conductance Modal Analysis.*

1. INTRODUCTION

Since the first experimental observation of thermal interface resistance, characterizing the exact modal contributions to interface heat transfer has long been a challenge. In this regard, it has been shown that details of atomic positions around the interface can either decrease [1] or increase[2] thermal interface conductance (G), and anharmonicity can become increasingly important especially above cryogenic temperatures, which has been investigated both theoretically [3] and experimentally [4]. Therefore, inclusion of these two effects into interface heat transfer analysis seems essential. We recently proposed a formalism termed interface conductance modal analysis (ICMA) [5, 6] that is able to determine the modal contributions to interface heat transfer by full inclusion of anharmonicity and detailed configuration of atoms around the interface in the calculations. The details of ICMA is presented elsewhere [5, 6], but in general, ICMA is based on calculating normal modes of the system using lattice dynamics and then simulating the structure using molecular dynamics (MD) and projecting the atomic velocities at each time-step in the simulation onto these identified normal modes to determine the individual modal contributions to heat transfer across the interface (Q). ICMA can be used in either non-equilibrium MD (NEMD) or equilibrium MD (EMD) to ultimately obtain the modal contributions to G. By changing the crystallinity of the sides of the interface we can have four options at the interface of Si and Ge: 1) cSi/cGe, 2) cSi/aGe, 3) aSi/cGe, and 4) aSi/aGe (See Fig. 1). Here, using ICMA and NEMD, we examine the heat transfer across these interfaces. We show that crystallinity of the materials have a huge impact on heat transfer across interfaces, and having amorphous materials at the sides of the interface can increase thermal interface conductance to a large degree.

2. SIMULATION AND METHODOLOGY

In this report, we use ICMA in its NEMD format. The modal contributions to the heat flow Q_n [5], are calculated and used in post processing, which leads to the calculation of modal thermal

conductance (G_n).Using the definition of G in NEMD simulations (i.e., $G = \frac{\overline{Q}}{\Delta T}$, where $\overline{Q}$ is the time-averaged heat flux in the NEMD simulation, and ΔT is the imposed temperature gradient across the sides of the interface), the modal description (G_n) takes the form of,

$$G_n = \frac{\overline{Q_n}}{\Delta T} \qquad (1)$$

LAMMPS package [7] and Tersoff inter-atomic potential [8] with a time step of 0.5 fs are used for the simulations. For the crystalline side the number of unit cells along x, y, and z directions are chosen to be equal to 3, 3, and 24 for both Si and Ge sides (1728 atoms). The same number of atoms is also used to make the amorphous structure. Interfaces are perpendicular to the z direction, and periodic boundary conditions are applied to all three directions. A region with a length of 20 $\mathring{A}$ is chosen in the middle of each side as heat baths. After relaxing the structure under the isobaric and isothermal ensembles (NPT) for 0.5 ns and canonical ensemble (NVT) for another 0.5 ns, a thermal power equal to 24.3 nW is input to the system from the hot heat bath and extracted from the system from the cold bath. The system is simulated for 2 ns to reach steady state. We then averaged the modal heat flux contributions for 2 ns and used Eq. (1) to calculate the modal contributions to the interface conductance. Statistical errors were reduced by averaging over 5 independent ensembles.

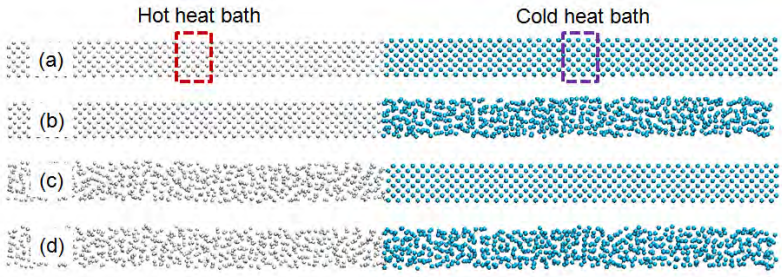

FIGURE 1. Four different interfaces between Si and Ge structures by accounting for both crystalline and amorphous materials at the sides of the interface. (a) cSi/cGe, (b) cSi/aGe, (c) aSi/cGe and (d) aSi/aGe. Heat bath positions are shown in panel (a) and are the same for other interfaces.

3. RESULTS

The result of thermal interface conductance for different interfaces are shown in Table. I. It can be seen that when both sides of the interface are amorphous, thermal interface conductance is larger than the case when both sides are crystalline. Even making one side to be amorphous increases the thermal interface conductance. Similar observations on the effect of amorphous sides on thermal interface conductance can be found in literature [9]. One explanation on how amorphous sides can lead to an increase in thermal interface conductance can be provided by considering the power spectrum of atomic vibrations (i.e., the density of states (DoS)). Correspondingly, we calculated the power spectra of the atoms at two sides of the interface [10]. Figure.2 shows the DoS for the vibrations of atoms in two the two of the considered structures. It can be seen that for the case of having amorphous materials on the sides of the interface, the overlap area is considerably larger compared to the case of having crystalline materials at the sides. We have also quantified the overlap area for the four considered structures, the result of which can be seen in Table. I. The fact

that thermal interface conductance and DoS follow the same trend for all the considered structures show that the DoS overlap can present a simple explanation for the increase in thermal interface conductance, but it does not provide answers to the detailed questions about the exact mechanism behind this observed phenomenon.

Structure	$G\left(MW\ m^{-2}\ K^{-1}\right)$	DoS overlap(%)
cSi/cGe	212.3	13
cSi/aGe	614.9	23
aSi/cGe	706.1	45
aSi/aGe	857.8	49

TABLE 1. Thermal interface conductance (G) for the four considered interfaces. The calculated error for each reported value of G and DoS overlap are less than 3% and 2%, respectively.

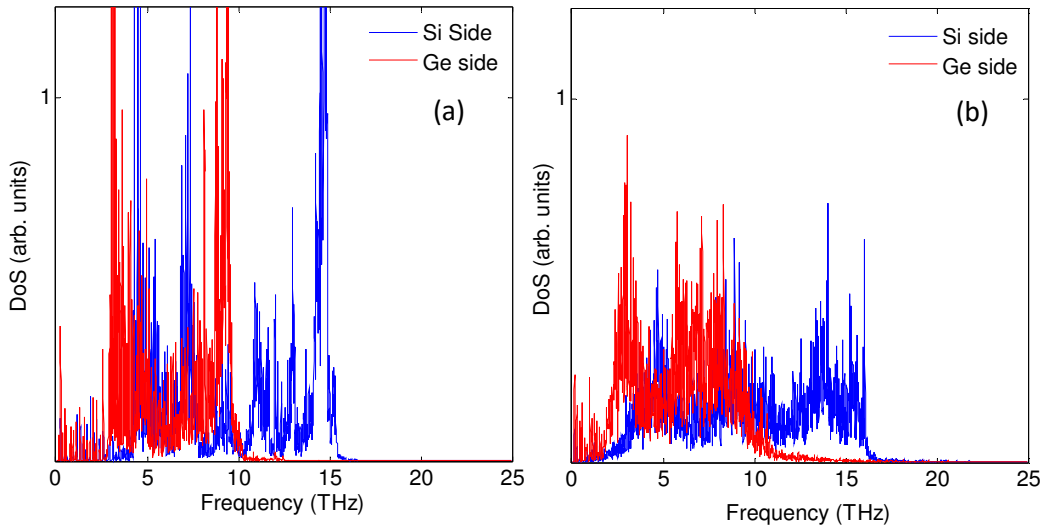

FIGURE 2. DoS for (a) cSi/cGe and (b) aSi/aGe structures. The more distributed vibrational energy present in the amorphous structure helps to enhance the DoS overlap.

In the next step, we present the modal thermal interface conductance accumulation functions for the four considered interfaces (see Fig. 3). It can be seen that even one amorphous side at the interface drastically changes the accumulation function compared to having crystalline structures on both sides of the interface. Another observation is that the large contribution from modes of vibration present around 12-13 THz is disappeared by introducing amorphous sides to the interface. The negative contributions to G calculated for aSi/cGe is an interesting observation, which is not contradicting the second law of thermodynamics, since the total value of conductance has been determined to be positive. However, observing such negative contributions to conductance simply demonstrates the possibility of having negative correlations between different modes of vibration present in the system.

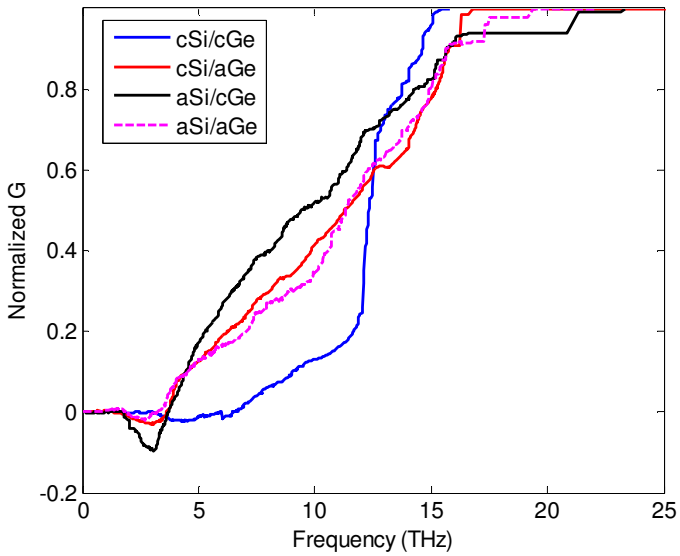

FIGURE 3. Normalized thermal interface accumulation functions for different Si/Ge structures.

4. CONCLUSIONS

This study showed that even by having constant interaction forces around the interface, thermal interface conductance has the potential to vary significantly just by changing the crystallinity of the sides of the interface. More study is needed to pinpoint whether the observed variations in thermal interface conductance are related to the local disorder caused by amorphous structure around the interface or to the nature of vibrational modes at the bulk of the amorphous structures (e.g., propagons, diffusons, and locons).

REFERENCES

[1] L. Sun and J. Y. Murthy, "Molecular dynamics simulation of phonon scattering at silicon/germanium interfaces," *Journal of Heat Transfer,* vol. 132, p. 102403, 2010.

[2] Z. Tian, K. Esfarjani, and G. Chen, "Enhancing phonon transmission across a Si/Ge interface by atomic roughness: First-principles study with the Green's function method," *Physical Review B,* vol. 86, p. 235304, 2012.

[3] Y. Chen, D. Li, J. Yang, Y. Wu, J. R. Lukes, and A. Majumdar, "Molecular dynamics study of the lattice thermal conductivity of Kr/Ar superlattice nanowires," *Physica B: Condensed Matter,* vol. 349, pp. 270-280, 2004.

[4] P. E. Hopkins, R. J. Stevens, and P. M. Norris, "Influence of inelastic scattering at metal-dielectric interfaces," *Journal of Heat Transfer,* vol. 130, p. 022401, 2008.

[5] K. Gordiz and A. Henry, "A formalism for calculating the modal contributions to thermal interface conductance," *New Journal of Physics,* vol. 17, p. 103002, 2015.

[6] K. Gordiz and A. Henry, "Phonon transport at interfaces: Determining the correct modes of vibration," *Journal of Applied Physics,* vol. 119, p. 015101, 2016.

[7] S. Plimpton, "Fast parallel algorithms for short-range molecular dynamics," *Journal of computational physics,* vol. 117, pp. 1-19, 1995.

[8] J. Tersoff, "Modeling solid-state chemistry: Interatomic potentials for multicomponent systems," *Physical Review B,* vol. 39, p. 5566, 1989.

[9] M. Li, J. Zhang, X. Hu, and Y. Yue, "Thermal transport across graphene/SiC interface: effects of atomic bond and crystallinity of substrate," *Applied Physics A,* pp. 1-10.

[10] K. Gordiz and S. M. V. Allaei, "Thermal rectification in pristine-hydrogenated carbon nanotube junction: A molecular dynamics study," *Journal of Applied Physics,* vol. 115, p. 163512, 2014.

Fourth International Conference on Computational Methods for Thermal Problems
THERMACOMP2016, July 6-8, 2016, Georgia Tech, Atlanta, USA
N. Massarotti, P. Nithiarasu and Y. Joshi (Eds.)

Thermal transport analysis of mini-channel heat sink partially filled with metal foam sandwiched on the fin sides

YongTong Li, MingHai, Xu Liang Gong*
College of Pipeline & Civil Engineering, China University of Petroleum (East China),Qingdao, 266580, China
(* Corresponding author: lgong@upc.edu.cn)

ABSTRACT

A mini-channel heat sink partially filled with metal foam sandwiched on fin sides is proposed to enhance convective heat transfer and reduce the pressure drop. The thermal and hydrodynamic performance of heat sink is numerically investigated by using Brinkman–Darcy and local thermal non-equilibrium models. The thermal performance of heat sink partially filled metal foam is compared with traditional heat sink. A parametric study is also conducted to investigate the Reynolds number, dimensionless metal foam thickness and porosity on the thermal performance and pumping power. The results show that heat sink partially filled with metal foam can enhance the convective heat transfer and the heat transfer performance is improved with the increase of dimensionless metal foam thickness. It also shows that when the dimensionless metal foam thickness is larger than 0.6, the heat transfer performance can be enhanced but it is also accompanied with drastic increase in pumping power. A proper insertion of porosity is of significance, the porosity ranges from 0.8-0.9 is recommended to enhance heat transfer with a moderate in pumping power consumption.

Keywords: Metal foam heat sink, Brinkman–Darcy model, local thermal non-equilibrium

1. INTRODUCTION

The attractive thermal performances of open-cell metal foam, such as large specific surface area, high effective thermal conductivity and strong fluid mixing capability, which makes it favourable in modern thermal applications[1]. Particularly, metal foam has a promising future in the thermal management of high power density electronic device.

Recently, numerous investigations have been conducted to enhance the convective heat transfer in heat sink by fully inserting metal foam [2-4]. These studies indicated that a significant heat transfer enhancement can be achieved when metal foams are inserted. However, the enhancement of heat transfer comes at the expense of excess pressure drop or pumping power. So the researchers attempted to improve the cooling performance by partially inserting or non-uniform inserting metal foams[5,6]. It is found that the heat transfer performance of metal foam heat sink can be improved if the insertion of metal foam configuration and pore densities conditions are properly designed[7,8].

The literature reviews show that the high pressure drop is the main obstacle for the application of heat sink fully filled with metal foam; however, with a proper design of the geometrical configuration, significant heat transfer enhancement and pressure drop reduction can be achieved simultaneously. In this paper, a design of heat sink partially filled with metal foam sandwiched on the fin sides is proposed to enhance the heat transfer and reduce pressure drop across the heat sink, in which the thickness of metal foam is symmetrically inserted on the two sides of the fins. The pertinent parameters, such as porosity, Reynolds number and dimensional metal foam thickness on the thermal performance are investigated in detail.

2. PHYSICAL MODEL AND MATHMATICAL FORMULATION

The schematic of the mini-channel heat sink partially filled with metal foam sandwiched on the fin sides is shown in Fig. 1(a). The dimension of metal foam heat sink is L_x, L_y and L_z, respectively. The channel height and width are H_c and W_c, respectively. The vertical fin width is denoted by W_r, and the thickness of the substrate wall and the cover wall are δ_1 and δ_2, respectively. A single unit is adopted for computation, as shown in Fig.1(b). Pure water is selected as the coolant. The bottom wall is supplied to a constant heat flux q_w to simulate the high power chip. The other walls are kept adiabatic.

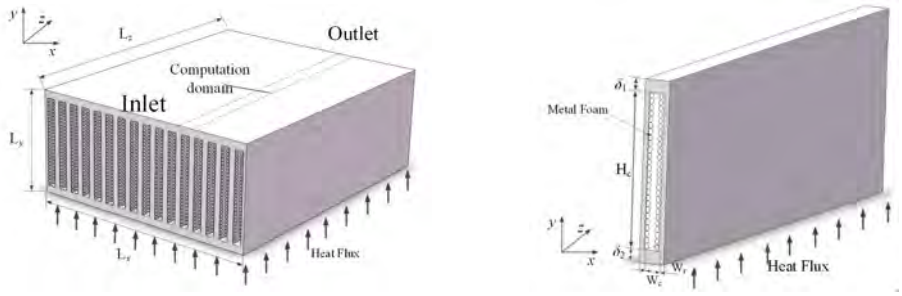

Fig.1 Physical model: (a) metal foam heat sink (b) the computational domain

The fluid flow is considered to be laminar, incompressible and steady flow through the metal foam region. The Brinkman extended Darcy model [9] is adopted for modelling fluid flow in partially filled metal foam region. The local thermal non-equilibrium energy equation is employed to describe the heat transfer process in fluid saturated metal foam domain.

Continuity equation:

$$\nabla \cdot (\varepsilon \rho \vec{V}) = 0 \tag{1}$$

Momentum equation:

$$\frac{\rho_f}{\varepsilon^2}(\vec{V}\cdot\nabla)\vec{V} = -\nabla\langle P\rangle_f + \mu_{f,eff}\nabla^2\vec{V} - (\frac{\mu_f}{K} + \frac{\rho_f C_F}{\sqrt{K}}|\vec{V}|)\vec{V} \tag{2}$$

Energy equation:

Fluid energy equation:

$$\left(\rho c_p\right)_f (\vec{V}\cdot\nabla T) = \nabla\cdot(\varepsilon k_f \nabla T) + h_{sf} a_{sf}(T_s - T_f) \tag{3}$$

Solid energy equation:

$$0 = (1-\varepsilon)\nabla\cdot(k_s \nabla T_s) - h_{sf} a_{sf}(T_s - T_f) \tag{4}$$

In the above equations, ε is the porosity; μ_{eff} is effective viscosity; T_s and T_f are the temperatures of the fluid and solid phase; k_{eff} is the effective thermal conductivity; K, C_F, h_{sf}, a_{sf} are the permeability, inertial coefficient, interfacial heat transfer coefficient and specific area, respectively.

The pumping power is written as:

$$P_{pum} = Q\Delta p \tag{5}$$

Where Q is the volume flow rate of the channel; ΔP is pressure drop.

The average nusselt number is written as:

$$Nu_m = \frac{h_m D_h}{k_f} = \frac{q_w A^{"} D_h}{(\overline{T}_w - T_{in})Ak_f} \tag{6}$$

Where the q_w is the applied heat flux; D_h is the hydraulic diameter; $\overline{T}_w$ is the average temperature of the wetted wall; k_f is the fluid thermal conductivity.

3. RESULTS

The heat transfer performance for the metal foam heat sink and the conventional channel heat sink at various Reynolds number is shown in Fig.3. The simulations are conducted at fixed ε=0.8, K=4.73×10^{-10}, α=0.5. It can be seen from Fig.3 that, as the Reynolds number increases, the average nusselt number both increases for metal foam channel and smooth channel. Compared with the conventional heat sink, the heat transfer is enhanced when the fin sides are filled with metal foam. The reason is that high thermal conductivity metal foam can conduct more heat generated from the bottom wall, and then it is dissipated by the coolant; Also, the metal foam can both enhance the convective surface and the fluid mixing, so the convective heat transfer is enhanced.

Fig.4 shows the comparison of Nu_m with Reynolds number for metal foam heat sink and conventional heat sink. It shows that the insertion of metal foam significantly increases the pressure drop, especially when the fluid flows through the channel with high velocity. This is only the case that the channel is partially filled with metal foam (α=0.5). So, the pressure drop can be unimaginable large if

the channel is fully inserted with metal foam, and it will limit its application because of the limited pumping power, especially in the electronic cooling regions.

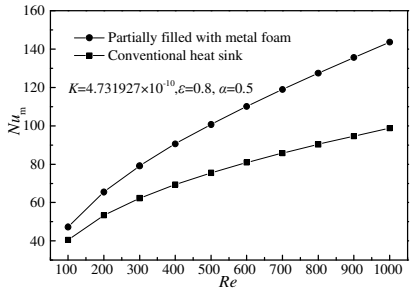

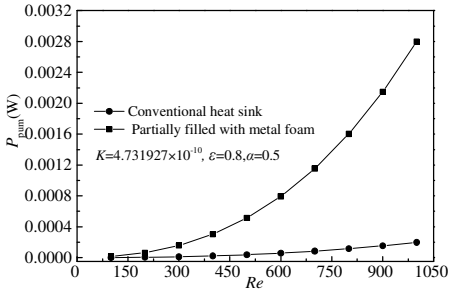

Fig. 3 Comparison of average nusselt number with Reynolds number Fig. 4 Comparison of pumping power with Reynolds number

To analyze the thermal transport process in mini-channel heat sink partially filled with metal foam sandwiched on the fin sides, the simplified heat transfer path in the metal foam heat sink is shown in Fig.5. The heat generated by the high power electronic device is conducted from the bottom substrate and then continuously transported by the solid fin and the metal foam; the heat then will dissipated by the coolant. Because the heat sink is made of high thermal conductivity copper material, the thermal resistance at the substrate is neglected, so the simplified overall thermal resistance of the heat sink is expressed as equation(7). Fig.6 shows the overall thermal resistance with Reynolds number.

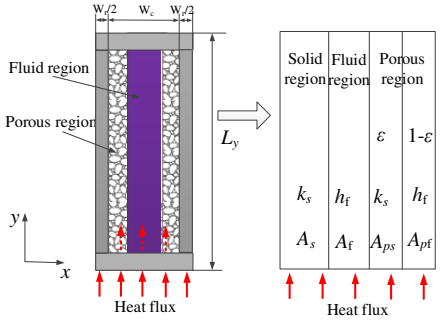

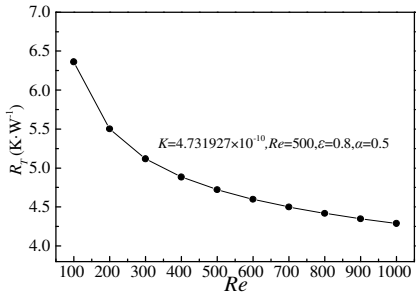

Fig. 5 Schematic of simplified heat transfer path in the metal foam heat sink Fig. 6 variation of thermal resistance with Reynolds number

$$R_T = R_{T,cd} + R_{T,cv} = \frac{H_c}{k_s A_s} + \frac{H_c}{k_s(1-\varepsilon)A_{ps}} + \frac{1}{h_f \varepsilon A_{pf}} + \frac{1}{h_f A_f} \tag{7}$$

The dimensionless metal foam thickness is the ratio of two sides metal foam thickness to the channel width. The effect of dimensionless metal foam thickness on the average nusselt number is shown in Fig.7. By increasing the dimensionless metal foam thickness, means that metal foam will occupy more volume in the channel and it will tend to the fully filled type, which in return the thermal performance is dramatically increased. However, as the dimensionless metal foam thickness increased, the supplied pumping power is also accompanied by a drastic increase, as shown in Fig.8. So, when the pumping power is the first priority to be considered, the fully filled or the closely fully filled metal foam heat sink may not be accepted in applications.

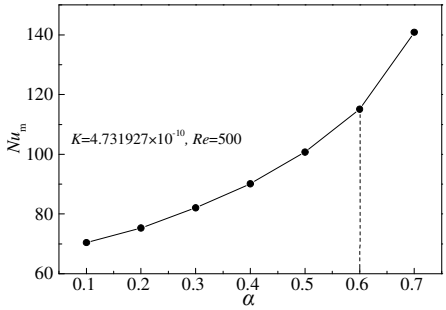

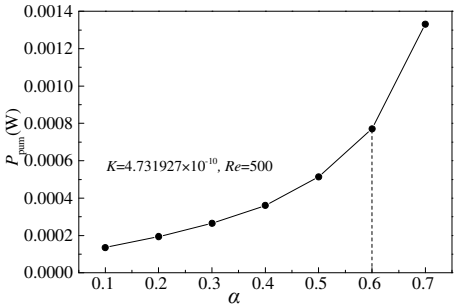

Fig. 7 The effect of dimensionless metal foam thickness on average nusselt number Fig. 8 The effect of dimensionless metal foam thickness on pumping power

The porosity of metal foam on the effect of thermal resistance of heat sink is shown in Fig.9. It shows that with an increase of porosity, the corresponding thermal resistance increases. Because increasing the porosity leads to the decrease of effective thermal conductivity of metal foam, and the conductive thermal resistance of metal foam sharply increased. In reverse, as the increase of porosity, the pumping power is sharply decreased, as shown in Fig.10. As the increase of porosity, the viscous resistance is reduced. When the porosity is closing to 1, the metal foam heat sink tends to the conventional heat sink, and the pumping power will keep constant.

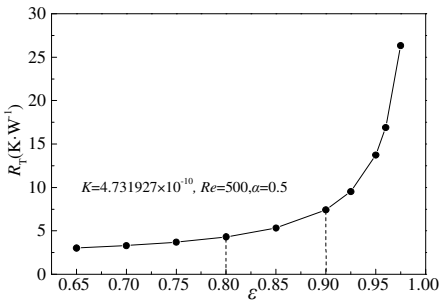

Fig. 9 The effect of porosity on average nusselt number

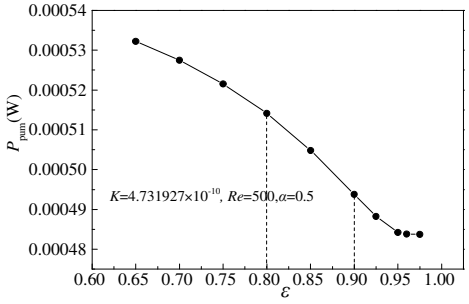

Fig. 10 The effect of porosity on pumping power

4. CONCLUSIONS

In this work, a mini-channel heat sink partially filled with metal foam sandwiched on the two sides of fins is proposed to enhance heat transfer and reduce the pressure drop across the heat sink. Hydrodynamic and thermal performance are investigated by considering the effect of Reynolds number, dimensionless metal foam thickness and porosity. The conclusions can be drawn as follows:

(1) Compared with conventional heat sink, mini-channel heat sink filled with metal foam on the fin sides can enhance the thermal performance and it will be more remarkable when Reynolds number is high.

(2) As the dimensionless thickness of metal foam increase, the thermal performance of heat sink is increased; but the highly consumed pumping power increases as a penalty. In applications, the heat sink partially filled with metal foam (α<0.6) is a better choice when the pumping power is limited.

(3) When the porosity is higher than 0.9, the thermal resistance of metal foam heat sink increases sharply. So, the porosity ranges from 0.8-0.9 is recommended to enhance the thermal performance with a moderate pumping power consumption.

REFERENCES

[1] Lu T J. Ultralight porous metals: from fundamentals to applications[J]. Acta Mechanica Sinica, 2002, 18(5): 457-479.

[2] Bhattacharya A, Mahajan R L. Finned metal foam heat sinks for electronics cooling in forced convection[J]. Journal of Electronic Packaging, 2002, 124(3): 155-163.

[3] Singh R, Akbarzadeh A, Mochizuki M. Sintered porous heat sink for cooling of high-powered microprocessors for server applications[J]. International Journal of Heat and Mass Transfer, 2009, 52(9): 2289-2299.

[4] Hung T C, Huang Y X, Yan W M. Thermal performance of porous microchannel heat sink: Effects of enlarging channel outlet[J]. International Communications in Heat and Mass Transfer, 2013, 48: 86-92.

[5] Ko K H, Anand N K. Use of porous baffles to enhance heat transfer in a rectangular channel[J]. International Journal of Heat and Mass Transfer, 2003, 46(22): 4191-4199.

[6] Chen K C, Wang C C. Performance improvement of high power liquid-cooled heat sink via non-uniform metal foam arrangement[J]. Applied Thermal Engineering, 2015, 87: 41-46.

[7] Yang J, Zeng M, Wang Q, et al. Forced convection heat transfer enhancement by porous pin fins in rectangular channels[J]. Journal of Heat Transfer, 2010, 132(5): 051702.

[8] Hung T.C., Huang Y.X., Yan W.M. Thermal performance analysis of porous-microchannel heat sinks with different configuration designs[J]. International Journal of Heat and Mass Transfer, 2013, 66: 235-243.

[9] Xu H J, Qu Z G, Lu T J, et al. Thermal modeling of forced convection in a parallel-plate channel partially filled with metallic foams[J]. Journal of Heat Transfer, 2011, 133(9): 092603.

Fourth International Conference on Computational Methods for Thermal Problems
THERMACOMP2016, July 6-8, 2016, Georgia Tech, Atlanta, USA
N. Massarotti, P. Nithiarasu and Y. Joshi (Eds.)

CONJUGATED HEAT TRANSFER IN COMPLEX GEOMETRIES VIA TOTAL INTEGRAL TRANSFORMATION AND SINGLE DOMAIN FORMULATION

José Luiz Zanon Zotin
Centro Federal de Educação Tecnológica Celso Suckow da Fonseca, CEFET/RJ, Itaguaí, RJ, Brasil, jlzzotin@gmail.com

Diego Campos Knupp
Instituto Politécnico, Universidade do Estado do Rio de Janeiro – IPRJ/UERJ, Nova Friburgo, RJ, Brasil, diegoknupp@iprj.uerj.br

Renato Machado Cotta
Comissão Nacional de Energia Nuclear, CNEN, Rio de Janeiro, and Universidade Federal do Rio de Janeiro, POLI & COPPE/UFRJ, Brasil, renato.cotta@cnen.gov.br

ABSTRACT

This work further advances the solution of transient conjugated heat transfer problems for complex geometrical configurations through the Generalized Integral Transform Technique (GITT), here combining a single domain formulation and a total integral transformation scheme based on a multidimensional eigenvalue problem. An application is considered more closely to illustrate the approach for a two-dimensional geometry, consisting of a horseshoe-like microchannel within a rectangular substrate. The results presented demonstrate the adequacy of the solution methodology for the thermal analysis and design of microfluidic systems with complex shapes.

Key Words: *Generalized Integral Transform Technique, Conjugated Heat Transfer, Single Domain Formulation, Total Integral Transformation*

1. INTRODUCTION

The analysis and design of thermal microsystems such as micro-heat exchangers and micro-reactors, aiming at more efficient processes at the micro-scale, has been quite extensively exploited in different application contexts, as brought by the fairly recent miniaturization revolution. It should be highlighted that since the pioneering works of Perelman [1] and Luikov et al. [2], the modelling of problems involving conjugated convection and conduction heat transfer phenomena has caught the attention of the scientific community, towards a more accurate analysis when compared to the classical correlations for internal convection, which neglect the wall participation in the heat transfer process. When dealing with the heat transfer analysis in micro-devices, such as micro-heat exchangers and micro-reactors, the conjugation effects can be very important due to the relative large dimensions of the substrate in which the microchannels are etched.

Recently, Knupp et al. [3] proposed the analysis of conjugated heat transfer problems through a combination of integral transforms and a single domain formulation strategy, resulting in a hybrid analytical-numerical solution for this class of problems. The single domain formulation is achieved by representing the thermal properties appearing in the model as piecewise functions, in order to describe all sub-regions of the domain (fluid and solid regions) and, therefore, allowing the conjugated problem to be modelled employing only one energy equation for the whole domain. The resulting thermal problem is then solved employing the hybrid numerical-analytical method known as the Generalized Integral Transform Technique (GITT) [4]. The methodology was demonstrated to be very accurate, motivating its use in practical problems in which the conjugation effects should

not be neglected, including the analysis of forced convection inside channels with arbitrarily shaped cross-sections [5,6]. The present work implements a total transformation scheme, in opposition to the partial transformation scheme employed in previous works [5,6], employing a multidimensional diffusive eigenvalue problem. The current approach provides a more general and automatic hybrid numerical-analytical solution for conjugated heat transfer in complex geometries, though with some penalty on convergence rates as compared to more dedicated solution alternatives that incorporate longitudinal diffusion and convection within the proposed eigenvalue problem and/or incorporate convergence enhancement techniques.

2. PROBLEM FORMULATION AND SOLUTION METHODOLOGY

Consider steady laminar incompressible internal flow in an arbitrarily shaped two-dimensional channel, undergoing transient convective heat transfer. The channel substrate is considered to participate on the heat transfer process through both transversal and longitudinal heat conduction. The single domain dimensionless formulation for this problem can be written as:

$$\frac{\partial\theta(X,Y,t)}{\partial t}+U(X,Y)W(X,Y)\frac{\partial\theta(X,Y,t)}{\partial X}+Pe\,V(X,Y)W(X,Y)\frac{\partial\theta(X,Y,t)}{\partial Y} = \frac{1}{Pe^2}\frac{\partial}{\partial X}\left(K(X,Y)\frac{\partial\theta(X,Y,t)}{\partial X}\right)+\frac{\partial}{\partial Y}\left(K(X,Y)\frac{\partial\theta(X,Y,t)}{\partial Y}\right) \tag{1.a}$$

with the following boundary and initial conditions in the example here considered:

$$\theta(X,Y,0)=0;\quad \theta(0,Y,t)=1;\quad \theta(X,0,t)=0;\quad \left.\frac{\partial\theta}{\partial X}\right|_{X=Lx}=0;\quad \left.\frac{\partial\theta}{\partial Y}\right|_{Y=Ly}=0; \tag{1.b-f}$$

First of all, a filter is proposed based on the steady two-dimensional heat conduction equation, in the form, $\theta(Y,Z,t)=\theta^*(Y,Z,t)+\theta_f(Y,Z)$, which allows for achieving homogeneous boundary conditions in both space coordinates. Instead of considering a one-dimensional eigenvalue problem to yield a partial integral transformation on the transversal direction only, either accounting or not for longitudinal diffusion within the eigenproblem, a two-dimensional purely diffusive eigenproblem is considered instead, as represented in the following integral transform pair:

$$\text{Transform:}\quad \bar{\theta}_i(t)=\int_0^{Ly}\int_0^{Lx}\widetilde{\Omega}_i(X,Y)\theta^*(Y,Z,t)dXdY \tag{2.a}$$

$$\text{Inverse:}\quad \theta^*(X,Y,t)=\sum_{i=1}^{\infty}\widetilde{\Omega}_i(X,Y)\bar{\theta}_i(t) \tag{2.b}$$

where the normalized eigenfunctions $\widetilde{\Omega}_i(X,Y)$ are obtained from the solution of the following 2-D eigenproblem, with similar boundary conditions as in eqs.(1.c-f):

$$\frac{\partial^2\widetilde{\Omega}_i(X,Y)}{\partial X^2}+\frac{\partial^2\widetilde{\Omega}_i(X,Y)}{\partial Y^2}+\beta_i^2\widetilde{\Omega}_i(X,Y)=0 \tag{3}$$

Operating on Eq. (1.a) with $\int_0^{Ly}\int_0^{Lx}\widetilde{\Omega}_i(X,Y)(.)$dX dY, the transformed ODE system is obtained:

$$\frac{d\bar{\theta}_i(t)}{dt}+\sum_{j=1}^{\infty}A_{ij}\bar{\theta}_{ij}(t)=\bar{g}_i\quad with\quad \bar{\theta}_i(0)=\bar{f}_i \tag{4.a,b}$$

Problem (4) can be analytically solved in terms of the matrix exponential function to provide explicit expressions for the transformed temperatures, $\bar{\theta}_i(t)$. Then, the inverse formula (2.b) is employed to yield the filtered temperature field $\theta^*(X,Y,t)$.

3. RESULTS AND DISCUSSION

The geometry considered involves a horseshoe like microchannel within its substrate, as illustrated in Figure 1, with the x-component of the velocity field presented in the fluid (water) region and with zero velocity at the solid (acrylic) region. Figure 2 depicts the calculated temperature field together with some isotherms. One can clearly notice the effects of the convection in the fluid region, distorting the isotherms in the microchannel region. Table 1 provides the convergence behaviour of the expansion, Eq. (2.b), for some selected points in both the solid and fluid regions, where results are converged to three significant digits for a truncation order of N < 400. Table 1 also shows the results obtained by a numeric simulation with the Comsol Multiphysics software, where is possible to notice an agreement to two significant digits in comparison with the present methodology. The results show the feasibility of employing a total transformation scheme together with the single domain formulation in order to solve conjugated heat transfer problems in complex geometries.

A convergence analysis was also undertaken, considering two different procedures for reordering of the terms in the eigenfunction expansions, namely, the traditional scheme through the sum of the squared eigenvalues, and a more elaborate one when the eigenvalues are reordered based on the diagonal of the coefficients matrix A_{ij}. In this analysis, a sufficiently large number of diagonal elements of this matrix were calculated and sorted in ascending order, and the first four hundred correspondent eigenvalues were used for calculation. Although the results are not significantly

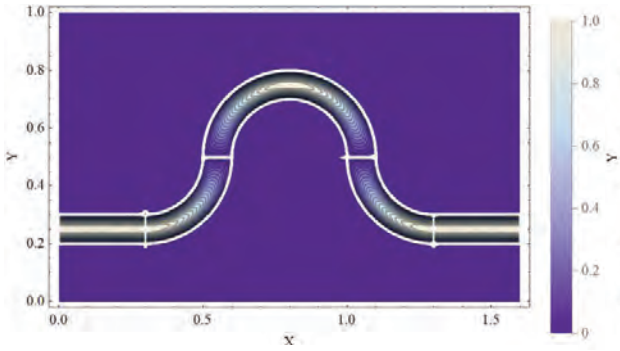

Figure 1: X-component velocity field within a horseshoe like channel (parabolic flow)

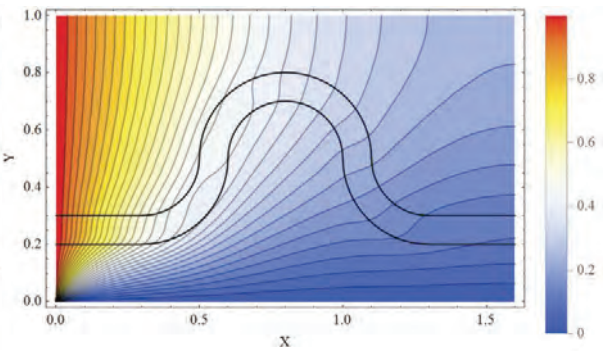

Figure 2: Computed steady temperature field and isotherms in a horseshoe like channel.

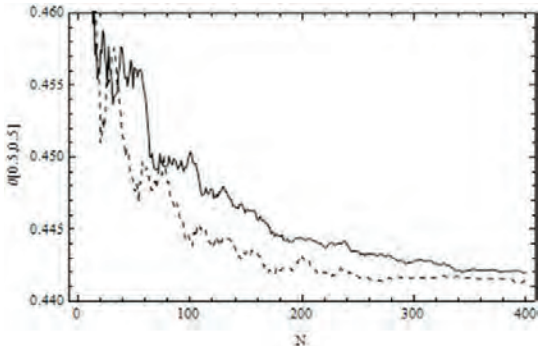

Figure 3: Convergence comparison at X = 0.5 and Y = 0.5. The dashed line corresponds to the matrix diagonal reordering scheme.

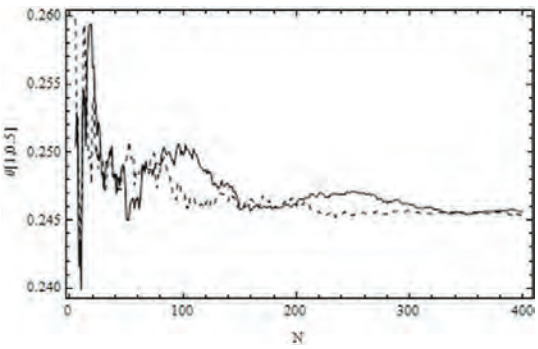

Figure 4: Convergence comparison at $X = 1$ and $Y = 0.5$. The dashed line corresponds to the matrix diagonal reordering scheme.

different, it is possible to notice in Figures 3 and 4 a slightly better convergence rate with the matrix diagonal reordering scheme, in relation to the traditional sum of the squared eigenvalues scheme.

N	$\theta(Y,Z), at\ X=0.1$			$\theta(Y,Z), at\ X=0.25$			$\theta(Y,Z), at\ Y=0.25$		
	$Y=0.1$	$Y=0.4$	$Y=0.7$	$Y=0.1$	$Y=0.4$	$Y=0.7$	$X=0.25$	$X=0.75$	$X=1.5$
40	0.54098	0.84764	0.89491	0.31052	0.63804	0.73238	0.57969	0.21257	0.10320
160	0.53301	0.84937	0.89171	0.29591	0.64935	0.73364	0.57562	0.2087	0.10251
300	0.53338	0.84919	0.89129	0.29734	0.64648	0.73463	0.57424	0.20828	0.10177
360	0.53351	0.84944	0.89151	0.29733	0.64730	0.73489	0.57434	0.20802	0.10199
400	0.53356	0.84981	0.89121	0.29741	0.64764	0.73448	0.57408	0.20795	0.10190
COMSOL	0.53160	0.85149	0.89320	0.29569	0.65310	0.73912	0.57770	0.21008	0.10662

TABLE 1. Convergence behaviour of the computed steady temperatures at selected positions and comparison with COMSOL results.

4. CONCLUSIONS

This work solves conjugated heat transfer problems combining a single domain formulation and a total integral transformation scheme from a purely diffusive two-dimensional eigenproblem, allowing for the solution of more complex geometries in comparison with the partial integral transformation scheme employed in previous works. As an application, conjugated heat transfer due to a horseshoe like microchannel in a rectangular substrate is considered. The results demonstrate the feasibility of the proposed approach in automatically handling more complex geometries, consisting of an attractive solution methodology for the thermal analysis and design of micro-systems. The research should now proceed towards the implementation of convergence enhancement techniques, for example through the proposition of a 2-D eigenproblem with space variable coefficients, through other expansion reordering rules, by taking into account the convective terms in the auxiliary problem, and/or application of integral balance schemes.

REFERENCES

[1] Perelman, T. L. (1961). On conjugated Problems of Heat Transfer. *Int. J. of Heat and Mass Transfer*, 3, 294-303.

[2] Luikov, A. V., Aleksashenko, V. A., & Aleksashenko, A. A. (1971). Analytical methods of solution of conjugated problems in convective heat transfer. *Int. J. of Heat and Mass Transfer*, 14, 1047-1056.

[3] Knupp, D. C., Naveira-Cotta, C. P., & Cotta, R. M. (2012). Theoretical analysis of conjugated heat transfer with a single domain formulation and integral transforms. *Int. Comm. in Heat and Mass Transfer*, 39, 355-362.

[4] Cotta, R. M. (1993). Integral Transforms in Computational Heat and Fluid Flow. Boca Raton, FL.: CRC Press.

[5] Knupp, D.C., Cotta, R.M., & Naveira-Cotta, C.P. (2015). Fluid Flow and Conjugated Heat Transfer in Arbitrarily Shaped Channels via Single Domain Formulation and Integral Transforms. *Int. J. Heat and Mass Transfer*, 85, 479-489.

[6] Knupp, D.C., Naveira-Cotta, C. P., Renfer, A., Tiwari, M. K., Cotta, R.M., and Poulikakos, D. (2015). Analysis of Conjugated Heat Transfer in Micro-Heat Exchangers via Integral Transforms and Non-Intrusive Optical Techniques, Int. J. Num. Meth. Heat & Fluid Flow, 25 (6), 1444-1462.

Fourth International Conference on Computational Methods for Thermal Problems
THERMACOMP2016, July 6-8, 2016, Georgia Tech, Atlanta, USA
N. Massarotti, P. Nithiarasu and Y. Joshi (Eds.)

PERFECT ABSORPTION IN HBN/METAL GRATING HYBRID ANISOTROPIC STRUCTURES

Bo Zhao and Zhuomin M. Zhang
G.W. Woodruff School of Mechanical Engineering
Georgia Institute of Technology, Atlanta, Georgia 30332, USA
E-mail: zhuomin.zhang@me.gatech.edu

ABSTRACT

Hybrid structures consisting of two-dimensional materials and periodic nanostructures show great potential to create unique radiative properties. Their accurate simulation requires an algorithm that can model anisotropic materials. In this work, an anisotropic rigorous coupled-wave analysis algorithm is developed that can calculate the radiative properties of periodic multilayer structures that contain anisotropic materials. Using this algorithm, a hybrid structure consisting of hexagon boron nitride and Ag grating is demonstrated that can enable perfect absorption in mid-infrared range. This work may facilitate the design of hybrid structures with unexplored radiative properties.

Key Words: *Anisotropic RCWA, Perfect Absorption, hBN, Metal Gratings.*

1. INTRODUCTION

Emerging two-dimensional (2D) materials offer enormous potentials to revolutionize current microelectronic, optoelectronic, and photonic devices as well as energy harvesting systems. The most popular 2D materials include graphene, hexagonal boron nitride (hBN), TMDCs (transition metal dichalcogenides, such as MoS_2), and recently emerged black phosphors. Due to their atomically thin layer and relatively short light-matter interaction path, most 2D materials are not good thermal absorbers. Recent studies show that, by combining graphene with periodic metal gratings, coupled resonances can be created and strongly enhance the absorption [1-3]. The hybridization of 2D materials with metamaterials provides a new route to design nanostructures with unique radiative properties, which is of critical importance in energy harvesting, radiative cooling, and photo detecting applications [4]. However, the atomically thin thickness of 2D materials induces a natural anisotropy in the out-of-plane direction for their optical properties. Some of them, such as black phosphors, even has an in-plane anisotropy, which leads to a strong biaxial behavior. The anisotropy requires a permittivity tensor to describe and makes the modeling much more challenging, especially when 2D materials are combined with periodic nanostructures.

Commercial simulation packages, such as Lumerical and COMSOL, can include the anisotropic effect, but the simulations suffer from convergence issues and long simulation time. Traditional rigorous coupled-wave analysis (RCWA), on the other hand, is fast and more convenient to model periodic structures but only suitable for isotropic media. The most promising efficient method would be anisotropic RCWA and it was proposed in the early 1990s [5]. However, the algorithm has not been widely used due to the extreme complexity and potential convergence problem, which has been noted in the late 1990s [6]. While this issue has been resolved for most isotropic RCWA codes, it has not been implemented in the anisotropic algorithm yet.

In this work, an anisotropic RCWA algorithm is developed to deliver fast and accurate simulation results for multilayer periodic uniaxial and biaxial anisotropic media. The algorithm is applied to model the radiative properties of a hybrid structure consisting of hBN and Ag grating. It is shown that the phonon-polaritonic waveguide modes in hBN and magnetic polaritons (MP) in Ag gratings can couple with each other and enable coherent absorption with an absorptance close to one. The algorithm and results may facilitate the design of hybrid structures with unique radiative properties.

2. NUMERICAL ALGORITHM

A schematic of an anisotropic multilayer structure is depicted in Fig. 1. The number of the layer is denoted as l and the range is 1 to N. Each layer can be either grating or film by adjusting l_x and l_y. The incident medium is set to be isotropic. The dielectric tensor for the l-th layer is $\overline{\overline{\varepsilon_l}}$, which contains only the diagonal terms. The incident medium, the intermediate layers (N layers in total), and the substrate can be categorized as region I, II, and III, respectively. The electromagnetic wave in each region is expressed as Fourier series based on the period of both x- and y- directions. The coefficients of the series terms are left unknown and later solved by using the boundary conditions. Specifically, the electric field in the region I can be written as

$$\mathbf{E}_{\mathrm{I}} = \mathbf{E}_{\mathrm{inc}} \exp\left(ik_{x,\mathrm{inc}}x + ik_{y,\mathrm{inc}}y + ik_{z,\mathrm{inc}}z\right) + \sum_m \sum_n \mathbf{E}^{\mathrm{r}}_{mn} \exp\left(ik_{x,m}x + ik_{y,n}y - ik^{r}_{z,mn}z\right) \tag{1}$$

where $\mathbf{E}_{\mathrm{inc}}$ is a unit vector describing the direction of the electric field of the incident wave. The second term on the right-hand side is the reflected wave. $\mathbf{E}^{\mathrm{r}}_{mn}$ is the complex amplitude of the (m, n) order reflected wave, whose wave vector is

$$k^{r}_{z,mn} = \begin{cases} \sqrt{k_{\mathrm{I}}^2 - k_{x,m}^2 - k_{y,n}^2} & , \quad \varepsilon_{\mathrm{I}} k_0^2 \geq k_{x,m}^2 + k_{y,n}^2 \\ i\sqrt{k_{x,m}^2 + k_{y,n}^2 - k_{\mathrm{I}}^2} & , \quad \varepsilon_{\mathrm{I}} k_0^2 < k_{x,m}^2 + k_{y,n}^2 \end{cases} \tag{2}$$

where ε_{I} is the dielectric function of the incident medium, and $k_{x,m}$ and $k_{y,n}$ are determined by the Bloch-Floquet condition: $k_{x,m} = k_{x,\mathrm{inc}} + 2\pi m/\Lambda_x$ and $k_{y,n} = k_{y,\mathrm{inc}} + 2\pi n/\Lambda_y$.

In the region II, the electric and magnetic field can be expressed as

$$\begin{aligned} \mathbf{E}_{\mathrm{II}} &= \sum_m \sum_n \boldsymbol{\chi}_{mn}(z) \exp\left(ik_{x,m}x + ik_{y,n}y\right) \\ \mathbf{H}_{\mathrm{II}} &= i\sqrt{\frac{\varepsilon_0}{\mu_0}} \sum_m \sum_n \boldsymbol{\gamma}_{mn}(z) \exp\left(ik_{x,m}x + ik_{y,n}y\right) \end{aligned} \tag{3}$$

The coefficient $\boldsymbol{\chi}_{mn}(z)$ and $\boldsymbol{\gamma}_{mn}(z)$ are related by Maxwell's equations. The substrate (region III) in general is a biaxial medium. The (m, n) order transmitted plane wave in this region is with a wave vector $\left(k_{x,m},\, k_{y,n},\, k^{t}_{z,mn}\right)$. The electric field inside can be written as

$$\mathbf{E}_{\mathrm{III}} = \sum_m \sum_n \sum_{j=1}^{2} E^{t}_{j,mn} \mathbf{p}_{j,mn} \exp\left(ik_{x,m}x + ik_{y,n}y + ik^{t}_{j,z,mn}(z - Z)\right),\ Z = \sum_{l=1}^{N} d_l \tag{4}$$

in which

$$\mathbf{p}_{j,mn} = N_{j,mn} \begin{pmatrix} \left(\omega^2 \mu \varepsilon_{\mathrm{III},yy} - k_{x,m}^2 - k_{j,z,mn}^{2,t}\right)\left(\omega^2 \mu \varepsilon_{\mathrm{III},zz} - k_{x,m}^2 - k_{y,n}^2\right) - k_{y,n}^2 k_{j,z,mn}^{2,t} \\ k_{x,m}k_{y,n}k_{j,z,mn}^{2,t} - k_{x,m}k_{y,n}\left(\omega^2 \mu \varepsilon_{\mathrm{III},zz} - k_{x,m}^2 - k_{y,n}^2\right) \\ k_{x,m}k_{y,n}^2 k^{t}_{j,z,mn} - k_{x,m}k^{t}_{j,z,mn}\left(\omega^2 \mu \varepsilon_{\mathrm{III},yy} - k_{x,m}^2 - k_{j,z,mn}^{2,t}\right) \end{pmatrix} \tag{5}$$

is the polarization vector for the electric field and $N_{j,mn}$ is a coefficient that normalizes $\mathbf{p}_{j,mn}$. Index j can take 1 or 2 since there are two allowed wave vectors for each order. The magnetic field can be obtained from the electric field based on Maxwell's equations. The complex amplitudes are then solved by matching the tangential component of the electric and magnetic field between different layers. This is done by complicated matrix manipulations. Once the coefficients are obtained, the reflectance, transmittance, as well as the field distribution in each layer can be calculated.

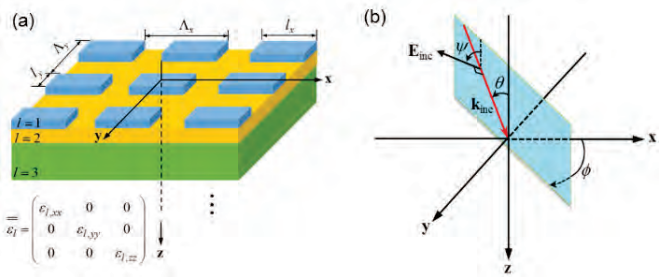

FIGURE 1. (a) Schematic of a periodic multilayer structure consisting of anisotropic materials; (b) the plane of incidence and the polarization of the incident electric field.

3. RESULTS

The developed algorithm is applied to calculate a proposed hybrid structure, which consists of a hBN film on a metal grating, as shown in Fig. 2(a). The hBN film thickness, *d*, is fixed at 30 nm in this work. The grating is made of silver and its period in the *x*-direction is Λ. The trench height and width are denoted as *h* and *b*, respectively. For transverse magnetic (TM) waves, magnetic polaritons or MPs can be excited inside the grating [7] and cause an emittance peak as shown in Fig. 2(b). The geometries of the grating are given in the figure. The hBN film is a uniaxial medium with two mid-infrared Reststrahlen bands shown as the shaded regions in Fig. 2(b). The in-plane and out-of-plane dielectric functions include the contributions from the in-plane phonon vibrations ($\omega_{\mathrm{TO},\perp} = 1370$ cm^{-1} and $\omega_{\mathrm{LO},\perp} = 1610$ cm^{-1}) and out-of-plane phonon vibrations ($\omega_{\mathrm{TO},\parallel} = 780$ cm^{-1} and $\omega_{\mathrm{LO},\parallel} = 830$ cm^{-1}), respectively, which are given by

$$\varepsilon_m = \varepsilon_{\infty,m}\left(1 + \frac{\omega_{\mathrm{LO},m}^2 - \omega_{\mathrm{TO},m}^2}{\omega_{\mathrm{TO},m}^2 - i\gamma_m\omega - \omega^2}\right) \tag{6}$$

where $m = \parallel, \perp$. The other parameters used are $\varepsilon_{\infty,\parallel} = 2.95$, $\gamma_{\parallel} = 4$ cm^{-1}, $\varepsilon_{\infty,\perp} = 4.87$, and $\gamma_{\perp} = 5$ cm^{-1}. Since the damping rates of the vibrations are low, the in-plane dielectric function has a different sign with the out-of-plane dielectric function in the two Reststrahlen bands, making hBN a hyperbolic material that can support multiple orders of phonon-polaritonic waveguide modes [8]. These modes have high quality factors and may be used to create coherent thermal emission. However, the wave vectors required by the waveguide modes are too large to be supported by propagating waves in vacuum. Thus, the absorptance spectrum of hBN film only shows a low peak

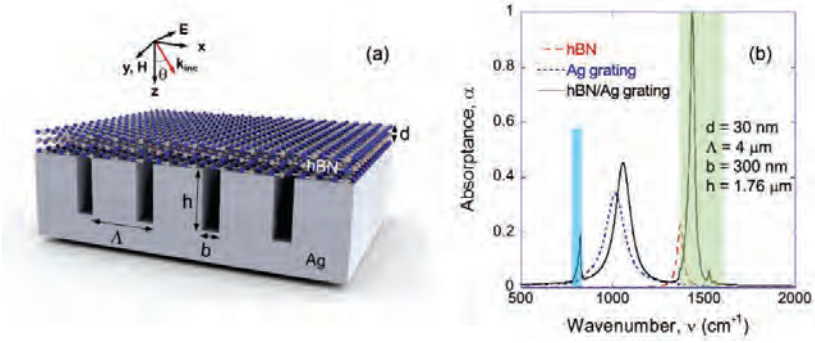

FIGURE 2. (a) Schematic of the hBN-covered 1D grating nanostructure for a plane TM wave incident at an angle of θ. (b) Absorptance of a 30-nm hBN film, a plain Ag grating and a hBN-covered grating for TM waves at normal incidence.

close to $\omega_{TO,\perp}$, as shown in Fig. 2(b). However, after combining with a Ag grating, a perfect absorption peak is created, indicating a strong coupling between MPs in the grating and the waveguide modes in hBN film in the higher Reststrahlen band.

Depend on the frequency of MP, the coupling can also happen in the lower Reststrahlen band. This can be demonstrated in Fig. 3, in which the absorptance for plain gratings and hybrid structures are given as a function of the trench height. The two bright bands in (a) indicate the excitation of the first order MP (MP1) and the second order MP (MP2). When h becomes larger, MPs are pushed to the lower frequency and coupled with the waveguide modes in the lower Reststrahlen band, resulting a perfect absorption at $h = 2.4$ μm as shown in Fig. 3(b). The white lines show the Reststrahlen bands. Meanwhile, the waveguide modes couple with MPs differently in the two Reststrahlen bands, as indicated by the shape of the bands. This may due to the different hyperbolicity of the waveguide modes. Note that the hBN film thickness can be tuned to allow more orders of waveguide mode to couple with MPs. The grating geometries can also be modified and enable tunable perfect absorption.

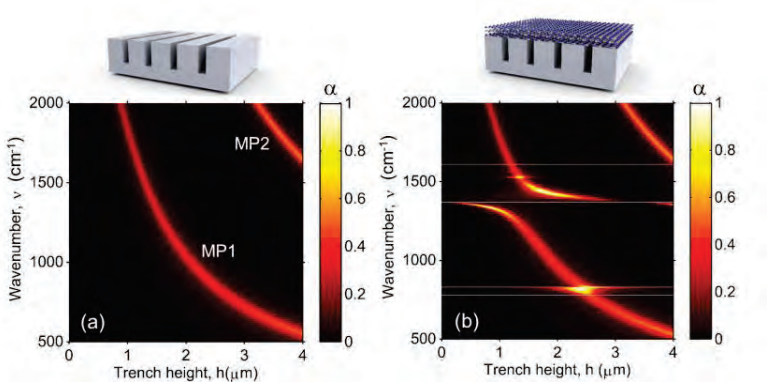

FIGURE 3. Absorptance contour for (a) plain gratings and (b) hBN-covered gratings.

4. CONCLUSIONS

In this work, an anisotropic RCWA algorithm is developed that is able to simulate multilayer periodic anisotropic media. The hybrid structure consisting of hBN and Ag grating is demonstrated that can create strong couplings between the phonon-polaritonic waveguide modes in hBN and MPs in Ag gratings. The coupled resonances enable perfect absorption in the two Reststrahlen bands and can be tuned by the geometries of the hybrid structure. The results show a great potential to create unique radiative properties using hybrid structures with 2D materials and metamaterials.

REFERENCES

[1] B. Zhao, J. M. Zhao, Z. M. Zhang, *Applied Physics Letters*, 105, 031905, 2014.
[2] B. Zhao, J. M. Zhao, Z. M. Zhang, *Journal of the Optical Society of America B*, 32, 1176-85, 2015.
[3] B. Zhao, Z. M. Zhang, *ACS Photonics*, 2, 1611-8, 2015.
[4] Z. M. Zhang, *Nano/Microscale Heat Transfer*, McGraw-Hill, New York, 2007.
[5] E. N. Glytsis, T. K. Gaylord, *Journal of the Optical Society of America A*, 7, 1399-420, 1990.
[6] L. Li, *Journal of the Optical Society of America A*, 13, 1870-6, 1996.
[7] B. Zhao, Z. M. Zhang, *Journal of Quantitative Spectroscopy and Radiative Transfer*, 135, 81-9, 2014.
[8] S. Dai, Z. Fei, Q. Ma, A. S. Rodin, M. Wagner, A. S. McLeod, M. K. Liu, W. Gannett, W. Regan, K. Watanabe, T. Taniguchi, M. Thiemens, G. Dominguez, A. H. C. Neto, A. Zettl, F. Keilmann, P. Jarillo-Herrero, M. M. Fogler, D. N. Basov, *Science*, 343, 1125-9, 2014.

MINI SYMPOSIUM

MULTISCALE METHODS IN THERMAL SIMULATIONS

MINI SYMPOSIUM ORGANISED BY PRATAP VANKA AND
YOGENDRA JOSHI

Fourth International Conference on Computational Methods for Thermal Problems
THERMACOMP2016, July 6-8, 2016, Georgia Tech, Atlanta, USA
N. Massarotti, P. Nithiarasu and Y. Joshi (Eds.)

Multi-Length Scale Electro-Thermal Simulations of GaN High Electron Mobility Transistors

Qing Hao, Hongbo Zhao, Yue Xiao
Aerospace and Mechanical Engineering, University of Arizona, Tucson, AZ 85712,
qinghao@email.arizona.edu

ABSTRACT

Overheating has largely limited the performance of GaN-based high electron mobility transistors (HEMTs) as high-power and high-frequency electronic devices. In this work, a multi-length scale simulation technique is developed and demonstrated in a 2D GaN-on-SiC HEMT. For the transistor region, coupled electron and phonon Monte Carlo (MC) simulations are used to address the phonon emission by hot electrons and phonon transport within the ~10 μm transistor region. Away from the transistor, conventional Fourier analysis is invoked so that heat transfer across the whole macroscale device can still be considered. Energy-dependent electron and phonon transport, either within a material or across an interface, can be incorporated into the simulation. Beyond 2D HEMTs, this technique can be applied to more complicated 3D devices for accurate prediction of device characteristic.

Key Words: *Multi-length scale, coupled electron and phonon MC simulations, HEMT.*

1. INTRODUCTION

With their high radio-frequency (RF) power density, operation frequency, and breakdown voltage, GaN-based devices exhibit significant advantages over silicon-based devices for high-power amplifications. One of the most widely used GaN devices is the high electron mobility transistor (HEMT). In a GaN HEMT, two-dimensional electron gas (2DEG) is formed on the interface between GaN and its ternary alloy (e.g., AlGaN). With its high carrier mobility and carrier density, such 2DEG can transport a large current for power electronics. Currently, GaN HEMTs have demonstrated a record-breaking 40 W/mm RF power output level as power amplifiers and >10 kV breakdown voltage as power-switching devices [1]. However, such superior device performance is largely restricted by the significant overheating within a GaN-based device, which would dramatically reduce the charge carrier mobility and lower the output current [2]. Due to the challenges in thermal management, commercial GaN HEMTs are still limited to 2–4 W/mm output power. In addition to the deteriorated performance, the strong overheating will also shorten the lifetime of GaN devices, which is critical to their long-term applications [3].

Experimentally, various approaches have been proposed to improve the thermal management of GaN HEMTs. To provide theoretical guidance for better thermal designs, a multi-length scale electro-thermal simulation of a GaN HEMT is needed. The length scale spans from a few nanometers in the hot spot region to hundreds of micrometers across the device substrate. Along the conduction channel of a transistor, heat is generated as acoustic or optical phonons emitted by hot electrons that gain energy from an ultra-high electrical field. Non-propagating optical phonons further decay into acoustic phonons that eventually carry heat across the whole millimeter- or centimeter-sized device.

The challenge in the electro-thermal simulations of GaN HEMTs lies in that detailed electron and phonon transport cannot be considered for the whole macroscale device due to the huge computational load. In existing studies, simplifications must be taken and often lead to large discrepancy with the experimental data. In this work, coupled electron and phonon Monte Carlo

(MC) simulations are performed for the micrometer transistor region (Figure 1). The electron MC simulations will track the movement and scattering of individual charge carriers and provide phonons emitted by hot electrons. The phonon emission will be further input into the phonon MC simulations to update the phonon temperatures that further affect electron scattering in electron MC simulations. The two simulations are thus carried out in an iterative way to achieve self-consistency. Energy-dependent electron and phonon transport can be fully considered in these MC simulations. To further predict the temperature profile of the entire macroscale device, the phonon MC simulation is coupled with the conventional Fourier analysis for regions away from the transistor.

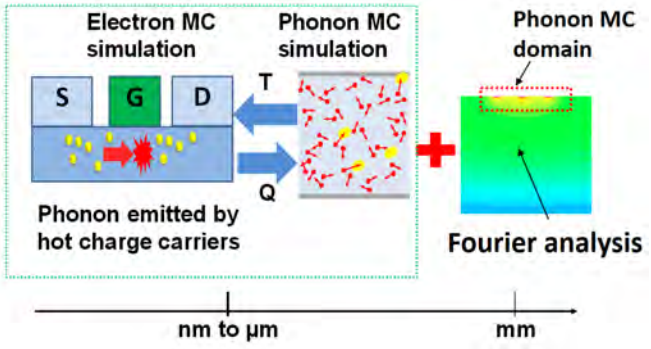

Figure 1. Scheme of multi-length scale electro-thermal simulations of a GaN HEMT.

2. METHODS

MC technique is used to simulate the electron or phonon transport in the transistor region of a HEMT device. In this technique, the motion of electrons and phonons is treated classically. The electron MC simulation is for the 2DEG along the conduction channel. For a given source-gate voltage, the electric field along the channel is first calculated, and is used to accelerate the electrons. The scattering mechanisms for electrons are with polar optical phonons, acoustic phonons, and intervalley optical phonons [4]. Since the 2DEG are confined in the GaN/AlGaN interface on the undoped GaN side, ionized impurity scattering is ignored. The local heat generation rate is counted by tracking the phonon emission during the simulation. For simplicity, only the highest longitudinal optical phonons, with energy of 91.2 meV, is considered.

For the phonon MC simulation, we used the deviational MC method [4] which can improve the computational efficiency by orders of magnitudes and thus enable simulations of ~10 μm domain sizes. In this new method, phonons are drawn from the deviation of the phonon distribution function from the Bose-Einstein distribution (i.e., equilibrium distribution function) at a reference temperature. Instead of solving for all phonons corresponding to the distribution function, only simulating these deviational phonons allows dramatic reduction of simulated phonons. We only consider acoustic phonons in the phonon MC simulations and the emitted optical phonons decay into acoustic phonons to be included in the simulation.

Different materials are present in a GaN HEMT device which normally features multiple layers. The rather complicated phonon dispersions of the materials are simplified as an isotropic sine-shape dispersion (Born-von Karman dispersion), with identical one longitudinal acoustic (LA) and two transverse acoustic (TA) branches. The Umklapp processes of the phonon-phonon scatterings are considered, as well as the phonon scattering with impurities. By fitting temperature-dependent thermal conductivities, we can determine all parameters in these scattering mechanisms. The interface thermal resistance is considered using phonon transmissivity from one material to another using the diffuse mismatch model [5].

Our electron and phonon MC simulations are coupled, and the basic relations are the following: In the 2DEG region, electron MC can output the phonon generation by hot electrons, but needs local phonon temperatures to determine the scattering rates of electrons; in the transistor region, phonon MC simulation can output phonon temperatures, but needs phonon generation by the 2DEG and the temperature of the domain boundary. The size of the phonon MC simulation domain (> 10 μm) is larger than the mean free paths of majority phonons so that thermal equilibrium between phonons and the local temperature can be assumed on the phonon MC domain boundary. The coupled simulation starts with a guessed phonon temperature profile in electron MC simulations to produce the phonon generation by 2DEG. For the whole device, the heat generation rate of generated phonons is fed into ANSYS, using the Fourier's law, to update the temperatures on the phonon MC domain boundary. The coupled electron and phonon MC simulations can then be used to refine the phonon generation and phonon temperatures of the transistor region. These steps can now be iterated and self-consistency can be achieved by comparing the subsequent temperature profiles.

3. RESULTS

The four-layer structure of our simulated 2D GaN HEMT is illustrated in Figure 2. From the top to bottom, there are a 30-nm-thick AlGaN layer, a 2.5-μm-thick GaN layer, a 60-nm-thick AlN buffer layer, and the substrate SiC with 500 μm thickness. The source, gate, and drain are on top of the AlGaN layer, and are all 1 μm wide, and 1 μm apart. The horizontal length of the whole device is chosen to be 500 μm. In our simulation, the drain-to-source and gate-to-source voltages are 15 V and 0V, respectively.

For electron MC simulation, the convergence is achieved relatively fast. we compare the classical Joule heating with the heat generation rate from electron MC simulation in Figure 3. The Joule heating is calculated as $\boldsymbol{J}\cdot\boldsymbol{E}$, and is the macroscopic version of the energy dissipation of electrons driven by an electric field $\boldsymbol{E}$. For a small electric field on the left half of the figure, Joule heating does not differ largely from the heat generation rate as phonon emission. However, the peak heat generation rate is overestimated with $\boldsymbol{J}\cdot\boldsymbol{E}$. This trend agrees with the early work on Si by Pop *et al.* [6].

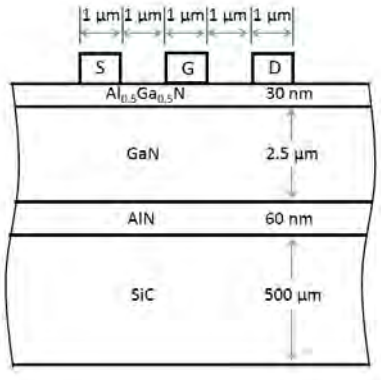

Figure 2. Schematic diagram of the cross section of the simulated GaN HEMT

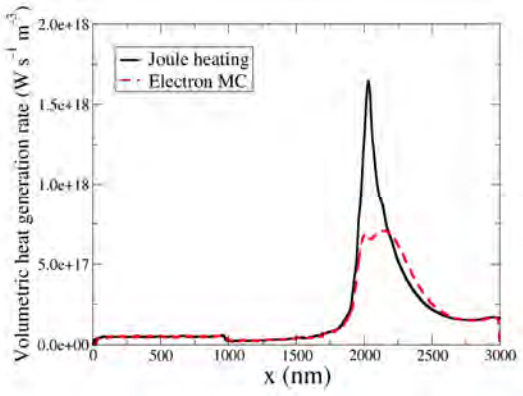

Figure 3. Comparison between volumetric Joule heating and heat generation rate corresponding to phonon emission.

We used ANSYS to simulate the temperature profile for the whole 500 μm × 500 μm device. Part of the calculated temperature is shown in Figure 4(a). The phonon MC simulation domain is 12 μm × 5.59 μm, and more than 60 million phonons are used in the MC simulation. The final temperature profile is shown in Figure 4(b).

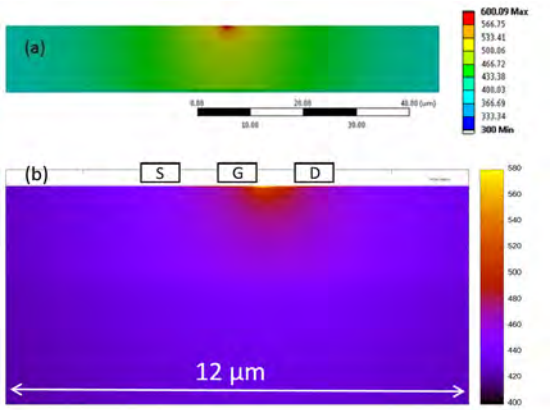

Figure 4. Temperature profile close to heat generation region from (a) ANSYS calculation, and (b) converged phonon MC simulation.

4. CONCLUSIONS

We have demonstrated a multi-length scale simulation for GaN HEMTs, which employs coupled electron and phonon MC simulations for the transistor region and conventional Fourier analysis away from the transistor. Deviational phonon MC technique is used in the phonon simulation, so that realistic transistor size can be simulated with reasonable computational load, which can be 3–5 orders of magnitude larger than the possible system size simulated with traditional MC technique. This hybrid simulation technique allows simulations of GaN HEMTs that are further cooled within the substrate, e.g., active cooling by single-phase or two-phase flows. Our generic method can be applied to other devices where overheating is critical to the device performance.

This material is based on research sponsored by Defense Advanced Research Agency (DARPA) under agreement number FA8650-15-1-7523. The U.S. Government is authorized to reproduce and distribute reprints for Governmental purposes notwithstanding any copyright notation thereon.

REFERENCES

[1] M. Yanagihara, Y. Uemoto, T. Ueda, T. Tanaka, and D. Ueda, Recent advances in GaN transistors for future emerging applications. *physica status solidi (a)*, 206, 1221-1227, 2009.

[2] Y.-R. Wu and J. Singh, Transient study of self-heating effects in AlGaN/GaN HFETs: Consequence of carrier velocities, temperature, and device performance. *Journal of Applied Physics*, 101, 113712, 2007.

[3] M. Rosker *et al.*, The DARPA wide band gap semiconductors for RF applications (WBGS-RF) program: Phase II results, The International Conference on Compound Semiconductor Manufacturing Technology, Tampa, FL, 2009.

[4] J.-P.M. Péraud and N.G. Hadjiconstantinou, Efficient simulation of multidimensional phonon transport using energy-based variance-reduced Monte Carlo formulations. *Physical Review B*, 84, 205331, 2011.

[5] Q. Hao, Influence of structure disorder on the lattice thermal conductivity of polycrystals: A frequency-dependent phonon-transport study. *Journal of Applied Physics*, 111, 014309, 2012.

[6] E. Pop, R.W. Dutton, and K.E. Goodson, Analytic band Monte Carlo model for electron transport in Si including acoustic and optical phonon dispersion. *Journal of Applied Physics*, 96, 4998-5005, 2004.

Fourth International Conference on Computational Methods for Thermal Problems
THERMACOMP2016, July 6-8, 2016, Georgia Tech, Atlanta, USA
N. Massarotti, P. Nithiarasu and Y. Joshi (Eds.)

A COMPARISON BETWEEN DIFFERENT LIFTING RELATIONS FROM MACROSCOPIC VARIABLES TO LATTICE BOLTZMANN DISTRIBUTION FUNCTIONS

Zi-Xiang Tong, Ming-Jia Li, Ya-Ling He *, Wen-Quan Tao
Key Laboratory of Thermo-Fluid Science and Engineering of Ministry of Education

School of Energy and Power Engineering, Xi'an Jiaotong University, Xi'an, Shaanxi, 710049, China

E-mail: yalinghe@mail.xjtu.edu.cn

ABSTRACT

The lifting relations for the reconstruction of the distribution functions of lattice Boltzmann method (LBM) from the macroscopic variables are compared. The single-relaxation-time (SRT) and multiple-relaxation-time (MRT) models with both first- and second- order expansions are studied. The results show that the lifting relations for SRT-LBM are more precise, but the relations for MRT-LBM are more stable. The differences between the first and second order models are small, For the MRT-LBM, the modified models should be used to insure the continuity of the velocity.

Key Words: *Lattice Boltzmann Method, Coupling Method, Initial Condition, Boundary Condition.*

1. INTRODUCTION

Multiscale processes are frequently meeting in heat transfer and fluid flow problems [1]. In the multiscale processes, the sub-processes always cover different time and spatial scale and are described by different governing equations. The multiscale numerical methods are needed for this kind of problems. One of the multiscale methods is to employ different numerical methods for different sub-processes according to the scale and couple them at the interfaces. This methodology has been adopted for various problems ranging from atomistic scale to macroscopic scale [1].

This paper focuses on the coupling between lattice Boltzmann method (LBM) and macroscopic methods. The LBM has been coupled with different macroscopic methods to simulate various multiscale transport processes [2-3]. Recently, Velivelli and Bryden [4-5] coupled LBM with alternating direction implicit method and vorticity-stream function method to solve the 2-D Burgers' equation and backward facing step flow. Salimi et al. [6-7] used the hybrid LBM and finite volume method (FVM) to simulate the flow and heat transfer around a porously covered square cylinder. They all found that the hybrid method is more efficient for the multiscale problems.

An important problem in the coupling methods is the information transfer from macroscopic methods to LBM because LBM contains more variables. The relations are called reconstruction operators (RO) in the following paper. For the single-relaxation-time (SRT) LBM, Tong and He [8] have derived a generalized RO for different lattice Boltzmann models and only first-order derivatives are considered in their derivations. Salimi and Taeibi-Rahni [9] also have developed a RO for the multiple-relaxation-time (MRT) LBM, in which the second-order derivatives were taken into consideration.

In order to choose the proper lifting relations in the coupling simulation, the precisions of the different ROs should be evaluated, which is the main purpose of the present paper. The models in this work can be also used as the initial and boundary conditions for LBM [10].

2. DERIVATIONS OF DIFFERENT RECONSTRUCTION OPERATORS

The derivation starts from the evolution equation of the MRT-LBM:

$$\mathbf{f}\left(\mathbf{x}+\mathbf{e}\delta t, t+\delta t\right)-\mathbf{f}\left(\mathbf{x},t\right)=\mathbf{M}^{-1}\mathbf{S}\mathbf{M}\left(\mathbf{f}-\mathbf{f}^{\mathrm{eq}}\right) \tag{1}$$

in which $\mathbf{f}(\mathbf{x}, t)$ is the vector of distribution functions at location $\mathbf{x}$ and time t. $\mathbf{e}_i$ is the ith discrete velocity. The $\mathbf{f}^{\mathrm{eq}}$ is the vector of the equilibrium distribution functions. $\mathbf{S}$ is a diagonal relaxation matrix and $\mathbf{M}$ is the transformation matrix which transforms $\mathbf{f}$ and $\mathbf{f}^{\mathrm{eq}}$ into the moment $\mathbf{m}$ and $\mathbf{m}^{\mathrm{eq}}$.

By the Chapman-Enskog expansions, the expressions for $\mathbf{m}$ can be derived as

$$\mathbf{m}^{(\mathrm{M2})}=\mathbf{m}^{\mathrm{eq}}-\delta t\mathbf{S}^{-1}\hat{\mathbf{D}}\mathbf{m}^{\mathrm{eq}}-\delta t\mathbf{S}^{-1}\hat{\mathbf{D}}\left(\mathbf{I}-\mathbf{S}/2\right)\hat{\mathbf{m}}^{(1)} \tag{2}$$

$$\hat{\mathbf{D}}=\mathbf{M}\mathbf{D}\mathbf{M}^{-1},\ \mathbf{D}_1=\mathrm{diag}\left(\partial/\partial t+\mathbf{e}_0\cdot\partial/\partial\mathbf{x},\ldots,\partial/\partial t+\mathbf{e}_{Q-1}\cdot\partial/\partial\mathbf{x}\right),\ \hat{\mathbf{m}}^{(1)}=-\delta t\mathbf{S}^{-1}\hat{\mathbf{D}}\mathbf{m}^{\mathrm{eq}} \tag{3}$$

This model is the same as the RO derived in Ref. [9] and is denoted by M2 model. By ignoring the second-order derivatives, the M1 model is given by

$$\mathbf{m}^{(\mathrm{M1})}=\mathbf{m}^{\mathrm{eq}}-\delta t\mathbf{S}^{-1}\hat{\mathbf{D}}\mathbf{m}^{\mathrm{eq}} \tag{4}$$

The corresponding first-order (S1) and second-order (S2) models for SRT-LBM is given by

$$\mathbf{f}^{(\mathrm{S1})}=\mathbf{f}^{\mathrm{eq}}-\delta t\tau\mathbf{D}\mathbf{f}^{\mathrm{eq}} \tag{5}$$

$$\mathbf{f}^{(\mathrm{S2})}=\mathbf{f}^{\mathrm{eq}}-\delta t\tau\mathbf{D}\mathbf{f}^{\mathrm{eq}}+\delta t^2\tau\left(\tau-1/2\right)\mathbf{D}^2\mathbf{f}^{\mathrm{eq}} \tag{6}$$

By taking the moments of $\mathbf{f}$, the results shows that all the above models can conserve the mass but do not conserve the momentum. The velocities can not be transferred exactly to the LBM and an error related to the stress term in the Navier-Stokes equations is observed. A correction term can be added to the S1 model to conserve the momentum in the S1M model [11]

$$f_i^{(\mathrm{S1M})}=f_i^{\mathrm{eq}}-\delta t\tau\left(D_i f_i^{\mathrm{eq}}-\mathbf{e}_i\cdot\left(\nabla\cdot\boldsymbol{\tau}\right)/\omega\right) \tag{7}$$

in which $\boldsymbol{\tau}$ is the deviatoric stress tensor and $\omega=\sum_i e_{i,x}e_{i,x}$. As for the MRT-LBM, the correction is simpler. Because the conservation values are just the elements of the moment vector $\mathbf{m}$, these elements can be directly assigned the macroscopic values with out the derivatives. By this procedure, we define the M1M and M2M models corresponding to Equations (4) and (2) separately.

3. NUMERICAL RESULTS

The decaying Taylor vortex is used to compare the precisions of the different models [10]. The initial and boundary conditions are calculated by the ROs based on the analytical solution. Then, the relative errors between the simulation velocities and the analytical velocities are calculated after a time period when the velocities are about 1/10 of the initial values. The influences of the initial velocity U_0, viscosity υ, spatial and time steps are studied and the results are show in FIGURE 1. When the viscosity is small, the errors tend to grow with the decreasing of the viscosity, but the models are divergent when the viscosity is large. Also, the errors increase with the initial velocities. All the models are second-order convergence in space. The SRT models are more precise than the MRT models, but the MRT models are more stable. The differences between the S1, S2 and S1M models are small, but the M1 and M2 models are instable. The modified ROs for the MRT-LBM should be used in the coupling simulations.

Then, the coupling method is adopted to simulate the flow past a circular cylinder. The computational domain is show in FIGURE 2, in which the domain is divided into an LBM region, an FVM and an overlapping region for information transfer. The relative errors of the velocities between the LBM and FVM in the overlapping region are calculated and show in FIGURE 3. The results also show that the SRT models are more precise and the MRT models are more stable. The

differences between the first-order and second-order models are small, but the M1 and M2 models are instable.

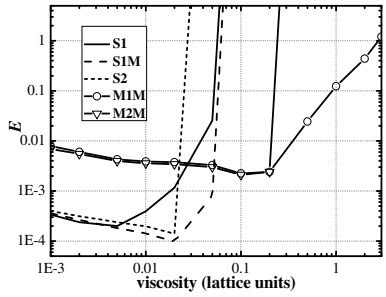

(a) Errors with varying viscosity

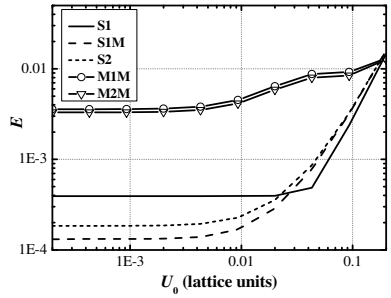

(b) Errors with varying initial velocity

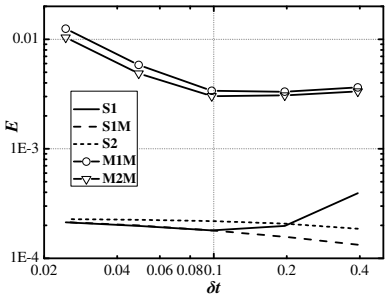

(c) Errors with varying δt

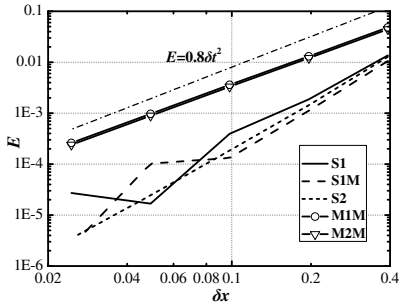

(d) Errors with varying δx

FIGURE 1. The relative velocity errors of decaying Taylor vortex for different viscosities, initial velocities, spatial and time steps (M1 and M2 models are instable and not plotted)

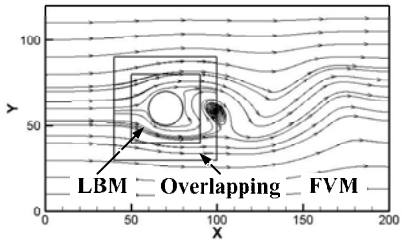

FIGURE 2. Computational domain for the flow past a circular cylinder

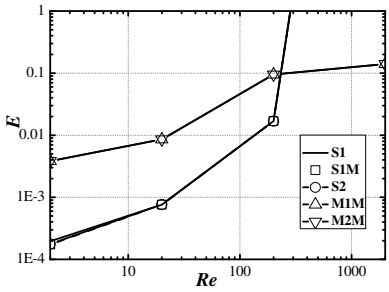

(a) Errors with varying Reynolds numbers

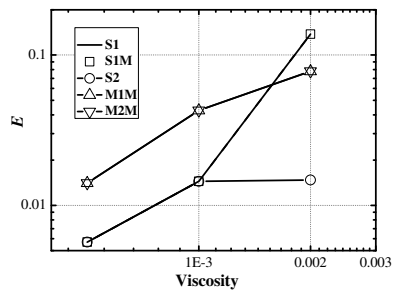

(b) Errors with varying viscosity for Re=200

FIGURE 3. Relative errors between the velocities of LBM and FVM in the overlapping region

4. CONCLUSIONS

The simulation results show that the SRT models are more precise, but the MRT models are more stable. The differences between the first- and second-order models are small, so the first-order models can be used due to its convenience. However, for the MRT-LBM, the modified models should be used.

ACKNOWLEDGEMENTS

This work was supported by the National Key Basic Research Program of China (973 Program) (2013CB228304, 2013CB228303).

REFERENCES

[1] Y.L. He, W.Q. Tao, Multiscale simulations of heat transfer and fluid flow problems, *Journal of Heat Transfer*, 134, 031018, 2012.

[2] H.B. Luan, H. Xu, L. Chen, D.L. Sun, Y.L. He and W.Q. Tao, Evaluation of the coupling scheme of FVM and LBM for fluid flows around complex geometries, *International Journal of Heat and Mass Transfer*, 54, 1975-1985, 2011.

[3] L. Chen, Y.L. He, Q. Kang and W.Q. Tao, Coupled numerical approach combining finite volume and lattice Boltzmann methods for multi-scale multi-physicochemical processes, *Journal of Computational Physics*, 255, 83-105, 2013.

[4] A.C. Velivelli, K.M. Bryden, Domain decomposition based coupling between the lattice Boltzmann method and traditional CFD methods-Part I: Formulation and application to the 2-D Burgers' equation, *Advances in Engineering Software*, 70, 104-112, 2014.

[5] A.C. Velivelli, K.M. Bryden, Domain decomposition based coupling between the lattice Boltzmann method and traditional CFD methods–Part II: Numerical solution to the backward facing step flow, *Advances in Engineering Software*, 82, 65-74, 2015.

[6] M.R. Salimi, M. Taeibi-Rahni, F. Jam, Pore-scale simulation of fluid flow passing over a porously covered square cylinder located at the middle of a channel, using a hybrid MRT-LBM–FVM approach, *Theoretical and Computational Fluid Dynamics*, 29, 171-191, 2015.

[7] M.R. Salimi, M. Taeibi-Rahni, F. Jam, Heat transfer analysis of a porously covered heated square cylinder, using a hybrid Navier–Stokes–lattice Boltzmann numerical method, *International Journal of Thermal Sciences*, 91, 59-75, 2015.

[8] Z.X. Tong, Y.L. He, A unified coupling scheme between lattice Boltzmann method and finite volume method for unsteady fluid flow and heat transfer, *International Journal of Heat and Mass Transfer*, 80, 812-824, 2015.

[9] M.R. Salimi, M. Taeibi-Rahni, New lifting relations for estimating LBM distribution functions from corresponding macroscopic quantities, based on equilibrium and non-equilibrium moments, *Journal of Computational Physics*, 302, 155-175, 2015.

[10] Y.L. He, Y. Wang and Q. Li, *Lattice Boltzmann Method: Theory and Applications*, Science Press, 2008.

[11] P.A. Skordos, Initial and boundary conditions for the lattice Boltzmann method, *Physical Review E*, 48, 4823, 1993.

Fourth International Conference on Computational Methods for Thermal Problems
THERMACOMP2016, July 6-8, 2016, Georgia Tech, Atlanta, USA
N. Massarotti, P. Nithiarasu and Y. Joshi (Eds.)

MULTI SCALE THERMAL MODELING IN GaN HEMTs

Ajit K Vallabhaneni
G.W. Woodruff School of Mechanical Engineering, Georgia Institute of Technology, Atlanta, GA 30332, ajit.vallabhaneni@me.gatech.edu

Satish Kumar
G.W. Woodruff School of Mechanical Engineering, Georgia Institute of Technology, Atlanta, GA 30332, satish.kumar@me.gatech.edu

ABSTRACT

High temperatures at hot spot is one of the main reasons for performance degradation of Gallium Nitride (GaN) based high electron mobility transistors (HEMT). Accurate estimate of hot spot temperatures during the design is essential to enhance their reliability. However, the Fourier law underestimates the hot spot temperature as it cannot capture the ballistic effects. Hence, alternate approaches using Boltzmann Transport Equation (BTE) are necessary to model thermal transport in such devices. But a complete BTE across the entire domain is prohibitively expensive. So, multi scale approaches that encapsulates both methods across different length scales are required. In this work, we developed a model that captures the ballistic effects near the heat source using the BTE model and diffusive effects far from the heat source using Fourier model. Using this model, we can simulate thermal transport across the entire GaN device including the substrate and accurately predict the hot spot temperature in reduced time.

Key Words: *Boltzmann Transport Equation, Fourier law, Finite Volume Method, Phonon*

1. INTRODUCTION

AlGaN/GaN based HEMTs (AG-HEMTs) are the strong candidates for the future high power amplifiers due to the superior properties of AlGaN/GaN hetero-structure such as high carrier saturation velocity, wide band gap, breakdown field and thermal conductivity [1]. Hot spot formation and stresses at elevated temperatures due to Joule heating leads to performance degradation in these devices. These issues have limited the widespread realization of AG-HEMTs. It is essential to have a model that can predict the spatial temperature distribution accurately to optimise the design. However, the standard Fourier law is inadequate to predict thermal behaviour when the size of the heat source is same as that of the phonon mean free path. Its inability to capture the ballistic effects can lead to severe under estimation of hot spot temperatures as demonstrated by Narumanchi *et al* [2]. Using BTE (based on the particle nature of the phonons) would address this problem as it can capture the ballistic effects. But such models are so computationally expensive that would make them almost impossible to apply across large domains. However, it should be noted that the ballistic effects are present only in the vicinity of the heat source. The diffusive behaviour will be recovered away from the hot spots and a Fourier model would be adequate to model the thermal transport. Hence, we developed a model in which both the BTE and Fourier models are coupled together through a common interface across which they exchange information on heat flux and temperature. This information is applied as boundary conditions in both domains to

ensure continuity in heat flux and temperature (if the material is same). The schematic of the GaN HEMT device used in our model is shown in Figure 1.

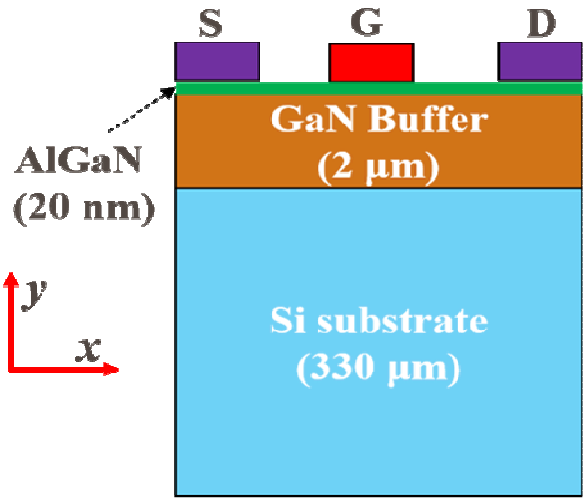

FIGURE 1. Schematic of the Computational domain of AlGaN/GaN based HEMTs. Source (S), Gate (G) and Drain Contacts has been shown.

2. MAIN BODY

BTE is a semi-classical approach that is widely used to simulate energy transport in semiconductors. The description of the BTE along with its discretization is presented in Ref. [3] and not provided here. In the current work, Finite Volume method is used to solve both the BTE and Fourier models. In every iteration, the BTE is solved first and the heat flux at the interface with Fourier domain is computed. This heat flux is used as a constant heat flux boundary condition for solving the Fourier model and then the interface temperature is computed. This in turn would serve as an isothermal boundary condition for BTE and the entire process is repeated until convergence. This exchange of information would prevent any energy loss and ensure continuity in both heat flux and temperature. If the materials are different, the thermal boundary resistance would lead to a temperature drop. Here, we demonstrate the effectiveness of this model in two cases. First, we considered a GaN buffer layer 50 μm wide and 2 μm thick with channel (6.5 μm wide and 6 nm thick) on top. Here, we divided the 50 μm wide domain into three regions of 17.5 μm, 15 μm, and 17.5 μm width. The first and last regions are modeled using Fourier model whereas the central region of 15 μm which includes the channel of HEMT is modelled using BTE. The extent of the BTE domain is determined based on the phonon mean free path. Joule heating in the channel is the primary heat source and is obtained from solving the hydrodynamic electro- thermal equations using the Sentaurus package. The second case is the GaN buffer layer (26.5 μm wide) with channel sitting on top of a silicon substrate (26.5 μm wide and 33 μm thick) as shown in Figure 1. Here, we modeled the entire GaN layer with BTE and the Silicon substrate with Fourier. A contact resistance of 3.3×10^{-8} m^2K/W is used at the interface [4].

3. RESULTS

The temperature profile across the lateral dimension for the first case is presented in Figure 2. First we obtained the temperature profile using the Fourier model (black) and then with the full BTE model (blue). Then we obtained temperature profile from our multi scale model (shown in red) and compared it with the full BTE case. The temperature variation is smooth across the interfaces which makes the temperature profiles in both cases identical. A major portion of the input energy from heat source leaves the domain through the bottom face which has isothermal boundary conditions (at 300 K). Heat flow in the lateral direction is comparatively low due to the high aspect ratio of the physical domain. Since the BTE domain is reduced by one-third, correspondingly the time taken for each iteration also reduced significantly. The time taken to solve the Fourier equation once within the same iteration is negligible when compared to that of the BTE. As mentioned before, the Fourier model significantly under predicts the temperature at the location of hot-spot (see Figure 2).

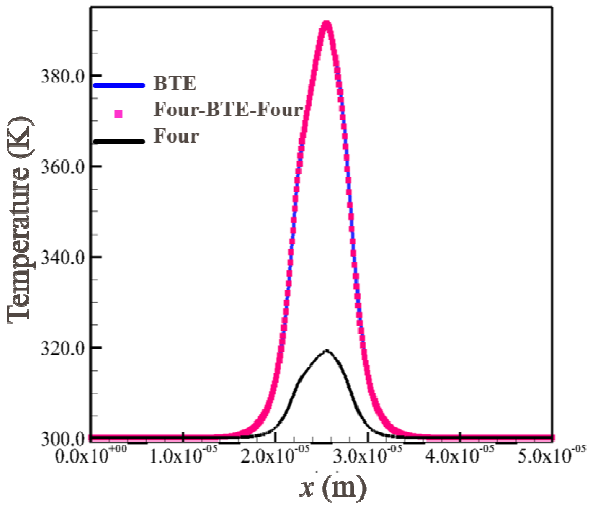

FIGURE 2. Temperature variation along the *x* direction at the middle of GaN Buffer

The spatial temperature variation across the entire domain of GaN HEMT corresponding to the second case is shown below in Figure 3. The region above the black dotted line is the buffer region which is modeled using non-gray BTE whereas the region below the line is the silicon substrate. A small temperature drop is observed across the interface due to the contact resistance and also due to the scattering of the ballistic phonons. The contact resistance is much lower in comparison with the thermal resistance of the Si substrate (~ 2.5×10^{-6} Km^2/W) considered here. It can be observed that the maximum temperature in the channel region is 506 K which is much higher than the average temperature of GaN buffer. The thermal conductivity of the substrate and the contact resistance between substrate and GaN buffer can play a significant role in lowering the maximum temperature in the device. The developed model can be employed to accurately estimate the hot-spot temperature considering the effects of these resistances.

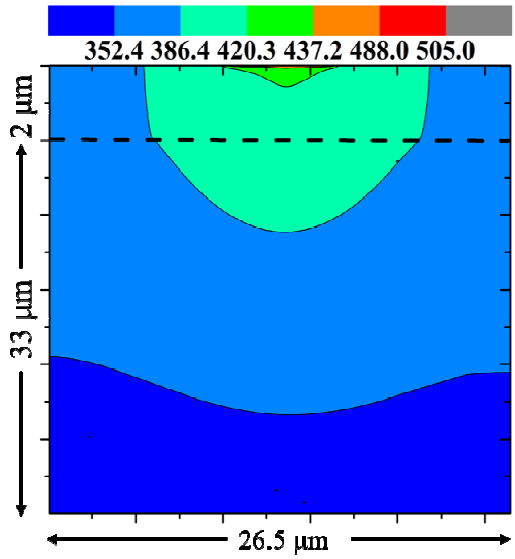

FIGURE 3. Temperature distribution in the computational domain of GaN HEMT

4. CONCLUSIONS

We have developed a multi scale thermal model that encapsulates both BTE and Fourier models and applied this to GaN HEMTs. The BTE-Fourier coupling approach is validated by comparing it with full BTE model. Our results demonstrate that the current model can be used to predict the hot spot temperature accurately and also reduce computational time significantly. These techniques would be quite useful in modeling large scale electronic devices, such as multi-finger GaN power amplifiers, rapidly without compromising on accuracy.

REFERENCES

[1] U. K. Mishra, P. Parikh, and Y.-F. Wu, "AlGaN/GaN HEMTs-an overview of device operation and applications," *PROCEEDINGS-IEEE,* vol. 90, pp. 1022-1031, 2002.

[2] S. V. Narumanchi, J. Y. Murthy, and C. H. Amon, "Comparison of different phonon transport models for predicting heat conduction in silicon-on-insulator transistors," *Journal of Heat Transfer,* vol. 127, pp. 713-723, 2005.

[3] J. M. Loy, S. R. Mathur, and J. Y. Murthy, "A Coupled Ordinates Method for Convergence Acceleration of the Phonon Boltzmann Transport Equation," *Journal of Heat Transfer,* vol. 137, p. 012402, 2015.

[4] X. Chen, F. N. Donmezer, S. Kumar, and S. Graham, "A Numerical Study on Comparing the Active and Passive Cooling of AlGaN/GaN HEMTs," *Electron Devices, IEEE Transactions on,* vol. 61, pp. 4056-4061, 2014.

Fourth International Conference on Computational Methods for Thermal Problems
THERMACOMP2016, July 6-8, 2016, Georgia Tech, Atlanta, USA
N. Massarotti, P. Nithiarasu and Y. Joshi (Eds.)

Hierarchical Multiscale Simulations for Data Center Cooling

S. P. Vanka
Department of Mechanical Science and Engineering, University of Illinois at Urbana-Champaign, 1206 W Green Street, Urbana, IL, 61801, USA, spvanka@illinois.edu

Jayati Athavale, Minami Yoda, Yogendra Joshi
G.W.Woodruff School of Mechanical Engineering, Georgia Institute of technology, Atlanta, GA 30332, USA, yogendra.joshi@me.gatech.edu

ABSTRACT

Accurate computation of the cooling of data centers is a challenging multiscale problem with scales spanning several orders of magnitude. Several hierarchical levels of models have been developed in the literature. These range from network based models to more complex turbulent CFD models based on Reynolds-averaged formulations. In this paper, we summarize these approaches, and describe some techniques to significantly accelerate the CFD models. Three techniques, namely the multigrid method, multilevel refinement, and GPU based parallel computing, are described.

Key Words: *Data center cooling, hierarchical models, GPU, multigrid method*

1. INTRODUCTION

With the explosive growth of the need to store data, efficient and adequate cooling of the storage devices and information technology (IT) hardware in data centers has become an important problem in the heat transfer community. A typical data center is a large warehouse of heat generating electronic equipment that need to be adequately cooled. Air-cooling is the predominant way in which cold air is circulated through the racks and the heat is dissipated to the outside environment through vapor compression chillers, cooling towers, or air venting. A problem formechanical engineers is providing adequate air flow and heat transfer, such that the maximum allowable temperature of the electronic component is not exceeded under various IT hardware utilizations.

The entire problem of data centers has multiple scales, as seen in Figure 1. At the smallest scale (currently ~20 nm) is the integrated circuit of transistors, resistors, memory, and other components. The microchip (~ cm scale) is the basic unit that dissipates the heat, which is transferred by chip level cooling through heat pipes, heat sinks, and chip package level fans. A computer unit or a storage device (~ tens of cm) may have several of these in one module, and several are mounted as one rack (~1 m). A large data center (~hundreds of m) has several bays of such racks, with parallel rows arranged along aisles (~10 m). The airflow to the data centers is commonly supplied through perforated floor tiles, with the hot return air taken out through the ceiling or side vents, and sent either to cooling units, or discharged. Thus, analysis of the cooling problem in data centers consists of studying heat transfer and fluid flow at several scales. Although the phenomena are mostly characterized by continuum physics, the disparate scales of geometry require innovative ways to balance accuracy with speed and cost of computation. The purpose of this paper is to provide a perspective of data center cooling analysis methodologies by presenting various tools that have been previously pursued and new computational tools that can be developed in future to address this important heat transfer problem.

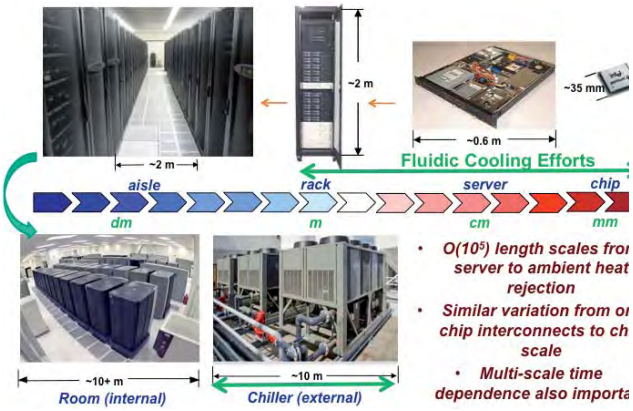

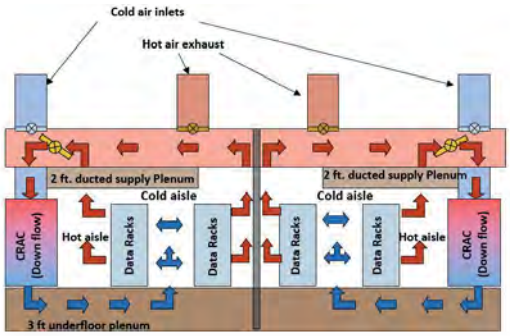

Fig. 1 The multi-scale heat transfer in data centers. *Fig. 2 Typical computational representation*

2. THE PROBLEM CONSIDERED

Figure 2 is a typical illustration of the data center, where the room is shown in two dimensions, and the racks are shown as rectangular blocks in elevation view. The CRAC (Computer Room Air Conditioners) are the suppliers of cold air to the plenum, which in turn distributes the cold air through the floor tiles. The air then returns through the overhead plenum back to the inlets of the CRAC. The objective is to maintain the air distribution such that there is adequate cooling to all the racks, and within the racks. It can be seen that the problem is a complex issue of air flow and heat transfer. As the air is circulating, complex flow patterns can develop throughout the room, resulting in inadequate flow to some of the racks, which can then become overheated. The flows are in general turbulent, and buoyancy may play a role in some regions of the room.

3.HIERARCHY OF ANALYSIS APPROACHES

The goal of a data center engineer is to maximize productivity, while ensuring reliable and energy efficient operation, which requires making sure adequate thermal management is provided to the IT equipment, without overcooling. IT component temperatures fluctuate because of the changing operating conditions, as well as under idle conditions of the servers. The supply flow rate of the air is however usually kept constant. To improve energy efficency, the CRAC can also be controlled to optimize the cooling energy consumption. Hence, one requirement for computational thermal models is they be fast. However, good accuracy is also desired, which results in a very demanding issue. There have been a number of computational approaches that have been proposed and used by industry. Because of the extensive literature available, it is not possible to review all these works. Hence we will describe very briefly the various approaches only in principle, and cite only one or two works as examples.

The simplest approach may be the one based on a network of resistances for pressure drop and flow rate [1]. In this, the data center is represented in the form of various flow paths with resistances to flow. The flow paths can be through the racks, and also through the open space. The pressure drop ~ flow rate correlations are in the form of algebraic relations, which can be very quickly solved to satisfy the flow balances and pressures at junctions. This network can be also constructed in time with flow capacitances and time dependent flows. Such networks can be used with control strategies and tuned to give desired responses. However, the major drawback of this approach is calibration and constant “tuning” to get agreement with sensor data.

The second simpler approach is based on a potential flow methodology. A potential flow neglects viscous terms in the Navier-Stokes equations, and also assumes that the flow is irrotational. This allows the flow velocities to be computed by solving the potential flow equation. The velocities are calculated from the gradients of a scalar potential. This approach has been pursued by several researchers, for example by [2]. The main advantage of this approach is also speed, with a somewhat more realistic simulation of the flow field behavior. The network approach and the potential method have also been coupled [1] by treating the rack flow using resistance networks and the open area using the velocity potential. This brings in the multiscale approach, with different grid resolutions corresponding to the rack airflow paths and the open air space. The potential equation is an elliptic equation, and its solution can be benefited from techniques such as multigrid / multilevel methods and GPU computing that will be mentioned in the next section. The velocities provided by the potential flow method are then used to compute the temperatures by solving an energy equation (with or without diffusion).

4. COMPUTATIONAL FLUID DYNAMICS

In order to improve accuracy of the flow field computations, a large number of researchers have developed codes to solve the complete Navier-Stokes equations. This requires solution of a set of nonlinear partial-differential equations at high resolution to minimize the discretization errors. Several researchers have used the SIMPLE algorithm and its derivatives ([3]). Several commercial codes have been used [4] which implement sophisticated pre- and post processors for easy representation of the data center geometry. However, the computer times required by current CFD software are significantly longer than what the engineers would like to spend, and hence CFD is used only sparingly only when new geometrical configurations are considered, and not for small deviations in operating conditions.

In this paper, we discuss three new ideas that can reduce the computer times significantly, and can also increase the grid resolution so that new features of the geometry and flow can be captured. In addition, we also describe a hierarchical refinement strategy that can integrate the rack and the interior flow without the use of the network approach. Using convergence acceleration techniques, inexpensive parallel computing, and hierarchical refinement, current CFD techniques can be significantly improved. We describe these ideas below.

Multigrid Techniques: The multigrid technique is an acceleration technique for convergence on fine grids. The multigrid concept is well established, but its effective use as a CFD accelerator has not been fully exploited. The multigrid method is based on the concept that a numerical iterative algorithm is traditionally slow to converge on fine grids because of the low frequency errors. To accelerate the convergence of these low frequency errors, a series of coarse grids is constructed, and the low freqency part of the errors is transferred (interpolated) and solved on the coarser grids. Done properly, the convergence of multigrid methods is independent of the grid resolution, and hence one can theoretically converge a solution on a grid with a million nodes at the same rate as the convergence on a grid with 1000 nodes. This dramatic improvement in the rate of convergence, however, can only be obtained if the entire set of momentum and continuity equations are transferred and solved on the coarser grids and their implied corrections are interpolated back to the finer grid. Only then the desired rate of convergence is maintained on grids at any spatial resolution.

Multilelevel Resolution: The multigrid concept, which deploys a number of coarse and fine grids, can be combined with local refinement and multilevel coupling. Certain regions of finer scale can be refined with a finer grid while others with small variations in temperatures can be represented with coarser resolution. These grids can be generated as a nested refinement. The finer resolved grids can be implicitly coupled with the coarser grid regions, thus preserving the two-way interactions. In principle, the number of levels is arbitrary, hence the refinement can span several orders of magnitude in scale. Another interesting multiscale analysis is to treat some of the regions

as inviscid [6]. This way the work involved in solving the turbulence equations is reduced for the inviscid regions. The coupling between the viscous and inviscid regions preserves mass and momentum balances at the interfaces.

Acceleration through Graphics Processing Units (GPU): GPUs [7] consist of a large number of cores which can perform arithmetic very fast. However, because of the special architecture of the GPU, it is necessary to reorganize the numerical algorithm, as well as the program structure such that the communication and computation as well as data access are executed optimally. In order to benefit from the GPU's architecture, the numerical algorithm must be data parallel. Also, the data must be supplied fast enough for the cores to perform computations. The GPU is designed with massive multithreading, where a single thread can be thought of as the smallest unit of execution. Instructions for the GPU are written in the form of "kernels" which are similar to a function in the C or FORTRAN programming languages. GPUs are best used for explicit computations, but implicit computations can be performed by suitably arranging the computational sequence. The multigrid algorithm has been previously implemented with the SIMPLE algorithm and on a GPU to solve very large scale flow problems. For example, a 2D recirculating flow using a multigrid SIMPLE algorithm converged in about 15 V-cycles, and a steady state solution on a grid with 16 million control volumes (4096 x 4096) was obtained in under one minute on a GPU [7]. There is potential for conducting very fast CFD calculations with several millions of control volumes in a few minutes on an inexpensive GPU. Such software are currently not available, although multigrid techniques have been previously developed for data centers [4].

5. CONCLUSIONS

Computer models of different levels of sophistication have been previously developed for cooling of data centers. CFD based models are commonly used, but the long computer times are a deterrent for their routine use. The multiscale CFD problem can be accelerated by using techniques such as multigrid techniques, local refinement, inviscid-viscous coupling, and using low cost, GPUs. Combining these technologies can reduce the computing time for CFD of a data center significantly.

REFERENCES

[1] X. Zhang, C. Hesley, J. W. VanGilder and Z. R. Sheffer, *Compact modeling of data center air containment systems* ASME International Technical Conference and Exhibition, IPACK 2013-73325, 2013.

[2] M. Toulouse, G. Doljac, V. Carey, C. Bash, *Exploration of a potential-flow-based compact model of air-flow transport in data centers,* in: International Mechanical Engineering Congress and Exposition (IMECE), November 13–19, Lake Buena Vista, Florida, USA, 2009.

[3] S. V. Patankar, *Airflow and cooling in a data center*, *Journal of Heat Transfer*, 2010, v. 132, p. 073001.

[4] Fluent, ANSYS Inc.

[5] J. D. Rambo and Y. K. Joshi, *Multi-scale modeling of high power density data centers*, ASME International Electronic Packaging Technical Conference and Exhibition, InterPACK 2003, v 1, p. 521-527, 2003.

[6] E. Cruz and Y. K. Joshi, *Coupled inviscid-viscid solution method for bounded domains: application to data center thermal management*, Int. J. Heat Mass Transfer, 2015, v. 85, p. 181-194.

[7] S. P. Vanka, *2012 Freeman Scholar Lecture: Computational Fluid Dynamics on Graphics Processing Units*, *Journal of Fluids Engineering*, 2013, vol. 135, p. 061401.

MINI SYMPOSIUM

COMPUTATIONAL BIOHEAT TRANSFER

MINI SYMPOSIUM ORGANISED BY PERUMAL NITHIARASU

Fourth International Conference on Computational Methods for Thermal Problems
THERMACOMP2016, July 6-8, 2016, Georgia Tech, Atlanta, USA
N. Massarotti, P. Nithiarasu and Y. Joshi (Eds.)

MODELLING AN HEAT-RELATED ILLNESS

Alberto Coccarelli, Dimitris Parthimos
School of Medicine, Cardiff University, Heath Park, Cardiff, U.K., coccarellia@cardiff.ac.uk, parthimos@cf.ac.uk

Hayder Hasan, Perumal Nithiarasu
College of Engineering, Swansea University, Bay campus, h.m.hasan.743207@swansea.ac.uk, p.nithiarasu@swansea.ac.uk

ABSTRACT

In the proposed study we investigate the conditions for the coming up of Heat Stroke (HS) when a human body is subjected to hot thermal stress. The bio-heat transfer model adopted encompass arterial convection, solid tissue conduction and thermo-regulatory mechanisms. Furthermore it accounts for many anatomical and physiological details. The blood and solid tissue variables are computed through two coupled solvers. The time occurring to reach the HS condition is computed for different external environment situations. The ageing factor on thermal balance is also analysed.

Key Words: *Heat transfer, heat stroke, thermo-regulation, finite elements.*

1. INTRODUCTION

A heat-related illness can be defined as a medical condition occurring as a result of heat exposure. Even short periods of high temperatures may be the cause of serious health problems. For instance we refer to the heat wave experienced in France in August 2003, which resulted in 14,800 excess deaths [1]. In summer the risk obviously rises significantly. These illness encompasses a spectrum of conditions that range from minor illnesses, like heat cramps or rash, to life-threatening medical emergencies like heat syncope, heat exhaustion or heat stroke. The latter disease is probably the most serious heat-related disorder. In [2] heat stroke (HS) is defined as “a life-threatening illness characterized by an elevation in core body temperature to above 40°C with central nervous system (CNS) dysfunction that results in delirium, convulsions, or coma in the absence of any other cause of CNS dysfunction, and skin dryness“. It occurs as a consequence of body's thermoregulation failure: with the body temperature fast increasing, the sensible and latent emissions are not sufficient to cold down the body, and the temperature continue to rise. HS can involve permanent disability or even death whether emergency treatment is not given. The high risk category for such disease are older people and children, especially whether they live in space with an absent or poor conditioning system. They result more vulnerable than others because they adjust to heat more slowly. Other risk factors are insufficient water consumption, having chronic diseases, using medications that involve vasoconstriction or abusing of alcohol.
To characterize HS onset we propose to simulate the thermodynamics state evolution of a body exposed to a rigid hot environment. For doing that, we adopted the human thermal model proposed in [3]. It consists of a multisegmental solid tissue model coupled with a fluid dynamics one representing the larger arterial tree.

2. METHODOLOGY

Arterial flow

To represent the larger arterial system the model proposed by Low et al. [4] is adopted; this is a branching network characterized by bifurcations and cross sectional discontinuities. Reflections due

to network singularities and terminals are also accounted for. The flow is considered incompressible, laminar and pressure is linked to area via a non-linear relation. Characteristic variables are used for prescribing inlet and outlet variables and also for transmitting information in discontinuities between segments [5,6]. For the fluid inlet point, the aortic valve is modelled, while the pumping action of the heart is modelled as a prescribed forward pressure source. To model branch ending, tapering vessels are used. The inlet node of the fluid network is supposed to be in thermal equilibrium with the surrounding tissue. At exiting nodes temperature is extrapolated if velocity is positive; otherwise it is set equal to that of the surrounding tissue. The numerical scheme used for solving the set of flow and temperature equations is the explicit form of locally conservative Taylor Galerkin method (LCG) [7].

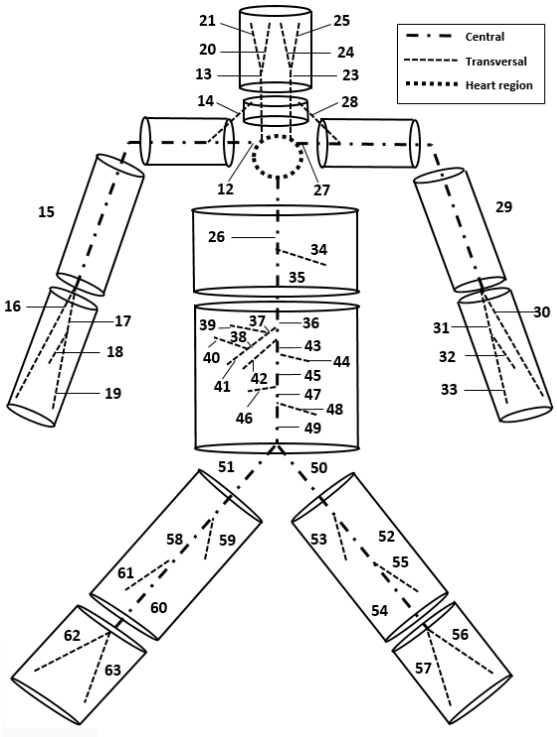

FIGURE 1. Architecture of solid tissue and arterial systems (details can be found in [3]).

Solid tissues

For the solid tissue representation, we adapted the model proposed by Fiala et al. [1] in order to match the two physical systems. The body consists of fourteen multilayer cylindrical elements representing head, neck, shoulders, thorax, abdomen, thighs, legs, arms and forearms. Heat transfer between arteries and veins is not considered as blood velocity in veins is significantly lower than that of arteries and temperature of back flow is close to that of the surrounding tissue. The heart represents the inlet of the fluid network and is not included in any cylinders. An exhaustive description on the arrangement of the arteries within the solid tissue can be found in [3]. In order to evaluate tissue temperature, the one-dimensional bioheat transfer equation in cylindrical coordinates is solved. We know that tissues receive heat from large arteries by convection and from small ones by perfusion. For a cylindrical section, convection contribution is evaluated at the nodes in which arterial vessels are localized. For vessel located along cylinder axes prescribing inner convection is straightforward while for the transversal ones is slightly different. We assume their convection contributions may be seen as an inner heat source in the nodes in which they lie. Perfusion is modeled through perfusion coefficients and assumed to be proportional to the temperature

difference between average weighted larger arterial and the tissue temperature. Under exercise conditions an increment in metabolic activity occurs; it is modeled by increasing the volumic heat generation in the muscle involved. The conduction problem in the walls along radial direction is solved using the forward Euler method. As the domain accounts for more than one tissue layer at the interface between two layers, continuity of flux is imposed. We include respiration losses by considering a negative volumetric heat source in all the lung nodes. The flux exchanged between the skin layer and the outside environment is the sum of the convection losses to the ambient air, radiation losses with surrounding surfaces and sources and evaporation of moisture from the skin.

Thermoregulatory mechanisms

The state of thermoneutrality exists when the core and mean skin temperatures are respectively around 36.8°C and 33.7°C. If thermoneutrality is not satisfied, different mechanisms may occur. Whenever core temperature drops below a determined threshold shivering occurs; thus the volumetric heat generation rise linearly until core temperature reaches a lower saturation threshold; after such limit all metabolic activities are reduced. Sweating occurs for increasing skin temperature and involves latent heat losses at the external surface of the body. Vasoconstriction and vasodilatation of skin vessels allow to vary the amount of flow and thus heat transport in the peripheral regions. We model them assuming perfusion ratio at skin nodes depends directly on the core and skin temperatures.

3. RESULTS

The framework has already been tested against experimental measurements for hot exposure condition (see FIGURE 2). For evaluating the ageing factor, we carried out the same simulations modifying some constitutive parameters according to [10]. In such a preliminary study we simulate body temperature evolution for the following conditions: 1 h at (28.1°C,43 % R.H.), 2h at (47.8°C,27 % R.H.). From FIGURE 3 we can observe that, after an initial transition stage, both temperatures rise dramatically. After 2 h of hot exposure , while the skin temperature seems to stabilise, the core one keeps increasing and HS will be reached soon. This could be read as thermo-regulation failure: sweating and vasomotion are not able to discharge inner energy towards outside environment.

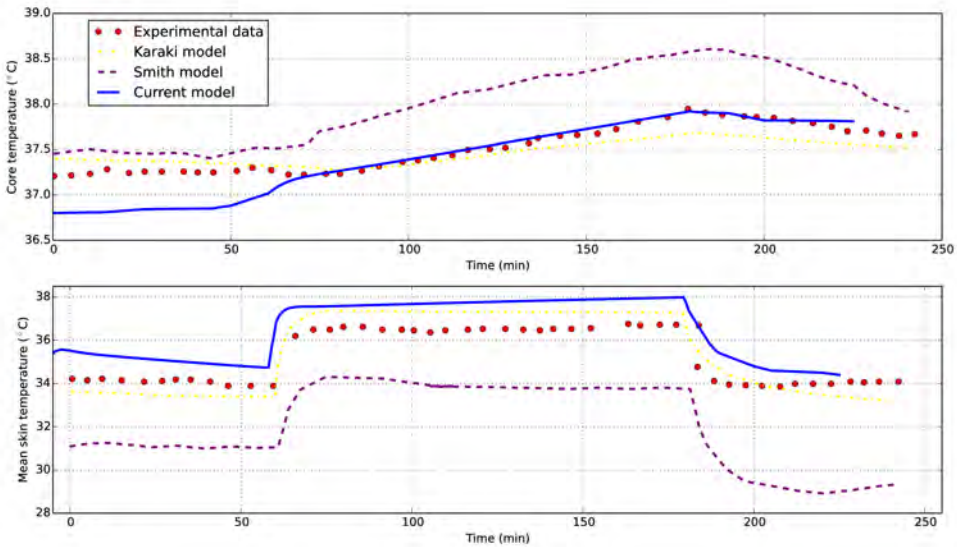

FIGURE 2. Experimental validation for the hot exposure case proposed in [3].

4. CONCLUSIONS

The theoretical model suggests that after 2 hours of hot exposure the global body balance results unpaired. Further investigation on metabolic response to heat must be carried out.

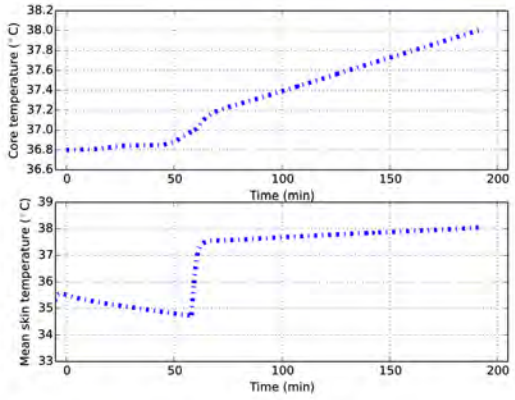

FIGURE 3. Body thermal response for the hot exposure case considered.

REFERENCES

[1] Dhainaut JF, Claessens YE, Ginsburg C, Riou B. Unprecedented heat-related deaths during the 2003 heatwave in Paris: consequences on emergency departments. Crit Care. 2004;8:1–2.

[2] Hadad E, Cohen-Sivan Y, Heled Y, Epstein Y. Clinical review: Treatment of heat stroke: should dantrolene be considered? Crit Care. 2004.

[3] Coccarelli A., Boileau E., Parthimos D., Nithiarasu P. An advanced computational bioheat transfer model for a human body with an embedded systemic circulation. Biomechanics and Modeling in Mechanobiology, to appear(DOI: 10.1007/s10237-015-0751-4), 2016.

[4] K. Low, R. van Loon, I. Sazonov, R. L. T. Bevan, and P. Nithiarasu. An improved baseline model for a human arterial network to study the impact of aneurysms on pressure-flow waveforms. International Journal for Numerical Methods in Biomedical Engineering, 28:1224–1246, 2012.18

[5] J.P. Mynard and P. Nithiarasu. A 1D arterial blood flow model incorporating ventricular pressure, aortic valve and regional coronary flow using locally conservative Galerkin (LCG) method. Communications in Numerical Methods in Engineering, 24:367–417, 2008.

[6] A. Coccarelli and P. Nithiarasu. A robust finite element modelling approach to conjugate heat transfer in flexible elastic tubes and tube networks. Numerical Heat Transfer, Part A Applications, 67:513–530, 2015.

[7] P. Nithiarasu. A simple locally conservative galerkin (lcg) finite-element method for transient conservation equations. Numerical Heat Transfer Part B - Fundamentals, 46:357–370, 2004.

[8] D. Fiala. A computer model of human thermoregulation for a wide range of environmental conditions: The passive system. Journal of Applied Physiology, 87:1957–1972, 1999.

[9] C. Smith. A transient, Three Dimensional Model of the Human Thermal System. PhD thesis, Kansas State University, 1991.

[10] M.A. Zulliger, N. Stergiopulos. Structural strain energy function applied to the ageing of the human aorta. Journal of Biomechanics, 40(14): 3061-3069. 2007.

Fourth International Conference on Computational Methods for Thermal Problems
THERMACOMP2016, July 6-8, 2016, Georgia Tech, Atlanta, USA
N. Massarotti, P. Nithiarasu and Y. Joshi (Eds.)

INVESTIGATION OF THERMOFLUID DYNAMICS IN A HUMAN EYE: NUMERICAL MODELING OF AQUEOUS HUMOR FLOW IN POROUS TISSUES

A. Mauro[1,2], N. Massarotti[1], M. Salahudeen[1]
[1]Dipartimento di Ingegneria, Università degli Studi di Napoli "Parthenope", Isola C4, Centro Direzionale di Napoli, 80143 Napoli, Italy

[2]Università Telematica Pegaso, Piazza Trieste e Trento n. 48, 80132 Napoli, Italy

M.R. Romano
Dipartimento di Neuroscienze e scienze riproduttive ed odontostomatologiche, Università degli Studi di Napoli Federico II, Via S. Pansini n. 5, 80131 Napoli, Italy

V. Romano
Dipartimento di Oftalmologia, Seconda Università degli Studi di Napoli (SUN), Via S. Pansini n. 5, 80131 Napoli, Italy

P. Nithiarasu
Zienkiewicz Centre for Computational Engineering, College of Engineering, Swansea University, Swansea SA2 8PP, United Kingdom

ABSTRACT

Numerical modelling of Aqueous Humour (AH) flow in the Anterior Chamber (AC) of a human eye is investigated. The geometry reconstruction from the scan of a human eye is performed using an in-house image acquisition tool. Both the healthy and glaucoma induced eye conditions are simulated using different permeability values for the porous tissues. In addition, flow due to a implanted Silicon Shunt Device (SSD), used for glaucoma treatment, is also analysed. The results show that there is a significant improvement, in terms of decrease in Intraocular Pressure (IOP), is achieved with the use of SSD.

Key Words: *Eye, Glaucoma, Numerical modelling, glaucoma treatment*

1. INTRODUCTION

Glaucoma treatment in a human eye is a major concern for ophthalmologists as it is the second leading cause of blindness. One of the causes of glaucoma is the increased resistance to Aqueous Humor (AH) flow of Trabecular Meshwork (TM) at the iris-cornea angle, resulting in adverse pressure gradient at the AC of the eye. Medical researchers are still working on the treatment of glaucoma using different techniques including medications and surgical methods. The constraints involved in testing surgical implants for glaucoma treatment techniques have led to the use of computational solutions. Exploiting numerical modelling for the prediction and feasibility of various glaucoma treatment techniques has reduced the time taken to develop newer methods.

Many authors have implemented mathematical modelling techniques in assessing the use of medications in human eyes. It has been shown that the drug applied enters the eye through cornea by diffusion and circulates inside the eye by convection[1,2]. Among the surgical techniques, laser surgery has received a great deal of attention. Such techniques are numerically analysed by applying laser source parameters. The implementation of Pennes bio-heat equation provides the possibility of finding the actual temperature inside the human eye. Another method of treating glaucoma is Trabeculectomy, which is an invasive surgical method for cutting the tissue in an eye to provide an alternative AH pathway. The use of ocular drainage devices is the latest trend in

curing glaucoma and the studies involving practical feasibility of using these devices are ongoing [3, 4].

The studies related to computational modelling of surgical ocular drainage device are less common compared to laser surgery and medications. In the present work, a novel drainage device, the Silicon Shunt Device (SSD) [4], is introduced to counteract the effects of high IntraOcular Pressure (IOP) in a glaucoma induced eye. The flow of AH inside AC is numerically simulated, incorporating Trabecular Meshwork (TM), sclera, choroid and Schlemm's Canal (SC). Vertical and supine position of the eye are considered for healthy and glaucoma induced eye conditions. AH velocity and IOP are analysed for each case. The implant of SSD has significantly reduced IOP by reducing resistance to AH outflow.

2. PROBLEM DESCRIPTION

Figure 1 shows a 2D scanned image of eye and the computational domain, that is made of Anterior Chamber (AC) enclosed by cornea, lens and iris. In addition, the Trabecular Meshwork (TM) is modelled along with Schlemm's canal at the surface of cornea. The AC depth is measured as 3.54 mm and cornea thickness as 0.5 mm.

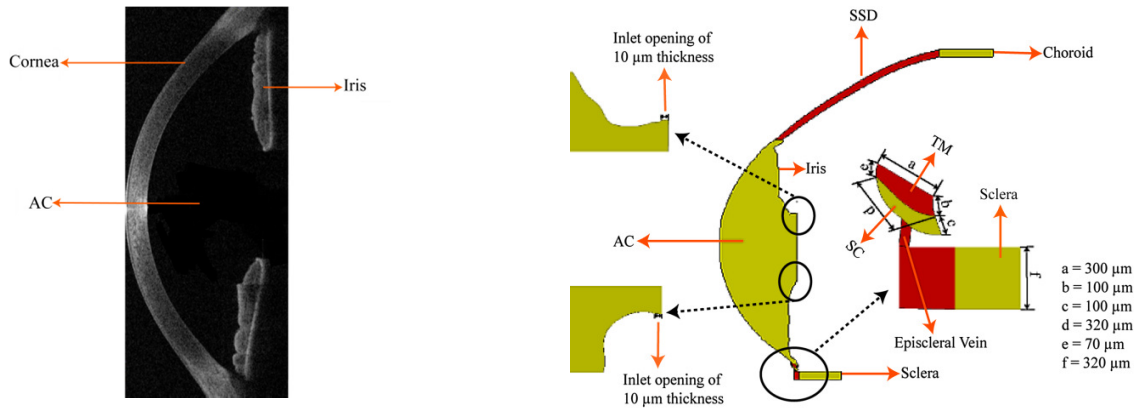

FIGURE 1. Eye Image (left) and computational domain (right).

The computational domain is extracted from the eye image using an in-house image acquisition tool. The extracted portion of the eye is meshed using triangular elements. The Trabecular Meshwork (TM) has been reproduced with a length of 300µm ('a'). The open space of thickness 10µm between iris and lens serves as the inlet opening for AH to flow towards AC. The width of TM at anterior and posterior portion is 70µm ('e') and 100µm ('b') respectively. Schlemm's Canal (SC) of diameter 320µm ('d') and thickness 100µm ('c') is placed at the top of TM. Episcleral vein connects SC to sclera of thickness 320µm ('f'). A novel Silicon Shunt Device(SSD) of length 8mm and 320µm is connected at TM to provide an alternate AH pathway towards posterior suprachoroidal space. The outlet of SSD is connected to choroid of thickness 320 µm.

3. MATHEMATICAL MODEL

The laminar, incompressible AH flow and heat transfer is solved using the following generalized porous flow medium equations.

Continuity equation

$$\frac{1}{\varepsilon}\frac{\partial u_i}{\partial x_i} = 0$$

Momentum equation

$$\frac{\rho_f}{\varepsilon}\left[\frac{\partial u_i}{\partial t}+\frac{\partial}{\partial x_j}\left(\frac{u_i u_j}{\varepsilon}\right)\right]=-\frac{1}{\varepsilon}\frac{\partial}{\partial x_i}\left(p_f\varepsilon\right)+\frac{\mu_e}{\varepsilon}\frac{\partial^2 u_i}{\partial x_i^2}+\left(\rho_{ref}-\rho_f\right)g\gamma_i-\frac{\mu_f u_i}{\kappa}-\frac{1.75}{\sqrt{150}}\frac{\rho_f}{\sqrt{\kappa}}\frac{|V|}{\varepsilon^{3/2}}u_i$$

Energy equation

$$\left[\varepsilon\left(\rho c_p\right)_f-(1-\varepsilon)\left(\rho c_p\right)_s\right]\frac{\partial T}{\partial t}+\left(\rho c_p\right)_f u_i\frac{\partial T}{\partial x_i}=k\left(\frac{\partial^2 T}{\partial x_i^2}\right)$$

The flow and thermal fields are solved taking into account also buoyancy effects, due to the temperature difference among cornea, lens and iris, obtaining a mixed convection regime. No slip boundary conditions are provided at iris, cornea and lens. A mass flow rate of 3μL/min is provided at the inlet for AH flow. The outlet of SSD and Schlemm's canal is exposed to a pressure of 9 mm Hg. Buoyancy effects are incoporated using Boussinesq approximation. The outer surface of cornea is set to 35°C while lens is set to 37°C. A convective temperature boundary condition is provided at the iris with heat transfer coefficient of 5 W/m^2 and free stream temperature of 37°C. The thermal and physical properties of AH is assumed to be equal to that of water. The governing equations along with boundary conditions are solved using an in-house finite element code.

4. RESULTS

Numerical simulation is carried out for AH flow and heat transfer in AC of human eye for healthy and glaucoma induced conditions. In healthy eye condition, a permeability value of 2 x 10^{-15} m^2 with a porosity of 0.2 is provided at TM while the glaucoma induced eye conditions are simulated for permeability value of 2x10^{-16} m^2 with a porosity of 0.15. Vertical and supine positions of the eye are considered for the analysis, where the direction of gravitational acceleration is varied for different alignments. A temperature difference of 2°C is enough to create natural convection of AH inside AC. The flow behavior is different in vertical and supine positions of the eye. In the vertical position of the eye, AH emanates from the inlet moves along the centerline position towards the cornea surface and thereafter flow towards the iris-cornea angle entering TM, thus forming a single convection current. In case of supine position, AH from different inlets move towards the centerline diverges at the midpoint to form two different pathways, thus creating symmetric counter rotating convection currents. The velocities are larger in vertical position compared to the supine position. However, the AH velocities for healthy and glaucoma conditions are almost similar at AC in the range of 10^{-5}-10^{-4} m/s. There is a lesser AH velocity near TM for the glaucoma induced eye compared to the healthy eye.

The higher resistance of AH flow at TM creates an elevated IOP in AC. A favorable IOP of 11 -14 mm Hg is permissible for healthy eye condition and an IOP of above 20 mm Hg is possible for a glaucoma induced eye. In our study, for healthy eye conditions, the pressure ranges between 11 and 14 mm Hg is obtained which are within the acceptable limits. On the other hand, a pressure value of 22 mm Hg is obtained with a permeability value of 2x10^{-16} m^2, which is quite high for glaucoma conditions. The pressure drop at the TM is higher for glaucoma induced eye, which corroborates that the higher resistance in TM is responsible for glaucoma.

The SSD inlet is connected at one of the TM towards suprachoroidal space and the outlet of SSD is opened to AC. Numerical analysis of AH flow inside AC is carried out by adding SSD which is connected to choroid of thickness 320 μm in the eye model. The choroid and sclera is treated as a porous medium with permeability value of 5x10^{-14} m^2. The case for vertical and supine positions of eye are studied for the AH flow using SSD. Figure 2 shows the velocity vectors inside the eye for vertical and supine positions. Convection currents are formed at AC due to the temperature difference.Velocity fields of AH at the AC is higher for vertical position compared to the supine

position. It is evident from the inlet velocity of 8.28 x 10^{-6} m/s in SSD that it provides less resistance to AH flow compared to inlet velocity of 1.87 x 10^{-7} m/s at TM. The use of SSD in a glaucoma eye has reduced the IOP to an optimum value between 11-15 mm Hg. The reduction in IOP corroborates the fact that implanting SSD has provided an alternate AH flow, thus creating a favourable pressure conditon in AC. The pressure drop is more at TM due to the higher viscous resistance and low permeability.

The permeability values have a significant effect in IOP values. In order to get the approximate pressure values, proper parameters have to be set for porous tissues. The permeability values at TM is of order 10^{-15}-10^{-16} m^2 which can actually mimic the physical conditions. IOP of 12-15 mm Hg is obtained with SSD, which is comparable with IOP for healthy eye. The use of SSD has significant effect on the IOP and at the same time it provides an alternate AH outflow with reduced pressure drop.

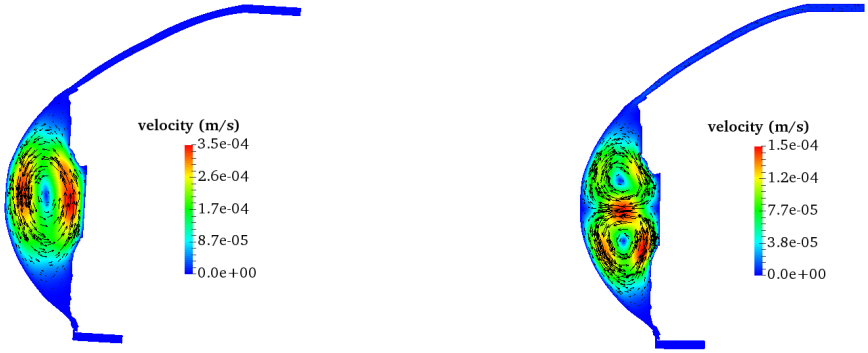

FIGURE 2. Velocity contous and vectors for vertical position (left) and supine position (right).

5. CONCLUSIONS

In this study, healthy and glaucoma induced eye conditions are numerically analysed for different eye positions. The use of permeability values aids the study to simulate the porous tissues for mimicking the healthy and glaucoma induced eye conditions. An ocular drainage device, SSD, is studied to understand the flow parameters, velocity and pressure inside AC. The main outcomes are: (i) the AH velocity at TM for a healthy eye is more than for a glaucoma induced eye; (ii) the AH velocity of SSD is higher compared to velocity at TM; (iii) the use of SSD has provided a significant reduction in IOP by allowing an alternate AH outflow.

ACKNOWLEDGMENTS

The authors gratefully acknowledge the financial support of TeVR Project CUP E62I15000760008.

REFERENCES

[1] Han Chen, Numerical investigation of topical drug transport in anterior human eye, *International Journal of Heat and Mass transfer*, 85(2015), 356-366.

[2] T R Crowder, Numerical simulation of fluid pressure in Human eye, *Applied mathematics and computation*, 219(2013), 11119-11133.

[3] Adam Villamarin, 3D simulation of aqueous flow in human eye, *Medical Engineering and Physics,*34(2012), 1462-1470

[4] V. Romano, F. Romano, A. Mauro, R. Vinciguerra, L. Rinaldi, M. Angi, M.R. Romano, C. Costagliola, Glaucoma Surgery: potential of a new uveoscleral outflow shunt. *Acta Ophthalmologica*, under review.

Fourth International Conference on Computational Methods for Thermal Problems
THERMACOMP2016, July 6-8, 2016, Georgia Tech, Atlanta, USA
N. Massarotti, P. Nithiarasu and Y. Joshi (Eds.)

NUMERICAL SIMULATION OF SUPRACHOROIDAL SHUNTS FOR TREATMENT OF GLAUCOMA

A. Mauro[1,2], N. Massarotti[2]
[1]Università Telematica Pegaso, Piazza Trieste e Trento n. 48, 80132 Napoli, Italy,

[2]Dipartimento di Ingegneria, Università degli Studi di Napoli "Parthenope", Isola C4, Centro Direzionale di Napoli, 80143 Napoli, Italy

M.R. Romano
Dipartimento di Neuroscienze e scienze riproduttive ed odontostomatologiche, Università degli Studi di Napoli Federico II, Via S. Pansini n. 5, 80131 Napoli, Italy

V. Romano
Dipartimento di Oftalmologia, Seconda Università degli Studi di Napoli (SUN), Via S. Pansini n. 5, 80131 Napoli, Italy

P. Nithiarasu
College of Engineering, Swansea University, Swansea SA2 8PP, United Kingdom

ABSTRACT

A numerical investigation of Aqueous Humor (AH) flow in SOLX® Gold Micro Shunt (GMS) and a novel Silicon Shunt Device (SSD) is presented, with the aim of reducing IntraOcular Pressure (IOP) for treatment of glaucoma. The generalised porous medium model is solved to simulate AH flow through the devices and the surrounding tissues. In the GMS, probable stagnation regions were found, due to very small AH velocity values and to the surrounding tissues, creating blockage and malfunction of the device. The simple microtubular geometry of the novel SSD allows to have a regular AH flow and facilitates surgeons in the choice of shunts with different diameter, based on patients needs, avoiding post-operative complications.

Key Words: *Eye, Ocular Pathology, Surgery, Devices, Modeling, Finite element method*

1. INTRODUCTION

Glaucoma is the second leading cause of blindness in human eye. The primary reason of glaucoma is the abnormality of Intra Ocular Pressure (IOP) involved with death of retinal ganglion cells in the inner retina and loss of their axons in the optic nerve [1, 2]. The increase of IOP is due to the blockage of trabecular meshwork, which reduces Aqueous Humor (AH) outflow from the eye. The adverse effects of IOP can be rectified by using various medical and surgical techniques which can improve the eye vision to a certain extent. Drug delivery (medical) techniques, paramedical techniques which involve laser treatment, and surgical techniques can be used for treatment of glaucoma. Among surgical techniques, filtration procedures (trabeculectomy) or implantation of drainage devices allow to create a path for AH outflow between Anterior Chamber (AC) and sub-conjunctival space of eye. Due to post-surgical complications in filtration procedure, a second category of surgical techniques was introduced, creating a link between the AC and the Suprachoroidal Space (SCS). Two examples of devices used in this category are the SOLX® Gold Micro Shunt (GMS) and the novel Silicon Shunt Device (SSD).

The present work is focused on the analysis of fluid dynamics of GMS and SSD by using the Characteristic Based Split (CBS) numerical scheme [3]. The concept of this paper derives from the collaboration between engineers and medical researchers, aimed at the optimization of ocular drainage devices. The objective of the work is to compare the performance of GMS (commercially available) and a novel SSD devices, in order to provide doctors with useful information for the optimization of such devices.

2. DESCRIPTION OF TWO SHUNTS

The SOLX®GMS is a non-valved flat-plate drainage device made of 24-K medical-grade (99.95%) gold. It consists of micro channels creating a flow based on hydrostatic pressure difference between the (Anterior Chamber) AC and the Anterior SupraChoroidal (supraciliary) Space (ASCS) through uveoscleral region. The GMS width, length and thickness are 2.5 mm, 5.2 mm, and 44 μm, respectively. The microchannels width and height are 24 μm and 50 μm, respectively. The inflow compartment of the GMS contains 60 holes of 100 μm in diameter and one 300 μm diameter hole on both plates of the device and 10 additional 50 μm lateral openings, that allow the inflow of AH. The outflow compartment contains a grid of 117 holes of 110 μm in diameter on both the plates of the shunt and 12 additional 50 μm openings, to allow the outflow of AH.

The novel SSD is a microtube made of silicon that connects AC to the Posterior SupraChoroidal Space (PSCS) of a silicon microtube with length, interior and exterior diameter of 8.0 mm, 320 μm and 640 μm, respectively.

3. MATHEMATICAL MODEL AND NUMERICAL METHODOLOGY

The mathematical procedure employed is based on the generalized approach for solving AH fluid dynamics in free fluids and porous media. The single phase fluid flows inside the device and encounters the scleral and choroidal tissues surrounding the outflow sections of the device, simulated as porous media. The present generalised mathematical model has the flexibility in easily reducing to Navier-Stokes equations, just setting $\varepsilon \to 1$ and $\kappa \to \infty$, and to simulate free fluid – porous medium interface problems, by providing appropriate values for porosity and permeability values. The governing equations, solved by using the Characteristic Based Split (CBS) scheme [3], are reported in the following:

Mass conservation equation

$$\frac{1}{\varepsilon}\frac{\partial u_i}{\partial x_i} = 0 \tag{1}$$

Momentum conservation equation

$$\frac{\rho}{\varepsilon}\frac{\partial u_i}{\partial t} + \frac{\rho}{\varepsilon^2}u_j\frac{\partial u_i}{\partial x_j} = -\frac{\partial p_f}{\partial x_i} + \frac{\mu_{eff}}{\varepsilon}\frac{\partial \tau_{ij}}{\partial x_j} - \frac{\mu_f}{\kappa}u_i - \rho_f\frac{F}{\sqrt{\kappa}}|\mathbf{u}|u_i \tag{2}$$

4. COMPUTATIONAL DOMAINS AND BOUNDARY CONDITIONS

The computational domains and boundary conditions of GMS and novel SSD are shown in Figure 1. The human tissues (sclera and choroid) have been reproduced as porous media with permeability of $2.5\text{x}10^{-13}$ m^2 and the thickness has been considered equal to 0.3 mm. The upper and lower surfaces of holes and the lateral openings of the inflow compartment of the GMS are subject to the AC pressure, such as the inlet section of the SSD. For both the devices, the surfaces of the porous tissues in correspondence of the outflow compartment are subject to the ASCS pressure.

For the GMS, the AC pressure value considered in the simulations is 18.2 mmHg (2426 Pa), corresponding to the mean value measured by Melamed et al. within their clinical study [4]. The ASCS pressure value has been taken equal to 17.4 mmHg (2320 Pa), corresponding to a pressure difference between AC and ASCS of 0.8 mmHg, on the basis of the only experimental data available in the literature, reported by Emi et al. [5].

For the SSD, the AC pressure value considered in the simulations is 12 mmHg (1600 Pa), corresponding to the mean value measured by some of the present authors in a pilot study on

patients after surgical insertion of the SSD [2]. The PSCS pressure value has been taken equal to 8.3 mmHg (1107 Pa) [5].

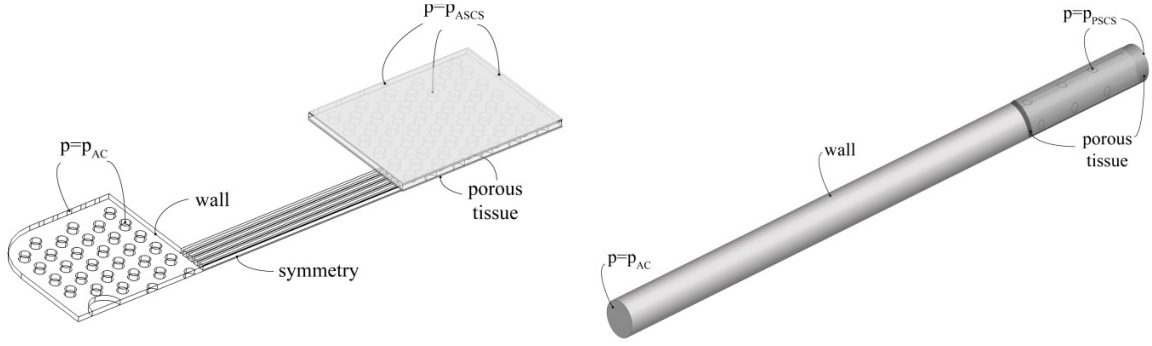

(a) (b)

FIGURE 1. Computational domain and boundary conditions for (a) SOLX®GMS and (b) novel SSD

5. RESULTS

The volumetric flow rate of AH drained by the GMS is found to be 1.04 µl/min, which is quite less compared to the normal flow rate in human eye of 2.2-3.1 µl/min [6]. AH enters the GMS and is accelerated towards the microchannels. The velocity of AH at the microchannels is high compared to the inlet and outlet section. Therefore, the internal fluid dynamics of the GMS is characterized by evident velocity gradients of several orders of magnitude between different areas of the shunt. In the regions near the inlet and outlet sections, the velocity values are found out to be smaller than 10^{-5} mm/s, and AH flow is practically absent (Figure 2). The possible cause of these stagnation regions is related to the surrounding vessels and tissues inducing blockage of the flow and malfunction of the device. Moreover, the small pressure gradient between AC and ASCS results in decreased AH flow. If the outflow was targeted towards PCSC, the higher pressure gradient would have led to an increased outflow. But, probably in order to avoid hypotonic conditions, the GMS outlet has been designed for implantation in the ASCS.

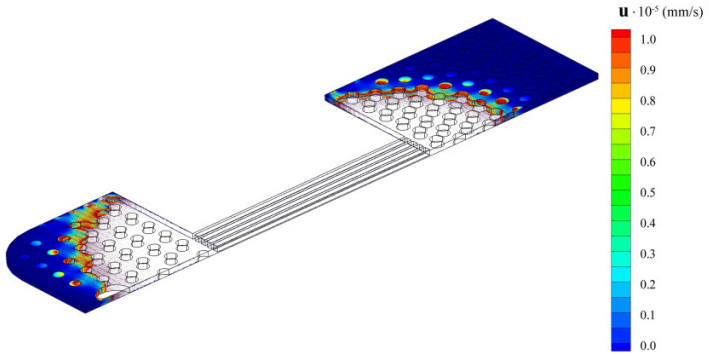

FIGURE 2. Velocity field in the GMS: stagnation zones.

As concerns the novel SSD, an AH volumetric flow rate of 2.57 µl/min is obtained, therefore significantly higher than the value corresponding to GMS and comparable to normal human values. In fact, the simple microtubular geometry of SSD has the advantage of less AH accumulation, as compared to the complex geometry of GMS. The simplicity in design of SSD allows doctors to have the flexibility of choosing different diameters, depending on the patient specific needs, such a preoperative IOP values or other medical considerations. A modified SSD has been designed by adding radial holes of 100 µm diameter at the lateral surface of outlet section, in order to control the flow rate of AH. The calculated AH volumetric flow rate (drainage) obtained varying the

diameter of the SSD and the number of 100 μm diameter radial holes is reported in Table 1. Surgeons could use these values to choose the SSD that best fits patient specific needs, in order to avoid post-operative complications.

D (μm) / **n. holes**	**320**	**280**	**250**
0	2.57	1.92	1.52
3	3.28	2.68	2.27
6	4.01	3.40	2.99
12	5.48	4.85	4.40

TABLE 1. AH volumetric flow rate (μl/min) through the novel SSD.

6. CONCLUSIONS

In this work, the authors employ the generalized porous medium model to analyze the fluid dynamics of the SOLX® Gold Micro Shunt (GMS) and the novel Silicon Shunt Device (SSD), taking into account the presence of the surrounding human tissues. These devices are implanted by surgeons in human eyes to reduce the IOP towards physiological values, in order to cure eyes with glaucoma.

The main outcomes of the study are: (*i*) The AH flow in GMS encounters stagnation areas and low velocity regions, due to probable obstruction of inlet and outlet holes by the surrounding tissues and vessels, creating blockage and malfunction of the device; (*ii*) The novel SSD allows to obtain an AH drainage comparable to normal human values, thanks to its regular microtubular geometry; (*iii*) The AH outflow that best fits patient specific needs can be chosen by the surgeon, implanting one of the different configurations of SSD, with three possible diameters and/or employing a variable number of radial holes.

The authors believe that the present numerical simulation approach, employing the generalized porous medium model, represents a useful tool to study the fluid dynamics of ocular drainage devices and to design these shunts, limiting post-operative complications.

ACKNOWLEDGMENTS

The authors gratefully acknowledge the financial support of TeVR Project CUP E62I15000760008.

REFERENCES

[1] W.H.M. Franzco, D-Y. Yu, Surgical management of glaucoma: a review, *Clinical and Experimental Ophthalmology,* **40,** 388-399, 2012.

[2] V. Romano, F. Romano, A. Mauro, R. Vinciguerra, L. Rinaldi, M. Angi, M.R. Romano, C. Costagliola, Glaucoma Surgery: potential of a new uveoscleral outflow shunt. *Acta Ophthalmologica*, under review.

[3] F. Arpino, N. Massarotti, A. Mauro, Efficient three-dimensional FEM based algorithm for the solution of convection in partly porous domains, *International Journal of Heat and Mass Transfer*, 54, 4495–4506, 2011.

[4] S. Melamed, G.J.B. Simon, M. Goldenfeld, G. Simon, Efficacy and Safety of Gold Micro Shunt Implantation to the Supraciliary Space in Patients With Glaucoma. A Pilot Study, *Archives of Ophthalmology*, 127, 264-269, 2009.

[5] K. Emi, J.E. Pederson, C.B. Toris, Hydrostatic Pressure of the Suprachoroidal Space, *Investigative Ophthalmology & Visual Science*, 30, 233-238, 1989.

[6] J.W. McLaren, Measurement of aqueous humor flow, *Experimental Eye Research*, 88, 641-647, 2009.

Fourth International Conference on Computational Methods for Thermal Problems
THERMACOMP2016, July 6-8, 2016, Georgia Tech, Atlanta, USA
N. Massarotti, P. Nithiarasu and Y. Joshi (Eds.)

Modelling Energy Transport in a Human Respiratory System

Perumal Nithiarasu
Biomedical Engineering and Rheology Group, Zienkiewicz Centre for Computational Engineering
College of Engineering, Swansea University, Swansea SA2 8PP, UK
e-mail:P.Nithiarasu@swansea.ac.uk;
website: http://www.swansea.ac.uk/staff/academic/engineering/nithiarasuperumal/

ABSTRACT

In this paper, energy transport in human respiratory tract is modelled using the finite element method. The upper and lower respiratory tracts are approximated as a one-dimensional domain with varying cross sectional area and the radial heat conduction in the tissue is approximated using one dimensional cylindrical coordinate system. The governing equations are solved using one-dimensional linear finite elements with convective and evaporative boundary conditions on the wall. The study of full breathing cycle indicates that evaporation is the main mode of heat transfer and convection plays almost negligible role in the energy transport. This is in line with the results obtained from animal experiments.

Key Words: *human respiratory system, heat transfer, convection, evaporation, finite element method.*

1. INTRODUCTION

The surface area of human respiratory tract varies between 30 and 100 m^2. This provides a surface to volume ratio of between 5000 and 17000 m^2/m^3. Such large values clearly make the human respiratory tract extremely compact. Since engineers consider a heat exchanger with a surface to volume ratio of more than 700m^2/m^3 as a compact heat exchanger, the human respiratory tract truly is such a heat exchanger. Thus, understanding the structure of the respiratory tract and transport within it may be of great interest to heat exchanger researchers.

One of the prominent features of lungs is that approximately 700 million interconnected alveolar sacs exchange heat and gas with blood. A typical alveolus is about 200μm in size. In addition, blood capillaries surrounding the alveolar sacs efficiently transfer carbon dioxide and heat to the air via the respiratory system. Since the temperature at the interface between blood and alveoli is approximately the body temperature, the heat transfer coefficient between the alveolus and air may be calculated to be between 0.2 and 5 W/m^{2o}C. This clearly shows that the hear transfer coefficient is lower than that of natural convection range, yet the lung is very efficient in transferring energy.

The heat transfer mechanisms in respiratory tract include convective and latent heat losses[1]. Numerical modelling of these heat transfer mechanisms is complex. In this paper an attempt is made to study the heat transport using a one-dimensional convection-diffusion model. The details of the models, solution procedure and results are discussed below.

2. MATHEMATICAL MODEL AND FINITE ELEMENT SOLUTION

The two main mechanisms of heat transfer in a respiratory tract are convection and latent heat of evaporation from the wall. The convective heat transferred from or to the respiratory tract walls may be written as

$$Q_c = hPL(T_w - T_a) \tag{1}$$

where h is the heat transfer coefficient, P is the perimeter, L is the length of the passage along which heat is transferred, T_w is the wall temperature and T_a is the local air temperature. In a lumped fashion the heat transfer due to convection may be written as

$$Q_c = \dot{m} c_p (T_b - T_{ai}) \tag{2}$$

where $\dot{m}$ is the mass flow rate, T_b is the body temperature and T_{ai} is the inlet air temperature. Heat transfer as a result of latent heat of vaporisation may be written as

$$Q_L = \frac{\lambda \dot{m}}{\rho} (\phi_e - \phi_a) \tag{3}$$

where λ is the latent heat of water evaporation, ρ is the density of air and ϕ_e and ϕ_a are the absolute humidities of expired and inspired air respectively. The absolute humidities may be defined as

$$\phi_e = \frac{10^6 M_w e^*}{R T_b} \tag{4}$$

and

$$\phi_a = \frac{10^6 M_w e}{R T_b} \tag{5}$$

where M_w is the mol mass of water (18.016 g/mol), R is the molar gas constant (8.3143 J/Mol K), e^* (kPa) is the saturation vapour pressure of the air at T_b and e (kPa) is the partial vapour pressure of air at T_a. The vapour pressures may be calculated as [1]

$$e(T) = 0.61075 \times 10^{\left\{\frac{7.5T}{T+237.5}\right\}} \tag{6}$$

The total heat transferred in a respiratory tract is therefore $Q = Q_c + Q_L$.

Although the above lumped model is useful to study different scenarios, it is not a robust model for predicting temperature distribution in space and time. A time dependent model in three dimensions will be the most comprehensive model for a respiratory system. However, the structural complexities of lungs can be extremely difficult to deal with using three dimensional spatial models. The one-dimensional models on the other hand are simple and fast. The one-dimensional energy equation governing energy transport in a human respiratory tract may be written as

$$\rho c_p A \left(\frac{\partial T}{\partial t} + u \frac{\partial T}{\partial x} \right) - \frac{\partial}{\partial x} \left(kA \frac{\partial T}{\partial x} \right) + hP(T - T_b) + \frac{\lambda \dot{m}}{\rho} P(\phi_b - \phi) = 0 \tag{7}$$

where A is the cross sectional area, k is the thermal conductivity of air and P is the perimeter. Since the respiratory tract wall temperature is not constant, a model to determine the wall temperature is essential. The simplest form of heat conduction model is a one-dimensional model in the radial direction originating from the respiratory tract wall. Such a model for heat conduction through the wall may be written as

$$\rho c_p A \frac{\partial T}{\partial t} - \frac{\partial}{\partial x} \left(kA \frac{\partial T}{\partial x} \right) + hP(T - T_a) = 0 \tag{8}$$

Equation 7 along with appropriate initial and boundary conditions is solved in the present work using an explicit Taylor Galerkin method and the heat conduction equation 8 is solved using standard explicit Galerkin method[2]. As seen in these equations, the interface is linked through a convective heat

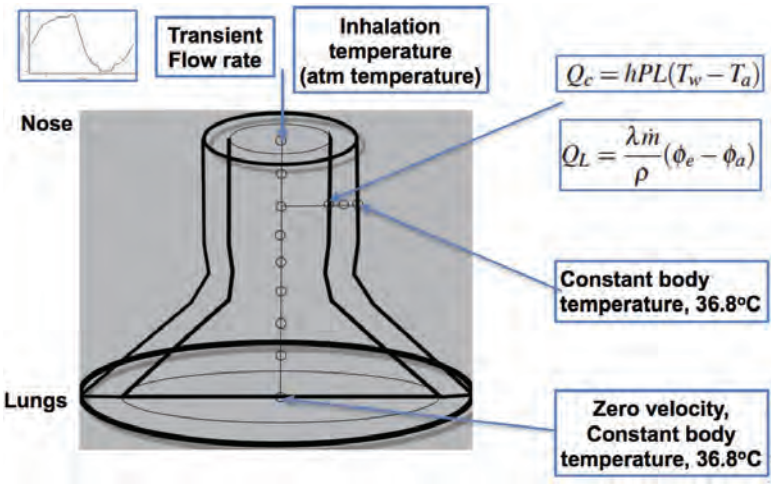

FIGURE 1. One-dimensional approximation of human respiratory tract and boundary conditions.

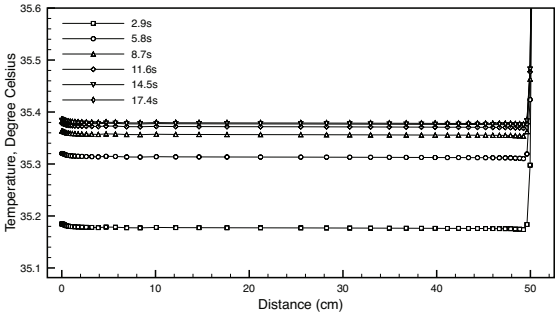

FIGURE 2. Convergence. Air temperature distribution at the end of each breathing cycle.

transfer boundary condition. Figure 1 shows the approximate model of the respiratory tract along with boundary conditions. As seen, a breathing flow rate cycle is imposed at the inlet and at the interface between the air and wall, a convective heat transfer boundary condition is imposed. At the lung end of the tract, the temperature is assumed to be that of the body temperature at 36.8^o C. Only part of the wall of thickness 0.2mm is considered. At 0.2mm from the airway, the tissue is assumed to reach the body temperature as shown.

3. RESULTS

As shown in Figure 1, the inlet flow variations and boundary conditions are imposed and solutions are obtained continuously for a number of breathing cycles. As seen in Figure 2, the solution takes a few cycles to reach a converged state. The air temperatures are plotted at the end of each cycle in Figure 2. As seen the results needed at least four cycles to converge. All the remaining results are therefore are obtained at least after five breathing cycles.

Figure 3(a) shows the relative importance of convection and evaporation heat transfer. As seen the temperature distribution is dominated by evaporation heat transfer. The convection effect is very small compared to evaporation heat transfer. Figure 3(b) shows the air temperature variation with time along the respiratory tract at an atmospheric temperature of 20^oC. As seen, at the inhalation phase of the breathing cycle, the air temperature in the entire tract is cooled down to below 33^o celsius before the temperature is increased towards the body temperature during exhalation part of the cycle. Thus, the duration of the breathing cycle plays an important role in determining the transient as well as the exhaled air temperature. The duration of the breathing cycle assumed here is 2.9s.

Figure 4(a) shows the wall temperature variation over a breathing cycle at an atmospheric temperature of 20^oC. As seen the wall temperature also follows a similar pattern to that of the air temperature.

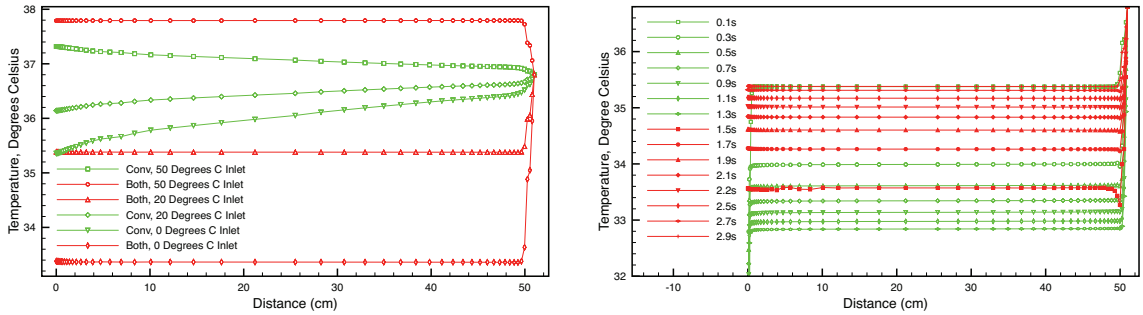

(a) Comparison of convection and evaporation mechanisms at different atmospheric temperatures.

(b) Temperature variation with time at an atmospheric temperature of 20^oC

FIGURE 3. Air temperature variation

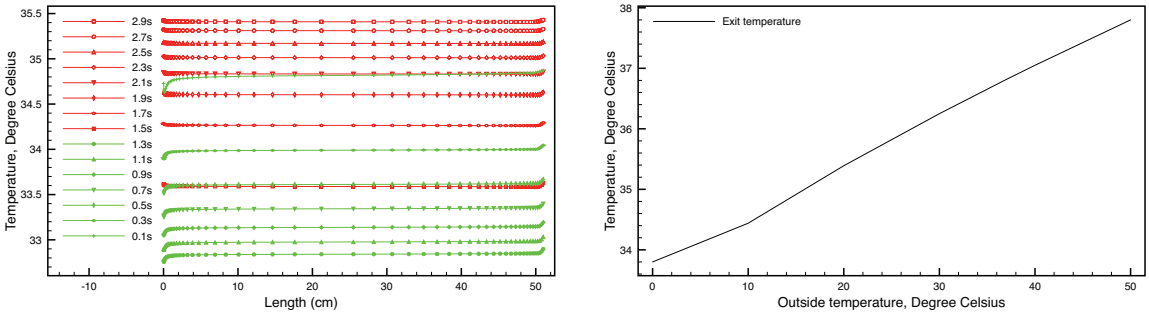

(a) Wall temperature variation with time at an atmospheric temperature of 20^oC

(b) Exhaled air temperature at various atmospheric temperatures.

FIGURE 4. Wall and exhaled temperature variations

The wall is initially cooled down during the inhalation part of the cycle and it heats up as the air is exhaled. Figure 4(b) shows the exhaled air temperature at different atmospheric temperatures. As seen the exhaled air temperature varies linearly with the atmospheric temperature. A very similar pattern was observed in sheep experiments[1].

4. CONCLUSIONS

In the present work, an attempt has been made for the first time to computationally model the energy transport in a respiratory tract. Although the model presented is one-dimensional in nature, the results appear to be physically meaningful and qualitatively reflects the result produced by animal experiments[1]. The results may be further refined by including thermoregulatory mechanisms in the soft tissue.

REFERENCES

[1] Roberto Gomes da Silva, Newton LaScala Jr, Alvaro Edison Lima Filho, and Marcelo Carlos Catharin, Respiratory heat loss in the sheep: a comprehensive model, *Int J Biometeorol*, 46, 136-140, 2002.

[2] P.Nithiarasu, R.W. Lewis and K.N. Seetharamu, *Fundamentals of the finite element method for heat, mass and fluid flow*, Wiley, February 2016.

Fourth International Conference on Computational Methods for Thermal Problems
THERMACOMP2016, July 6-8, 2016, Georgia Tech, Atlanta, USA
N. Massarotti, P. Nithiarasu and Y. Joshi (Eds.)

STATE ESTIMATION PROBLEMS IN PRF-SHIFT MAGNETIC RESONANCE THERMOMETRY

César C. Pacheco*, Helcio R. B. Orlande, Marcelo J. Colaço
Department of Mechanical Engineering
Federal University of Rio de Janeiro – POLI/COPPE
Centro de Tecnologia, Sala I-136, Cidade Universitária, Rio de Janeiro, Brazil
cesar.pacheco@poli.ufrj.br helcio@mecanica.ufrj.br colaco@ufrj.br

George S. Dulikravich
Department of Mechanical and Materials Engineering, MAIDROC Laboratory
Florida International University
10555 West Flagler St., EC 3462, Miami, Florida 33174, USA
dulikrav@fiu.edu

(*Corresponding author)

ABSTRACT

The calculation of temperature shifts *via* PRF-Shift MR Thermometry is herein performed under a Bayesian framework. This formulation aims to result in more robust temperature measurements, accounting for known uncertainties in some important parameters.

Key Words: *Heat Transfer, MR Thermometry, State Estimation Problems.*

1. INTRODUCTION

Non-intrusive quantification of temperature in living tissue has become a very important feature in developing more robust and reliable thermal therapies. Several methodologies designed for this purpose are available, wherein the PRF-Shift Magnetic Resonance (MR) Thermometry is the most widely used due to its robustness and near tissue-independency [1]. In this technique, the temperature values are calculated using phase mapping. These values, acquired by MR equipment, are usually noisy and propagate uncertainties to the indirect temperature measurements. In this work, these uncertainties are quantified by recasting this problem as a state estimation problem, which enables the use of techniques that have been successfully used in other areas [2], [3].

2. FORWARD AND INVERSE PROBLEM

The calculation of temperature shifts via phase mapping in the PRF-Shift MR Thermometry is given by Eq. (1) [1]. Here, $\Phi(T_2)-\Phi(T_1)$ stands for the phase difference measured within a GRE-type pulse sequence, α represents the linear relationship between temperature and chemical shift, γ is the gyromagnetic ratio, t_{TE} is the echo time and B_0 is the externally imposed magnetic field.

$$\Delta T = T_2 - T_1 = \frac{\Phi(T_2)-\Phi(T_1)}{\alpha\gamma t_{TE} B_0} \tag{1}$$

In order to process the noisy measurements of phase shift we recast this problem in the form of a state estimation problem, given by an evolution and an observation model, respectively given by

$$\mathbf{x}_{n+1} = \mathbf{F}\mathbf{x}_n + \mathbf{w}_{n+1} \tag{2}$$

$$\mathbf{y}_n = \mathbf{H}\mathbf{x}_n + \mathbf{v}_n \tag{3}$$

In these equations, $\mathbf{x}$ is the state vector, $\mathbf{y}$ is the observation vector, $\mathbf{w}$ is the evolution noise and $\mathbf{v}$ is the observation noise. Both of these noise vectors are Gaussian with zero mean and known covariance matrices $\mathbf{Q}$ and $\mathbf{R}$, respectively. Within the proposed approach, the state vector is the temperature shift, while the observation vector contains the phase shift.

$$\mathbf{x}_n = \mathbf{\Delta T}_n \qquad \text{and} \qquad \mathbf{y}_n = \mathbf{\Delta \Phi}_n \tag{4}$$

By noticing that the model given by Eq. (1) is linear, it might be possible to estimate the sought variables sequentially by using the Kalman filter (KF) [2]–[4]. An evolution model based on the heat conduction equation, presented by Eq. (5), is also considered. This partial differential equation is a particular case of the well-known bioheat equation [5], without perfusion terms. In this model, all boundaries are considered as thermally insulated. The initial condition is discussed below.

$$\rho c_p \partial_t \Delta T = k \nabla^2 \left(\Delta T \right) \tag{5}$$

After the assembling of the required matrices for the KF, it follows that the resulting system is linear and time-invariant (LTI). In this particular case, an approximation of the KF equations can be performed, resulting in the *steady-state Kalman filter* (SSKF) [4]. In comparison with the original KF, the SSKF is orders of magnitude faster and can easily provide the required temporal resolution for situations like monitoring and controlling of thermal therapies. The equations for the SSKF are

$$\mathbf{P}_\infty = \mathbf{F}\mathbf{P}_\infty\mathbf{F}^T - \mathbf{F}\mathbf{P}_\infty\mathbf{H}^T \left(\mathbf{H}\mathbf{P}_\infty\mathbf{H}^T + \mathbf{R} \right)^{-1} \mathbf{H}\mathbf{P}_\infty\mathbf{F}^T + \mathbf{Q} \tag{6}$$

$$\mathbf{K}_\infty = \mathbf{P}_\infty\mathbf{H}^T \left(\mathbf{H}\mathbf{P}_\infty\mathbf{H}^T + \mathbf{R} \right)^{-1} \tag{7}$$

$$\hat{\mathbf{x}}_n^+ = \left(\mathbf{I} - \mathbf{K}_\infty\mathbf{H} \right) \mathbf{F}\hat{\mathbf{x}}_{n-1}^+ + \mathbf{K}_\infty\mathbf{y} \tag{8}$$

3. RESULTS

In this work, the synthetic phase measurements were simulated by solving a 2D heat conduction problem, similar to the one given by Eq. (5). The phase measurements were calculated through Eq. (1). Gaussian noise with zero mean and standard deviation of 10% of the maximum phase shift observed was added to the measurements. These synthetic measurements were considered available throughout a 24 x 24 uniform grid with domain dimensions 12 cm x 12 cm. The MR [6] and thermal [7] parameters used both in the measurements simulation and in the SSKF are presented in Eqs. (9) and (10), respectively. Figure 1 shows the initial condition and the temperature distribution at t = 100 s.

$$\gamma = 42.57 \text{ MHz/T}, \quad t_{TE} = 18 \text{ ms}, \quad \alpha = -0.01 \text{ ppm/ºC}, \quad B_0 = 1.5 \text{ T} \tag{9}$$

$$\rho c_p = 4180 \text{ kJ/m³ºC}, \quad k = 0.60 \text{ W/mºC} \tag{10}$$

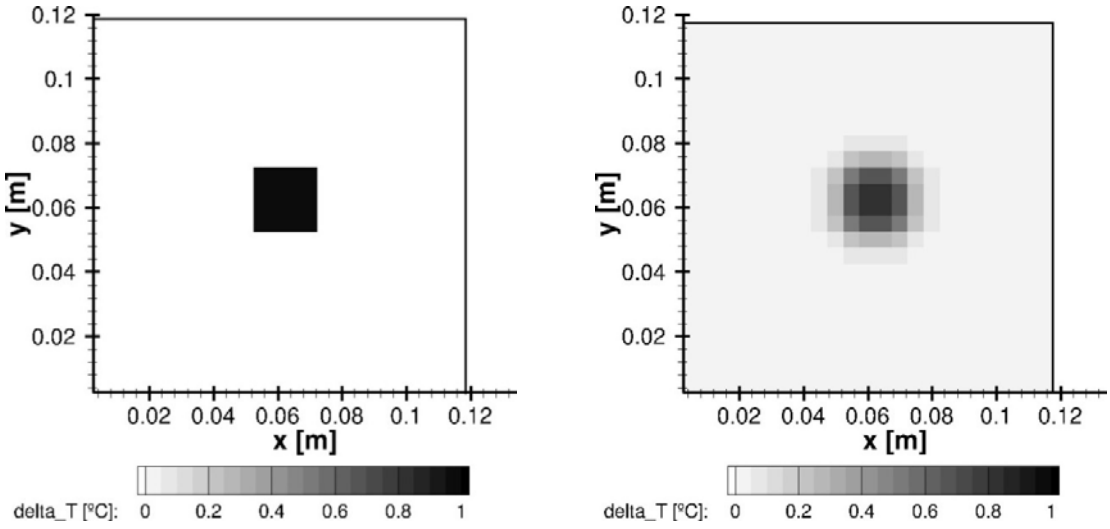

(a) (b)

FIGURE 1. Contour plots for exact temperature at (a) t = 0 s, and (b) t = 100 s.

Figure 2 presents the temperature shift estimates at t = 100 s, obtained by directly inverting Eq. (1) (Figure 2a) and by applying the proposed approach (Figure 2b). Comparing these results with Figure 1b clearly shows the improved performance of the proposed approach. The time evolution of a voxel within the central region is tracked and shown in Figure 3a. Once again, one can observe that the proposed approach produces estimates with better agreement with the reference temperature values. This improvement is better observed in Figure 3b, where the temperature errors for both approaches are shown. The SSKF method outperformed the direct inversion throughout the simulation time, resulting in temperature erros significantly smaller than the ones obtained *via* direct inversion.

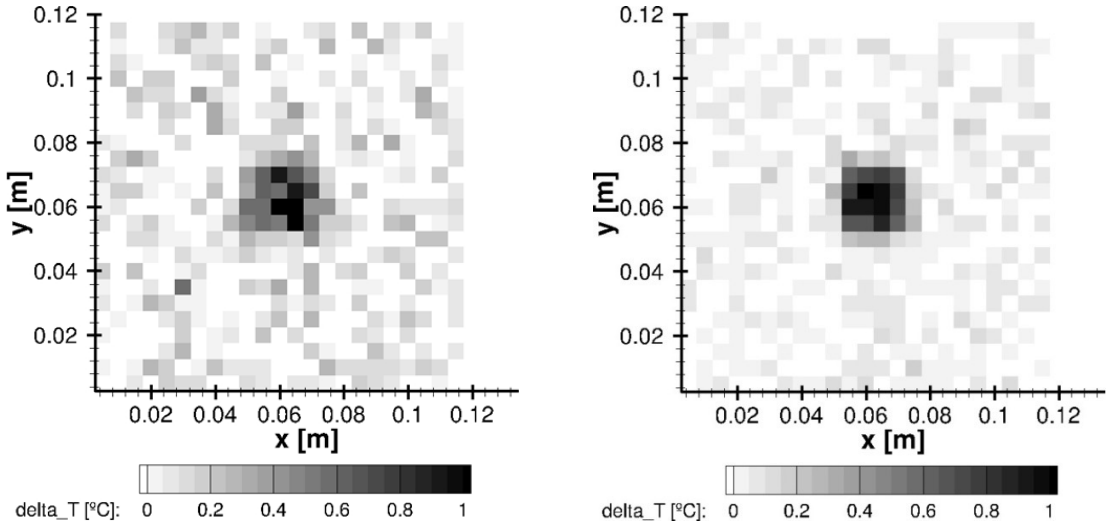

(a) (b)

FIGURE 2. Contour plots for temperature at t = 100 s calculated through (a) direct inversion, and (b) proposed approach using SSKF.

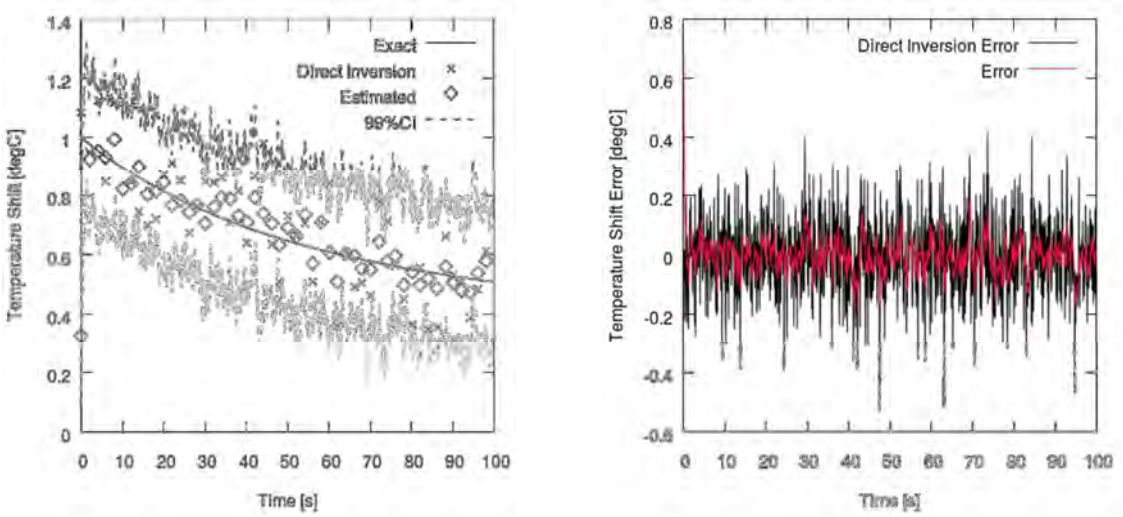

(a) (b)

FIGURE 3. Time evolution of (a) temperature at the central region and (b) temperature errors at the heated region for both methods.

4. CONCLUSIONS

The proposed approach resulted in temperature shift estimates that are in excellent agreement with the reference values and that have better quality in comparison with the temperature shift values obtained through direct inversion, with the added benefit of quantifying the uncertainty of the estimates.

REFERENCES

[1] Y. Ishihara, a Calderon, H. Watanabe, K. Okamoto, Y. Suzuki, K. Kuroda, and Y. Suzuki, "A precise and fast temperature mapping using water proton chemical shift.," *Magn. Reson. Med.*, vol. 34, no. 6, pp. 814–823, 1995.

[2] J. P. Kaipio and E. Somersalo, *Statistical and Computational Inverse Problems*. Springer Science+Business Media, Inc, 2004.

[3] H. R. B. Orlande, M. J. Colaço, G. S. Dulikravich, F. L. V. Vianna, W. B. da Silva, H. M. Fonseca, and O. Fudym, "State Estimation Problems in Heat Transfer," *Int. J. Uncertain. Quantif.*, vol. 2, no. 3, pp. 239–258, 2012.

[4] D. Simon, *Optimal State Estimation: Kalman, H∞, and Nonlinear Approaches*. John Wiley & Sons, Inc., 2006.

[5] H. H. Pennes, "Analysis of Tissue and Arterial Blood Temperatures in the Resting Human Forearm," *J. Appl. Physiol.*, vol. 1, no. 2, pp. 93–122, Aug. 1948.

[6] C. Mougenot, B. Quesson, B. D. de Senneville, P. L. de Oliveira, S. Sprinkhuizen, J. Palussière, N. Grenier, and C. T. W. Moonen, "Three-dimensional spatial and temporal temperature control with MR thermometry-guided focused ultrasound (MRgHIFU)," *Magn. Reson. Med.*, vol. 61, no. 3, pp. 603–614, 2009.

[7] M. N. Ozisik, *Heat Transfer: A Basic Approach*, 2nd ed. McGraw-Hill, 1985.

MINI SYMPOSIUM

VALIDATION, VERIFICATION AND EXPERIMENTAL UNCERTAINTY QUANTIFICATION FOR HEAT AND FLUID FLOW PROBLEMS

MINI SYMPOSIUM ORGANISED BY F. ARPINO, G. CORTELLESSA, F. IANNETTA, N. MASSAROTTI, A. MAURO, F. SCARANO AND A. SCIACCHITANO

Fourth International Conference on Computational Methods for Thermal Problems
THERMACOMP2016, July6-8, 2016, Georgia Tech, Atlanta, USA
N. Massarotti, P. Nithiarasu and Y. Joshi(Eds.)

SCHLIEREN AND MIE SCATTERING TECHNIQUES FOR THE ECN "SPRAY G" CHARACTERIZATION AND 3D CFD MODEL VALIDATION

L. Allocca[1], M. Costa[1], S.Y. Lee[2], A. Montanaro[1], D. Piazzullo[3], V. Rocco[1]
[1]CNR - Istituto Motori, Viale Marconi 4, 80125, Naples, Italy

[2]Michigan Technological University, Houghton, MI, 49931, USA

[3]Università degli Studi "Tor Vergata", Via del Politecnico 1, 00133 Rome, Italy

l.allocca@im.cnr.it, m.costa@im.cnr.it, sylee@mtu.edu, a.montanaro@im.cnr.it, daniele.piazzullo@students.uniroma2.eu, v.rocco@im.cnr.it

ABSTRACT

Key Words: *Spray Injection, GDI, CFD, Schlieren, Mie-Scattering.*

1. INTRODUCTION

The beneficial impact of direct injection strategy (DI) on spark ignition (SI) engine performances is largely recognized in terms of fuel economy and emissions reduction [1]. DISI engines operate at higher compression ratios with respect to port fuel injection (PFI) ones, resulting in higher thermal efficiencies and power outputs. Moreover, different injection strategies can be chosen, so the greater control over the air-to-fuel ratio allows operating under lean fuel conditions, in the stratified charge mode, approaching the efficiencies and emission indexes of compression ignition engines. On the other hand, today engines strongly differ from yesterday ones, due to their complexity and high number of sub-systems, so that traditional tools and techniques used for their design are often insufficient for the required challenges of high power output and low environmental impact. In this change of perspective, from a test-first culture to an analysis-led design process, numerical simulation tools, as CFD (computational fluid dynamics) models, are becoming increasingly important to accelerate the time to market of high-efficiency clean power units for transportation [2]. Present work aims at giving a contribution to the validation of 3D CFD models for the simulation of the in-cylinder thermo-fluidynamic processes underlying energy conversion, in particular by giving a detailed experimental insight into the dynamics and impact over walls of multi-hole sprays for DISI applications through combined schlieren and Mie scattering techniques.

2. EXPERIMENTAL SETUP

Experimental tests aimed at collecting detailed information about the phase transition of the multitude of droplets compounding the spray in their impact against hot walls and the consequent complex heat transfer mechanisms between the solid, liquid and gaseous media, were performed in a constant volume combustion vessel optically accessible by three quartz windows allowing the admittance to the investigated area. The chosen multi-hole injector was located on the top of the vessel in a holder including a jacket for the temperature control of the nozzle nose and connected to a chiller for fluxing a cooling liquid. The fuel is supplied through a common rail system and heated by an electrical resistance, with the temperature controlled by a J-type thermocouple located in the rail. A cooling cup surrounding the injector mount was used to control the injector nozzle temperature. Both the injector and the fuel temperature were kept at 363 K. A more complete description of the experimental setup is reported in [3].
A Delphi solenoid-activated eight holes electro-injector was used, 0.165 mm in diameter, L/d=2

having a static flow of 15 cc/s @10.0 MPa. A single-component fuel, iso-octane, was used as fluid [ρ=690 kg/m3@298 K]. The used injector was chosen from Engine Combustion Network (ECN) for the gasoline characterization (Spray G), with precise specification. The tests were carried out by injecting 10 mg of fuel at the injection pressure of 20.0 MPa and injection duration of 680 µs. An 80 mm in diameter aluminum flat plate was positioned 19.5 mm downstream the injector tip and placed orthogonally to the injector axis. The wall temperature was fixed at 373 K and monitored in temperature by a J-type thermocouple, located in the center of the plate at 1.0 mm under the impinging surface. The ambient temperature inside the vessel was kept constant at the same wall temperature.

The impinging GDI (gasoline direct injection) spray morphology was investigated by optical techniques before and after impingement on a heated wall. Schlieren technique is sensible to the refraction index gradient caused by the density gradient of the fuel, hence it is able to collect information about the space distribution of both the liquid and vapor. A single optical technique however does not allow accurately evaluating the boundaries between the phases, being these linked to the choice of the threshold levels. For this reason, the spray was characterized by two synchronized optical techniques, schlieren for the vapor and Mie scattering for the liquid, working in alternative and quasi-simultaneous mode. A sketch of the combined z-shaped schlieren and Mie-scattering optical setup is shown in figure 1a. The camera was equipped with a 90 mm objective, f =1:2.8, and realizing a spatial resolution of 9.6 pixel/mm. A "syncout" signal, derived from the C-Mos camera, triggered the light sources powering the LEDs on its odd and even frames for schlieren and elastic scattering, respectively. Both the LEDs durations were 8µs and their time arrangements were straddled of the change of the frame of the C-Mos. The resulting time difference between the schlieren image and the elastic scattering one was no longer than 15µs. Figure 1b shows a sketch of the footprint of the 8 jet position on the nozzle and a photo of the whole spray on the right. The injector was mounted so to acquire the evolving fuel with the spray #1 oriented orthogonally with respect to the camera axis.

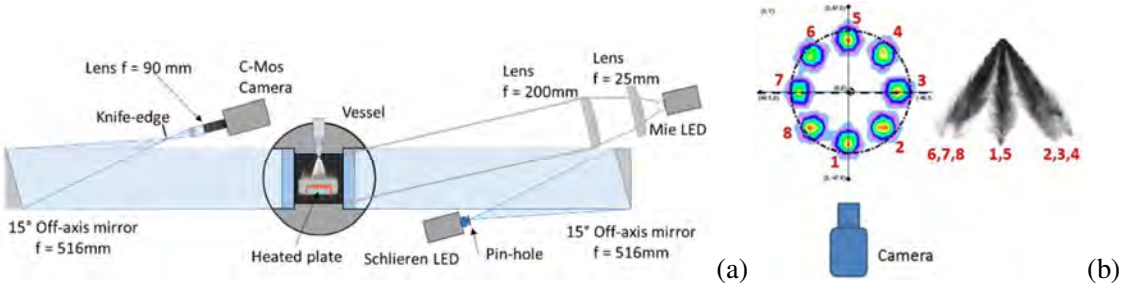

FIGURE 1. Optical setup: (a) spray orientation with respect to the camera positioning; (b) jet position and whole spray image.

3. NUMERICAL MODEL

The 3D sub-model able to simulate the dynamics of the gasoline spray issuing from the considered injector was developed in the context of the software AVL Fire™ [4], in such a way to simulate the performed experiments. The followed approach is the classical coupling between the Eulerian description of the gaseous phase and the Lagrangian description of the liquid phase. The governing equations are here not reported for the sake of brevity; the interested reader may refer to the book by Ramos ref. [5]. Details about the model and its application to different GDI injectors under various injection pressures are reported in ref. [6].

The results of the comparison between the 3D numerical simulation and the experimental campaign relevant to the spray before impact are summarized in figure 2, where the penetration lengths as measured on jet # 1 and on the corresponding calculated jet are reported as a function of time starting form the time of SOI (start of injection). The computational mesh for the spray validation is

a cylinder whose diameter and height are 100x100 mm; the total number of cells is 720000. If the injection pressure is 20.0 MPa in a vessel under standard air conditions, the free spray dynamics of a heated fuel at 363 K seems well reproduced by the 3D CFD tool.

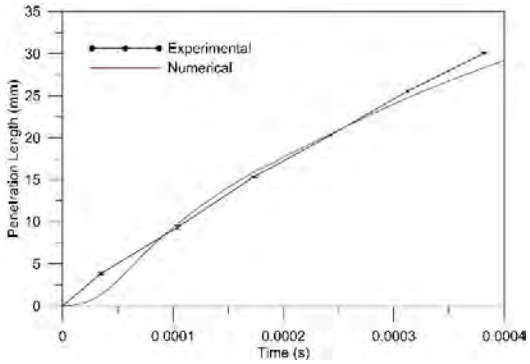

FIGURE 2. Comparison between calculated and measured penetration length of the ECN "Spray G"

4. RESULTS

The detailed information of a spray impact over a heated thin wall distant 19.5 mm from the injector is obtained thanks to the experimental setup based on the combined optical techniques of schlieren and Mie-scattering are reported in figure 3, together with the numerical simulation reproduced in the same operative conditions. Now the computational grid considered is a cylinder of diameter and height of 80x20 mm respectively, in which a wall condition is imposed on the side opposite to the injector location in order to simulate the presence of the thin wall. The injection pressure is still 20.0 MPa of a heated fuel at 363 K, in ambient and wall temperature fixed at 373 K.

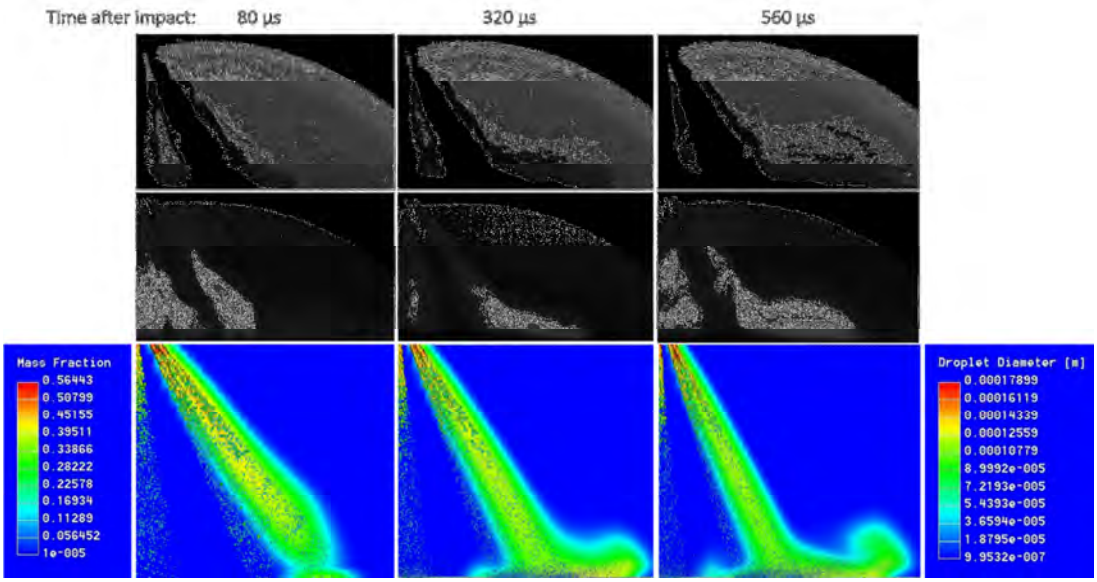

FIGURE 3. Schlieren (top), Mie-scattering (middle) and computed (bottom) spray images for different times after the impact. The computed fuel mass fraction is on a plane cutting the spray axis.

The spray behavior is quite well reproduced in terms of droplet impingement, although the numerical results show an underestimation of the vapor diffusion in terms of thickness, possibly related to a spray impingement model not correctly reproducing the actual droplet outcome after

impact. Indeed, figure 4 gives a quantitative measure of the error between the numerical and experimental results in terms of vapor thickness and radial width from the spray axis. Per each experimental image, the distance of the farthest point of the rebound fuel from the injector axis (equivalent to the intersection of the spray-axis #1 with the wall) in radial direction is considered as width value, while the highest one with respect to the plate is considered as thickness for both the liquid and vapor phases. The numerical data are taken by the same procedure on the contour of the isosurfaces of fuel mass fractions. In particular, the most external value of 10^{-5} has been considered as indicative of the limit between ambient air and evaporated fuel vapour.

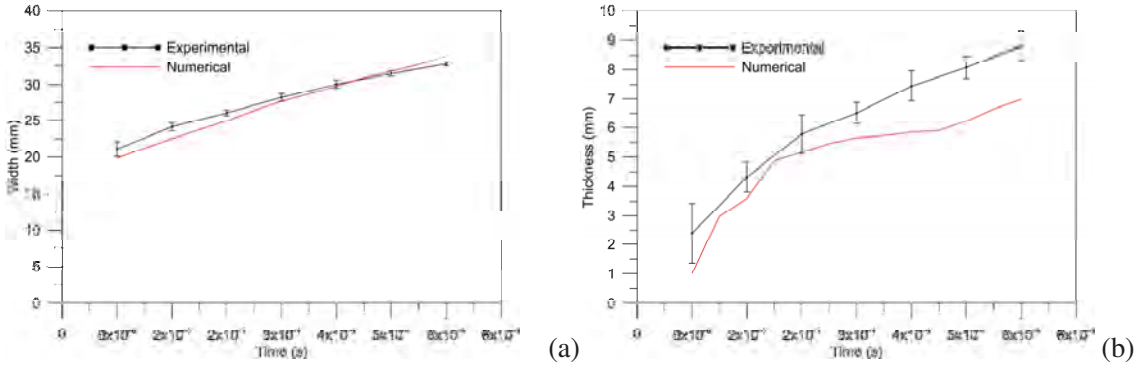

FIGURE 4. Experimental and numerical spray measurements of spray width (a) and thickness (b)

5. CONCLUSIONS

Present work considers the impact of a multi-hole spray over a hot wall. The experimentally collected data of the droplet behavior before and after impact resulting from the coupling between two optical techniques are compared with numerical simulations performed through a properly developed 3D CFD model of the spray dynamics. The main aim of the work is the validation of a predictive numerical model suitable of being included within simulations of entire engine working cycles.

An underestimation of the vapor diffusion is noticed in still air conditions, that could be reduced by properly acting on the details of the submodel for the spray impact and rebound. In any case, the vapor diffusion under actual engine operation is surely intensified, due to the charge motion and the high level of turbulence intensity characterizing the in-cylinder processes of real engines.

REFERENCES

[1] F. Zhao, D.L. Harrington, M.C. Lai, Automotive Gasoline Direct-Injection Engines, *SAE International Book Publication*, Warrendale, pp. 195-222, 2002.

[2] A.C. Alkidas, Combustion Advancements in Gasoline Engines, *Energy Conversion and Management,* 48: 2751-2761, 2007.

[3] L. Allocca, A. Montanaro, R. Di Gioia, G. Bonandrini, Spray Characterization of a Single-Hole Gasoline Injector under Flash Boiling Conditions, *SAE Technical Paper 2014-32-0041*, doi:10.4271/2014-32-0041, 2014.

[4] https://www.avl.com/web/ast/fire

[5] J. I. Ramos, Internal Combustion Engine Modelling, *Hemisphere Publishing Corporation*, New York, 1989.

[6] L. Allocca, M. Costa, U. Sorge, CFD optimization for GDI spray model tuning and enhancement of engine performance, *Advances in Engineering Software* 49:43-53, 2012.

Fourth International Conference on Computational Methods for Thermal Problems
THERMACOMP2016, July 6-8, 2016, Georgia Tech, Atlanta, USA
N. Massarotti, P. Nithiarasu and Y. Joshi (Eds.)

Numerical and experimental comparison of velocity derived quantities in rectangular cavity flows

F. Iannetta*, A. Sciacchitano, F. Arpino*, F. Scarano****
* Department of Civil and Mechanical Engineering, Università degli Studi di Cassino e del Lazio Meridionale, via G. Di Biasio 43, Cassino, Italy – f.iannetta@unicas.it, f.arpino@unicas.it

** Faculty of Aerospace Engineering, Department of Aerodynamics, Delft University of Technology, Kluyverweg 1, 2629 HS Delft, Netherlands – A.Sciacchitano@tudelft.nl, F.Scarano@tudelft.nl

ABSTRACT

This work proposes a comparison between numerical and experimental velocity derived quantities in rectangular cavity flows. Two and three dimensional particle image velocimetry (PIV) measurements are conducted at Reynolds numbers between 6,500 and 19,500 over rectangular cavities of different aspect ratios. Experiments are compared with results from Computational Fluid Dynamics (CFD) simulations performed employing different turbulence modeling approach: Reynolds Averaged Navier Stokes (RANS), Detached Eddy Simulation (DES) and Large Eddy Simulation (LES). A dedicated uncertainty analysis of the PIV data is conducted for a conclusive validation of the turbulence models employed in the CFD simulations.

Key Words: *PIV, CFD validation, turbulence model, measurement uncertainty, cavity flow.*

1. INTRODUCTION

Particle Image Velocimetry (PIV) has become the preferred technique for aerodynamic investigation and validation of Computational Fluid Dynamics (CFD) results, given its known advantages (non-intrusive, quantitative, full-field). In PIV, small tracer particles are inserted in the flow and carried by the fluid. A laser illuminates the particles twice within a thin light sheet, which defines the measurement domain. The light scattered by the particles is captured by a digital camera. The displacement of the particle images is measured with spatial cross-correlation analysis, returning the flow velocity once divided by the time separation between the two exposures. CFD simulations are a very powerful tool for predicting the behavior of turbulent flows [1]. Due to their versatility and the low cost, they are routinely used for engineering analysis and design ranging from the aerospace to the chemical and biomedical sectors [2], [3]. CFD simulations often require validation by experiments, in particular to assess the validity and accuracy of the assumptions made in the turbulence models [4], [5]. The aim of the present work is to perform a tailored experiment with the purpose of validating computer simulations of the turbulent flow over rectangular cavities with various aspect ratios. Since the first study of Rossiter [6] on rectangular cavity flow by wind tunnel measurements, several researchers have investigated such geometry due to the many applications in aerospace and civil engineering [7]. Recently, Atvars et al. [8] studied the problem in the transonic flow regime by PIV. The same authors also conducted CFD simulations with unsteady RANS, with a k-ε turbulence model. The CFD results could not capture the unsteady characteristics of the flow field, in particular pressure fluctuations and Rossiter's modes.

A meaningful validation of CFD results with PIV data requires a careful estimate of the measurement uncertainty, which is not often considered. Sciacchitano et al. [9] have recently introduced an a-posteriori approach for uncertainty quantification of PIV data. Wieneke and Sciacchitano [10] have further discussed the propagation of the baseline uncertainty from

instantaneous velocity to derived quantities of interest (e.g. turbulence kinetic energy, TKE). the present work, PIV measurements corroborated with uncertainty quantification are collected, to evaluate the adequacy and accuracy of RANS and DES simulations on cavity flows.

2. METHODOLOGY

The experiments are performed at the Aerodynamic Laboratories of TU Delft in the M-tunnel, an open-circuit, open-test-section wind tunnel with cross section of 40×40 cm2 and maximum velocity of 35 m/s. A wooden flat plate-cavity model spans the entire test section. The cavity height is H = 2 cm and several lengths are considered: W = {8, 16, 24} cm. In the abstract, results from W = 24 cm are presented. The resulting length-to-depth aspect ratio is W/H=12. A sketch of the model geometry is shown in figure 1. The measurements are conducted at three different values of the free-stream velocity: u_∞= {5, 10, 15} m/s, which correspond to Reynolds numbers ReH = 6,500, 13,500 and 19,500, respectively. The static air temperature is monitored with an RTD sensor and is kept constant at T=21°C.

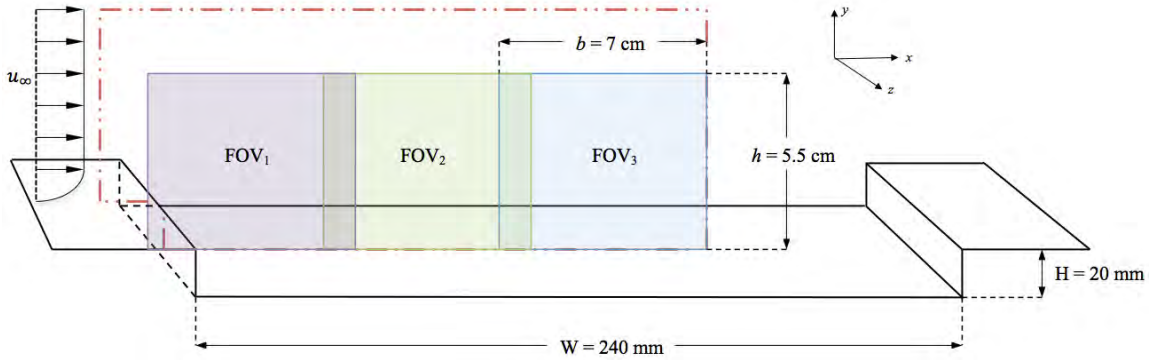

FIGURE 1. Schematic representation of the model geometry and the measurement domain.

A SAFEX seeding generator is used to produce water-glycol droplets of 1 μm median diameter. Planar two-components (2C), stereoscopic and tomographic PIV measurements are conducted. For the 2C, three *LaVision Imager LX 2MP* interline CCD cameras (1628 × 1236 pixels, pixel pitch of 4.4 μm) are equipped with 75 mm focal length objectives. Each field of view (FOV) is approximately 7 × 5.5 cm^2 with a digital imaging resolution of 21.3 px/mm. The three cameras yield a total FOV of approximately 18 × 5.5 cm^2 (figure 2). The lens aperture is set to f#=3.9. Measurements are conducted in the centerline plane. The illumination is provided by an Nd:YAG laser (Quantel *EverGreen,* 200 mJ/pulse at 15 Hz). The time interval between pulses is set to achieve a particle image displacement of roughly 20 pixels in the free-stream region and is equal to Δt={135, 70, 45} μs depending upon the free stream velocity. Sets of 500 uncorrelated image pairs are acquired at frequency of 8.3 Hz. System synchronization and image acquisition are controlled with an acquisition computer via a PTU9 timing unit and LaVision Davis 8.1.2 software. The CFD simulations are conducted employing RANS, DES and LES methods. The comparison will focus upon the uncertainty of the results arising from variations of the boundary conditions estimated from the PIV uncertainty analysis. The work will discuss in details the distinct role played by the different CFD methods (including turbulence modeling) and that of the mismatch between the experimental conditions and those applied in the numerical simulations.

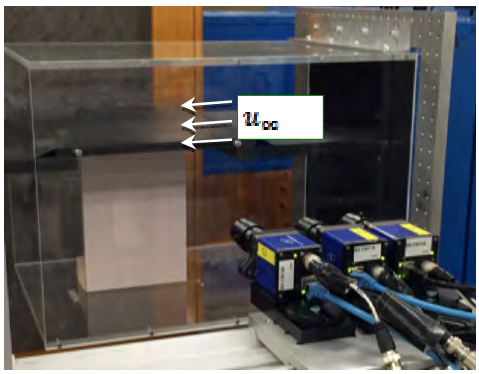

FIGURE 2. Experimental arrangement for planar PIV measurements (cameras position).

3. RESULTS

Figure 3-top left shows the time-averaged velocity field for the free-stream velocity u_∞ =10 m/s. After separation from the cavity edge (x = 0 mm, y = 20 mm), a shear layer is formed that generates a large recirculation region centered at x/H = 3 (x = 60 mm).

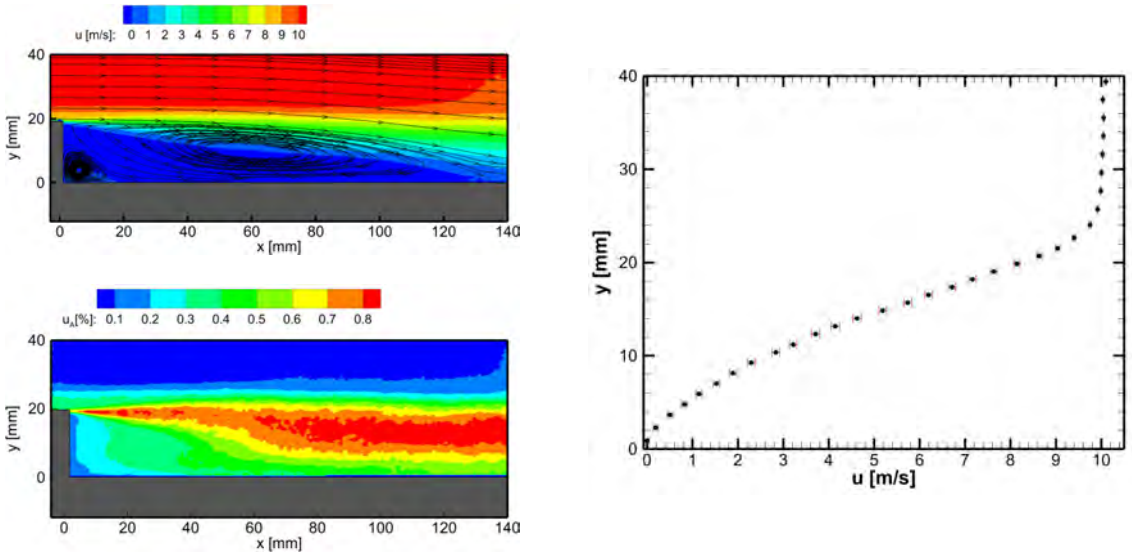

FIGURE 3. Measured mean velocity field with streamlines for u_∞ =10 m/s (top left), flow is from left to right; uncertainty contours in the mean velocity field (bottom left).Velocity profile of the x-component over the reattachment point inside the cavity (right).

The flow reattaches at x=130 mm (x/H = 6.5). A second small recirculation region, counter-rotating with respect to the main one, is found in the immediate vicinity of the cavity wall (x ~ 5 mm). The results agree well with those reported in literature [11]. Figure 3-right illustrates the time-averaged velocity profile at the flow reattachment location. Uncertainty bars at 68% confidence level are computed from the standard deviation of the streamwise velocity as discussed in [10]. The type A

measurement uncertainty is about 0.06 % in the free-stream region, while it increases up to 0.57 % close to the wall.

4. CONCLUSIONS

The present study proposes a comparison between experimental and numerical results on a cavity flow. Some preliminary results of the velocity field in a closed rectangular cavity by planar PIV have been shown. The goal of the work is to build a comprehensive benchmark for the validation of CFD codes. Stereoscopic and tomographic PIV measurements will be presented, along with the uncertainty of velocity and derived quantities, to allow a comparison with CFD simulations for validation of the numerical results.

REFERENCES

[1] B. Ma, V. Ruwet, P. Corieri, R, Theunissen, M. Riethmuller, C. Darquenne, CFD simulation and experimental validation of fluid flow particle transport in a model of alveolated airways, *Journal of Aerosol Science*, 40 (5):403 – 141, 2010.

[2] J. Sheng, H. Meng, R. Fox,Validation of CFD simulations of a stirred tank using particle image velocimetry data, *Canadian Journal of Chemical Engineering*, 76 (3):611 – 625, 1998.

[3] F. Arpino, G. Cortellessa, A. Mauro, Transient thermal analysis of natural convection in porous and partially porous cavities, *Numerical Heat Transfer; Part A: Applications*, Volume 67, Issue 6, 19, Pages 605-631, 2015.

[4] M. D. Ford, PIV – measured versus CFD – predicted flow dynamics in anatomically realistic cerebral aneurysm models, *Journal of Biomechanical Engineering*, 130 (2): 021015, 2008.

[5] M. Scungio, F. Arpino, G. Cortellessa, G. Buonanno, Detached eddy simulation of turbulent flow in isolated street canyons of different aspect ratios, *Atmospheric Pollution Research*, Volume 6, Issue 2, Pages 351-364, 2015.

[6] J. E. Rossiter, Wind – Tunnel experiments on the flow over rectangular cavities at subsonic and transonic speeds, technical report no.ARC R&M 3438, Aeronautical Research Council, UK, 1964.

[7] C. Heigermoser, F. Scarano. M. Onorato, Investigation of the flow in a rectangular cavity using tomographic and time – resolved PIV, *26th International Congress of the Aeronautical Sciences,* 2008.

[8] K. Atvars, K. Knowles, S.A. Ritchie, N.J. Lawson, Experimental and computational investigation of an 'open' transonic cavity flow, *3rd International Symposium on Integrating CFD and experiments in Aerodynamics*, 2007.

[9] A. Sciacchitano, B. Wieneke, F. Scarano, PIV uncertainty quantification by image matching, *Measurements Science and Technology*, 24, 2013.

[10] A. Sciacchitano, B. Wieneke, PIV uncertainty propagation, *11th International Symposium on Particle Image Velocimetry – PIV15*, 2015.

[11] S.D. Hall, T.J. Barber, A detailed CFD and experimental investigation of a benchmark turbulent backward facing step flow, *Integrating CFD and Experiments*, pp. 1 - 12, 2003.

Fourth International Conference on Computational Methods for Thermal Problems
THERMACOMP2016, July 6-8, 2016, Georgia Tech, Atlanta, USA
N. Massarotti, P. Nithiarasu and Y. Joshi (Eds.)

NUMERICAL AND EXPERIMENTAL INVESTIGATION OF THE PERFORMANCE OF A CAR PROTOTYPE FOR THE SHELL ECO MARATHON

M. Scungio*, F. Arpino, F. Iannetta, A. Frattolillo, G. Cortellessa, L. Fuoco
Department of Civil and Mechanical Engineering, University of Cassino and Southern Lazio, via G. di Biasio 43, 03043 Cassino (FR), Italy,
*m.scungio@unicas.it

ABSTRACT

The *Eco-Marathon* is a challenge organized by Shell in which student teams from around the world compete in designing and building of energy-efficient vehicles. The events spark debate about the future of mobility and inspire young engineers to push the boundaries of fuel efficiency. The aim of the present work consists of the numerical and experimental investigation of the aerodynamic performance of a *Shell Eco Marathon* prototype designed by a group of students of the University of Cassino, Italy. The car design has been carried on by means of detailed 3D CFD modelling with a commercial code Comsol Multiphysics®. The numerical tool has been validated against experiments conducted at the Laboratory of Industrial Measurements (LaMI) of the University of Cassino. In particular, a scale model of the car has been investigated in an open chamber wind tunnel by means of the *Particle Image Velocimetry* (PIV) technique, for different free stream velocities within the range 11 – 23 m/s. Measurements have been associated to a proper uncertainty analysis. The experimental data has been compared to numerical results obtained employing different turbulence models and the validated numerical tool has been applied to the simulation of the full scale car model, allowing to analyse the wake flow structures, and evaluate the overall drag coefficient.

Key Words: *drag coefficient, wind tunnel, particle image velocimetry, numerical simulation, wake flow.*

1. INTRODUCTION

In the light of energy efficiency and fuel saving objectives, aerodynamic forces and moments analysis of road vehicles are of great interest for the decrease of aerodynamic resistance, and in particular for the drag force. The major contribution to aerodynamic drag arises from shape (or pressure) drag [1]. In the automotive industry, a survey of the scientific literature shows that even though in the last years the scientific research allowed a decrease of the drag force for commercial vehicles of almost 33%, a further improvement results to be challenging [2], [3]. The major contribution to a car's drag is due to the wake flow behind the vehicle. The location at which the flow separates determines the size of the separation zone, and consequently the drag force [4]. Other studies found that almost 85% of body drag is due to pressure drag, and most of this drag is generated at the rear end of the model [5]. The aim of the present work consists of the numerical and experimental investigation of the aerodynamic performance of a Shell Eco Marathon prototype: averaged velocity field measurements have been conducted on a 1:18 scaled model at the Laboratory of Industrial Measurements (LAMI) of the University of Cassino, employing an open chamber wind tunnel and the Particle Image Velocimetry (PIV) technique. Besides experiments, 3D numerical simulations have been performed and numerical results were validated against experiments. The validated numerical model was then applied to the prediction of aerodynamic performance of the full scale model and represents a useful tool for future optimization of the prototype shape aimed at further improvement of energetic efficiency.

2. METHODS

The velocity field around the car prototype was characterized by means of wind tunnel and PIV measurement equipment available at the LaMI. A sketch of the measurement domain adopted for the PIV measurements in the wind tunnel, the computational domain and a detail of the adopted mesh is reported in Figure 1.

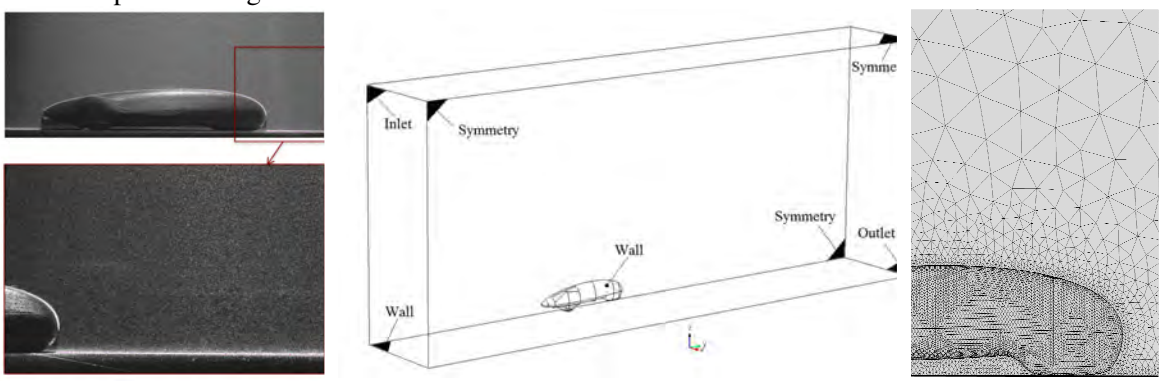

FIGURE 1. PIV measurement domain, computational domain and detail of the numerical grid adopted for the wake flow analysis.

At the inlet, the y-component of the velocity was imposed, reproducing the same velocity profile as obtained from the PIV measurements (17 m/s in the free stream). Zero pressure condition was imposed at the exit, while on the base of the domain and on the model surface, a wall boundary condition was imposed. Finally, a symmetry condition was imposed an all the other sides. The whole computational domain has the dimensions of 500 mm of height (z-axis), 900 mm of depth (y-axis) and 200 mm of width (x-axis). The car model has a length of 15 mm (L) and is positioned at a distance of 300 mm from the inlet. The maximum computational grid size in the free stream is equal to 20 mm. A grid refinement was made on the Nebula model surface and on the base of the domain (wall), using a minimum grid size of 1 mm with a growth rate of 1.3. The resulting unstructured computational grid is composed of about 3.8 million of tetrahedral elements. A grid sensitivity analysis was made, and a maximum error between two consecutive meshes was maintained under 5%.

3. RESULTS

In Figure 2 are reported the results in terms of profiles of the horizontal and vertical components of the velocity, obtained with the k-ε and k-ω RANS models, evaluated on the symmetry plane of the computational domain. On the same figure, a comparisons with data obtained from PIV analysis are reported in order to evaluate which turbulence model shows the better performance on reproducing the experimental velocity profiles. From an overall overview of the Figure 2, it could be concluded that even if the two turbulence models adopted show comparable performance, the k-ε model results more suitable in reproducing the recirculation pattern of the wake flow in terms of horizontal component of the velocity. Once analysed the performance of the turbulence models, and verified the overall better performance of the k-ε model by comparing numerical results with PIV measurements in wind tunnel, a simulation of the full scale Nebula car prototype moving at 50 km/h has been realised in order to analyse the wake flow characteristics and to evaluate the drag coefficient of the car. In Table 1 are reported the values of viscous and pressure forces acting on the vehicle surface in the y-direction, calculated post processing the data obtained from numerical simulation of the 1:1 car model dimensions. As can be seen, the greatest contribution to the drag force is due to the pressure force which has values higher than viscous component. The force acting on the bottom of the car surface (-1.42 N) results greater than that acting on the top (-0.778 N). The total force on the y-direction, including viscous and pressure components, results equal to 2.198 N

at 50 km/h. By calculating the reference front vehicle surface, A, from geometrical data equal to 0.297 m^2, the drag coefficient of the Nebula prototype under examination, C_d, results equal to 0.0658.

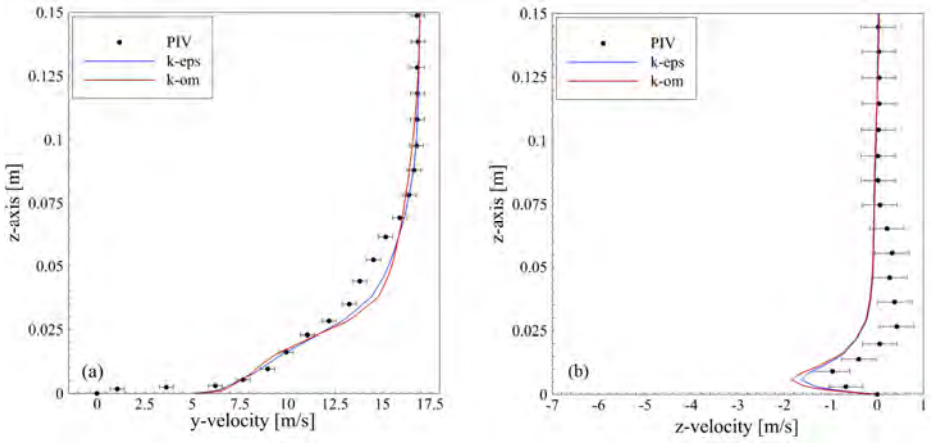

FIGURE 2. Profiles of vertical and horizontal components of the velocity on the symmetry plane at 17m/s: horizontal component at L+45 mm (a) and vertical component at L+45 mm (b).

	Front-top	Front-bottom	Back-top	Back-bottom	Total
Viscous force (N)	-0.129	-0.110	-0.079	-0.051	-0.369
Pressure force (N)	0.218	-0.641	-0.788	-0.618	-1.829
Total force (N)	0.089	-0.751	-0.867	-0.669	-2.198

TABLE 1. Viscous and pressure forces acting on the vehicle surface in the y-direction, calculated post processing the numerical data for different zones of the car model.

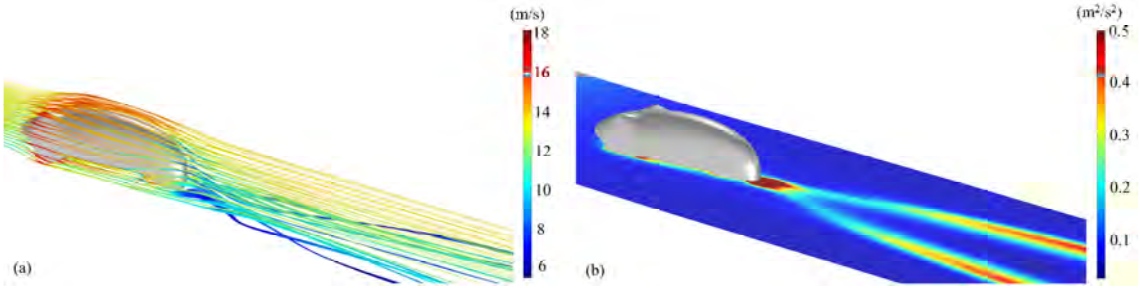

FIGURE 3. 3D streamlines (a), and turbulent kinetic energy on the x-y plane, plotted at 12 cm from the base of the computational domain (b). The streamline colour is related to the velocity magnitude and their thickness is proportional to the turbulent kinetic energy.

In Figure 3 are reported the streamlines of the wake flow behind the Nebula prototype: the streamlines colour is related to the velocity magnitude while their thickness is proportional to the turbulent kinetic energy. The zone corresponding to the base of the wake flow is characterized with thick streamlines, which means high turbulent kinetic energy, but low velocity magnitude. The same behaviour of low velocity magnitude and high turbulent kinetic energy could be observed at the wake flow behind the front wheels. With the aim of Figure 4, which reports the velocity and pressure fields on the symmetry plane, it could be explained the vortex generation mechanism at the back of the car, as the interaction of three behaviour: a high speed stream along the side walls of the car; a slow speed zone at the back, and a main flow along the top of the vehicle. The vortex structures in the wake flow is originated when the high speed flow moving on the side wall of the car enters in the slow speed zone at the back. At this point the interaction with the main flow gives a twirling motion to the mixed stream, changing its direction, and creating the longitudinal vortices.

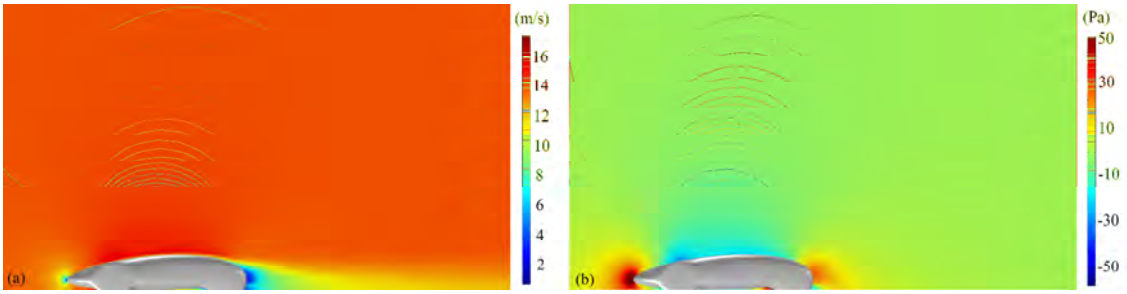

FIGURE 4. Velocity magnitude (a) and pressure field (b) around the Nebula model on the symmetry plane for the full scale simulation.

4. CONCLUSIONS

In the present paper, numerical simulations of the wake flow behind a Shell Eco Marathon vehicle prototype, called Nebula, were carried out using RANS turbulence model and the commercial CFD software Comsol Multiphysics. In order to verify the suitability of the numerical model, results from k-ε and k-ω turbulence models simulations, in terms of horizontal and vertical components of the velocity, were compared with experimental data from wind tunnel investigation made out with Particle Image Velocimetry (PIV) technique. In order to experimentally analyse the wake flow characteristics with PIV method, a scale model of the Nebula prototype was realised by means of 3D printer, working on a fused deposition modelling (FDM) principle. The printed model was adequately studied in a closed circuit wind tunnel facility available in the Laboratory of Industrial Measurement (LaMI) of the University of Cassino and Lazio Meridionale. Once verified which turbulence model were more suitable for the reproduction of the flow around the Nebula prototype, a 1:1 scale simulation was carried out in order to study the wake flow characteristics and evaluate its drag coefficient. From the numerical analysis, it was found that the most suitable RANS turbulence model for the simulation of the wake flow of the Nebula car is the standard k-ε model, which is able to correctly reproduce the horizontal velocity component of the wake flow, even if a little discrepancy with experimental data could be observed with the vertical velocity component.
A very low value of the drag coefficient, C_d, of the prototype under investigation was found, and equal to 0.0658. It was also found that the total force acting on the bottom of the car surface (-1.42 N) results greater than that acting on the top (-0.778 N), due to the formation of two recirculation vortices in the car wake flow, while the flow on the upper surface results almost completely attached. From the numerical simulation, it was found an overall good performance of the Nebula prototype in terms of aerodynamic efficiency, finding a very low air resistance, comparable with other concept/experimental cars.

REFERENCES

[1] Aljure, D. E., O. Lehmkuhl, et al. (2014). "Flow and turbulent structures around simplified car models." *Computers and Fluids* 96: 122-135.

[2] Brulle, R. V. (1977). "Feasibility investigation of the giromill for generation of electrical power. Technical discussion, vol. II." *Energy Research and Development Administration*; COO/2617-76/1/2.

[3] Lazar, E., B. DeBlauw, et al. (2010). "A practical approach to PIV uncertainty analysis". *27th AIAA Aerodynamic Measurement Technology and Ground Testing Conference*, 2010.

[4] Nishio, S. (2008). "Uncertainty analysis: Particle imaging velocimetry (PIV)." *International Towing Tank Conference*, Section 7.5-01-03-03.

[5] Stanislas, M. and J. C. Monnier (1997). "Practical aspects of image recording in particle image velocimetry." *Measurement Science and Technology* 8(12): 1417-1426.

Fourth International Conference on Computational Methods for Thermal Problems
THERMACOMP2016, July 6-8, 2016, Georgia Tech, Atlanta, USA
N. Massarotti, P. Nithiarasu and Y. Joshi (Eds.)

VALIDATION OF THERMAL MODELS OF SINGLE PHASE THERMAL MANAGEMENT FLOW LOOPS

Mark S. Spector
ONR

Yogendra Joshi
Georgia Institute of Technology

John Doty
University of Dayton

Bart Eussen
National Aerospace Laboratory, NL

Martin Cerza
US Naval Academy

Consideration of thermal management for current military platforms typically occurs late in the development cycle and is based on unvalidated component and subsystem models. Often, thermal control problems surface only after a new technology has been designed and implemented. These problems can force restrictions on the platform's operational capabilities, and they can result in an inefficient allocation of resources. In order to address these issues, the NATO Science and Technology Organization (STO) created a technical team 'Validation of Thermal Models for Air, Land, Sea and Space Vehicles' to assess thermal model validation methodologies in order to strengthen design practices for future military platforms. This team has designed and fabricated a common test bed which is being circulated among national laboratories for experimental characterization. The test bed (Fig. 1) is a single-phase fluid loop that represents a common design of power amplifier liquid cold plates. Various thermal models of the test bed are being formulated. Comparison between models and measured performance will lead to improved understanding and quantification of uncertainty as it influences the validation process. A statistically-based uncertainty quantification (UQ), sensitivity analysis (SA), and uncertainty propagation (UP) process has been developed to support model-based verification and validation (V&V) for thermal systems. This paper will present initial results of this process and discuss opportunities for further engagement with the thermal engineering community.

For the selected testbed, steady heat transfer rate is the major quantity of interest. In Fig. 1, we have three areas in the test rig where heat transfer rate may be determined based upon experimental measurements. These are:

1) Heat transfer rate from the heater power input to the cold plate and then to the flow loop ($\dot{Q}_{cold\ plate \rightarrow flow}$). This heat transfer rate occurs in device 'B' Cold Plate. The directionality for $\dot{Q}_{cold\ plate \rightarrow flow}$ is typically from the heater elements to the cold plate and is therefore assumed to be heat transfer in to the system with an assumed positive sign.

2) Heat transfer rate from the flow loop to the air heat exchanger ($\dot{Q}_{flow \rightarrow Air\ HX}$). This heat transfer rate occurs in device 'C' Air Heat Exchanger. The directionality for $\dot{Q}_{flow \rightarrow Air\ HX}$ is typically from the flow loop to the ambient and is therefore assumed to be heat transfer out of the flow system with an assumed negative sign. Note: if the ambient temperature is higher than the flow loop temperature, the heat transfer rate will be *into* the flow system.

3) Heat transfer rate from the flow loop to the braised heat exchanger ($\dot{Q}_{flow \rightarrow braised\ HX}$). This heat transfer rate occurs in device 'D' Braised Heat Exchanger. The directionality for $\dot{Q}_{flow \rightarrow braised\ HX}$ is typically from the flow loop to the braised heat exchanger fluid and is therefore assumed to be heat transfer out of the flow system with an assumed negative sign.

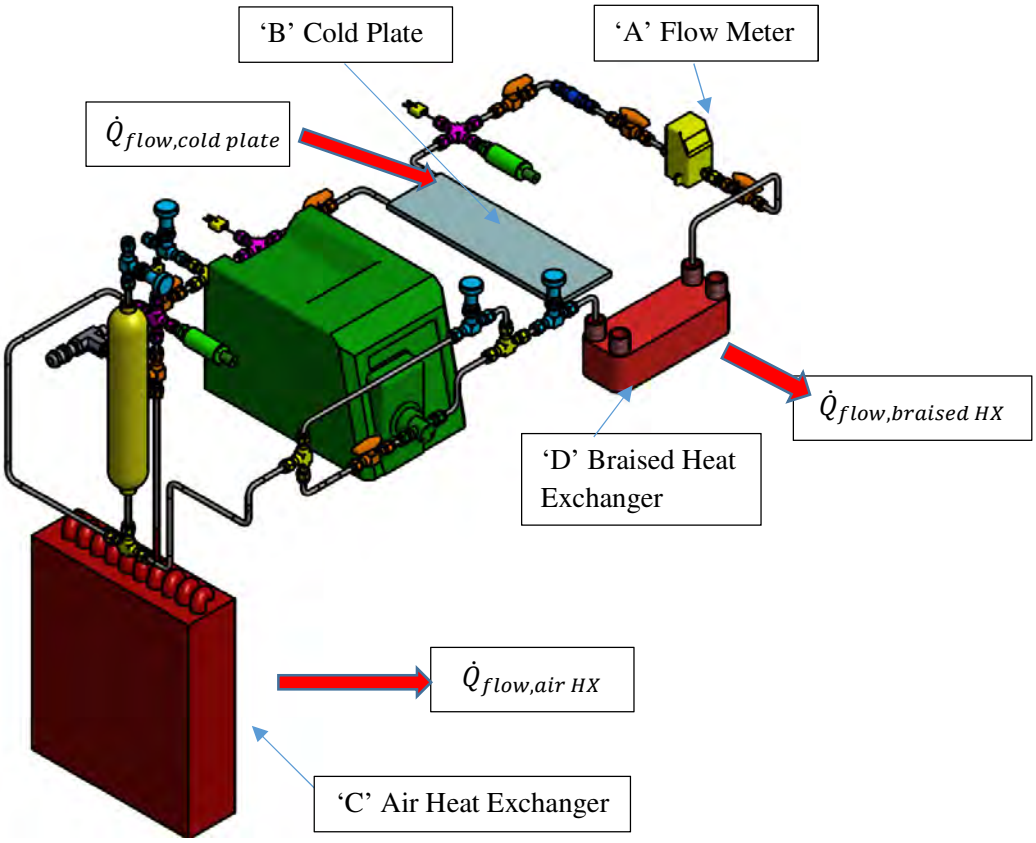

Figure **Errore. Nel documento non esiste testo dello stile specificato.**: CAD drawing of testbed with flow loop heat transfer locations.

As an example of how to perform a pre-planning estimate of the trends and magnitudes of uncertainties over a desired test range, we use the heat transfer rate for the cold plate to the flow loop as given by:

$$\dot{Q}_{cold\ plate \rightarrow flow} = \rho_{flow}\ \dot{\mathcal{V}}_{flow} C_{p,flow}\left(T_{flow,2} - T_{flow,3}\right) \quad (1)$$

where

ρ_{flow} density of the working fluid evaluated at the average temperature $1/2(T_{flow,2} + T_{flow,3})$,

$\dot{\mathcal{V}}_{flow}$ volumetric flow rate of the working fluid, and

$C_{p,flow}$ specific heat at constant pressure of the working fluid, also evaluated at the average temperature $(T_{flow,2} + T_{flow,3})/2$.

and $T_{flow,2}$ and $T_{flow,3}$ are the mean fluid temperatures measured at the exit and inlet of the cold plate, respectively. In order to understand how uncertainties in the quantities on the right-hand side of Equation (1) propagate to the quantity of interest ($\dot{Q}_{cold\ plate \rightarrow flow}$) on the left-hand side, we need to understand the uncertainties present in the terms on the right-hand side. We first isolate the uncertainties using the product rule of normalized uncertainties applied to Equation (1):

$$\left(\frac{U_{\dot{Q}_{cold\ plate \rightarrow flow}}}{\dot{Q}_{cold\ plate \rightarrow flow}}\right)^2 = \left(\frac{U_{\rho_{flow}}}{\rho_{flow}}\right)^2 + \left(\frac{U_{\dot{\mathcal{V}}_{flow}}}{\dot{\mathcal{V}}_{flow}}\right)^2 + \left(\frac{U_{C_{p,flow}}}{C_{p,flow}}\right)^2 + \left(\frac{U_{\Delta T_{flow,2 \rightarrow flow,3}}}{\Delta T_{flow,2 \rightarrow flow,3}}\right)^2 \quad (2)$$

where

$U_{\dot{Q}_{cold\ plate \rightarrow flow}}$ uncertainty in heat transfer rate from cold plate to the flow loop,

$U_{\rho_{flow}}$ uncertainty in the density of the working fluid,

$U_{\dot{\mathcal{V}}_{flow}}$ uncertainty in the volumetric flow rate,

$U_{C_{p,flow}}$ uncertainty in the specific heat of the working fluid, and

$U_{\Delta T_{flow,2 \rightarrow flow,3}}$ uncertainty in the temperature difference in the flow loop across the cold plate.

Equation (2) represents the propagated variance in heat transfer rate from cold plate to the flow loop.

Properties of the working fluid are typically estimable within +/- 1%. As we are uncertain of the magnitudes of the uncertainties for flow rate previously estimated we use two levels of uncertainty as $U_{\dot{\mathcal{V}}_{flow}}$=+/- 0.01 LPM and +/- 0.02 LPM. Similarly, we use two levels of uncertainty for temperature difference as $U_{\Delta T_{flow,2 \rightarrow flow,3}}$=+/- 0.1 C and +/- 0.2 C. We also investigate a flow rate range from 0.1 to 2.0 LPM and two temperature differences of 5 C and 75 C. This preliminary uncertainty analysis should cover the range of values and uncertainties potentially achieved in the experimental investigation phase.

The results of the uncertainty investigation illustrated in Figure 2 show that the sensitivity is largest at low flow rates, as indicated by the largest gradients in relative uncertainty below flow rates of approximately 0.5 LPM. This influence is indicated in the figure with annotation '1'. The largest influence of the flow rate upon the response is annotated '2' in the figure and occurs at the lowest flow rates. Fig. 2 also shows the influence of the *magnitude* of temperature difference (ΔT) upon the

response $\%\left(\frac{U_{\dot{Q}_{cold\ plate\rightarrow flow}}}{\dot{Q}_{cold\ plate\rightarrow flow}}\right)$ at two levels of ΔT. The first level, ΔT_1, has a magnitude equal to 5 C; and the second, ΔT_2, has a magnitude equal to 75 C. It is apparent that there is minimal influence of ΔT upon the response at low flow rates but a much larger influence at higher flow rates. This influence is indicated in the figure with annotation '3'.

Fig. 2 also shows two levels of $U_{\Delta T}$: the first, annotated as $U_{\Delta T_1}$, has a magnitude equal to 0.1 C; and the second, annotated as $U_{\Delta T_2}$, has a magnitude equal to 0.2 C. It is apparent that there is minimal influence of $U_{\Delta T}$ upon the response at low flow rates but a much larger influence at higher flow rates. Additionally, we note that there is a larger influence of $U_{\Delta T}$ upon the response at higher levels of temperature difference (ΔT). Lastly, we investigate the influence of uncertainty in flow rate ($U_{\dot{\forall}_{flow}}$) upon the response $\%\left(\frac{U_{\dot{Q}_{cold\ plate\rightarrow flow}}}{\dot{Q}_{cold\ plate\rightarrow flow}}\right)$ at two levels of $U_{\dot{\forall}_{flow}}$. The first level $U_{\dot{\forall}_{flow_1}}$ has a magnitude equal to 0.01 LPM, and the second level $U_{\dot{\forall}_{flow_2}}$ has a magnitude equal to 0.02 LPM. It is apparent that there is minimal influence of $U_{\dot{\forall}_{flow}}$ upon the response at low flow rates but a much larger influence at higher flow rates. This influence is indicated in the figure with annotation '3'. The largest influence of the $U_{\dot{\forall}_{flow}}$ upon the response is annotated as approximately 4%. In total, Fig. 2 suggests for purposes of validation, that the minimum flow rate be approximately 0.5 LPM, with the caution that the difference in uncertainties will be highest in this region but that the magnitudes of uncertainties will likely be smallest.

The paper will report on experimental heat transfer data guided by uncertainty analysis described above. The uncertainty analysis will be used to reconcile the differences between the simulations and measurements.

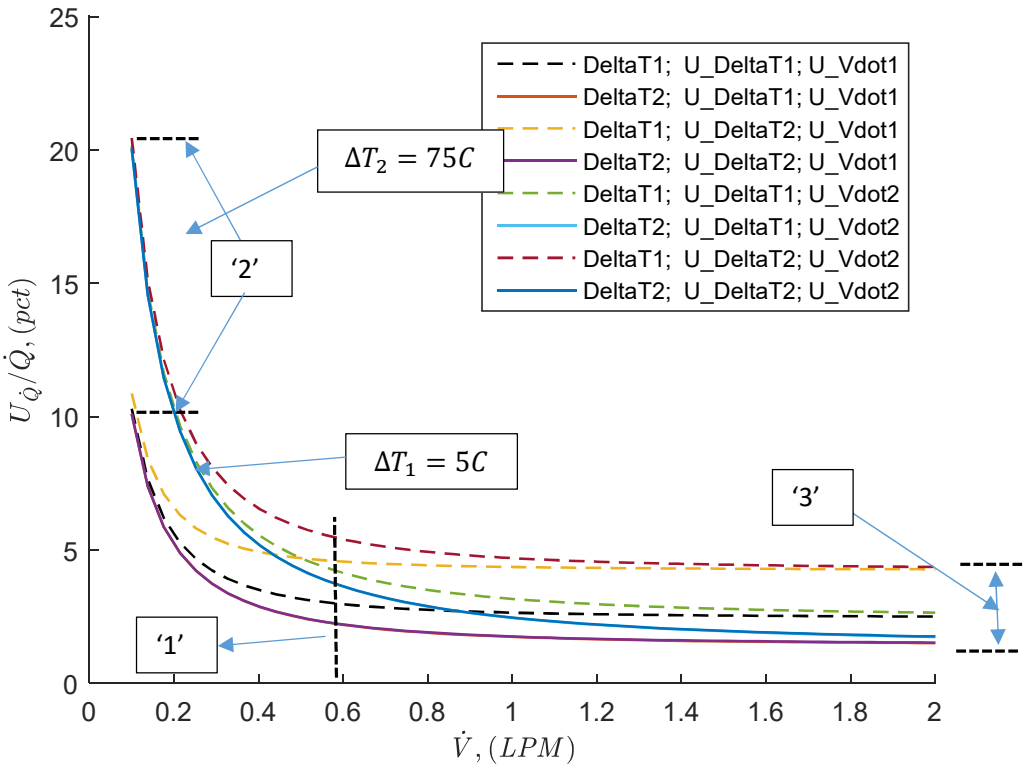

Figure 2: Propagated uncertainty for heat transfer rate from cold plate to the flow loop.

PARALLEL SESSIONS

PARALLEL SESSION

CONDUCTION, CONVECTION AND RADIATION

Fourth International Conference on Computational Methods for Thermal Problems
THERMACOMP2016, July 6-8, 2016, Georgia Tech, Atlanta, USA
N. Massarotti, P. Nithiarasu and Y. Joshi (Eds.)

OPERATING ROOMS: NUMERICAL MODELING OF HEAT AND MASS TRANSPORT PHENOMENA

Alberto Carotenuto[1], Nicola Massarotti[1], Alessandro Mauro[1, 2], Domenico Sainas[1]
[1]Dipartimento di Ingegneria, Università degli Studi di Napoli "Parthenope", Isola C4, Centro Direzionale di Napoli, 80143 Napoli, Italy

[2]Università Telematica Pegaso, Piazza Trieste e Trento n. 48, 80132 Napoli, Italy,

ABSTRACT

The operating room is the environment inside of hospitals that requires the greatest deal of attention in the choice of the devices for air supply, diffusion and recovery. The design of Heating Ventilation and Air Conditioning (HVAC) systems dedicated to these environments plays a crucial role, in order to drastically reduce the risk of infections for patients, in addition to the maintenance of adequate thermo-hygrometric comfort conditions for the medical team. The proper design of such systems must take into account air distribution and pollutants transport within the operating room. In the present work, the authors numerically simulate heat and fluid flow inside the room, and CO_2 distribution.

Key Words: ***Airflow, Operating Room, CO_2***

1. INTRODUCTION

The air quality in an operating room is one of the key factor for reducing the post-operative infection rates of surgical procedures. It has been reported that 80-90% of bacterial contamination observed in an open wound comes from the ambient air [1]. Therefore, a lower risk of sepsis has been reported thanks to a cleaner air injection in operating rooms. Several guidelines are available for a correct design of HVAC systems for operating rooms, depending on the country legislations. The Italian standard is provided by ISPESL guideline [2], which defines the security and hygiene environmental standard for operating rooms. This standard quotes other Italian regulations regarding fresh air supply in an operating room D.P.R. 14/01/97 [3] and the UNI EN ISO 14644-2: 2015 [4], which specifies the minimum requirements for a monitoring plan of cleanroom or clean zone performance related to air cleanliness by particle concentration. In USA, there is the ANSI/ASHARAE/ASHE Standard 170-2013 [5], which defines ventilation systems design requirements in order to provide environmental control for comfort and asepsis in health care facilities. The aim of the present work is to develop a numerical model able to reproduce the thermo-fluid dynamic phenomena and contaminant concentration inside operating rooms. The aim of this paper is to adapt the model proposed by Romano (2015) in order to analyse another parameter respect the particulate, namely the carbon dioxide concentration (CO_2) [6].

2. CASE STUDY

The geometry of the operating room considered as case study are reported in Figure 1. The net height of the room is 3.00 m. The operating room is provided with a unidirectional ceiling diffuser composed of 23 terminal HEPA H14 filters, installed in a plenum of 3.00m x 3.00m. The main characteristic of this ceiling filter system is the differentiation of the supply air velocity. The supply air at the ceiling filters has a temperature of 20°C and 50% relative humidity.

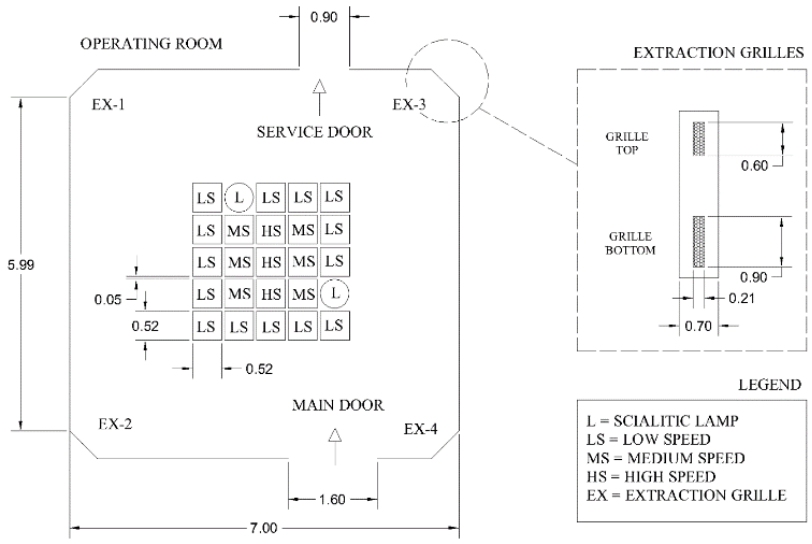

Figure 1. Isometric view of the operating room taken into account for the case study

3. GOVERNING EQUATIONS AND BOUNDARY CONDITIONS

The numerical model is based on the following partial differential equations:

Mass conservation equation $$\nabla \cdot (\boldsymbol{U}) = 0$$

Momentum conservation equation $$\rho \boldsymbol{U} \cdot \nabla(\boldsymbol{U}) = \mu \nabla^2 \boldsymbol{U} - \nabla \boldsymbol{p} + \boldsymbol{F}$$

Energy conservation equation $$\boldsymbol{U} \cdot \nabla \boldsymbol{T} = \frac{\lambda}{\rho \boldsymbol{c_p}} \nabla^2 \boldsymbol{T}$$

Species conservation equation $$\boldsymbol{U} \cdot \nabla(\boldsymbol{CO_2}) = \boldsymbol{D_{CO_2}} \nabla^2 \boldsymbol{CO_2}$$

Where ρ is the fluid density and $\boldsymbol{U}$ = (u, v, w) is the velocity vector. The authors consider a RANS approach for Newtonian fluid and incompressible flow, and employ a standard k-$\boldsymbol{\varepsilon}$ method to solve turbulence field. The values of CO_2 flux from nostrils of the medical staff and the patient are considered equal to 2.14 mol/m^{2}s and 0.32 mol/m^{2}s, respectively [7].

	Surface area (m^2)	Heat flux (W/m^2)	Fluid-dynamics boundary conditions (m/s)
Medical Staff (4 medical doctors)	2.26	44.2	U=0
Patient	1.51	66.3	U=0
Medical equipment	1.76	170	U=0

Operating table	1	-	U=0
Scialitic lamp	0.56x2	215x2	U=0
Air inlet – LS filter	0.27x14	-	U=0.25
Air inlet – MS filter	0.27x6	-	U=0.35
Air inlet – HS filter	0.27x3	-	U=0.45
Outlet air – Top extraction	0.13x4	-	P=0 Pa
Outlet air – Bottom extraction	0.19x4	-	P=0 Pa
OT floor	47.9	-	U=0

TABLE 1. Boundary conditions and parameters employed in the simulations.

4. RESULTS

Figure 2 (left) shows that the laminar flow diffusers with filtering ceiling above the surgical table provide unidirectional airflow by hindering air stagnation, thanks to the overpressure generated in the aseptic core. Furthermore, the differential velocity of the ceiling diffuser influences the airflow path behaviour around the surgical lamp and the operating table, and outside the critical zone. The differential air velocities imposed by the ceiling filters, with decreasing intensity from the center to the borders, allow the air released by the HS (High speed) filters to follow a preferential escape path towards the external surgical area, without being influenced by the airflow released by the outer filter MS (Medium Speed) and LS (Low Speed) filters.
Figure 2 (right) shows that the maximum CO_2 concentration is smaller than the limits imposed by the standards [8,9]. In particular, the larger concentration is present in the area near the surgical team. With the proposed numerical approach, it is possible to optimize the evacuation of CO_2 from the surgical table, for example working on the positioning of the scialitic lamps or of the inlet and outlet grilles.

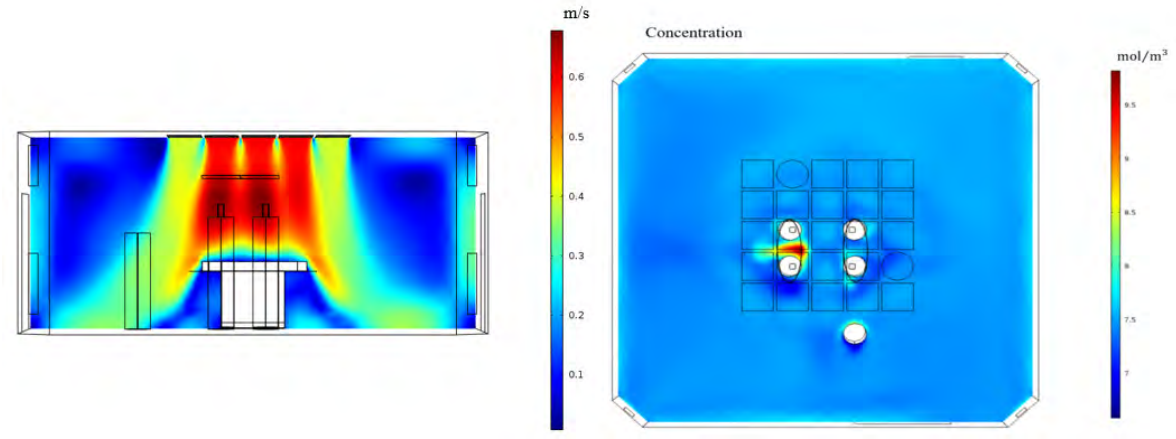

FIGURE 2. Velocity magnitude (left) and CO_2 concentration on a horizontal plane (right).

5. CONCLUSIONS

This work has proven that the numerical modelling approach can be successfully applied to the simulation of the real performance of an operating room in terms of air velocity, carbon dioxide concentration and temperature distributions. In particular, the authors have investigated the distribution of carbon dioxide (CO_2) emitted by medical staff and patient inside the operating room. The typical value of concentration of carbon dioxide in atmospheric air is 350 ppm [10]. Therefore, the effectiveness of a differential airflow diffusion system provides a reduction of the carbon dioxide concentration on the operating table and an improvement of air cleaning, so avoiding stagnation areas outside the aseptic area. Sure enough, the results have shown that the carbon dioxide concentration ranges between 418ppm at 1.4m from the floor and 968ppm at 1.7m from the floor. This results are compliant to guideline. Finally, has been obtained thanks to an overpressure generation in the aseptic area, as evidenced by results shown in figure 2.

REFERENCES

[1] Nelson J.P., The operating room environment and its influence on deep wound infection in the hip, ***Proceedings of the 5th Scientific Meetings of Hip Society***. C.V. Mosby, St. Louis, 1977

[2] ISPESL Department of Occupational Hygiene, Guidelines for the Definition of Safety Standards and Environmental Health Departments Operators (In Italian), 2009

[3] Decreto del Presidente della Repubblica, Italy, 14th Genuary 1997.

[4] ISO 14644-2:2015 Cleanrooms and associated controlled environments – Part 2: Monitoring to provide evidence of cleanroom performance related to air cleanliness by particle concentration.

[5] Standard 170-2013, Ventilation of health care facilities, ANSI/ASHRAE/ASHE, Tullie Circle, Atlanta, United State of America, 2013.

[6] F. Romano, Numerical and experimental analysis of airborne particles control in an operating theater, ***Building and Environment***, 89, 369-379, 2015.

[7] C. Balocco, Numerical Investigation of different Airflow Schemes in a Real Operating Theater, ***Biomedical Science and Engineering***, 8, 73-89, 2015

[8] European Standard EN 13779: 2007 – Ventilation for non-residential buildings – Performance requirements for ventilation and room conditioning systems, 2007.

[9] DIN 1946-2, Thermal performance of building products and components – Specific criteria for the assessment of a laboratories measuring heat transfer properties – Part 2: Measurements by the guarded hot plane method, 1999.

[10] ASTM standard D 6245-07 standard guide for using indoor carbon dioxide concentration to evaluate indoor air quality and ventilation. American Society for Testing and Materials, 2002.

Forth International Conference on Computational Methods for Thermal Problems
THERMACOMP2016, July 6-8, 2016, Georgia Tech, Atlanta, USA
N. Massarotti, P. Nithiarasu and Y. Joshi (Eds.)

A one-dimensional numerical model to determine thermal and optical performance of a PCM-filled double glazing unit

Dong Li, Yumeng Zheng, Changyu Liu, Xiaoyan Liu, Hanbing Qi, Guozhong Wu
School of architecture and civil engineering, Northeast Petroleum University, Fazhan Lu Street, Daqing 163318, China, lidonglvyan@126.com

ABSTRACT

Phase change material (PCM) applied in the double glazing structure can improve its thermal performance, but which has an effect on the optical performance of the glazing unit. A one-dimensional numerical model was developed to analyze the thermal and optical performance of the PCM-filled double glazing unit. The model structure, the main implemented equations and the adopted hypotheses were illustrated in detail. The comparison between numerical simulations and experimental data of a PCM-filled double glazing unit was also presented. The results show that the numerical tool can predict well the thermal and optical performance of the PCM-filled double glazing unit.

Key Words: *Double Glazing Unit, PCM, Thermal Performance, Optical Performance.*

1. INTRODUCTION

Glazing unit is an indispensable part of a building, which provides passive solar energy gain and air ventilation. However, effect of the glazing unit on energy loss from building envelope becomes much more drastic when the glazing area is large. Thermal performance of a glazing unit is depending on the thermal mass of glazing structure. An alternative practice to enhance the thermal mass of glazing units is to increase its thermal storage capacity. An effective approach to increase thermal storage capacity of glazing units is to incorporate PCM in the glazing structure.

Ismail et al. [1] developed one dimensional radiation and heat conduction model of double glass window filled with PCM, and found that the solar heat gain coefficient of double glass window filled with PCM is in the range of 0.65-0.80. Li et al. [2] proposed two optical parameters to calculate the solar absorptance and transmittance of the glass window filled with PCM (PCMW), and numerically investigated the thermal performance of PCMW, and found that the peak temperature on the interior surface of the PCMW reduced by 10.2□, and the heat entered into the building through the PCMW reduced by 39.5%. Li et al. [3] also found that the thermal insulation and load shifting effects of PCMW enhance with the increasing fusion latent heat of PCM and the optimal melting temperature of PCM applied in PCMW was 25-31□. Goia et al. [4] introduced optical properties of PCM in solid and liquid state to a numerical model of heat transfer calculation in the glazing units filled with PCM, which describes the thermo-physical behavior of a PCM layer in combination with other transparent materials to perform numerical analyses on various PCM glazing units. Gowreesunker et al. [5] investigated the thermal and optical performance of a PCM-glazed unit using the T-history method and spectrophotometry principles, and also used the optical constants (i.e. extinction coefficient and refractive index) to calculate the optical properties of PCM layer.

The recent studies show that optical performance of PCM in different phase state plays an important role in the thermal mass of PCM glazing unit [2-6], and the characterization of the thermal mass of the PCM layer affect considerably the thermal performance of the PCM glazing units. In the present work, a one-dimensional numerical model was developed to analyze the thermal and optical performance of the PCM-filled double glazing unit.

2. PHYSICAL AND MATHEMATICAL MODELS

Fig. 1 shows the details of a modeling double glazing unit filled with PCM. For the double glazing unit filled with PCM, the heat transfer is calculated in three regions as shown in Fig.2, which are the outer glass layer, internal glass layer and PCM layer in the middle.

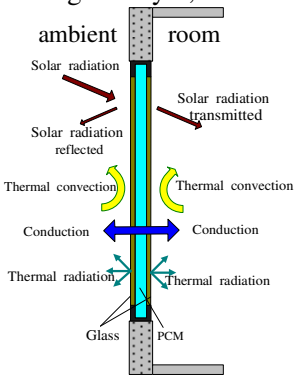

FIGURE 1. Double glazing unit

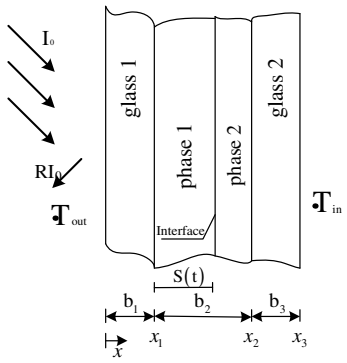

FIGURE 2. Layout of double glazing unit

Assumptions for the mathematical model have been listed as follows: (1) The heat transfer through the glazing unit is simplified to one-dimensional unsteady heat transfer process. (2) The convection within the PCM layer is neglected. (3) The radiative exchange between the two glass surfaces facing the cavity filled with PCM is neglected too. And the PCM both liquid state and solid state is highly non-transparent to the long-wave radiation. (4)The glass and PCM are considered to be thermally homogeneous and isotropic media, and the thermal properties of the materials are temperature independent. (5) The scattering effect of PCM is omitted.

A one-dimensional unsteady energy equation for glass regions is given as Eq. (1)

$$\rho_{\mathrm{g}} c_{\mathrm{P,g}} \frac{\partial T}{\partial \tau} = k_{\mathrm{g}} \frac{\partial^2 T}{\partial \mathrm{x}^2} + \emptyset. \tag{1}$$

Where, τ is time(s).T is temperature (K). ρ_{g}, k_{g} and $c_{\mathrm{P,g}}$ are density(kg/m^3), thermal conductivity (W/m·K) and specific heat (J/kg·K) of glass, respectively. $\emptyset$ is radiative source term (W/m^3).

The one-dimensional unsteady energy equation for PCM region is given as

$$\rho_{\mathrm{p}} \frac{\partial H}{\partial \tau} = k_{\mathrm{p}} \frac{\partial^2 T}{\partial \mathrm{x}^2} + \emptyset. \tag{2}$$

Where, H is the specific enthalpy of PCM (J/kg). ρ_{p} and k_{p} are density(kg/m^3), thermal conductivity (W/m·K) of PCM, respectively.

The specific enthalpy of PCM in Eq. (2) is calculated by

$$H = \int_{T_{\mathrm{ref}}}^{T} c_{\mathrm{P,p}} \mathrm{d}T + \beta Q_{\mathrm{L}}; \beta = 0, T < T_{\mathrm{s}}; \beta = \frac{T - T_{\mathrm{s}}}{T_l - T_{\mathrm{s}}},\ T_s \le T \le T_l; \beta = 1, T > T_l. \tag{3}$$

Where, T_{ref} is the reference temperature (K). $c_{\mathrm{P,p}}$ is specific heat (J/kg·K) of PCM. Q_{L} is the latent heat of PCM in the whole phase change process (J/kg). β is the local liquid fraction in calculation region. T_{s} and T_{l} is the temperature that the phase of PCM starts to change from solid to liquid (K), and the temperature that the phase of PCM completely changes into liquid(K), respectively.

The radiative source term for each layer is given as following. when the calculation node is in the glass 1, phase 1 , phase 2 and glass 2 as shown in Fig.2,

$$\emptyset = \frac{A_{\mathrm{g1}} I_{\mathrm{sol}}}{L_{\mathrm{g1}}}; \emptyset = \frac{T_{\mathrm{g1}} A_{\mathrm{p1}} I_{\mathrm{sol}}}{L_{\mathrm{p1}}}; \emptyset = \frac{T_{\mathrm{g1}} T_{\mathrm{p1}} A_{\mathrm{p2}} I_{\mathrm{sol}}}{L_{\mathrm{p2}}}; \emptyset = \frac{T_{\mathrm{g1}} T_{\mathrm{p1}} T_{\mathrm{p2}} A_{\mathrm{g2}} I_{\mathrm{sol}}}{L_{\mathrm{g2}}} \tag{4}$$

Where, I_{sol} is solar radiation (w/m^2). T_{g1}, T_{p1}, T_{p2} and T_{g2} is solar transmittance of glass 1 layer, phase 1 layer, phase 2 layer and glass 2 layer, respectively. A_{g1}, A_{p1}, A_{p2} and A_{g2} is solar absorptance of glass 1 layer, phase 1 layer, phase 2 layer and glass 2 layer, respectively. L_{g1}, L_{p1}, L_{p2} and L_{g2} is the thickness (m) of glass 1 layer, phase 1 layer, phase 2 layer and glass 2 layer, respectively. The transmittance and absorptance are calculated as the reference [6].

The solar reflectance R, transmittance T and absorptance A of a PCM-filled glazing unit are given as

$$T = T_{\mathrm{g1}} T_{\mathrm{p1}} T_{p2} T_{g2} \tag{5a}$$

$$A = A_{g1} + T_{g1}A_{p1} + T_{g1}T_{p1}A_{p2} + T_{g1}T_{p1}T_{p2}A_{g2} \quad (5b)$$

$$R = 1 - T - A \quad (5c)$$

The mathematical boundary conditions for the calculation domain are given as following. In the exterior surface of outer glass is exposed to solar radiation, and the boundary condition at x=0 is given as

$$-k_g \frac{\partial T}{\partial x} = q_{rad} + h_{out}(T_{out} - T_{a,out}) \quad (6)$$

Where, q_{rad} is radiative heat exchange between exterior surface of outer glass with the outdoor environment (w/m^2). h_{out}, T_{out} and $T_{a,out}$ is the convective heat transfer coefficient of the exterior surface of outer glass(W/m^2·K), temperature of the exterior surface of outer glass (K), and ambient temperature (K), respectively. The radiative heat exchange with the outdoor environment q_{rad} is given by

$$q_{rad} = q_{rad,air} + q_{rad,sky} + q_{rad,ground} \quad (7)$$

Where, $q_{rad,air}$, $q_{rad,sky}$ and $q_{rad,ground}$ is radiative heat exchange with the air, sky and ground (w/m^2), respectively.

The radiation heat flux $q_{rad,air}$, $q_{rad,sky}$ and $q_{rad,ground}$ is calculated as the reference [4] .

In the inner surface of internal glass near to indoors environment, the boundary condition at x=x_3 is given as [4]

$$-k_g \frac{\partial T}{\partial x} = h_{in}(T_{in} - T_{a,in}) - \varepsilon\sigma(T_{in}^4 - T_{a,in}^4) \quad (8)$$

Where, h_{in} ,T_{in} and $T_{a,in}$ is the convective heat transfer coefficient of the inner surface of internal glass (W/m^2 K), temperature of the inner surface of internal glass (K), and indoors air temperature (K), respectively.

The equations together with the boundary conditions are solved by using an explicit finite difference scheme as the procedure of reference [4] is used.

3. RESULTS

The numerical procedure is validated with the experimental parameters in the literature [3]. The outdoor air temperature and solar radiation intensity, temperature on the interior surfaces of the double glazing filled with PCM can be attained from Fig.6 to Fig.8 in the reference [3]. The thermophysical properties of materials can be attained from Table 2 in the reference [3].The extinction coefficient and refractive index of glass is 19 m^{-1} and 1.5 [5], respectively. The emissivity of the glass is 0.88. The refractive index of PCM is 1.3, and the extinction coefficients of solid and liquid PCM is 50 and 40 m^{-1}, respectively [5]. The initial temperature of the domain is 23℃. The comparison of heat flux (without transmitted solar energy) and temperature on the interior surfaces, optical performance of the double glazing filled with PCM between numerical results in this work and available in the literature [3] are shown in Fig.3.

As shown in Fig.3, the numerical and the literature results have different characteristic in different time region. Before the time at 7:00, the difference between numerical and the literature results is huge, and the reason is that the effect of initial temperature in the double glazing filled with PCM in the experimental is not omitted when heat conduction plays an important role in the heat transfer process, but which is omitted in the calculation because it can be reached the rational periodic condition. In the time region 7:00-11:00, the numerical results have a good agreement with the literature results, and the reason is that the effect of initial temperature in the double glazing filled with PCM in the experimental can be eliminated after running 7 hours, and both phase change of PCM and radiation transfer play an important role in this heat transfer process. However, in the time region 11:00-14:00, the difference between numerical and the literature results is also huge, and the reason is that radiation transfer plays an important role in this heat transfer process when the phase of PCM is liquid in this time region, but we can not give the exact optical parameters of PCM, which leads to the bigger numerical error. In the time region 14:00-22:00, the numerical

results have a good agreement with the literature results, and the reason is that both phase change of PCM and radiation transfer play an important role in this heat transfer process.

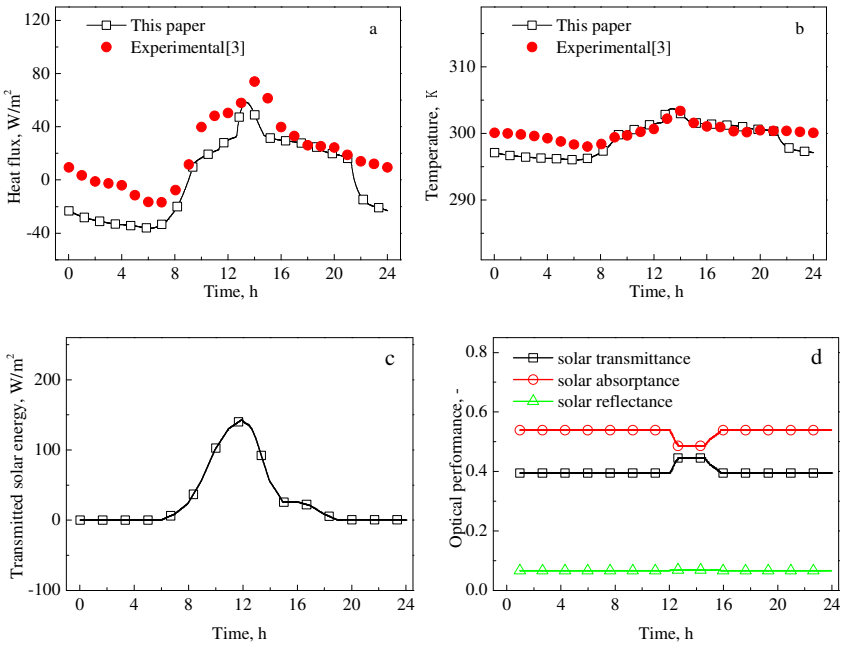

FIGURE 3. Thermal and optical results of the double glazing filled with PCM (a: heat flux; b: temperature; c: transimitted solar energy; d: optical performance)

4. CONCLUSIONS

A one-dimensional numerical model was developed to analyze the thermal and optical performance of the PCM-filled double glazing unit. And the model can predict well the thermal and optical performance of the PCM-filled double glazing unit.

REFERENCES

[1] K.A.R. Ismai, C.T. Salinas, and J.R. Henriquez, Comparison between PCM filled glass windows and absorbing gas filled windows, *Energy and Buildings*, 40, 710–9, 2008.

[2] S.H. Li, K.C. Zhong, Y. Zhou, and X. Zhang, Comparative study on the dynamic heat transfer characteristics of PCM-filled glass window and hollow glass window, *Energy and Buildings*, 85, 483–92, 2014.

[3] K.C. Zhong, S.H. Li, G. Sun, S. Li, and X. Zhang, Simulation study on dynamic heat transfer performance of PCM-filled glass window with different thermophysical parameters of phase change material, *Energy and Buildings*, In press, 2015.

[4] F. Goia, M. Perino, and M. Haase, A numerical model to evaluate the thermal behaviour of PCM glazing system configurations, *Energy and Buildings*, 54, 141–53, 2012.

[5] B.L. Gowreesunker, S.B. Stankovic, S.A. Tassou, and P.A. Kyriacou, Experimental and numerical investigations of the optical and thermal aspects of a PCM-glazed unit, *Energy and Buildings*, 61, 239–49, 2013.

[6] D. Li, Y. Zheng, Z. Li, and H. Qi, Optical properties of a liquid paraffin-filled double glazing unit, *Energy and Buildings*, 108, 381-386, 2015.

Fourth International Conference on Computational Methods for Thermal Problems
THERMACOMP2016, July 6-8, 2016, Georgia Tech, Atlanta, USA
N. Massarotti, P. Nithiarasu and Y. Joshi (Eds.)

Inhomogeneities inside thermal bridges: effects on heat and vapor transport

Paola Iodice[1], Nicola Massarotti[2], Alessandro Mauro[1,2]
[1]Università Telematica Pegaso, Piazza Trieste e Trento n. 48, 80132 Napoli, Italy,
alessandro.mauro@unipegaso.it, paola.iodice@unipegaso.it

[2]Dipartimento di Ingegneria, Università degli Studi di Napoli "Parthenope", Centro Direzionale,
Isola C4, Napoli, Italy, massarotti@uniparthenope.it, alessandro.mauro@uniparthenope.it

ABSTRACT

The importance of calculating the effect of thermal bridges in buildings energy consumption is growing, due to recent energy saving regulations applied in different countries. The widespread use of insulating materials to reduce energy requirements of buildings, often employed for intermediate insulation of building envelope, makes thermal bridges a crucial point in the energy analysis of the building envelopes. Furthermore, heat losses through thermal bridges often lead to building pathologies due to moisture condensation. Therefore, thermal bridges need to be correctly characterized in the building design stage in order to reduce heat losses and avoid materials degradation. The authors numerically simulate, by using finite elements, the dynamic three-dimensional (3D) heat and vapor transport in inhomogeneous thermal bridges and building envelopes. The aim of the present work is to show the importance of taking into account the presence of inhomogeneities in building materials for the calculation of actual heat losses and water condensation in 3D thermal bridges.

Key Words: *inhomogeneity; dynamic; thermal dispersions.*

1. INTRODUCTION

Nowadays, a great deal of attention has been given to the efficient energy use in the heating and cooling sector, and building envelopes play a crucial role in the reduction of the energy consumption and the related costs. In fact, buildings are responsible for about 40% of final energy consumption in the European Union and, as a consequence, for a considerable amount of total CO_2 emissions.

In this scenario, the use of numerical tools, required by the standards for the characterization of thermal bridges [1], should be extended to the verification of hygrothermal performance of these structures, given the complexity of solving analytically the governing equations. In these analyses, the thermal and hygrometric properties employed for each material of the building envelope assume a crucial role. These properties are available for most building components [2-4], or must be certified by the manufacturer and are commonly used in design calculations. However, problems may arise for inhomogeneous materials, such as concrete, heavily used in the existing building envelopes. In fact, the presence of the steel framework strongly influences the thermal conductivity and the hygrometric properties of the inhomogeneous concrete structure. The adoption of the value of thermal conductivity of simple concrete may cause significant errors in the calculation of the actual heat losses. Furthermore, neglecting the presence of the metal framework, some areas of possible water condensation may be ignored, thus preventing the subsequent corrective action.

Therefore, the authors' aim in this work is to show the importance of taking into account the presence of inhomogeneities inside construction materials. This approach, referred to as "microscopic", requires to reproduce the inhomogeneities (i.e. steel framework), with their physical properties, inside the geometry under investigation.

2. THE NUMERICAL MODEL

The mathematical model employed in the present work for the simulation of heat and mass transfer through a three-dimensional thermal bridge consists in the unsteady equations for heat and vapor transport through homogeneous permeable medium. To employ the present microscopic approach, the governing equations are therefore written for each isotropic homogeneous material that is found in a typical building envelope:

Heat transfer by conduction

$$\rho c \frac{\partial T}{\partial \vartheta} = \lambda \nabla^2 T \tag{1}$$

Vapor diffusion

$$\frac{\partial p_v}{\partial \vartheta} = \delta \nabla^2 p_v \tag{2}$$

The governing equations (1) and (2) are solved with the following boundary and initial conditions:

$$\begin{aligned}
&T(x,y,z,\vartheta=0) = T_0; \quad p_v(x,y,z,\vartheta=0) = p_{v,0} \quad \text{in the whole computational domain} \\
&h_{c,i}\left[T_{\infty,i} - T_{P,i}(x,y,z,\vartheta)\right] = -\lambda \left.\frac{\partial T(x,y,z,\vartheta)}{\partial n}\right|_{P,i}; \quad p_v = p_{v,i} \quad \text{on the interior surfaces} \\
&h_{c,e}\left[T_{\infty,e}(\vartheta) - T_{P,e}(x,y,z,\vartheta)\right] = -\lambda \left.\frac{\partial T(x,y,z,\vartheta)}{\partial n}\right|_{P,e}; \quad p_v = p_{v,e}(\vartheta) \quad \text{on the exterior surfaces} \\
&\left.\frac{\partial T(x,y,z,\vartheta)}{\partial n}\right|_P = 0; \quad \left.\frac{\partial p_v(x,y,z,\vartheta)}{\partial n}\right|_P = 0 \quad \text{on the remaining (lateral) surfaces}
\end{aligned} \tag{3}$$

where T_0 and $p_{v,0}$ are the initial temperature and partial pressure of vapor, respectively, $h_{c,i}$ and $h_{c,e}$ are the convective heat transfer coefficients of the interior and exterior environment, respectively, $T_{\infty,i}$ and $T_{\infty,e}$ are the interior and exterior environment temperatures, respectively, $T_{P,i}$ and $T_{P,e}$ are the temperatures of the interior and exterior surfaces, respectively, $p_{v,i}$ and $p_{v,e}$ are the partial pressures of vapor in the interior and exterior environment.

The values of the time-dependent exterior temperature and time-dependent relative humidity are calculated for the city of Aosta in Italy on the basis of the technical standard [5], that reports the methodology to be employed for the definition of the reference year to be used to reproduce the climatic conditions.

The simple mathematical model described above is solved by using the well known Finite Element Method [6].

3. RESULTS

The geometry considered for the numerical analysis is similar to the one proposed in the technical standard [1], opportunely modified to reproduce a structure adopted in actual constructions. In particular, a pillar is inserted at the corner, and the presence of interior and exterior plasters and of tiles is considered.

Furthermore, in order to show the importance of taking into account the presence of internal inhomogeneities of the materials employed in constructions to correctly estimate heat losses and condensation, two different cases are considered: the pillar and the slab are made of concrete of natural aggregates with closed structure (case 1); a steel framework in the pillar and a brick-

concrete slab are considered (case 2). The 3D structures for the two cases of modified thermal bridge are reported in Figure 1. The physical properties of the materials employed in the modified thermal bridge, taken from the technical standards [3-5], together with their geometrical characteristics, are reported in Table 1.

From the obtained numerical results, reported in Table 2 in terms of the heat flux transferred by the interior and exterior surfaces of the thermal bridge, it is possible to appreciate significant differences between case 1 and case 2. The difference on the heat flux calculated for case 1 and case 2, due to the presence of inhomogeneities in case 2, reaches the 16%. Obviously, these results depend on the geometry and on the construction characteristics of the structures considered in the simulations, and the percentage gap can increase for larger amount of steel or smaller bricks.

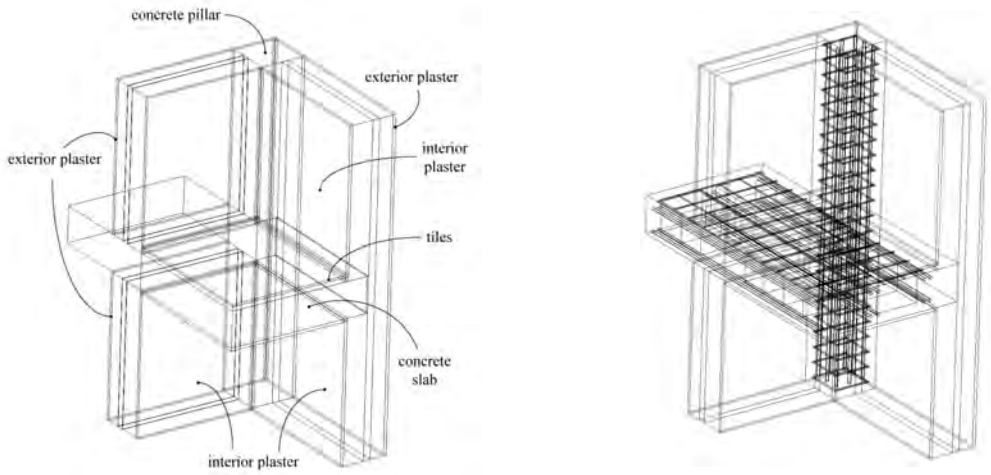

FIGURE 1. Three dimensional geometry: case 1 (left), case 2 (right).

Material	**Thermal conductivity** λ $\left(\mathrm{W}/\left(\mathrm{m}\cdot\mathrm{K}\right)\right)$	**Vapor permeability** $\delta\cdot 10^{12}$ $\left(\mathrm{kg}/\left(\mathrm{m}\cdot\mathrm{s}\cdot\mathrm{Pa}\right)\right)$	**Densiy** ρ $\left(\mathrm{kg}/\mathrm{m}^3\right)$	**Heat capacity** c $\left(\mathrm{J}/\left(\mathrm{kg}\cdot\mathrm{K}\right)\right)$	**Thickness** s $\left(\mathrm{m}\right)$
Exterior plaster	0.70	18	1400	1000	0.02
Solid brick	0.72	27	1800	840	0.10
Insulation	0.04	3.2	30	1250	0.04
Hollow brick	0.30	27	800	840	0.12
Interior plaster	0.35	18	1200	1000	0.02
Malta	0.90	9.0	1800	1000	0.03
Tiles	1.4	9.0	2300	840	0.015
Concrete - pillar	1.2	3.0	2000	1000	0.30
Concrete - slab	1.2	3.0	2000	1000	0.25
Steel - framework	52	0.0	7800	500	-

TABLE 1. Properties of the employed materials.

	Heat flux $\left(\mathrm{W/m^2}\right)$	Rate of condensed water $\left(10^{-5}\ \mathrm{g/s}\right)$
	interior surfaces	whole structure
Thermal bridge (case 1)	-6.3	3.31
Thermal bridge (case 2)	-7.3	3.71
Percentage difference	16%	12%

TABLE 2. Heat flux transferred by the interior and exterior surfaces and rate of condensed water for the two configurations of thermal bridge.

5. CONCLUSIONS

In this work, the authors solve unsteady conduction heat transfer and vapor diffusion in three-dimensional (3D) inhomogeneous thermal bridges, by using the finite element method. The authors highlight the importance of using a microscopic approach to take into account the inhomogeneities present in structures commonly employed in building envelopes, such as steel-concrete pillars or brick-concrete slabs, in order to estimate heat losses and water condensation in 3D thermal bridges.

The heat flux transferred and the water condensation in the 3D thermal bridge considered varies of 16%, ad 12%, respectively, when the presence of inhomogeneities in the employed materials is considered in detail by using a microscopic approach.

It is important to consider the inhomogeneities inside construction materials, by using the present microscopic approach, in order to correctly simulate heat and mass transfer in 3D thermal bridges, and to highlight critical local phenomena in building envelopes. The present 3D numerical approach can be a useful tool both in the design stage of building envelopes and in the energy certification of existing constructions for giving detailed local information on complex structures, and could be used together with lumped parameter models that are capable to reproduce the global behaviour of entire buildings.

REFERENCES

[1] UNI EN ISO 10211:2008 Thermal bridges in building construction - Heat flows and surface temperatures – detailed calculation; 2008.

[2] UNI 10351:1994 Materiali da costruzione - Conduttività termica e permeabilità al vapore; 1994.

[3] UNI EN 12524:2001 Building materials and products - Hygrothermal properties - Tabulated design values; 2001.

[4] UNI EN ISO 10456:2008 Building materials and products - Hygrothermal properties - Tabulated design values and procedures for determining declared and design thermal values; 2008.

[5] UNI EN ISO 15927-4: 2005 Hygrothermal performance of buildings - Calculation and presentation of climatic data Part 4: Hourly data for assessing the annual energy use for heating and cooling; 2005.

[6] R.W. Lewis, P. Nithiarasu, K.N. Seetharamu, Fundamentals of the finite element method for heat and fluid flow, John Wiley & Sons, Chichester, 2004.

Fourth International Conference on Computational Methods for Thermal Problems
THERMACOMP2016, July 6-8, 2016, Georgia Tech, Atlanta, USA
N. Massarotti, P. Nithiarasu and Y. Joshi (Eds.)

Heat transfer enhancement in PCM storage tanks through topology optimization of finning material distribution

Alberto Pizzolato, Vittorio Verda
Politecnico di Torino, Corso Duca degli Abbruzzi 24, 10129, Turin, Italy
alberto.pizzolato@polito.it, vittorio.verda@polito.it

Adriano Sciacovelli
School of Chemical Engineering; University Of Birmingham, UK
a.sciacovelli@bham.ac.uk

ABSTRACT

Latent Heat Thermal Energy Storage provides very high energy density and nearly constant operating temperatures. However, it suffers of very low thermal conductivity that considerably limits the heat transfer rate. The insertion of highly conductive fins looks the most promising option for heat transfer enhancement but raises the fundamental question of how to optimally distribute a limited amount of highly conductive material. In this paper, we show that density-based topology optimization is a very powerful tool to generate optimized devices for heat transfer enhancement in finned shell-and-tube PCM storage tanks. We consider 2D steady-state diffusion with uniform heat generation and we minimize the global heat transfer resistance. The topological designs reduces the maximum overheating of more than 84 % compared to a previous design obtained by parameter shape optimization.

Key Words: *Heat Transfer Enhancement, PCM Storage Tank, Topology optimization*

1. INTRODUCTION

Latent Heat Thermal Energy Storage (LHTES) shows two of the most desirable properties for a storage system, such as a high energy density and nearly costant operating temperatures. However, the large scale adoption of cheap paraffinic Phase Change Material as a storage mean still holds back due to its poor thermal conductivity, which considerably limits the heat transfer rate. This is the reason why heat transfer enhancement techniques have been largely adopted in the past to improve the performances of LHTES: One of the possibilities is to utilize fins of a high conductivity material such as aluminium, whose design should be optimized to maximize the heat transfer performances. To this aim, topology optimization looks the most powerful approach compared to the standard parameter-based shape optimization. It allows to dramatically enlarge the space of design degrees of freedom, by optimizing the distribution of high conductivity finning material on a ground domain. To the knowledge of the Authors, only one work [1] has been devoted to the application of the tools of topology optimization for heat transfer enhancement in PCM-based devices. That paper dates back to 2006 and suffers of a poor resolution, due to the limited computational performances achievable at the time.

2. MODELING AND OPTIMIZATION

We have considered 2D steady-state heat diffusion as a valuable representation of the problem. As a matter of facts, besides the very first instants of the process, solidification is ruled by pure heat conduction and buoyancy-induced currents can be neglected [2]. Furthermore, assuming that an homogenous phase transition across the domain can be modelled as a constant heat source, we let the transient term decay. In mathematical terms:

$$k\frac{\partial^2 T}{\partial x_i \partial x_j} = q \qquad \text{in } \Omega \tag{1}$$

Where q is the volumetric heat generation rate here set to 224 KW/m$^{3.}$ This value has been calculated considering the average thermal power obtainable from a volume of 0.02 m^3 of PCM that completely releases its latent heat in 30 minutes. Based on this physics, we are solving an optimization problem of the form:

$$\begin{aligned} &\text{minimize:} \quad f(T,\rho) = \int_\Omega qT(\rho)dA \\ &\text{subject to:} \quad \mathrm{R}(T,\rho) = 0 \\ &\qquad\qquad \int_\Omega \rho dA - vf \cdot A_\Omega < 0 \\ &\qquad\qquad 0 \le \rho \le 1 \end{aligned} \tag{2}$$

In Eq. (2), f is the objective functional, i.e. the global thermal compliance. Note that in diffusion problems with uniform heat generation, this optimization problem is completely equivalent to the minimization of the mean integral temperature and thus of the global thermal resistance. The objective functional is dependent on the state variable field T and on the design variable field ρ, i.e. the normalized density of high conductivity material. The equality constraint forces the residual function of Eq. (1) to zero, while the first inequality constraints sets a higher limit to the volume fraction vf of high conductivity material in the computational domain, here set to 0.1. All the relevant boundary conditions are summarized in Figure 1.

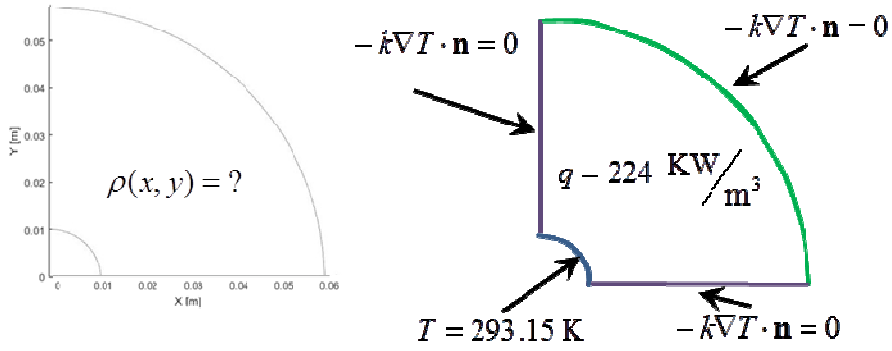

FIGURE 1. Overview of the 2D computational domain and boundary conditions

The objective functional sensitivities needed to drive the optimization algorithm are calculated through the discrete adjoint method, which can be described with:

$$\frac{df}{d\boldsymbol{\rho}} = \frac{\partial f}{\partial \boldsymbol{\rho}} - \boldsymbol{\lambda}^T \frac{\partial \mathbf{R}}{\partial \boldsymbol{\rho}} \qquad \frac{\partial \mathbf{R}}{\partial \mathbf{T}}^T \boldsymbol{\lambda} = \frac{\partial f}{\partial \mathbf{T}}^T \tag{3}$$

where λ is the vector of adjoint variables, i.e. the Lagrange multipliers. Note that every variable in bold is a column vector obtained through the discretization of the corresponding continuous field. Hence, the calculation of the adjoint sensitivities are obtained by solving an additional (always linear) FEM problem in the adjoint space.

3. NUMERICAL IMPLEMENTATION

Since the objective of the optimization problem is to end up with binary designs, i.e. the normalized density of the high conductivity material should ideally take the value of 0 and 1, the intermediate designs should be made unattractive by a suitable interpolation scheme. In this paper, this is achieved by penalizing the thermal conductivity of intermediate designs with the SIMP approach [3] (Solid Isotropic Material with penalization). The relaxed conductivity field can be written as:

$$\mathbf{k}(\boldsymbol{\rho}) = k_{\min} + (k_{\max} - k_{\min})\boldsymbol{\rho}^{p} \tag{4}$$

where k_{min} is the thermal conductivity of the PCM (here set to 0.2 W/m^{2}K) and k_{max} is the thermal conductivity of the alluminum fin (here set to 120 W/m2K). p is a penalization parameter that is raised during the optimization history following a continuation scheme from the starting value of 1 to the final value of 3. Furthermore, also the load vector needs to be interpolated to avoid heat generation in non-PCM regions. This is done with a simple linear interpolation of the form:

$$\mathbf{q}(\boldsymbol{\rho}) = q_{\max}(1 - \boldsymbol{\rho}) \tag{5}$$

where q_{max} is the heat flux vector in the PCM region. To avoid ill-posedness of the optimization problem, which results in mesh-dependency and checkerboard density fields, we have used the density filter as proposed in [4]. The governing equations are discretized using linear quadrilateral finite elements for a total number of state degrees of freedom of 109.4k and design degrees of freedom of 108.8k. Regularity of the grid was ensured to guarantee isotropy of the filter operator. The linear systems of both the adjoint and the primal problem are solved with the MUltifrontal Massively Parallel sparse direct solver (MUMPS). The optimization is conducted through the gradient-based Method of Moving Asymptotes (MMA) by K. Svanberg [5]. Convergence test is designed to check if the L^1 norm of the normalized density vector update step is below 0.01. The whole procedure has been implemented in the interactive COMSOL-Matlab environment.

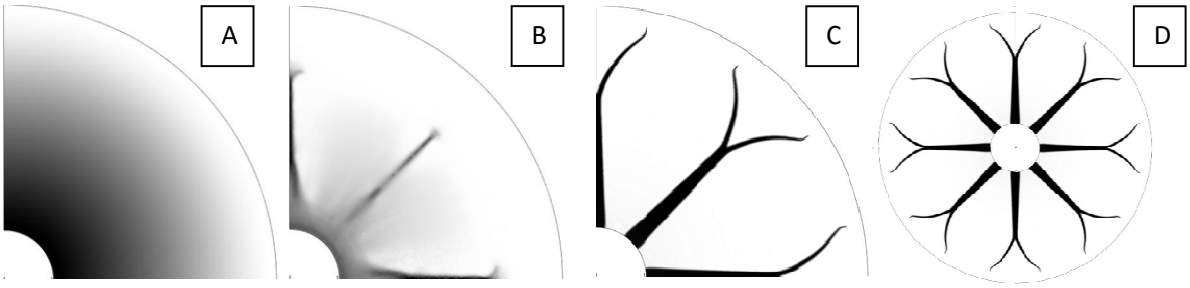

FIGURE 2. A-C: Convergence history: Iteration 2 (A), iteration 50 (B) and iteration 120 (C). D: Final design obtained by exploiting the symmetry condition.

4. RESULTS

Figure 2.A-C shows the convergence history obtained selecting an initial homogenous distribution of finning material. During the iterative procedure, more and more highly conductive material is concentrated on 8 equally spaced branches with single bifurcation and the tip of each branch shows a further alignment in the radial direction. The full final optimized design (Figure 2.D) shows many similarities with the constructal design originated from the point-to-area maximum access problem.
In order to show the potential of topology optimization for the design of heat transfer devices, we compare the performances of the topological design with the ones of an optimized design obtained

through parametric shape optimization [2] (degrees of freedoms are reduced to 3 angles and 2 lengths). The temperature fields for the two cases are plotted in Figure 3.A-B. The objective function is decreased from 83.55 MW K to 7.03 MW K and the integral mean temperature is curtailed from the original 372.4 K of the parametric design to the 314.3 K of the topological design. Finally, the maximum temperatures calculated in the domain are 488.7 K and 324.1 K for case A and case B respectively, meaning the topological design brings an 84 % cut-down of the maximum overheating.

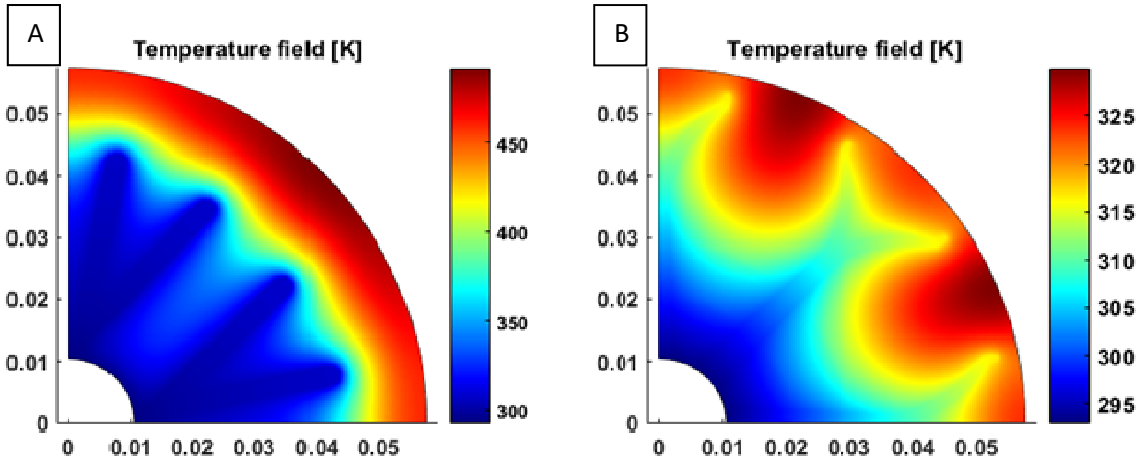

FIGURE 3. A: Temperature field obtained with the optimized design calculated in [2] through parametric optimization. B: Temperature field obtained with the optimized design calculated through topology optimization of finning material

5. CONCLUSIONS

The present work uses the tools of density-based topology optimization to design the best fins for maximizing heat transfer performance of PCM thermal storage tanks. The design obtained consists of 8 equally spaced variable thickness branches with single bifurcation. Compared to a previously optimized design, obtained by using parameter shape optimization with 5 degrees of freedom in the design space, the maximum overheating is reduced by more than 84 %, bringing down the maximum temperature from 488.7 K to 324.1 K and the integral mean temperature from 372.4 K to 314.3 K.

REFERENCES

[1] Srinivas, V. S. S., & Ananthasuresh, G. K. (2006). Analysis and topology optimization of heat sinks with a phase-change material on COMSOL multiphysics™ platform. In *Proc. COMSOL Multiphys. User's Conf* (pp. 1-7).

[2] Sciacovelli, A., Gagliardi, F., & Verda, V. (2015). Maximization of performance of a PCM latent heat storage system with innovative fins. *Applied Energy*, *137*, 707-715.

[3] Bendsøe, M. P. (1989). Optimal shape design as a material distribution problem. *Structural optimization*, *1*(4), 193-202.

[4] Svanberg, K. (2002). A class of globally convergent optimization methods based on conservative convex separable approximations. *SIAM journal on optimization*, *12* (2), 555-573.

[5] Wang, F., Lazarov, B. S., & Sigmund, O. (2011). On projection methods, convergence and robust formulations in topology optimization. *Structural and Multidisciplinary Optimization*, *43*(6), 767-784.

Fourth International Conference on Computational Methods for Thermal Problems
THERMACOMP2016, July 6-8, 2016, Georgia Tech, Atlanta, USA
N. Massarotti, P. Nithiarasu and Y. Joshi (Eds.)

HEATLINE AND ENTROPY GENERATION BASED ANALYSIS OF NATURAL CONVECTION IN POROUS CAVITIES WITH CURVED WALLS SUBJECTED TO RAYLEIGH-BENARD HEATING

Pratibha Biswal, Tanmay Basak*
Department of Chemical Engineering, Indian Institute of Technology Madras,
Chennai - 600036,
E-mail: biswal.pratibha9@gmail.com, *Corresponding author, E-mail: tanmay@iitm.ac.in.

ABSTRACT

The computational study of natural convection within porous enclosures with curved (concave/convex) horizontal walls is carried out via the heatline and entropy generation approach. The numerical simulation has been carried out for air at Prandtl numbers, $Pr_m = 0.7$ for various Darcy numbers ($10^{-5} \leq Da_m \leq 10^{-2}$) at a high Rayleigh number, $Ra_m=10^6$ with different wall curvatures. The heatlines approach, (mathematically represented as heatfunction) is employed for the heat flow visualization. In addition, the localized entropy generation due to heat transfer and fluid friction are also illustrated for various wall curvatures. Finally, the optimal situation is recommended based on the less entropy production and high heat transfer rate.

Key Words: *Rayleigh-Benard heating, Heatfunction, Entropy generation, Curved surfaces, Nusselt number, Finite element method.*

1. INTRODUCTION

During the natural convection, the shapes and geometrical configurations of enclosed cavities significantly influence the characteristics of flow and heat transfer rates. The analysis of natural convection within complex cavities is also mathematically challenging based on the complexity in implementation of boundary conditions and calculation of various field variables along the complicated walls. The finite element method is more beneficial in handling the complex boundary conditions and complex domains compared to the finite difference and finite volume techniques. In addition, the accuracy achieved by the finite element method is more compared to the finite difference and finite volume techniques even with coarser grids.

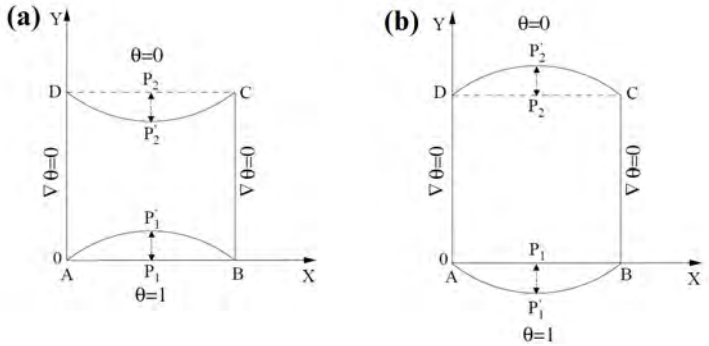

FIGURE 1: Schematic diagram of the computational domain for the (a) concave and (b) convex cases.

In addition to the spatial distribution of the isotherms (θ) and streamlines (ψ), the heatline (Π) approach [1] is employed in the present work to visualize the heat flow during natural convection. Also, the entropy generation approach [2] is employed to study the associated irreversibilities during natural convection (S_θ and S_ψ). The coupled partial differential equations are solved via the Galerkin finite element method [3] with penalty parameter. Further, the finite element approach

offers special advantage over finite difference or finite volume methods as the elemental basis functions are employed for accurate evaluation of gradients or derivatives of velocity and temperature in entropy generation equation. Note that, for complex cavities with the curved wall(s), the calculation of derivative terms in the entropy generation problem becomes cumbersome by finite difference/finite volume approach. The Gaussian quadrature based finite element method which provides smooth solutions at the interior domain including the corner regions. The finite element method is advantageous especially for the curved surfaces where implementation of finite difference/finite volume method becomes cumbersome. The current work is the first attempt for the investigation of entropy generation during natural convection using elemental basis functions via Galerkin finite element method for porous curved domains with Rayleigh-Benard heating.

2. MATHEMATICAL MODELING AND SIMULATIONS

The computational domain based on the semi-infinite approximation assumption is shown in Fig. 1(a) and (b) for the concave and convex surfaces, respectively. The momentum transport in porous medium is based on Darcy-Brinkman-Forchheimer model. Under various simple assumptions [4], the governing equations for natural convection in porous media are obtained as follows:

$$\frac{\partial U}{\partial X}+\frac{\partial V}{\partial Y}=0 \tag{1}$$

$$U\frac{\partial U}{\partial X}+V\frac{\partial U}{\partial Y}=-\frac{\partial P}{\partial X}+\mathrm{Pr_m}\left(\frac{\partial^2 U}{\partial X^2}+\frac{\partial^2 U}{\partial Y^2}\right)-\frac{\mathrm{Pr}_m}{Da_m}U-\frac{1.75}{\sqrt{150}}\frac{U\sqrt{(U^2+V^2)}}{\sqrt{Da_m}} \tag{2}$$

$$U\frac{\partial V}{\partial X}+V\frac{\partial V}{\partial Y}=-\frac{\partial P}{\partial Y}+\mathrm{Pr_m}\left(\frac{\partial^2 V}{\partial X^2}+\frac{\partial^2 V}{\partial Y^2}\right)-\frac{\mathrm{Pr}_m}{Da_m}V-\frac{1.75}{\sqrt{150}}\frac{V\sqrt{(U^2+V^2)}}{\sqrt{Da_m}}+Ra_m\mathrm{Pr_m}\theta \tag{3}$$

$$U\frac{\partial \theta}{\partial X}+V\frac{\partial \theta}{\partial Y}=\frac{\partial^2 \theta}{\partial X^2}+\frac{\partial^2 \theta}{\partial Y^2} \tag{4}$$

The definitions of the dimensional parameters and solution procedure are presented elsewhere [4]. The governing equations are subjected to the thermal boundary condition based on the hot bottom wall, cold top wall and adiabatic side walls [see Fig. 1(a-b)]. The no-slip velocity boundary condition is valid along all the solid walls. Further, the streamfunction (ψ) and heatfunction are evaluated using the finite element method [3-5]. The calculation of the entropy generation and Nusselt number is carried out by the Galerkin finite element method with the weighed residuals [3-6].

3. RESULTS AND DISCUSSION

The isotherms are significantly distorted within the cavity for all the concave cases [see Fig. 2(a-c)]. Multiple streamline cells are seen within the cavity for all the cases. The highly distorted heatlines are accompanied by the closed loop heatlines for all the cases. It may be noted that, $S_{\theta,max}$ is observed at the central portion of the cavity for the cases 1 and 2 whereas, $S_{\theta,max}$ for the case 3 is seen at the left and right portions of the core. It may also be noted that, $S_{\psi,}$ is significant along all the solid walls and $S_{\psi,max}$ is found to occur at the left and right portions of the concave walls for all the cases.

The isotherms are strongly compressed towards almost entire convex walls and at the middle portion of the cavity for all the cases [Fig 3(a-c)]. Comparatively larger streamline cells with the higher streamfunction are observed for all the convex cases [see Fig. 3(a-c)]. Mainly closed loop heatlines are seen and the end-to-end heatlines take complex path from the bottom to the top wall. The magnitudes of S_θ at the core are very less for all the cases. Note that, $S_{\theta,max}$ is observed at the mid point of the top and bottom walls for the case 1. On the other hand, $S_{\theta,max}$ is located at the left and right portion of the mid horizontal axis for the cases 2 and 3. The velocity gradients are quite high at the side walls for the cases 1 and 2 in contrast to the case 3. Note that $S_{\psi,max}$ is located near

the top and bottom portions of the side walls for the cases 1 and 2 whereas, $S_{\psi,max}$ for the case 3 is located near the left and right portions of the horizontal curved walls.

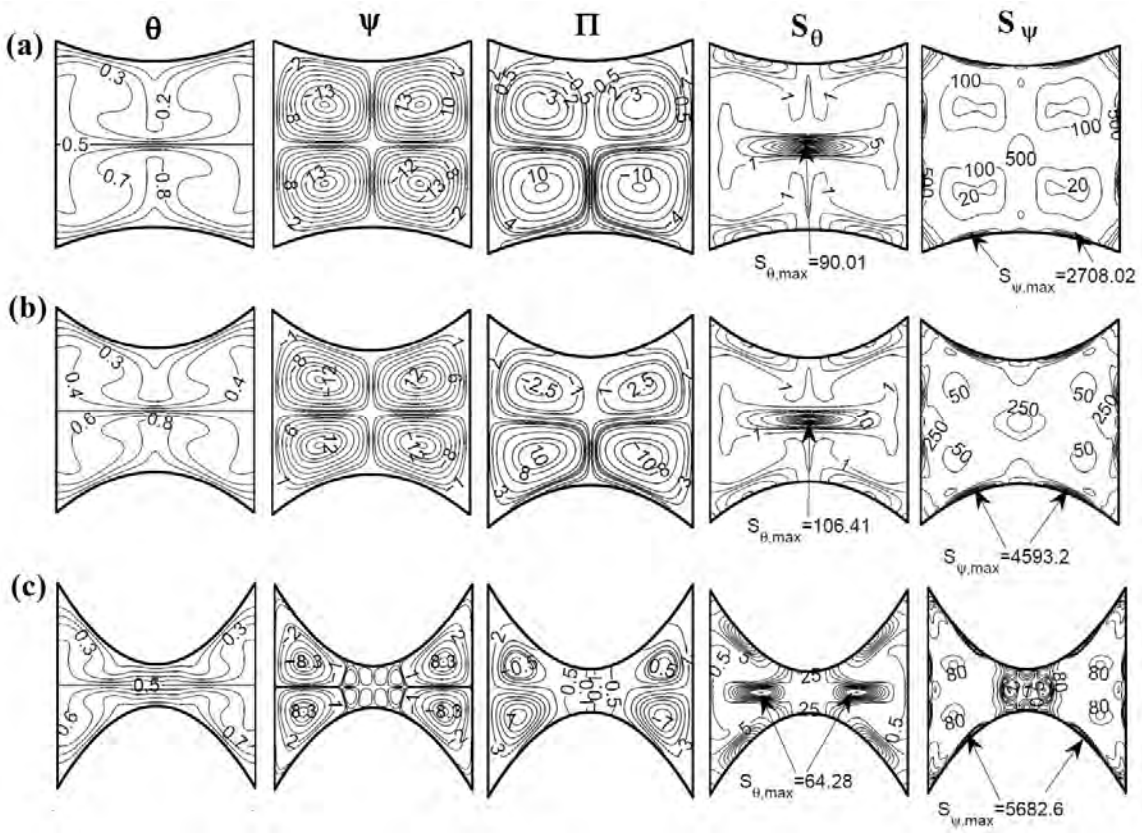

FIGURE 2: Isotherms (θ), streamlines (ψ), heatlines (Π), entropy generation due to heat transfer (S_θ) and entropy generation due to fluid friction (S_ψ) at Pr_m=0.7 and Da_m=10^{-2} for the concave cases [(a) case 1, (b) case 2 and (c) case 3]

4. CONCLUSION

The effects of the concavities and convexities as well as various thermal parameters on the heat transfer rate during Rayleigh-Benard convection discussed. The heat transfer visualization from the bottom to the top wall is described by the heatline approach. In addition, the entropy generation due to the heat transfer and fluid friction are examined for various wall curvatures. It was established that, the case 3 with the high wall concavity is more beneficial compared to the cases 1 and 2 of the concave domain for all Da_m based on the minimum entropy generation rates. On the other hand, the case 1 with the less wall convexity is more beneficial compared to the cases 2 and 3 of the convex domain for all Da_m based on the minimum entropy generation rates.

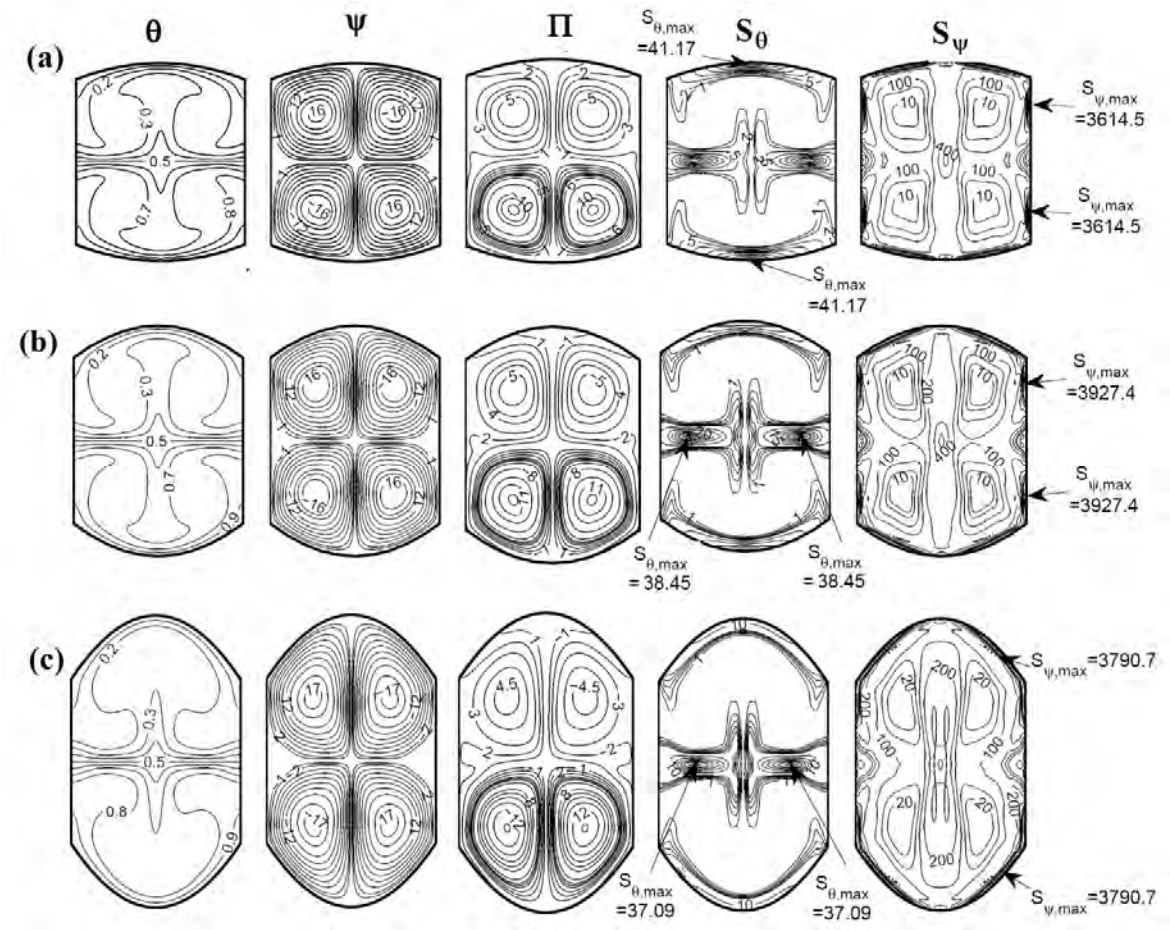

FIGURE 3: Isotherms (θ), streamlines (ψ), heatlines (Π), entropy generation due to heat transfer (S_θ) and entropy generation due to fluid friction (S_ψ) at Pr_m=0.7 and Da_m=10^{-2} for the convex cases [(a) case 1, (b) case 2 and (c) case 3].

REFERENCES

[1] S. Kimura, and A. Bejan, The heatline visualization of convective heat transfer*, Journal of Heat Transfer T ASME*, 105, 916-919, 1983.

[2] A. Bejan, *Entropy Generation through Heat and Fluid Flow,* Wiley, 1994.

[3] J. N, Reddy, *An Introduction to the Finite Element Method,* McGraw-Hill, 1993.

[4] A. K. Singh, T. Basak, A. Nag and S. Roy, Role of entropy generation on thermal management during natural convection in tilted porous square cavities, *Journal of the Taiwan Institute of Chemical Engineers*, 50, 153-172, 2015.

[5] P. Biswal and T. Basak, Bejan's heatlines and numerical visualization of convective heat flow in differentially heated enclosures with concave/convex side walls, *Energy*, 64, 69-94, 2014.

[6] P. Biswal and T. Basak*,* Entropy generation based approach on natural convection in enclosures with concave/convex side walls*. International Journal of Heat and Mass Transfer*, 82, 213-235, 2015.

Fourth International Conference on Computational Methods for Thermal Problems
THERMACOMP2016, July 6-8, 2016, Georgia Tech, Atlanta, USA
N. Massarotti, P. Nithiarasu and Y. Joshi (Eds.)

A NUMERICAL INVESTIGATION ON AERO-THERMODYNAMIC CHARACTERISTICS OF A NOSE CONE IN WIND TUNNEL AND NEAR SPACE FLIGHT ENVIRONMENT

Lin Shen, Jianhua Wang, Wenjie Dong

Department of Thermal Science and Energy Engineering, University of Science and Technology of China, Hefei, 230027, PR China. sforest@mail.ustc.edu.cn, jhwang@ustc.edu.cn, dwj150mc@mail.ustc.edu.cn

ABSTRACT

A numerical comparison of the aero-thermodynamic characteristics of a nose cone between a ground arc-heating wind tunnel and real space flight with an altitude of 30km is carried out. The results indicate that at same stagnation temperature, the temperature, pressure and heat flux along the nose cone surface are higher in wind tunnel than that in altitude 30km, and the differences are caused by different heating principles in the two environments.

Key words: *Aero-thermodynamic, Arc-heating, Hypersonic, Wind tunnel, Near-space environment*

1. INTRODUCTION

With the development of spaceflight and aviation technologies, advanced thermal protection system (TPS) becomes more and more important, especially for the hypersonic vehicles in near space. In order to develop more effective TPS to meet the extreme environments, a large number of assessment tests and mechanism experiments are carried out by ground experimental devices [1]. Therein, considering accuracy and cost of experiments, the arc-heating wind tunnel, which can establish high enthalpy environments through a combined effect of aero-heating caused by lower Mach number free stream with arc-heating, has been widely used for estimating TPS.

It is clear that the thermodynamic environment of arc-heating wind-tunnel is different from that of the real aero-heating flight in near space, because there are essential differences between their heating principles, one is based on a combined effect of aero-heating with arc-heating and the other is based on purely aero-heating. Therefore, it is necessary to investigate the differences of aero-thermodynamic characteristics between the wind tunnel environment and real near space flight environment through numerical analysis. The aim of this work is to help the investigators, experimenters and designers of hypersonic vehicles understand the experimental data obtained by ground facilities, and rationally use the data source in TPS design.

2. WIND TUNNEL AND NEAR SPACE ENVIRONMENT

The arc-heating wind tunnel has been widely used to create a thermodynamic environment to simulate the supersonic or hypersonic flight in near space. It is clear that the aero-thermodynamic performances exhibited in ground arc-heating facilities are different from the real space flight. In ground experiments, to estimate the heat resisting property of TPS, an important indicator is the stagnation temperature. In this work, at the same stagnation temperature of 2380K, the differences of aero-thermodynamic characteristics between the ground wind-tunnel experiments environment and real space flight in altitude 30km are analyzed by numerical simulations. The schematic

configuration of arc-heating wind tunnel FD-4.1 in China Academy of Aerospace Aerodynamics (CAAA) is shown in Fig.1. The setting thermodynamic states of FD-4.1 experiment environment and altitude 30km for numerical simulations are listed in Tab.1. It is noted that the freestream static temperature and pressure in altitude 30km are set as the standard atmospheric parameters referring to the COESA (U.S.) Standard Atmosphere [2]. Besides, the freestream static temperature in wind tunnel is higher than that in altitude 30km due to arc-heating effect.

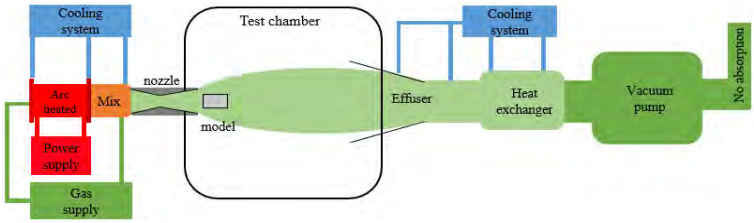

FIGURE 1. Schematic configuration of wind tunnel

Physical parameters	Wind tunnel	Altitude 30km
Freestream static temperature T_∞ / K	510	226
Freestream static pressure P_∞ / kPa	6	1.2
Freestream Mach number Ma_∞	4.3	7
Stagnation temperature T_0 / K	2380	2380

TABLE 1. Physical parameters of arc-heating wind tunnel and altitude 30km

3. NUMERICAL SIMULATIONS

The physical model used in this work is a wedged nose cone with a radius of 3mm, a width of 70mm and a length of 114mm. It is put in the center of freestream field with a computational domain of 300mm×600mm, as shown in Fig.2. Numerical simulations are carried out by using commercial software Ansys CFX 15.0. A constant inlet velocity at ambient pressure and a supersonic outlet are used as boundary conditions at the inlet and outlet of the computational domain. The upper and lower opening boundary conditions make the flow field not be limited within 300mm height. The SST turbulence model is used to solve Navier-Stokes equations, and RMS residuals less than 10^{-5} are given to confirm convergence.

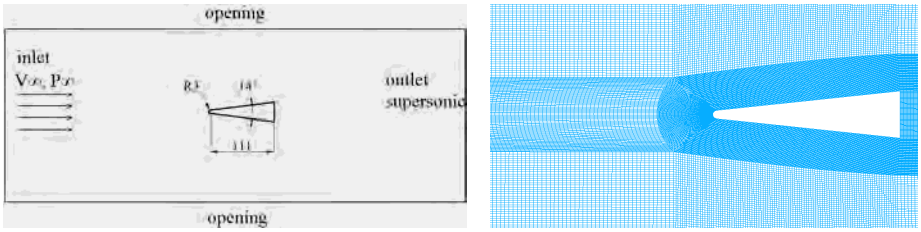

FIGURE 2. Simplified physical model and structured mesh

Using the parameters as shown in Tab.1, the temperature, pressure and heat flux in the computational domain are computed. Fig.3 (a) and (b) shows the temperature and pressure contour in the two environments. By comparison, two phenomena as followings can be found, 1) The bow shock wave patterns illustrated in real space environment are much closer to the model surface and the shock angle is smaller than that in wind tunnel environment. This phenomenon is reasonable, because these performances are basically dependent on Mach number. At the same stagnation

temperature 2380K, the corresponding Mach number in altitude 30km is much larger than that in wind tunnel experiment. 2) The surface temperature and pressure around the nose cone in wind tunnel are higher than that in altitude 30km. In order to conduct a quantificational comparison of thermodynamic characteristics between the two environments, the temperature and pressure along the centerline of nose cone surface are computed and their distributions are presented in Fig.4 (a) and (b).

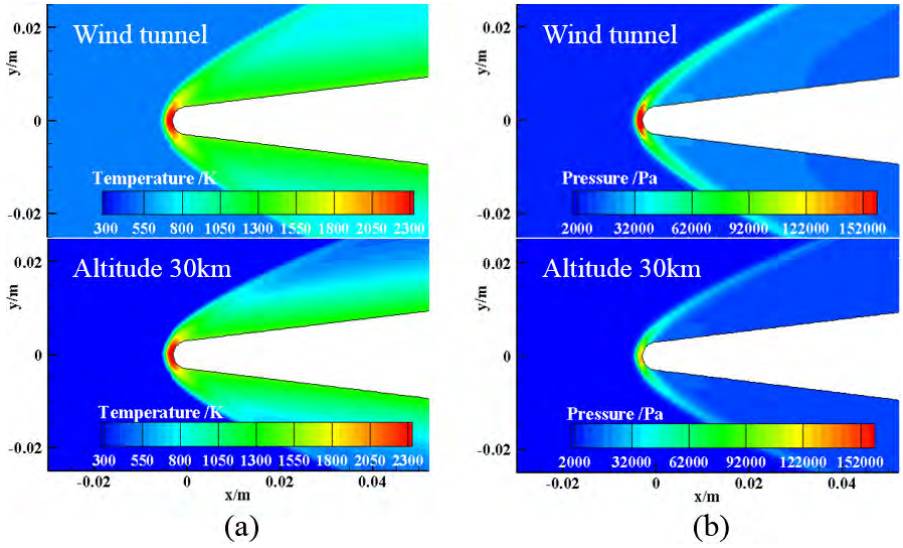

FIGURE 3. (a) Temperature and (b) Pressure contour in two environments

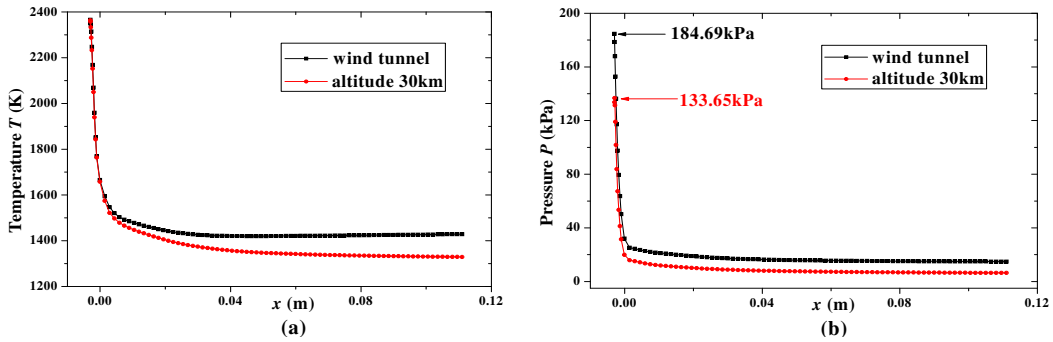

FIGURE 4. (a) Temperature and (b) Pressure distribution along the centerline of nose cone surface in two environments

Fig.4 (a) illustrates the temperature along the centerline of the nose cone surface in two environments at the same stagnation temperature 2380K. Except the stagnation point, at the other points, the temperature in wind tunnel is higher than that in altitude 30km. This phenomenon is reasonable, because all of the freestream in wind tunnel is heated by electric arc, and it implies that the nose cone in wind tunnel will suffer much severer thermal environment than that in real space flight of altitude 30km. Therefore, the ground experiments are usually conservative, i.e., if a TPS is through the high-temperature assessment tests in ground arc-heating wind tunnel, then the TPS is more likely to be successful in near space flight.

Fig.4 (b) illustrates the pressure along the centerline of the nose cone surface in two environments at the same stagnation temperature 2380K. It is clear that the pressure at the whole surface in wind

tunnel is higher than that in altitude 30km, especially at the stagnation point, 184.69kPa in wind tunnel and 133.65kPa in altitude 30km, respectively. This phenomenon is also reasonable that the freestream density and static pressure in the wind tunnel are much higher than that in altitude 30km, and it means that in an active TPS, to cool the stagnation region or the entire nose cone, the driving force to inject cooling media is much higher in ground experiments.

It is one of the most important tasks in hypersonic aircraft designs to study the heat flux distribution over a model surface, not only in an aerodynamic experiment, but also in a real flight condition. If we want to cool a nose cone model down to its surface temperature at 1000K, the heat flux variation over the model surface is exhibited in Fig.5. The heat flux in wind tunnel is slightly higher than that in real space, and this phenomenon corresponds well with the temperature distribution. By integrating the heat flux over the entire surface, the heat flow into the model can be calculated, as 2005.36W in wind tunnel and 1478.57W in altitude 30km, respectively. It implies that in an active TPS, in order to cool the nose cone surface to the constant temperature 1000K, the demands of coolants in near space flight is less than that in the wind tunnel. It is significant, because a decrease of coolant consumption can reduce the loads of flight vehicles to a certain degree.

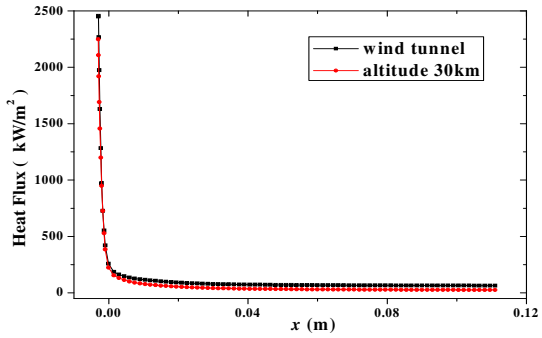

FIGURE 5. Heat flux distribution along the centerline of nose cone surface in two environments

4. CONCLUSIONS

Numerical simulations are used to study the aero-thermodynamic characteristics of a nose cone in the two environments, i.e., ground arc-heating wind tunnel and real space flight in altitude 30km. Under the condition of same stagnation temperature, the following three conclusions can be drawn: Firstly, the surface temperature of the nose cone in wind tunnel appears higher; Secondly, even though the stagnation temperature of two environments is the same, the stagnation pressure in wind tunnel is much higher; Thirdly, if the nose cone is cooled down to a constant surface temperature, the heat flow into the cone in wind tunnel is higher. In brief, the thermodynamic environment is much severer in wind tunnel.

REFERENCES

[1] P.S. Anton, E.C. Gritton, R. Mesic, P. Steinberg. Wind Tunnel and Propulsion Test Facilities: An Assessment of NASA's Capabilities to Serve National Needs, *Rand National Defense Research Inst Santa Monica CA*, 2004.

[2] COESA, U. S. Standard Atmosphere. 1976, *US Government Printing Office, Washington, DC* (1976).

Fourth International Conference on Computational Methods for Thermal Problems
THERMACOMP2016, July 6-8, 2016, Georgia Tech, Atlanta, USA
N. Massarotti, P. Nithiarasu and Y. Joshi (Eds.)

INFLUENCE OF TEMPERATURE DEPENDENT PROPERTIES ON DUSTY FLUID

Sadia Siddiqa, Naheed Begum
COMSATS Institute of Information Technology, Attock, Pakistan, saadiasiddiqa@gmail.com, Naheed.awan6@gmail.com
Md. Anwar Hossain
Department of Mathematics, University of Dhaka, Dhaka, Bangladesh, anwar.cfd@gmail.com

ABSTRACT

The influence of temperature dependent viscosity and thermal conductivity on dusty fluid flow is analyzed in this paper. Numerical solutions are given for the flow along vertical plate which is immersed in the dusty fluid. The viscosity and thermal conductivity are considered to be the linear function of temperature and their behavior is observed on commonly used fluid (water). It is concluded from this investigation that water with particles can increase the rate of heat transfer.

Key Words: *Variable Properties, Natural Convection, Two-Phase, Dusty Fluid, Vertical Surface*

1. INTRODUCTION

The investigations on flow of fluids with suspended particles have attracted the attention of numerous researchers due to their practical applications in various problem of atmospheric, engineering and physiological fields (see [1]). Farbar and Morley [2] were the first to analyze the gas-particulate suspension on experimental grounds. After that, Marble [4] studied the problem of dynamics of a gas containing small solid particles and developed the equations for gas-particle flow systems. Singleton [5] was the first to study the boundary layer analysis for dusty fluid and later on the dynamics of two-phase flow was investigated by numerous authors [6-7] under different physical circumstances.
In all the above analysis, considerations have been given to unifrom properties of the fluid. But literautre is replete with such examples (see Ref. [8-10]) where temperature dependent properties have significant influence over the flow characteristics. In the present analysis, consideration has been given to report the effects of variable viscosity and thermal conductivity on two-phase flow of dusty fluid by assuming the underlying expressions (see Ref. [11]):

$$\mu = \mu_\infty \left[1 + \frac{\varepsilon (T - T_\infty)}{T_w - T_\infty}\right], \quad \kappa = \kappa_\infty \left[1 + \frac{\gamma (T - T_\infty)}{T_w - T_\infty}\right] \tag{1}$$

Here μ_∞ and κ_∞ are the viscosity and thermal conductivity of the ambient fluid and ε and γ are respectively the viscosity variation parameter and thermal conductivity variation parameter. The solutions are calculated by using the implicit finite difference method and numerical results are displayed in the form of skin friction coefficient, heat transfer rate, velocity and temperature profiles by varying several controlling parameters.

2. PROBLEM FORMULATIOIN

Consider natural convection two-phase dusty fluid flow past a vertical plate by assuming the variable viscosity and thermal conductivity of the fluid. Initially, the system is having a uniform temperature T_∞. Suddenly, the surface of the plate is heated to a temperature $T + \Delta T$ and natural convection starts due to this. The dimensionless boundary layer equations for the two-phase flow can be written as: (for details see Ref. [3], [6], [7], [10]):

$$\frac{1}{2}U + \frac{1}{2}X\frac{\partial U}{\partial X} - \frac{1}{4}Y\frac{\partial U}{\partial Y} + \frac{\partial V}{\partial Y} = 0 \tag{2}$$

$$\frac{1}{2}U^2+\frac{1}{2}XU\frac{\partial U}{\partial X}+\left(V-\frac{1}{4}YU\right)\frac{\partial U}{\partial Y}=(1+\varepsilon\Theta)\frac{\partial^2 U}{\partial Y^2}+\varepsilon\frac{\partial U}{\partial Y}\frac{\partial\Theta}{\partial Y}+\Theta-D_\rho X(U-U_p) \tag{3}$$

$$\frac{1}{2}XU\frac{\partial\Theta}{\partial X}+\left(V-\frac{1}{4}YU\right)\frac{\partial\Theta}{\partial Y}=\frac{1}{\Pr}\left[(1+\gamma\Theta)\frac{\partial^2\Theta}{\partial Y^2}+\gamma\left(\frac{\partial\Theta}{\partial Y}\right)^2-\frac{2}{3}D_\rho X\left(\Theta-\Theta_p\right)\right] \tag{4}$$

$$\frac{1}{2}U_p+\frac{1}{2}X\frac{\partial U_p}{\partial X}-\frac{1}{4}Y\frac{\partial U_p}{\partial Y}+\frac{\partial V_p}{\partial Y}=0 \tag{5}$$

$$\frac{1}{2}U_p^2+\frac{1}{2}XU_p\frac{\partial U_p}{\partial X}+\left(V_p-\frac{1}{4}YU_p\right)\frac{\partial U_p}{\partial Y}=-X(U_p-U) \tag{6}$$

$$\frac{1}{2}XU_p\frac{\partial\Theta_p}{\partial X}+\left(V_p-\frac{1}{4}YU_p\right)\frac{\partial\Theta_p}{\partial Y}=-\frac{2X}{3\omega\Pr}\left(\Theta_p-\Theta\right) \tag{7}$$

Where

$$Gr=\frac{g\beta(T_w-T_\infty)L^3}{\nu^2},\ D_\rho=\frac{\rho_p}{\rho},\ \omega=\frac{c_s}{c_p},\ \Pr=\frac{\upsilon}{\alpha} \tag{8}$$

Here, Gr and Pr are respectively the Grashof number and Prandtl number, α the thermal diffusivity, β the volumetric expansion coefficient, ν the kinematic viscosity, g the gravitational acceleration, ρ and ρ_p are the density of carrier and particle phase, c_s and c_p are specific heat at constant pressure for carrier and particle phases, (U, V) and (U_p, V_p) are dimensionless velocity components of carrier and particle phase respectively in (X, Y) directions, (Θ, Θ_p) the temperature for carrier and particle phase, T_w the temperature of the surface of the plate, T_∞ the ambient fluid temperature, ε the viscosity variation parameter and γ the thermal conductivity variation parameter.
The boundary conditions to be satisfied are:

$$\begin{gathered}U(X,0)=V(X,0)=\Theta(X,0)-1=U_p(X,0)=V_p(X,0)=\Theta_p(X,0)-1=0\\ U(X,\infty)=U_p(X,\infty)=\Theta(X,0)=\Theta_p(X,\infty)=0\end{gathered} \tag{9}$$

The system of equations is discretized and then solved numerically by using implicit finite difference method developed by Thomas algorithim. After solving the above system, it is important to calculate the values of physical parameters like local skin friction coefficient, τ_w, and rate of heat transfer, Q_w. The mathematical expressions for these quantities are calculated as:

$$\tau_w=(1+\varepsilon)\left(\frac{\partial U}{\partial Y}\right)_{Y=0},\quad Q_w=-(1+\gamma)\left(\frac{\partial\Theta}{\partial Y}\right)_{Y=0} \tag{10}$$

In the next section, numerical solutions obtained are graphed and discussed as well.

3. RESULTS

In this analysis, the influence of variable viscosity and thermal conductivity has been reported on natural convection flow of two-phase flow along vertical surface. The system of equations are solved numerically via implicit finite difference method and it is found that the solutions are affected by two major physical parameters, tempertaure dependtent visosity paramter, ε, and thermal conductivity parameter γ. So we will focus our attention to report the effects of ε and γ on local skin friction coefficient, τ_w, rate of heat transfer, Q_w, velocity and temperature profiles of both phases. The results are calculated for metal particles in water: D_ρ = 10.0, Pr = 7.0, ω= 0.1.

In Fig. 1 attention has been given to the effects of variable viscosity parameter, ε, on τ_w and Q_w. Significant change is recorded in both quantities when variable viscosity parameter increases. Particularly, τ_w for ε = 0.0 is low and increases significantly by intestifying the viscosity parameter. This may happens because the large values of ε produce more resistance to flow and ultimately skin friction increases at the surface of the plate.

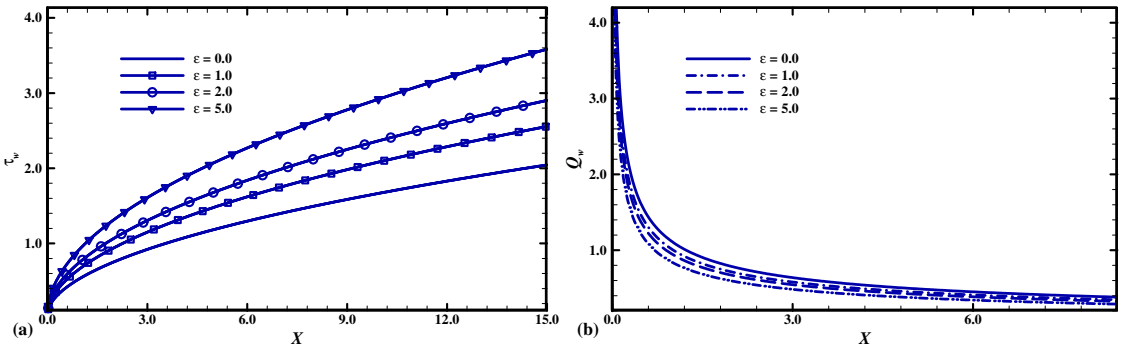

FIGURE 1 (a) τ_w (b) Q_w for $\varepsilon = 0.0, 1.0, 2.0, 5.0$, $\gamma = 1.0$.

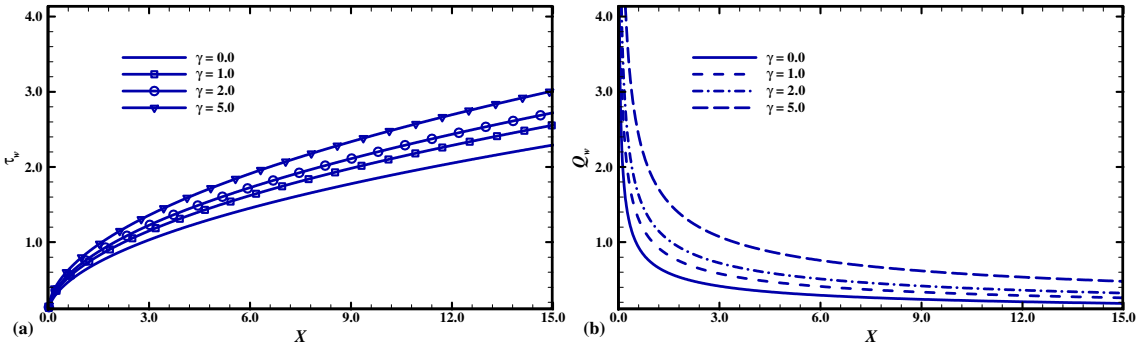

FIGURE 2 (a) τ_w (b) Q_w for $\gamma = 0.0, 1.0, 2.0, 5.0$, $\varepsilon = 1.0$.

For the purpose of discussion on the influence of parameter γ, Fig. 2 is plotted. It is evident from the figure that Q_w increases drastically as γ increases. The entire convective regime is hotter for the case of variable conductivity and the large temperature gradient in the thermal boundary layer promotes conductive heating near the surface of the plate. Moreover, in Fig. 2(a) the skin friction at the vertical surface also increases by magnifying the parameter γ.

In order to determine the change due to an increase in ε on velocity and temperature profiles, Fig. 3 is plotted. For comparison, suspension without particle cloud (pure water) is also presented. It is observed that velocities for carrier and fluid phase decreases for increasing values of ε and reverse behaviour is reported for the temperature profiles. It may happens because the large values of ε produces more resistance to flow and hence fluid velocity decreases.

Fig. 4 is plotted to visualize the influence of γ on τ_w and Q_w and it is reported that γ has a dominant effect on velocity and temperature of both phases. Higher values of γ contribute in magnifying the velocity and temperature profiles.

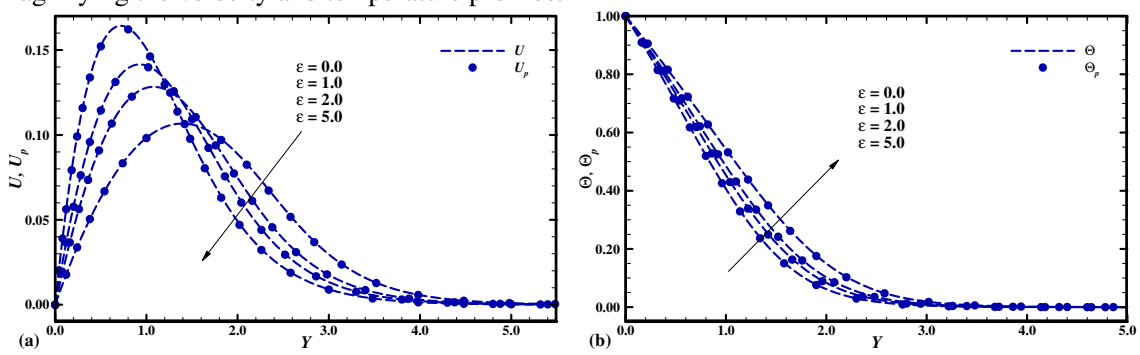

FIGURE 3 (a) Velocity (b) Temperature profiles for $\varepsilon = 0.0, 1.0, 2.0, 5.0$, $\gamma = 1.0$, $X = 20.0$.

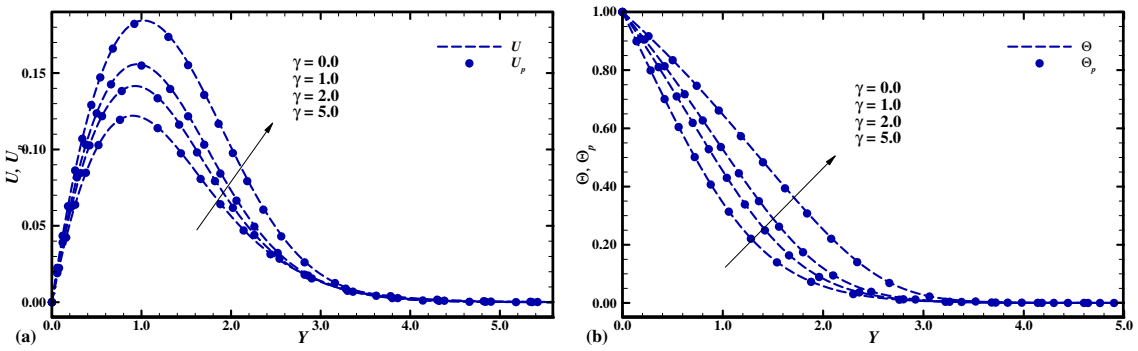

FIGURE 4 (a) Velocity (b) Temperature profiles for $\gamma = 0.0, 1.0, 2.0, 5.0$, $\varepsilon = 1.0$, $X = 20.0$.

4. CONCLUSIONS

This paper aims to compute numerical results of natural convection flow of dusty fluid along a vertical plate. The nonlinear system of boundary layer equations are iteratively solved step by step by using implicit finite difference method along with tri-diagonal solver. The problem is investigated to predict the characteristics of free convection fluid flow having variable fluid properties. Computational results are shown for the physical quantities, namely, skin friction coefficient, rate of heat transfer coefficient, velocity and temperature profiles. It is concluded from the results that rate of heat transfer is extensively promoted by increasing thermal conductivity parameter whereas the rate of skin friction depicts a considerable increase by increasing the viscosity parameter.

REFERENCES

[1] G. Rudinger, Fundamentals of gas-particle flow, *Elsevier Scientific Publishing Co.*, Amsterdam, 1980.

[2] L. Farbar and M. J. Morley, Heat transfer to flowing gas-solid mixtures in a circular tube, *Ind. Eng. Chem.*, 49, 1957, 1143-1150.

[3] Saffman, P. G., On the stability of laminar flow of a dusty gas, *J. Fluid Mech.*, 13, 1962, 120-128.

[4] F. E. Marble, Dynamics of a gas containing small solid particles, combustion and propulsion, *5th AGARD colloquium*, Pergamon press, 1963.

[5] R. E. Singleton, Fluid mechanics of gas-solid particle flow in boundary layers, Ph.D. Thesis, California Institute of Technology, 1964.

[6] S. Siddiqa, M. A. Hossain and S. C. Saha, Two-phase natural convection flow of a dusty fluid, *Int. J. Numer. Methods Heat Fluid Flow*, 45, 2015, 1542-1556.

[7] S. Siddiqa, M. A. Hossain and M. N. Nasir, Dynamics of Two-phase dusty fluid flow along a wavy surface, Submitted in: *Int. J. Numer. Methods Heat Fluid Flow*.

[8] N. G. Kafoussius, E. W. Williams, The effect of temperature-dependent viscosity on the free convection laminar boundary layer flow past a vertical isothermal flat plate, *Acta Mechanica,* 110, 1997, 123-137.

[9] M. A. Hossain, M. S. Munir, H. S. Takhar, Natural convection flow of a viscous fluid about a truncated cone with temperature dependent viscosity, *Acta Mechanica,* 140, 2000, 171-181.

[10] M. A. Hossain, M. S. Munir, I.Pop, Natural convection with variable viscosity and thermal conductivity from a vertical wavy cone, *Int. J. Therm. Sci.*,40, 2001,437-443.

[11] J. Chrraudeau, Influence de gradients de proprieties physiques en convection force application au.

Fourth International Conference on Computational Methods for Thermal Problems
THERMACOMP2016, July 6-8, 2016, Georgia Tech, Atlanta, USA
N. Massarotti, P. Nithiarasu and Y. Joshi (Eds.)

THERMAL RADIATION EFFECTS ON TWO-PHASE DUSTY FLUID PAST A VERTICAL WAVY SURFACE

Sadia Siddiqa, Naheed Begum
COMSATS Institute of Information Technology, Attock, Pakistan, saadiasiddiqa@gmail.com, Naheed.awan6@gmail.com
Md. Anwar Hossain
Department of Mathematics, University of Dhaka, Dhaka, Bangladesh, anwar.cfd@gmail.com

ABSTRACT

The purpose of present analysis is to investigate the influence of thermal radiation on natural convection flow of two-phase flow past a vertical wavy surface. The dimensionless equations are solved numerically by the implicit finite difference method. The aim is to predict the enhancement of heat transport due to large values of thermal radiation parameter and surface heating parameter. It is recorded that the rate of heat transfer enhances extensively when the thermal radiation parameter R_d is penetrated into the mechanism of dusty fluid model.

Key Words: *Thermal Radiation, Natural Convection, Two-Phase, Dusty Fluid, Wavy Surface*

1. INTRODUCTION

The investigations on flow of fluids with suspended particles have attracted the attention of numerous researchers due to their practical applications in various problem of atmospheric, engineering and physiological fields (see [1]). Farbar and Morley [2] were the first to analyze the gas-particulate suspension on experimental grounds. After that, Marble [4] studied the problem of dynamics of a gas containing small solid particles and developed the equations for gas-particle flow systems. Singleton [5] was the first to study the boundary layer analysis for dusty fluid and later on the dynamics of two-phase flow was investigated by numerous authors [6-7] under different physical circumstances.

In all the above analysis, considerations have been given to smooth surfaces only. But sometimes it is very important to exploit the roughened surfaces in industries and the distribution of heat transfer for incompressible fluid from a non-uniform vertical surface was initially encountered by Yao [8] and Moulic and Yao [9]. Keeping the work of [8] and [9] in view, several investigations have been done for numerous practical situations as given in [7], [10]. In the present analysis consideration has been given to the effects of radiative heat transfer (for information on radiation see [10]) on natural convection flow of two phase dusty fluid moving along a vertical wavy surface. Present paper reports the effects of thermal radiation on natural convection flow of a two-phase model and the solutions are calculated by using the implicit finite difference method. Numerical results are displayed in the form of skin friction coefficient, heat transfer rate, velocity and temperature profiles by varying several controlling parameters.

2. PROBLEM FORMULATIOIN

Consider natural convection flow of two-phase dusty fluid past a vertical wavy plate under the influence of thermal radiation. The boundary layer analysis outlined below allows the shape of the wavy surface, $\sigma(\hat{x})$, to be arbitrary, but our detailed numerical work will assume that the surface exhibits sinusoidal deformations defined as: $\hat{y}_w = \sigma(\hat{x}) = \hat{a}\sin(\pi\hat{x}/L)$ (where $\hat{a}$ is the dimensional amplitude of the wavy surface and L the characteristic length associated with the uneven surface) . Initially, the system is having a uniform temperature T_∞. Suddenly, the surface of the plate $\hat{y} = 0$ is heated to a temperature $T + \Delta T$ and natural convection starts due to this. Fig. 1 shows the geometry of the wavy surface.

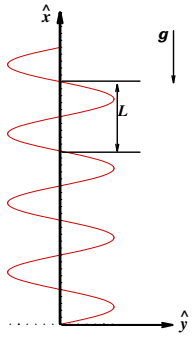

FIGURE 1. Physical Model

The dimensionless boundary layer equations for the two-phase flow can be written as: (for details see Ref. [3], [6], [7]):

$$X\frac{\partial U}{\partial X}+\frac{1}{2}U-\frac{1}{4}Y\frac{\partial U}{\partial Y}+\frac{\partial V}{\partial Y}=0 \tag{1}$$

$$\left(\frac{1}{2}+\frac{X\sigma_X\sigma_{XX}}{\left(1+\sigma_X^2\right)}\right)U^2+XU\frac{\partial U}{\partial X}+\left(V-\frac{1}{4}YU\right)\frac{\partial U}{\partial Y}=\left(1+\sigma_X^2\right)\frac{\partial^2 U}{\partial Y^2}+\frac{1}{\left(1+\sigma_X^2\right)}\Theta+D_\rho\alpha_d X^{1/2}(U_p-U) \tag{2}$$

$$XU\frac{\partial\Theta}{\partial X}+\left(V-\frac{1}{4}YU\right)\frac{\partial\Theta}{\partial Y}=\frac{1}{\mathrm{Pr}}\left[\frac{\partial}{\partial Y}\left(1+\frac{4}{3}R_d\left(1+(\theta_w-1)\Theta\right)^3\right)\frac{\partial\Theta}{\partial Y}\right]+\frac{2}{3\mathrm{Pr}}D_\rho\alpha_d X^{1/2}\left(\Theta_p-\Theta\right) \tag{3}$$

$$X\frac{\partial U_p}{\partial X}+\frac{1}{2}U_p-\frac{1}{4}Y\frac{\partial U_p}{\partial Y}+\frac{\partial V_p}{\partial Y}=0 \tag{4}$$

$$\left(\frac{1}{2}+\frac{X\sigma_X\sigma_{XX}}{\left(1+\sigma_X^2\right)}\right)U_p^2+XU_p\frac{\partial U_p}{\partial X}+\left(V_p-\frac{1}{4}YU_p\right)\frac{\partial U_p}{\partial Y}=-\alpha_d X^{1/2}(U_p-U) \tag{5}$$

$$XU_p\frac{\partial\Theta_p}{\partial X}+\left(V_p-\frac{1}{4}YU_p\right)\frac{\partial\Theta_p}{\partial Y}=-\frac{2}{3\gamma\mathrm{Pr}}\alpha_d X^{1/2}\left(\Theta_p-\Theta\right) \tag{6}$$

where

$$Gr=\frac{g\beta(T_w-T_\infty)L^3}{\nu^2},\ \theta_w=\frac{T_w}{T_\infty},\ R_d=\frac{4\sigma^* T_\infty^3}{\kappa\left(\alpha_r+\sigma_s\right)},\ D_\rho=\frac{\rho_p}{\rho},\ \gamma=\frac{c_s}{c_p},\ \alpha_d=\frac{L^2}{\nu\tau_m Gr^{1/2}} \tag{7}$$

The boundary conditions to be satisfied are:

$$U(X,0)=V(X,0)=\Theta(X,0)-1=U_p(X,0)=V_p(X,0)=\Theta_p(X,0)-1=0$$
$$U(X,\infty)=U_p(X,\infty)=\Theta(X,0)=\Theta_p(X,\infty)=0 \tag{8}$$

The system of equations is discretized and then solved numerically by using implicit finite difference method developed by Thomas algorithim. After solving the above system, it is important to calculate the values of physical measurements like local skin friction coefficient, τ_w, and rate of heat transfer, Q_w. The mathematical expressions for these quantities are calculated as:

$$\tau_w=\sqrt{1+\sigma_X^2}\left(\frac{\partial U}{\partial Y}\right)_{Y=0},\quad Q_w=-\sqrt{1+\sigma_X^2}\left(1+\frac{4}{3}R_d\theta_w^3\right)\left(\frac{\partial\Theta}{\partial Y}\right)_{Y=0} \tag{9}$$

In the next section, numerical solutions obtained from the above algorithm are graphed and discussed as well.

3. RESULTS

In this analysis, the influence of thermal radiation has been reported on natural convection flow of two-phase flow along vertical wavy surface. The system of equations are solved numerically via implicit finite difference method and it is found that the solutions are affected by two major parameters, radiation parameter R_d and surface heating parameter θ_w. So we will focus our attention to report the effects of R_d and θ_w on local skin friction coefficient, τ_w, rate of heat transfer, Q_w,

velocity and temperature profiles of both phases. The results are calculated for metal particles in water: $D_\rho = 10.0$, Pr = 7.0, $\gamma = 0.1$.

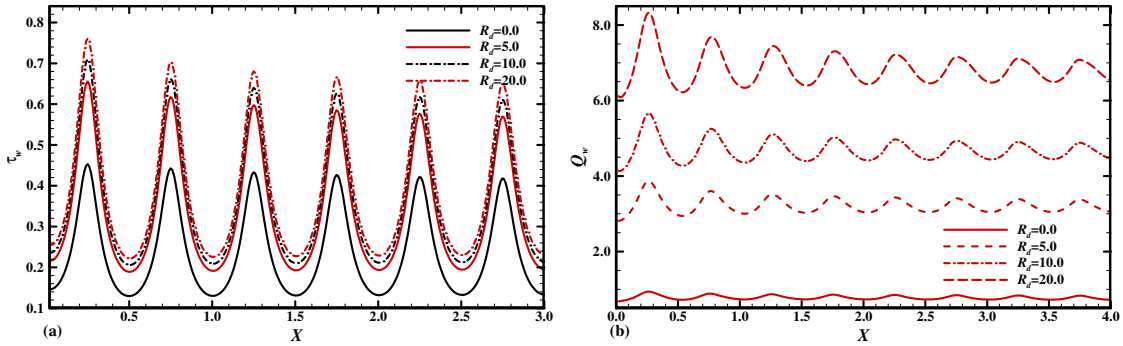

FIGURE 2 (a) τ_w (b) Q_w for R_d = 0. 0, 5.0, 10.0, 20.0, $\alpha_d = 0.5$, $a = 0.3$, $\theta_w = 1.1$.

In Fig. 2 attention has been given to the effects of thermal radiation parameter, R_d, on τ_w and Q_w. Both the quantities increase significantly when thermal radiation parameter increases. Particularly, heat transfer for R_d = 0.0 is very low and this factor act as a heat source which enhances the temperature of the radiating fluid and as a result heat is transferred more at the surface. Radiation parameter not only enhances the rate of heat transfer but also develops the amplitude of the harmonic wave with dominant surface curvature.

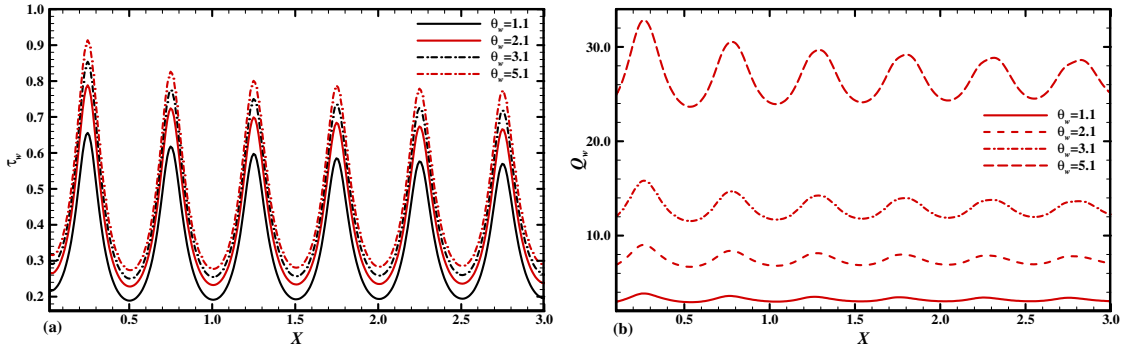

FIGURE 3 (a) τ_w (b) Q_w for θ_w = 1.1, 2.1, 3.1, 5.1, R_d = 5.0, $\alpha_d = 0.5$, $a = 0.3$.

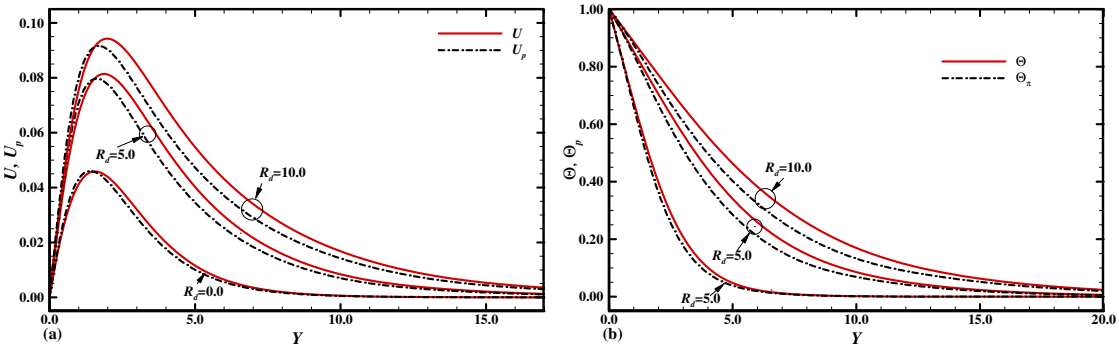

FIGURE 4 (a) Velocity (b) Temperature profiles for R_d = 0. 0, 5.0, 10.0, $\alpha_d = 0.5$, $a = 0.3$, $\theta_w = 1.1$.

Fig. 3 shows the effect of θ_w on τ_w and Q_w and found notable influence on Q_w. Such behavior is expected because increment in θ_w leads to an increase in the temperature of the wavy surface and ultimately fluid particles accelerates more rapidly in the vicinity of the uneven surface. Moreover, in Fig. 3(b) small surface temperature corresponds to the waves having negligible amplitude which ultimately recovers the solutions for flat surface case. For the purpose of the discussion of the influence of R_d, and θ_w, on velocity and tempererature profiles, Figs. 4 and 5 are plotted. For comparison, suspension without particle cloud (pure water) is also presented. It is observed that velocities and temperatures for carrier and fluid phase increases for increasing values of R_d and θ_w. It is interesting to note that at every stage the particle phase velocity, U_p, and particle phase

temperature Θ_p is sufficiently higher than the carrier phase velocity U, and carrier phase temperature Θ. Particulary in Fig. 5 it is reported that the effect of surface heating parameter θ_w has a dominant effect on velocity and temperature of particle phase.

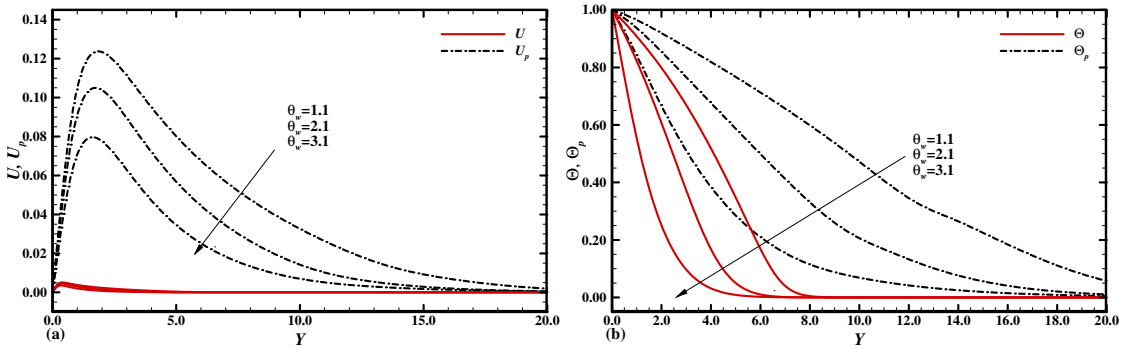

FIGURE 5 (a) Velocity (b) Temperature profiles for $\theta_w = 1.1, 2.1, 3.1$, $R_d = 5.0$, $\alpha_d = 0.5$, $a = 0.3$.

4. CONCLUSIONS

This paper aims to compute numerical results of influence of radiation effects on natural convection flow of two-phase flow along a vertical wavy surface. The nonlinear system of boundary layer equations are iteratively solved step by step by using implicit finite difference method along with tri-diagonal solver. The problem is investigated to predict the characteristics of free convection fluid flow in presence of radiation effects. Computational results are shown for the physical quantities, namely, skin friction coefficient, rate of heat transfer coefficient, velocity and temperature profiles. It is concluded from this study that thermal radiation extensively promotes the heat transfer coefficient near the surface of the wavy surface. In addition, R_d and θ_w enhances the amplitude of the waves representing the rate of heat transfer.

REFERENCES

[1] G. Rudinger, Fundamentals of gas-particle flow, *Elsevier Scientific Publishing Co.*, Amsterdam, 1980.

[2] L. Farbar and M. J. Morley, Heat transfer to flowing gas-solid mixtures in a circular tube, *Ind. Eng. Chem.*, 49, 1957, 1143-1150.

[3] Saffman, P. G., On the stability of laminar flow of a dusty gas, *J. Fluid Mech.*, **13**, 1962, 120-128.

[4] F. E. Marble, Dynamics of a gas containing small solid particles, combustion and propulsion, *5th AGARD colloquium*, Pergamon press, 1963.

[5] R. E. Singleton, Fluid mechanics of gas-solid particle flow in boundary layers, Ph.D. Thesis, California Institute of Technology, 1964.

[6] S. Siddiqa, M. A. Hossain and S. C. Saha, Two-phase natural convection flow of a dusty fluid, *Int. J. Numer. Methods Heat Fluid Flow*, 45, 2015, 1542-1556.

[7] S. Siddiqa, M. A. Hossain and M. N. Nasir, Dynamics of Two-phase dusty fluid flow along a wavy surface, Submitted in: *Int. J. Numer. Methods Heat Fluid Flow*.

[8] L. S. Yao, Natural convection along a vertical wavy surface, *J. Heat Transfer*, 105, (1983) 465-468.

[9] S. G. Moulic, L. S. Yao, Natural convection along a wavy surface with uniform heat flux, *J. Heat Transfer*, 111, (1989) 1106-1108.

[10] S. Siddiqa, M. A. Hossain and S. C., Natural convection flow with surface radiation along a vertical wavy surface, *Numerical Heat Transfer, Part A: Applications*, 64, 400-415, 2013.

[11] S. Siddiqa, M. A. Hossain, S. C. Saha, The effect of thermal radiation on the natural convection boundary layer flow over a wavy horizontal surface, *Int. J. of Thermal Sciences*, 84, 143-150, 2014.

Fourth International Conference on Computational Methods for Thermal Problems
THERMACOMP2016, July 6-8, 2016, Georgia Tech, Atlanta, USA
N. Massarotti, P. Nithiarasu and Y. Joshi (Eds.)

NUMERICAL MODELING OF CONVECTIVE FLOWS STRUCTURED AT ISOTHERMAL DIFFUSION IN VERTICAL CYLINDRICAL CHANNELS AT DIFFERENT PRESSURES

D.B. Zhakebayev
Department of Mathematical and Computer modeling, Kazakh National University named after al-Farabi, al-Farabi 71, 050038, Almaty, Kazakhstan, dauren.zhakebaev@kaznu.kz

V.N. Kosov, Y.V. Kosov
Institute of Experimental and Theoretical Physics, Kazakh National University named after al-Farabi, al-Farabi 71, 050038, Almaty, Kazakhstan, kosov_vlad_nik@list.ru, y.kossov@mail.ru

ABSTRACT

The problem of emergence of structuralized convective flows at an isothermal ternary diffusion in a vertical cylindrical channel is solved by the methods of numerical simulation. The modeling process is based on the joint solution of the Navier-Stokes equation, the diffusion equations and the equation of continuity. It is shown that at a certain pressure in the system arise essentially non-linear distributions of concentrations of components that lead to non-linear distribution of the gas mixture density that is the cause of convective structures.

Key Words: *Convection, Diffusion, Instability, Pressure.*

1. INTRODUCTION

If in isothermal binary gas mixture, the heavy density gas is on the top, then in the system occurs (generates) a concentration gravitational convection. The opposite direction of the gradient density of the mixture leads to a diffusion type of mixing. However, the addition of a third component to the mixture may lead to the occurrence of new effects which are contrary to the above stated data. Studying the velocity of leveling the concentrations in multicomponent diffusion at different pressures in vertical channels the convective flows were recorded [1,2]. The anomalous of convection was that it took place under the conditions where the light density binary mixture was in the upper part of the channel, and the third, heavier density gas was placed in the lower part.

The systematic study of these problems by methods of stability theory [3,4] allowed to form approaches to the study of the most common features in defining the boundary of the transition from one mode (diffusion) to another (convection). As it is shown in [5], mathematical research is based on the linearization system of equations of continuum medium mechanics for the isothermal two-component systems with respect to small perturbations. The resulting homogeneous system of linear differential equations with time-independent coefficients has a solution of this type $\exp(-i\omega t)$. If among the found $\omega = \omega_0 + i\omega_1$ exist those, for which $\omega_1 > 0$, then the state will be unstable. For the ternary mixture in the terms of Rayleigh numbers have been defined the borders of regime change "diffusion - concentration convection." However, the proposed in [5,6] approach did not allow to explore the issues related to the formation of convective flows determining mainly the transfer of components of the mixture in the course of time. The purpose of this study is to explore the formation of structuralized flows in isothermal gas mixtures at different pressures in the course of time by means of a 2-D modelling.

2. MATHEMATICAL MODEL OF DIFFUSION INSTABILITY

Numerical simulation of the process is based on the Navier-Stokes equation, the continuity equation

and equations of the concentration in the Descartes' (Cartesian) coordinate system:

$$\begin{cases} \dfrac{\partial \vec{u}_i}{\partial t} = -\nabla p + \nabla^2 \vec{u} + (R_1 c_1 \tau_{11} + R_2 c_2)\vec{\gamma} \\ \operatorname{div} \vec{v} = 0 \\ \dfrac{\partial c_1}{\partial t} + \vec{v}\nabla c_1 = \dfrac{1}{Pr_{11}}\nabla^2 c_1 + \dfrac{A_2}{A_1}\dfrac{1}{Pr_{12}}\nabla^2 c_2 \\ \dfrac{\partial c_2}{\partial t} + \vec{v}\nabla c_2 = \dfrac{A_1}{A_2}\dfrac{1}{Pr_{21}}\nabla^2 c_1 + \dfrac{1}{Pr_{22}}\nabla^2 c_2 \end{cases} \quad (1)$$

where D_{ij}^* - practical diffusion coefficient, $Pr_{ii} = \nu / D_{ii}^*$ - diffusion Prandtl number, $R_i = g\beta_i A_i d^4 / \nu D_{ii}^*$ - partial Rayleigh number, $\tau_{ij} = D_{ij}^* / D_{22}^*$ - parameters that define the relationship between the practical diffusion coefficients.

We study the process when a binary mixture 0.5312Ar + 0.4688He, located at the top of a vertical cylindrical channel and the pure gas (N_2) - at the bottom, in which, provided the condition of the occurrence of instability. For physical quantities are specified the following boundary conditions: on all borders of the cylinder condition of solid wall $u_i\big|_{x_i=0, x_i=L_i} = 0,\ i = 1,2$, and for the concentration components we use boundary conditions $\partial C / \partial n\big|_{x_i=0, x_i=L_i} = 0,\ i = 1,2$.

For the numerical solution of the problem of gas motion in the cylinder area is used the splitting scheme by physical parameters.

$$\begin{aligned} &1.\ \frac{\bar{u}^* - \bar{u}^n}{\Delta t} = -\bar{u}^n \nabla \bar{u}^* + \Delta \bar{u}^* + \tau_{11} Ra_1 C_1 + Ra_2 C_2, \\ &2.\ \Delta p = \frac{\nabla \bar{u}^*}{\Delta t}, \\ &3.\ \frac{\bar{u}^{n+1} - \bar{u}^*}{\Delta t} = -\nabla p \\ &4.\ \frac{\bar{C}_1^{n+1} - \bar{C}_1^n}{\Delta t} = -\left(\bar{u}^{n+1}\nabla\right)\bar{C}_1^* + \frac{1}{Pr_{11}}\Delta \bar{C}_1^* + \frac{1}{Pr_{12}}\Delta \bar{C}_2^* \\ &5.\ \frac{\bar{C}_2^{n+1} - \bar{C}_2^n}{\Delta t} = -\left(\bar{u}^{n+1}\nabla\right)\bar{C}_2^* + \frac{1}{Pr_{21}}\Delta \bar{C}_1^* + \frac{1}{Pr_{22}}\Delta \bar{C}_2^* \end{aligned} \quad (2)$$

In the first stage the equation of Navier-Stokes is solved without taking into consideration the pressure. To approximate the convective and diffusive terms in the equation used a compact scheme of higher accuracy order where the compact approximation for convective terms of equations of motion of the third, and for the diffusion terms of the fourth order accuracy [7]. The intermediate velocity field is solved by the method of fractional steps in using the sweep method.

In the second stage is solved the Poisson equation, obtained from the continuity equation in view of the velocity field of the first stage. In order to solve the two-dimensional Poisson equation developed an original algorithm, where the matrix sweep method is used [8]. The obtained pressure field on the third stage is used to recalculate the final velocity field. The fourth stage is the final concentration using velocity fields.

3. RESULTS

Calculated by the scheme (1) - (2) concentrations of components at different pressures and mixing times are shown in Fig. 1-2. Calculations were carried out for the system 0.5312Ar + 0.4688He-N_2 on an uniform rectangular grid with the same pitch in all coordinate directions. The total number of nodes of the computational grid constitutes 256x256. The pressure is selected in the range of P=0,2 – 3,0 MPa at T=298K. The taken time step was to be 0.005 seconds. In the calculations the instability of mechanical balance was recorded at P = 1.7 MPa, which corresponds to the experimental data [1, 2], in which at pressure P = 1.6 MPa was recorded a significant discrepancy between the experimental and calculated in the assumption of the diffusion component concentrations.

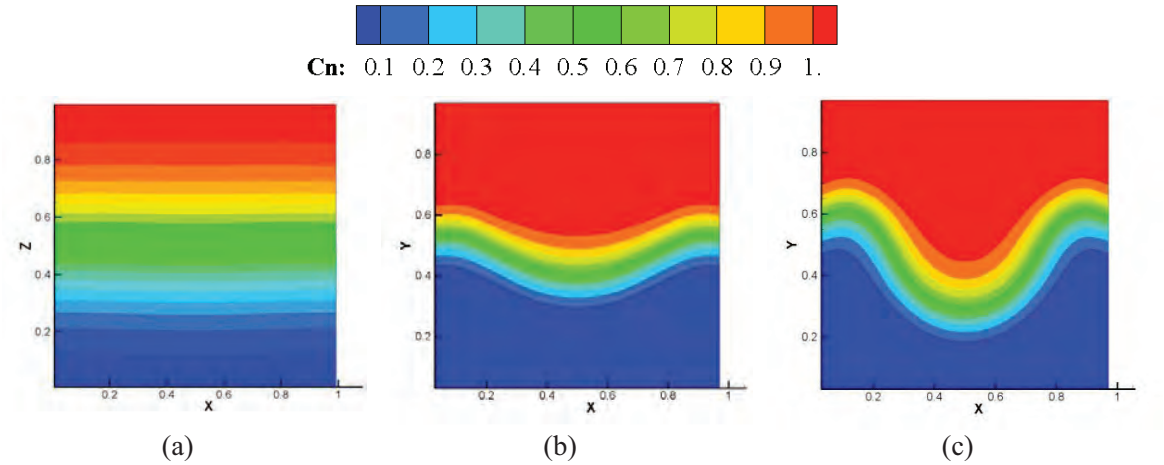

(a) (b) (c)

FIGURE 1. The dynamics of changes in concentration time for different pressure and time of mixing in the system 0.5312Ar+0.4688He- N_2 by T=298 K.

a) P=1.5 MPa, t = 13.5 sec; b) P=2.0 MPa, t = 13.5 sec; c) P=2.0 MPa, t = 18 sec.

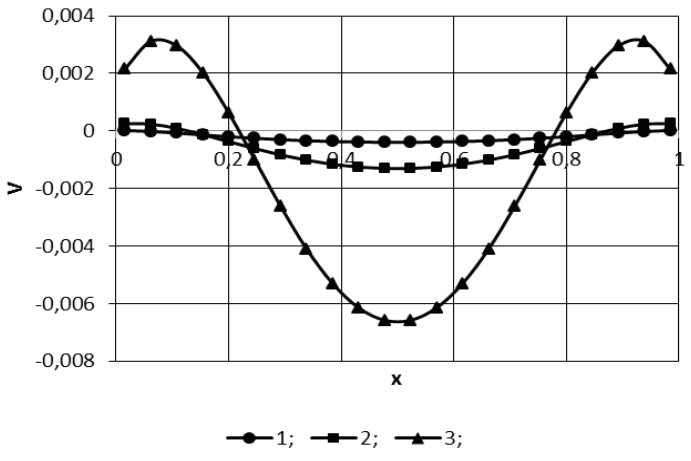

FIGURE 2. Profile velocity V(x) in section y=0.5 at the exact time t = 13.5 sec:
1) P = 0.5 MPa; 2) P = 1.5 MPa; 3) P = 2.0 MPa;

Figure 1a shows the concentration changes of components in consecutive at P = 1.5MPa. The diffusion is observed in the system. A similar pattern in the distribution of concentrations is typical for all mixing time. Increasing the pressure to P = 2.0MPa in the system marks nonlinearity

distribution of concentration (Figure1b), which is the cause of the nonlinear distribution of density of the mixture in the vertical cylindrical channel. In its turn nonlinearity in the density distribution can lead to instability of mechanical equilibrium of mixture. In figure 2 is given the profile in section y = 0.5, which shows the change in the rate of vertical velocity while increasing pressure. Significant nonlinearity in the rate of change of the vertical velocity falls on the pressure P = 2.0MPa, which corresponds to the experimental data [1,2], which was fixed regime change "diffusion - convection". Later there might arise conditions in the gravity field for the formation of convective structures, consisting mainly of the heaviest density component (Figure 1c). Apparently it is exactly this type of current observed in [2,5], where the experimentally recorded convective flows associated with the primary transfer of the component with the desired properties.

4. CONCLUSIONS

There have been offered a mathematical model for the numerical simulation of a complex mass transfer in isothermal ternary gas mixtures at different density. There has been worked out a numerical algorithm to solve the mass transfer of components of mixture in a confined cylindrical channel, where the decision for the area takes the cross section of the cylinder. On the basis of numerical simulation studied the effect of pressure for the systems, where the occurrence of convection is due to the instability of mechanical equilibrium of mixture. Received the critical value of pressure connected with the transition "diffusion - convection."

The part of the results obtained due to the financial support of the grant of the Committee of Science of the Ministry of Education and Science of the Republic of Kazakhstan №3482 / GF4.

REFERENCES

[1] Yu.I. Zhavrin, N.D. Kosov, S.V. Belov, and S.B. Tarasov, S.B., Effect of Pressure on the Diffusion Stability in Some Three-Component Gas Mixtures*, Journal of Technical Physics,* 54, 943-948, 1984.

[2] V.N. Kosov, V.D. Seleznev, and Yu.I. Zhavrin, Separation of components during isothermal mixing of ternary gas systems under free-convection conditions, *Technical Physics,* 42, 1236-1237, 1997

[3] G.Z. Gershuni, E.M. Zhukhovitskii, *Convective Stability of Incompressible Fluids,* Keter, Jerusalem, 1976.

[4] D.D. Joseph, *Stability of Fluid Motions,* Springer, Berlin, 1976

[5] V.N. Kosov, V.D. Seleznev, *Anomalous Onset of the Free Gravitational Convection in Isothermal Ternary Gas Mixtures*, Yekaterinburg, Ural Branch Russian Academy of Science, 2004, (in Russian)

[6] V.N. Kosov, I.V. Poyarkov, and O.V. Fedorenko, Numerical modelling of gravitational convection in three-component gas mixtures in the cylindrical channel, *2nd International Conference on Computational Methods for Thermal Problems, September 5-7, 2011, Dalian, China*, 228-231

[7] N.T. Danaev, D.B. Zhakebaev, and A.U. Abdibekov, Algorithm for solving nonstationary three-dimensional Navier-Stokes equations with large Reynolds numbers on multiprocessor systems, *Notes on Numerical Fluid Mechanics and Multidisciplinary Design*, 115, 313–326, 2011

[8] U.S. Abdibekov, B.T. Zhumagulov, and D.B. Zhakebaev, Numerical modelling of non-homogeneous turbulence on cluster computing system, *Notes on Numerical Fluid Mechanics and Multidisciplinary Design*, 115, 327–338, 2011.

Fourth International Conference on Computational Methods for Thermal Problems
THERMACOMP2016, July 6-8, 2016, Georgia Tech, Atlanta, USA
N. Massarotti, P. Nithiarasu and Y. Joshi (Eds.)

NUMERICAL INVESTIGATION OF LAMINAR RAYLEIGH-BÉNARD CONVECTION OF POWER-LAW FLUIDS IN SQUARE CROSS-SECTIONAL CYLINDIRICAL ANNULAR CAVITY

Sahin Yigit, Nilanjan Chakraborty
School of Mechanical & Systems Engineering, Newcastle University, Newcastle-Upon-Tyne, UK,
s.yigit1@ncl.ac.uk, nilanjan.chakraborty@ncl.ac.uk

ABSTRACT

Steady-state laminar natural convection of power-law fluids in square cross-sectional cylindrical annular cavity heated from bottom wall (i.e. Rayleigh-Bénard configration) has been numerically investigated under the assumption of axisymmetry. The numerical simulations have been conducted for a range of different values of nominal Rayleigh number Ra, the nominal Prandtl number Pr, power-law index n and the internal radius to enclosure height ratio r_i / L (i.e. $10^3 \le Ra \le 10^5$; $10 \le Pr \le 10^4$; $0.6 \le n \le 1.8$ and $0 \le r_i / L \le 16$) for both constant wall temperature (CWT) and constant wall heat flux (CWHF) boundary conditions.

Key Words: *Heat Transfer, non-Newtonian, Natural Convection, Cylindrical Annular Cavity.*

1. INTRODUCTION

Natural convection in enclosures has been analysed extensively for Newtonian fluids (where the relation between shear stress and strain rate is linear). However, limited attention has been given to the natural convection of non-Newtonian power-law fluids despite their growing practical importance in engineering applications (i.e. food and chemical industries, solar power systems and cooling of electronic devices). The laminar Rayleigh-Bénard convection of shear-thinning fluids in rectangular enclosure has been analysed numerically [1] and experimentally [2] and in both cases a strengthening of convective transport with shear thinning has been reported. The effects of Ra, Pr, n [3] on laminar Rayleigh-Bénard convection of power-law fluids in square enclosures have recently been numerically invastigated and correlations for mean Nusselt number have been proposed to account for increasing extent of shear-thinning with decreasing n. Furthermore, the numerical findings in Ref. [3] have been utilised to identify different regimes of laminar natural convection regimes of power-law fluids considering for the effects of Ra, Pr, n. Natural convection of power-law fluids in annular cylindrical cavity is more relevant than the rectangular cavities for applications such as cooling of cylindrical tanks, chemical and food processing etc. However, natural convection of power-law fluids in cylindrical annular space is yet to be analysed in detail. This analysis aims to address this gap in existing literature and the main objective of this study are:

i) To demonstrate the effects of Ra, Pr, n on steady-state laminar Rayleigh-Bénard convection of power-law fluids in square cross-sectional cylindrical annular cavity for different values of r_i / L.

ii) To provide physical explanations for the above effects based on numerical findings.

2. MATHEMATICAL BACKGROUND AND NUMERICAL METHODOLOGY

According to the power-law (Ostwald-De Waele) model the viscous stress tensor τ_{ij} is defined as follows:

$$\tau_{ij} = 2\mu_a e_{ij} = 2K(2e_{kl}e_{kl})^{(n-1)/2} e_{ij} \tag{1}$$

where $e_{ij} = 0.5(\partial u_i / \partial x_j + \partial u_j / \partial x_i)$ is the rate of strain tensor, K is the consistency and n is the power-law index. The apparent viscosity μ_a decreases (increases) with increasing shear rate for $n<1$ ($n>1$). Thus, the fluids with power-law indexes with $n<1$ ($n>1$) are referred to shear-thinning (shear-thickening) fluids, where $n=1$ for Newtonian fluids.

Using dimensional analysis, it is possible to show that the mean Nusselt number for natural convection of power-law fluids in square cross-sectional cylindrical annular enclosure can be expressed as: $Nu = f_1(Ra, Pr, n, r_i / L)$, where the nominal Rayleigh and Prandtl numbers for power-law fluids can be defined for CWT and CWHF configurations in the following manner:

$$Ra_{CWT} = \frac{g\beta(T_H - T_C)L^{2n+1}}{\alpha^n (K/\rho)};\ Ra_{CWHF} = \frac{g\beta q L^{2n+2}}{\alpha^n k (K/\rho)} \text{ and } Pr = (K/\rho)\alpha^{n-2} L^{2-2n} \tag{2}$$

where g, β, T_H, T_C, q, α, k and ρ are the acceleration due to gravity, volume expansion coefficient, hot wall temperature, cold wall temperature, wall heat flux, thermal diffusivity, thermal conductivity and density respectively. For the current analysis the differentially heated horizontal walls are considered to be subjected to constant wall temperatures (CWT) constant wall heat flux (CWHF) as shown in Fig.1.

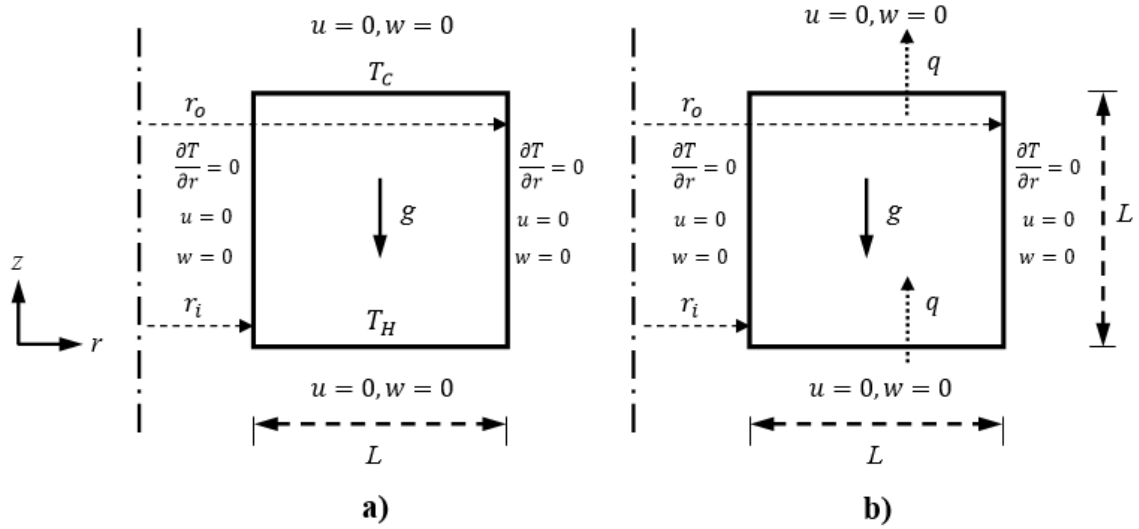

FIGURE 1. Schematic diagram of simulation domain: a) CWT, b) CWHF configurations

The steady-state conservation equations of mass, momentum and energy equations in cylindrical coordinates are solved in the framework of the finite-volume methodology. The well-known SIMPLE semi-implicit pressure based algorithm is used for the coupling between pressure and velocity. A detailed grid independence analysis has been conducted using a number of different non-uniform meshes in order to establish grid independent results for Newtonian (i.e. $n=1$), shear-thinning fluids ($n<1$) and shear-thickening fluids ($n>1$). The simulation results have been benchmarked with respect to previous findings for Newtonian [4] and power-law fluids [5] respectively.

3. RESULTS & DISCUSSION

The variation of $\overline{Nu} = \int_{r_i}^{r_i+L} 2\pi r Nu(r)dr / [\pi(r_i+L)^2 - \pi r_i^2]$ with r_i / L for different values of nominal Ra for both CWT and CWHF boundary conditions for shear-thinning ($n = 0.6$), Newtonian ($n = 1$) and shear-thickening ($n = 1.8$) fluids at $Pr = 10^3$ is shown in Fig. 2.

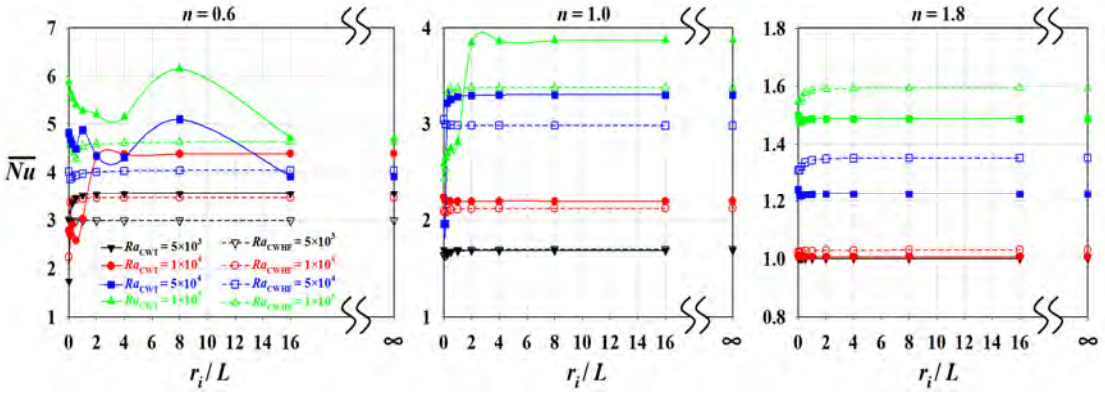

FIGURE 2. Variation of $\overline{Nu}$ with r_i / L for different values of nominal Ra for both CWT and CWHF boundary conditions for $n = 0.6$ (1st column), 1.0 (2nd column) and 1.8 (3rd column) at $Pr = 10^3$.

It can be seen from Fig. 2 that $\overline{Nu}$ does not always show a monotonic increase with increasing Ra despite strengthening of buoyancy forces. This non-monotonic trend of $\overline{Nu}$ is relative prevalent for small values of r_i / L but whereas the value of $\overline{Nu}$ approaches the value obtained for square enclosures ($r_i / L \to \infty$) for large values of r_i / L in the case of both CWT and CWHF boundary conditions.

CWT					CWHF				
r_i/L \ Ra	5×10^3	10^4	5×10^4	10^5	r_i/L \ Ra	5×10^3	10^4	5×10^4	10^5
0	a	a	a	a	0	c	a	a	a
1	c	b	b	a	1	c	c	b	b
8	c	c	b	b	8	c	c	b	b
16	c	c	d	d	16	c	c	b	b
Square	c	c	d	d	Square	c	c	e	e
Flow Patterns									
a		b		c		d		e	
									

FIGURE 3. Flow patterns for different values of Ra for both CWT and CWHF boundary conditions for $n = 0.6$ and $Pr = 10^3$.

This non-monotonic variation of $\overline{Nu}$ with increasing Ra can be explained by change in the flow patterns. The schematic depiction of the flow patterns for different values of Ra and r_i / L for both

CWT and CWHF boundary conditions is shown in Fig.3 for $n = 0.6$ and $Pr = 10^3$. Moreover, Table 1 lists the nominal values of critical Rayleigh number Ra for the onset of convection and these critical Ra values have been estimated by reducing Ra in steps of 50 (250) for shear thinning and Newtonian (shear thickening) fluids from the one-cell flow pattern with $\overline{Nu} > 1.001$.

n	Ra_{CWT}				Ra_{CWHF}			
	r_i / L				r_i / L			
	0	1	16	Square	0	1	16	Square
0.6	750	800	800	800	650	650	650	650
0.8	1400	1550	1550	1600	1150	1150	1150	1150
1	2250	2600	2600	2600	1700	1700	1700	1700
1.4	3250	3500	3500	3500	2000	2000	2000	2000
1.8	5000	5000	5000	5000	2500	2500	2500	2500

Table 1. The value of Ra at which $\overline{Nu}$ deviates from unity in the third decimal place (i.e. $\overline{Nu} >$ 1.001) for different values of n and r_i / L for both CWT and CWHF boundary conditions at $Pr = 10^3$.

4. CONCLUSIONS

It is found that convective transport is stronger for CWT boundary condition than for CWHF boundary condition for large (small) values of Ra (n) for a given set of values of n, Ra, Pr and r_i / L but an opposite trend is observed for small (large) values of Ra (n). The mean Nusselt number $\overline{Nu}$ does not show a monotonic increase with increasing (decreasing) Ra (n) especially for small values of r_i / L due to a change in flow pattern (i.e number of convection cells). However, the mean Nusselt number $\overline{Nu}$ and flow patterns for large values of r_i / L approach those for square enclosures ($r_i / L \to \infty$) for both CWT and CWHF boundary conditions. Additionally, the critical Rayleigh number Ra_{crit} for the onset of convection is found to be independent of r_i / L for both CWT and CWHF boundary conditions.

REFERENCES

[1] M. Lamsaadi , M. Naïmi , M. Hasnaoui, Natural convection of non-Newtonian power law fluids in a shallow horizontal rectangular cavity uniformly heated from below, *Heat Mass Transfer* 41, 239-249, 2005.

[2] H. Inaba, C. Daib and A. Horibe, Natural convection heat transfer of micro-emulsion phase-change material slurry in rectangular cavities heated from below and cooled from above, *Int. J. Heat Mass Transfer*, 46, 4427-4438, 2003.

[3] O. Turan, F. Fotso-Choupe, J. Lai, R.J. Poole and N. Chakraborty, Boundary condition effects on laminar natural convection of power-law fluids in a square enclosure heated from below with differentially heated horizontal walls, *Ind. Eng. Chem. Res.*, 53, 456-473, 2014.

[4] G. de Vahl Davis, Natural convection of air in a square cavity: A bench mark numerical solution, *Int. J. Numer. Meth. Fluids*, 3, 249–264, 1983.

[5] G. B. Kim, J.M. Hyun, H. S. Kwak, Transient buoyant convection of a power law non-Newtonian fluid in an enclosure, *Int. J. Heat Mass Transfer*, 46, 3605-3617, 2003.

PARALLEL SESSION

REACTIVE HEAT AND MASS TRANSPORT

Fourth International Conference on Computational Methods for Thermal Problems
THERMACOMP2016, July 6-8, 2016, Georgia Tech, Atlanta, USA
N. Massarotti, P. Nithiarasu and Y. Joshi (Eds.)

Non-equilibrium Framework Applicable at all Spatial and Temporal Scales Using Steepest-Entropy-Ascent Quantum Thermodynamics

Guanchen Li and Michael R. von Spakovsky
Department of Mechanical Engineering, Virginia Tech
Blacksburg, VA 24061, USA
guanchen@vt.edu, vonspako@vt.edu

ABSTRACT

Steepest-entropy-ascent quantum thermodynamics (SEAQT) is a novel non-equilibrium first-principles thermodynamic-ensemble based framework, which has successfully been applied to a variety of systems from quantum spin systems to mesoscopic solid oxide fuel cell systems to macroscopic systems. Based on recent developments by the authors, this framework has become an approach applicable to the study of non-equilibrium phenomena across all temporal and spatial scales. This paper provides an overview of some of the key theoretical aspects of this framework developed by the authors including the density of states method, which effectively extends the framework to infinite-dimensional state spaces, and the concepts of hypo-equilibrium state and non-equilibrium intensive properties, which lead to a fundamental generalization of the stable equilibrium framework to the non-equilibrium realm even that far from equilibrium.

Key Words: *non-equilibrium thermodynamics, steepest-entropy-ascent quantum thermodynamics.*

1. INTRODUCTION

Conventional approaches for studying non-equilibrium phenomena are of two types. The first is based on the mechanics of individual particles or quantum states. The mechanics is acquired from first-principles (i.e., Newton's law or quantum mechanics) using, for example, molecular dynamics (MD) and kinetic theory (KT) or from stochastic dynamics using, for example, Monte Carlo (MC) simulations. These approaches contain all the details of the mechanical features of the system (e.g., particle position and velocity at any instant of time, particle collisions, etc.) needed to arrive at a set of macroscopic properties, resulting, however, in a huge computational burden. The second type is based on an ensemble view with the laws of thermodynamics acting as first principles. Onsager's theory, linear response theory, and fluctuation theory are examples of this type of approach. However, the applicability of these methods is limited in the non-equilibrium realm. Local-equilibrium or near-equilibrium assumptions are needed, and limitations to steady state or the use of an environmental reservoir are also necessary in many applications.

In contrast to these conventional approaches, the SEAQT framework attempts to explain non-equilibrium phenomena from a first-principle, thermodynamic-ensemble viewpoint. Irreversibility is captured via intrinsic entropy generation using the steepest entropy ascent principle rather than from collisions or some scattering process, which means system state evolution is entropy-driven and the laws of thermodynamics act as first principles. The equation of motion is developed on the basis of a gradient dynamics in system state space instead of the microscopic mechanics of more traditional approaches and can be regarded as resulting from a pattern of the more microscopic mechanical model. In a manner similar to the way at stable equilibrium one can view the "Maxwellian distribution" as an invariant pattern even though the mechanical details of the individual particle states constantly change, steepest entropy ascent can also be viewed as a changing global pattern or effect of the details of the mechanics in relaxation. Thus, without including all of the details of the more microscopic model (i.e., of the mechanics), the pattern of this model serves as a modification of the more macroscopic model (i.e., of the non-equilibrium thermodynamics). This, of course, greatly simplifies the computational complexity, while the clear physical meaning and geometrical description of the SEA landscape facilitates the discovery of

general but unique patterns of relaxation in the non-equilibrium realm at any scale. As an example of computational time, to model a transient multi-phase, multi-component, multi-scale system (i.e., a solid oxide fuel cell (SOFC) cathode) with heat conduction, an externally applied field, diffusion, and multiple coupled electrochemical reaction pathways [1] requires only a few hours on a PC workstation. In general, the SEAQT framework has successfully been applied to a variety of systems from quantum spin to mesoscopic to macroscopic systems [1-6].

2. GENERAL THEORY

A general equation of motion can be written using the generalized form of the Ginzburg-Landau equation [7, 8] expressed as

$$\frac{d}{dt}\alpha(t) = X^H_{\alpha(t)} + Y^H_{\alpha(t)} \tag{1}$$

where $\alpha(t)$ represents the state evolution trajectory, $X^H_{\alpha(t)}$ and $Y^H_{\alpha(t)}$ are functions of the system state $\alpha(t)$ and represent the reversible symplectic dynamics and irreversible relaxation dynamics, respectively. If the reversible symplectic dynamics vanishes, the equation of motion describes a pure relaxation process. In SEAQT, the irreversible part is explained from an entropy generation viewpoint and is given using the steepest entropy ascent principle [9], which can be presented as a local variational principle: maximize $\dot{S}(\dot{\boldsymbol{x}}) = (\dot{\boldsymbol{x}}, \boldsymbol{g_S})$ subject to $\dot{E} = (\dot{\boldsymbol{x}}, \boldsymbol{g_E}) = 0$, $\dot{I} = (\dot{\boldsymbol{x}}, \boldsymbol{g_E}) = 0$, $(\dot{\boldsymbol{x}}, \dot{\boldsymbol{x}}) = \xi(\boldsymbol{x})$ with $\delta\dot{\boldsymbol{x}} \neq 0$, $\delta\boldsymbol{x} = 0$. Here, $\boldsymbol{x}$ represents the state of the system, and (,) is the inner product of the vector in system state space. The third constraint on $\dot{\boldsymbol{x}}$ indicates that only the direction of $\dot{\boldsymbol{x}}$ is of interest. This variational principle is in microscopic state space, which contrasts with the variational principle in the macroscopic state space spanned by conjugate fluxes and forces presented later for the Onsager relations. If the system is defined by its energy eigenlevels $\{\epsilon_i\}$ and system state is represented by the probability distribution $\{p_i\}$ among the energy eigenlevels. The equation of motion takes the form on the left of Eq. (2), namely,

$$\frac{dp_j}{dt} = \frac{1}{\tau}\frac{\begin{vmatrix} p_j \ln p_j & p_j & \epsilon_j p_j \\ \langle s\rangle & 1 & \langle e\rangle \\ \langle es\rangle & \langle e\rangle & \langle e^2\rangle \end{vmatrix}}{\begin{vmatrix} 1 & \langle e\rangle \\ \langle e\rangle & \langle e^2\rangle \end{vmatrix}}, \qquad \frac{dP_j}{dt} = \frac{1}{\tau}\frac{\begin{vmatrix} P_j \ln P_j/n_j & P_j & E_j P_j \\ \langle s\rangle & 1 & \langle e\rangle \\ \langle es\rangle & \langle e\rangle & \langle e^2\rangle \end{vmatrix}}{\begin{vmatrix} 1 & \langle e\rangle \\ \langle e\rangle & \langle e^2\rangle \end{vmatrix}} \tag{2}$$

The number of energy eigenlevels (or the dimension of state space) of a system can be small (e.g., such as that for a quantum spin system) or almost infinite (e.g., such as that for a macroscopic ideal gas at room temperature). To enable solving the equation of motion for a system with an infinite-dimensional state space, the density of states method developed in [3, 4] can be used to reduce the dimension of the state space to a finite manageable one. It is based on the observation that neighbouring eigenlevels with similar initial conditions have similar time evolutions and contributions to the system intensive properties. Thus, these eigenlevels can be combined to form one energy eigenlevel of degenercy n_j at energy $E_j = \sum\epsilon_i/n_j$ with initial probability $P_j = \sum p_i$, where the summation is over the neighboring eigenlevels. The equation of motion then takes the form given on the right of Eq. (2). By doing this, the SEAQT framework can be applied to systems at all temporal and spatial scales.

The solution of the SEA-QT equation of motion exhibits some convenient properties. Based on the developments of the authors, the non-equilibrium relaxation captured by this equation of motion can be completely described using the concepts of hypo-equilibrium state and non-equilibrium intensive properties [3, 4]. The energy eigenlevels of the system $\{\epsilon_i\}$ can be divided into to M sets $\{\epsilon_i^K\}$ (degeneracy $\{n_i^K\}$) with i=1, 2, 3,..., K=1, 2,..., M, so that system state can be represented by the distributions $\{p_i^K\}$ in M subspace energy eigenlevels. If the probability distribution in one subspace, for example, the K^{th} subspace yields to the canonical distribution of parameter β_K, the temperature of the K^{th} subspace is defined to be $T^K = 1/(\beta_K k_b)$. Given a way to divide the energy eigenlevels and provided the system probability distributions in the M subspaces are all canonical distributions,

the state of the system can be called a M^{th}-order hypo-equilibrium state [3], which can be described uniquely by the total probability in each subspace ($\{p^K\}$) and the temperature of each of the subspaces ($\{T^K\}$). Li and von Spakovsky [3] have proven that the system retains a M^{th}-order hypo-equilibrium state throughout the non-equilibrium relaxation process if it initially starts out in such a state. The solution to Eq. (2), thus, becomes

$$p_i^K(t) = \frac{p^K(t)}{Z_K(\beta^K(t))} n_i^K e^{-\beta^K(t)\epsilon_i^K} = n_i^K e^{-\alpha^K(t)-\beta^K(t)\epsilon_i^K} \tag{3}$$

where α^K and β^K are called non-equilibrium intensive properties in the K^{th} subspace and correspond to the extensive properties p^K and E^K. As a result, each subspace has temperature defined throughout the entire non-equilibrium relaxation process.

3. NON-EQUILIBRIUM THERMODYNAMIC RELATIONS

Both the particle number and energy evolution of the K^{th} subspace can be obtained from Eq. (2) by summation over one subspace such that

$$\frac{dp^K}{dt} = \frac{1}{\tau} p^K(\alpha^K - \alpha) + \frac{1}{\tau} E^K(\beta^K - \beta) \tag{4}$$

$$\frac{dE^K}{dt} = \frac{1}{\tau} E^K(\alpha^K - \alpha) + \frac{1}{\tau} \langle e^2 \rangle^K(\beta^K - \beta) \tag{5}$$

where α, β are found from Eq. (2), $\langle e^2 \rangle$ is the contribution of the K^{th} subspace to the expectation value of the second moment of the energy of the system, and p^K and E^K are the probability and energy, respectively, in the K^{th} subspace. When a system is in a M^{th}-order hypo-equilibrium state and undergoes a pure relaxation process, a relation for the evolution of the extensive properties evolution in one subspace exists and is given by

$$dS^K = \beta^K \frac{dE^K}{dt} + (\alpha^K - 1)\frac{dp^K}{dt} \tag{6}$$

where S^K is the entropy in the K^{th} subspace. This is the Gibbs relation for the subspace where the physical meaning of β^K and that of α^K is

$$\beta^K = \left(\frac{\partial S^K}{\partial E^E}\right)_{p^K} = \frac{1}{T^K}, \qquad \alpha^K - 1 = -\frac{\mu^K}{T^K}, \qquad \mu^K = \left(\frac{\partial E^K}{\partial p^K}\right)_{S^K} \tag{7}$$

Here T^K is the subspace temperature and μ^K is its chemical potential with respect to the subspace probability p^K. The differential change in the total entropy or in this case the entropy generation is then expressed as

$$dS = \sum_K dS^K = \sum_K (\alpha^K - \alpha) dp^K + \sum_K (\beta^K - \beta) dE^K \tag{8}$$

where both energy ($\sum dE^K = 0$) and probability ($\sum dp^K = 0$) conservations have been applied. With $J_E^K = dE^K/dt$ and $J_p^K = dp^K/dt$ defined as the internal fluxes of energy and probability inside the system and $X_p^K = \beta^K - \beta$ and $X_E^K = \alpha^K - \alpha$ as their corresponding conjugate forces, the Casimir condition can be written as

$$\frac{dS}{dt} = \sum_K X_E^K J_E^K + \sum_K X_p^K J_p^K \tag{9}$$

The Onsager relations are now acquired from Eqs. (4) and (5) in the form of $\boldsymbol{J} = \boldsymbol{\Lambda X}$, where $\boldsymbol{\Lambda}$ is symmetric and positive definite, so that

$$J_p^K = \frac{1}{\tau} p^K X_p^K + \frac{1}{\tau} E^K X_E^K, \qquad J_E^K = \frac{1}{\tau} E^K X_p^K + \frac{1}{\tau} \langle e^2 \rangle X_E^K \tag{10}$$

Finally, the quadratic dissipation potential in force representation [10] is

$$\Xi(\boldsymbol{X}, \boldsymbol{X}) = \frac{1}{2} \langle \boldsymbol{X}, \boldsymbol{\Lambda X} \rangle \tag{11}$$

Thus, from the entropy generation of a non-equilibrium isolated system derived from the relaxation gradient dynamics of SEAQT, which are based on the geometry of system state space, one is able to arrive at the Onsager relations and the quadratic dissipation potential using the concepts of hypo-

equilibrium state and non-equilibrium intensive properties. One can also arrive at these relations and this potential using a variational principle in system state space as is done in [11]. Of course, the Onsager relations and quadratic dissipation potential correspond to a variational principle in the space spanned by conjugate forces and fluxes as well [10]. A detailed Onsager investigation using the concepts of hypo-equilibrium state and non-equilibrium intensive properties are found in [3, 4]. For a general discussion of the Onsager relation in SEAQT using the language of quantum mechanics, the reader is referred to [11].

4. CONCLUSIONS

Using the density of states method, SEAQT becomes an approach practically applicable to all temporal and spatial scales. The reader is referred to [1, 3-6] for applications. Using the concept of hypo-equilibrium state, the non-equilibrium intensive properties together with the extensive properties provide a complete description of the non-equilibrium relaxation process and are in effect a fundamental generalization of the stable equilibrium framework to the non-equilibrium realm even that far from equilibrium. As also shown above, the relaxation process, which is the evolution of an isolated system in non-equilibrium, can also be described using an Onsager type of investigation, arriving at a set of non-equilibrium thermodynamic relations such as the Gibbs relation, the Casimir condition, the Onsager relations, the Clausius inequality (not shown above), etc. Thus, SEAQT results in a new, less computationally intensive, non-equilibrium thermodynamic approach for modeling reactive and non-reactive systems at any scale as well as across scales.

REFERENCES

[1] G. Li, M. R. von Spakovsky, Study of the transient behavior and microstructure degradation of a SOFC cathode using an oxygen reduction model based on steepest-entropy-ascent quantum thermodynamics, *ASME 2015 IMECE*, IMECE2015-53726, 2015.

[2] C., Sergio, G. P. Beretta, and M. R. von Spakovsky. Steepest-entropy-ascent quantum thermodynamic modeling of decoherence in two different microscopic composite systems. *Phys. Rev. A*, 91, 1, 013848, 2015.

[3] G. Li and M. R. von Spakovsky, Steepest-entropy-ascent quantum thermodynamic modelling of the relaxation process of isolated chemically reactive systems using density of states and the concept of hypo-equilibrium state, *Phys. Rev. E*, 2015, in publication.

[4] G. Li, *Non-equilibrium thermodynamic approach based on steepest-entropy-ascent quantum thermodynamics applicable across all temporal and spatial scales*, Ph.D. dissertation, advisor: M. R. von Spakovsky, Virginia Tech, Mechanical Engineering Dept., 2015.

[5] G. Li, O. Al-Abbasi, and M. R. von Spakovsky, Atomistic-level non-equilibrium model for chemically reactive systems based on steepest-entropy-ascent quantum thermodynamics, *Journal of Physics: Conference Series*, 538, 1, 012013, 2014.

[6] G. Li, M. R. von Spakovsky, Application of steepest-entropy-ascent quantum thermodynamics to predicting heat and mass diffusion from the atomistic up to the macroscopic level, *ASME 2015 IMECE*, IMECE2015-53581, 2015.

[7] M. Grmela and H. C. Öttinger, Dynamics and thermodynamics of complex fluids. i. development of a general formalism, *Phys. Rev. E*, 56, 6620–6632, 1997.

[8] H. C. Öttinger and M. Grmela, Dynamics and thermodynamics of complex fluids. ii. Illustrations of a general formalism, *Phys. Rev. E*, 56, 6633–6655, 1997.

[9] G. P. Beretta, Nonlinear model dynamics for closed-system, constrained, maximal-entropy-generation relaxation by energy redistribution, *Phys. Rev. E*, 73, 026113, 2006.

[10] I. Gyarmati, E. Gyarmati, and W. F. Heinz, *Non-equilibrium thermodynamics*, Springer, 1970.

[11] G. P. Beretta, Nonlinear quantum evolution equations to model irreversible adiabatic relaxation with maximal entropy production and other nonunitary processes, *Reports on Mathematical Physics*, 64, 1-2, 139–168, 2009.

Fourth International Conference on Computational Methods for Thermal Problems
THERMACOMP2016, July 6-8, 2016, Georgia Tech, Atlanta, USA
N. Massarotti, P. Nithiarasu and Y. Joshi (Eds.)

Non-equilibrium Predictions of Diffusion in Closed and Open Systems at Atomistic Levels Using Steepest-Entropy-Ascent Quantum Thermodynamics

Aimen M. Younis, Michael R. von Spakovsky
Mechanical Engineering Department, Virginia Tech
Blacksburg, Virginia, 24061, USA,
younis@vt.edu, vonspako@vt.edu

ABSTRACT

The principal approach found in the literature for predicting the non-equilibrium phenomenon of diffusion in closed systems at atomistic levels is equilibrium-based. The purpose of such an approach is to describe the phenomenon of diffusion at states very close to equilibrium. In order to understand diffusion at states far from equilibrium, an atomistic-level approach, which makes no limiting equilibrium assumption, is needed. Such an approach is intrinsic quantum thermodynamics (IQT), and it is the application of its mathematical framework steepest-entropy-ascent quantum thermodynamics (SEAQT), which is used here to predict diffusion in both closed and open atomistic-level systems. The closed system is that of He^3 diffusing in He^4, while the open system is that of O_2 diffusing in a tin anode. Both systems are first defined geometrically and the energy eigenstructure of each established. The SEAQT equation of motion without mass interaction terms is then applied to the non-equilibrium state evolution of the isolated, closed system, while that with mass interactions is applied to the transient state evolution of the open system. Both systems are initially prepared in states far from stable equilibrium after which each is allowed to evolve to stable equilibrium in the case of the closed, isolated system and to steady state in the case of the open system. Results show in detail the non-equilibrium and transient thermodynamic paths that the closed and open systems take, respectively.

Key Words: *non-equilibrium thermodynamics, diffusion, steepest-entropy-ascent quantum thermodynamics.*

1. INTRODUCTION

Intrinsic quantum thermodynamics (IQT) and its mathematical framework steepest-entropy-ascent quantum thermodynamics (SEAQT) are used to model and describe the non-equilibrium phenomenon of diffusion at atomistic levels [1]. The SEAQT framework is able to describe the evolution in state of a system undergoing a dissipative process based on the principle of steepest entropy ascent or locally maximal entropy generation. The dynamical postulate of this theory was formulated originally to predict the evolution dynamics of closed, isolated systems composed of a single particle, an assembly of indistinguishable particles, or a field or alternatively a set of distinguishable particles, fields, or some combination of these [2]. More recently the SEAQT equation of motion has been extended to model a larger class of systems, namely, those involving heat and/or mass interactions [3-5]. This framework is used here to develop a non-equilibrium-based model for an isolated system in which He^3 diffuses in He^4. The model developed is able to predict the non-equilibrium and equilibrium characteristics of diffusion as well as capture the differences in behavior of fermions (He^3) and bosons (He^4). The SEAQT framework is also used to develop the transient and steady-state model for an open system in which O_2 diffuses through a tin anode. Two forms of the SEAQT equation of motion are used. The first only involves the dissipative term and is applied to the state evolution of the isolated system as its state relaxes from

some initial non-equilibrium state to stable equilibrium. The second form of this equation, the so-called extended SEAQT equation of motion, is applied to the transient state evolution of an open system undergoing a dissipative process as well as mass-interactions with two mass reservoirs [1, 3, 5]. In this case, the state of the system relaxes from some initial transient state to steady state. Model predictions show that the non-equilibrium thermodynamic path that the isolated system takes significantly alters the diffusion values from those of the equilibrium-based models for isolated atomistic-level systems found in the literature. Nonetheless, the SEAQT equilibrium predictions for He^3 and He^4 capture the same trends as those found in the literature [6], providing a point of validation for the SEAQT framework. For the open system, there are no comparable studies in the literature with which to compare since the SEAQT results presented here are completely original to this work.

2. SEAQT MODEL

In modeling the non-equilibrium time evolution of state of these systems, both the system energy eigenvalue problems and the non-linear SEAQT equation of motion must be solved. The former establish the so-called energy eigenstructure of the system, while the latter determines the unique non-equilibrium thermodynamic path taken by the system. The SEAQT equation of motion without mass interaction terms is then applied to the non-equilibrium state evolution of the isolated, closed system, while that with mass interactions is applied to the transient state evolution of the open system. Both systems are initially prepared in states far from stable equilibrium after which each is allowed to evolve to stable equilibrium in the case of the closed, isolated system and to steady state in the case of the open system. For the former, the boson and fermion distribution functions are based on the non-equilibrium density operator of the SEAQT description and are defined by an ensemble of two particles (i.e., either two He^3 diffusing into two He^4 or vice versa). For two identical particles of mass m in a one-dimensional box of length L, the energy eigenvalue problem for translation only (since the particles are monatomic) is given by

$$e_{tr} = \frac{\hbar^2 \pi^2}{2\, m\, L^2}(k_1^2 + k_2^2)\ ,\ k_1, k_2 = 1,2,\ldots \tag{1}$$

where $e_{tr}$is the translational energy eigenvalue, $\hbar$ is the reduced Planck's constant, m is the mass of the particles, k_1 and k_2 are the quantum numbers for the two-particle energy eigenlevels, and x_1 and x_2 are the positions of the two particles. In the case of an open system, the energy eigenvalues for translation, vibration, and rotation for the oxygen molecule are given by a set of numerical values for translation and a set of closed-form relations for vibration and rotation. For translation, the following governing equation is solved numerically:

$$\frac{-\hbar^2}{2\, m_{o_2}}\left(\frac{\partial^2\psi(\vec{r})}{\partial x^2} + \frac{\partial^2\psi(\vec{r})}{\partial y^2} + \frac{\partial^2\psi(\vec{r})}{\partial z^2}\right) + V(\vec{r})\,\psi(\vec{r}) = e_{tr}\,\psi(\vec{r}) \tag{2}$$

Here, $\psi(\vec{r})$ is the eigenfunction; $\vec{r}$ is the position vector as a function of $x, y,$ and z; m_{o_2} is the mass of the oxygen molecule O_2; and $V(\vec{r})$ is the potential energy that describes the interactions between the oxygen molecule and the tin atoms. These interactions are captured by the Lennard-Jones-Devonshire potential. Eq. (2) is solved numerically by using finite element analysis with a structured grid. For both vibration and rotation, the energy eigenvalues are given by

$$\varepsilon_v^{vib} = v\left(v + {}^1/_2\right)\omega\hbar^2, \qquad \varepsilon_J^{rot} = \frac{J(J+1)\,\hbar^2}{2\,\mu\, r^2} \tag{3}$$

where v is the vibrational quantum number, which takes values of v =0,1,2, …; ω is the vibrational frequency; $\hbar$ is Plank's modified constant, J is the rotational quantum number that takes values of J = 0,1,2, …; μ is the reduced mass; and r the distance between two atoms. The SEAQT equation of motion with two mass interactions for the systems considered here is the following:

$$\frac{d\rho}{dt} = \frac{-i}{\hbar}[H,\rho] + \frac{1}{2k_b\,\tau_D}\{\Delta M,\rho\} + \frac{1}{2k_b\,\tau_{G_1}}\{\Delta G_1,\rho\} - \frac{1}{2k_b\,\tau_{G_2}}\{\Delta G_2,\rho\} \tag{4}$$

where k_b is Boltzmann's constant, ρ is the density or so-called "state" operator, H is the Hamiltonian operator, t is the time, G is a Massieu-like mass interaction operator, and M is the non-equilibrium Massieu disspative operator. τ_D, τ_{G_1}, and τ_{G_2} are the relaxation times that play an important role in scaling and adjusting the relative strengths of each of the operators, i.e., the dissipation and the mass interactions. Subscripts 1 and 2 stand for the inlet and outlet of the open system, respectively. The anti-commutator operators $\{.\}$ are defined as

$$\{\Delta M,\rho\} = \Delta M\,\rho + \rho\,\Delta M, \quad \{\Delta G_i,\rho\} = \Delta G_i\,\rho + \rho\,\Delta G_i\,,\ i = 1,2 \tag{5}$$

In the case of a closed system, the last two terms in Eq. (4) vanish because the closed system undergoes a dissipative process only. Based on the choice of initial conditions, which ensure that both systems undergo a pure relaxation process, the first term to the right of the equals in Eq. (4), the so-called Schrödinger term, also vanishes.

3. RESULTS

Figure 1 shows the energy-entropy diagram of the Fermion gas (He^3) in the closed, isolated system. Also shown is the non-equilibrium thermodynamic path of the time evolution of system state from a state initially at non-equilibrium, i.e., A_0, to a final state at stable equilibrium, i.e., A_{se}. The initial energy of the system, which has an energy eigenstructure based on 100 energy eigenvalues, is picked to be consistent with a temperature at stable equilibrium of 1 K. The non-equilibrium thermodynamic path is then generated by the SEAQT equation of motion. Figure 2 shows the entropy of the system increasing very rapidly at the beginning of the evolution and then slowing its increase to reach the maximum entropy value at stable equilibrium. At the beginning of the evolution, the entropy generation rate $\dot{S}$ has a peak value and then decreases to zero at stable equilibrium. Note that the entropy generation rate always remains positive.

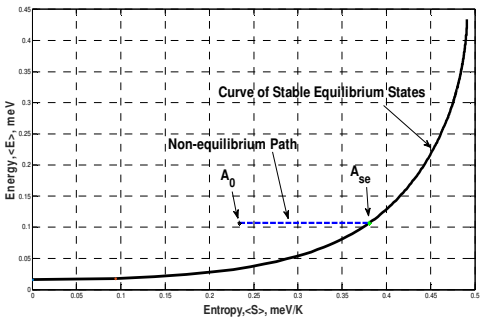

FIGURE 1. Energy-entropy diagram at $T_{se} = 1$ K for a Fermion gas (He^3) where A_0 and A_{se} represent the initial and final states, respectively.

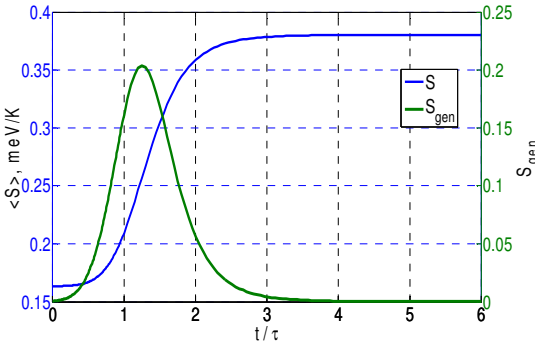

FIGURE 2. Entropy and entropy generation rate as a function of dimensionless time at $T_{se} = 1$ K for He^3.

Figure 3 shows the state of the open system relaxing from its initial non-equilibrium state (green circle) to that of steady state (red circle). At the initial non-equilibrium state, the energy, entropy and number of particles of the system are low, after which they increase along the steepest entropy ascent path to steady state. Figure 4 shows that the steady state diffusivity values of oxygen are lower than those for the transient states. Furthermore, the lowest steady state value occurs at the center of the box, i.e., at $x = 5$ nm, while the steady state values at the inlet and outlet surfaces are approximately the same. Thus, the steady state spatial distribution of the diffusivity of oxygen is symmetric in the x-direction, while those in the transient region are clearly not.

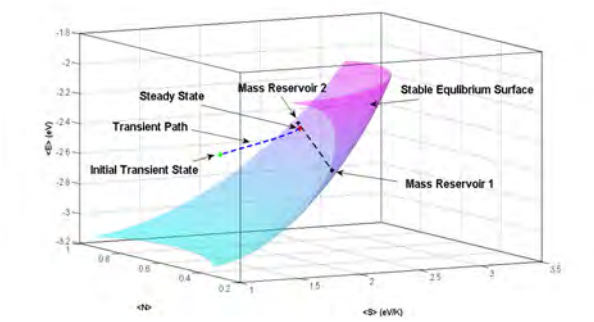

FIGURE 3. Non-equilibrium thermodynamic path (blue curve) that describes the transient relaxation of state of the open system towards steady state. The green and red dots represent the initial and steady states of the system, respectively.

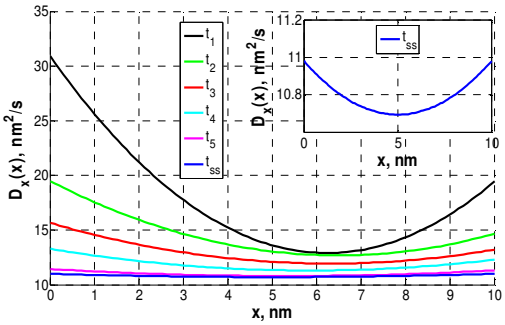

FIGURE 4. Temporal and one-dimensional spatial evolutions of diffusivities for the open system of oxygen diffusion through the tin anode as the system relaxes from an initial transient state to steady state.

4. CONCLUSIONS

The SEAQT framework is an effective approach for modeling and describing the non-equilibrium effects of diffusion for both closed and open systems. As outlined here and as demonstrated in [1], the SEAQT results underline the limitations of using a purely equilibrium-based approach for predicting what is in essence a non-equilibrium process, particularly in regions far from equilibrium. Though limited to atomistic scales and very low temperatures in this work, the SEAQT framework, as demonstrated in [4], is applicable across all spatial and temporal scales, providing a single fundamental kinematic and dynamic description. The computational advantages of such an approach, which intrinsically satisfies all the laws of physics (classical or quantum) and thermodynamics, are significant for multi-scale, multi-physics modeling.

REFERENCES

[1] Younis, A.M., "Modeling the non-equilibrium phenomenon of diffusion in closed and open systems at an atomistic level using steepest-entropy-ascent quantum thermodynamics," Ph.D. dissertation, advisor: M.R. von Spakovsky, M.E. Dept., Virginia Tech, Blacksburg, VA (2015).

[2] Beretta, G.P., "Nonlinear model dynamics for closed-system, constrained, maximal-entropy-generation relaxation by energy redistribution," *Physical Review E*, 73(2), 026113 (2006).

[3] Smith, C.E., "Intrinsic Quantum Thermodynamics: Application to Hydrogen Storage on a Carbon Nanotube and Theoretical Consideration of Non-Work Interactions," Ph.D. dissertation, advisor: M.R. von Spakovsky, M.E. Dept., Virginia Tech, Blacksburg, VA (2012).

[4] Li, G. and von Spakovsky, M.R., "Steepest-entropy-ascent quantum thermodynamic modeling of the relaxation process of isolated chemically reactive systems using density of states and the concept of hypo-equilibrium state," *Physical Review E*, in publication (2015).

[5] Smith, C.E. and von Spakovsky, M.R., "Comparison of the non-equilibrium predictions of intrinsic quantum thermodynamics at the atomistic level with experimental evidence," *Journal of Physics: Conference Series*, 380**,** 012015 (2012).

[6] Ozturk, Z. and Sisman, A., "Quantum size effects on the thermal and potential conductivities of ideal gases,". *Physica Scripta*, 80(6), 065402, (2009).

PARALLEL SESSION

HEAT AND MASS TRANSFER IN POROUS MEDIA

Fourth International Conference on Computational Methods for Thermal Problems
THERMACOMP2016, July 6-8, 2016, Georgia Tech, Atlanta, USA
N. Massarotti, P. Nithiarasu and Y. Joshi (Eds.)

TWO-PHASE EXPLICIT CBS PROCEDURE FOR COMPRESSIBLE VISCOUS FLOW TRANSPORT IN POROUS MATERIALS

Fausto Arpino, Gino Cortellessa
Dipartimento di Ingegneria Civile e Meccanica, Università degli Studi di Cassino e del Lazio Meridionale, via G. Di Biasio 43, Cassino, Italy, f.arpino@unicas.it, g.cortellessa@unicas.it

Vito Fernicola
Istituto Nazionale di Ricerca Metrologica (INRIM), Strada delle Cacce, 91 - 10135 Torino, v.fernicola@inrim.it

ABSTRACT

In this paper the finite element based Artificial Compressibility (AC) Characteristic-Based Split (CBS) algorithm is applied, for the first time, to the heat and mass transfer in porous media with associated phase change in a single physical domain. The procedure can be used for the resolution of problems characterized by the coexistence of a two-phase zone and single-phase regions with irregular and moving phase interfaces in between. The obtained results have been compared with the numerical data available in the scientific literature.

Key Words: *Porous media, Heat Transfer, Finite Elements, Multiphase, mixture model*

1. INTRODUCTION

Two phase flow and heat transfer in porous media occur in a wide spectrum of engineering disciplines. Examples include heat and moisture transfer in insulation materials, latent heat storage, drying processes, geothermal systems, oil reservoir engineering, multiphase packed-bed reactors, condensation improvement. The strongly nonlinear and coupled nature of the governing equations and the presence of moving and irregular interfaces, between the single and two-phase sub regions in a domain of interest, represents difficult aspects to be taken into account. To the authors knowledge, the numerical procedures adopted in the scientific literature for the resolution of two-phase flows in porous media are only implicit. In the last two decades the AC approach has received increasing attention, mainly due to the following reasons: i) low computing requirements; ii) easy parallelization; iii) possibility to solve transient flows in a memory efficient manner, by using explicit pseudo time marching that allows to avoid solutions with large matrices; iv) superior convergence.
The AC-CBS algorithm was successfully employed by the authors to solve the governing generalized porous medium equations in the case of natural, forced and mixed convection problems [1-3]. In this work, the authors analyse the performance of a new version of the numerical algorithm for the solution of multiphase flow through fluid saturated porous media in which the two phases are viewed as constituents of a binary mixture. The numerical procedure is verified for a transpiration cooling problem with coolant phase

change. The effects of coolant mass flow rate on the distribution of temperatures and saturations were studied.

2. GOVERNING EQUATIONS

The conservation equations are given below for mass (continuity), momentum (Darcy's law), and energy, governing two-phase flow in porous media and stationary conditions using the two-phase mixture model. The porous material in the enclosure is assumed to be homogeneous and isotropic. The fluid is assumed to have constant physical properties in each phase, but the properties of the two-phase mixture vary with the relative amounts of each phase.

Mass conservation equation

$$\frac{\partial \rho}{\partial t} + \frac{\partial \left(\rho u\right)_i}{\partial x_i} = 0 \tag{1}$$

Momentum conservation equation

$$\frac{\partial \rho_f \left(s\right) u_i}{\partial t} + \frac{1}{\varepsilon} u_j \frac{\partial \rho_f \left(s\right) u_i}{\partial x_j} = -\varepsilon \frac{\partial p_f}{\partial x_i} + \mu_{eff}\left(s\right) \frac{\partial \tau_{ij}}{\partial x_j} - \varepsilon \frac{\mu_f \left(s\right)}{\kappa} u_i \tag{2}$$

Fluid Energy conservation equation

$$\frac{\partial \left(\gamma_h \left(s\right) uH\right)_i}{\partial x_i} = \frac{\partial}{\partial x_i} \Gamma_h \frac{\partial H_i}{\partial x_i} + \frac{\partial \left(f\left(s\right) K \Delta \rho \mathbf{g} h_{fg} / \nu_v\right)_i}{\partial x_i} + q_{sf} \tag{3}$$

Solid Energy conservation equation

$$\frac{\partial}{\partial x_i} k_{s,eff} \frac{\partial T_s}{\partial x_i} = q_{sf} \tag{4}$$

The fluid energy equation is described usually with temperature. Here, to include the three states of the fluid (liquid, two-phase and vapour) in the Two Phase Mixture Model (TPMM), a volumetric pseudo enthalpy is introduced to replace the fluid temperature. It represent a monotonic function of the thermodynamic state during the single to two-phase transition. The conservation equations are valid throughout the calculation domain, in both the one and two-phase regions. It is assumed that $h \approx c_p T$, and therefore H is related to T in the single-phase region, and to s (liquid saturation) in the two-phase region. Therefore the energy equation represents a temperature equation in the single-phase region and reduces to an equation for liquid saturation in the isothermal two-phase region.
The mass and momentum conservation equations (Darcy equation) represent a simplified form of the generalized mathematical model and the simplification related to the convective and diffusive terms is valid because of the low Reynolds number in the kind of problems investigated. The energy equation, however, required some manipulations. In fact to include the three states of the fluid (liquid, two-phase and vapour) in the TPMM, enthalpy and saturation were introduced to replace fluid temperature. The temperature and liquid saturation are recovered from the pseudo volumetric enthalpy by the relations reported in [4]. The variables and coefficients in the above differential equations can be calculated by the saturation. The mixture variables and properties are synthetized in [4].

3. PROBLEM DESCRIPTION AND RESULTS

The heat and mass transfer with phase change was verified considering a physical model of transpiration cooling with phase change. It consists in an homogenous and isotropic porous matrix with a thickness L equal to 0.1 m crossed by a liquid fluid injected from one side and heated from the other side, where it leaves the porous material in a gaseous state. The computational domain and the boundary conditions are reported in Figure 1. The upper surface of the matrix is exposed to a heat flux of Q_{in}, liquid coolant is injected from reservoir at a temperature T_{in} with a mass flow rate of $\dot{m}_{in}$ into the pores of the porous matrix. A symmetry condition is imposed on the side surfaces. A continuous mass flows against the gravitation from the bottom to the top of the domain was considered. A constant value of pressure, p_{out}, was imposed at the outlet section of the computational domain. The pseudo-mixture enthalpy at the inlet was defined by the inlet-temperature [4].
During the crossing the fluid was heated from the top by a heat source $\dot{Q}_{in}$ and starts to boil. The Neumann boundary condition for the enthalpy at exit was given in [4].

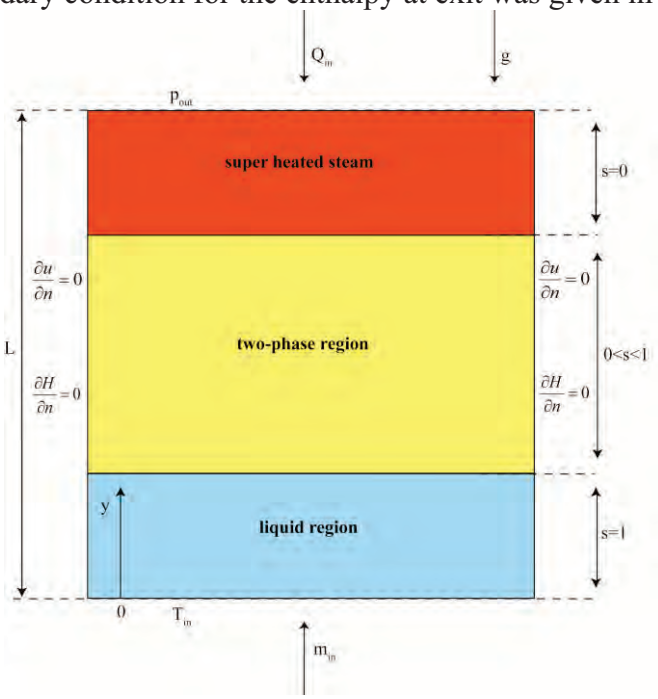

FIGURE 1. Physical model of transpiration cooling with phase change. Computational domain and boundary conditions.

The physical model reported in Figure 1 was analyzed by two-dimensional simulations considering pure water as coolant. A computational unstructured mesh of 50034 free triangular elements was chosen on the basis of a sensitivity analysis (the nodal variation of the solution between two subsequent meshes is lower then 1%). Figure 2 illustrates the comparisons with the results of Droste [5] in terms of temperature variations of fluid and solid, and saturation distribution within the porous matrix at different coolant mass flow rates, 0.3, 0.5, 0.8, and 1.0 $kg/(m^2 s)$, when the heat flux is $1.0 \cdot 10^6 J/(m^2 s)$, porosity is 0.35, and sphere diameter is $5 \cdot 10^{-4} m$. Form the figures, it can be found that a higher coolant mass flow rate can delay liquid evaporation, reduce the area of two-phase region and vapour region, thus the temperatures at the hot surface decrease.

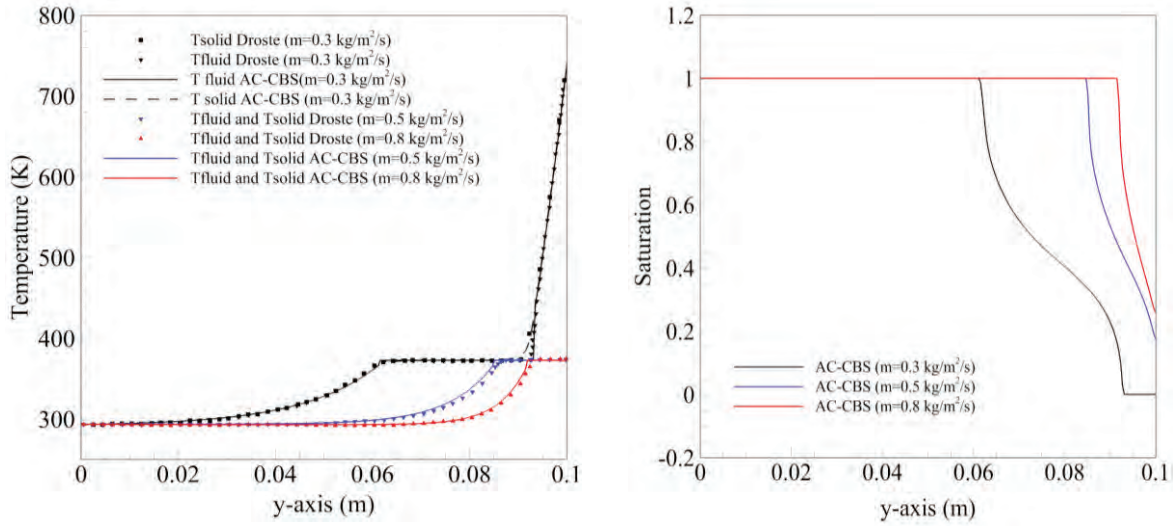

FIGURE 2. Temperature and saturation variation using different coolant mass flow rate equal to 0.3, 0.5 and 0.8 (kg/m^2/s).

4. CONCLUSIONS

In this paper the AC-CBS algorithm is applied, for the first time for the solution of multiphase flow through fluid saturated porous media. An unified set of mass, momentum and energy conservation equations was obtained for transport processes in both single and two phase regions. Therefore a single computational domain and a fixed grid can be used for the entire physical domain. The fully explicit numerical methodology was applied successfully to an important post-dry-out heat transfer problem featuring two moving phase interfaces. A significant advantage is that it involves modest computational cost comparable to those for single-phase counterparts of similar complexity. It was found that an increase in the coolant mass flow rate can delay liquid evaporation, reduce the area of two-phase region and vapour region, thus the temperatures at the hot surface decrease. The present algorithm provides a powerful routine tool for the numerical modelling of complex two-phase transport processes in porous media.

REFERENCES

[1] G.C. F. Arpino, M. Dell'Isola, N. Massarotti, A. Mauro, High Order Explicit Solutions for the Transient Natural Convection of Incompressible Fluids in Tall Cavities, Numerical Heat Transfer, Part A: Applications, vol. 66(8), pp. 839-862, 2014

[2] F.Arpino, G. Cortellessa and A. Mauro, Transient Thermal Analysis of Natural Convection in Porous and Partially Porous Cavities, Numerical Heat Transfer, Part A, vol. 67, pp. 605–631, 2015

[3] N. Massarotti, M. Ciccolella, G. Cortellessa and A. Mauro, New benchmark solutions for transient natural convection in partially porous annuli, International Journal of Numerical Methods for Heat and Fluid Flow, vol. 26(3-4), pp. 1187-1225, 2016

[4] J. X. Shi and J.H. Wang, A Numerical Investigation of Transpiration Cooling with Liquid Coolant Phase Change, Transp Porous Med, vol. 87, pp. 703–716, 2011

[5] D. Droste, F. Lindner, Ch. Mundt and M. Pfitzner, Numerical Computation of Two-Phase Flow in Porous Media, 2013 Comsol Conference, Rotterdam

Fourth International Conference on Computational Methods for Thermal Problems
THERMACOMP2016, July 6-8, 2016, Georgia Tech, Atlanta, USA
N. Massarotti, P. Nithiarasu and Y. Joshi (Eds.)

MACRO-SCALE MODELLING OF HEAT SINKS WITH HIGHLY CONDUCTIVE PERIODICALLY ARRANGED FINS

G. Buckinx, M. Baelmans
KU Leuven, Department of Mechanical Engineering, Celestijnenlaan 300A, 3001, Leuven, Belgium

ABSTRACT

A macro-scale model is presented for accurate modelling of heat sinks with highly conductive periodically arranged fins. The macro-scale model is based on a spatial filtering technique which yields exact results for the periodically developed regime in isothermal fins. The accuracy of this macro-scale model, as well as its capability to predict the overall heat sink performance, is compared to that of a corresponding porous medium model derived via volume-averaging.

Key Words: *Fins, Heat Sink, Macro-Scale, Volume-Averaging.*

1. INTRODUCTION

The design of finned heat sinks crucially depends on reduced models that accurately describe the flow and heat transfer within these devices. In a number of studies, e.g. [1,2], the reduced models for finned heat sinks are derived from the volume-averaged models that describe the flow and heat transfer through a porous medium in a spatially averaged or 'macro-scale' sense. In our previous work [3,4], which builds upon the work of Quintard and Whitaker [5], we have shown theoretically that the former volume-averaged models for porous media do not accurately describe the macro-scale flow and heat transfer through spatially periodic solid structures, such as the fins of a heat sink. Therefore, this paper applies our new spatial filtering technique [3,4], to derive a one-dimensional macro-scale model for heat sinks consisting of an array of highly conductive fins. First, the DNS equations for the flow and temperature in the heat sink are averaged to obtain the planar equations for the height-averaged flow and temperature in the heat sink. Subsequently, the planar velocity, pressure and temperature are filtered with a suitable weighting function to obtain a one-dimensional macro-scale heat sink model. This macro-scale heat sink model holds exactly when the fins and base-plate of the heat sink have the same constant temperature. Our modelling approach is illustrated in a case study for a heat sink with square fins. In this case study, the accuracy of the macro-scale model is compared to the planar model as well as the corresponding volume-averaged porous model.

2. PLANAR FLOW AND TEMPERATURE EQUATIONS

We consider a heat sink consisting of a fin array on a base-plate with all fins having the same cross-sectional shape in every plane parallel to the base-plate, as depicted in FIG. 1.

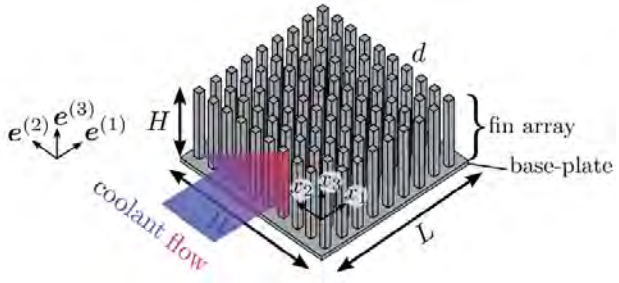

FIGURE 1. Heat sink consisting of an array of square pin-fins.

When the coolant flow through the heat sink is directed mainly parallel to the base-plate, the three-dimensional incompressible flow equations can be reduced to the two-dimensional planar flow equations, which yield the average flow velocity $\boldsymbol{v}$ and average pressure p over the height H of the fin array:

$$\nabla^{\nu} \cdot v = \varphi_3 \tag{1}$$

$$\rho_{\mathrm{f}} \frac{\partial^{\nu} \boldsymbol{v}}{\partial \mathrm{t}} + \rho_{\mathrm{f}} \nabla^{\nu} \cdot (\boldsymbol{vv}) = -\nabla^{\nu} p + \nabla^{\nu} \cdot \mu_f (\nabla^{\nu} \boldsymbol{v} + (\nabla^{\nu} \boldsymbol{v})^T) + \boldsymbol{\Psi_3} \tag{2}$$

The planar flow velocity $\boldsymbol{v}$ and pressure p in the planar flow equations (1) and (2) are defined as the average of the original flow and pressure *distributions* over the coordinate x_3, perpendicular to the base-plate. The closure terms φ_3 and $\boldsymbol{\Psi_3}$ arise in the planar flow equations due to the height-averaging procedure. Under the assumption that the velocity field is parallel to the base-plate and that the velocity profile has a parabolic shape over the height of the fin array, the closure terms can be approximated as $\varphi_3 \simeq 0$ and $\boldsymbol{\Psi_3} \simeq -\frac{1}{5}\rho_{\mathrm{f}} \nabla^{\nu} \cdot (\boldsymbol{vv}) - \frac{12}{H^2}\mu_f \boldsymbol{v}$.

The average temperature T over the height of the fin array is governed by the planar temperature equation,

$$\rho \frac{\partial^{\nu}(\mathrm{cT})}{\partial \mathrm{t}} + \rho \nabla^{\nu} \cdot (\boldsymbol{v} c T) = \nabla^{\nu} \cdot (k \nabla^{\nu} T) + \psi_3 \,, \tag{3}$$

where the thermal closure term ψ_3 can be approximated as $\psi_3 \simeq h_b(T_s - T) + (1 - \xi)\rho \nabla^{\nu} \cdot (\boldsymbol{v} c T)$, when the temperature T_s of the fins and base-plate is constant and all other heat sink boundaries are adiabatic. The former approximation for ψ_3 with $h_b = 2.692 \frac{k_f}{H^2}$ and $\xi = 1.0571$ is derived by assuming that the temperature profiles over the fin array height at different positions in the main flow direction are self-similar separable functions of the coordinate x_3, perpendicular to the base-plate.

As a case study, we have numerically resolved the planar flow and temperature in a heat sink consisting of 10×10 equidistant square fins of side d and spacing $l_1 = 2d$ on a square base-plate. The total pressure drop Δp_{tot} over the heat sink, the fluid inlet temperature T_{in} as well as the fluid properties are prescribed (see TABLE 1).

W/L	H/d	L/d	$\mathrm{Re} = \frac{\mathrm{d}}{\nu}\sqrt{\Delta p_{tot}/\rho_f}$	Pr
1	2	20	50	10

TABLE 1. Parameters for this case study.

2. MACRO-SCALE HEAT SINK MODEL

Sufficiently far from the coolant flow inlet in the heat sink, where the flow is periodically developed, the following Darcy-like relation is often assumed in the literature:

$$|\nabla P| = \frac{\Delta p}{\ell_1} = \mu_f K_{app}^{-1} U. \tag{4}$$

The scalar apparent permeability K_{app} in (4) relates the 'mean pressure gradient' ∇P in the developed flow or the pressure drop Δp over a single fin unit to the 'mean velocity' U through the fin array. When U is defined equal to the volume-averaged (planar) velocity $|\langle \boldsymbol{v} \rangle|$ over a single fin unit, we can determine K_{app} in function of $|\langle \boldsymbol{v} \rangle|$ by solving the periodic flow equations for an imposed pressure gradient ∇P on a single fin unit [3]. For our case study, this constant value of K_{app} is plotted in FIGURE 2.

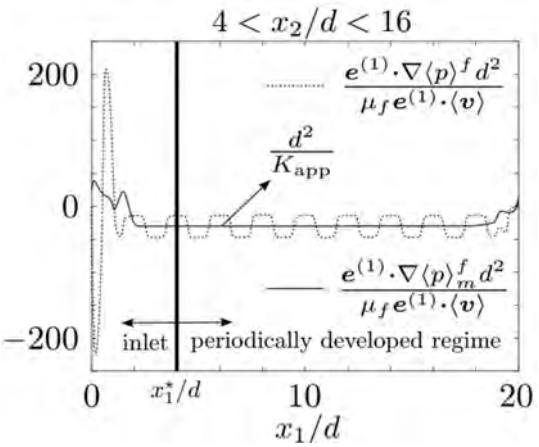

FIGURE 2. Ratio of macro-scale pressure gradient to macro-scale velocity.

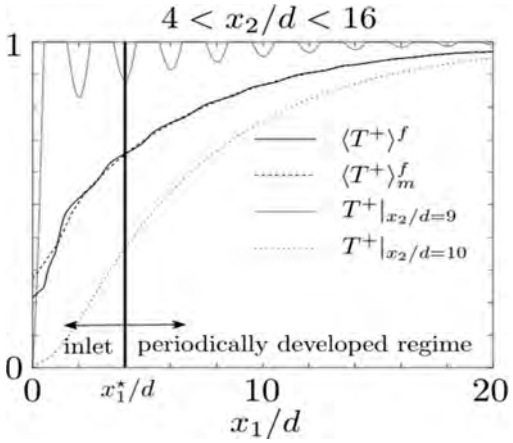

FIGURE 3. Dimensionless macro-scale temperature profiles, $T^+ = (T - T_{in})/(T_s - T_{in})$.

FIGURE 2 shows that the constant permeability K_{app} as calculated from a single fin unit, does not correspond to the ratio of the volume-averaged velocity $\langle \boldsymbol{v} \rangle$ to the gradient of the volume-averaged pressure $\nabla \langle p \rangle^f$. Hence, the heat sink fin array is not adequately modelled by the macro-scale flow equation for a porous medium based on volume-averaging:

$$\left|\nabla \langle p \rangle^f\right| \neq |\nabla P| = \frac{\Delta p}{\ell_1} = \mu_f K_{app}^{-1} |\langle \boldsymbol{v} \rangle| \,, \tag{5}$$

Instead, it can be shown [10] that the correct macro-scale momentum equation for the core of the heat sink is given by

$$|\nabla \langle p \rangle_m^f| = |\nabla P| = \frac{\Delta p}{\ell_1} = \mu_f K_{app}^{-1} |\langle \boldsymbol{v} \rangle|, \tag{6}$$

where the appropriate constant macro-scale pressure gradient $|\nabla \langle p \rangle_m^f|$ in the periodically developed flow regime is obtained through a double volume-average: $\left|\nabla \langle p \rangle_m^f\right| = |\nabla \langle \langle p \rangle^f \rangle|$.

In the literature, e.g. [7], an empirical 'overall heat transfer coefficient' h_M, which is assumed to be spatially constant, is introduced to obtain the following one-dimensional model for the 'mean fluid temperature' T_M in an isothermal heat sink:

$$T_M = \left(T_M|_{x_1^\star} - T_s\right) e^{-(\lambda_T)(x_1 - x_1^\star)} + T_s \quad \text{with} \quad \lambda_T = h_M/(\rho_f c_f U) \quad \text{for } x_1 \geq x_1^\star \,. \tag{7}$$

As illustrated by FIGURE 3, it is the filtered planar temperature $\langle T \rangle_m^f$ based on the matched weighting function of [4], that satisfies a macro-scale temperature equation similar to (7):

$$\langle T \rangle_m^f = \left(\langle T \rangle_m^f|_{x_1^\star} - T_s\right) e^{-(\lambda_T)(x_1 - x_1^\star)} + T_s \quad \text{with} \quad \lambda_T \simeq (h_{fs} + h_b)/(\rho_f c_f |\langle \boldsymbol{v} \rangle|) \,, \tag{8}$$

when the heat transfer is periodically developed after the inlet region ($x_1 \geq x_1^\star$). The heat transfer coefficient h_{fs} in (8) represents the macro-scale interfacial heat transfer from the fins towards the coolant flow and is indeed spatially constant for the macro-scale temperature $\langle T \rangle_m^f$. Consequently, h_{fs} is easily governed by solving the periodic temperature field [11] around a single fin unit. If one would replace $\langle T \rangle_m^f$ in (7) by the volume-averaged temperature $\langle T \rangle^f$, λ_T and h_{fs} would be no longer spatially constant, as can be seen in FIGURE 4.

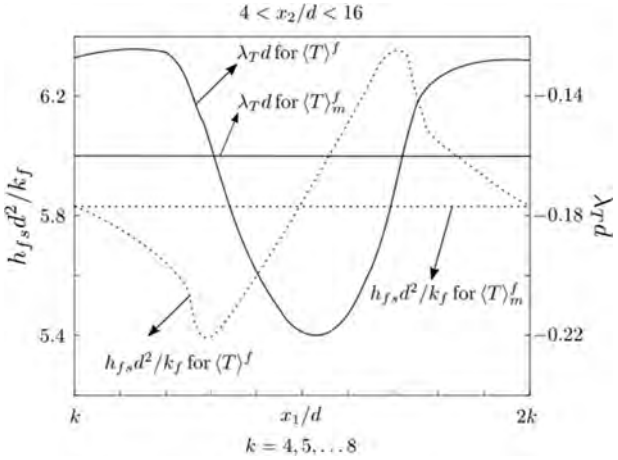

FIGURE 4. Interfacial heat transfer coefficient and macro-scale temperature exponent.

4. RESULTS AND CONCLUSION

From the results of the case study, it is concluded that the presented macro-scale model is in perfect agreement with the results obtained by DNS of the planar flow and temperature. At least, perfect agreement holds over the part of the core where the flow and heat transfer regime are periodically developed. The volume-averaged porous model fails to predict the correct macro-scale flow through the core, if the spatial dependence of the apparent permeability and heat transfer coefficient is neglected. Nevertheless, the latter approach has been common practice.

REFERENCES

[1]. S. Kim, D. Kim, and D. Lee, "On the local thermal equilibrium in microchannel heat sinks," Int. J. Heat Mass Transf., vol. 43, no. 10, pp. 1735 – 1748, 2000.

[2]. A. Horvat and I. Catton, "Numerical technique for modeling conjugate heat transfer in an electronic device heat sink," Int. J. Heat Mass Transf., vol. 46, no. 12, pp. 2155–2168, 2003.

[3]. G. Buckinx and M. Baelmans, "Multi-scale modelling of flow in periodic solid structures through spatial averaging," J. Comp. Phys., vol. 291, pp. 34–51, 2015.

[4]. G. Buckinx and M. Baelmans, "Macro-scale heat transfer in periodically developed flow through isothermal solids," J. Fluid Mech., vol. 780, pp. 274–298, 2015.

[5]. M. Quintard and S. Whitaker, "Transport in ordered and disordered porous media II: Generalized volume averaging," Transp. Porous Media, vol. 14, no. 2, pp. 179–206, 1994.

[6]. S. Whitaker, "The Forchheimer equation: A theoretical development," Transp. Porous Media, vol. 25, no. 1, pp. 27–61, 1996.

[7]. R.W. Knight, J.S. Goodling and D.J. Hall, "Optimal thermal design of forced convection heat sinks-analytical," J. Electron Packaging, vol. 113, pp. 313-321, 1991.

Fourth International Conference on Computational Methods for Thermal Problems
THERMACOMP2016, July 6-8, 2016, Georgia Tech, Atlanta, USA
N. Massarotti, P. Nithiarasu and Y. Joshi (Eds.)

LINEAR STABILITY ANALYSIS OF NATURAL CONVECTION IN PARTIALLY POROUS TALL ANNULI

Michela Ciccolella, Nicola Massarotti, Alessandro Mauro
Dipartimento di Ingegneria, University of Naples "Parthenope", Centro Direzionale, Isola C4, 80143 Naples, Italy,
michela.ciccolella@uniparthenope.it, massarotti@uniparthenope.it, alessandro.mauro@uniparthenope.it

Gino Cortellessa
[2]Dipartimento di Ingegneria Civile e Meccanica, University of Cassino and Lazio Meridionale, Via G. Di Biasio 43, 03043 Cassino (FR), Italy, g.cortellessa@unicas.it

ABSTRACT

The paper focuses on linear stability analysis of natural convection in partially porous tall annular cavities. In order to analyze the dependence of this phenomenon on the cavity geometry, different values of radii ratio (r_o/r_i) have been considered; moreover, the influence of porous layer is investigated by considering several values of Da numbers and by changing the position of the internal porous domain. A transient Artificial Compressibility version of CBS algorithm is introduced here for the solution of the generalized Navier-Stokes equations; a dual time stepping approach is introduced in the scheme in order to employ a local time stepping procedure, suitable for applications in problem involving free fluid- porous medium interfaces. The numerical results highlight that linear stability of free convection in partially porous tall annuli is strongly affected both by the geometry and porous layer, as transient oscillations tend to disappear as radii ratio increases and Da number decreases; moreover, also the position of the porous layer seems to affect the stability analysis, as this trend is more noticeable when the porous domain is near the cold wall.

Key Words: *Linear Stability, AC-CBS, Natural Convection, Partially porous annuli*

1. INTRODUCTION

Stability of free convection in partially porous domains is very important as several industrial and environment applications, involve the interaction between a saturated porous medium and a free fluid which saturate it. Although stability analysis of natural convection in tall vertical annuli has been much discussed in scientific literature [1], there are no works focused on the magnitude of this phenomenon in partially porous tall annuli. For this reason, a fully explicit finite element based algorithm has been developed here to analyze the influence of the presence of a porous layer on the oscillatory behavior of thermal field.

2. NUMERICAL MODEL

A generalized porous medium model is employed here for modeling transient free convection in a partially porous annulus, assuming local thermal equilibrium, uniform properties of the porous medium, incompressibility of the fluid and the axial symmetry.
The Boussinesq approximation is invoked for the incorporation of buoyancy effects into the generalized Navier-Stokes equations; for the detailed description of the mathematical model reader can refer to ref. [2]. The PDEs constituting the generalized porous medium model were numerically solved using the transient AC–CBS algorithm. The governing equations were discretized in time along the flow characteristics, and in space using the standard Galerkin procedure; a dual time stepping procedure is introduced to deal with transient terms adding a true transient term to either the first or fourth step of the algorithm. These additional terms are discretized over real time to the third order of approximation. The reader can find a detailed description of the proposed algorithm, completed by a computational stability analysis and model validation, in ref [2].

3. RESULTS

In this section, the numerical results obtained for transient natural convection in partially porous tall annuli with AR of 4:1 are presented. The computational domain and the boundary conditions employed are shown in Fig. 1; the input parameters used in the simulations are the following: $Ra=3.6 \cdot 10^6$, Pr=0.71, ε=0.5, Fo=0, Da variable from 10-5 to 1 and ro/ri changing in the range 1-3. A constant unitary value of the annular thickness ($r_o - r_i=1$) and a real-time step of 0.1 has been considered in all simulations. In order to analyze the transient behavior of the natural convection, five probe points have been identified: these points are presented in Fig. 1 and their coordinates are reported in Table 1. An unstructured triangular mesh composed by 14478 elements and 7679 nodes has been selected on the basis of a mesh sensitivity analysis for the simulations; the mesh is refined near all the boundaries of computational domain.

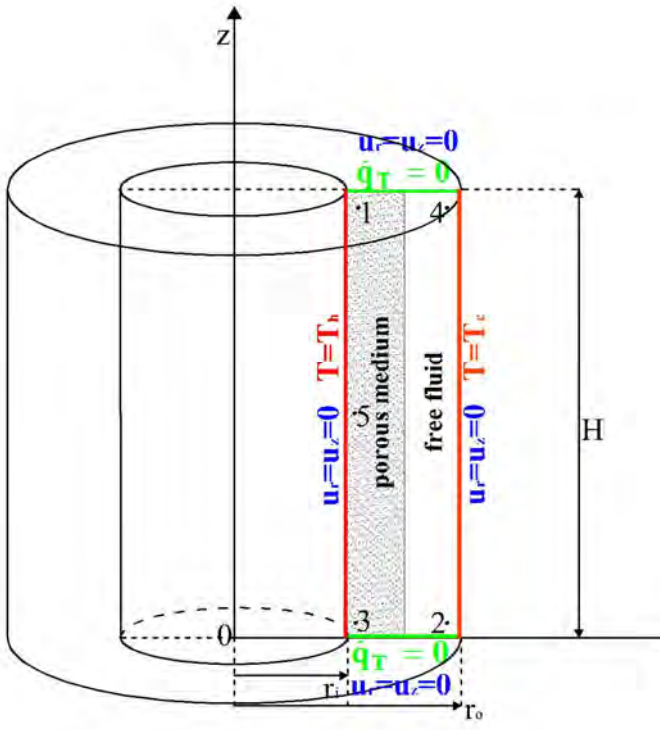

Point	r	z	
1	r_i + 0.091	3.685	
2	r_i + 0.910	0.315	
3	r_i + 0.091	0.315	
4	r_i + 0.910	3.685	
5	r_i + 0.091	2.00	

TABLE 1- *Non-dimensional coordinates of points from 1 to 5*

FIGURE 2- Computational domain and boundary conditions employed for the analysis of natural convection in a partially porous annulus

Two different configurations have been analyzed: a first one with the porous layer is on the left side of the computational domain (case A) and a second one obtained by exchanging the sub-domains (case B). Transient oscillations are quantitatively represented in Fig. 2 and 3; in particular, Fig. 2 shows transient thermal behavior for case A (on the left side) and for case B (on the right one) for different values of Darcy numbers. The analysis of the results highlights that for high values of Da the presence of the porous layer increases the linear stability only in the configuration A, as transient oscillations tend to disappear approaching steady state only in this case. However, it is important to underline that for very low Da numbers, steady state is reached in both cases.

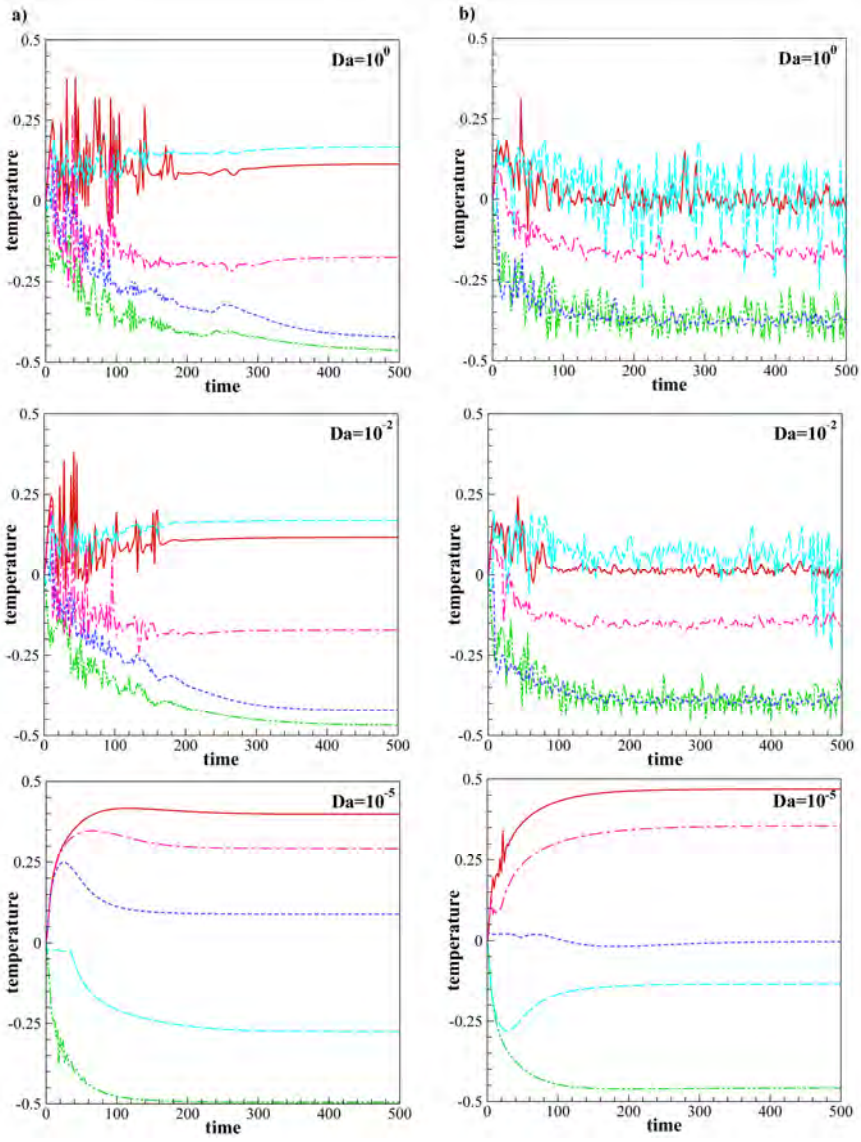

FIGURE 2- Temperature variation over time obtained at points from 1 to 5 (see Fig. 1) for case A (on the left) and case B (on the right) for different Da and Ra=3.4 · 10^6 (r_o/r_i=2)

In order to investigate the behavior of the flow regime with the annulus radius, several analyses have been carried out by changing the radius ratio r_o/r_i in the range between 2 and 1.1. As transient oscillations seems to affect natural convection for high value of Darcy number, the reference value of Da=1 has been assumed for all the simulations. Figure 3 shows the results obtained from these analyses both for the case study A (on the left) and B (on the right). In the first case, for all values of r_o/r_i, oscillations dampen and the flow is not oscillatory in time on all the considered points. As the value of radii ratio decreases, it is possible to observe an increase of the time necessary to reach the steady state. A different trend is observed for the results related to case B as transient oscillations do not disappear for all the values of radii ratios examined here. Finally, it can be noted that in both cases, the amplitude of this oscillations increases with the decrease of the value of radii ratio.

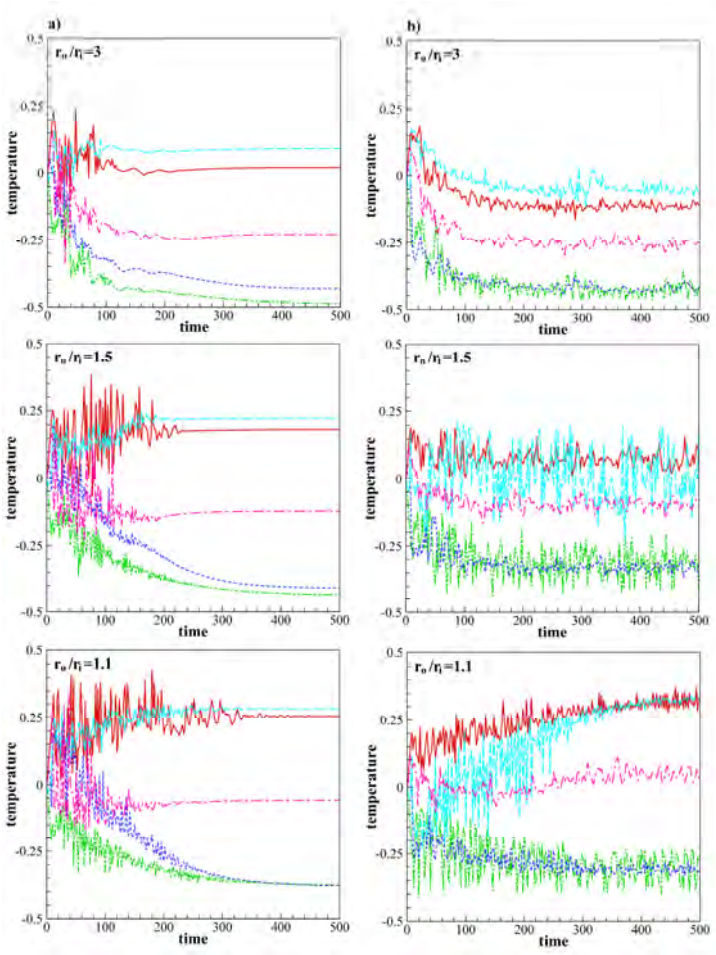

FIGURE 3- Temperature variation over time obtained at points from 1 to 5 (see Fig. 1) for case A (on the left) and case B (on the right) for different r_o/r_i and Ra=3.4 · 10^6 (Da=1)

4. CONCLUSIONS

In the paper, a properly stabilized fully matrix-inversion free scheme, employing an adaptive local time stepping procedure, is introduced for the analysis of linear stability in partially porous annular enclosures. Several analyses have been conducted by changing the properties and the position of porous domains and also the geometry of the cavity: in particular, several values of Da and ro/ri has been considered. The results highlights that not only the properties of the porous layer but also its position strongly affects linear stability of free convection, which can be enhanced or not changing the position of internal porous domain: only for low values of Da the stability seems to be enhanced in both cases.

REFERENCES

[1] M. Bhowmik, P. Bera, and J. Kumar, Non-isothermal Poiseuille flow and its stability in a vertical annulus filled with porous medium, International Journal of Heat and Fluid Flow, 56, 272-83, 2015

[2] M.Ciccolella, G. Cortellessa, N. Massarotti and A. Mauro, New benchmark solutions for transient natural convection in partially porous annuli, *International Journal of Numerical Methods for heat and fluid flow*, in press.

Fourth International Conference on Computational Methods for Thermal Problems
THERMACOMP2016, July 6-8, 2016, Georgia Tech, Atlanta, USA
N. Massarotti, P. Nithiarasu and Y. Joshi (Eds.)

EXAMINATION OF TWO APPROACHES FOR DETERMINING INTERFACIAL CONDUCTION COEFFICIENT IN POROUS MEDIA

Massimo Cimmino, Bantwal R. (Rabi) Baliga
Department of Mechanical Engineering, McGill University
817 Sherbrooke St. W., Montreal, Quebec H3A 0C3, Canada
massimo.cimmino@mail.mcgill.ca, bantwal.baliga@mcgill.ca

ABSTRACT

Unsteady two-dimensional finite volume simulations on a microscopic representative cell are undertaken for the evaluation of interfacial conduction heat transfer coefficient for porous media. Two approaches are compared: 1) volumetric heat sources of opposite signs are prescribed in the two phases; and 2) different uniform initial temperatures are imposed in the two phases. Sample results are presented and comparatively discussed. Relevance to geothermal systems is indicated.

Key Words: *Porous Media, Local Thermal Non-Equilibrium, Interfacial Conduction Coefficient.*

1. INTRODUCTION

Practically viable computer simulations of fluid flow and heat transfer in porous media are usually based on volume-averaged mathematical models. When unsteady heat transfer between the fluid and solid phases in the porous medium is to be simulated, it is necessary to use a so-called two-temperature (or local thermal non-equilibrium) model, which involves separate volume-averaged energy equations for the solid and fluid phases, with terms to account for the thermal energy exchange between these phases. In the energy equations of such two-temperature models, in addition to the prescription of parameters such as porosity, effective thermal conductivities, and specific (per unit volume) interfacial area, it is also necessary to specify an interfacial heat transfer coefficient. Correlations for the interfacial convection heat transfer coefficient based on data from experimental works and also numerical simulations of representative unit cells have been proposed, for example, by Wakao and Kaguei [1] and Kuwahara et al. [2], respectively, but these correlations are not designed for cases in which the fluid phase is stagnant. Quintard and Whitaker [3] and Rees [4] have proposed analytical and numerical methods for the evaluation of the interfacial conduction heat transfer coefficient, based on prescriptions of suitable volumetric source terms in the solid and/or fluid phases. However, in most practical heat transfer applications involving porous media, there are no volumetric source terms in the solid and fluid phases. The objective of this work is to compare two different approaches (and the results) for the evaluation of the interfacial conduction heat transfer coefficient: 1) by imposing volumetric heat sources in the two phases; and 2) by prescribing different initial temperatures in the two phases. Some comments related to applications involving geothermal heat exchangers are also presented.

2. MAIN BODY

A representative microscopic periodic unit cell of the porous medium considered in this investigation is shown in Figure 1. The cell has a unit depth, and width and height L. The solid phase (shown in grey) occupies a H x H square region in the cell. The porosity of the porous medium is given by the volume fraction of the fluid phase (shown in white): $\varepsilon = 1 - H^2/L^2$.

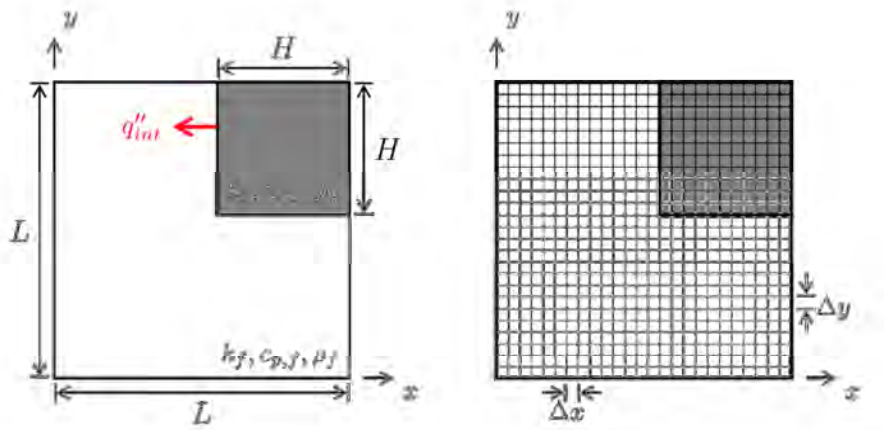

FIGURE 1. Representative microscopic periodic unit cell (left) and finite volume grid (right)

Within the microscopic representative unit cell (Figure 1), the following equations govern unsteady two-dimensional heat conduction in the solid and fluid phases (no forced or natural convection):

$$\rho_s c_{p,s} \frac{\partial T^s}{\partial t} = \frac{\partial}{\partial x}\left(k_s \frac{\partial T^s}{\partial x}\right) + \frac{\partial}{\partial y}\left(k_s \frac{\partial T^s}{\partial y}\right) + S_s, \quad x \geq L - H \text{ and } y \geq L - H \tag{1}$$

$$\rho_f c_{p,f} \frac{\partial T^f}{\partial t} = \frac{\partial}{\partial x}\left(k_f \frac{\partial T^f}{\partial x}\right) + \frac{\partial}{\partial y}\left(k_f \frac{\partial T^f}{\partial y}\right) + S_f, \quad \text{elsewhere} \tag{2}$$

where ρ_s, $c_{p,s}$, and k_s are the density, specific heat, and thermal conductivity of the solid phase; ρ_f, $c_{p,f}$, and k_f are the density, specific heat, and thermal conductivity of the fluid phase; and S_s and S_f denote volumetric heat sources in the solid and fluid phases (when applicable). Continuity of the normal heat flux and temperature is imposed at the interface between the phases.

The above-mentioned mathematical model was solved using a finite volume method [5] for two approaches: 1) following Quintard and Whitaker [3], equal and opposite (in magnitude and sign) total rates of heat generation are prescribed in the two phases; and 2) different uniform initial temperatures in the two phases are imposed, with zero source terms. The spatial periodicity of the porous media allows imposition of the adiabatic condition on the boundaries of the unit cell.

Dimensionless initial conditions and volumetric source terms for the first approach are given by:

$$\theta = \frac{T - T_{ini}}{S_f L^2 / k_f} = 0, \qquad \text{at } t^* = \alpha_f t / L^2 = 0 \tag{3}$$

$$S_s^* = \frac{(1-\varepsilon)}{\varepsilon}, \qquad S_f^* = -1 \tag{4}$$

Dimensionless initial conditions for the second approach (zero source terms) are given by:

$$\begin{cases} \theta = \dfrac{T - T_{ini}^f}{T_{ini}^s - T_{ini}^f} = 1, & x \geq L - H \text{ and } y \geq L - H \\ \theta = 0, & \text{elsewhere} \end{cases}, \qquad \text{at } t^* = 0 \tag{5}$$

The interfacial conduction heat transfer coefficient is calculated using the following equations:

$$h = \frac{1}{\bar{T}^s - \bar{T}^f}\left[\frac{\int_{\text{interface}} q''_{int}\, ds}{2H}\right] \tag{6}$$

$$\bar{T}^s = \frac{1}{H^2}\iint_{\text{solid region}} T^s dxdy\,, \qquad \bar{T}^f = \frac{1}{L^2 - H^2}\iint_{\text{fluid region}} T^f dxdy \tag{7}$$

where h is the interfacial conduction heat transfer coefficient; $\bar{T}^s$ and $\bar{T}^f$ are the average temperatures in the solid and fluid phases, respectively; and q''_{int} is the normal interfacial heat flux from the solid phase to the fluid phase (see Figure 1).

3. RESULTS

Unsteady finite volume simulations were undertaken for the two approaches. The porosity of the porous medium was varied from $\varepsilon = 0.10$ to $\varepsilon = 0.90$ and the thermal conductivity ratio between the solid and fluid phases was varied from $k_s/k_f = 0.01$ to $k_s/k_f = 100$. Only one ratio of the thermal diffusivity ratio $\alpha_s/\alpha_f = 1$ was considered in this (preliminary) work. Based on numerous exploratory simulations, satisfactory time step and spatial grid sizes were selected for the final runs: $\Delta t = \left(L^2/\alpha_f\right)/1000$; and $\Delta x/L = \Delta y/L \cong 0.01$.

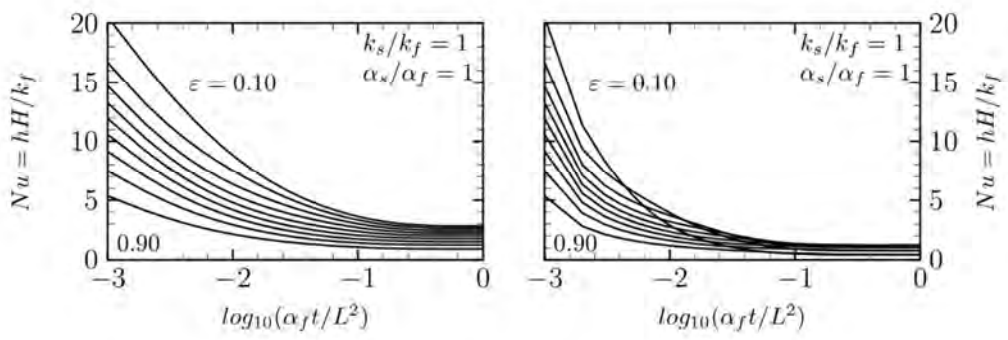

FIGURE 2. Time-variation of the interfacial conduction heat transfer coefficient for the first (left) and second (right) approaches

Sample results for the time variation of the interfacial heat transfer coefficient are shown in Figure 2. These results are represented in terms of a conduction Nusselt number, $Nu = hH/k_f$, for a thermal conductivity ratio $k_s/k_f = 1$. In both approaches, the interfacial heat transfer starts at a high value, due to the initially large temperature gradients at the interface between the phases, and reaches an asymptotic regime around time $t = \left(L^2/\alpha_f\right)/10$. For geothermal applications in soils, the particle size can vary from 0.002 mm (silt) to 10 mm (gravel) [6]; the corresponding times to reach the asymptotic regime vary from $2.8\text{x}10^{-6}$ s to 70 s, using a water thermal diffusivity of $\alpha_f = 1.43\text{x}10^{-7}$ m^2/s. Considering that simulations of geothermal heat exchange systems are typically undertaken using time steps of the order of one hour, the aforementioned time-asymptotic values of the conduction Nusselt number should be appropriate for use in the corresponding models.

The time-asymptotic values of the conduction Nusselt number for the parameters considered here are shown in Figure 3 for the two approaches. The numerical results for $k_s/k_f = 1$ were verified

against the analytical Fourier series solutions. In the first approach, the conduction Nusselt number monotonically decreases with increasing porosity; and it also decreases with decreasing values of the thermal conductivity ratio. In the second approach, the conduction Nusselt number reaches a maximum value around $\varepsilon = 0.5$ for all thermal conductivity ratios; and it decreases with decreasing values of the thermal conductivity ratio, as per the first approach. The values of time-asymptotic conduction Nusselt number obtained using the first approach are also significantly higher than those computed using the second approach. These two approaches are fundamentally different, hence the differences in the corresponding results. The second approach is recommended; as there are no significant rates of heat generation in the solid and fluid phases in most fluid flows in porous media.

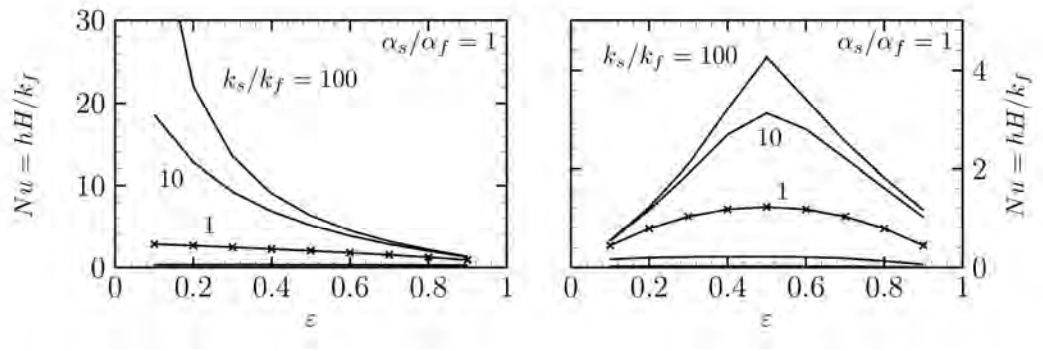

FIGURE 3. Effects of porosity and thermal conductivity ratio on the interfacial conduction heat transfer coefficient for the first (left) and second (right) approaches (**x** indicates analytical solution)

4. CONCLUSIONS

Interfacial conduction heat transfer coefficients were calculated from the results of unsteady two-dimensional finite volume simulations on a representative microscopic periodic unit cell. The first approach consisted in imposing equal and opposite total rates of heat generation in the solid and fluid phases. The second approach consisted in prescribing different initial temperatures in the two phases. Interfacial conduction heat transfer coefficients were calculated for simple square-domain geometries, for various different values of the solid and fluid thermal conductivities and porosity. Extensions of this work will be devoted to the evaluation of the interfacial conduction heat transfer coefficient for different (non-square) geometries and a suitable range of values of (α_s/α_f).

REFERENCES

[1] N. Wakao and S. Kaguei, *Heat Transfer in Packed Beds*, Gordon and Breach, New York, 1982.

[2] F. Kuwahara, M. Shirota, and A. Nakayama, A numerical study of interfacial convective heat transfer coefficient in two-energy equation model for convection in porous media, *International Journal of Heat and Mass Transfer*, 44, 1153-59, 2001.

[3] M. Quintard, and S. Whitaker, One- and two-equation models for transient diffusion processes in two-phase systems, *Advances in Heat Transfer*, 23, 369-464, 1993.

[4] D.A.S. Rees, Microscopic modeling of the two-temperature model for conduction in heterogenous media, *Journal of Porous Media*, 13, 125-43, 2010.

[5] B.R. Baliga and N. Atabaki, Control-Volume-Based Finite-Difference and Finite-Element Methods, in *Handbook of Numerical Heat Transfer*, 2nd Edition, 191-224, 2006.

[6] J. Bear and A.D. Cheng, *Modeling Groundwater Flow and Contaminant Transport*, Vol. 23, Springer Sciences & Business Media, 2010.

Fourth International Conference on Computational Methods for Thermal Problems
THERMACOMP2016, July 6-8, 2016, Georgia Tech, Atlanta, USA
N. Massarotti, P. Nithiarasu and Y. Joshi (Eds.)

USING FLOW OBSTRUCTIONS IN ELECTRO-OSMOTIC SYSTEMS FOR FLUID FLOW ENHANCEMENT

Simona Di Fraia, Nicola Massarotti, Alessandro Mauro
Dipartimento di Ingegneria, Università degli Studi di Napoli "Parthenope", Napoli, Italy,
Centro Direzionale, Isola C4, 80143, Napoli, Italy,
simona.difraia@uniparthenope.it, massarotti@uniparthenope.it, alessandro.mauro@uniparthenope.it

Perumal Nithiarasu
Biomedical Engineering and Rheology Group, Zienkiewicz Centre for Computational Engineering,
Swansea University, Swansea SA2 8PP, United-Kingdom,
p.nithiarasu@swansea.ac.uk

ABSTRACT

A numerical investigation of Electro-Osmotic Flow (EOF) in plain channels and channels with obstructions is presented. The aim of the work is to analyse fluid flow enhancement in EO systems due to flow obstructions. The results show that the introduction of flow obstructions allows to increase the range of channel width in which EOF is effective, and to produce higher fluid flow rates than those corresponding to plain channels. The results also show that beyond a channel width of 100μm, EOF driven systems are possible only if flow obstructions are employed.

Key Words: *Electro-osmotic Flow, Finite element, CBS, Width effect, Micro-channels.*

1. INTRODUCTION

Electro-osmosis driven systems are used for pumping, cooling, mixing and separation processes. The working principle of these systems is based on the interaction between solids and electrolytes. A solid surface in contact with an electrolytic solution becomes spontaneously charged. As a consequence, the ions of the solution form a high concentration region close to the surface, called Electric Double Layer (EDL) [1]. When an external electric field is applied, the ions tend to move towards the electrode that presents the opposite charge, in order to restore the electro-neutrality of the system. As a result, the nearby ions are also dragged and Electro-Osmotic Flow (EOF) is generated. As the distance from the charged surface increases, the EOF effect weakens; hence, EOF is effective at micro- and nano-scale. In plain channels, only the walls are active with a prescribed potential, while in presence of flow obstructions inside channels, the obstructions' boundaries can also be considered as charged surfaces. As a consequence, EOF can potentially be enhanced.

There are very few experimental works concerning EOF in porous media since the small scale of the phenomenon makes the collection of data very difficult. Numerical modelling is then particularly appropriate, but many simplifying hypotheses are necessary [2]. For this reason, the authors analyse EOF in a porous channel with prescribed geometric characteristics, using a microscopic approach, that provides details of the quantities of interest [3].

The aim of the work is to clearly define the effectiveness of using flow obstructions to enhance EOF. As presented in Section 2, EOF is modelled by employing two sets of equations, one to study the electrical field, and the other, based on Navier Stokes equations, for fluid flow. The finite element method is used to discretize the sets of equations and the Characteristic Based Split (CBS) algorithm [4,5] is used to solve the Navier Stokes equations. The computational domain and the boundary conditions used in the study are described in Section 3. In order to highlight the effectiveness of using flow obstructions, a comparative study between micro-channels with and without obstructions is presented in Section 4. Finally, some conclusions are drawn in Section 5.

2. MATHEMATICAL MODEL AND SOLUTION PROCEDURE

Electro-kinetic effects, responsible for EOF, are studied through a Laplace equation for external potential, ϕ, and a Poisson-Boltzmann equation for the Electric Double Layer (EDL) potential, ψ. Fluid flow is modelled by using Navier Stokes equations for incompressible fluids, modified by introducing a source term in the momentum equation to take into account the electro-kinetic forces [6]. The non-dimensional form of these equations is given as follows:

Electro-kinetic effects

External potential $\sigma\nabla^2\phi = 0$

EDL potential $\nabla^2\psi = -(\kappa L_{ref})^2 \sinh(\psi)$

Fluid flow

Continuity $\frac{1}{\beta^2}\frac{\partial p}{\partial t} = -\rho\frac{\partial u_i}{\partial x_i}$

Momentum $\rho\left[\frac{\partial u_i}{\partial t} + \frac{\partial\left(u_j u_i\right)}{\partial x_j}\right] = -\frac{\partial p}{\partial x_i} + \frac{1}{\mathrm{Re}}\frac{\partial \tau_{ij}}{\partial x_i^2} + J\sinh(\psi)\left(\frac{\partial\phi}{\partial x_i}\right)$

where σ is the electrical conductivity of the working fluid, κ, known as Debye-Hűckel parameter, is the reciprocate of the EDL thickness

$$\kappa = \left(\frac{2n_0 z^2 e^2}{k_B T \varepsilon\varepsilon_0}\right)^{1/2}$$

in which n_0 is the ionic number concentration in the bulk solution, z is the valance of the ions, e is the elementary charge, k_B is the Boltzmann's constant, T is the temperature measured in kelvin, ε is the dielectric constant of the electrolyte, ε_0 is the permittivity of vacuum, and L_{ref}, is a reference length, defined as follows:

$$L_{ref} = \frac{\Phi A_{chan}}{L_{chan}}$$

in which Φ is the porosity, A_{chan} and L_{chan} are the area of cross section and the length of the channel, respectively. In plain channels, L_{ref} corresponds to the channel width, consistent with the quantity commonly used in previous works concerning EOF, while in channels with flow obstructions, its use should take into account flow enhancement due to the charge of obstruction boundaries. In the continuity equation, β is the artificial compressibility parameter [4, 5]. The stabilization procedure for the CBS scheme applied to the Navier-Stokes equations can be found in [4]. The dimensionless form of the governing equations for forced convection is obtained through the following non-dimensional scales:

$$x_i^* = \frac{x_i}{L_{ref}}; \quad \sigma^* = \frac{\sigma}{\sigma_{ref}}; \quad \phi^* = \left(\frac{ze\phi}{k_B T_{ref}}\right); \quad \psi^* = \left(\frac{ze\psi}{k_B T_{ref}}\right); \quad \rho^* = \frac{\rho}{\rho_{ref}}; \quad u_i^* = \frac{u_i}{u_{ref}};$$

$$t^* = \frac{t u_{ref}}{L_{ref}}; \quad p^* = \frac{p - p_{ref}}{\rho_{ref} u_{ref}^2}; \quad \mathrm{Re} = \frac{\rho_{ref} u_{ref} L_{ref}}{\mu}; \quad J = \left(\frac{2n_0 k_B T_{ref}}{u_{ref}^2 \rho_{ref}}\right); \quad u_{ref} = \frac{E_x \varepsilon\varepsilon_0 \zeta}{\mu}.$$

Both the Laplace and Poisson-Boltzmann equations are solved explicitly, by adding a pseudo time term which becomes negligible when a steady state solution is reached. They are temporally discretized using a forward difference approach and spatially discretized through the standard Galerkin finite element method. The solution of Laplace and Poisson-Boltzmann equations is implemented into the source term of the momentum equation. The modified incompressible Navier Stokes equations are temporally discretized by using the Characteristic Based Split algorithm [5].

3. COMPUTATIONAL DOMAIN AND BOUNDARY CONDITIONS

The walls and any solid boundary are assumed to be active with a prescribed non-dimensional zeta potential and to obey no-slip velocity boundary conditions. With reference to Figure 1, an applied

external potential difference between inlet and outlet is considered and the normal velocity gradients are assumed to be zero at both inlet and outlet. The computation starts with prescribed zero velocity components as initial condition. A 2D unstructured mesh refined near all solid boundaries is employed, to capture the local variation in both internal potential and velocity. A mesh sensitivity study has been carried out in order to find grid independent results.

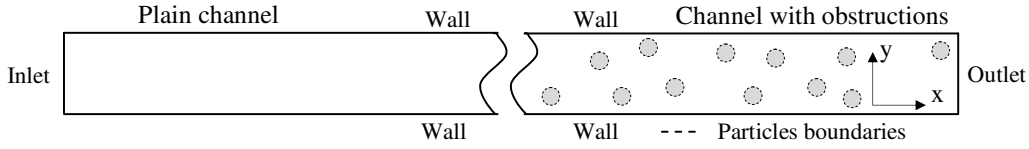

FIGURE 1. Boundary conditions.

4. RESULTS

A silicon micro-channel, characterized by an aspect ratio of 10, with deionized water as working fluid is considered in the present work. Regular circular obstructions are considered. The width of the micro-channel is varied from 5μm to 300μm, while the porosity is varied from 0.8 to 0.4, by increasing particles size.

For channel width lower than 30 μm, the average velocity is higher in plain channels than in channels with obstructions. As expected, in smaller channels the drag resistance induced by flow obstructions is higher than EOF pressure and, as a consequence, the velocity is lower. As the width is increased, this trend is reversed and introduction of obstructions increases the range of effectiveness of EOF. EDL potential is confined close to the charged surfaces: the insertion of obstructions increases the specific charged surface area, enhancing EDL potential distribution, as shown in Figure 2. As a consequence, EOF is affected, since EDL potential distribution appears in the source term of momentum equation.

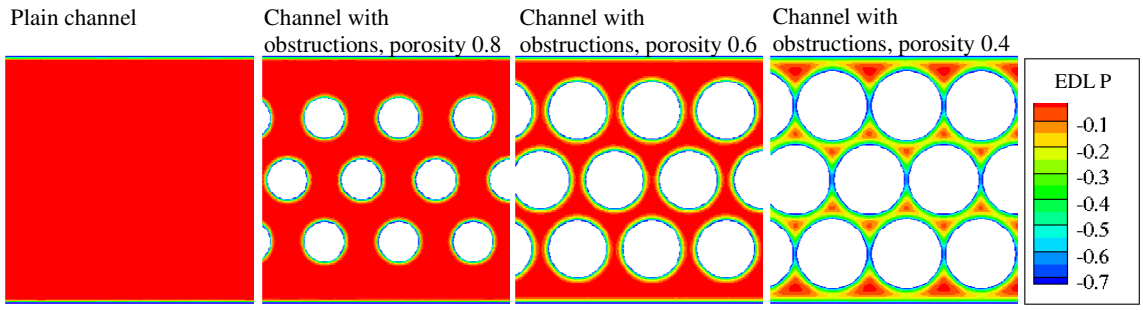

FIGURE 2. EDL potential (EDL P) distribution for plain channel and channels with obstructions, at width of 150μm.

The average velocity calculated at several channel widths is reported in Table 1, where the line indicates the threshold value beyond that the velocity starts to decrease.

Channel width (μm)	Velocity in plain channel (m/s)	Velocity in channel with obstructions (m/s)		
		Porosity 0.8	Porosity 0.6	Porosity 0.4
5	$9.6 \cdot 10^{-6}$	$5.4 \cdot 10^{-7}$	$1.2 \cdot 10^{-7}$	$2.0 \cdot 10^{-8}$
30	$1.3 \cdot 10^{-5}$	$5.7 \cdot 10^{-6}$	$2.6 \cdot 10^{-6}$	$6.1 \cdot 10^{-7}$
120	$1.7 \cdot 10^{-6}$	$6.2 \cdot 10^{-6}$	$6.1 \cdot 10^{-6}$	$4.0 \cdot 10^{-6}$
180	-	$6.5 \cdot 10^{-7}$	$4.9 \cdot 10^{-6}$	$4.8 \cdot 10^{-6}$
300	-	-	-	$2.6 \cdot 10^{-6}$

TABLE 1. Average velocity at different widths.

In order to assess the effectiveness of using obstructions to enhance EOF, the flow rate is determined for different channel widths. As shown in Figure 3, the micro-channels without obstructions appear to be effective up to a channel width of 80μm, while beyond a width of 100μm, the introduction of flow obstructions enhances the fluid flow rate. The range of effectiveness increases as the porosity is decreased: beyond a channel width of 240μm, EOF is advantageous only if an effective porosity of 0.4 is employed.

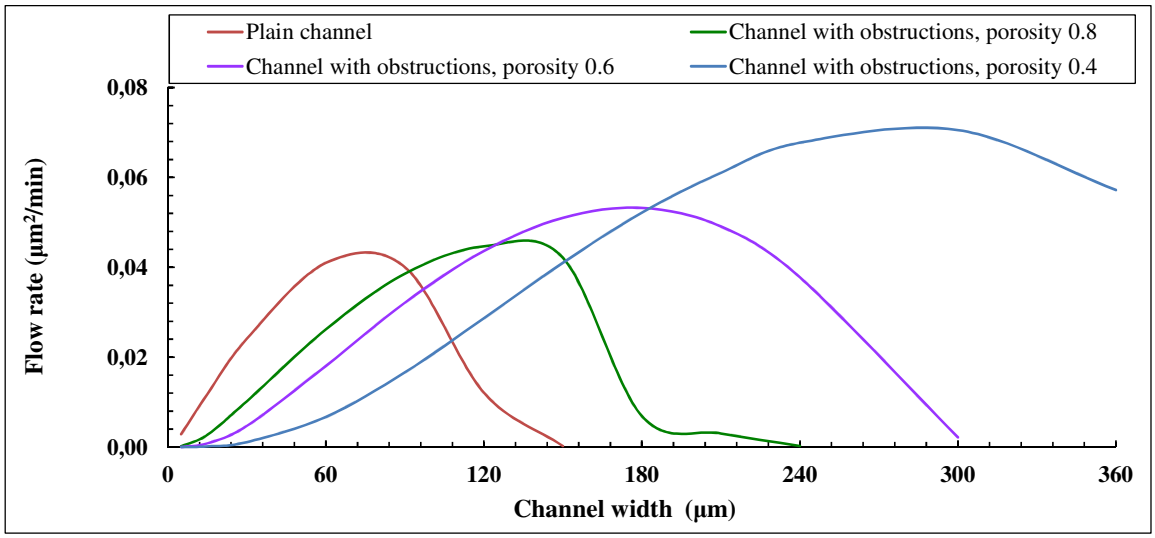

FIGURE 3. Flow rates for plain channels and channels with obstructions, at different widths.

5. CONCLUSIONS

Electro-osmotic flow through micro-channels with and without flow obstructions has been investigated. The introduction of obstructions increases the effectiveness of electro-osmotic flow driven systems: for channel width larger than 100μm, higher flow rate can be ensured only by using flow obstructions. The results indicate that for wider micro-channels, decreasing the porosity by using larger obstructions allows to increase the flow rate.

REFERENCES

[1] R.F. Probstein, *Physicochemical hydrodynamics: an introduction*. John Wiley & Sons, 2005.

[2] N. Scales, Modelling electroosmotic and pressure-driven flow in porous media for micro-fluidic applications. PhD thesis, Carleton University Ottawa, 2004.

[3] N. Massarotti, P. Nithiarasu, A. Carotenuto. Microscopic and macroscopic approach for natural convection in enclosures filled with fluid saturated porous medium, *International Journal of Numerical Methods for Heat and Fluid Flow*, 13(7), 862–886, 2003.

[4] F. Arpino, G. Cortellessa, M. Dell'Isola, N. Massarotti, A. Mauro, High Order Explicit Solutions For Transient Natural Convection of Incompressible Fluids in Tall Cavities, *Numerical Heat Transfer, Part A: Applications*, 66: 839–862, 2014.

[5] P. Nithiarasu, R.W. Lewis, K.N. Seetharamu, *Fundamentals of the Finite Element Method for Heat and Mass Transfer*. Wiley, second edition, 2016.

[6] Patankar NA, Hu HH, Numerical simulation of electroosmotic flow, *Analytical Chemistry*, 70(9), 1870–1881, 1998.

Fourth International Conference on Computational Methods for Thermal Problems
THERMACOMP2016, July 6-8, 2016, Georgia Tech, Atlanta, USA
N. Massarotti, P. Nithiarasu and Y. Joshi (Eds.)

EFFECTS OF PERMEABILITY ON TWO-DIMENSIONAL TRANSPIRATION COOLING

Wenjie Dong, Jianhua Wang, Lin Shen
Department of Thermal Science and Energy Engineering, University of Science and Technology of China, Hefei 230027, PR China, dwj150mc@mail.ustc.edu.cn, jhwang@ustc.edu.cn, sforest@mail.ustc.edu.cn

ABSTRACT

This paper presents numerical investigations to simulate the process of two-dimensional coolant moving, absorbing heat and evaporating in three porous plates, which have the same size and thermal properties except their permeability. From comparisons of numerical results of the three plates, the influences of the permeability on coolant flow and cooling characteristics are discussed. The discussion indicates that the performance of transpiration cooling with liquid phase-change can be greatly optimized by a reasonable design of uneven permeability of porous matrix.

Key Words: *Transpiration Cooling, Permeability, Efficiency.*

Nomenclature

T	temperature, K	$\dot{m}$	interfacial mass transfer rate, $kg \cdot m^{-3} \cdot s^{-1}$
s	phase saturation	$\mathbf{v}$	velocity vector, $m \cdot s^{-1}$
p	pressure, Pa	$\mathbf{g}$	gravity vector, $m \cdot s^{-2}$
K	permeability, m^2	H	specific enthalpy, $J \cdot kg^{-1}$
k	thermal conductivity, $W \cdot m^{-1} \cdot K^{-1}$	c_p	specific heat at constant pressure, $J \cdot kg^{-1} \cdot K^{-1}$

Greek symbols

ρ	density, $kg \cdot m^{-3}$	ε	porosity	μ	dynamic viscosity, $N \cdot s \cdot m^{-2}$

Subscripts

l	liquid	v	vapor	s	solid

1. INTRODUCTION

In recent years, with the development of hypersonic aerospace vehicles, an enhanced transpiration cooling with liquid coolant phase change has been gradually deemed to be the most potential approach of active thermal protection techniques for the leading edge and nose of hypersonic vehicles. Foreest et al. (2011) [1] and Zhao & Wang (2014) [2] estimated the transpiration cooling features with liquid phase change by the experiments conducted in the DLR's Arc Heated Wind Tunnel and the Arc-heated Supersonic Free Jet Facility of CAAA, respectively. Their experimental results demonstrate that the cooling using water as coolant is extremely effective, because the phase change of liquid water within pores released a large number of heat-latent. Despite existence some expensive experiments pertaining transpiration cooling with coolant phase change, the mechanism, principle, numerical evaluation and prediction of transpiration cooling effect in real space environment are the points of emphasis currently.

In fact, some researchers have studied the features of transpiration cooling by numerical method. Using a local thermal non- equilibrium two-phase mixture model (LTNE-TPMM), Shi & Wang [3] analyzed the influences of parameters (porosity, particle diameter, and thermal conductivity of solid

matrix) on the phase interface locations. Using an improved model, He & Wang [4] discussed the fluid flow characteristics and the influence of coolant injection rate on the efficiency of transpiration cooling. However, these investigations were carried out by the assumption of uniform permeability, but most of real transpiration cooling problems are three- or two-dimensional. Therefore it is necessary to discuss the influences of uneven permeability on the characteristics of coolant moving and absorbing heat and evaporating.

2. PHYSICAL AND MATHEMATICAL MODEL

The steady-state transpiration problems studied in this paper is as shown in Fig.1. Three porous plates have the same size with a thickness of 0.1m and a length of 0.4m, but different permeability variations. The permeability of plate 1 and 2 is constant, at 1.5×10^{-13} and 0.75×10^{-13}, respectively, whereas the permeability of plate 3 decreases linearly in x direction from 1.5×10^{-13} to 0.75×10^{-13}. The upper surface of the plates is exposed to a heat flux of q(x), which decreases exponentially in x direction. Liquid coolant is injected from opposite direction into the pores with a mass flow rate of $m=0.27kg/m^2$.

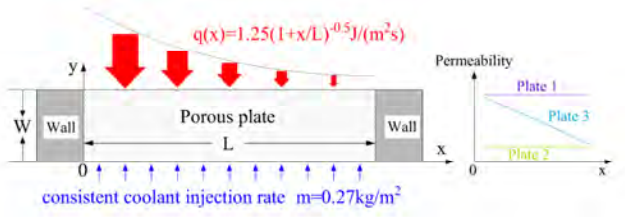

FIGURE 1. Two-dimensional model of transpiration cooling of porous plate

Conversation equations and constitutive relations

Mass

$$\begin{cases} Liquid: & \nabla\cdot(\rho_l \varepsilon s \mathbf{v}_l) = -\dot{m} \\ Vapor: & \nabla\cdot[\rho_v \varepsilon (1-s)\mathbf{v}_v] = \dot{m} \end{cases}$$

Momentum

$$\begin{cases} Liquid: & -\nabla p_l - \rho_l \mathbf{g} - \dfrac{\mu_l}{K_l}\varepsilon s \mathbf{v}_l = 0 \\ Vapor: & -\nabla p_v - \rho_v \mathbf{g} - \dfrac{\mu_v}{K_v}\varepsilon (1-s)\mathbf{v}_v = 0 \end{cases}$$

Energy

$$\begin{cases} Liquid\ region: & \nabla\cdot(\rho_l \varepsilon \mathbf{v}_l H_l) = \nabla\cdot\left(\dfrac{\varepsilon k_l}{c_{p,l}}\nabla H_l\right) + q_{sf} \\ Two\ phase\ region: & (H_v - H_l)\dot{m} = q_{sf} \\ Vapor\ region: & \nabla(\rho_v \varepsilon \mathbf{v}_v H_v) = \nabla\cdot\left(\dfrac{\varepsilon k_v}{c_{p,v}}\nabla H_v\right) + q_{sf} \\ Solid: & \nabla\cdot[(1-s)k_s \nabla T_s] = q_{sf} \end{cases}$$

Relative permeability

$$K_l(s) = K\cdot s^n,\quad K_v(s) = K\cdot(1-s)^n$$

Fluid-solid heat transfer

$$q_{sf} = h_{sf}(T_s - T_f)$$

Boundary conditions

$y=0,\ 0\le x\le L$	$y=W,\ 0\le x\le L$	$0\le y\le W,\ x=0\ or\ L$
$\rho_l v_{in} = m(x)$	$p = p_0$	$u_f = 0$
$h_c(T_s - T_c) = k_{s.eff}\dfrac{dT_s}{dy}$	$k_{s.eff}\dfrac{dT_s}{dy} = q(x)$	$k_{s.eff}\dfrac{dT_s}{dx} = 0$
$h_c(T_s - T_c) = \rho_l v_{in} c_{p.l}(T_f - T_c)$	$k_{f.eff}\dfrac{dT_f}{dy} = 0$	$k_{f.eff}\dfrac{dT_f}{dx} = 0$

TABLE 1. Conversation equations, constitutive relations and boundary conditions

3. NUMERICAL SOLUTION

Coolant evaporating within pores may result in the appearance of three regions: liquid region, two-phase region and vapor region. Fluid flow and heat transfer are described separately in each region

by a series of conservation equations shown in Tab. 1. Through the comparison of numerical result independence on three meshes, which have element numbers 200×800, 250×1000 and 400×1600, respectively, the fixed-grid mesh with 250×1000 elements is chosen.

The solution procedure is briefly described as follows: 1). Assume initial properties, and there is no phase change in porous matrix; 2). Solve the governing equations listed in Tab. 1; 3). Calculate fluid temperature and saturation in the interested domain; 4). Determine the interface location of single- and two-phase regions according to liquid saturation; 5). Solve energy equation, mass and momentum equations; 6). Return to step 3, iteration, until convergence is achieved.

4. RESULTS AND DISCUSSIONS

By comparing the simulated results of the three porous plates, the influences of uneven permeability on transpiration cooling effect are discussed.

Using plate 1, whose permeability is constant, at 1.5×10^{-13}, Figs. 2(a-d) exhibit a series of numerical results of liquid saturation, solid temperature, fluid pressure and coolant vectors, respectively. As illustrated in Fig. 2(a), the area of vapor phase region in left hand side is larger than that in right hand side. It is reasonable, because the heat flux in left hand side is higher than that in right hand side. As illustrated in Fig. 2(b), the temperature in the top left corner is much higher than the others, and the highest local temperature achieves to 1800.7K. This phenomenon can be explained by the fact that the heat flux in left hand side is higher, but the coolant injection rate is uniform. From Figs. 2(c-d), one can find the movement characteristics of coolant and the pressure variations, i.e. in liquid region, the movement direction of coolant is from left to right in Fig. 2(d), which leads to a larger velocity concentration in top right corner, and in Fig. 2(c), the pressure in left hand side is higher than that in right hand side, which results in the coolant flowing to right hand side; in vapor phase region, the coolant vectors show a movement from right to left and the pressure in right hand side is higher than that in left hand side.

Using plate 2, whose permeability is constant, at 0.75×10^{-13}, Figs. 3(a-d) exhibit similar numerical results of liquid saturation, solid temperature, fluid pressure and coolant vectors, respectively, i.e. the interfaces between single- and two-phase regions in Fig. 3(a) and the temperature profile over the solid plate in Fig. 3(b), as well as the fluid flow characteristics shown in Fig. 3(d) are approximately the same with those in Fig. 2(a),(b) and (d). However, the local pressure in Fig. 3(c) is much larger than that in Fig. 2(c). This is reasonable, because the permeability of plate 2 is half of plate 1, while the other properties and boundary conditions of plate 1 and plate 2 are the same.

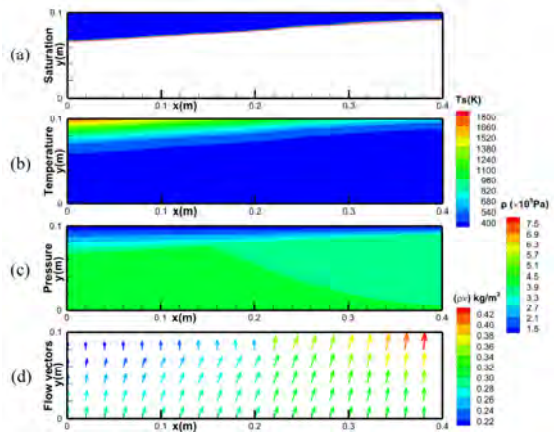

FIGURE 2. Distributions within plate 1

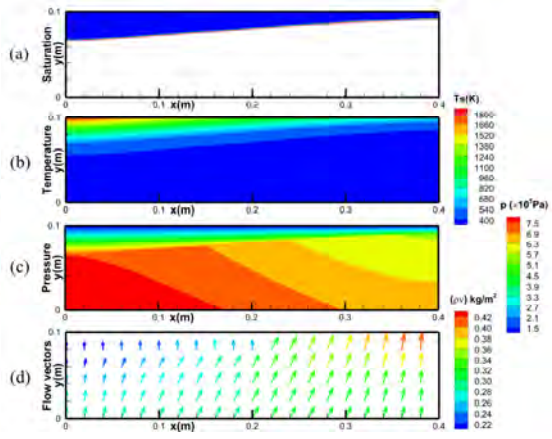

FIGURE 3. Distributions within plate 2

Using plate 3, whose permeability decreases linearly in x direction from 1.5×10^{-13} to 0.75×10^{-13}, Figs. 4(a-d) also exhibit a series of numerical results of liquid saturation, solid temperature, fluid pressure and coolant vectors, respectively. As depicted in Figs. 4(a) and (b), the interfaces of single- and two-phase regions are approximately horizontal, and isotherms are approximately horizontal, too, but the highest local temperature achieves to 1324.8K. From Fig. 4(d), one can find that the movement direction of coolant flow is from right hand side to left hand side in domain of interest, which leads to a larger velocity concentration in top left corner. In Fig. 4(c), it is observed that pressure contours fall slightly from right side to left side. It is worth noting that the left vectors close to the hot surface is larger than right vectors, and the heat flux in left hand side is also larger than that in right hand side. This phenomenon is valuable, because it induces us to consider that coolant moves from the part with low permeability to the part with high permeability, which leads to a larger velocity concentration in the part with high heat flux, as a result, a uniform temperature distribution is obtained, as shown in Fig. 4(b). Compared with the numerical results of plate 1 and 2, the numerical results of plate 3 exhibit that the coolant flow direction is totally changed by the design of uneven permeability distribution and the performance of transpration cooling is optimazed.

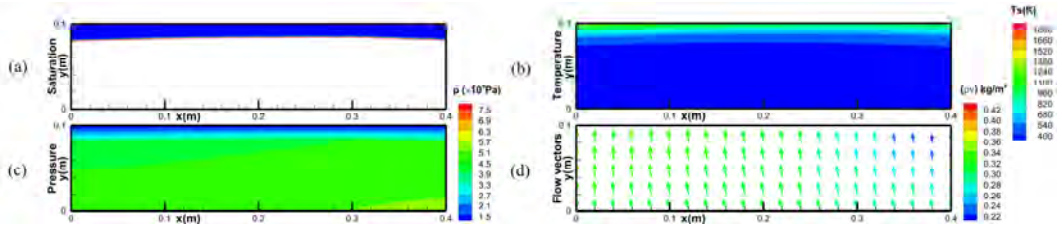

FIGURE 4. Distributions within porous plate 3

5. CONCLUSIONS

Simulations are conducted to study two-dimensional, steady state transpiration cooling problems using the porous plates with different permeability distributions. From the comparison of the numerical results of the different permeability distributions, the performance of transpiration cooling is optimized by the design of an uneven permeability distribution, i.e. permeability is higher in the part where heat flux is higher, too. Obviously, using numerical method in this paper, engineers can easily design the most reasonable permeability distribution of porous materials to optimize the performance of transpiration cooling.

REFERENCES

[1] A.V. Foreest, M. Sippel, A. Guelhan, B. Esser, B.A.C. Ambrosius, K. Sudmeijer, Transpiration cooling using liquid water, *Journal of Thermophysics and Heat Transfer*, 23, 693-702, 2006.

[2] L.J. Zhao, J.H. Wang, An experimental investigation on transpiration cooling under supersonic condition using a nose cone model, *International Journal of Thermal Sciences*, 84, 207-213, 2014.

[3] J.X. Shi, J.H. Wang, A numerical investigation of transpiration cooling with liquid coolant phase change, *Transport in Porous Media*, 87, 703-716, 2011.

[4] F. He, J.H. Wang, Modeling and simulation of transpiration cooling with phase change, *Applied Thermal Engineering*, 58, 173-180, 2013.

Fourth International Conference on Computational Methods for Thermal Problems
THERMACOMP2016, July 6-8, 2016, Georgia Tech, Atlanta, USA
N. Massarotti, P. Nithiarasu and Y. Joshi (Eds.)

DESIGN OF COMPRESSED GRAPHITE/PCM THERMAL BATTERIES

Anne Mallow, Samuel Graham
Georgia Institute of Technology, 771 Ferst Drive Atlanta GA 30332
amallow3@gatech.edu, sgraham@gatech.edu

Kyle Gluesenkamp, Omar Abdelaziz
Oak Ridge National Laboratory, 1 Bethel Valley Road Oak Ridge TN 37831
gluesenkampk@ornl.gov, abdelazizoa@ornl.gov

ABSTRACT

The thermal charging performance of compressed expanded natural graphite foam saturated with a phase change material is modeled under constant heat flux and constant temperature conditions. This phase change moving boundary problem is solved with the effective heat capacity method. The graphite composite properties are modeled using empirically determined volume-averaged density, specific heat, latent heat, and thermal conductivity measurements for each composite. After being experimentally validated for constant temperature boundary conditions of 60°C and constant flux boundary conditions of 0.39 W/cm^2, 1.22 W/cm^2, and 1.55 W/cm^2 for graphite bulk densities of 23, 50, 100, 143 kg/m^3, the use of this model is demonstrated in the design of a thermal battery. The objectives of minimizing size and refrigerant charge while maximizing heat capacity and thermal charging rate are studied as a function of the parameters graphite bulk density, thermal battery dimensions, and refrigerant tube configuration.

Key Words: *Compressed Expanded Natural Graphite, Phase Change Material, Thermal Energy Storage, Numerical Methods*

1. INTRODUCTION

Phase change materials (PCMs) have the ability to store thermal energy as latent heat over a nearly isothermal temperature range. Compared to sensible heat storage, properly chosen PCMs can store an order of magnitude more energy when undergoing phase change. However, since their low thermal conductivity significantly limits the rate of thermal charging and discharging, increasing the thermal performance of PCMs is crucial to the widespread adoption of thermal energy storage technologies. One of the methods used to increase the thermal charging of PCMs is the insertion of highly conductive porous foams within the PCM. Compressed expanded natural graphite (CENG) foams are an attractive thermal enhancement material due to their high thermal conductivity and low density combined with being an inexpensive alternative to metal. Furthermore, CENG foams can be easily molded into various shapes to accommodate any geometry and maximize contact between the composite and the heat source.

The latent heat and thermal conductivity of the solid can be used to characterize the PCM/CENG composite as a function of the bulk density of the graphite foam. While latent heat of the PCM decreases due to the addition of graphite, thermal conductivity of the PCM increases [1-3]. The thermal conductivity of composites formed with CENG bulk densities greater than 50 kg/m^3 is found to be anisotropic [1]. In addition to studying the influence of CENG bulk density on the storage properties of the PCM composite, applications such as thermal management of a battery pack [2], thermal storage in a solar hot water system [3], and general application in constant temperature conditions [4] have been considered. However, comparison of the effectiveness of the CENG on the thermal response of the PCM remains a function of the thermal conductivity of the solid composite. This work focuses on the

development of an experimentally validated PCM/CENG composite model to be used in the design of PCM thermal batteries to predict charging behavior without relying on experiments. This model will be used to optimize the design of the thermal battery considering the size, mass, heat capacity, thermal charging rate, refrigerant charge, and cost of the system.

2. MODELING APPROACH

Modeling latent heat thermal storage materials introduces an additional degree of non-linearity into the heat transfer problem since thermal energy is stored or released at a nearly constant temperature during phase change. In order to describe the temperature distribution through the homogenous medium, the evolution of the phase change boundary through the material must be understood. This moving boundary problem, referred to as the Stefan problem, can be solved analytically, though only feasible for basic 1D analysis, or numerically. The two most common numerical solution methods are referred to as the enthalpy method and the effective heat capacity method [5].

These approaches can be extended to study the heat transfer within foams saturated with a phase change material. The small pore size of graphite foam allows the composite to be modeled as a homogeneous material with thermophysical properties adjusted as a function of the bulk density. One method of solving this composite material heat transfer problem is by using the volume averaging technique, which uses the relative density, $\gamma = V_{foam}/V_{total}$, of the material to adjust the thermophysical properties of each material in the system by its respective volume in the composite [6]. A common assumption that has been experimentally validated for heat transfer in porous media with phase change is that natural convection is suppressed within the pores [7]. With this assumption in addition to assuming thermal equilibrium between the boundary of the foam and PCM, the governing equation can be transformed with the effective heat capacity as Equation 1 [7]. Note that phase change may occur over a range of temperatures, denoted by ΔT, and that the melting temperature is described as T_{melt} such that $T_{solid} = (T_{melt} - \Delta T/2)$ and $T_{liquid} = (T_{melt} + \Delta T/2)$.

$$\left(\rho(T)c_p(T)\right)_{composite}\frac{\partial T}{\partial t} = \nabla\cdot\left(k_{composite}\nabla T\right) \tag{1}$$

or

$$\left[(1-\gamma)\left(\rho c_p\right)_{PCM} + (\gamma)\left(\rho c_p\right)_{foam}\right]\frac{\partial T}{\partial t} = \nabla\cdot\left(k_{eff}\nabla T\right)$$

where,

$$\left(\rho c_p\right)_{PCM} = \begin{cases} \rho c_{p_{solidPCM}} & T < T_{solid} \\ \rho\left[\dfrac{L}{(\Delta T)} + \left(c_p\right)_{solidPCM}\right] & T_{solid} \le T \le T_{liquid} \\ \rho c_{p_{liquidPCM}} & T > T_{liquid} \end{cases}$$

In this work, the effective heat capacity method is used to model CENG foams saturated with PCM. This model requires knowledge of the density and specific heat in both the solid and liquid phase as well as the latent heat and thermal conductivity of the composite. Density and specific heat for the solid and liquid pure PCM were obtained from the manufacturer; for the graphite, these properties were based on published values. Relative density for each CENG foam was used to adjust both the specific heat and density to represent each composite. Latent heat and thermal conductivity was measured for each composite with differential scanning calorimetry and a Hot Disk Thermal analyzer, respectively. The thermophysical measurements and calculations were used in combination with Equation 1 to model the thermal charging performance of the each composite with $\Delta T_{solid-solid}$ = 14°C and $\Delta T_{solid-liquid}$ = 15°C as calculated from DSC measurements. The model is validated with prior experimental data by

comparing the bottom temperature profile over time under various boundary conditions (60°C, 0.39 W/cm^2, 1.22 W/cm^2, and 1.55 W/cm^2) for various bulk densities of graphite (23, 50,100, 143 kg/m^3).

3. RESULTS

The prior experimental setup is modeled using COMSOL 4.4 to compare bottom temperature profiles of different graphite composites to the respective experimental values. The 3D phase change heat transfer problem was solved for the geometry shown in Figure 1 (left), which shows a 0.75 mm layer of thermal grease between the applied boundary condition and the CENG/PCM sample. The boundary condition was applied to the top surface, while the remaining sides were exposed to natural convection to represent the any heat loss. Figure 1 (right) shows comparison of the 23 kg/m^3 and 100 kg/m^3 samples exposed to various boundary conditions.

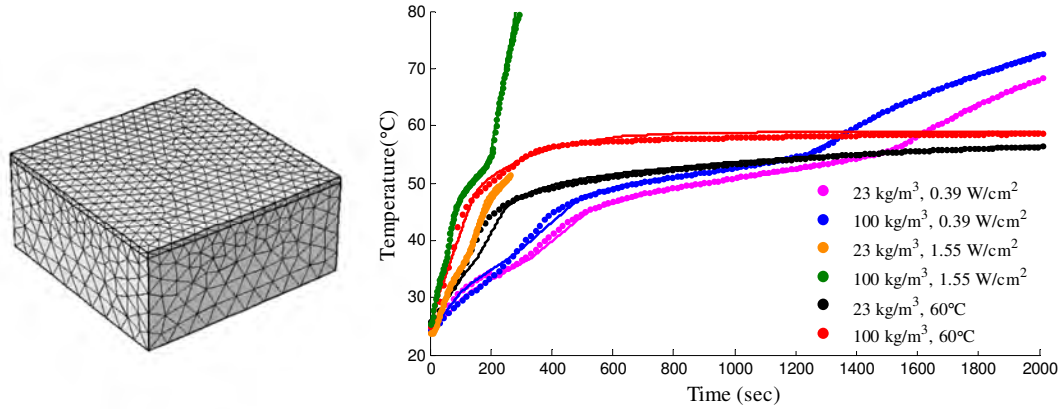

FIGURE 1. Modeled geometry 2.54x2.54x1.27cm (left); Comparison of FEA model to experimental results. Solid and dotted lines represent numerical and experimental results, respectively (right)

There is less than 10% error between the time to end of melt for the model and the experiments, which indicates the validity of the model in designing heat exchangers with the PCM composites. The application of this model is demonstrated by designing a thermal battery to store 170 W for a period of 2 hour, or 1224 kJ, of heat from a refrigerant passing through the battery at 48°C. The design of such a condenser requires knowledge of thermal charging behavior for PCM composites as well as adhering to constraints of size, mass, heat capacity, thermal charging rate, and refrigerant charge.

To determine the impact of the graphite bulk density on other design constraints of the thermal battery, the volume averaged effective heat capacity method was used to find the melt distance, x, defined as the radial distance from the refrigerant tubing that PCM has undergone phase change after 2 hours as shown in Figure 2 (left). The melt distance as a function of bulk density was used to calculate the phase change heat exchanger (PCHX) mass and volume, refrigerant charge, and length of refrigerant tubes for a unit that stores 1224 kJ of thermal energy. In general, as the bulk density increases, the increased thermal conductivity results in a greater melt distance that decreases the refrigerant charge and number of refrigerant tubes. Furthermore, as the bulk density increases, the latent heat decreases due to the addition of graphite. This means that the mass and volume of the heat exchanger increases to store the required amount of energy. Results are shown in Figure 2 (right).

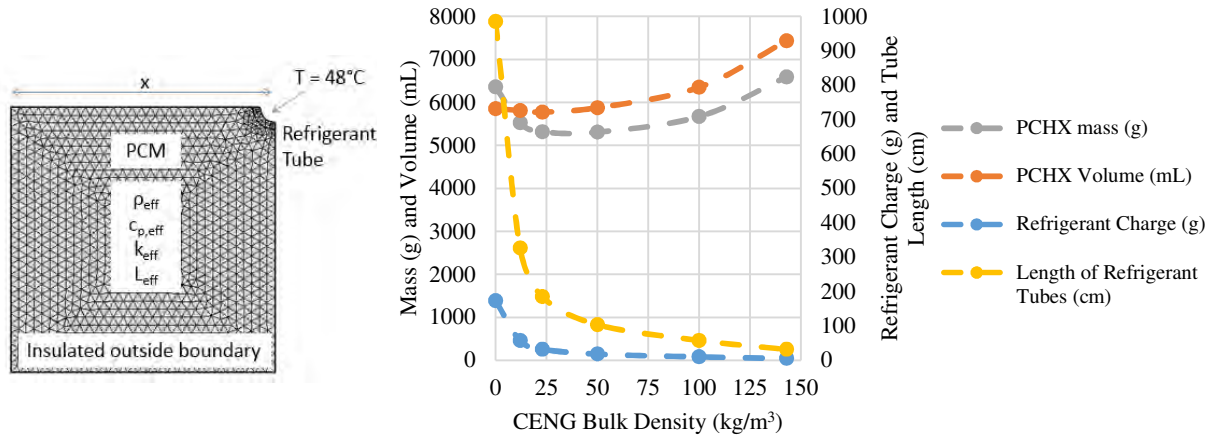

FIGURE 2. CENG modeled geometry (left); Summary the impact of CENG bulk density on design parameters (right)

4. CONCLUSIONS

A 3D phase change model was developed and validated for CENG/PCM composites; the phase change moving boundary problem was solved using the effective heat capacity method with the addition of the graphite using the volume averaging assumption. The model was used to demonstrate the ability to design a thermal battery based on the objectives of minimizing size and refrigerant charge while maximizing heat capacity and thermal charging rate.

REFERENCES

[1] X. Py, R. Olives, and S. Mauran, "Paraffin/porous-graphite-matrix composite as a high and constant power thermal storage material," *International Journal of heat and mass transfer,* vol. 44, pp. 2727-2737, 2001.

[2] A. Mills, S. Al-Hallaj, M. Farid, and J. R. Selman, "Thermal conductivity enhancement of phase change materials using a graphite matrix," *Applied Thermal Engineering,* vol. 26, pp. 1652-1661, 2006.

[3] D. Haillot, V. Goetz, X. Py, and M. Benabdelkarim, "High performance storage composite for the enhancement of solar domestic hot water systems: Part 1: Storage material investigation," *Solar energy,* vol. 85, pp. 1021-1027, 2011.

[4] Y. Zhong, S. Li, X. Wei, Z. Liu, Q. Guo, J. Shi*, et al.*, "Heat transfer enhancement of paraffin wax using compressed expanded natural graphite for thermal energy storage," *CARBON,* vol. 48, pp. 300-304, 2010.

[5] M. Iten and S. Liu, "A work procedure of utilising PCMs as thermal storage systems based on air-TES systems," *Energy Conversion and Management,* vol. 77, pp. 608-627, 2014.

[6] Z. Chen, M. Gu, and D. Peng, "Heat transfer performance analysis of a solar flat-plate collector with an integrated metal foam porous structure filled with paraffin," *Applied Thermal Engineering,* vol. 30, pp. 1967-1973, 2010.

[7] K. Kota, L. Chow, and Q. Leland, "Laminar film condensation driven latent thermal energy storage in rectangular containers," *International Journal of Heat and Mass Transfer,* vol. 55, pp. 1208-1217, 2012.

PARALLEL SESSION

NUMERICAL METHODS

Fourth International Conference on Computational Methods for Thermal Problems
THERMACOMP2016, July 6-8, 2016, Georgia Tech, Atlanta, USA
N. Massarotti, P. Nithiarasu and Y. Joshi (Eds.)

A NOVEL REINITIALIZATION TECHNIQUE TO CONSERVE MASS AND ENHANCE ACCURACY IN VOF METHOD

S. P. Bhat, J. C. Mandal
Aerospace Engineering Department, IIT Bombay, India, mandal@aero.iitb.ac.in

ABSTRACT

A novel reinitialization technique for mass conservation and reduction of diffusion error in VOF method is presented. This technique is general enough to be easily extended to unstructured mesh. The efficacy of the present technique is demonstrated by computing a few standard test problems.

Key Words: *Volume of Fluid, Reinitialization, Mass Conservation, Sharp Interface Capturing.*

1. INTRODUCTION

The volume of fluid (VOF) method is one of the very popular approaches for solving multi-fluid flows. In this method, accurate positioning of fluid interface plays a vital role as it allows accurate calculation of surface forces and realistic visualization of the flow. In this method, an advection equation of volume fraction C, given by equation,

$$\frac{\partial C}{\partial t} + u\frac{\partial C}{\partial x} + v\frac{\partial C}{\partial y} = 0 \tag{1}$$

is added to the Navier-Stokes equations to solve a two-fluid system. This equation is solved in volume tracking methods, like VOF, for interface capturing. The piecewise linear interface calculation (PLIC) technique in VOF has been very successful for interface capturing which is extensively studied in [1, 4]. The PLIC technique is not simple to extend to unstructured meshes due to its dependence on mesh geometry for flux calculation [2]. Therefore, the need for a more elegant and general approach of reconstruction of fluid interface and calculation of interface fluxes is felt. An alternative approach may be to use Riemann solver with solution reconstruction. However, the major drawback with this approach is the high diffusion at fluid interface with lower order solution reconstruction. Also, high-order non-total-variation-diminishing (non-TVD) method can introduce spurious oscillations in the solution near discontinuities (fluid interfaces). In addition, the very-high-order methods are computationally expensive. A new method for maintaining the sharp fluid interface is therefore presented here, which can be used with moderate order of solution reconstruction approach along with a Riemann solver. The new reinitialization technique is tested with a first order and well-known high-order solution reconstructions based on Weighted Essentially Non-Oscillatory (WENO) approach of third and fifth order of accuracy [5].

2. NOVEL REINITIALIZATION TECHNIQUE

The reinitialization of VOF function is based on the marching squares method [3]. The marching squares method is widely used in computer graphics visualization for producing contour lines and it can be easily extended to any cell geometry. This method with few modifications is adopted here for calculation of total mass for a given volume fraction level. In this approach, we begin by setting total mass equal to zero and interpolating the cell center values to the cell nodes. Every cell node is then evaluated to check whether its value is above or below the volume fraction level and it is

marked as 1 or 0 respectively. The cell which has all four nodes marked as 1 is contained inside the volume fraction, therefore the area of the cell is added to total mass. On the other hand, the cell with all nodes marked as 0 are ignored. All the remaining cells contain the interface line corresponding to the volume fraction being considered. These cells fall in one of the 14 cases (case 1 through 14) as shown in FIGURE 1 and the appropriate mass (area in 2D) is added to total mass. The calculated total mass obviously may not be equal to the exact mass of the tracked fluid. Therefore, we start with 0.5 as the initial guess value, and iterate to converge to the volume fraction level corresponding to the exact mass using the bisection method up to an accuracy of 10^{-6}. Once the volume fraction level which conserves the mass is obtained, the volume fraction field is reinitialized with the volume fraction obtained from FIGURE 1. It may be noted that, frequent reinitialization of VOF field is not required, especially in case of high order methods, as the diffusion is well controlled, and unnecessary reinitialization adds to the computational overhead. Also, less frequent reinitialization will lead to accumulation of diffusion error. Hence, there exists an optimal reinitialization frequency for a given problem depending on the method of solution reconstruction.

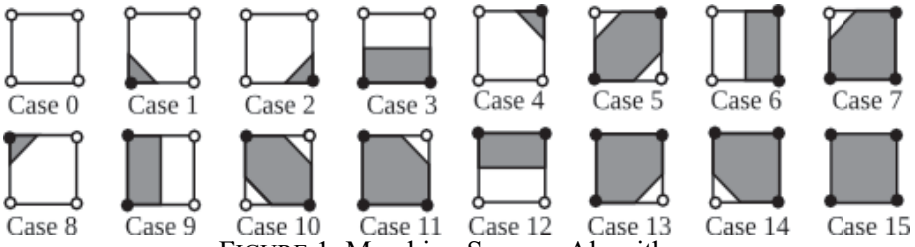

FIGURE 1. Marching Squares Algorithm

3. ERROR CALCULATION

Let the exact solution of equation (1) for the i^{th} cell be C_i^e and the numerical solution be C_i^n. The L_1- and L_2-norm of error in the solution for the i^{th} cell can then be defined as,

$$\epsilon_{L1} = \frac{1}{N}\sum^{N} \epsilon_i\,; \quad \epsilon_{L2} = \sqrt{\frac{1}{N}\sum^{N} (\epsilon_i)^2}\,; \quad \text{where,} \qquad \epsilon_i = |C_i^e - C_i^n|$$

4. RESULTS AND DISCUSSION

The performance of the new reinitialization technique is demonstrated by solving two standard test problems. The contour plots of reinitialized solution are plotted only for a reinitialization frequency of 40 iterations and for a mesh size of 160×160.

Test Problem 1 - Translation of Square Volume: A square volume of side 0.2 is placed in a uniform velocity field given by $\vec{V} = (1, -1)$. The computational domain has dimensions of $[0,1] \times [0,1]$, and the square volume is placed at time $t = 0$ with its left-bottom corner at $(0.4, 0.4)$. The contour plots of the VOF function for different reconstruction methods are shown in FIGURE 2 with the initial position of the square shown using dashed line. The error plots and the computing time plots are shown in FIGURE 3 and FIGURE 4 respectively.

Test Problem 2 - Circular Volume in Transient Shear Velocity Field: A circular volume of radius 0.2π is placed in a transient shearing velocity field given by,

$$\vec{V}(x,y,t) = \begin{cases} (\sin(x)\cos(y), -\cos(x)\sin(y)), & t < T/2 \\ (-\sin(x)\cos(y), \cos(x)\sin(y)), & t \geq T/2 \end{cases}; \text{ where, } T = 8$$

The computational domain has dimensions of $[0, \pi] \times [0, \pi]$, and the circular volume is placed at time $t = 0$ with its center at $(0.5\pi,\ 0.2 + 0.2\pi)$. The contour plots of final solution (at $t = T = 8$) of the VOF function for different reconstruction methods and the maximum extent of shear (shown

as dashed line at $t = 4$) are shown in FIGURE 5. The error plots and the computing time plots are shown in FIGURE 6 and FIGURE 7 respectively.

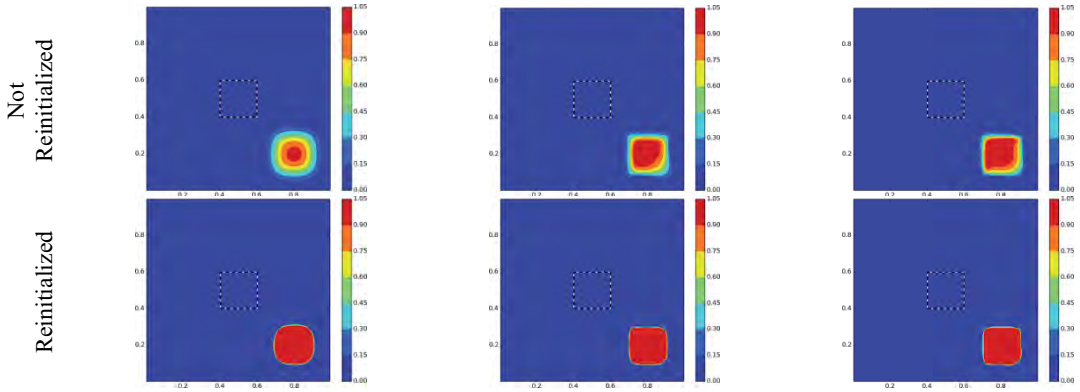

FIGURE 2. Translation of Square Volume

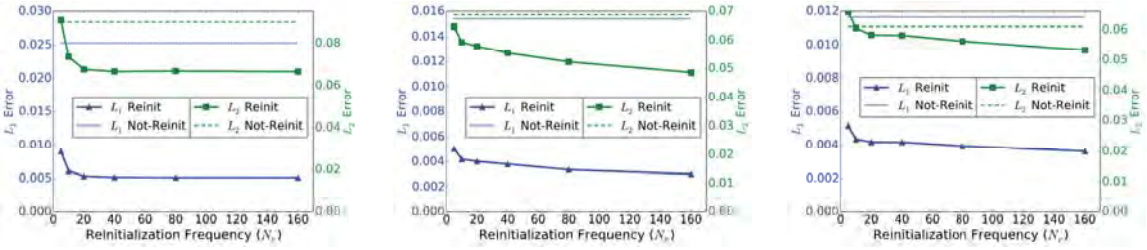

FIGURE 3. Error Plots - Translation of Square Volume

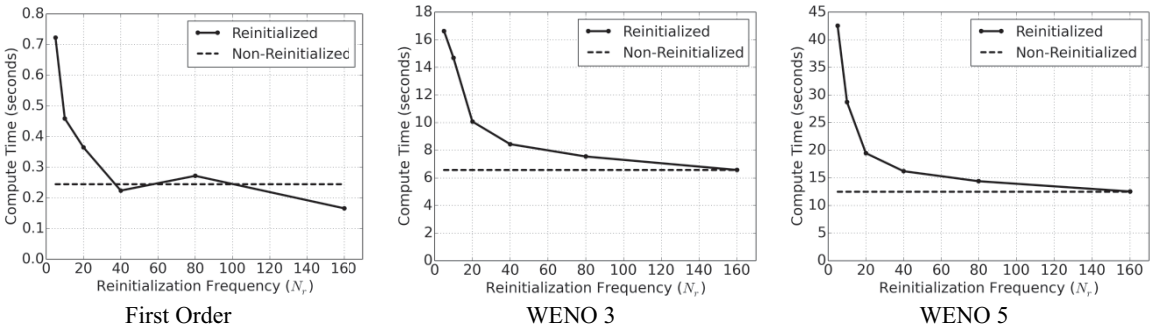

FIGURE 4. Computation Time - Translation of Square Volume

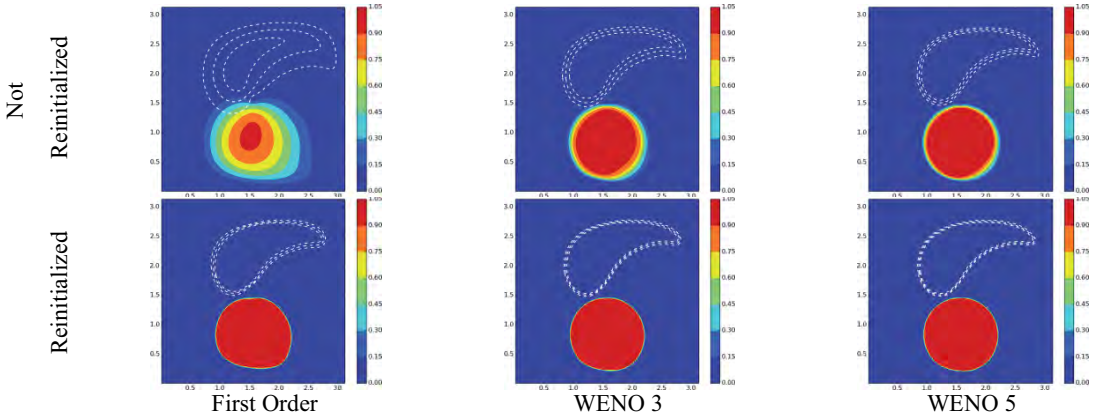

FIGURE 5. Circular Volume in Transient Shear Velocity Field

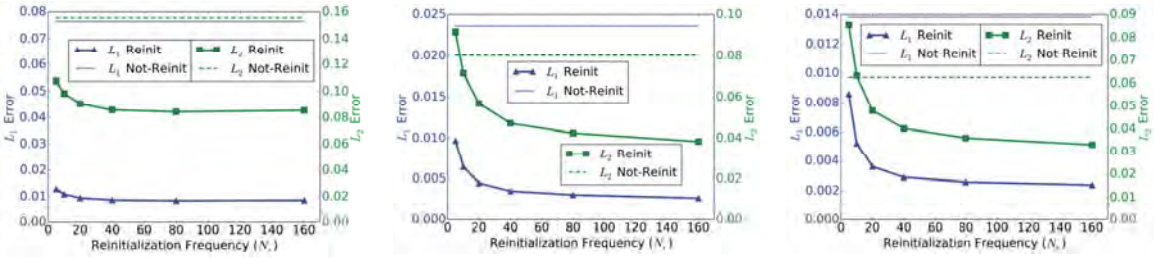

First Order WENO 3 WENO 5

FIGURE 6. Error Plots - Circular Volume in Transient Shear Velocity Field

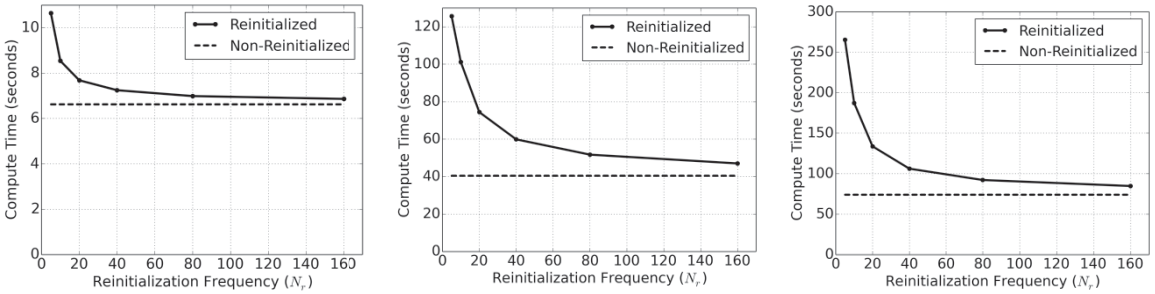

First Order WENO 3 WENO 5

FIGURE 7. Computation Time - Circular Volume in Transient Shear Velocity Field

4. CONCLUSIONS

The commonly used techniques in the VOF method, using geometry based interface reconstruction, like PLIC, maintain very sharp fluid interfaces and also conserve mass. However, they are found to be complicated to extend to unstructured mesh, which is required for analysis of flow over complex geometries. The Riemann solver based methods, on the other hand, can be easily extended to unstructured mesh but suffer from the problem of diffused fluid interface. The reinitialization technique proposed here, overcomes the shortcomings of these two methods. This technique is based on the marching squares method which is commonly used in computer graphics and visualization. The new method is found to successfully conserve mass and restrict the diffusion error introduced by Riemann solver based methods. Also, this methodology can be easily extended to unstructured mesh. It is observed from solved test cases that the method maintains very sharp interfaces between the fluids. The high order solution reconstruction methods, do not diffuse the interfaces too much in few iterations, hence the reinitialization of the VOF function can be carried out less frequently to reduce computational cost.

REFERENCES

[1] E. Aulisa, et al. Interface reconstruction with least-squares fit and split advection in three-dimensional Cartesian geometry. *Journal of Computational Physics*, 225(2):2301—2319, 2007.

[2] Kei Ito, et al. A volume-conservative PLIC algorithm on three-dimensional fully unstructured meshes. *Computers & Fluids*, 88:250—261, 2013.

[3] William E. Lorensen, Harvey E. Cline. Marching cubes: A high resolution 3D surface construction algorithm. *Computer Graphics*, 21(4):163—169, 1987.

[4] William J Rider, Douglas B Kothe. Reconstructing Volume Tracking. *Journal of Computational Physics*, 141:112—152, 1998.

[5] Chi-wang Shu. ENO and weighted ENO schemes for hyperbolic conservation laws. In *Advanced Numerical Approximation of Nonlinear Hyperbolic Equations* .Springer Berlin Heidelberg, 1997.

Fourth International Conference on Computational Methods for Thermal Problems
THERMACOMP2016, July 6-8, 2016, Georgia Tech, Atlanta, USA
N. Massarotti, P. Nithiarasu and Y. Joshi (Eds.)

ASYMPTOTIC APPROACH AND BOUNDARY ELEMENT METHOD FOR CALCULATION OF SLOW PHASE TRANSITIONS

Iuliia Brazaluk, Dmytro Yevdokymov
Oles Honchar Dnipropetrovsk National University, Gagarin ave., 72, Dnipropetrovsk,, 49010, Ukraine brazaluk_jv@ukr.net, devd@mail.ru

ABSTRACT

Actual and important in practical applications problem of heat and mass transfer with phase transitions is considered in particular case of Stefan problem under small Stefan number. This case implies unmovable phases and relatively large latent specific heat of phase transformation in comparison with heat capacities of the phases. An asymptotic approach with Stefan number as a small parameter is applied for simplification of the problem. It is shown that boundary element method is high effective for numerical solution of obtained series of boundary-value problems. The developed approach is illustrated by several examples of numerical calculations.

Key Words: *Phase Transition, Stefan Problem, Stefan Number, Small Parameter Method, Boundary Element Method.*

1. INTRODUCTION

Last decades phase transformation processes attracted growing attention in computational heat and mass transfer, because their consideration leads to complicated problems with specific kind of non-linearity. A lot of approaches were proposed for phase transition calculation. Slow phase transformations (phase transformation under small Stefan number) are widespread in natural processes, however they are worse investigated, than ordinary fast phase transformations. The reason of such situation is difficulties in numerical solution of correspondent problems, because traditional finite difference and finite element methods are evidently non-effective for that kind of problems, because they require a huge number of time steps. The quasi-stationary approximation (Leybenzon approximation) [1] was only tool for such problems during long time, however it requires asymptotically small Stefan number. Small parameter method is applied to the problem in paper [2], it gives an opportunity to consider the problem under any Stefan number less than 1. The natural development of that approach is application of small parameter method together with some numerical method to two- and three-dimensional Stefan problems.

2. MAIN BODY

Consider two-phase Stefan problem in dimensionless form:

$$\frac{\partial \theta_1}{\partial \tau_{st}} \mathrm{St} = \Delta\theta_1, \tag{1}$$

$$\frac{\partial \theta_2}{\partial \tau_{st}} f_a \mathrm{St} = \Delta\theta_2, \tag{2}$$

here the Stefan number $\mathrm{St} = \frac{C(T_n - T_{p.t.})}{\sigma}$ is determined for first phase by traditional way [2], $f_a = \frac{Fo_1}{Fo_2} = \frac{a_1}{a_2}$, $\tau_{st} = \frac{\tau\lambda_1(T_n - T_{ф.п.})}{L^2\sigma\rho}$, $Fo_1 = \frac{\tau a_1}{L^2}$, $Fo_2 = \frac{\tau a_2}{L^2}$.

Let, for the sake of easy, the first kind boundary conditions are prescribed on the outer boundaries of phases, thus

$$\theta_1\big|_{\Gamma_1} = \theta_{1s}, \tag{3}$$

$$\theta_2\big|_{\Gamma_2} = \theta_{2s}, \tag{4}$$

$$\theta_1\big|_{\Gamma_{p.t.}} = 0, \tag{5}$$

$$\theta_2\big|_{\Gamma_{p.t.}} = 0, \tag{6}$$

and Stefan condition

$$\frac{\partial\theta_1}{\partial n} - f_\lambda \frac{\partial\theta_2}{\partial n} = \frac{\partial n^*}{\partial\tau_{st}}, \tag{7}$$

where $f_\lambda = \lambda_2/\lambda_1$. Smallness of Stefan number is a result of existence of two different time scales in the Stefan problem for slow phase transition. The first one is determined by heat conduction process and the second one is determined by interphase boundary motion. The second process is slower than the first one. The Stefan number is relation of mentioned time scales.

According to small parameter method the dimensionless temperature fields in the phases are represented as two series [3, 4]

$$\theta_1 = \theta_1^0(x,y,z,\tau) + \sum_{k=1}^{\infty} St^k \theta_1^k(x,y,z,\tau), \tag{8}$$

$$\theta_2 = \theta_2^0(x,y,z,\tau) + \sum_{k=1}^{\infty} St^k \theta_2^k(x,y,z,\tau). \tag{9}$$

As a result the dimensionless two-phase Stefan problem is reduced to following series of the problems

$$\Delta\theta_1^0 = 0, \quad \Delta\theta_1^1 = \frac{\partial\theta_1^0}{\partial\tau}, \ldots., \quad \Delta\theta_1^i = \frac{\partial\theta_i^{i-1}}{\partial\tau}, \ldots \tag{10}.$$

$$\Delta\theta_2^0 = 0, \quad \Delta\theta_2^1 = f_a \frac{\partial\theta_2^0}{\partial\tau}, \ldots.., \quad \Delta\theta_2^i = f_a \frac{\partial\theta_2^{i-1}}{\partial\tau}, \ldots \tag{11}$$

with boundary conditions

$$\theta_1^0\big|_{\Gamma_1} = \theta_{1s}, \quad \theta_1^0\big|_{\Gamma_{p.t.}} = 0, \ldots, \quad \theta_1^i\big|_{\Gamma_1} = 0, \ldots, \quad \theta_1^i\big|_{\Gamma_{p.T.}} = 0, \ldots \tag{12}$$

$$\theta_2^0\big|_{\Gamma_2} = \theta_{2s}, \quad \theta_2^0\big|_{\Gamma_{p.t.}} = 0, \ldots, \quad \theta_2^i\big|_{\Gamma_2} = 0, \ldots, \quad \theta_2^i\big|_{\Gamma_{p.t.}} = 0, \ldots \tag{13}$$

and Stefan condition

$$\frac{\partial\theta_1^0}{\partial n} - f_\lambda \frac{\partial\theta_2^0}{\partial n} = \frac{\partial\eta^0}{\partial\tau}, \ldots, \quad \frac{\partial\theta_1^i}{\partial n} - f_\lambda \frac{\partial\theta_2^i}{\partial n} = \frac{\partial\eta^i}{\partial\tau}, \ldots \tag{14}$$

where all variables are dimensionless. The relations (14) must be complemented by some initial conditions and can be considered as series of Cauchy problems for phase transition boundary position. The first equations and boundary conditions in (10) - (14), which describes the temperature approximations indicated by index “0”, coincide with well-known quasi-stationary approximation. Note that for one-dimensional (in space) case for any Stefan problems the boundary-value problems indicated by “0” and “1” can be integrated analytically but the following

approximations requires some numerical method for solution of mentioned Cauchy problem. Such solutions were built for one-phase and two-phase one-dimensional (in ordinary Cartesian, polar and spherical coordinate systems) Stefan problems with different boundary conditions on the outer boundaries. There are particular cases of one-dimensional Stefan problems, analytical solutions of which are known. The mentioned analytical solutions were used to check the approach accuracy. As a result, it is shown that accuracy of test problem solutions is enough high.

However the temperature fields must be determined numerically in two-dimensional and three-dimensional cases. Boundary element method [5, 6] is used in the present work to this end. It supposes transformation of equations (10), (11) into boundary integral equations

$$C(x_0)\theta_1^0(x_0) = \int\limits_{\Gamma_1 \cup \Gamma_{p.t.}} \varphi_0(x, x_0)\frac{\partial \theta_1^0}{\partial n}ds - \int\limits_{\Gamma_1 \cup \Gamma_{p.t.}} \theta_1^0 \frac{\partial \varphi_0(x, x_0)}{\partial n}ds, \quad (15)$$

$$C(x_0)\theta_2^0(x_0) = \int\limits_{\Gamma_2 \cup \Gamma_{p.t.}} \varphi_0(x, x_0)\frac{\partial \theta_2^0}{\partial n}ds - \int\limits_{\Gamma_2 \cup \Gamma_{p.t.}} \theta_2^0 \frac{\partial \varphi_0(x, x_0)}{\partial n}ds, \quad (16)$$

……

$$C(x_0)\theta_1^i(x_0) = \int\limits_{\Gamma_1 \cup \Gamma_{p.t.}} \varphi_0(x, x_0)\frac{\partial \theta_1^i}{\partial n}ds - \int\limits_{\Gamma_1 \cup \Gamma_{p.t.}} \theta_1^i \frac{\partial \varphi_0(x, x_0)}{\partial n}ds + \int\limits_{D_1} \varphi_0(x, x_0)\frac{\partial \theta_1^{i-1}}{\partial \tau}dx, \quad (17)$$

$$C(x_0)\theta_2^i(x_0) = \int\limits_{\Gamma_2 \cup \Gamma_{p.t.}} \varphi_0(x, x_0)\frac{\partial \theta_2^i}{\partial n}ds - \int\limits_{\Gamma_2 \cup \Gamma_{p.t.}} \theta_2^i \frac{\partial \varphi_0(x, x_0)}{\partial n}ds + \int\limits_{D_2} \varphi_0(x, x_0)\frac{\partial \theta_2^{i-1}}{\partial \tau}dx, \quad (18)$$

where φ_0 is fundamental solution of Laplace equation. Equations (15) - (18) are solved numerically by well-known boundary element algorithm [5, 6]. According to that algorithm, the boundaries of phases are fragmented by boundary elements and temperatures and thermal fluxes are assumed constant on every boundary element. Thus, the system of linear algebraic equations with respect to unknown values of temperature or thermal flux on elements is formed. Solving mentioned systems of linear algebraic equations, corresponding to every boundary integral equation (15) - (18) we can obtain the temperature distribution with required accuracy at some instant, that is under specific shape of interphase boundary. Then new position of interphase boundary must be determined using the Stefan condition (14). To build new interphase boundary relation (14) must be considered as an ordinary differential equation, and correspondent Cauchy problem must be solved numerically. The Euler method is used for this aim in the present work. If it is necessary, the problems (15) - (18) can be solved by boundary element method for new shape of the interphase boundary. Such time-stepping process can be continued during any time interval. The main advantage of proposed time-stepping approach in comparison with time-stepping finite difference and finite element methods is time discretization with respect to slow time scale determined by interphase boundary motion unlike finite difference and finite element methods, which requires time discretization with respect to fast time scale determined by heat conduction process.

3. RESULTS

The proposed approach is illustrated by following examples of numerical calculations. Melting process of cylinder, which had initial circular shape, is shown on fig. 1 and 2 under different conditions of heating.

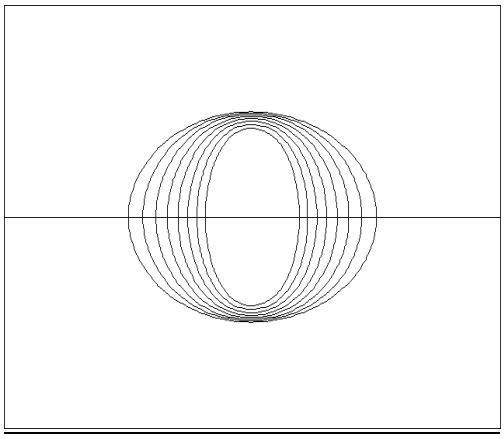

Fig. 1. Sequence of phase transformation boundary positions under side heating

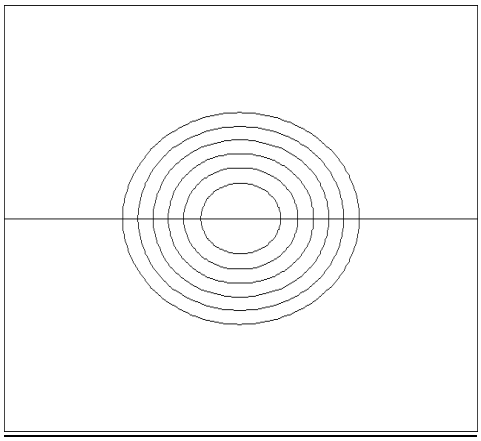

Fig. 2. Sequence of phase transformation boundary positions under multifold heating

4. CONCLUSIONS

Some conclusions can be made It is evident that the above proposed approach is more general and has more opportunities than earlier existing computational methods for slow phase transitions. It gives an opportunity to effectively calculate of the processes in more broad band of Stefan numbers. Enough high accuracy of the proposed algorithms is confirmed by the series of test calculations. The results of calculations can be used in investigations of a number of processes, first of all, in investigations of slow phase transformations in microgravity and in environment. They also can be used in design of space-rocket technique.

REFERENCES

[1] L.I. Rubinstein, *The Stefan Problem,* AMS Translations of Mathematical Monographs, Vol. 27, Amer. Math. Soc., Providence, R.L., 1971.

[2] G.S.H. Lock, J.R. Gunderson, D. Quon, J.K. Donnelly, A study of onedimensional ice formation with particular reference to periodic growth and decay, *International Journal of Heat and Mass Transfer,* v.12, N 11, 1969.

[3] Bevza E.K., Yevdokymov D.V., Kochubey O.O. Boundary element method application for solution of Stefan problem for slow phase transition // *Bulletin of Kharkov National University,* № 590. – P. 26-31, 2003. (in Russian)

[4] Bevza E.K., Yevdokymov D.V., Kochubey O.O. Mathematical modelling of phase transformation processes in microgravity conditions // *Bulletin of Donetsk university. Series A. Natural sciences*, № 2. – P. 249-253, 2002. (in Russian)

[5] C.A. Brebbia, J.C.F. Telles, L.C. Wrobel, *Boundary element techniques*, Springer-Verlag, Berlin, New York, 1984.

[6] P.K. Banerjee, R. Butterfield, *Boundary element methods in engineering science,* McGrow-Hill, London, New York, 1981.

Fourth International Conference on Computational Methods for Thermal Problems
THERMACOMP2016, July 6-8, 2016, Georgia Tech, Atlanta, USA
N. Massarotti, P. Nithiarasu and Y. Joshi (Eds.)

MODELING OF MELTING WITH SOLID BULK MOTION

Y. Kozak, G. Ziskind
Department of Mechanical Engineering, Ben-Gurion University of the Negev, Beer-Sheva 84105, Israel, kozaky@post.bgu.ac.il, gziskind@bgu.ac.il

ABSTRACT

The present work deals with a novel numerical method for modeling solid-liquid phase change problems. The new method involves a full solution of the conservation equations, namely, continuity, momentum and energy on a fixed grid via the enthalpy method. This approach allows proper coupling between the enthalpy method and the solid bulk motion. Two physical effects are investigated: sinking of the solid bulk at a constant velocity and natural convection in the melt. The separate effect of each of these phenomena is tested, and also the effect of both of them combined together. It is found that the melting patterns are completely different for each one of the cases. However, sinking at the chosen, relatively low, velocity does not affect significantly the melting rate.

Key Words: *PCM, Enthalpy Method, Natural Convection*

1. INTRODUCTION

Solid-liquid phase change modeling is essential for many engineering applications, including latent-heat thermal energy storage or thermal management of electronic equipment. Design of these systems requires to take into account different complex physical phenomena such as volume change, natural convection in the melt, and solid bulk motion which interacts with the already melted liquid phase. One of the leading methods for solid-liquid phase change modeling is the enthalpy method [1]. This method allows to solve arbitrary geometries on a fixed grid without any need to track the solid-liquid interface. An improved version of the enthalpy method, which can take into account convection in the melt, is known as the enthalpy-porosity method [2]. This method utilizes a momentum sink term that mimics the Kozeny–Carman equation for porous media. Recently, an improved enthalpy method that is coupled with solid sinking motion was suggested [3]. The main drawback of this approach is that it does not include thermal convection in the melt. In the current work a new formulation for the enthalpy method is suggested. This new approach allows proper modeling of the interaction between the solid bulk motion and the natural convection in the cavity. Also, the new method does not require any arbitrary constants, such as the mushy zone constant in the enthalpy-porosity formulation [3], or high effective viscosity [4] that can cause numerical stiffness. The different effects of two physical phenomena, namely, solid bulk motion at a constant velocity and natural convection in the melt, are investigated and discussed.

2. MODELING

The modeling approach in this paper involves a full solution of the conservation equations, while taking into account the phase change via an enthalpy method.

The following assumption are used:

- The PCM (phase-change material) volume change is neglected
- Natural convection is taken into account with the Boussinesq approximation
- The PCM properties are constant
- 3-D effects are neglected

- The flow is laminar and incompressible
- The PCM is a pure material

The equations that govern the problem are:

Continuity equation:

$$\frac{\partial u}{\partial x}+\frac{\partial v}{\partial y}=0 \tag{1}$$

where u and v are the x and y velocity components, x and y are Cartesian coordinates.

Momentum equations:

$$\frac{\partial u}{\partial t}=-\frac{\partial\left(u^2\right)}{\partial x}-\frac{\partial(uv)}{\partial y}+\frac{\mu}{\rho}\left(\frac{\partial^2 u}{\partial x^2}+\frac{\partial^2 u}{\partial y^2}\right)-\frac{1}{\rho}\frac{\partial p}{\partial x}+f_x \tag{2}$$

$$\frac{\partial v}{\partial t}=-\frac{\partial(uv)}{\partial x}-\frac{\partial\left(v^2\right)}{\partial y}+\frac{\mu}{\rho}\left(\frac{\partial^2 v}{\partial x^2}+\frac{\partial^2 v}{\partial y^2}\right)-\frac{1}{\rho}\frac{\partial p}{\partial y}+g_y\left[1-\beta\left(T-T_m\right)\right]+f_y \tag{3}$$

where t is time, μ is the PCM dynamic viscosity, ρ is the PCM density, p is pressure, g_y is the gravitational acceleration, T_m is the PCM melting temperature, β is the volumetric expansion coefficient, f_x and f_y are momentum sources.

Energy equation:

$$\frac{\partial \tilde{H}}{\partial t}=-\rho c_p\left[\frac{\partial(uT)}{\partial x}+\frac{\partial(vT)}{\partial y}\right]+k\left(\frac{\partial^2 T}{\partial x^2}+\frac{\partial^2 T}{\partial y^2}\right) \tag{4}$$

where $\tilde{H}$ is the enthalpy per unit volume in a PCM cell, c_p is the specific heat capacity of the PCM, k is the thermal conductivity of the PCM and T is temperature.

The phase change is taken into account by updating the temperature distribution according to the enthalpy distribution:

$$T=\begin{cases} T_{init}+\dfrac{\tilde{H}}{\rho c_p} & \tilde{H}<\rho c_p\left(T_m-T_{init}\right) \\ T_m & \rho c_p\left(T_m-T_{init}\right)<\tilde{H}<\rho\left[c_p\left(T_m-T_{init}\right)+L\right] \\ T_{init}+\dfrac{\tilde{H}-\rho L}{\rho c_p} & \tilde{H}>\rho\left[c_p\left(T_m-T_{init}\right)+L\right] \end{cases} \tag{5}$$

where T_{init} is the PCM initial temperature and L is the PCM specific latent heat.

The solid bulk interaction with the fluid in the cavity is modeled by the momentum sources f_x and f_y, which are interpolated at the solid cells' boundaries. The problem is discretized with the finite-difference method for a rectangular domain on a staggered grid, where the x and y velocity components are defined at the cell boundaries and the pressure and temperature are defined at the cell centers.

The boundary conditions include no-slip, no-penetration, zero pressure gradient and constant temperature at the walls. Only half of the domain is solved due to symmetry. The PCM properties used in the simulations are the same as in [3].

3. RESULTS

The cavity dimensions chosen for this work are 52×52 mm, where the initial solid is assumed to be a 26×26 mm square which is initially at the center of the cavity. The solid initial temperature is assumed to be the melting temperature, while the liquid is initially at a temperature slightly higher than the melting temperature.

Figure 1 shows three different cases that were studied: melting of a sinking solid with a constant velocity of 10^{-5} m/s (the velocity is intentionally taken small to proceed in the future to sinking under gravity), melting of a constrained solid with natural convection and melting of a sinking solid with natural convection. Fully solid PCM cells are colored in blue and fully liquid PCM cells are colored in red. It can be seen that the melting patterns for the different cases are completely different. For the case where the solid is constrained, natural convection currents erode the solid from its side and bottom, and the solid bulk remains at the center of the cavity through the whole melting process. For the second case, where the solid sinks without natural convection, the solid is approaching the bottom of the cavity, while the slow currents created from its slow descent motion erode the solid only slightly. The third case that involves both natural convection and sinking motion shows a combination of the two former patterns: the solid is approaching the bottom of the cavity and also natural convection erodes the solid from the side while its bottom remains relatively flat because of the sinking motion.

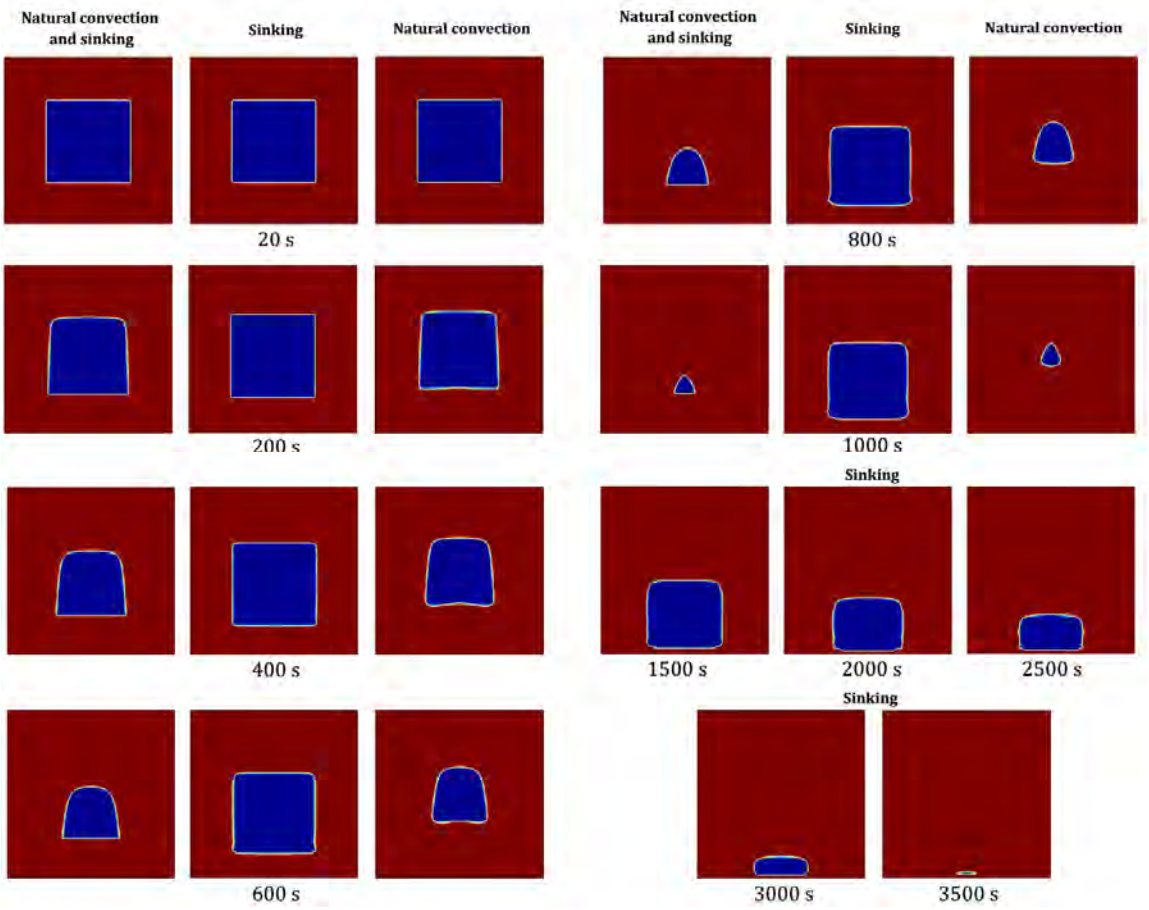

FIGURE 1. The phase fields at different instances for the three tested cases.

Figure 2 shows the melt fraction evolution for the three different cases. It can be seen that when only sinking motion is involved the melting time is more than three times longer than for the cases with natural convection. It seems that for the chosen velocity the sinking motion accelerates the melting only slightly, and natural convection enhances the melting rate quite noticeably.

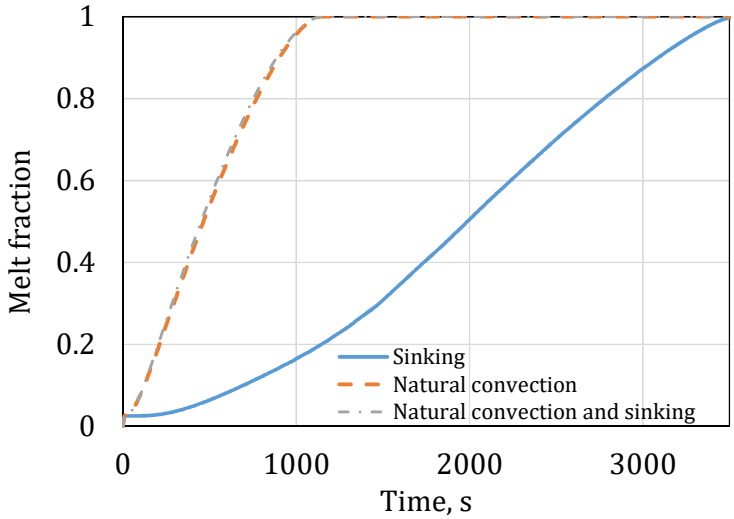

FIGURE 2. The melt fraction for the three different cases.

4. CONCLUSIONS

In the current work a new model based on the enthalpy method is suggested. The model includes full solution of the conservation equations and takes into account solid bulk motion and natural convection in the melt. The effect of these two physical phenomena is investigated by the model for specific conditions. It is found that the melting patterns are completely different under these conditions, while the melting rate is mostly affected by natural convection and not by the solid bulk motion. In the future, this model will be coupled with the force balance on the solid bulk to allow full interaction between the solid and the fluid.

REFERENCES

[1] N. Shamsundar, E.M. Sparrow, Analysis of multidimensional conduction phase change via the enthalpy model, *ASME Journal of Heat Transfer*, 97, 333-340, 1975.

[2] V.R. Voller, C. Prakash, A fixed grid numerical modeling methodology for convection-diffusion mushy region phase-change problems, *International Journal of Heat and Mass Transfer*, 30, 1709-1719, 1987.

[3] Y. Kozak, T. Rozenfeld, G. Ziskind, Close-contact melting in vertical annular enclosures with a non-isothermal base: theoretical modeling and application to thermal storage, *International Journal of Heat and Mass Transfer*, 72, 114-127, 2014.

[4] Y. Asako, M. Faghri, M. Charmchi, P.A. Baharami, Numerical solution for melting of unfixed rectangular phase-change material under low-gravity environment, *Numerical Heat Transfer, Part A*, 25, 191-208, 1994.

Fourth International Conference on Computational Methods for Thermal Problems
THERMACOMP2016, July 6-8, 2016, Georgia Tech, Atlanta, USA
N. Massarotti, P. Nithiarasu and Y. Joshi (Eds.)

CONVECTIVE PRESSURE FLUX SPLIT SCHEME FOR COMPUTING INCOMPRESSIBLE FLOWS ON UNSTRUCTURED GRIDS

J. C. Mandal, Shainath Kalamkar

Aerospace Engineering Department, Indian Institute of Technology Bombay, Mumbai, India.

ABSTRACT

In this paper, an extension of convective pressure flux split scheme [4] for solving incompressible flow equations in artificial compressibility formulation on unstructured grids is presented. A new approach to define artificial dissipation term used in the numerical scheme is proposed which helps its application to unstructured grids. Numerical results of a few benchmark problems are presented to demonstrate the efficacy of the present method.

Key Words: *Artificial compressibility formulation, Divergence free velocity field, Finite volume method, Convective pressure flux splitting scheme, Unstructured grid*

1. INTRODUCTION

Over the years, many numerical schemes have been developed for computing incompressible flows. Of late, numerical schemes based on artificial compressibility formulation [1] have drawn considerable attention due to its ability to use well developed compressible flow algorithms for the computation of incompressible flows. The upwind schemes such as Roe and HLLC schemes are often used to compute inviscid fluxes in artificial compressibility formulation. These upwind schemes, originally developed for compressible flows, add numerical dissipation to provide stabilization when discontinuities like shock waves are encountered in flows. However, so much of dissipation is not required due to absence of discontinuities in the incompressible flows. It is also understood that the convective waves have preferred directions of propagation, whereas pressure disturbances propagate in all directions in case of incompressible flows. These features are not completely imitated by the conventional upwind methods mentioned above. If convective and pressure fluxes are separated out in the governing equations, then different numerical treatments of these fluxes are possible in order to incorporate the wave propagation nature into the discretization process. Separating out convective and pressure fluxes is done in the AUSM method [2] for compressible flows. That may be the reason, Vierendeels et al. [3] have considered AUSM flux splitting and used upwind differencing for convective flux term, while central differencing for the pressure flux term. Modified versions of Vierendeels method has been presented in reference [4]. In the modified approach, a technique to achieve divergence free velocity field is introduced. The major limitation of the schemes presented in references [3,4] is the use of uniform Cartesian grids. This is mainly due to the way artificial dissipation term in the continuity equation is defined. In this paper, we propose a new expression for the artificial dissipation term that is applicable to non-uniform and unstructured grids. Finally, the proposed scheme is successfully applied to solve a few benchmark problems on unstructured grids.

2. GOVERNING EQUATIONS

Governing equations of two dimensional artificial compressibility formulation for incompressible flow can be written as

$$\frac{\partial U}{\partial t}+\frac{\partial F}{\partial x}+\frac{\partial G}{\partial y}=0 \tag{1}$$

where $U=\left[P,u,v\right]^T$, $F=F^{inv}-F^{vis}$ and $G=G^{inv}-G^{vis}$. Superscripts inv, $visc$ denote the inviscid and viscous fluxes respectively, where

$$F^{inv}=\left[\beta u,u^2+P,uv\right]^T;\ G^{inv}=\left[\beta v,uv,v^2+P\right]^T;$$

$$F^{vis}=\left[0,2\nu\left(\frac{\partial u}{\partial x}\right),\nu\left(\frac{\partial v}{\partial x}+\frac{\partial u}{\partial y}\right)\right]^T;\ G^{vis}=\left[0,\nu\left(\frac{\partial v}{\partial x}+\frac{\partial u}{\partial y}\right),2\nu\left(\frac{\partial v}{\partial y}\right)\right]^T.$$

Here u and v are the Cartesian components of velocity, P and ν are kinematic pressure and dynamic viscosity respectively. The symbol β denotes artificial compressibility parameter.

3. FORMULATION

Finite volume formulation of governing equations can be obtained by using the integral form of the governing equations (1) as

$$\iint_{\Omega}\frac{\partial U}{\partial t}+\oint_{A}\left[Fn_x+Gn_y\right]dA=0 \tag{2}$$

where n_x and n_y are the components of unit normal vector on the surface of area A enclosing the volume Ω. The discretized form of the equation (2) on a finite volume Ω_i with K faces can be written as

$$\Omega_i\frac{\Delta U}{\Delta t}+\sum_{k=1}^{K}\left[Fn_x+Gn_y\right]_k\Delta s_k=0$$

where the Δs_k is the length of the k^{th} edge surrounding the cell i.

3.1 *Inviscid flux computation*

Inviscid flux normal to any cell interface between left cell L and right cell R is given by $\mathbf{F}=F^{inv}n_x+G^{inv}n_y$. The Face normal flux in convective pressure flux split method is taken as $\mathbf{F}=u_n\left[\beta,u,v\right]_{L/R}^T+p\left[0,n_x,n_y\right]^T$, where $u_n=\left[\left(u_Ln_x+v_Ln_y\right)+\left(u_Rn_x+v_Rn_y\right)\right]/2$ and $p=\left(p_L+p_R\right)/2$. The L or R states in the convective term are selected based on the following criterion,

$$\left[\cdot\right]_{L/R}=\begin{cases}\left[\cdot\right]_L\ if\ u_n\geq 0\\ \left[\cdot\right]_R\ if\ u_n<0\end{cases}$$

The above discretization requires an artificial dissipation term to be added to the continuity equation for stability. The expressions for the artificial dissipation term used in [3,4] are applicable only to uniform Cartesian grids. In order to overcome the above limitations a new type of artificial dissipation term is introduced in the present approach based on the observations of the upwind schemes. Realizing that any upwind scheme can be written as a summation of central difference term and an artificial dissipation term, we have considered Roe scheme to define the artificial dissipation for the continuity equation as

$$\left[-\frac{(P_R-P_L)(\tilde{u}+\tilde{a})-(u_R-u_L)\beta}{4\tilde{a}}\left|\tilde{u}-\tilde{a}\right|-\frac{(u_R-u_L)\beta-(P_R-P_L)(\tilde{u}-\tilde{a})}{4\tilde{a}}\left|\tilde{u}+\tilde{a}\right|\right].$$

where values with tilde are Roe averages of respective variable. Thus, this for expression artificial dissipation term is applicable to non-uniform and unstructured grids. A factor ε is multiplied with the dissipation term before adding to the continuity equation used for progressively reducing the dissipation at every time iteration. The value of ε may be tuned depending on a problem for achieving better values of divergence free velocity field. Left and right states for unwind discretization of convective term are obtained using linear solution dependent weighted least squares (SDWLS) [5] reconstruction while variables used for pressure flux and artificial dissipation are reconstructed using least square.

3.2 *Viscous flux computation*

Derivatives of velocity components required for viscous fluxes are calculated in a central differencing manner. Green Gauss theorem is applied over Courier diamond path [6] for the evaluation of these derivatives at the cell interfaces.

4. RESULTS AND DISCUSSION

To validate the present method, three test cases namely lid driven square cavity, lid driven cavity with forward step and lid driven semicircular cavity are solved. For all the three cases the top lid is moving in positive x direction with unit velocity and on solid wall no slip boundary condition is imposed. The initial value of the parameter ε is taken as 1 and at each time iteration it is reduced by 0.1% till the dissipation term reaches 10^{-8}. Results of all the cases are compared with the results obtained using upwind method of Roe and the results reported in the literature. For all the test cases Reynolds number 1000 is used.

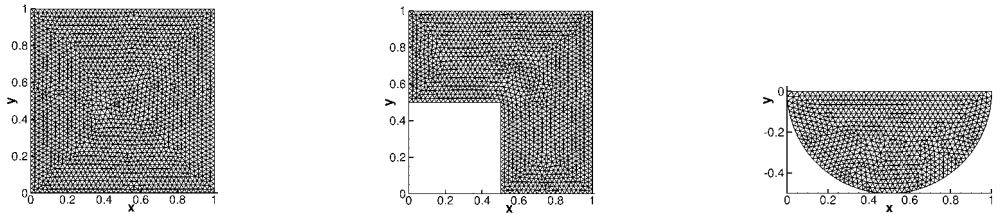

(a) (b) (c)

Figure 4.1 Grids used for (a) lid driven square cavity (b) lid driven cavity with forward step and (c) semicircular lid driven cavity

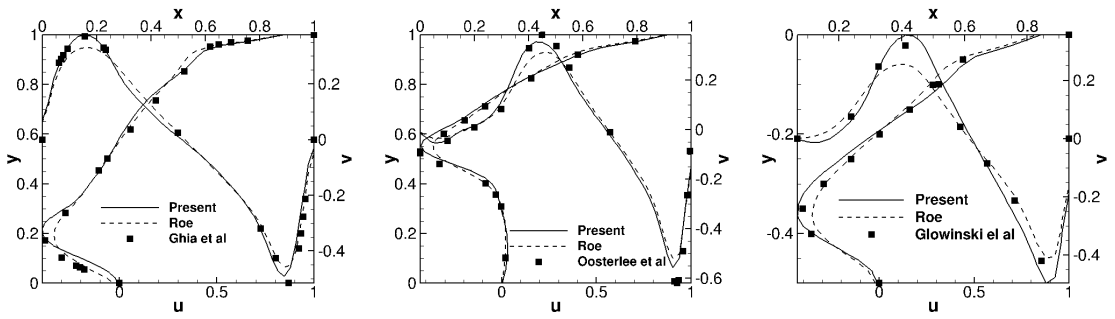

(a) (b) (c)

Figure 4.2 Variation of u and v velocities for (a) lid driven square cavity (b) lid driven cavity with forward step and (c) semicircular lid driven cavity

In lid driven square cavity test case, the computational domain is discretized into uniformly distributed triangular unstructured grid with 3588 cells as shown in Figure 4.1(a). Figure 4.2(a) shows the comparison of velocity plots. It is observed that the present method is able to capture the velocity profile reported in literature [7] very accurately as compared to the Roe's scheme.

In lid driven cavity with forward step problem, the computational domain is discretized into uniformly distributed triangular unstructured grid with 2678 cells as shown in Figure 4.1(b). The results obtained are compared with the results reported in the literature [8]. Figure 4.2(b) shows the comparison of velocity plots. It is found that the present scheme produces more accurate results than Roe scheme.

In semicircular lid driven cavity case, the domain is discretized into uniformly distributed triangular unstructured grid with 1487 cells as shown in the Figure 4.1(c). Figure 4.2(c) shows the comparison of velocity plots with the results reported in literature [9]. In this case also the present method captures velocity profile closer to the literature as compared to Roe's scheme.

4. CONCLUSION

A new approach to define artificial dissipation term in the convective pressure flux split scheme [4] has been proposed that allows its application to non-uniform and unstructured grids. The efficacy of the proposed method has been successfully demonstrated by computing a few benchmark problems on unstructured grids.

REFERENCES

[1] A.J. Chorin, A numerical method for solving incompressible viscous flow problems, *Journal of Computational Physics*, 2, 12-26, 1967.

[2] M. Liou and C.J. Steffen, Jr, A new flux splitting scheme, *Journal of Computational Physics*, 107, 23-39, 1993.

[3] J. Vierendeels, K. Riemslagh and E. Dick, A multigrid semi-implicit line method for viscous incompressible and low Mach number flows on high aspect ratio grids, *Journal of Computational Physics*, 154, 310-341, 1999.

[4] S. R. Kalamkar and J. C. Mandal, Convective-pressure flux split algorithm for incompressible flow computation using artificial compressibility formulation, *International Journal of Numerical Methods for Heat and Fluid Flow,* 26, 384-408, 2016.

[5] J. C. Mandal and Sundeep P. Rao, High Resolution Finite Volume Computations on Unstructured Grids using Solution Dependent Weighted Least Squares Gradients, *Computers & fluids*, 44,23-31, 2011.

[6] W. Coirier and K. Powell, Solution-adaptive Cartesian cell approach for viscous and inviscid flows, *AIAA Journal,* 34, 938-945, 1996.

[7] K. N. Ghia, U. Ghia and C.T. Shin, High-Re solutions for incompressible flow using Navier-Stokes equations and multigrid method, *Journal of Computational Physics*,48, 387-411,1982.

[8] C. W. Oosterlee, P. Wesseling, A. Segal and E. Brakkee. (1993). Benchmark solutions for the incom-pressible navierstokes equations in general coordinates on staggered grids, *International Journal for Numerical Methods in Fluids*, 17,301-321, 1993.

[9] R. Glowinski, G. Guidoboni, and T Pan, Wall-driven incompressible viscous flow in a two-dimensional semi-circular cavity, *Journal of Computational Physics*, 216,76-91, 2006.

Fourth International Conference on Computational Methods for Thermal Problems
THERMACOMP2016, July 6-8, 2016, Georgia Tech, Atlanta, USA
N. Massarotti, P. Nithiarasu and Y. Joshi (Eds.)

UNSTEADY TEMPERATURE FIELDS UNDER DETONATION COMBUSTION ON BASIS OF STRINGS METHOD

Nikolay Svetushkov
Moscow Aviation Institute (National Research University),
4, Volokolamskoy shosse, Moscow, Russia, 125993,
svt.n.n@mail.ru

ABSTRACT

The paper presents a new method of calculating the thermal loads on the walls of the combustion chamber during detonation burning, which is important in the development of industrial detonation engines, including spin detonation and burning. As a mathematical model was used a simplified description of the process, based on parabolic partial differential equations, thus reflecting the main features of the propagation of a detonation wave in the combustion chamber. The article is detailed derivation of this equation, and the key assumptions used in its preparation. In order to solve the resulting equations and make numerical calculations were used a new approach - a method of strings based on the integral representation of the heat equation.

Key Words: *Detonation Combustion, Heat Transfer Simulation, Numerical Methods, Integral Equations, Software.*

1. INTRODUCTION

Recently, there is a significantly practical interest in detonation combustion in gas mixtures. Since the pressure and temperature of the combustion products at the detonation burning is several times higher than conventional (slow) combustion (e.g., by burning a stoichiometric hydrogen-air mixture, the temperature and pressure increase is approximately twice), it is natural to propose for increasing engine power. Despite the fact there are a large number of works on the detonation combustion (e.g. [1]), the question remains about the temperature in the wave front, and in the area of chemical reactions. Moreover, it is a research area for the behaviour of the waves, depending on the size and geometry of the channels (diaphragms and obstacles) of the engine, and the impact on the detonation of turbulence and vortices flow.

The main problem when constructing detonation combustion engines is to improve heat transfer from the combustion products on the walls of the chamber. This task arises due to the high temperatures in the detonation wave and increased heat transfer coefficient as a result of disruption of the boundary layer. Obviously, the thermal load on the combustion chamber wall depends on various factors - such as temperature and size of the detonation wave front, the speed of its movement, the direction of gas flow and temperature field distribution in the combustion products after passing wave.

The aim of the work was approbation of the previously developed «strings method» [2,3] to calculate the heat load on the combustion chamber wall. Due to the fact that the method of the strings based on the integral representation of heat transfer process, we can use all of its advantages:

- assessment of the accuracy of decisions on the error function,
- the lack of oscillation at high temperature gradients,
- good convergence on large size grid partitioning.

2. SIMPLIFIED PARABOLIC EQUATIONS

In order to fully carry out simulation of the detonation of the combustion process is necessary to use the kinetic equation, which would determine the type and speed of the chemical reactions (including set and the value of specific heat for each of the reactions), and, accordingly, to find an overall density of heat power depending on the concentration of the initial component in the reaction mixture and its temperature, pressure, and heat and mass transfer to take into account. Simulation of detonation combustion process in such a setting is a rather complex mathematical problem as a narrative point of view and as to find the numerical solution of the whole system of equations obtained.

In order to simplify mathematical model for further calculations, it was decided to introduce the detonation wave front to form at a known speed of a moving heat source forms a predetermined specific spatial power density of heat release. This assumption is justified even more, due to the fact that during detonation of fuel oxidation exact mechanism has not been studied fully [1].

General law of conservation of energy [e.g.4] was used to get the parabolic equations written in the form of partial differential equations (work mass and surface forces can be neglected). In order to describe the behavior of the combustion products (unknown mass flows in the equations), depending on the temperature distribution, one can use these natural simplified assumptions:

- under the influence of the large absolute value of forces (pressure) the direction of the mass flow vector can be considered directly proportional to depend on the pressure gradient,
- pressure is also directly proportional to the temperature,

which implies that the mass flow can be simply assumed to depend directly proportional to the temperature gradient. Thus the final equation for the temperature distribution in the gas flow function takes the following form:

$$\rho c_v \frac{\partial T}{\partial t} = \frac{\partial}{\partial x} K_x \frac{\partial}{\partial x} T + \frac{\partial}{\partial y} K_y \frac{\partial}{\partial y} T + q(x, y, t) \tag{1}$$

where:

$$K_x = c_v \rho R D_x T + k_x$$
$$K_y = c_v \rho R D_y T + k_y \tag{2}$$

and: T- temperature, ρ - gas density, R - universal gas constant, $\tilde{n}_v$ - specific heat at constant volume, $k_{x,y}$. - thermal conductivity (this may depend on the temperature), $D_{x,y}$ - effective thermal conductivity coefficients that determine the velocity of the gas as a function of temperature.

The derivation of (1) - (2) is based on the mass flow due to the temperature gradient, which imposes significant limitations on its application for arbitrary flows: it is impossible to adequately describe the various vortex flow and return, challenging obstacles and walls, etc. However, it makes it possible to model good regular stationary gas streams and irrotational (laminar) flow from the heat source. At the same time the main task is the description of the movement of the heat source, i.e, detonation combustion must explicitly define the position of the detonation wave front at any given time.

3. NUMERICAL RESULTS

The numerical model was described by a linear model of the dimensionless ratio of the nozzle channel length to its width as a 10 to 1 (cross-section of the channel is constant). It was decided to

use advantages of integral equations and select a test grid area with a small number of points (10x100), which allowed not only worsen the results obtained, and perform calculations on a personal computer with several minutes. The movement of the detonation wave front was described by means of special software environment as a moving heat source of constant power, having a configuration in the form of a plane wave crest (Figure 1).

FIGURE 1. The model region, the computational grid and the detonation wave front as a moving heat source (shown by its position in the different times with a constant time-step)

The results of the calculations are presented in the figure below. This flow was modelled when the effective thermal conductivity of the X-axis (K_x) was 10 times greater than the effective thermal conductivity in the transverse direction (K_y).

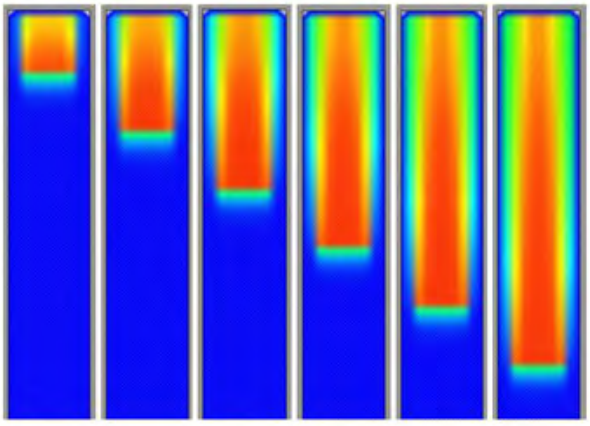

FIGURE 2. Field temperature during flow (K_x = 10* K_y) at different time points.

The nature of the flow shown in Figure 2, said that in this case stands preheating zone before the shock wave, which is observed in experiments, as well as significantly increase the size of the high-temperature "loop." As seen from the picture of the flow quality has rather natural behavior as the real processes of detonation combustion. Variation of free parameters ($K_{x,}or\ K_{y)}$ allows you to change the shape of the plume behind the detonation wave, as well as the size of the zone preheating ahead of the wave.

4. CONCLUSIONS

The numerical calculations showed that the proposed simplified description of the detonation of the combustion process based on parabolic equations is in qualitative agreement with the processes observed in the pulse detonation engine. The strings method showed rapid convergence, and the

numerical results were not observed "nonphysical" oscillations. In order to make this approach be useful for the calculations of thermal loads on the detonation engine wall one should determine free parameters - K_x and K_y . That can be made on terms of maximum accordance with experimental results. Then, it's quite simple to use this model to perform calculations with given the thermal parameters of the engine wall.

REFERENCES

[1] S.M. Frolov, *Impul'snye detonacionnye dvigateli,* red., M: Torus Press, 2006, 592 s.

[2] N.N. Svetushkov, Integral approach for the numerical modeling quenching process of forming rolls, *Proc. of 6th International Symposium on Advances in Computational Heat Transfer, Rutgers University, Piscataway, USA*, ID 259, 2015.

[3] N.N. Svetushkov, Metod strun v zadachah mnogomernoj nestacionarnoj teploprovodnosti, *Informacionnye tehnologii,* 2014. № 12. S. 14-19.

[4] D.A.Anderson, J.C.Tannehil and R.H. Pletcher, *Computational fluid mechanics and heat transfer*, 2nd Edition, Hemisphere Publishing Corporation, 1984.

Forth International Conference on Computational Methods for Thermal Problems
THERMACOMP2016, July 11-13, 2016, Georgia Tech, Atlanta, USA
N. Massarotti, P. Nithiarasu and Y. Joshi (Eds.)

Numerical simulation of energy harvesting eel in a viscous flow

Emad Uddin,

National University of Sciences and Technology (NUST), Islamabad, Pakistan,
emaduddin@smme.nust.edu.pk

Hyung Jin Sung

Department of Mechanical Engineering, KAIST 291 Daehak-ro, Yuseong-gu, Daejeon 305-701,
hjsung@kaist.ac.kr

ABSTRACT

Inspired by the energy harvesting eel, a flexible flag behind a D-shape half cylinder in a uniform viscous flow was simulated by using the immersed boundary method. The downstream flag was strongly influenced by the vortices shed from the upstream cylinder in vortex-vortex and vortex-body interactions. The flexible flag was subjected to passive flapping to optimize the geometric and the flow parameters, which were subsequently used in the actively flapping flag. In this study the dependence of the bending energy of the passively flapping flexible flag was examined in detail for multiple parameters, these optimized parameters were used in the active flapping motion to investigate the effect of the phase difference, the amplitude of the pitching and heaving motion. The maximum bending energy was observed for the range of the phase difference and the amplitudes. Constructive and destructive vortex interaction modes, unidirectional and bidirectional bending and the different flapping frequency were found which explained the variations in the bending energy on the downstream flag

Key Words: *Immersed boundary method, fluid structure interaction, energy harvesting eel.*

1. INTRODUCTION

The interaction of the vortex and the flexible flag in wake of a bluff body is a common occurrence in nature and in engineering fields. Renewable energy from small-scale hydro, modern biomass, wind, solar, geothermal and biofuels accounted for global energy consumption was 2.7% in 2008, increased to 5.8% in 2012 and is growing very rapidly [1]. From a hydrodynamic point of view, experimental evidence has supported the assertion that the appropriate synchronization of the positioning in of flag in the wake of the bluff body can be advantageous by increasing the hydrodynamic resistance due to wake interactions and introducing significant energy harvesting [2, 3, 4, 5 and 6]. Tang et al. [7] analytically analyzed a flutter-mill to generate electricity. The swept area for a single device can thus be wide and shallow, allowing large systems to be installed in shallow water. Subsequently, multi-mega watt devices can be envisaging for a wider range of the resource areas. There are only a few numerical work on this to give a reliable physical explanation, e.g., Manela and Howe [9] put a cylindrical pole attached with the flag in order to make periodical shedding vortices. Their model neglected the interaction of the flag motion on the motion of fluid. Interactions between flexible structure and its surrounding vortices play a crucial role.

The current study provides the dynamics of flow around a flexible flag (eel) in the wake of a D-shaped half cylinder subjected to a two-dimensional uniform viscous flow. There are some analytical and numerical studies on the energy harvesting eel but the detail investigation and optimization of the parameters is the missing link [10]. The dependence of the bending energy on the streamwise gap distance between the D-shaped half cylinder and the downstream flag, the length and the bending rigidity of the downstream flag, effect of the bending energy on the actively flapping downstream flexible flag for the variable pitching and heaving phase difference, and the pitching and heaving amplitude were examined in detail.

2. PROBLEM FORMULATION

A flexible flag in the wake of a D-shaped half cylinder was subjected to the two-dimensional viscous flow. A schematic diagram of the geometric configuration and the coordinate system is shown in figure 1. The fluid domain was defined by an Eulerian coordinate system, and a separate Lagrangian coordinate system was applied to the flexible flag. The flexible flag in a viscous flow were modeled using an improved immersed boundary method (Huang *et al.* [11]), in which the governing equations of the fluid flow and the flexible flag was solved in each coordinate system, and the interactions among components was calculated using a feedback law.

The fluid motion was governed by the incompressible Navier–Stokes and continuity equations,

$$\frac{\partial \boldsymbol{u}}{\partial t} + \boldsymbol{u}\cdot\nabla\boldsymbol{u} = -\nabla p + \frac{1}{\mathrm{Re}}\nabla^2\boldsymbol{u} + \boldsymbol{f}\ , \tag{1}$$

$$\nabla\cdot\boldsymbol{u} = 0, \tag{2}$$

where $\boldsymbol{u}$ is the velocity vector, p is the pressure, $\boldsymbol{f}$ is the momentum force applied to enforce the no-slip conditions along the immersed boundary, and the Reynolds number Re is defined by $\mathrm{Re} = \rho_0 U_\infty L/\mu$, with ρ_0 the fluid density, U_∞ the free stream velocity, L the flag length, and μ the dynamic viscosity.

The flag motion was governed by

$$\frac{\partial^2 \boldsymbol{X}}{\partial t^2} = \frac{\partial}{\partial s}\left(T\frac{\partial \boldsymbol{X}}{\partial s}\right) - \frac{\partial^2}{\partial s^2}\left(\gamma\frac{\partial^2 \boldsymbol{X}}{\partial s^2}\right) - \boldsymbol{F} \tag{3}$$

where s denotes the arc length, $\boldsymbol{X} = \boldsymbol{X}(s,t)$ the position, T the tension force, γ the bending rigidity, $\boldsymbol{F}$ the Lagrangian force exerted on the flexible flag by the fluid. The bending rigidity is defined as EI, with E the Young's modulus and I the second moment of area, which gives the non-dimensional value γ.

The interaction force between the flow and the structure was calculated using the feedback force

$$\boldsymbol{F} = \alpha\int_0^t \left(\boldsymbol{U}_{ib} - \boldsymbol{U}\right)d\tau + \beta\left(\boldsymbol{U}_{ib} - \boldsymbol{U}\right), \tag{4}$$

where α and β are large negative free constants, $\boldsymbol{U}_{ib}$ is the fluid velocity obtained by interpolation at the immersed boundary, and $\boldsymbol{U}$ is the velocity of the flag expressed by $\boldsymbol{U} = d\boldsymbol{X}/dt$. On the other hand, $\boldsymbol{X}_{ib}$ and $\boldsymbol{U}_{ib}$ denote, respectively, the position and velocity of the immersed boundary, which were determined using the local Eulerian fluid velocity, as expressed by

$$\boldsymbol{U}_{ib}(s,t) = \int_\Omega \boldsymbol{u}(\boldsymbol{x},t)\delta(\boldsymbol{X}(s,t) - \boldsymbol{x})d\boldsymbol{x}\ , \tag{5}$$

where δ( ) denotes a smoothed approximation of the Dirac delta function, and Ω_f is the fluid region. Equation (6) provides an interpolation of the Eulerian fluid velocity at the Lagrangian points. In physics, equations (4) – (6) represent a stiff spring system. This system connected the Lagrangian points on the immersed boundary to the surrounding fluid particles. After obtaining the Lagrangian force $\boldsymbol{F}$, the expression was transformed to the Eulerian form using the smoothed Dirac delta function,

$$\boldsymbol{f}(\boldsymbol{x},t) = \frac{\rho_1}{\rho_0 L_r}\int_\Gamma \boldsymbol{F}(s,t)\delta(\boldsymbol{x} - \boldsymbol{X}(s,t))ds\ . \tag{6}$$

where $\rho = \rho_1/(\rho_0 L)$, based on the non-dimensionalization steps, and Ω_s denotes the structure region. After discretization, the force was applied over a width of several grids, which supported the smoothed delta function.

3. RESULTS

3.1 Passive flapping

A schematic diagram of the problem setup and the coordinate system for the downstream flag in the wake of the D-shaped half cylinder subjected to a uniform flow is plotted in figure 1.

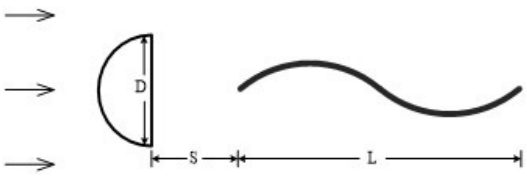

Figure 1. Schematic of the energy harvesting flag behind a half cylinder.

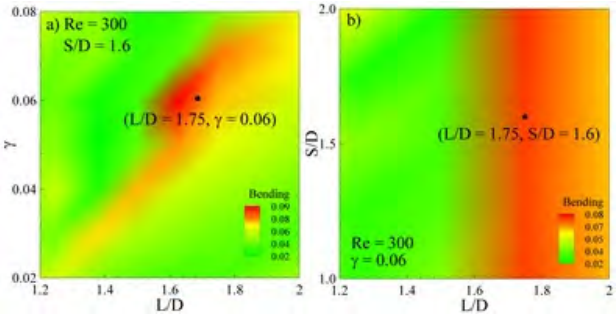

Figure 2. Contours of the bending energy for different a) L/D and γ and b) L/D and S/D.

A quantitative characterization of the interaction behaviour was supplemented by qualitative evaluations of the flag deformations and the vorticity contours within the flow, which provided an intuitive understanding of the vortex–flexible body interactions. Three parameters were chosen for optimization within the following ranges: the streamwise gap distance between the D-shaped half cylinder and the downstream flag ($1 \leq S/D \leq 2$), the bending coefficient of the flag ($0.02 \leq \gamma \leq 0.08$) and the length of the flag ($1.2 \leq L/D \leq 2.0$).

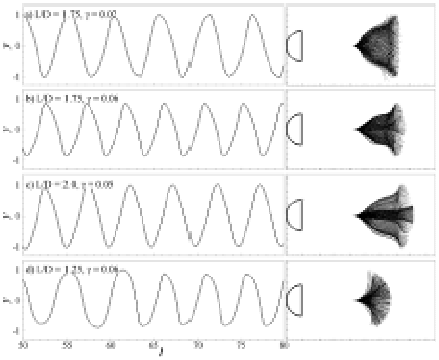

Figure 3. Evolutions of the tail position and corresponding flag deformations

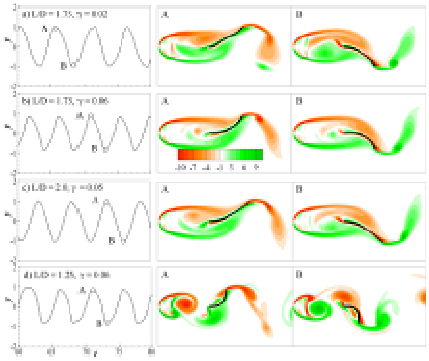

Figure 4. Contours of vorticity for different L/D and γ.

The bending energy E_b of the downstream flag as a function of the length and the bending coefficient of the flag is plotted in figure 2a showing high and low bending energy regions. For the less flexible flag in figure 3 (a), the flag get significant deformation by the influence of the upstream vortices, this changes the flag shape significantly, resulting in decreasing the dominant frequency. The increase in the stiffness in figure 3 (a) causes more resistance to the upstream vortices, which decreases the effect of the upstream vortices resulting in the low deformation of the flag as well as increase in the dominant frequency which is near the natural frequency of the flag in a uniform flow. In figure 4 for the length below 1.5, the flag effects the upstream vortices by increasing the shear resistance to the upstream vortices which delays/blocks the upstream vortices and causes the two vortices to combine and create a shear layer for the downstream flag. The creation of the shear layer causes suction zone in-front of the downstream flag, Beal et. al. [8] reported the suction zone for the S/D<2.0, and this study reveals that it is also dependent on the L/D ratio by the action of increased shear resistance. The second map (figure 2b) showed the map between the length and the gap distance. The unidirectional/constrained deformation is attributed to the low bending energy. As the length is increased to L/D=1.75 provides the sufficient surface area of the flag to exert more viscous forces on the flag to cause the bidirectional curvature flapping.

3.2 Active flapping

Figure 9 shows the phase difference and amplitude maps. The bending energy is calculated for different phase difference in the pitching and heaving motion (figure 9a), the phase difference shows a very regular trend, the minimum bending energy is obtained when the difference between the pitching and heaving phase is 0.5π, mathematically low bending energy is obtained when $\phi_{pitching} - \phi_{heaving} = 0.5\pi$.

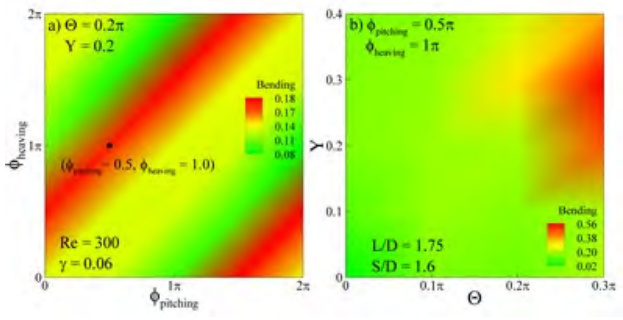

Figure 9. Contours of the bending energy for a) different

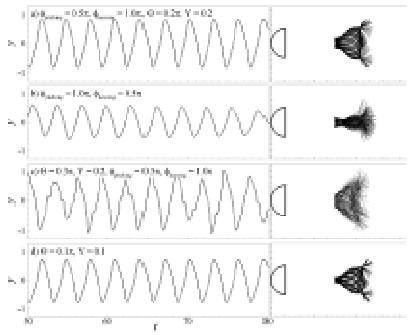

Figure 10. Evolutions of the tail position

$\Phi_{pitching}$ and $\Phi_{heaving}$ and b) the amplitude map. and corresponding flag deformations Figure 10 (a, b) shows the high bending energy case for $\phi_{pitching} = 0.5\pi$; $\phi_{heaving} = 1.0\pi$ and for low bending energy case for $\phi_{pitching} = 1.0\pi$; $\phi_{heaving} = 0.5\pi$, respectively. The frequency of the tail flapping is the same for both cases, but the amplitude of the tail flapping is different. This vortex interception and slaloming mode can be observed by analyzing the vortices shed from the flag, the upcoming vortices are coming at the same frequency for both cases (figure 10a, b). The map between the pitching and the heaving amplitudes (Θ and Y) in figure 9b) shows the region for the optimal pitching and heaving phase difference for highest bending energy.

4. CONCLUSIONS

The dynamics of energy harvesting flexible flag behind a half cylinder undergoing passive and active flapping modes subjected to a uniform viscous flow by using the immersed boundary method. The increase in the bending stiffness is accompanied by the increase in the flag deformation as well as the dominant and the flapping frequency is increased. Constructive mode is observed for the optimal bending energy region when the streamwise distance is increased. Also the unidirectional curvature is attributed to the low bending energy while the bidirectional curvature is attributed to the high bending energy case. The tail vortices corresponding to the high bending energy case has higher energy than the low bending energy case, this depicted the energy harvesting By analysing the passive flapping we obtained the optimal parameters were used in active flapping to obtain the optimal phase difference and the amplitude of the pitching and the heaving motion, which gives us the optimal design as well as the relationship between the bending energy and the interaction modes of the D cylinder and the flag-in-fluid system suggested a mechanism by which advantages may be gained via the vortex-flexible body interactions in the energy harvesting eel.

This work was supported by the Creative Research Initiatives (No: 2012-0000246) of the National Research Foundation of Korea and NUST, Pakistan.

REFERENCES

[1] REN21, Renewables 2014 Global Status Report, 2014, pp. 21-25.
[2] J.J. ALLEN, A.J. SMITS, 2001, Energy harvesting eel, Journal of Fluids and Structures, vol. 15, no. 3–4, pp. 629–640.
[3] BARRERO-GIL, A., ALONSO, G. & SANZ-ANDRES, A. 2010 Energy harvesting from transverse galloping. Journal of Sound and Vibration 329 (14), 2873–2883.
[4] BERNITSAS, M. M., RAGHAVAN, K., BEN-SIMON, Y. & GARCIA, E. M. H. 2008 VIVACE (Vortex Induced Vibration Aquatic Clean Energy): a new concept in generation of clean and renewable energy from fluid flow. J. Offshore Mech. Arct. Eng. 130, 041101.
[5] PENG, Z. & ZHU, Q. 2009 Energy harvesting through flow-induced oscillations of a foil. Phys. Fluids 21, 123602.
[6] SINGH, K., MICHELIN, S. & DE LANGRE, E. 2012 The effect of non-uniform damping on flutter in axial flow and energy harvesting strategies. Proc. R. Soc. A 468, 3620–3635
[7] L. TANG, M.P. PAÏDOUSSIS, J. JIANG, Cantilevered flexible plates in axial flow: Energy transfer and the concept of flutter-mill, Journal of Sound and Vibration 326, 2009, pp. 263-276.
[8] D. BEAL, F. HOVER, M. TRIANTAFYLLOU, J. LIAO, G. LAUDER, Passive propulsion in vortex wakes, J. Fluid Mech. 549 (2006) 385–402.
[9] A. MANELA, M. HOWE, The forced motion of a flag, J. Fluid Mech. 635 (2009) 439–454.
[10] J. ELDREDGE, Dynamically coupled fluid–body interactions in vorticity-based numerical simulations, J. Comput. Phys. 227 (2008) 9170–9194.
[11] HUANG, W.-X., SHIN, S. J. & SUNG, H. J., 2007 Simulation of flexible filaments in a uniform flow by the immersed boundary method. J. Comput. Phys. 226, 2206-2228.

PARALLEL SESSION

HIGH PERFORMANCE COMPUTING

Fourth International Conference on Computational Methods for Thermal Problems
THERMACOMP2016, July 6-8, 2016, Georgia Tech, Atlanta, USA
N. Massarotti, P. Nithiarasu and Y. Joshi (Eds.)

Adaptive Cell-Factor Algorithm for Unified Direct Simulation Monte Carlo Approach of Continuous, Transitional and Molecular Flows

Matthew Henry, Andrei Fedorov
George W. Woodruff School of Mechanical Engineering, Georgia Institute of Technology, Atlanta, GA 30332, USA, MathUHenry@GATech.edu, AGF@GATech.edu

ABSTRACT

A new approach has been developed for a Direct Simulation Monte Carlo (DSMC) of gas flow spanning the Knudsen number from 0.01 (continuous flow) to 1 (molecular flow) using a single domain and unified framework for discretizing the governing equations. This technique is based on introducing a dynamically adjusting "cell factor", which represents the ratio of physical particles (molecules) to simulation "proxy" particles, to always maintain sufficient particles per cell for simulation accuracy, yet keeping the number of simulation particles to a minimum for computational efficiency. We outline the fundamental principles of the adaptive algorithm, demonstrate its viability as a DSMC technique, and discuss some of its applications.

Key Words: *Direct Simulation Monte Carlo, Molecular Gas Dynamics.*

1. INTRODUCTION

Simulation of transitional and molecular gas flow regimes are commonly approached with the DSMC technique in which each simulation particle represents a large number of real particles and local properties are calculated for cells based on the particles in each cell. The DSMC technique produces accurate results for molecular, transitional, or continuum flow regimes; however, it is typically applied to the problems involving only one of these flow regimes and requires special treatment under conditions when all three flow regimes are realized within the same computational domain. The involvement of multiple regimes implies significant variation of particle density from one location to another such that a scalar factor that represents the ratio of the real molecules to the simulation particles and is commonly set to a fixed value for all cells in the simulation domain necessarily results in too few particles per a cell in molecular flow regime for accurate results or too many particles per another cell in continuous flow regime for computational efficiency.

Several techniques have been applied to circumvent this problem. The simplest approach is to accept the computational inefficiency and provide the necessary computer memory and time to run a simulation with an excessive number of particles. Another alternative, if the region of interest is in the continuum regime, is to custom tailor the cell sizes to increase in regions where particle densities decrease as in the case of an expanding nozzle.[1] More recently it has become common to automate cell transitions between a Navier Stokes solver and DSMC.[2,3] The latter approach is particularly effective when the majority of the domain is in the continuum flow regime, the minority of the domain requires the DSMC approach, and transition regions are small relative to the continuum regions so that they don't add more computational overhead. However, it offers little advantage when the minority of domain regions are in the continuum regime and most of the flow is either in molecular or transitional regimes.

Here, we introduce an adaptive algorithm, which adjusts cell factors according to cell populations, to allow DSMC simulations to seamlessly transition between flow regimes where the transition boundaries are not known a-priori or are not readily defined. By allowing each cell to have its own ratio between simulation particles and physically real particles, the simulation can capture the full range of flow regimes using uniform computational representation of the flow physics throughout

the simulation domain.

2. ADAPTIVE ALGORITHM DEVELOPMENT

When a particle moves from one cell to another cell with a different factor, it can either split into two particles or merge with another particle to halve or double its representation of real particles; therefore, each cell factor must relate to all other factors by a power of two. The challenge is how to split or merge particles without distorting the velocity distribution; without adding or deducting net mass, energy, or momentum from the simulation; and without biasing the simulation. Several strategies were considered to accomplish this.

When two particles merge, as is necessary when two particles move to a cell with a higher factor or when a cell is being adjusted to a higher factor, only the velocity of one particle can be preserved because any combination or averaging of the velocities will distort the local velocity distribution. The discarded particle velocity may be greater or lower, but the cumulative average of the velocities deleted is equal to that of the velocities preserved. The potential error that a merging event introduces is equal to the resolution error of the cell with the higher factor (half of a particle), so the important aspect of this error is that it not be directionally biased. Because 50% of all merged particles have their velocity data discarded, none of their information persists beyond the merge event. Therefore it is not necessary to match particles for merging events; each particle may be merged or discarded based on a random variable.

When one particle is split into two, velocity information must be provided to the additional particle. If the velocity is cloned from the original particle, then the velocity distribution will be distorted such that the velocity variance, and therefore gas temperature, is artificially diminished. Alternatively, the velocity information is seeded from the current cell properties of temperature and mean velocity. Statistical errors may influence subsequent cell properties that feedback into further seeding of velocity information. This makes the adaptive algorithm unsuitable for a closed system, but is a lesser concern when the simulated flow has both an inlet and an outlet. Mechanisms can be applied to enforce the conservation of mass; however, intrinsic to this algorithm is the loss of strict energy and momentum conservation. The method can only be valid if there is no directional bias to erroneous gains and losses in energy and momentum. To test this, argon gas flow is simulated at $50 m/s$, $674 Pa$, and $355 K$ in a system that is made closed by periodic boundary conditions along the axis of flow and specular boundary conditions on the walls such that total energy and axial momentum should be constant. The domain is 20 cells long along the flow axis and 10 cells high by 10 cells wide with the cell dimension of $1 \mu m$. The cell properties are calculated when a cumulative of 70 particles are sampled in a cell and the converging cell properties are calculated according to Equation 1 (for temperature T) where α is 0.5. All cells are held to a constant cell factor except at the axial cell positions 10 and 11, which are divided by four. As flow passes across these cells, particles are forced to split and merge, introducing statistical error to the simulation. The chart of energy and momentum versus simulation time in Figure 1 show that while the values are not perfectly conserved, they have no net directional bias. Because the variation is due only to random walk, the physics of the simulation is not compromised by the adaptive algorithm.

$$T = \alpha T_{new} + (1 - \alpha) T_{old} \tag{1}$$

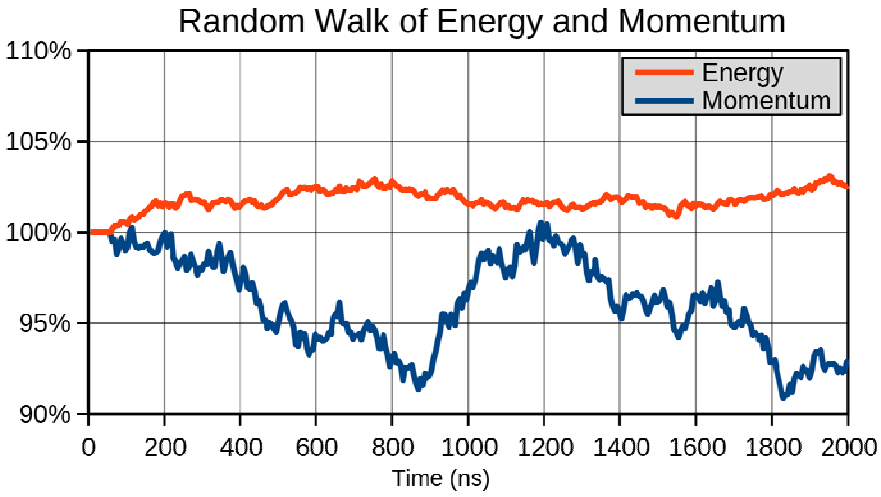

FIGURE 1. Tracking the changes in energy and axial momentum in a closed system with periodic boundary conditions shows that both properties, though not strictly conserved, have no net bias and are subject only to random walk.

In the case of steady state solutions, particles from multiple time steps can be taken to calculate cell properties. To simulate a transient flow, simulation cells, called sub-cells, are clustered into larger property cells. Properties can be determined in a single time step by calculating the properties for a cluster of sub-cells, but the trade-off is a loss of spatial resolution. It may seem that the adaptive algorithm described precludes application to transient flow; however, its dependence on previous time steps can be reduced (or eliminated) by increasing the convergence rate α closer to one. As with normal DSMC, the sampling error can be reduced by increasing the number of sub-cells per a cell.

3. RESULTS

The development of the adaptive algorithm was motivated by the need to simulate a continuum gas jet expanding into a vacuum and impinging upon a substrate. Previous work in Electron Beam Induced Deposition (EBID) involved gas jets in the molecular or transitional flow regimes, which were readily simulated by ordinary DSMC to determine the flux of precursor molecules to the surface. Experiments have shown that 1) continuum gas jets introduce desirable deposition conditions and 2) the jet-surface interaction alter the precursor sticking and diffusion coefficients. One such configuration of interest for achieving enhanced surface diffusion is a heated argon jet of $0.48 kg/s$ exiting at sonic velocity from a $75 \mu m$ nozzle with the exit conditions of $674 Pa$ and $355.6°C$. Results from the modified DSMC, shown in Figure 2, provide critical insight into the surface flux distribution and the spatially resolved energy delivered to the substrate by the jet.

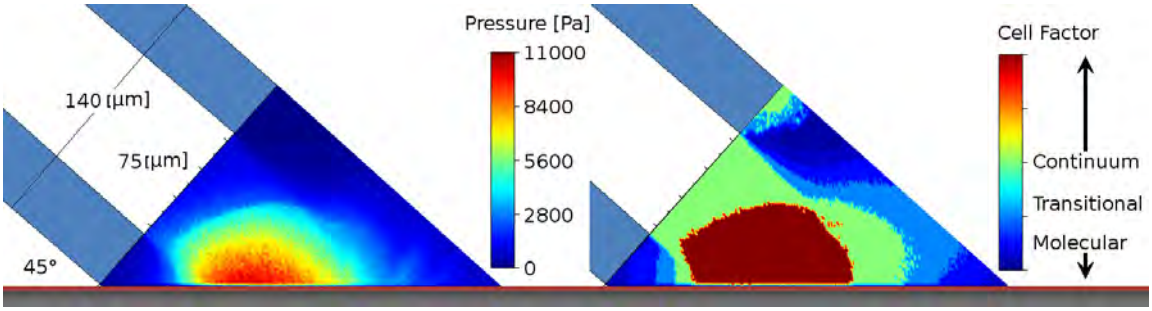

FIGURE 2. The DSMC with the adaptive algorithm revealed the jet structure of a continuum gas jet from a 75μm capillary. A stagnation region at the surface, with elevated pressure and temperature, is of interest to work in electron beam induced deposition. The variation of cell factors throughout the domain make it computationally expedient to perform this multi-scale simulation.

4. CONCLUSIONS

The adaptive algorithm developed for DSMC enables computationally efficient simulation of multi-scale gas flows without use of different computational descriptions of relevant physics for different locations/flow regimes in the domain. We have demonstrated the viability of the technique in terms of statistically conserving energy and momentum despite the fact that statistical error in conservation is the single deviation from conventional steady state DSMC. Further, by using only the most recent cell properties in an iterative algorithm, and by increasing the number of sub-cells used to calculate local properties, it is possible to perform transient simulations with the same fundamental trade-offs as faced by conventional DSMC implementation. Therefore, the adaptive algorithm reduces the computational requirements of multi-scale simulations without any loss of capability of DSMC in computing complex flows.

REFERENCES

[1] M. Darbandi, and E. Roohi, Applying a hybrid DSMC/Navier-Stokes frame to explore the effect of splitter catalyst plates in micro/nanopropulsion systems, *Sensors and Actuators A: Physical*, 189, 409-19, 2013.

[2] Y. Lian, Y. Chen, K. Tseng, J. Wu, B. Wu, and L. Yang, Improved parallelized hybrid DSMC-NS method, *Computers & Fluids*, 45, 254-60, 2011.

[3] K. Farber, P. Farber, J. Gräbel, S. Krick, J. Reitz, and P. Ueberholz, Development and validation of a coupled Navier-Stokes/DSMC simulation for rarefied gas flow in the production process for OLEDs, *Applied Mathematics and Computation*, 272, 648-56, 2015.

Fourth International Conference on Computational Methods for Thermal Problems
THERMACOMP2016, July 6-8, 2016, Georgia Tech, Atlanta, USA
N. Massarotti, P. Nithiarasu and Y. Joshi (Eds.)

Rapid Modelling Tools for Transient Thermal Response of Modular Data Centers

Rehan Khalid, Yogendra Joshi
Georgia Institute of Technology, rkhalid6@gatech.edu, yogendra.joshi@me.gatech.edu

Aaron Wemhoff
Villanova University, aaron.wemhoff@villanova.edu

ABSTRACT

Modular data centers provide a convenient way for deploying data center capacity in off grid locations, or to enhance the capability of existing infrastructure. Standardized yet customizable, modular data centers provide an easy means by which cloud-based infrastructure can be easily placed and operations controlled. This paper looks at the transient thermal response of modular data centers to dynamic loads, such as varying server load through change in user requirement over the cloud, and to changes in outside weather conditions. The effect of server thermal mass has also been accounted for in the study. The change in performance of the data center is reported through changes in the Power Usage Effectiveness (PUE) metric, and through change in the exergy destruction in the individual hot and cold aisles. The simulations are performed using EnergyPlus, an open source software provided by the Department of Energy. An in-house software DCE+ is used to perform the PUE and exergy destruction calculations and output the results.

Key Words: *Thermal Management, Modular Data Centers, Transient, EnergyPlus*

1. INTRODUCTION

Modular data centers are used in terrains where grid connected brick and mortar data centers can either not be built, such as oil fields and other harsh terrains, or they are used to enhance the capability of existing infrastructure by adding pre-configured modules. Since they consume significant energy, with typical 20%-50% towards cooling, this calls for systematic ways to monitor and control their power consumption.

In a typical data center, the servers contribute significantly to the thermal mass. This thermal mass has the ability to flatten swings in temperature variation inside the conditioned space, by absorbing energy following a sudden increase in workload, and releasing it with a certain delay, resulting in the moderation of the temperature rise during the transient. Hence, transient analysis of modular data centers needs to include the influence of thermal mass. The implementation of server thermal mass in models is important for development and deployment of control schemes.

Previous studies include a finite-difference server model by Pardey et al. [1] in conjunction with IBM. Their work is based on the individual analytical development by Pardey and VanGilder et al (2014) and Erden et al (2014). The goal of the present study is to implement a transient server thermal model, conjunction with an established energy modelling software package EnergyPlus. In order to do this integration, we have employed companion software that provides the appropriate input modification to enable a model of data centers, and post-processing of data center performance metrics. This paper discusses the transient server models and the complimentary software package to EnergyPlus, called DCE+.

2. TRANSIENT MODEL DEVELOPMENT

2.1 Dynamic Server Model Development. Treating the server as a blackbox with a stream of cooling air flowing through the server (over the electronic components). This can be effectively modelled as a single-stream heat exchanger and hence the ε-NTU method used for heat exchangers is readily applied. The model in [1] can be mathematically expressed as follows:

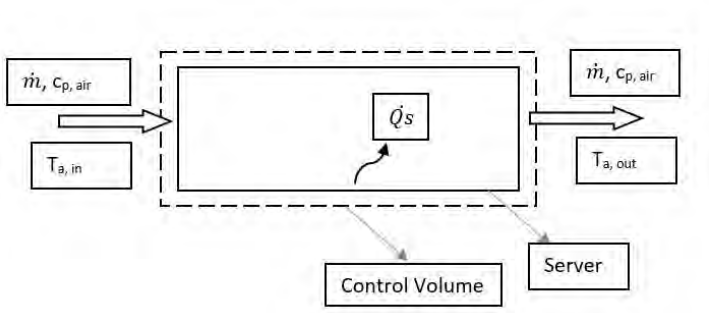

Figure 1: Control volume for a server treated as a blackbox

Energy balance for the server:

$$C_s \frac{dT_s}{dt} = \dot{Q}_s - \dot{C}_a\left(T_{a,out} - T_{a,in}\right) \tag{1}$$

Which in the steady-state reduces to

$$T_{a,ex} = \frac{\dot{Q}_s}{\dot{m}c_{p,a}} + T_{a,in} \tag{2}$$

Energy balance for the air stream:

Neglecting thermal storage in the air, the heat gained by the air is equal to that lost by the server times the server effectiveness of heat transfer. This leads to the expression

$$\dot{C}_a\left(T_{a,out} - T_{a,in}\right) = \varepsilon\dot{C}_a\left(T_s - T_{a,in}\right) \tag{3}$$

Solving Eqs. (1) and (3) simultaneously gives

$$C_s \frac{dT_s}{dt} = \dot{Q}_s - K\left(T_s - T_{a,in}\right) \tag{6}$$

where $K = \varepsilon\dot{C}_a$ (7) $\tau = \frac{C_s}{K}$ (8)

The capacitance C_s and effectiveness ε may be estimated using correlations from Pardey [1]:

$$C_s = 644M \qquad \varepsilon = 1 - 13(\rho')^{-1.87} \tag{9, 10}$$

where M is the server mass in kg and ρ' is the mass density of the server in kg/U, where 1U = 1.75”

The time derivative in Eq. (6) is discretized in EnergyPlus using forward differencing as

$$\frac{dT_s}{dt} = \frac{T_s - T_s^{old}}{\Delta t} \tag{11}$$

This approach allows for the updating of the server temperature in EnergyPlus as

$$T_s = \left(\frac{\tau}{\tau+\Delta t}\right)T_s^{old} + \left(\frac{\Delta t}{\tau+\Delta t}\right)\left[T_{a,in} + \frac{\Delta T_{ss}}{\varepsilon}\right] \tag{12}$$

Where $$T_s^0 = T_{a,in}^0 + \frac{\Delta T_{ss}^0}{\varepsilon} \quad (13)$$

Furthermore, the exit air temperature is modified to the following form:

$$T_{a,out} = \left[1 + \varepsilon\left(\frac{\Delta t}{\tau+\Delta t}\right) - \varepsilon\right] T_{a,in} + \varepsilon\left(\frac{\tau}{\tau+\Delta t}\right) T_s^{old} + \left(\frac{\Delta t}{\tau+\Delta t}\right) \Delta T_{ss} \quad (14)$$

Where ΔT_{ss} is the steady-state temperature difference obtained by making the time derivative term in Eq. (1) equal to zero, thus giving $$\Delta T_{ss} = \frac{\dot{Q}_s}{\dot{m} c_{p,a}} \quad (15)$$

Equations (12) through (15) are the relevant equations for the Schneider model that are implemented in EnergyPlus using the built-in Energy Management System (EMS) through EnergyPlus Runtime Language (ERL).

2.2 Implementation of the Dynamic Server Models. The EnergyPlus software package is designed for commercial and residential buildings, but important differences exist between these types of buildings and data centers:

1. HVAC analysis for commercial and residential buildings consists of dividing the interior space into zones where air is assumed to contain uniform properties (e.g., temperature). However, air-cooled data centers predominantly separate the airspace into hot and cold aisles to aid in computing efficiency.
2. Calculations on the total cooling load due to IT equipment in data centers is difficult to do manually.
3. Data centers contain different metrics for acceptable operating conditions than residential or commercial buildings.

Items 2 and 3 above call for an additional software capability to aid in the construction and evaluation of the energy modelling performed of data centers. Therefore, the Data Center EnergyPlus (DCE+) software package was created to aid in modeling of data centers. DCE+ acts as a wrapper software package to EnergyPlus per Fig. 1 below. In general, the user creates a base EnergyPlus input data file (IDF) using the OpenStudio and SketchUp software packages. This base IDF contains information related to building envelope construction, general cooling equipment, and climate information. The IDF also contains dummy values for electronic loads in the data center. DCE+ overwrites the electronic load information in the IDF to create a new IDF. DCE+ then calls EnergyPlus to perform energy calculations using the new IDF, and then DCE+ analyzes the output files to determine data center-specific performance metrics.

DCE+ updates the IDF by allowing users to build data center loads from scratch. Users define individual types of servers, then deploy these servers on types of racks. Groups of these types of racks are then implemented into rows of the data center. The total load from the IT equipment is then automatically calculated in DCE+ but may be

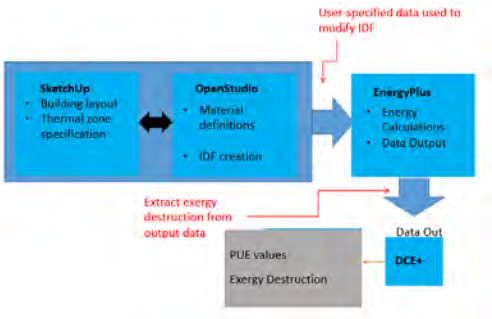

Figure 2. Application of DCE+ to modify the base IDF

manually overwritten by the user if desired.

DCE+ also determines the performance metrics associated with data center operation. The primary metric is the power utilization effectiveness (PUE), which is defined as the ratio of total power consumption to IT power consumption. The PUE is calculated from EnergyPlus output data for both summer and winter design days. Other metrics include the following:

- Water utilization effectiveness (WUE): the amount of water consumed in Liters per kWh of IT load. The WUE determination uses the water evaporation calculation in EnergyPlus from cooling towers.
- Exergy destruction calculations are performed based on the inlet and outlet air temperature of the data center. The IDF provides the IT load for each row ($\dot{Q}$), the row supply air mass flow rate ($\dot{m}$), and the supply air temperature (T_s). The return air temperature (T_r) for the row is calculated as

$$T_r = T_s + \frac{\dot{Q}}{\dot{m}c_{p,a}} \tag{18}$$

The exergy destruction in the row airspace is calculated as

$$\dot{\psi}_d = \dot{m}c_p \left(T_r - T_s - T_0 \ln\left(\frac{T_r}{T_s}\right)\right) \tag{19}$$

The use of exergy destruction as a metric represents a second-law thermodynamic efficiency. Exergy is the amount of useful energy available in the system, and the destruction of exergy indicates irreversible processes that lose available work that could be potentially recovered for waste energy harvesting.

REFERENCES

[1] Zachary M. Pardey Dustin W. Demetriou, Hamza Salih Erden, James W. VanGilder. Ezzat Khalifa, Roger R.Schmidt, Proposal for Standard Compact Server Model forTransient Data Center Simulations, *ASHRAE Transactions, 121*(1)

[2] Hamza Salih Erden, Ezzat Khalifa, Roger R.Schmidt, 2014, Determination of the LumpedCapacitance Parameters of Air-Cooled Servers through Air Temperature Measurements, *Journal of Electronic Packaging, 136*

[3] Application Guide for EMS, *EnergyPlus Version 8.3*

[4] Dell, PowerEdge R210 II, *Technical Guide*

Fourth International Conference on Computational Methods for Thermal Problems
THERMACOMP2016, July 6-8, 2016, Georgia Tech, Atlanta, USA
N. Massarotti, P. Nithiarasu and Y. Joshi (Eds.)

Single and Multiphase Flow Computations on Graphics Processing Units

S. P. Vanka, P. Kumar, K. Jin and B. G. Thomas
Department of Mechanical Science and Engineering, University of Illinois at Urbana-Champaign,
1206 W Green Street, Urbana, IL, 61801, USA, spvanka@illinois.edu

ABSTRACT

In recent years, graphics processing units (GPU) have become popular and powerful for solving problems in various scientific disciplines. GPUs have also been widely applied to solve problems of fluid flow and heat transfer. GPUs are essentially massively parallel processors with a large number of cores and fast access memory. In this paper we discuss our on going work on fluid flow analyses using GPUs.

Key Words: *Multiphase Flow, MHD, Non-Newtonian, Bubbly Flow, Graphics Processing Units.*

1. INTRODUCTION

This paper describes some of our recent work on using Graphics Processing Units (GPU) as a paradigm for performing large-scale scientific computations. In particular we are interested in computational fluid dynamics (CFD), which is important to a large number of mechanical, aerospace, chemical and biomedical industries. The objective of this paper is to provide our assessment of learning, implementing, and applying the codes to several problems of our current interest. The observed performances are quite attractive to pursue this new paradigm as a tool for CFD. The technology is continually improving, and new hardware platforms as well as software are being developed. Our current experiences relate to NVIDIA GPUs (specifically the Tesla K20 and K40) and programming them using CUDA (Compute Unified Device Architecture)

The GPU can be thought essentially as a massively parallel computer, capable of simultaneously executing instructions on a large number of arithmetic units. However, because of the special architecture of the GPU, it is necessary to reorganize the numerical algorithm as well as the program structure such that the communication and computation as well as data access are executed optimally. The architecture of a GPU is quite different than that of a CPU. A GPU is designed with more transistors dedicated to computation and less resources dedicated to data caching and flow control compared with a CPU, resulting in significant computational speed-up [1]. The GPU is designed to be a parallel processor by using massive multithreading, where a single thread can be thought of as the smallest unit of execution that executes instructions in a program. Instructions for the GPU are written in the form of “kernels" which are similar to a function in the C or FORTRAN programming languages.

2. NUMERICAL METHOD

Our in-house code, CUFLOW, solves the three-dimensional momentum and continuity equations in conjunction with Maxwell equations for magneto hydrodynamics (MHD), volume of fluid method (VOF) for multiphase flows, algebraic relations for strain-dependent non-Newtonian viscosity, and Lagrangian particle tracking for solid particles and microbubbles. The momentum and continuity equations are discretized on a collocated Cartesian grid using a finite volume method. The terms in the momentum equation are integrated with second-order accuracy in time and space using Adams-Bashforth time advancement. For multiphase flows computations, the convection term ($\nabla\cdot\rho\mathbf{uu}$) is computed geometrically with linear interpolation for the face velocity. To mitigate the issues caused by large density ratio between gas and liquid phases, the pressure gradient term is written at cell

faces and in the form of $(\nabla p/\rho)$. Coupling the pressure gradient and density together eliminates any ambiguity in density interpolation and leads to a robust method. The viscous term is computed by second order central differencing. Linear interpolation is used for face densities and viscosities.

3. IMPLEMENTATION ON GPU

CUFLOW has been implemented using PGI Fortran on a multi-GPU platform. The multi-GPU implementation is used to solve large problems with up to 100 million grid points. Domain decomposition is first performed to split the total domain between the different GPUs. One additional layer (halo cells) on each side of the domain is added to copy the data from the neighbouring domain and maintain the data continuity. The data transfer process between any two GPUs are shown in Figure 1a which describes the three steps for transferring the data from one node to another. In the first step, the data is copied from the node 0 GPU to the node 0 CPU by invoking a CUDA memory copy command; then in the second step the data is transferred from node 0 to node 1 via MPI send and receive commands, and in the last step the data is transferred from node 1 CPU to node 1 GPU via CUDA memory copy command. The memory copy from GPU to CPU and vice-versa, and data exchange between nodes are time expensive procedures therefore the asynchronous copy must be utilized to mask the overhead of data transfer with computation time. The Poisson type equations (Pressure Poisson Equation, electrical potential equation, MHD potential equation) are solved using a multi-grid V-cycle red-back successive over relaxation (SOR) method.

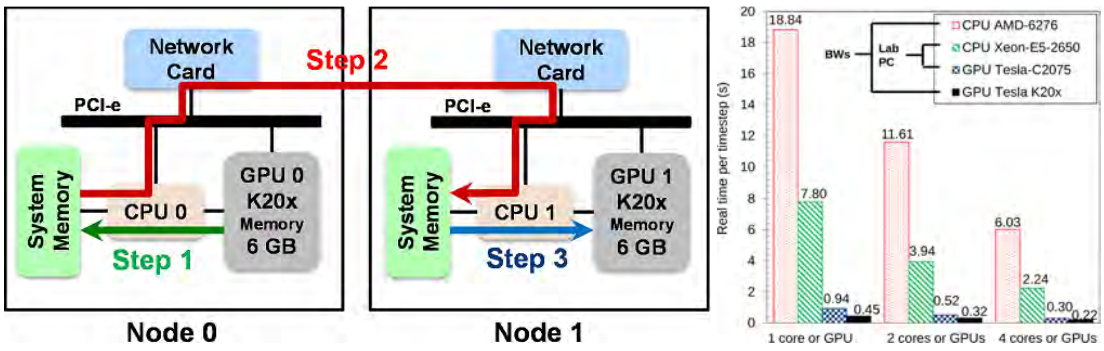

(a) (b)

FIGURE. 1 Multi GPU implementation and performance: (a) Steps for data transfer between two GPUs and (b) Speed up of CUFLOW on multiple CPUs and GPUs

The GPU implementation is 10-40 times faster than a single CPU performance depending on the number of GPU and CPU cores used. Figure 1(b) shows some timings of the code for a three-dimensional lid-driven cavity problem on a $128 \times 128 \times 512$ grid.

4. RESULTS

We present below results of three sets of calculations that involve VOF, magnetic fields and turbulent flows. Complete details of these calculations are presented elsewhere [2-4].

Rise of a single argon bubble in molten steel under a magnetic field

The motion and dynamics of argon bubbles are important to understand the process of inclusion removal in continuous casting of molten steel. When an external magnetic field is applied, the shape, moving path and the motion of the bubble are considerably modified.

In this study, we considered motion of 3 mm and 7 mm spherical bubbles rising in quiescent molten steel under a constant transverse magnetic field. Three different magnetic fields (of strength B = 0, 0.2 and 0.5 T) have been applied in the transverse direction of the bubble motion, and their effects on bubble rise velocity and vorticities are studied. Figure 2(a) shows the geometry of the problem and Figures 2(b) and 2(c) show the rise velocity as a function of time, bubble size and the magnetic field strength.

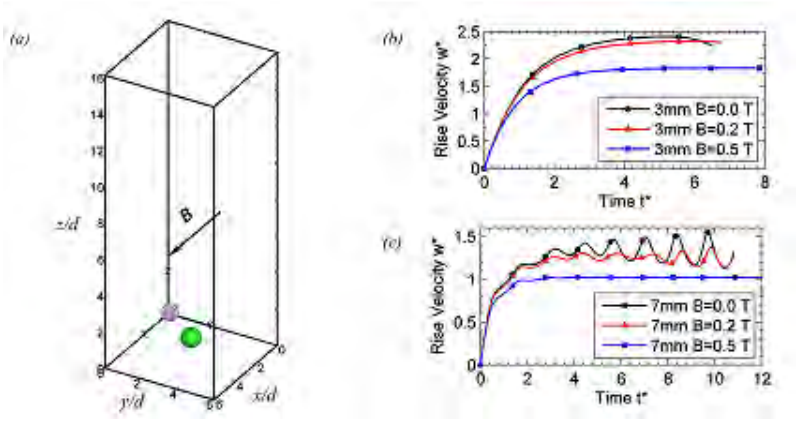

FIGURE 2: (a) Computational domain and the initial bubble location (b) Rise velocity of 3 mm argon bubble and (c) Rise velocity of 7 mm argon bubble.

Effect of confinement on bubble dynamics in a square duct:

In this work, we have studied effects of wall confinement on the bubble rise velocity and aspect ratio of the deformed bubble. We considered four Bond numbers (Bo = 1, 10, 50, 100), two Morton numbers (Mo = 0.001, 0.01) and three confinement ratios (CR = duct size/bubble diameter = 2, 3, 4). Figure 3 shows the various shapes that form as the bubble rises through the duct.

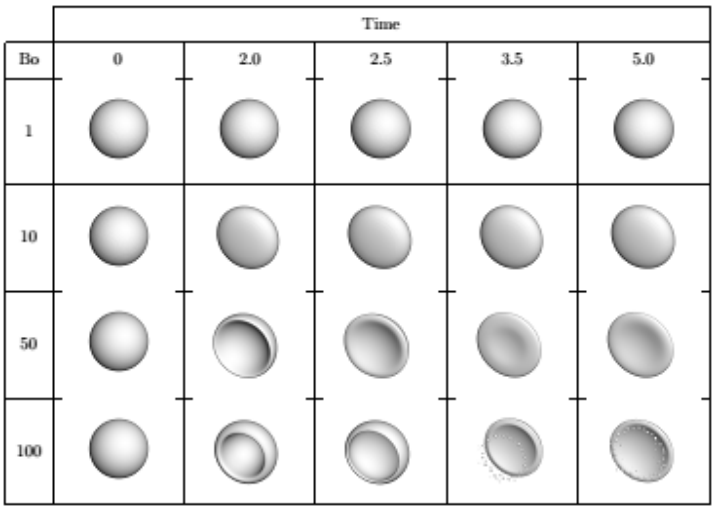

FIGURE 3: Transient bubble shapes for confinement ratio of 4 and Mo = 0.001

Turbulent flow in the mold region of a steel caster

The third problem we present result for is the flow in a continuous caster for which we conducted Large Eddy Simulation (LES) to study effects of Electromagnetic Braking (EMBr) system and submerged entry nozzle (SEN) depth on the flow field. The flow geometry is shown in Figure 4(a). Figures 4(b) and (c) show respectively the view from the top in a cross-section 1 cm below the free surface and contours of velocity magnitude in the central plane. These were obtained by averaging the time varying flows for several seconds of real time.

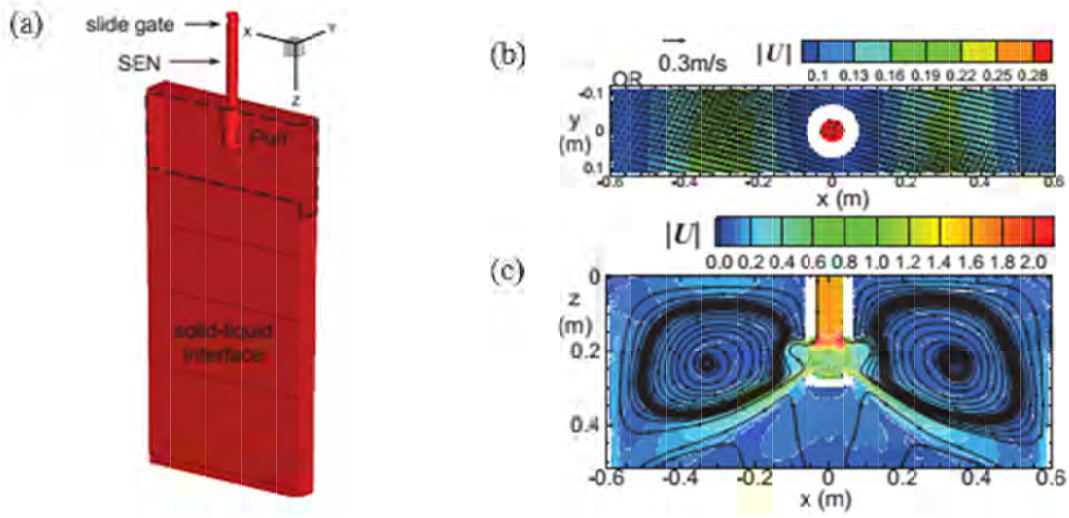

FIGURE 4: (a) Computational domain, (b) Contours of velocity magnitude at 1 cm below top surface (c) Contours of velocity magnitude in the central YZ plane

4. CONCLUSIONS

GPUs are new paradigms for scientific computing. They consist of a large number of cores which can perform arithmetic very fast. Thus they can speed up flow and heat transfer computations significantly. However, in order to benefit from the GPU's architecture, the numerical algorithm must be data parallel. Also, the data must be supplied fast enough for the cores to perform computations. Current data access is limited by the DDR5 memory bandwidth. This inherent limitation prevents exploitation of the full power of the many cores in the GPU. However, significant speed up is still seen. The cost / benefit issues of the GPU must be evaluated with respect to the pricing strategy of the GPUs and the available multiple core CPUs.

REFERENCES

[1] S. P. Vanka, *2012 Freeman Scholar Lecture: Computational Fluid Dynamics on Graphics Processing Units*, *Journal of Fluids Engineering*, 2013, vol. 135, p. 061401.

[2] K. Jin, P. Kumar, S. P. Vanka, B. G. Thomas, *Rise of an Argon bubble in liquid steel in the presence of transfer magnetic field*, *Physics of Fluids,* Under revision.

[3] P. Kumar, S.P. Vanka, *Effects of confinement on bubble dynamics in a square duct*, *International Journal of Multiphase Flow*, 2015, Vol. 77, pp. 32–47.

[4] K. Jin, S. P. Vanka, B. G. Thomas, *Large eddy simulations of the effects of EMBr and SEN submergence depth on turbulent flow in the mold region of a steel caster*, Under preparation.

PARALLEL SESSION

HEAT EXCHANGERS AND FUEL CELLS

Fourth International Conference on Computational Methods for Thermal Problems
THERMACOMP2016, July 6-8, 2016, Georgia Tech, Atlanta, USA
N. Massarotti, P. Nithiarasu and Y. Joshi (Eds.)

EXPERIMENTAL SET-UP AND THERMO HYDRO MECHANICAL MODEL FOR AN ENERGY PILE

M. Adinolfi, A. Mauro, R.M.S. Maiorano, N. Massarotti, S. Aversa
Università degli Studi di Napoli "Parthenope", Centro Direzionale, Isola C4, Napoli, Italy
marianna.adinolfi@uniparthenope.it, alessandro.mauro@uniparthenope.it,
rossella.maiorano@uniparthenope.it, massarotti@uniparthenope.it, aversa@uniparthenope.it

G. Normino, P. Marotta
Consorzio di Ricerca per l'Ambiente i Veicoli l'Energia e i Biocombustibili (CRAVEB), Centro Direzionale, Isola C4, Napoli, Italy

ABSTRACT

A limited number of installations are recorded about geothermal pile foundations and few information are available regarding the impact of thermal processes on their structural and geotechnical performance. Therefore, an experimental set-up has been realized by the geo-energy research group at the University of Napoli "Parthenope" consisting in the installation of heat exchangers and proper instrumentations in sheet-piles retaining wall for underground platform. A coupled multi-physical finite element model has been also developed to simulate the thermo-mechanical behaviour of a single pile.

Key Words: *Energy pile, experimental set up, thermo-hydro mechanical coupling.*

1. INTRODUCTION

The use of geothermal pile foundations is an environmental friendly way to extract/store up energy from/in the ground. The diffusion of this technology is rapidly growing [1], also for its economic advantages due to the reduction of installation costs with respect to traditional geothermal probes. The operating principle of these innovative structures is based on energy transfer between the ground and the fluid flowing inside probes inserted in the pile, in order to feed heat pumps dedicated to buildings heating and cooling [1]. Experimental tests have been conducted [2,3] on energy piles, showing that the thermally induced axial stress inside the pile is between about 50% and 100% of the theoretical fully restrained values [3]. However, it strictly depends on the end-restraint provided by the overlying structure, thermal loads and the properties of the foundation material. Several numerical approaches are available in the literature to model the coupled thermal, hydraulic and mechanical (THM) effects on energy piles and the surrounding soil [2,4]. The aims of this work are to describe the experimental set-up and to propose a proper finite element THM model allowing the simulation of complex soil-structure interaction phenomena for thermo-active piles in retaining walls, in order to evaluate the performance of the geothermal pile in the investigated area.

2. EXPERIMENTAL SET-UP

The experimental set-up has been realized in the construction site of the underground station of Piazza Municipio in Napoli, Italy (Figure1a). The train platform of the original project is located at 13.5 m below the ground level. A sheet pile wall is realized by means of forty-five bored piles (800 mm nominal diameter) and six of them have been used for the present set-up, by incorporating, in the concrete casting, the geothermal probes made of High Density PolyEthylene (HDPE). The average mechanical load on the foundation system is estimated to be smaller than 1200kN. The length of piles to support loads is equal to 11.40 m. The tested elements are located within the sheet-pile retaining wall as shown in Figure1b. The HDPE probes (32 mm nominal diameter) were

anchored to the pile reinforcing cage (Figure 1c). Different probes configurations have been provided: spiral, double and triple U-shaped. The reinforcement cage (details available in Figure 1.d-e) has been used also to support Optic Fiber Sensors (OFS), for strain and temperature measurements. In particular, about 180 m of OFS cables were installed in three of the six probes-equipped piles. Two methods of installation, one with the cable anchored continuously along the length of the reinforcement cage at regular steps and one with the cable strung between the top and bottom of the cage were used.

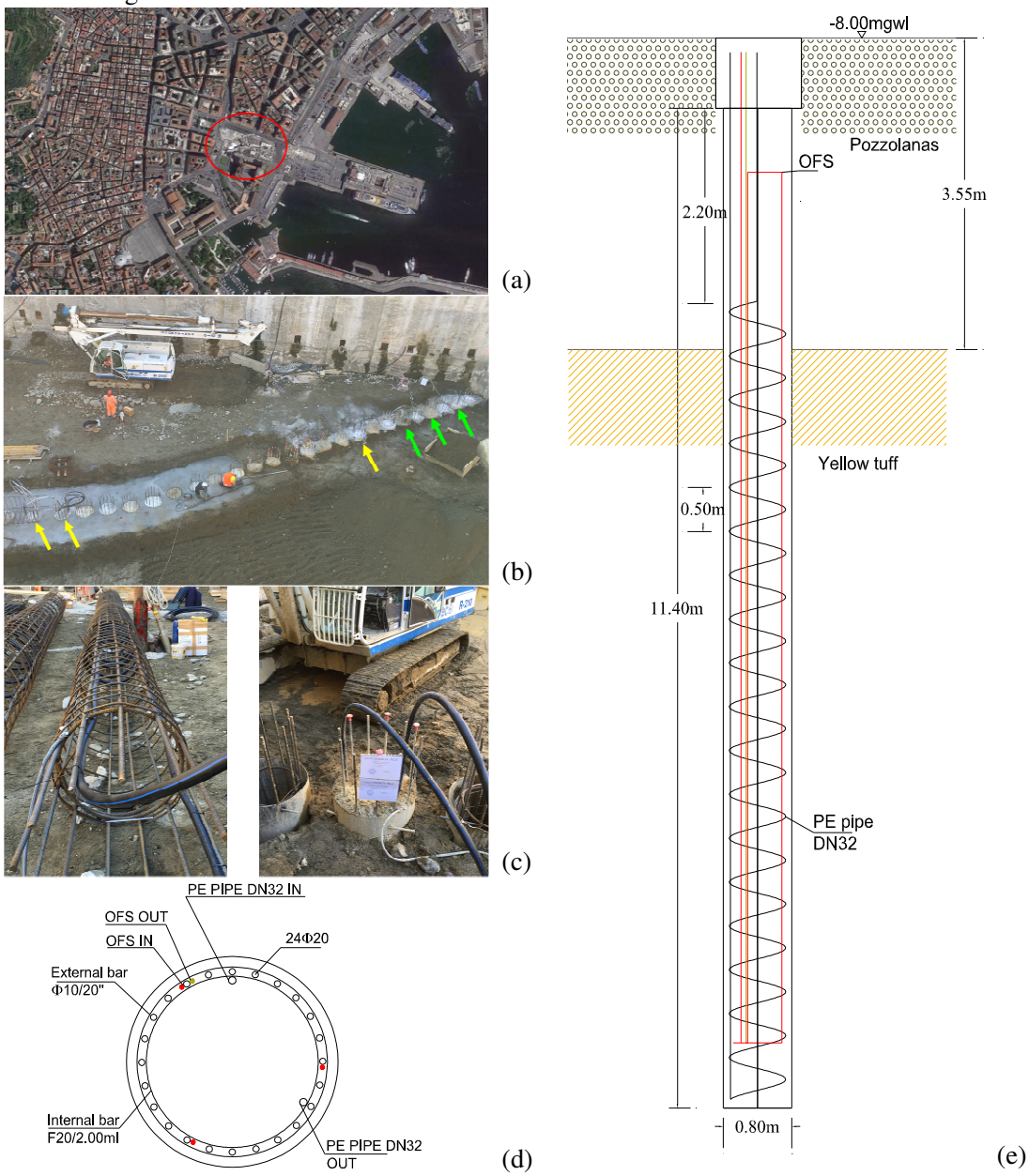

FIGURE 1. Experimental set up details: (a) Piazza Municipio construction site; (b) Retaining wall and positions of geothermal piles (green arrows indicate instrumented piles) ; (c) Set-up distribution of OFS cables and spiral heat exchanger pipe (before and after concrete casting); (d) Typical section of equipped pile; (e) Pile section: geometric and ground features.

As concerns strain measurements, three fibres, installed at 120° along the pile circumference, allow to extract the vectorial displacements of each pile section. The fourth optical cable was strung along

the pile for distributed temperature measurements and a traditional temperature sensor was used to obtain a reference temperature value. The monitoring system is made up by an optoelectronic reading unit, including all the electronic and optical components and cables. Ground conditions, relevant to the foundation designed at around 8.00 meters below ground water level (gwl), are typical for Neapolitan area: a superficial layer of granular pyroclastic products of volcanic activity called "pozzolanas" (3.55 m thick) overlies a lithified stratum of yellow tuff, at depth of 11.55 m below gwl, which extends for many meters under the piles toe. The water level is well above the top of the sheet pile wall; for this reason, all the ground is considered as saturated (Figure 1e).
The energy piles installation was undertaken within an active construction site. Therefore, the experimental campaign will be designed compatibly with all the other activities of the underground station. Moreover several additional in situ and laboratory tests will be realized to characterize the materials, including thermal conductivity and permeability tests on soil samples, integrity tests on the concrete, performance evaluation on heat exchangers and ground response tests.

3. MODEL

A coupled thermo-hydro-mechanical model has been developed to simulate one of the piles of the experimental set-up during the preliminary tests, to be carried out before the soil beneath the sheet pile wall will be excavated. The model has been validated against literature experimental data [3]. The geometric features are shown in Figure 1e, and the material properties are taken from the literature. The governing equations reproducing the mechanical behaviour of the solid skeleton, the heat conduction phenomena and the hydraulic motions in the soil mass are integrated. The model is based on the following assumptions: convection phenomena are negligible; soils are modelled as linear elastic materials (the applied mechanical loads are significantly smaller than the collapse values); displacements and deformations of the solid skeleton are small (linear kinematics); undrained conditions during loads application and hydrostatic pressures are neglected. Taking into account the previous assumptions, the applied equations are:

Pile and soils

$$\nabla\boldsymbol{\sigma}+\mathbf{b}=\mathbf{0} \quad \textit{Momentum conservation}$$

$$\boldsymbol{\varepsilon}^{\mathrm{T}}=1/3\cdot(\alpha_s\cdot\Delta T)\cdot\mathbf{1} \quad \textit{Thermal strain}$$

$$\rho\cdot C_p\cdot\frac{\partial T}{\partial t}-\lambda\cdot\nabla^2 T=0 \quad \textit{Energy balance}$$

$$\boldsymbol{\sigma}=\mathbf{D}^{\mathbf{e}}\left(\boldsymbol{\varepsilon}-\boldsymbol{\varepsilon}^{\mathrm{T}}\right) \quad \textit{Hooke's law}$$

Soils

$$\nabla\boldsymbol{\sigma}'+\nabla p=\nabla\boldsymbol{\sigma} \quad \textit{Terzaghi's principle}$$

$$\mathbf{v}=-\mathbf{k}\cdot\nabla p \quad \textit{Darcy's law}$$

$$\rho\cdot div\frac{\partial\mathbf{u}}{\partial t}-\rho\cdot\beta_{sw}\cdot\frac{\partial T}{\partial t}+\nabla\left(\rho\cdot\mathbf{v}\right)=0 \quad \textit{Mass conservation}$$

where $\boldsymbol{\sigma}$ is the total stress tensor (positive if tensile), $\mathbf{b}$ is volume external force vector, $\boldsymbol{\sigma}'$ is effective stress tensor (positive if tensile), which is the responsible of the mechanical behaviour of saturated soils, p is pore water pressure increase (positive if compressive), $\mathbf{D}^{\mathbf{e}}$ is elastic stiffness tensor, $\boldsymbol{\varepsilon}$ is strain tensor, $\boldsymbol{\varepsilon}^{\mathrm{T}}$ is thermal strain rate tensor, T is temperature, $\mathbf{1}$ is second order unit tensor, α_s is thermal volumetric expansion coefficient of the soil, β_{sw} is thermal volumetric expansion coefficient of the bi-phase mass, $\mathbf{u}$ is the deformation vector, $\mathbf{v}$ is the Darcy velocity vector, $\mathbf{k}$ is the permeability tensor, ρ is respectively fluid and soil density, $\mathbf{q}$ is the heat flux vector, $\boldsymbol{\lambda}$ is the thermal conductivity tensor of the soil and C_p is the soil heat capacity. The finite elements code Comsol Multiphysics v4.3 has been used and implemented for the computation of the axial-symmetric analysis in time dependent study. The mechanical Boundary Conditions (BCs) are: fixed constraint at the bottom and roller condition on the side. The thermal BCs are: constant temperature on the heat exchanger, adiabatic conditions on all external boundaries. The hydraulic BCs are: no flow on the right and bottom boundaries and zero pressure on the top. Ground initial conditions derive from the results obtained from steady-state simulations accounting for only gravity effects. The imposed load on the pile is 1200kN, while the temperature imposed on the pile assumes the dynamic behaviour reported in Figure 2a.

4. RESULTS

Pile head displacements (bottom Figure 2a) are smaller than 2 mm and reach the maximum value when both mechanical and cooling loads are applied. The analysis shows that the vertical displacement of the pile head follows the temperature changes. Analysing Figure 2b, when only mechanical load is applied, the axial load decreases with depth, because it is mainly carried by shaft resistance. The pile is contracted during the cooling phase (blue line of Figure 2b) while, during the heating phase, an increase of 550kN of the compressive load due to only heating phenomena can be appreciated at about 3m depth, with a consequent total load of 1750kN due to the combined thermo-mechanical effects (red line of Figure 2b).

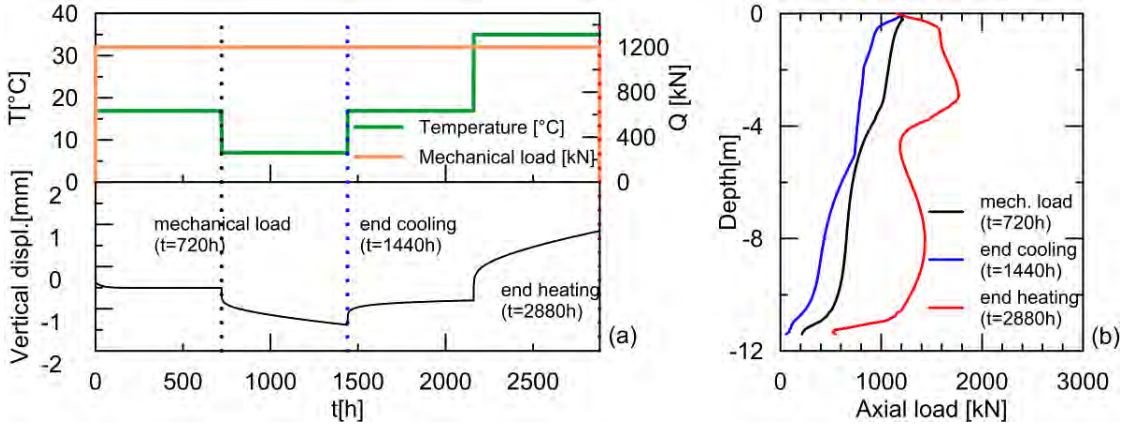

FIGURE 2. Model results: (a) Mechanic and thermal loads-time histories on top and pile head displacements on bottom; (b) Axial loads calculated at only mechanical load application and at the end of thermal phases.

5. CONCLUSIONS

In this paper it is described the experimental set-up of energy multi-piles system realized in the construction site of the underground station of Piazza Municipio in Napoli, Italy. A thermo-hydro-mechanical forecasting model has been developed to design the future experimental campaign and validated against experimental data [3]. The model has been also applied to the simulation of a pile of the experimental set-up. When the data of the campaign tests will be available, the results obtained with the present numerical model will be also compared with on-field experimental data.

ACKNOWLEDGMENTS

The authors gratefully acknowledge the financial support of GeoGrid project PON03PE_00171_1.

REFERENCES

[1] H. Brandl, Energy foundations and other thermo-active ground structures, *Geothecnique*, 56, 81-122, 2006.

[2] L. Laloui, M. Nuth, L. Vulliet, Experimental and numerical investigations of the behaviour of a heat exchanger pile, *Int. J. Numer. Anal. Meth. Geomech.*, 30, 763-781, 2006.

[3] P.J. Bourne-Webb, B. Amatya, K. Soga, T. Amis, C. Davidson, P. Payane, Energy pile test at Lambeth College, London: Geotechnical and thermodynamic aspects of pile response to heat cycles, *Geothecnique*, 59, 237-248, 2009.

[4] D. Salciarini, C. Tamagnini, E. Cinfrignini, Modellazione dei processi termo-idro-meccanici indotti in prossimità di pali geotermici, *IARG*, 2012.

Fourth International Conference on Computational Methods for Thermal Problems
THERMACOMP2016, July 6-8, 2016, Georgia Tech, Atlanta, USA
N. Massarotti, P. Nithiarasu and Y. Joshi (Eds.)

Transitional Fluid Flow Numerical Modelling in Sinusoidal Heat Exchanger Channels

Evaldas Greiciunas
EPSRC Centre for Doctoral Training in Fluid Dynamics, University of Leeds, Leeds LS2 9JT, United Kingdom, scegr@leeds.ac.uk

Duncan Borman
School of Civil Engineering, University of Leeds, Leeds LS2 9JT, d.j.borman@leeds.ac.uk

Jon Summers
School of Mechanical Engineering, University of Leeds, Leeds LS2 9JT, J.L.Summers@leeds.ac.uk

ABSTRACT

The study focuses on modelling heat transfer and fluid flow in a sinusoidal plate-fin heat exchanger channel at $10 \leq Re \leq 1000$. The aim is to investigate the modelling of unsteady flows from $Re \approx 200$, a regime that promotes fluid mixing and improves heat transfer [1]. The channel geometry is taken from a study by Zhang et al. [2], in which steady state simulations were presented. Steady and unsteady numerical simulations are undertaken; with the impact of different turbulence modelling assumptions considered. Predictions for $Re > 200$ were made using $k-\omega\ SST$ turbulence model. Results obtained agree to the observations by Rush et al. [1]. The study includes exploring and verifying simulation approaches for this regime. A further aim of the study is to compare Computational Fluid Dynamics (CFD) codes OpenFOAM and Ansys Fluent.

Key Words: *Heat Exchangers, Finite Volume, Forced Convection, OpenFOAM, Ansys Fluent.*

1. INTRODUCTION

A heat exchanger (HE) is a device which enables heat transfer between fluid streams or between solid and a fluid stream, provided that there is a temperature difference and a thermal contact [3]. HEs are crucial components in a wide array of industry: process, automotive, aerospace and many others. A common interest of researchers is to increase the compactness of HE systems [4] as compactness saves installation space and unit weight and, as explained in Kays and London [5], can enhance heat transfer. A measure of compactness is the hydraulic diameter, $d_h = 4\,A_C L/A_S$ [5] where A_c - cross sectional flow area, L - thickness of the HE and A_S - heat transfer surface area.

Bhutta et al. [6] carried out an extensive literature review of HE Computational Fluid Dynamics (CFD) studies. It revealed the adoption of two main numerical modelling methods. Namely, one based on a large scale analysis using a porous media approach to model HE matrices [7], and the other based on detailed flow and heat transfer analysis through small sections of the HE [2]. Detailed predictions enable friction and heat transfer characteristics to be applied in the design of HE matrices [7], [8]. There are a number of studies that employ a detailed flow analysis, e.g. Zhang et al. [2], Rosaguti et al. [9], Manglik et al. [10], all of which analyse the HE channel flow using a single period of geometry and assume that the flow is periodic and laminar. Unsteady behaviour of the flow occurring at the geometry dependent Reynolds number of a few hundred was the limit of the work presented in [2,9,10]. Reynolds number in this study is defined as $Re = \rho U_m S/\mu$. Here ρ - fluid density, U_m - mean flow velocity, S - channel width and μ – dynamic viscosity. The experimental evidence supporting the unsteady behaviour was found in the work of Rush et al. [1], who studied the flow through sinusoidal channels. They concluded that unsteady flow increases the heat transfer. Numerical simulations to solve a similar problem were presented for a similar geometry in [11], [12], however, both studies assumed the flow remained laminar.

In this work the focus is on detailed analysis through a single HE flow channel with emphasis on providing understanding of the unsteady behaviour. It quantifies the differences in heat transfer that

are observed when the flow is steady and unsteady, and also evaluates predictions of two CFD codes: OpenFOAM and FLUENT. Steady state results are obtained at the Reynolds number range $10 \leq Re \leq 200$ and data from [2] is used to verify predictions. Unsteady analysis is undertaken for Reynolds numbers in the range of $200 \leq Re \leq 1000$. To simulate the unsteady regime a range of turbulence modelling assumptions are considered (including use of $k-\omega\ SST$ model).

2. METHODOLOGY

The problem was set up using the non-dimensionalised geometry by Zhang et. al [2], which is parametrised by corrugation aspect and fin spacing ratios for the sinusoidal channel. The corrugation aspect ratio is defined as $\gamma = 2A/L$ and fin spacing ratio as $\epsilon = S/(2A)$ (Figure 1). The flow was modelled as two-dimensional, incompressible, steady state and periodic with the properties of air for low Reynolds number predictions. The walls were set at a constant temperature of $T_w = 350\,K$ whilst the flow inlet was set at $T_b = 300\,K$. The mathematical model of the problem consists of continuity of mass, momentum and energy equations using the assumptions above for laminar flow predictions [13]:

$$\nabla \cdot \mathbf{u} = 0$$

$$\rho \frac{\partial \mathbf{u}}{\partial t} + \rho(\mathbf{u} \cdot \nabla)\mathbf{u} = -\nabla p + \mu \nabla^2 \mathbf{u} + \mathbf{F}$$

$$\rho c_p \left(\frac{\partial T}{\partial t} + \mathbf{u} \cdot \nabla T \right) = \nabla \cdot k \nabla T + \Phi$$

Whilst for turbulent flow simulations RANS $k-\omega\ SST$ formulation was used [14]. A periodic condition was used to reduce computational complexity for simulations at $Re < 200$. This method requires only a single period of the channel (Figure 1) and the modifications to the model can be found in Patankar et al. [15].

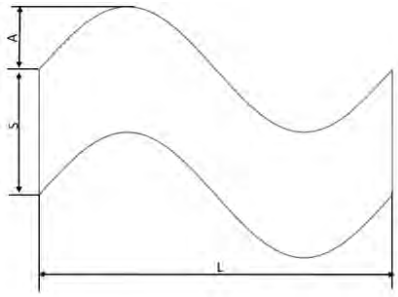

FIGURE 1. Schematic of a single period geometry.

Unsteady flow modelling ($Re \geq 200$) was carried out using the approach proposed by Zheng et al. [11]. This involved the whole channel of the HE, which consisted of seven sinusoidal periods (Figure 2). The flow was modelled as unsteady and, instead of periodic condition at the start and end of the domain, a velocity inlet and pressure outlet were used. Other flow properties were unchanged. Straight sections at the inlet and the outlet of the sinusoidal section were added to enable the flow to develop and prevent potential errors from flow reversal. The simulations provide detailed information about transient and spatial flow development inside the channel, and are significantly more computationally intensive than the low Reynolds number, steady and periodic cases. In addition, it provided information about flow development inside the channel.

3. RESULTS

Periodic simulations were undertaken at $10 \leq Re \leq 200$ and results in both OpenFOAM and Fluent are shown to be in strong agreement with those presented by Zhang et. al [6]. At $Re \approx 200$ it was observed that the flow becomes unsteady as identified by Rush et al. [7]. The flow contour

for an unsteady simulation at $Re = 400$ is shown in Figure 2b. As the flow is observed to be unsteady this is a snapshot of the changing flow field at time 0.18 s. The result is in contrast to the solution at $Re = 100$, shown in Figure 2a, where a steady flow field is observed. At $Re = 400$ mixing of the fluid stream is higher compared to $Re = 100$. Simulations at $Re > 200$ were carried out using a range of turbulence modelling assumptions (results using $k - \omega\ SST$ model are those shown in figure 2b). The need for an appropriate turbulence model was identified by simulating laminar and turbulent predictions for a range of Reynolds number cases. At low Reynolds number predictions agree well for both laminar and turbulence modelling cases, meanwhile at $Re \approx 200$ the solutions begin to differ. It should be noted that appropriately small time-steps must be used to observe the instability. To illustrate the effect unsteady mixing has on the flow, the pressure drop (Δp) across the channel length at $Re = 500$ is presented in Figure 3. It can be observed that pressure drop is also unsteady in nature and the predictions for the laminar and turbulence model cases are significantly different. This in turn have an effect on the resolved temperature fields. The impact of considering different turbulence models on the resulting heat transfer performance will be presented in the full paper, along with comparisons to validation data. Transient effects, heat transfer and pressure drop will be considered in the context of implementing these different turbulence modelling assumptions in both OpenFOAM and Fluent.

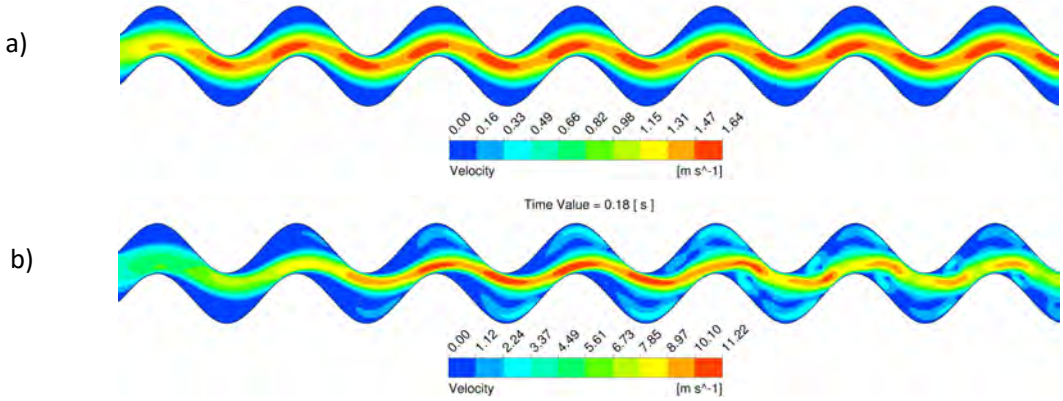

FIGURE 2. a) Steady state laminar ($Re = 100$) and b) transient $k - \omega\ SST$ ($Re = 400$) velocity contours using $\Delta t = 1 \times 10^{-5}$ s (Fluent), $\gamma = 0.375, \epsilon = 1.0$.

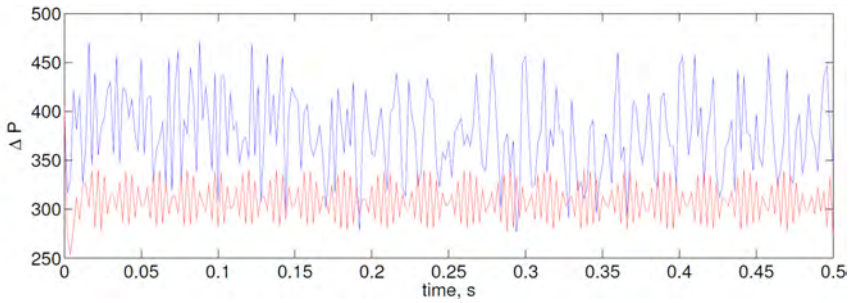

FIGURE 3. Flow pressure drop through a channel (ΔP) at $Re = 500$ versus simulation time. Red and blue lines are $k - \omega\ SST$ and laminar predictions with $\Delta t = 1 \times 10^{-5}\ s, \gamma = 0.375, \epsilon = 1.0$ (Fluent).

4. CONCLUSIONS

CFD modelling of HE channels is challenging as the flows are regularly in the transitional regime. Low Re number regime simulations were verified using the data from Zhang et al. [3]. Modelling of

the transitional regime requires far greater computational power as the flow is unsteady, requiring small time steps to resolve for small length scale velocity fluctuations. These cause fluid mixing and mean temperature differences through the channel to fluctuate periodically. OpenFOAM and Fluent CFD codes are used for comparison throughout the Re number range. To validate the transitional modelling approach, results will be presented alongside validation data in the full paper.

REFERENCES

[1] Rush, T. A., T. A. Newell, and A. M. Jacobi. "An experimental study of flow and heat transfer in sinusoidal wavy passages." *International Journal of Heat and Mass Transfer* 42.9 (1999): 1541-1553.

[2] Zhang, J. , J. Kundu, and R. M. Manglik. "Effect of fin waviness and spacing on the lateral vortex structure and laminar heat transfer in wavy-plate-fin cores." *International Journal of Heat and Mass Transfer* 47.8 (2004): 1719-1730.

[3] Rohsenow, W. M. Handbook of heat transfer. Vol. 3. New York: McGraw-Hill, 1998.

[4] Hesselgreaves, J . E. Compact heat exchangers: selection, design and operation. Gulf Professional Publishing, 2001.

[5] Kays, William Morrow, and Alexander Louis London. "Compact heat exchangers." (1984).

[6] Bhutta, M. M. A. , et al. "CFD applications in various heat exchangers design: A review." *Applied Thermal Engineering* 32 (2012): 1-12.

[7] Hayes, Andrew M., et al. "The thermal modeling of a matrix heat exchanger using a porous medium and the thermal non-equilibrium model." *International Journal of Thermal Sciences* 47.10 (2008): 1306-1315.

[8] Wen, Jian, et al. "An experimental and numerical investigation of flow patterns in the entrance of plate-fin heat exchanger." *International Journal of Heat and Mass Transfer* 49.9 (2006): 1667-1678.

[9] Rosaguti, Nathan R., David F. Fletcher, and Brian S. Haynes. "Low-Reynolds number heat transfer enhancement in sinusoidal channels." *Chemical engineering science* 62.3 (2007): 694-702.

[10] Manglik, Raj M., Jiehai Zhang, and Arun Muley. "Low Reynolds number forced convection in three-dimensional wavy-plate-fin compact channels: fin density effects." *International Journal of Heat and Mass Transfer* 48.8 (2005): 1439-1449.

[11] Zheng, Zhanying, David F. Fletcher, and Brian S. Haynes. "Transient laminar heat transfer simulations in periodic zigzag channels." *International Journal of Heat and Mass Transfer* 71 (2014): 758-768.

[12] Dai, Zhenhui, David F. Fletcher, and Brian S. Haynes. "Impact of tortuous geometry on laminar flow heat transfer in microchannels." *International Journal of Heat and Mass Transfer* 83 (2015): 382-398.

[13] Subrahmanyan Chandrasekhar. *Hydrodynamic and hydromagnetic stability*. Courier Corporation, 2013.

[14] Menter, Florian R. "Two-equation eddy-viscosity turbulence models for engineering applications." AIAA journal 32.8 (1994): 1598-1605.

[15] Patankar, S. V., C. H. Liu, and E. M. Sparrow. "Fully developed flow and heat transfer in ducts having streamwise-periodic variations of cross-sectional area." *Journal of Heat Transfer* 99.2 (1977): 180-186.

Fourth International Conference on Computational Methods for Thermal Problems
THERMACOMP2016, July 6-8, 2016, Georgia Tech, Atlanta, USA
N. Massarotti, P. Nithiarasu and Y. Joshi (Eds.)

Molecular dynamics simulation of oxygen transport characteristics in the MEA of PEMFC

Mahiro Kato
Tokyo Institute of Technology, Meguro-ku, Tokyo 152-8552 JAPAN

Asegun Henry, Samuel Graham
Georgia Institute of Technology, Atlanta, GA 30332-0405 U.S.A.

Hong Duc Doan, Kazuysohi Fushinobu
Tokyo Institute of Technology, Meguro-ku, Tokyo 152-8552 JAPAN

ABSTRACT

The polymer exchange membrane fuel cell (PEMFC) is a promising candidate for energy conversion applications in various applications such as automobile, co-generation systems for households, or emergency power supply. One of the issues for the large-scale commercialization of PEMFC is durability, which is affected by gas molecule transport in the membrane. Our previous study has shown that the diffusion coefficient of both of hydrogen and oxygen molecules increases with the increment of water content, and the ratio of hydrogen and oxygen diffusion coefficient in the membrane approaches the value in liquid water. From the previous study though, the atomic or molecular level transport mechanism cannot be fully revealed. To investigate the molecular level transport phenomena, in this study, classical molecular dynamics has been done to calculate diffusion coefficient of oxygen with different water content.

Key Words: *Proton exchange membrane fuel cell (PEMFC), molecular dynamics simulation, transport property.*

1. INTRODUCTION

PEMFC (Proton exchange membrane fuel cell,) or PEFC (polymer electrolyte fuel cell,) is an important energy conversion device option for the applications, such as automobile, co-generation system for households and emergency power supply, considering the possible alternatives of primary energy sources other than the fossil fuel and its local clean nature. Fuel cell-based co-generation systems for households have been commercially available since 2009 in Japan, and the cumulative market sales exceeded 100,000 units in 2014. Fuel cell vehicles have also been commercially since 2014.

One of the issues for the PEMFC is its durability. Previous studies have revealed cell degradation due to gas molecules cross-leaking [1]. The polymer electrolyte membrane, which is supposed to have gas barrier function, in fact have a very tiny amount of permeation of oxygen and hydrogen gas molecules during its operation. This cross-leaking of gas molecules results in the formation of hydrogen peroxide in the membrane under certain condition to degrade the membrane as well as degrading the cell performance.

Authors have experimentally measured the diffusion coefficient of oxygen and hydrogen in electrolyte membrane under operation conditions [2]. Limiting current technique is applied to measure the overall gas transport resistance along the thickness-wise direction of the membrane by using microprobe technique. The resistance is then analyzed to obtain the diffusion coefficient in the membrane by plotting the resistance versus thickness-wise position of the microprobe. The results showed the increasing trend of the diffusion coefficient of both oxygen and hydrogen with increasing membrane water uptake and with other parameters, as well as the unique trend of the

ratio of hydrogen to oxygen diffusion coefficients. The microprobe technique is so powerful that it measures gas molecule transport characteristics by means of simple experimental setup. It however cannot give more detailed insight of the reason why and how the diffusion coefficient is controlled by the water uptake and other parameters by visualizing the constitution and the behavior of each molecules or atoms. To the author's knowledge, it is a grand challenge to experimentally validate the question. From such viewpoint, molecular dynamics simulation is a very powerful tool to visualize the molecular level behavior of materials. By preparing a system of molecules and atoms under considerations, the technique visualizes the behavior of the system.

In this work, we have conducted a molecular dynamics simulation of oxygen molecules in Nafion membrane with water uptake. Present work focuses on the development of MD (molecular dynamics) simulation of the system. We chose oxygen molecules for the first step to see their behavior in Nafion with water uptake. Position of oxygen molecules is analyzed to calculate the mean square displacement (MSD) to obtain the diffusion coefficient. The result is the compared with experimental results.

2. NUMERICAL CALCULATION

Parameters of Nafion117 [3] with equivalent weight (EW) of 1100 g/eq is used in the simulation. Chemical formula of Nafion is shown in Fig. 1, where the parameter set of $x = 7$, $y = 1$, $n = 10$ is used in the simulation.

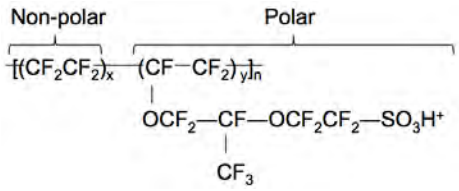

FIGURE 1. Chemical formula of Nafion

Present calculation employs Dreiding Force Field according to the previous works [4]. Modified parameter is used for the torsion force parameter [5] in order to match the density value with experimental data.

24 molecular chains of Nafion are randomly positioned in a 20 nm cubic cell with three dimensional periodic boundary condition. Water molecules are then added in the cubic cell so that the number of water molecules to be equal to the value of water uptake, λ ($= N_{H2O}/N_{SO3-}$), of either 3, 5, or 8, that is the number of water molecules per sulfo group. Functional relationship of λ to the relative humidity is taken from a literature [6]. Since all the protons are known to dissociate from sulfo group under the condition of λ is equal to or larger than 3 [7], hydronium ions of same amount to the sulfo group are added to neutralize the system. Three oxygen molecules are added in the system to calculate the diffusion coefficient in the medium.

After arranging the molecules and ions in the cell, following numerical procedure is conducted to aim at annealing the system and at obtaining a equilibrium state according to a previous work [5]: (1) both the temperature and the pressure are gradually increased to reach 800 K and 100 MPa by 50 ps, (2) temperature and pressure are maintained at same value for 100 ps, and (3) the temperature and the pressure are decreased to 353.15 K and 0 MPa by 50 ps. The processes (1) to (3) are repeated several times, and the system is maintained at constant temperature and pressure for 200 ps to obtain a state, which we consider as under equilibrium. Figure 2 shows typical system structure under equilibrium.

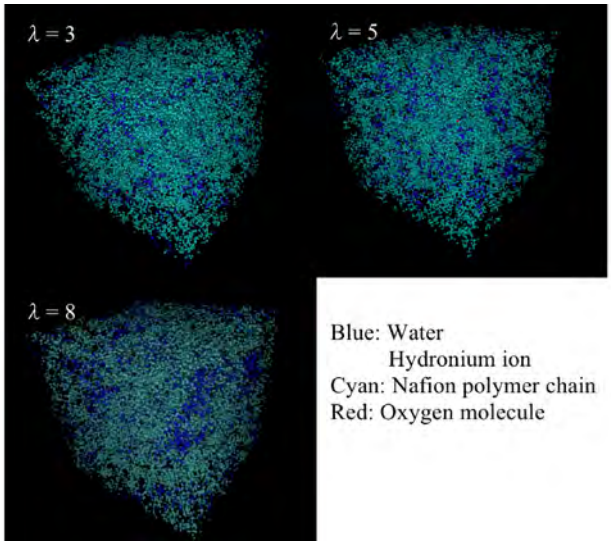

FIGURE 2. Nafion structure after annealing process

The value of density is then examined by omitting the oxygen molecules from the system and by changing the number of water molecules to find about 10% error at maximum.
Open-source molecular dynamics program LAMMPS is used for the simulation.

3. RESULTS

MSD of oxygen molecules are shown in Fig. 3.

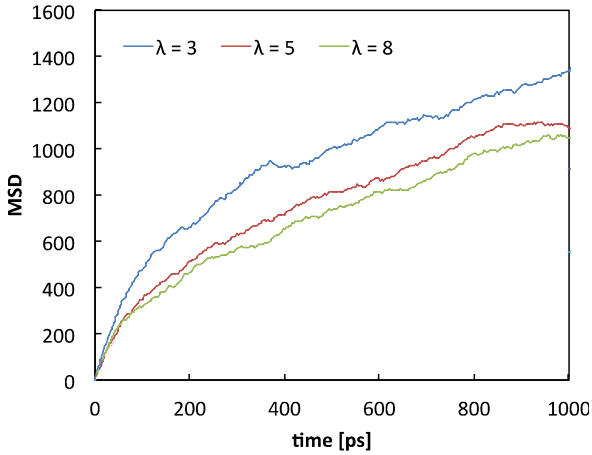

FIGURE 3. MSD (mean square displacement) of oxygen molecules

Diffusion coefficient of oxygen is then calculated from MSD by using Eq. (1)

$$D = \lim_{t\to\infty} \frac{1}{6t} \left\langle \left| r(t) - r(0) \right|^2 \right\rangle \tag{1}$$

where t is time, $r(t)$ is the position of oxygen molecule.
Figure 3 shows the increasing trend of MSD with increasing water uptake. Figure 4 shows the diffusion coefficient of the oxygen obtained by molecular dynamics simulation and our previous experimental data [2]. Numerical results agree well with the experimental data. The diffusion coefficient is found to increase with increasing water uptake.

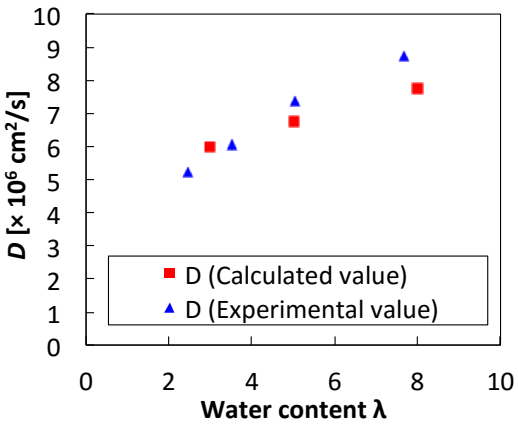

FIGURE 4. Diffusion coefficient of oxygen molecules. Experimental value at 1 atm, 353.15 K

4. CONCLUSIONS

Diffusion characteristics of oxygen in Nafion with water uptake is calculated by using molecular dynamics simulation in order to examine our previous experimental data. Calculated diffusion coefficient of oxygen increases with increasing water uptake, and the trend well agree with the experimental data. Further investigation is underway to examine more parametric dependence, such as the thermal condition, diffusion coefficient of hydrogen molecules, and the molecular level visualization of the system configurations.

5. ACKNOWLEGEMENT

MK and KF acknowledge the kind help of Prof. Takashi Tokumasu of Tohoku University and fruitful discussions with him. MK acknowledges the support from TiROP program of Tokyo Tech. Part of the research has been conducted by the support of Iwatani Foundation.

REFERENCES

[1] A. Ohma, S. Suga, S. Yamamoto, K. Shinohara, Membrane degradation behavior during open-circuit voltage hold test, J. Electrochem. Soc. 154(8), B757-B760, 2007

[2] M. Ohishi, Y. Ono, K. Fushinobu, Measurement of Gas Transport Characteristics in PEFC Electrolyte Membrane by Using Microprobes, Nanoscale and Microscale Thermophysical Engineering, 17(2), 69-78, 2013

[3] S. S. Jang, V. Molinero, T. Cagin, W. A. Goddard, III, Nanophase-segregation and transport in Nafion 117: Effect of monomeric sequence, J. Phys. Chem., B 108, 3149-3157, 2004.

[4] S. L. Mayo, B. D. Olafson, W. A. Goddard, Dreiding – A generic force-field for molecular simulations, J. Phys. Chem. 94, 8897-8909, 1990.

[5] T. Mabuchi, T. Tokumasu, Molecular Simulation of Proton and Water Transport in Hydrated Nafion Membrane, ECS Transactions, 50(2), 175-181, 2012.

[6] J. T. Hinatsu, M. Mizuhata, H. Takenaka, Water-uptake of perfluorosulfonic acid membranes from liquid water and water-vapor, *J. Elecgrochem. Soc.*, 141(66), 1493-1498, 1994

[7] C. Wang, J. K. Clark II, M. Kumar, S. J. Paddison, An ab initio study of the primary hydration and proton transfer of CF_3SO_3H and $CF_3O(CF_2)_2SO_3H$: Effects of the hybrid functional and inclusion of diffuse function, *Solid State Ionics*, 199-200, 6-13, 2011.

Fourth International Conference on Computational Methods for Thermal Problems
THERMACOMP2016, July 6-8, 2016, Georgia Tech, Atlanta, USA
N. Massarotti, P. Nithiarasu and Y. Joshi (Eds.)

EXPERIMENTAL VALIDATION OF A QUASY–3D CVFEM MODEL OF BOREHOLE HEAT EXCHANGERS

Esad Tombarević, Igor Vušanović
Faculty of Mechanical Engineering, University of Montenegro, Džordža Vašingtona bb, 81000 Podgorica, Montenegro. E-mail: esad.tombarevic@ac.me, igor.vusanovic@ac.me

ABSTRACT

This paper presents a quasi-three-dimensional CVFEM model of unsteady heat flow around a single U-tube borehole heat exchanger. The heat transfer model of the fluid circulating through the U tube is considered as one dimensional, while heat transfer through the pipe's wall, grout and the soil is considered as fully three dimensional. Equations of the mathematical model are simultaneously solved to arrive at the solution. The two components of the numerical model are separately verified through the comparison with available analytical solutions. Also, the integral model is verified against the available experimental data.

Key Words: *Borehole heat exchanger, CVFEM, Experimental validation*

1. INTRODUCTION

Borehole heat exchangers are often used to couple the heat pump with the ground to use it as a heat source or sink. This technical solution provides more efficient operation of the heat pump since the ground usually has more favourable temperatures than air to be used as a heat source in winter, or as a heat sink in summer. Heat extraction and rejection is performed by circulating of heat transfer fluid (usually water, brine or antifreeze solution) in a U-bended HDPE pipe buried in a vertical borehole. Borehole is backfilled with an appropriate grouting material which purpose is to improve heat transfer between the pipe legs and the surrounding soil.

Numerical models of heat flow taking place between the fluid circulating in the pipe and the surrounding soil are of crucial importance for the dimensioning and efficiency of long term operation of the system. Extensive review of systems and models is given in the paper by Yang [1]. Most of analytical models are based either on Kelvin's solution for the infinite line source [2] or Carslaw and Jaeger's solution for the cylindrical source [3]. Analytical models are attractive because of computational efficiency and have been incorporated in several design methods but with a number of simplifying assumptions. However, the geometry of the U-tube heat exchanger is more challenging. First, heat transfer within the borehole is not simple radial conduction. Then the temperatures of the circulating fluid in the two legs of the U-tube are different, and therefore the pipes do not exchange heat only with the soil, but also with each other. Therefore, it is evident that in general the borehole heat exchanger presents a transient three dimensional problem because the temperature of the circulating fluid changes with depth. Three-dimensional models offer the most general and accurate representation of heat transfer, but at the cost of considerable computation time.

2. PHYSICAL AND MATHEMATICAL MODEL AND NUMERICAL SOLUTION

The whole domain is divided in two parts: fluid circulating through the U pipe and solid that consists of the U tube, grout and soil. Mathematical model of the borehole heat exchanger consists of the two energy conservation equations, one for the fluid that circulates in the U pipe and another for the pipe, grout and soil. Neglecting the conductive heat transfer, energy equation for the fluid in the U-pipe is:

$$\rho_f c_f \frac{\partial T_f}{\partial t} + \rho_f c_f \frac{\partial}{\partial s}\left(v_f T_f\right) = \frac{4h}{d_{p,i}}\left(T_w - T_f\right) \tag{1}$$

where $d_{p,i}$ is the inner pipe diameter, ρ_f, c_f v_f and T_f are density, specific heat, velocity and temperature of the heat transfer fluid respectively, s is the downstream coordinate, T_w is the temperature of the pipe wall and h is the heat transfer coefficient. This equation is dicretized using control volume method with implicit integration in time and with quadratic upwind interpolation for convective kinetics. Temperature of the pipe wall in the source term on RHS of equation (1) is obtained from the solution of the heat transfer equation for the solid part of the domain.

Corresponding energy equation for the heat transfer for the U-pipe, grout and soil is:

$$\rho c \frac{\partial T}{\partial t} + \rho_w c_w u \frac{\partial T}{\partial x} + \rho_w c_w v \frac{\partial T}{\partial y} = \frac{\partial}{\partial x}\left(k \frac{\partial T}{\partial x}\right) + \frac{\partial}{\partial y}\left(k \frac{\partial T}{\partial y}\right) + \frac{\partial}{\partial z}\left(k \frac{\partial T}{\partial z}\right) \tag{2}$$

where ρ, c, k and T without subscripts are density, specific heat, thermal conductivity and temperature of U-pipe, grout and soil, while ρ_w, c_w, u and v are density, specific heat and discharge components of groundwater. Groundwater discharge components can be calculated using expressions for potential flow. Advective terms in equation (2) are omitted in the case when groundwater flow is negligible.

Numerical solution is elaborated in more details in Tombarević and Vušanović [4]. Thanks to the fact that the solid domain is sweepable, it is meshed by triangular prism elements with required number of divisions along the depth of the borehole in order to appropriately take into account the temperature change of heat transfer fluid with depth. Equation (2) is discretized using hybrid Control Volume Finite Element Method which is described in details in Voller [5]. Solutions of the two equations are coupled through the source term on the RHS of equation (1) and the boundary conditions on the pipe walls for equation (2) on the way that the continuity of heat flux on this mutual interface is preserved.

3. RESULTS AND DISCUSSION

Numerical solutions of equations (1) and (2) are separately verified through the comparison with available analytical solutions (see [3] and [6]). The integral model is verified through comparison with the available reference data sets from a large laboratory "sandbox" with a borehole and U-tube, provided by Beier et al. [7]. Large wooden box has a horizontal layout, with square vertical cross section where borehole in the form of an aluminium pipe is centred horizontally along the length of the box. U-tube made of HDPE is centred with spacers in the borehole which is then filled with a bentonite grout. The box is filled with sand which is saturated with water. Constant far field temperature (ground temperature away from the borehole) is simulated by circulating air of the constant temperature through the gap around sandbox and the outer surrounding box. The ends of the sand box are insulated. In the experiments, water is circulated through the U-tube and heated by means of an electric heater. Temperatures of water at the inlet and outlet of the U-tube, temperature of sand at various positions as well as the voltage and current at electric heater are recorded once every minute. Relevant borehole geometry and physical properties are given in Table 1.

TABLE 1. Relevant parameters for model validation

Parameter	Description	Value
L	Borehole length	18,30 m
d_b	Borehole diameter	0,126 m
$d_{p,i}$ / $d_{p,o}$	U-tube inner/outer diameter	0,02733 / 0,0334 m
s	Distance between centres of U-tube legs	0,053 m
k_p / k_g / k_s	Thermal conductivity of U-tube / grout / wet sand	0,39 / 0,73 / 2,82 W/mK
C_p / C_g / C_s	Heat capacity of U-tube / grout / wet sand	2137 / 3800 / 2600 kJ/m^{3}K

Two tests are performed. In the first, uninterrupted test, the circulating pump and the electric heater are operated constantly for the period of 52 hours, more or less without variations in the flow rate and electric power. Figure 1 and 2 show time variation of water temperatures at the outlet and sand temperatures at various locations within the sandbox. Calculated water temperatures and sand temperatures show good agreement with values measured in the experiment. RMSE for water temperatures is 0,1488°C, with maximum relative error of 0,71 %. Corresponding values for the borehole wall are 0,1994°C and 2,27 %.

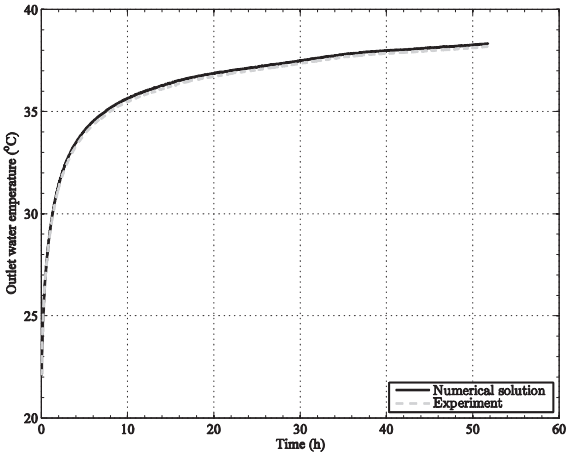

FIGURE 1. Uninterrupted test - water temperatures

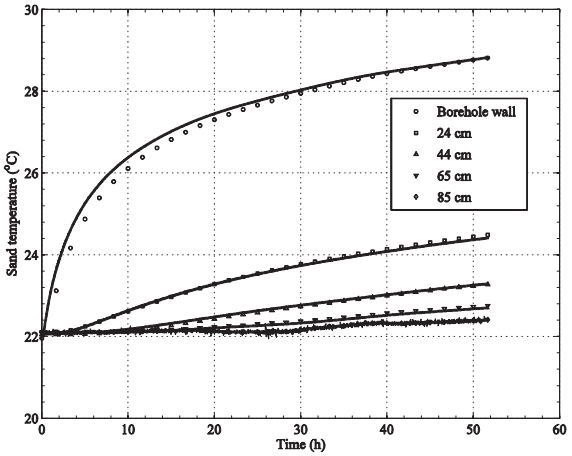

FIGURE 2. Uninterrupted test - sand temperatures

Another test performed includes a two hour interruption of the electric power to the heater and the circulating pump, between 9 and 11 hours of operation. During the interruption forced convection heat transfer coefficient on the RHS of eq. (1) turns into free convection coefficient which value of 137 W/m^2K is suggested by Kavanaugh [8]. Figures 3 and 4 compare the temperatures measured in the experiment with model predictions. It can be seen that the numerical model closely reproduces experimental data even in the case of fast temperature changes in the system. RMSE for water temperatures is 0,2230°C, with maximum relative error of 4,77 %. Corresponding values for the borehole wall are 0,1256°C and 3,03 %.

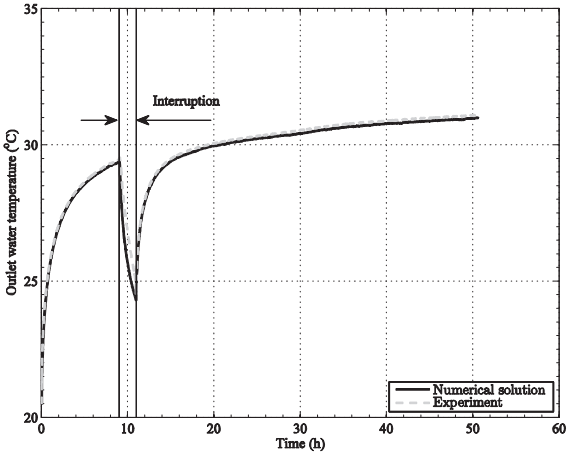

FIGURE 3. Interrupted test - water temperatures

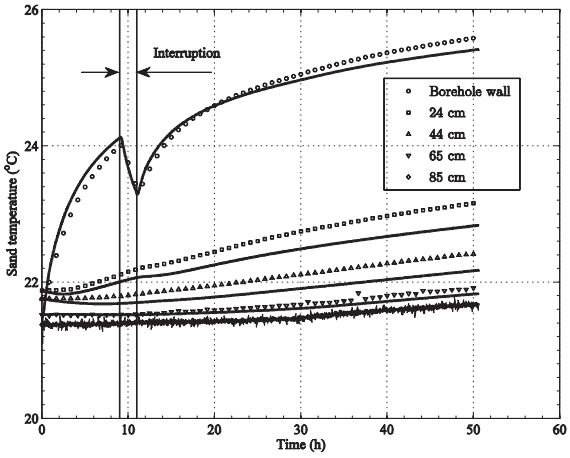

FIGURE 4. Interrupted test - sand temperatures

Similar agreements of numerical simulations and this experiment in terms of accuracy are achieved in Gallero et al. [9]. Deviations can be justified in part because of uncertainties in temperature measurements as well as independent measurements of heat conductivity of grout and wet sand. One of the greatest uncertainty in the input parameters is the estimated heat capacity of wet sand. Beier suggests the value 2 MJ/m^3K in private communication, but also uses the value of 3.2

MJ/m^{3}K in his other work [10]. All models uncertainties can be treated in accordance with new statistical method recently proposed by Fezi and Krane [11] used for modelling of solidification problems.

To the authors' knowledge, comparisons like those shown on 4, for the positions in the sandbox except the borehole wall are not published so far. Noticeable mismatch of numerical solution and experiment on Figure 4 are probably due to relatively high initial temperature differences within the wet sand, compared to the temperature rises caused by heat rejection at the end of the experiment.

4. CONCLUSION

The paper presents a quasi 3D numerical model developed for the simulation of thermal behaviour of single U tube borehole heat exchanger. The proposed model allows the unsteady calculation of temperature of heat transfer fluid as well as temperature distribution in the surrounding grout and soil. The model is experimentally validated against reference data sets for vertical borehole ground heat exchanger models. It is shown that the proposed quasi 3D model successfully reproduce the measured data. More details in forthcoming research will be addressed to the uncertainty in parameters used for model calculations, in order to estimate sensitivity of different model parameters on final results.

REFERENCES

[1] H. Yang, P. Cui and Y. Fang, Vertical-borehole ground-coupled heat pumps: A review of models and systems, *Applied Energy*, 87, 16-27, 2010.

[2] L.R. Ingersoll and H.J. Plass, Theory of the ground pipe source for the heat pump, *ASHVE Transactions*, 54, 339-48, 1948.

[3] H.S. Carslaw and J.C. Jaeger, *Conduction of Heat in Solids*, 2nd edition, Clarendon Press, Oxford, 1959.

[4] E. Tombarević and I. Vušanović, Numerical model of heat flow in a geothermal borehole heat exchanger, ThermaComp2014, June 2-4, 2014, Lake Bled, Slovenia.

[5] V.R. Voller, *Basic Control Volume Finite Element Method for Fluids and Solids*, IISc Research Monographs - Vol. 1, World Scientific, Singapore, 2009.

[6] M.Th. van Genuchten and W.J. Alves, Analytical Solutions of the One-Dimensional Convective-Dissipative Solute Transport Equation, Technical Bulletin Number 1661, United States Department of Agriculture, Washington DC, 1982.

[7] R.A. Beier, M.D. Smith and J.D. Spitler, Reference data sets for vertical borehole ground heat exchanger models and thermal response test analysis, *Geothermics*, 40, 79-85, 2011.

[8] S.P Kavanaugh, Simulation and experimental verification of vertical grouncoupled heat pump systems, Ph.D. dissertation, Oklahoma State University, 1984.

[9] F.J.G. Gallero, I.R. Maestre, P.A. Gomez and J.L.F. Blasquez, Numerical and experimental validation of a new hybrid model for vertical ground heat exchangers, *Energy Conversion and Management*, 103, 511-518, 2015.

[10] R.A. Beier, Transient heat transfer in a U-tube borehole heat exchanger, *Applied Thermal* Engineering, 62, 256-266, 2014.

[11] K. Fezi and M.J.M. Krane, Uncertainty quantification in solidification modelling, *IOP Conference Series: Materials Science and Engineering*, Volume 84, Issue 1, 2015.

PARALLEL SESSION

BOILING AND CONDENSATION

Fourth International Conference on Computational Methods for Thermal Problems
THERMACOMP2016, July 6-8, 2016, Georgia Tech, Atlanta, USA
N. Massarotti, P. Nithiarasu and Y. Joshi (Eds.)

CFD MODELING OF HIGH-SPEED CONDENSATION IN SUPERSONIC NOZZLES, PART II: R134a

Giulio Biferi, Federico Mazzelli
University of Florence, Via di Santa Marta 3, 50139, Florence, Italy
federico.mazzelli@unifi.it

Adrienne B. Little
ARPA-E, Washington, DC

Srinivas Garimella
Georgia Institute of Technology, Atlanta, GA 30032

Yann Bartosiewicz
Université Catholique De Louvain, Louvain-La-Neuve, Belgium

ABSTRACT

The present work performs CFD simulations of condensing flows inside a Laval nozzle. The intended application is the numerical modeling of supersonic ejectors with different working fluids: R718 (water) and R134a. Both these refrigerants are "wet" fluids, and their expansion inside supersonic nozzles can lead to non-equilibrium condensation that alters the pressure and Mach profiles, and induces thermodynamic losses. The numerical analysis of these phenomena requires modeling the microscopic behavior of the fluid where properties must be reproduced with a high level of fidelity. In part I of this work, the accuracy of the "wet steam" model available in the commercial CFD software was evaluated with a comparison with experimental results. In part II, the same wet steam model is adapted to reproduce the properties of R134a. The accuracy of this model is assessed though a comparison with the NIST REFPROPOP database as well as experimental results collected from a small-scale prototype ejector chiller.

Key Words: *CFD, Supersonic Ejectors, Non-equilibrium condensation, Wet Steam model, R134a*

1. INTRODUCTION

The effect of flow condensation on ejector performance has been a topic of discussion among researchers in the field. Many initial studies have speculated that the presence of condensation would be detrimental to ejector system performance. However, subsequent experimental work has found some performance improvement with the insertion of liquid droplets [1]. In an effort to gain further insights into these effects, Little and Garimella [2] investigated the performance of an ejector-based chiller using a wet R134a working fluid. Keeping ejector suction and outlet conditions constant, the degree of superheat at the motive nozzle inlet was changed to observe the effects of condensation on ejector performance. The experimental results in terms of coefficient of performance (COP) are presented in Fig. 1. The changing trend of the COP was attributed to the possible effect of condensation. To confirm this hypothesis, CFD simulations of the ejector primary nozzle are performed in the present study to provide an explanation for the observed changes and to make suggestions for future design improvements.

CFD calculations are carried out on the commercial CFD package ANSYS FLUENT v15. The numerical scheme and computational domain adopted for the computations are summarized in Fig. 2. To perform two-phase simulations, the wet steam model described in part I is adapted to reproduce the properties of R134a. This is done by inserting expressions for the second and third Virial coefficients found in the literature. The vapor specific heats, enthalpy, and entropy are

calculated based on such coefficients following a procedure explained by Young [4]. Moreover, polynomial equations were implemented to reproduce NIST data for the saturation curves, liquid density, liquid specific heats, and vapor and liquid transport properties (viscosity, thermal conductivity).

The accuracy of the proposed Virial equation is validated by comparison with results obtained by implementing the NIST REFPROP libraries built in ANSYS Fluent. This comparison is possible only for the first experimental state point in Fig. 1 because the whole flow within the nozzle is superheated. After validation of the model, CFD calculations are performed for all points shown in Fig. 1, and experimental data for the mass flow rates are compared with numerical results. A comparison is also made with simulations using the ideal gas equation of state.

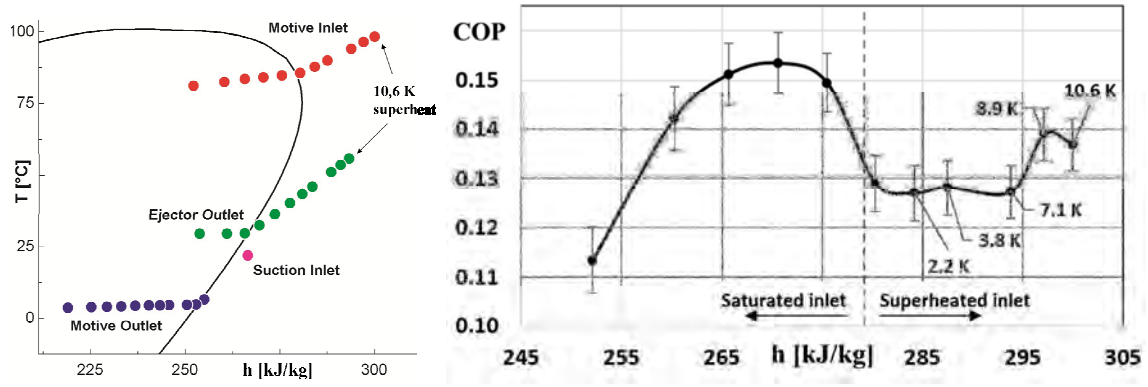

FIGURE 1. Experimental state points plotted on a T-h diagram (left image) and corresponding experimental change in COP (right image);

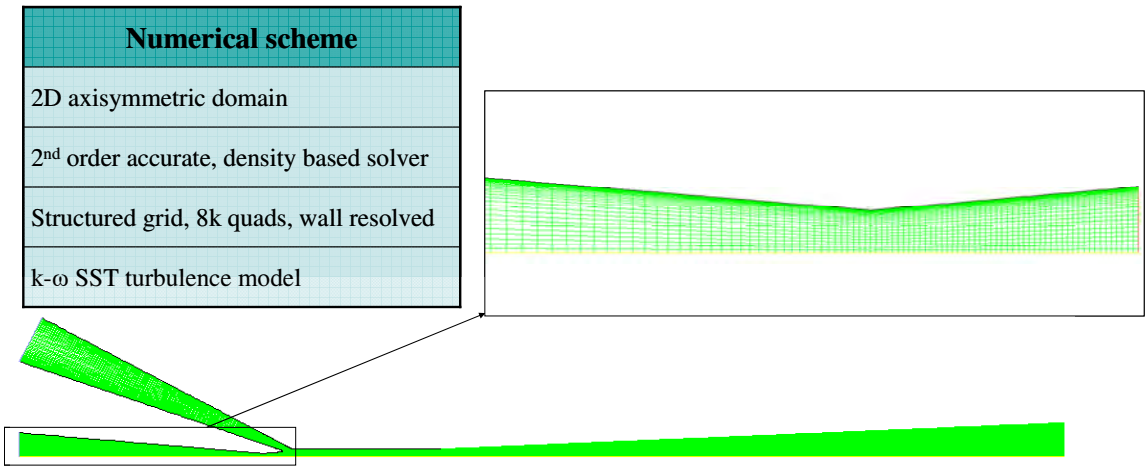

FIGURE 2. Numerical scheme and computational domain adopted for all the simulations

3. RESULTS

Figure 3 shows the trend of pressure, temperature, and velocity profiles along the nozzle axis. As can be seen, there is good agreement between the Virial equation of state and the NIST data. However, the ideal gas equation tends to give incorrect results for both temperature and velocity profiles. It should be noted that all simulations are performed near the critical conditions of the refrigerant (see left image of Figure 1), and poor results from the ideal gas equation should be

expected. By contrast, the good agreement between the Virial and NIST equations is surprising considering that only the first three terms of the series were retained.

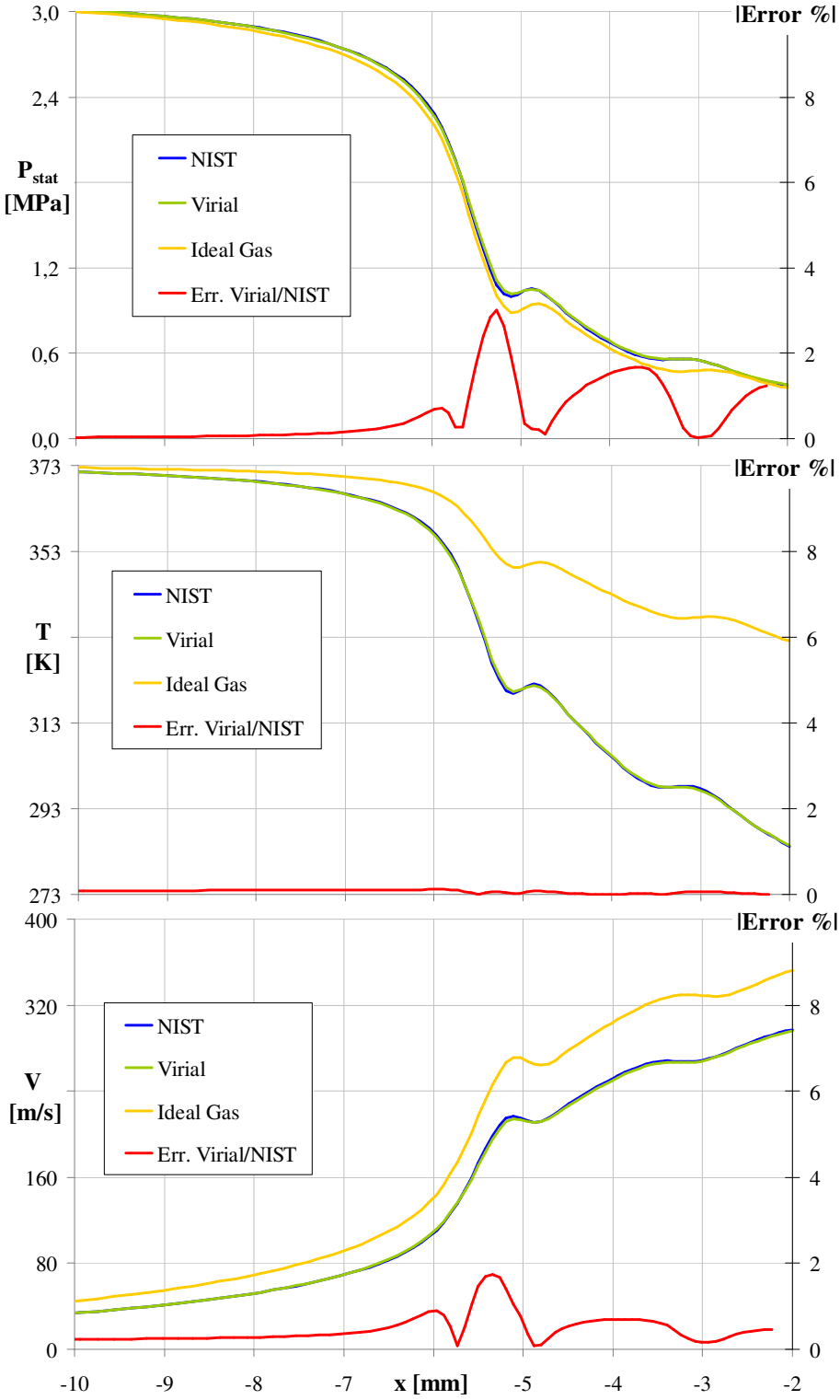

FIGURE 3. Trends of pressure, temperature, and velocity along the nozzle axis. Oscillations near *x=-5.5 mm* are due to a compression wave arising from the sharp edge of the throat (*x=-5.8 mm*).

Figure 4 shows the comparison between numerical and experimental data. Experiments were performed to maintain nearly constant mass flow rate while decreasing inlet enthalpy. This was achieved by accurately controlling the inlet pressure and temperature. Figure 4 shows that the Virial equation of state presents errors that are generally ±5%. This is in line with the differences between the NIST and Virial trend (in particular those near the throat, see Fig. 3). Moreover, the results for the Virial equation show a decreasing trend that begins when the inlet conditions are within the saturation region. This may be attributed to the fact that CFD results assume dry flow at the motive inlet. The wet steam model requires a certain degree of supercooling before condensation occurs, and condensation is always seen downstream of the throat under conditions where it does occur. As a result, condensation has no impact on the CFD mass flow rates. However, in experiments where saturated conditions exist at the inlet, the presence of liquid droplets in the motive flow may induce the onset of condensation before the nozzle throat, thus increasing the average density and mass flow rate passing through the nozzle. The failure of CFD simulation to reproduce this effect may explain the decrease in mass flow rate seen in Fig. 4. Sensitivity analyses are underway to test this hypothesis, in which the number of liquid droplets at the motive inlet are progressively decreased.

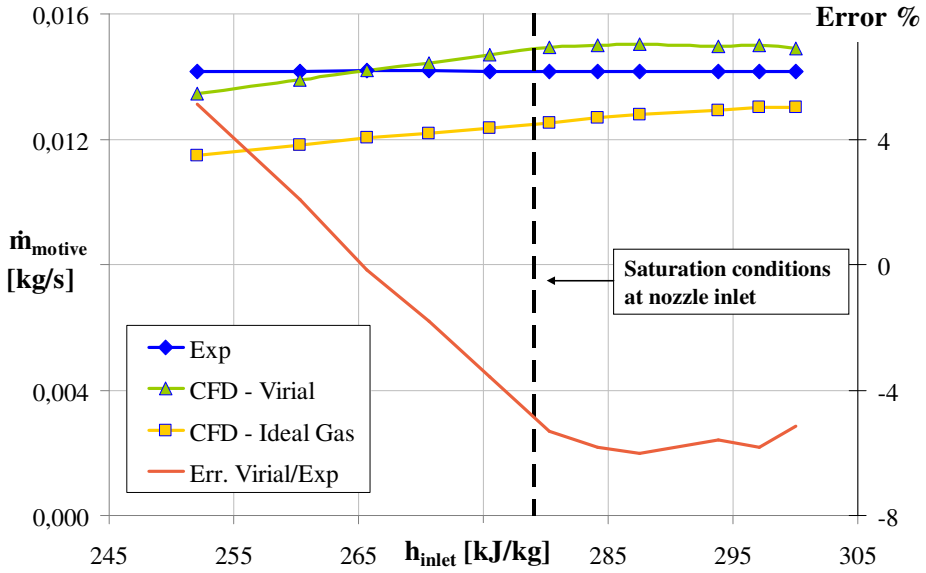

FIGURE 4. Comparison of mass flow rates for various inlet conditions

REFERENCES

[1] A. Hemidi, F. Henry, S. Leclaire, J.-M. Seynhaeve, Y. Bartosiewicz, CFD analysis of a supersonic air ejector. Part I: Experimental validation of single-phase and two-phase operation, *Applied Thermal Engineering* 29, 1523-1531, 2009.

[2] A. Little, S. Garimella, Ejector Refrigeration Systems for Waste Heat Recovery Applications: Effects of Condensation on Performance, *24th IIR International Congress of Refrigeration*, Yokohama, Japan, 2015.

[3] J.B. Young, An equation of state for steam for turbomachinery and other flow calculations, *Trans. ASME, J. Engng Gas Turbines and Power*, 110, 1–7, 1988.

Fourth International Conference on Computational Methods for Thermal Problems
THERMACOMP2016, July 6-8, 2016, Georgia Tech, Atlanta, USA
N. Massarotti, P. Nithiarasu and Y. Joshi (Eds.)

CFD MODELING OF HIGH-SPEED CONDENSATION IN SUPERSONIC NOZZLES, PART I: STEAM

Francesco Giacomelli, Federico Mazzelli, Adriano Milazzo
University of Florence, Via di Santa Marta 3, 50139, Florence, Italy
federico.mazzelli@unifi.it

ABSTRACT

The present work tries to tackle the CFD simulation of condensation inside a De Laval nozzle. The intended application is the numerical modelling of supersonic ejectors working with different fluids: R718 (water) and R134a (Freon). Both these refrigerants are "wet" fluid and their expansion inside supersonic nozzles can lead to non-equilibrium condensation that alter the pressure and Mach profiles and induce thermodynamic losses. The numerical analysis of these phenomena requires modelling the microscopic behaviour of the fluid whose properties must be reproduced with a high level of fidelity. In part I of this work, the accuracy of the wet steam model build in a commercial CFD software is evaluated by comparison with an experimental test case. In part II of the work, the same model is adapted to reproduce the properties of Freon.

Key Words: *CFD, Supersonic Ejectors, Non-equilibrium condensation, Wet-Steam model*

1. INTRODUCTION

In general there are two ways of testing nucleation and droplet growth theories, the first, more appropriate for fundamental physics, involves condensation in cloud and expansion chambers; the second, which is more suited for engineering investigations, deals with supersonic expansions in De Laval nozzles. As shown by many authors [1-2], the converging/diverging nozzle is a remarkable test bench for wet steam model theory. The advantages of this type of experiment are numerous: first of all, the "simplicity" of the steady isentropic flow. This can be easily reproduced by Q1D calculations and allows marking the effects of condensation by simple pressure measurements. Moreover, it has been demonstrated by Stodola [3] that for this type of expansion the effects of dust particles are entirely insignificant: in a typical expansion of steam 10^{15} *nuclei/cm*^{3} are spontaneously formed whereas a maximum credible concentration of dust particles might be 10^8 *nuclei/cm*^{3} [2]. The only drawback of nozzle experiments is that nucleation and droplet growth are tightly coupled and is hard to validate the theories separately (or check any possible correction or improvement that is introduced in the model, see [4]).

Among the many nozzle experiments that can be found in the literature, that of Moore et al. [5] appears to be one of the most popular test case for validating wet steam models [4][6]. In what follows, the ANSYS Fluent wet steam model is tested by comparison with a different, though still classical, nozzle experiment: that of Moses and Stein [7]. In order to test the wet steam model, the numerical results were compared with experimental data for the axial profiles of static pressure and liquid mass fraction. Simulations are performed using the commercial CFD package ANSYS FLUENT v15. The numerical scheme and computational domain adopted for these tests are described in Fig. 1 (more details will be provided in the full paper). The grid dependence was checked by comparison of three different meshes of respectively 6k, 12k and 24k quad elements. The independent solution was found for the intermediate mesh, which was retained for all subsequent calculations.

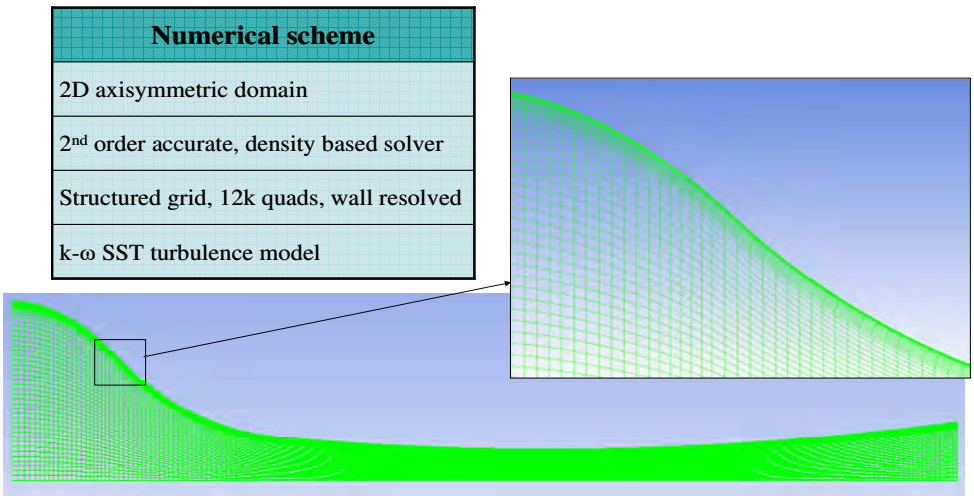

FIGURE 1. Numerical scheme and computational domain for the Moses and Stein [7] test case

3. RESULTS

Although Moses and Stein performed tests for a great number of different conditions [7], only for few experiments did the authors show the axial pressure profiles and liquid mass fraction measurements. In particular, Fig. 2 and 3 show the comparison between numerical and experimental pressure trends along the nozzle axis. As can be seen, for all the tested cases the agreement is excellent, both in terms of condensation starting position and asymptotic pressure trend.

The two sets of curves also show the main features and effects caused by the non-equilibrium condensation. Due to the concentrated heat release, the pressure curves deviate significantly from the hypothetical dry isentropic trend (the dotted curve on each figure). This brings about many undesirable effects. First of all, the non-equilibrium heat transfer between the two phases causes the entropy to increase, thus producing losses and reducing the nozzle efficiency. Secondly, the trends of pressure and Mach number are altered. This has consequences on the correct expansion of the jet exiting the nozzle.

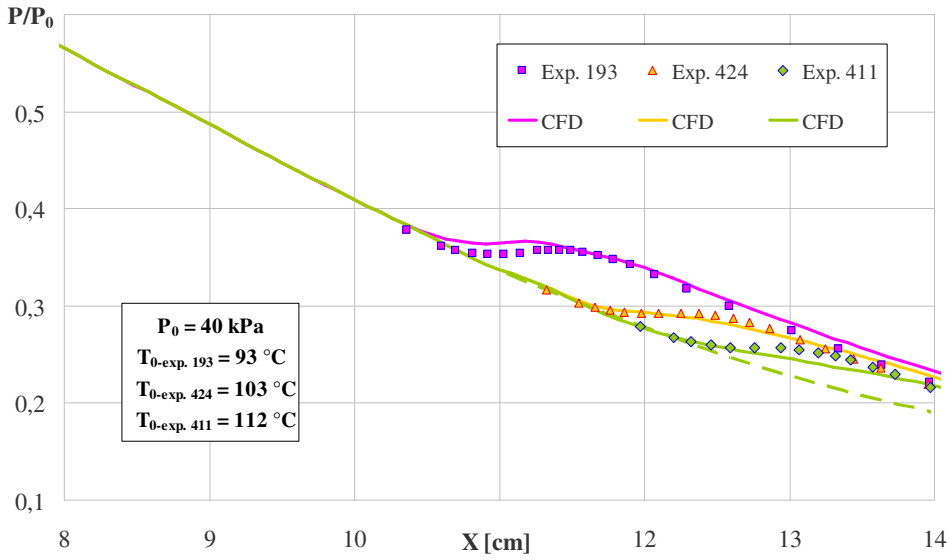

FIGURE 2. Axial trends of static pressure for three experiments with increasing inlet temperature

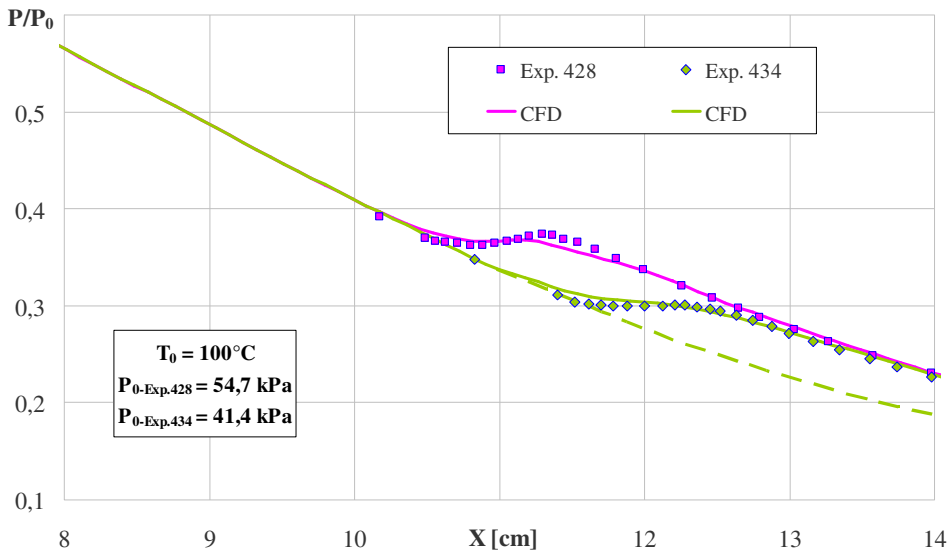

FIGURE 3. Axial trends of static pressure for two experiments with decreasing inlet pressure

The point at which the pressure differs from the isentropic value by 1 percent is commonly referred as the "onset of condensation". In their paper, Moses and Stein report data for this quantity in a wide range of conditions. In order to further test the accuracy of the wet steam model, additional simulations were performed to compare results for the onset of condensation. Tab. 6.1 shows a summary of the comparison. From inspection of the different cases, it can be seen that the difference between the experimental and numerical results is always around 1%. Moreover, a further validation is provided from the comparison of numerical and experimental trend for the liquid mass fraction (i.e. the ratio of the liquid mass to the total mass). Unfortunately, Moses and Stein report only one of such profiles. Nevertheless, even for this one case the agreement between theory and experiments is remarkable, as shown in Fig. 6.4.

Despite the surprisingly good agreement of all presented trends, the same good results may not hold true for supersonic ejector flows, where the presence of liquid droplets induces many unpredictable effects. This will be discussed in the full paper.

	T_0 [°C]	P_0 [Pa]	T_{onset} [°C]	P_{onset} [Pa]	x – Exp. [cm]	x – CFD [cm]	Error in X
Exp. 191	96,1	17812	-15,8	3906	13,26	13,37	*-0,8%*
Exp. 193	92,9	43023	12,8	15252	10,74	10,56	*1,7%*
Exp. 234	97,9	34957	6,4	11012	11,49	11,64	*-1,3%*
Exp. 244	110,4	26944	-6,0	6199	13,18	13,37	*-1,4%*
Exp. 248	108,8	19492	-17,5	3840	14,1	14,2	*-0,7%*
Exp. 252	101,2	40050	9,6	12292	11,5	11,47	*0,3%*

TABLE 1. Comparison of numerical and experimental data for the condensation onset conditions

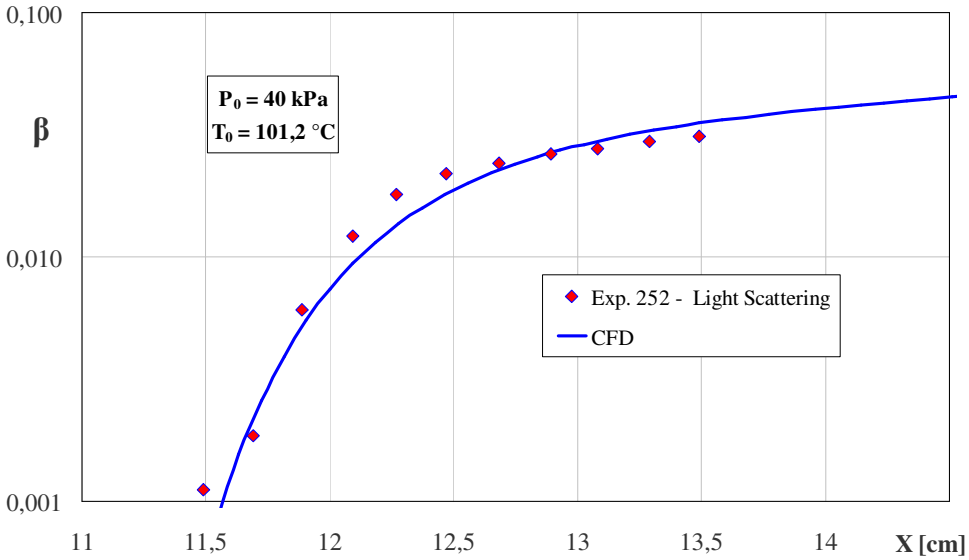

FIGURE 1. Axial trends of liquid mass fraction, comparison of experimental and numerical trends

4. CONCLUSIONS

The present work deals with CFD simulation of condensation inside a supersonic nozzle operating with steam. The intended application is the numerical modelling of supersonic ejectors. The accuracy of the wet steam model build in a commercial CFD package are evaluated by comparison with an experimental test case. The comparison results in remarkable agreement both in terms of pressure and liquid mass fraction profiles. However, the same good results may not be found in the simulation of a complete supersonic ejector, due to the possible alterations connected with the presence of liquid droplets.

REFERENCES

[1] P.P. Wegener, L.M. Mack, Condensation in supersonic and hypersonic wind tunnels, *in: Advances in Applied Mechanics,* Academic Press Inc., New York, NY, 1958.

[2] P.G. Hill, Condensation of water vapour during supersonic expansion in nozzles, *Journal of Fluid Mechanics*, 25, 593–620, 1966.

[3] A. Stodola, Steam and Gas Turbines, *New York: McGraw-Hill,* 1927

[4] F. Bakhtar, J.B. Young, A.J. White, D.A. Simpson, Classical Nucleation Theory and Its Application to Condensing Steam Flow Calculations, *Proceedings of the Institution of Mechanical Engineers, Part C: Journal of Mechanical Engineering Science,* 1315-1333, 2005.

[5] M.J. Moore, P.T. Walters, R.I. Crane, B.J. Davidson, Predicting the fog drop size in wet steam turbines, *In Wet steam 4,* 101–109, 1973.

[6] A.G. Gerber, Two-Phase Eulerian/Lagrangian Model for Nucleating Steam Flow, *Journal of Fluids Engineering*, Vol. 124, 465-475, 2002.

[7] C.A. Moses, G.D. Stein, On the Growth of Steam Droplets Formed in a Laval Nozzle Using Both Static Pressure and Light Scattering Measurements, *Journal of Fluids Engineering*, 100, 311–321, 1978

THERMACOMP2016, July 6-8, 2016, Georgia Tech, Atlanta, USA
N. Massarotti, P. Nithiarasu and Y. Joshi (Eds.)

SATURATED FILM BOILING IN REDUCED GRAVITY WITH APPLIED ELECTRIC FIELD

Vinod Pandey, Gautam Biswas and Amaresh Dalal
Department of Mechanical Engineering, Indian Institute of Technology, Guwahati 781039, India,
p.vinod@iitg.ernet.in, gtm@iitg.ernet.in, amaresh@iitg.ernet.in

ABSTRACT

In this paper, the influence of gravity on the flow dynamics during film boiling is presented through numerical simulations. The dominant effect of gravity in normal terrestrial conditions is found to be replaced by the electrohydrodynamic (EHD) forces due to the applied electric field in reduced gravity conditions. The increase in characteristic wavelength of disturbance due to low gravity impedes the rate of bubble growth and results in lateral merging of departing bubbles and significant increase in bubble volume. Combined level-set and volume of fluid (CLSVOF) method is incorporated for liquid-vapour interface capturing.

Key Words: *Film Boiling, EHD , CLSVOF .*

1. INTRODUCTION

Phase change phenomena have been considered as the most effective means of heat exchange in the present technological scenario. Boiling and condensation are thus studied to increase the overall efficiency of the heat transfer equipment in power generation, cryogenic storage system, air conditioning and other such industrial applications. In high temperature applications, the heating surface gets covered by a vapour layer and bubbles evolve from the liquid-vapour interface which facilitates the heat exchange from the vapour to the liquid phase. This particular physical condition is termed as film boiling which is strongly influenced and controlled by the presence of buoyancy force due to gravity. In normal terrestrial conditions on earth, the acceleration due to gravity is the most dominant factor that controls vapour flow physics in boiling. Other forces like capillary forces due to surface tension are often considered to have negligible effect due to the predominance of buoyancy force. The most dominant wavelength of disturbance in film boiling as defined by Zuber's [1] hydrodynamic theory is inversely proportional to the square root of gravity. Hence, in reduced gravity condition, the separation distance of detaching bubbles is much larger than in normal gravity. Also, the buoyancy force is reduced significantly and the counter force of surface tension which tends to keep the bubbles attached to the vapour volume becomes much more relevant [2]. Although it has been observed that the reduced gravity does not influence the nucleate boiling regime, it still has a significant effect in the transition and film boiling regime and can reduce the heat transfer rate up to 50% [3].

Di Marco and Grassi [4] observed the increased instability at the liquid-vapour interface with an applied electric field. At low intensity of the electric field, bubble growth and departure are sensitive to the acceleration due to gravity while at high enough intensities of the electric field the boiling is found to be almost unaffected with changing gravity. Increase in bubble size and horizontal spacing were also observed at reduced gravity conditions. The present work focuses on the numerical analysis of the changes in bubble growth mechanism in reduced gravity conditions under the influence of an applied electric field which tends to stimulate the bubble growth [5, 6], hindered by the reduced buoyancy force. The CLSVOF approach [7] is utilised in conjunction with the electric field model by Tomar et al. [8].

2. NUMERICAL FORMULATION

A single set of governing equations is utilized to simulate the fluid flow in boiling, occurring as a result of energy transfer from the vapour to the liquid region across the interface. These are

$$\nabla \cdot \mathbf{U} = 0 \tag{1}$$

$$\rho(\mathbf{U}_t + \nabla \cdot \mathbf{U}\mathbf{U}) = -\nabla p + \rho \mathbf{g} + \nabla \cdot (2\mu \mathbf{D}_v) + \mathbf{f}_{sv} + \mathbf{f}_v^E \tag{2}$$

$$\frac{\partial T}{\partial t} + \mathbf{U} \cdot \nabla T = \frac{k_g}{\rho c} \nabla^2 T \tag{3}$$

where $\mathbf{D}_v = 1/2\left\{(\nabla \mathbf{U}) + (\nabla \mathbf{U})^T\right\}$ is the deformation tensor and $\mathbf{f}_{sv} = \sigma \kappa \hat{\mathbf{n}} \delta$ is the surface tension volume force [9] which is non-zero only at the liquid-vapour interface. Here, $\hat{\mathbf{n}}$ is the unit normal vector at the interface, κ is the curvature, σ is the surface tension coefficient and δ is the surface Dirac delta function. The density and viscosity are defined on the basis of the smoothed void fraction field $\widetilde{F} = H(\phi)$ where $H(\phi)$ is the smoothed Heaviside function based on the level-set function which is assigned positive value on one side of the interface and negative on the other. At the interface, the mass conservation equation [Eq. (1)] also involves an additional source term due to the phase change across the liquid-vapour boundary. The temperature at the interface and the liquid region is considered to be invariable at the saturation temperature. The void fraction and level-set function are advected with velocity following the advection equations along the *x* and *y* directions [10]. The medium considered in the present simulations is saturated water near its critical pressure. A perfect dielectric without any free charge is considered. Under the electrostatic approximation, the curl of the electric field is zero i.e. $\nabla \times \mathbf{E} = 0$. This follows $\mathbf{E} = \nabla \psi$ which finally results in $\nabla \cdot (\varepsilon \varepsilon_0 \nabla \psi) = 0$, where ψ is the electric potential function. The term $\mathbf{f}_v^E = -\frac{1}{2}\mathbf{E}^2 \nabla \varepsilon_0 \varepsilon$ in the momentum equation [Eq. (2)] is the volumetric electric force term.

3. RESULTS AND DISCUSSIONS

To analyze the variation in bubble release pattern and its shape under normal and reduced gravity conditions, numerical simulations have been performed with and without the application of an electric field. The properties of the medium are taken at near critical pressure as mentioned in Pandey et al. [6]. Simulation is performed for a $3\lambda_B \times \lambda_B$ domain where λ_B is the Berenson's characteristic wavelength [6] corresponding to the normal gravity condition. It can be observed from Fig. 1(a) that the horizontal spacing between bubbles is increased significantly in reduced gravity conditions and the time taken for the formation of first set of bubbles is much more as compared in normal gravity conditions due to the reduced buoyancy forces. With the application of an electric field, the bubble growth rate again increases and the number of bubble formation sites also increases. Figure (1b) shows the variation of the height of the apex of the vapour bubble with time for both normal and reduced gravity conditions in the simulation of single bubble growth. It can be clearly observed that the maximum height of the bubble in reduced gravity is more than three times that of the one in normal gravity. The number of bubbles formed is five for normal gravity as compared to the single bubble formed in reduced gravity in the same time period. The rate of interface growth before bulging of the bubble starts is very low as compared to the growth rate after neck formation.

The change in bubble morphology in reduced gravity can be more clearly observed from Fig. (3), which shows the release of first set of bubbles in reduced gravity with an applied electric field of strength 2×10^5 V/m . As compared to a distinct bubble release pattern in normal gravity [Fig. (2)], the departing bubbles seem to interact with each other more vigorously resulting in their merging and formation of larger bubbles and vapour packets. The size of bubbles is comparatively very large with respect to that of the bubbles under normal gravity. The lateral merging is due to the increased dominance of capillary forces as compared to the buoyancy force.

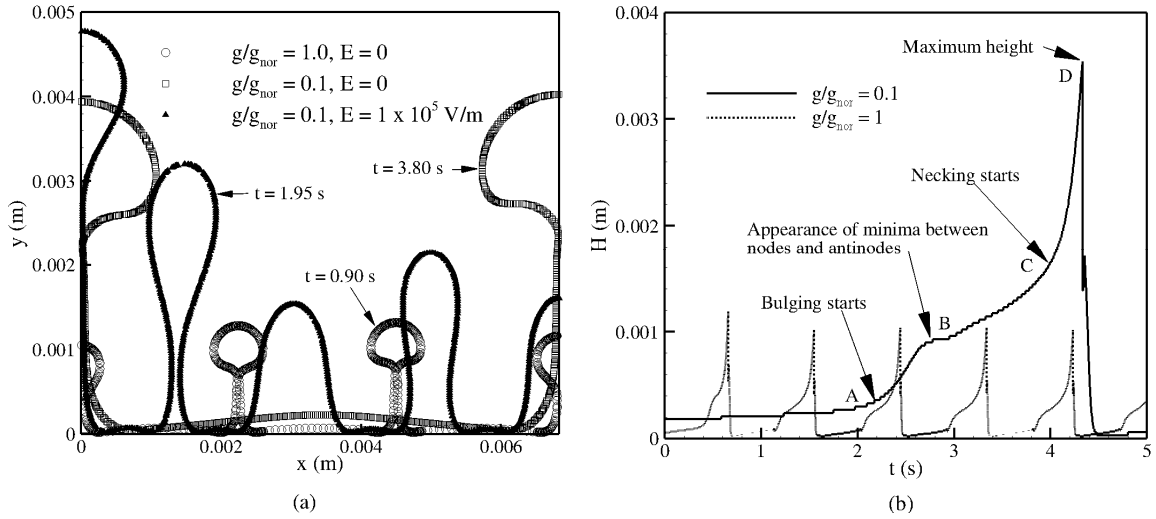

FIGURE 1. (a) Comparison of bubble morphology at reduced gravity (with and without electric field) with normal gravity for 18 K wall superheat. (b) Variation of apex height of bubble with time at normal and reduced gravity conditions.

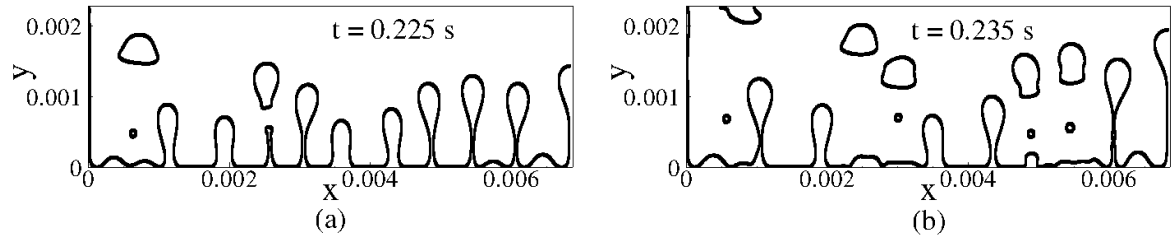

FIGURE 2. First set of bubble release in normal gravity (g_{nor}) at two different instants of time with an applied electric field of intensity 2×10^5 V/m .

4. CONCLUSIONS

The dynamics of bubble release is found to be significantly dependent on the acceleration due to gravity. Rate of bubble formation becomes much slower and the size of the bubble i.e. the bubble diameter and height reduces in reduced gravity condition. In case of multiple bubble formation in a larger domain with applied electric field, the bubbles are found to merge in the lateral direction leading to larger sizes of the released bubbles. Electric forces enhance the bubble growth rate due to the increased instability at the interface.

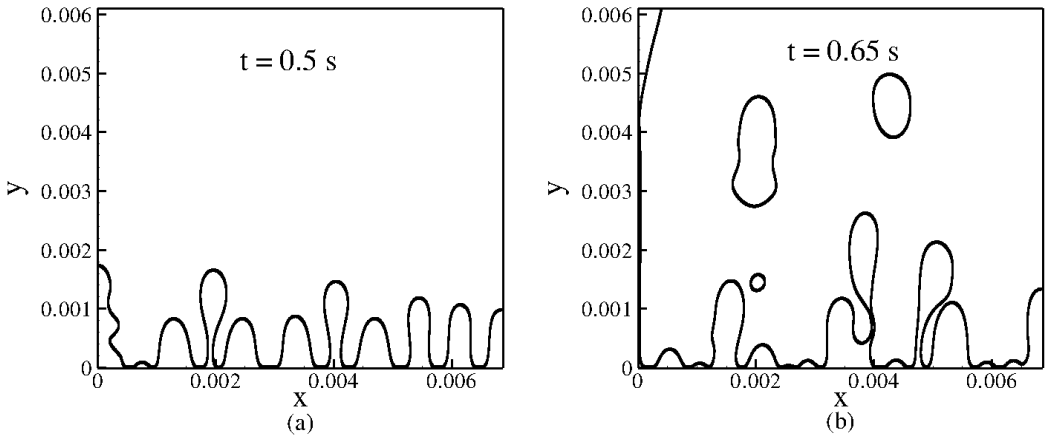

FIGURE 3. First set of bubble release in reduced gravity ($0.1g_{nor}$) at two different instants of time with an applied electric field of intensity 2×10^5 V/m .

REFERENCES

[1] N. Zuber, Hydrodynamic aspects of boiling heat transfer, *Ph.D. thesis, University of California, Los Angeles,* 1959.

[2] J. Straub, The role of surface tension for two-phase heat and mass transfer in the absence of gravity, *Experimental Thermal and Fluid Science*, 9, 253-273, 1994.

[3] J. Straub, Microscale boiling heat transfer under 0*g* and 1*g* conditions, *Int. J. Therm. Sci.,* 39, 490-497, 2000.

[4] P. D. Marco and W. Grassi, N. Massarotti, Motivation and results of a long-term research on pool boiling heat transfer in low gravity, *Int. J. Therm. Sci*., 41, 567–585, 2002.

[5] G. Tomar,, G. Biswas, A. Sharma, and S.W.J. Welch, Influence of electric field on saturated film boiling, *Phys. Fluids*, 21, 032107, 2009.

[6] V. Pandey, A. Dalal and G. Biswas, Bubble formation in film boiling including electro-hydrodynamic forces*, IUTAM Symposium on Multiphase flows with phase change: challenges and opportunities, Procedia IUTAM*, 15, 86-94, 2014.

[7] D. Gerlach, G. Tomar, G. Biswas and F. Durst, Comparison of volume-of-fluid methods for surface tension-dominant two-phase flows., *Int. J. Heat Mass Transf.,* 49, 740-754, 2006.

[8] G. Tomar, G. Gerlach, G. Biswas, N. Alleborn, A. Sharma, F. Durst, S. W. J. Welch and A. Delgado, Two-phase electrohydrodynamic simulations using a volume-of-fluid approach, *J. Comput. Phys.,* 227, 1267–1285, 2007.

[9] J. U. Brackbill, D. B. Kothe, and C. Zemach, A continuum method for modeling surface tension, *J. Comput. Phys.* 100, 335–354, 1992.

[10] E. G. Puckett, A. S. Almgren, J. B. Bell, D. L. Marcus, and W. J. Rider, A high order projection method for tracking fluid interfaces in variable density incompressible flows, *J. Comput. Phys.*, 130, 269-282, 1997.

Fourth International Conference on Computational Methods for Thermal Problems
THERMACOMP2016, July 6-8, 2016, Georgia Tech, Atlanta, USA
N. Massarotti, P. Nithiarasu and Y. Joshi (Eds.)

NUCLEATE BOILING PERFORMANCE EVALUATION OF DIFFERENT CAVITIES AT MESOSCALE LEVEL

Yutong Mu[a], Li Chen[a,b], Qinjun Kang[b], Ya-Ling He[a] and Wen-Quan Tao*[a]

Key Laboratory of Thermo-Fluid Science and Engineering, Ministry of Education, Xi'an Jiaotong University, 710049, P.R. China
Computational Earth Science Group, Los Alamos National Laboratory, Los Alamos, NM, USA
Corresponding email address: wqtao@mail.xjtu.edu.cn

ABSTRACT

The cavities behaviour for nucleation on roughened surface is numerically studied for the entire ebullition cycle based on a phase-change lattice Boltzmann method without introducing any artificial disturbances. The bubble departure diameter, departure frequency (BRF) and total boiling heat flux of an ebullition cycle are explored. It is demonstrated that cavity with circular groove shows the best performance for NBHT in terms of the averaged heat flux and BRF. The departure of the first bubble in triangular groove is the fastest while that in re-entrant groove is the slowest.

Key Words: *lattice Boltzmann method, Nucleate boiling, Cavity groove, Bubble dynamics.*

1. INTRODUCTION

Nucleate boiling heat transfer (NBHT) is one of the most challenging problems in convective heat transfer. This is because from physical point of view phase change is a nano-scale phenomenon, and from engineering point of view the influencing factors are so many that until 1990ties we still did not know many things about NBHT even at phenomenological level [1]. It is now widely recognized that the small-cavities on the surfaces can easily become the nucleation sites and according to this basic idea, extensive studies have been performed to enhance NBHT by changing the surface roughness. However, the details of boiling in such surfaces are still not understood completely. For example, we even cannot answer such a simple question as what kind of cavity has the best performance for NBHT. In the present study, we used the Shan-Chen pseudo-potential model together with an improved phase-change model [2] to simulate the nucleate boiling on roughened surfaces. In our study no any assumptions of existing vapor embryo and no an artificial disturbance of temperature or density are needed.

2. MAIN BODY

In the LB model, the motion of the fluid described by a set of density distribution functions is considered as a collective behavior of pseudo-particles on a mesoscopic level.

$$f_i(\mathbf{x}+c\,\mathbf{e}_i\,\Delta t, t+\Delta t)-f_i(\mathbf{x},t)=-\frac{1}{\tau_f}\left(f_i(\mathbf{x},t)-f_i^{eq}(\mathbf{x},t)\right)+F_i \tag{1}$$

where $f_i(\mathbf{x}, t)$ is the density distribution function at the lattice site $\mathbf{x}$ and time t, τ_f is the dimensionless relaxation time, $c=\Delta\mathbf{x}/\Delta t$ is the lattice speed with $\Delta\mathbf{x}$ and Δt as the lattice spacing and time step, respectively. A non-ideal fluid with the P-R equation of state (EOS) is considered

$$p=\frac{\rho RT}{1-b\rho}-\frac{a\alpha(T)\rho^2}{1+2b\rho-b^2\rho^2} \tag{2}$$

$$\alpha(T)=\left[1+\left(0.37464+1.54226\omega-0.26992\omega^2\right)\times\left(1-\sqrt{T/Tc}\right)\right]^2 \tag{3}$$

with $a = 0.45724(RT_c)^2/p_c$, $b = 0.1873RT_c/p_c$. In order to simulate the nucleation process of water, we choose G_f = -1, a = 3/49, b = 2/21, R = 1, ρ_c=2.541858, T_c=0.109383 and ω=0.344. The entropy balance equation neglecting the viscous dissipation is given by

$$\frac{\partial T}{\partial t}+\nabla\cdot(\mathbf{u}_r T)=\nabla(\alpha\nabla T)+T\left[1-\frac{1}{\rho c_v}\left(\frac{\partial p}{\partial T}\right)_\rho\right]\nabla\cdot\mathbf{u}_r \tag{4}$$

And the above equation is solved with the thermal LB model

$$h_i(\mathbf{x}+c\,\mathbf{e}_i\,\Delta t,t+\Delta t)-h_i(\mathbf{x},t)=-\frac{1}{\tau_T}\left(h_i(\mathbf{x},t)-h_i^{eq}(\mathbf{x},t)\right)+\omega_i\varphi \tag{5}$$

where h_i ($\mathbf{x}$, t) is the temperature distribution function, φ is the source term. It is worth noting that the above described numerical methods are basically the same as that adopted in [2]，where an artificial interruption should be added to start the nucleation; However, in our later presentation it will be shown that the above method can be used to predict the nucleation of a roughened surface without any artificial interruptions. In some sense the roughened surface can be regarded a kind of interruption, but it is the problem-inherent interruption, not artificially added. Hence the present study is physically more meaningful.

3. RESULTS

Bubble departure diameter D_d and departure frequency (BRF) f are two critical characteristic parameters during the nucleation process. Fritz [3] derived a relation between the departure diameter and gravity:

$$D_d \sim \left[\frac{\sigma}{g(\rho_l-\rho_g)}\right]^{0.5} \tag{6}$$

Figure 1 presents the simulation results of the effect of bubble departure diameter under various gravity accelerations. It is shown that the exponent of the fitting curve for our simulation results is -0.4875, which agrees quite well with the analytical result given by Fritz [3]. Figure 2 shows the simulated BRF under various gravity accelerations. The exponent of the fitting curve is -1.029, which agrees extremely well with the experimental work with the exponent of -1.05 [4].

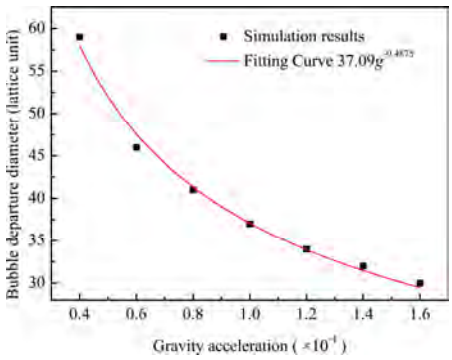

FIGURE 1. Bubble departure diameter vs. gravity.

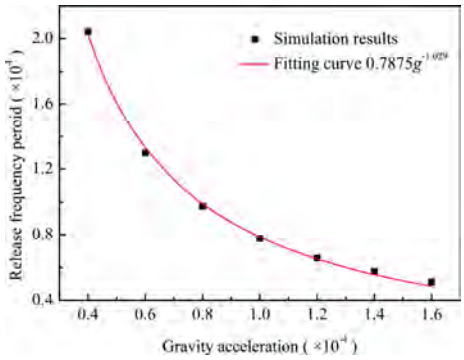

FIGURE 2. Bubble departure frequency vs. gravity.

Figure 3 shows the bubble formation, growth and departure process in three different cavity grooves. With the departure of the first bubble concerned, the bubble in the triangular

groove departs at t=15000Δt, which is the fastest among all the grooves in the present study. This might be caused by the fact that the triangular groove is not effective to trap vapor. The vapor necks in other grooves are larger than that in triangular one. However, the bubble in the re-entrant groove (Fig. 3(b)) departs at t=40000Δt, which is the slowest. This is mainly because before the departure the vapor should first fully fills the groove and then continually grows to a certain size at the top surface of the solid. When the first bubble detaches from the roughened surfaces, the remained vapor can be served as the nucleation site for the next bubble. It is also observed that a large amount of vapor is trapped in the circular and rectangular grooves, while only a small amount of vapor exists in the re-entrant and triangular groove. Therefore, even though among all the grooves the first bubble is firstly released in the triangular groove, the BRF of the triangular cavity is still low. The BRF for circular, re-entrant, triangular and rectangular grooves are 5650, 15300, 7400 and 7485 Δt, respectively. Therefore, circular groove can be used to enhance the NBHT.

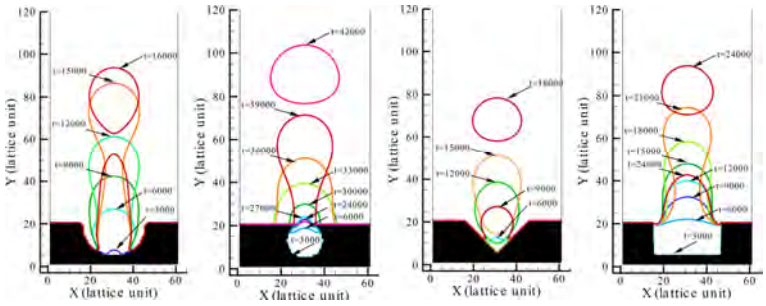

(a) (b) (c) (d)

FIGURE 3. Bubble nucleation process in different cavity grooves

The density and temperature distributions at t=30000Δt of four different cavity grooves are illustrated in Figure 4. One can see that the vapor temperature is lower than its surrounding because during the evaporation process heat flux goes from the surrounding to the bubble. In the cavity corners of the rectangular groove, the temperature is the lowest, which is also the three phase contact line. It can also be found that the re-entrant and rectangular grooves are fully occupied by the remained vapor.

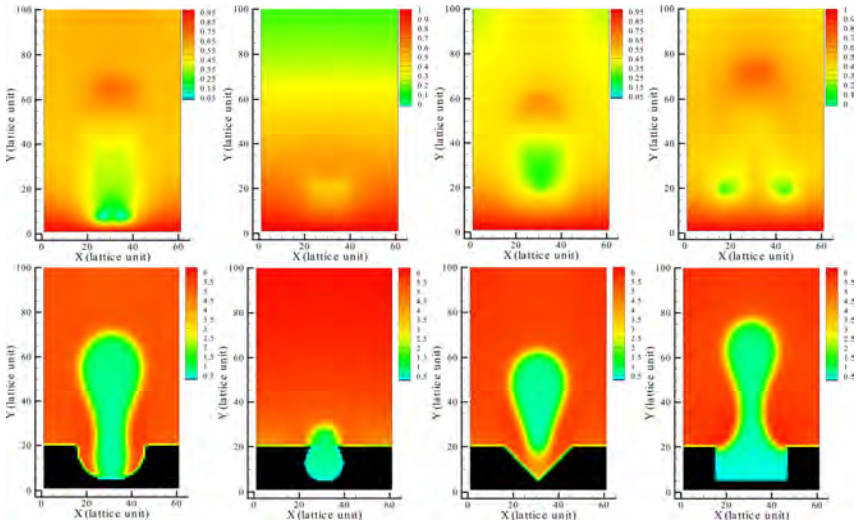

FIGURE 4. Snapshot of the non-dimensionless temperature and density distribution at 30000 Δt

The dimensionless total heat transfer rate of different cavity grooves are shown in Figure 5. The figure shows that the circular groove performs the best for NBHT. This result agrees well with reference [5]. The average dimensionless total heat fluxes during one period of the circular, re-entrant, triangular and rectangular grooves are 0.53276, 0.18809, 0.26604 and 0.29678, respectively. The detailed dimensionless local heat flux distribution, when the dimensionless total heat flux is at its maximum and minimum value, is shown in Figure 6. The highest local heat flux for the circular, re-entrant and triangular grooves lies at the middle part of the bottom, while the highest local heat flux for the rectangular groove lies under the two corners of the cavity. Generally, the local heat flux distributions for the rectangular and triangular grooves are much flatter compared with the other two grooves, this may be contributed to their specified structures.

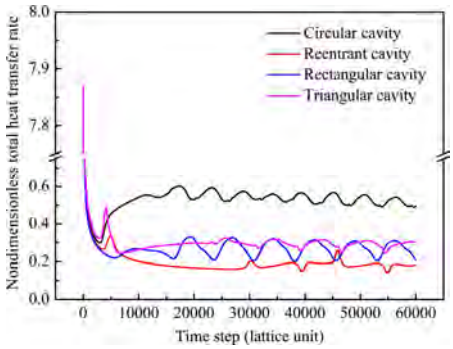

FIGURE 5. Total heat transfer rate vs. time.

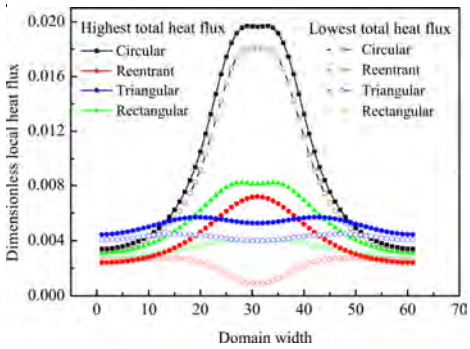

FIGURE 6. Local heat flux distribution in one period.

4. CONCLUSIONS

In this study, a phase-change lattice Boltzmann method is adopted and applied to the study of the nucleation boiling on surfaces with cavities. Without introducing any artificial interruptions, the actual nucleation process on roughened surfaces can be predicted by the adopted LBM. The main conclusions are as follows:

1. The generation of the first bubble in triangular groove is the fastest, while in re-entrant groove the slowest.

2. The surface with circular groove shows the best boiling heat transfer performance.

3. The BRF of the circular groove is the highest among all four studied grooves, and its local heat flux is also the highest in the most range of the surface; the local heat flux distributions of the re-entrant, rectangular and triangular grooves are much flatter.

REFERENCES

[1] J.H. Lienhard, Things we don't know about boiling heat transfer: 1988, *International Communications in Heat and Mass Transfer*, 15(4), 401-28, 1988.

[2] S. Gong, P. Cheng, A lattice Boltzmann method for simulation of liquid-vapor phase-change heat transfer, *International Journal of Heat and Mass Transfer*, 55(17-18), 4923-27, 2012.

[3] W. Fritz, Maximum volume of vapor bubbles, *Physik Zeitschr*, 36, 379-384, 1935.

[4] D. M. Qiu, V. K. Dhir, D. Chao, et al., Single-bubble dynamics during pool boiling under low gravity conditions[J]. *Journal of thermophysics and heat transfer*, 16(3), 336-45, 2002.

[5] C. D. Ghiu, Y.K. Joshi, Boiling performance of single-layered enhanced structures, *ASME Journal of Heat Transfer*, 127(7), 675-83, 2005.

PARALLEL SESSION

POWER PLANTS AND EQUIPMENT

Fourth International Conference on Computational Methods for Thermal Problems
THERMACOMP2016, July 6-8, 2016, Georgia Tech, Atlanta, USA
N. Massarotti, P. Nithiarasu and Y. Joshi (Eds.)

Finite volume model of a flat plate cogenerative collector: thermodynamic and experimental analysis

Francesco Calise
Department of Industrial Engineering, University of Naples Federico II P.le Tecchio 80, 80125, Naples, Italy, frcalise@unina.it

Rafal Damian Figaj, Laura Vanoli
Department of Engineering, University of Naples Parthenope, Centro Direzionale IS.C4, 80143, Naples, Italy, rafal.figaj@uniparthenope.it, laura.vanoli@uniparthenope.it

ABSTRACT

This paper presents a one-dimensional finite-volume model of an unglazed photovoltaic/thermal solar collector. The final goal of the model is an integration within an overall dynamic simulation environment. The type of collector consists of a conventional solar thermal device with a PV film covering the absorber. In particular, the collector includes a roll bond heat exchanger and the absorber encapsulates the PV film. The unglazed collector is not equipped with back insulation. The system was discretized along the longitudinal direction of the cogenerative collector. Mass and energy balances are considered for each finite-volume element of the discretized computational domain. The model allows one to evaluate both thermodynamic and electrical parameters for each element of the domain. The collector geometry and materials parameters are taken from a commercially available device. An experimental investigation is performed in order to validate the proposed model. Finally, a sensitivity analysis is also performed in order to evaluate the effect of the variation of the main design/environmental parameters on the energetic performance of the cogenerative collector.

Key Words: *PVT collector, Finite Volume, Experimental validation.*

1. INTRODUCTION

Over the last decades, the development and the application of renewable energy applications have become more and more important topics for designers and researchers. In this framework, solar energy is one of the most sustainable renewable energy sources. Traditionally, solar thermal collectors and photovoltaic panels are used to produce separately thermal and electrical energy, respectively. On the contrary, hybrid photovoltaic/thermal collector (PVT) technology allows one to produce simultaneously thermal and electrical energy using the available solar radiation [1]. Such configuration has the advantages of the production of thermal energy and the cooling of the photovoltaic module [2]. The application of hybrid PVT collectors leads to an increase of energy output per unit of collector area with respect to the traditional thermal or photovoltaic panels. In order to determine the performance of a cogenerative collector, a detailed analysis must be done. Although numerical and experimental investigations of PVT collectors have been widely discussed in scientific literature [3], there is a scarce focus on the investigation of PVT configurations without cover and insulation. For such reason, this paper presents a simplified finite-volume model of a commercially available photovoltaic/thermal solar collector. The final scope of this model is to obtain a fast and reliable simulation model to be integrated in complex dynamic simulation environments (e.g., TRNSYS, ENERGY Plus, etc.). In particular, a “Janus” PVT panel, manufactured by the Italian Company AV Project, has been considered (Figure 1) in order to perform the analysis. It is a commercial simple unglazed PVT collector, suitable for low temperature heating in summer season. The developed finite volume model has been validated against experimental data collected by an outdoor installation.

2. COLLECTOR DESCRIPTION AND NUMERICAL MODEL

The collector adopted was a roll bond type with the PV panel encapsulated into the absorber (Figure 1). The photovoltaic module was a high efficiency polycrystalline silicon panel and the aluminium absorber was equipped with a separated double circuit in order to distribute the cooling fluid across the absorber channels. The photovoltaic module and the absorber were bonded with a butyl resin. The collector configuration does not include any glass cover or back and insulation. In fact, the goal of this product is to obtain a cheap PVT collector suitable for low temperature heating in hot climates. The operating fluid, flowing inside the channels of the absorber, was water. The dimensions of the collector were 1644 mm of height and 992 mm of width. Moreover, the useful area of the photovoltaic module was 1.44 m^2 and the absorber plate was equipped with 48 channels. The shape of each channel was trapezoidal, with the lengths of the two parallel sides of 10 and 6.6 mm, and a height of 1.6 mm. The collector configuration allows one to operate the unit at a maximum operating flowrate of 100 l/h.

FIGURE 1. JANUS PVT COLLECTOR

The objective of this paper is to develop and validate a simulation model of the PVT collector under investigation. In particular, a 1-dimensional model has been developed (Figure 2).

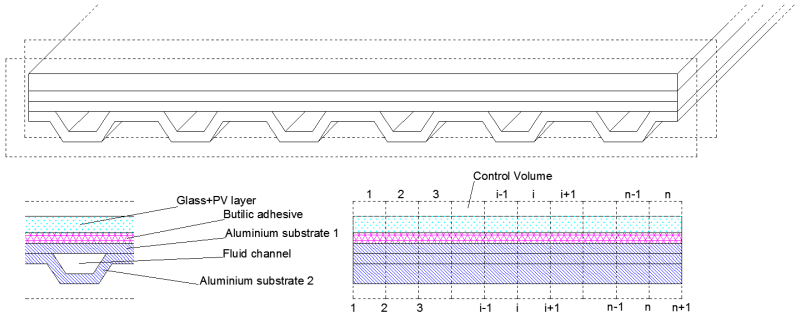

FIGURE 2. DISCRETIZATION OF THE COMPUTATIONAL DOMAIN

The model calculates the thermodynamic parameters and thermal and electrical powers along the direction of the heat transfer fluid passing through the PVT collector. The computational domain has been discretized along the longitudinal axis. Mass and energy balance equations have been implemented for each computational domain element using Engineering Equation Solver (EES) software. The collector was divided in five parts: glass cover/PV layer, butyl adhesive, aluminium substrate, fluid channels and roll bond aluminium substrate. The collector thermodynamic equilibrium and state conditions have been considered. Moreover, in the energy balances of each element kinetic and gravitational terms have been considered negligible. In addition to such assumptions, a uniform distribution and absorption of the solar radiation on the photovoltaic module surface have been assumed. The collector was discretized along its longitudinal axis in n elementary

slices, thus, n+1 nodes of the computational domain have been considered. For such domain, the inlet and outlet thermodynamic conditions for slice 1 and n, respectively, were the boundary conditions used for the simulation of the PVT collector. Furthermore, the temperature of the solid materials of each domain element (cover glass/PVT cell, bonding layer and aluminium absorber) was assumed constant. On the contrary, a linear variation of the fluid temperature in each element was assumed. In order to reduce the error of the linearization of the temperature profile, a number of 20 elements has been adopted during the simulation. Finally, the model parameters have been accurately selected in order simulate the collector surrounding environment.

3. RESULTS: EXPERIMENTAL INVESTIGATION AND MODEL VALIDATION

The PVT system installation consisted of a closed circuit loop with a tank, circulating pump and 4 cogenerative collectors (Figure 3).

FIGURE 3: SYSTEM SET-UP

The performed hydraulic configuration allowed a uniform fluid flow distribution among all the collectors. An experimental investigation of the PVT collector has been performed (Figure 4) with a pyrometer, Pt 100 thermoresistances (for duct and surface measurement) and an electromagnetic flowmeter.

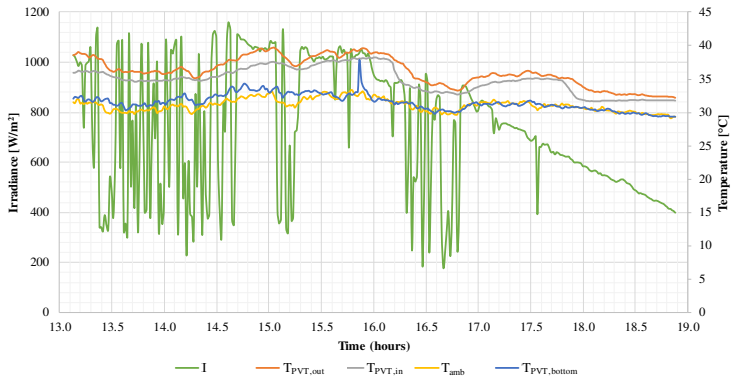

FIGURE 4: EXPERIMENTAL DATA

The same inlet/inlet outlet temperature of each collector is assumed due to the length of piping configuration. The measurements have been performed during an about 6-hour operation of the PVT system. During such operation the flow rate has been set to 5 l/min, thus, to 1.25 l/min per each collector. In this paper, some intervals of experimental data have been used to analyse the model results. In particular, two data intervals have been considered, one with a high radiation (over 1000 W/m^2, approximatively from 14.7 to 15.1 h) and with a low one (400-600 W/m^2, approximatively from 17.6 to 18.9 h). The selection of theses intervals is due to the steady state assumption done for

the proposed model and due to the oscillations present during some time intervals achieved by the experiments. The model was also analysed with the entire set of collected experimental data, however for sake of brevity the discussion is here omitted.

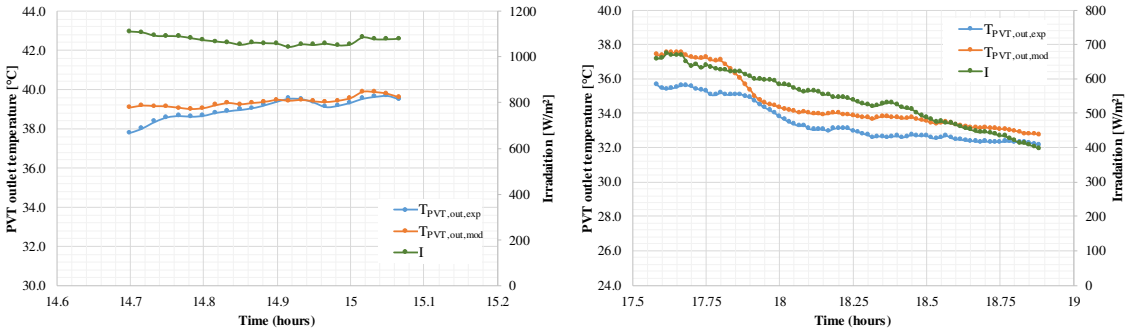

FIGURE 5: PVT OUTLET TEMPERATURE: EXPERIMENTAL DATA VS MODEL DATA; HIGH IRRADIATION (LEFT), LOW IRRADIATION (RIGHT)

In Figure 4 it is clearly shown that the developed model follows the experimental data trend, in particular it slightly overestimates the PVT outlet temperature for both high and low irradiation conditions. Maximum difference between experimental and model data is present for low irradiation conditions, and it is about 2.0°C between 17.55 and 17.80 h. Such differences are achieved because the model does not take into account: thermal capacity of the collector, unsteady operation. In addition, this deviation is also due to the lack of detailed information regarding the radiative properties of PV and back surface of the PVT collector. This is outlined by the time shift between the decrease of experimental and model PVT outlet temperature reported in Figure 4 (right), between 17.8 and 18.10 h. The mean difference between the experimental and model data was 0.354 and 1.015 °C for high and low irradiation data sets, respectively. The standard deviation of such difference resulted 0.321 and 0.484 °C for the same data sets. Moreover, the mean relative error, calculated as the ratio between the difference of experimental and model values and the measured one, resulted 0.00916 and 0.0300 for high and low irradiation conditions, respectively.

4. CONCLUSIONS

A finite volume model of a flat plate PVT collector without insulation has been developed, simulated and experimentally validated against of field measured data. The model follows the experimental data trend, however a slight overestimation of PVT outlet temperature is achieved. In particular, the mean temperature difference between experimental and model data resulted 0.354 and 1.015 °C for high and low irradiation data sets, respectively. Furtherer development will include a detailed analysis of the energy flows in order to enhance the model formulation, and the implementation of the model in dynamic simulation of solar plants.

REFERENCES

[1] Zondag HA, Flat-plate PV-Thermal collectors and systems: A review. *Renewable and Sustainable Energy Reviews,*12, 891-5.2008.

[2] Chow TT, A review on photovoltaic/thermal hybrid solar technology, *Applied Energy*, 87, 365-79, 2010.

[3] Shan F, Tang F, Cao L, Fang G, Performance evaluations and applications of photovoltaic-thermal collectors and systems, *Renewable and Sustainable Energy Reviews*, 33, 467-83, 2014.

Fourth International Conference on Computational Methods for Thermal Problems
THERMACOMP2016, July 6-8, 2016, Georgia Tech, Atlanta, USA
N. Massarotti, P. Nithiarasu and Y. Joshi (Eds.)

HEAT TRANSFER ANALYSIS OF A FLUIDIZED BED STRIPPER ASH COOLER

Ravi Inder Singh and Karan Ghule
Birla Institute of Technology and Science, Pilani-India, raviinder@pilani.bits-pilani.ac.in
ghulekaran@yahoo.in

ABSTRACT

A novel bubbling bed Stripper Ash Cooler for a circulating fluidised bed boiler has been proposed in this paper. To access the heat transfer performance of the proposed ash cooler, CFD techniques have been used. The well established Kinetic Theory of Granular Flow along with the Eulerian Eulerian numerical approach has been used to solve the heat transfer problem. The key parameters of study are the particle diameter, heat transfer coefficient and distribution of phases in the the ash cooler. The contours of temperature, phasic volume and velocity have also been analysed in this paper.

Key Words: *Stripper ash cooler, multiphase, Eulerian –Eulerian, Heat transfer*

1. INTRODUCTION

Circulating Fluidised Bed boilers have gained popularity in the last dacade due to advantages such as high heat transfer rate, fuel flexibilities and enhanced NOx control opportunities. However, a CFB boiler generates significant quantiy of ash which must be cooled to recover the waster heat and thus improve the overall efficacy of the power plant. From the economic perspective, handling of cold ash increased the life of ash handling equipment. Thus, there is immense encouragement to study the heat transfer characteristics of ash coolers. The fluidsation regime of the proposed stripper ash cooler is bubbling bed. The cold rig prototype is similar to stripper ash cooler used industry and it was made after scaling it down. The reason for choosing cold test rig is that high temperature is difficult to maintain at a laboratory level. Hence a CFD technique was employed to understand the heat transfer characteristics of the ash cooler. The key parameters under consideration are the velocity contours , heat transfer coefficient and distribution of phases in the the ash cooler.

2. EXPERIMENTAL AND NUMERICAL SETUP

2.1 Experimental setup

The cold-rig prototype developed is similar to the stripper ash cooler currently used in industry and is shown in figure 1. The sand is used instead of ash to observe the flow phenomena. A bed of sand in formed to observe the fluidization phenomena The primary fluidization air, supplied by a blower is directed into the ash cooler with the help of nozzles. The ash cooler has a vent on the top surface and is exposed to the atmosphere. This vent serves as an outlet for the air and also for the finer sand particles. The prototype is used to visualize the flow and CFD has been used to study the heat transfer characteristics of the ash cooler.

2.2 Computational Model

A 3 D computational model with dimensions 1.013 X 0.988 X 0.317 m was solved in commercial CFD software FLUENT 15.0 using a multiphase Eulerian-Eulerian method. A heat sink (U pipe

heat exchanger of diameter =10 mm) was immersed in the bed to improve the heat transfer. Drag model derived by Gidaspow and heat transfer model proposed by Gunn has been employed to set up the interaction between phases. The time step used for the computation was 0.001 s and the simulation was run for 5 seconds of real time. The phase coupled SIMPLE algorithm with second order upwind scheme has been used to solve the transport equations. The boundary conditions and initial conditions for the set up have been given in Table 1 and 2. The computational model is shown in figure 2. The hopper was not included in the domain to reduce the computational effort.

Name	Boundary Type	Boundary Conditions
Primary air inlet	Velocity Inlet	V= 6 m/s T = 313 K
Outlet	Pressure outlet	Gauge Pressure =0
Heat Exchanger	Constant Temperature Heat Sink	T= 850 K

TABLE 1. Boundary Conditions

Name	Initial Conditions
Height	0.2 m
Temperature	1073 K
Solid Volume Fraction	0.6

TABLE 2. Initial Conditions of bed

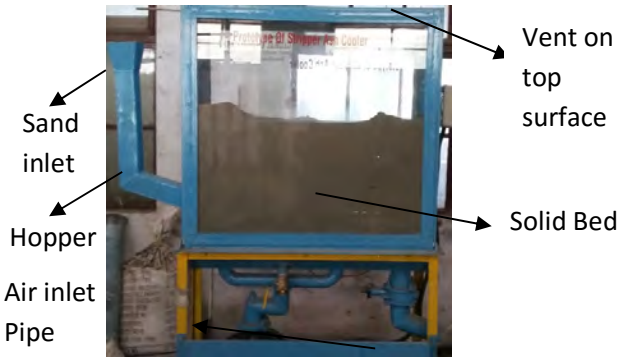

FIGURE 1. Prototype of Stripper Ash Cooler

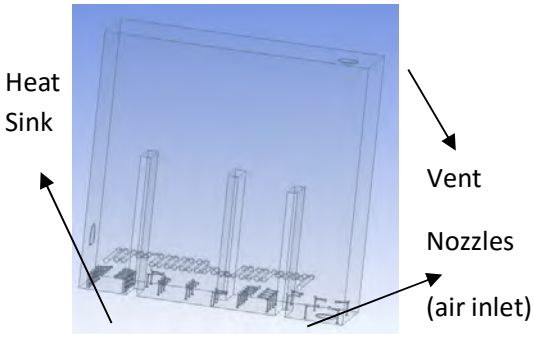

FIGURE 2. Computational Model

3. RESULTS

The transient CFD model was simulated for 5 seconds of real time and the results of the simulation are presented below.

3.1 Variation in instantaneous heat transfer coefficient between the bed and immersed tube

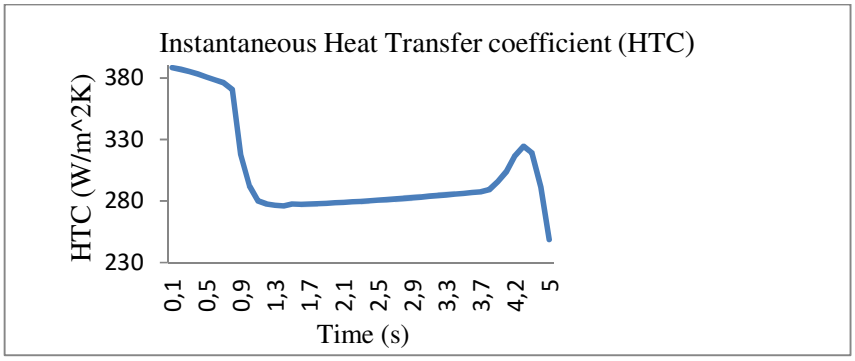

FIGURE 3. Variation in the heat transfer coefficient

3.2 Evolution of bubbles of air

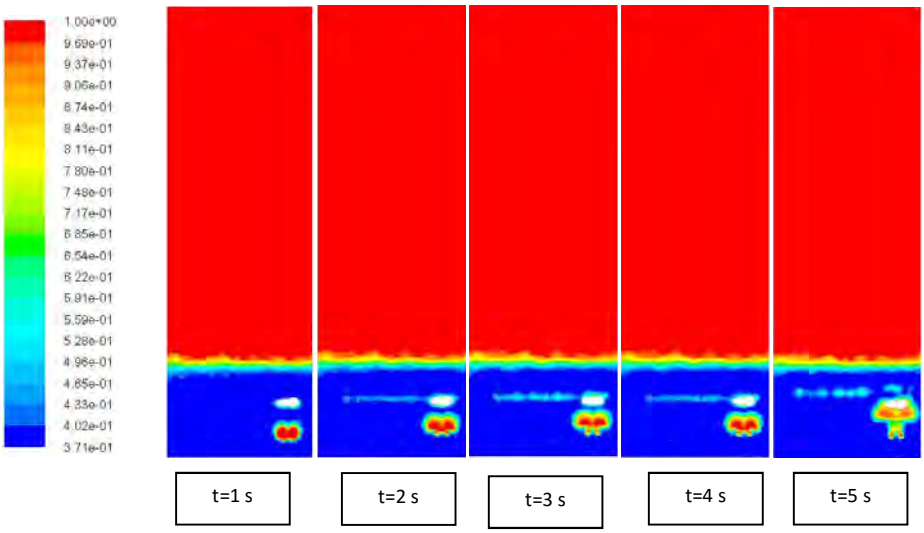

FIGURE 4. Evolution of bubbles

3.3 Velocity vectors of air

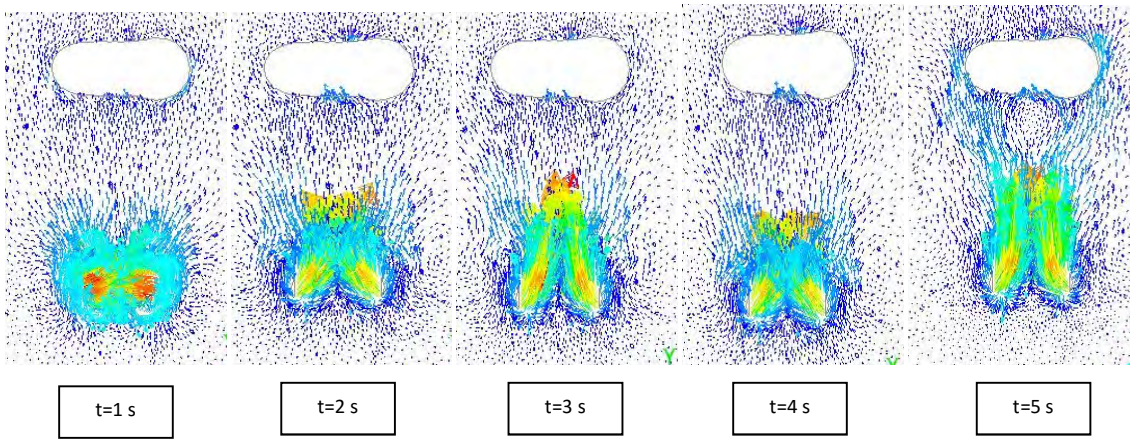

FIGURE 5. Velocity vectors of air around the nozzle and the heat sink at a vertical section

3.4 Temperature distribution of air

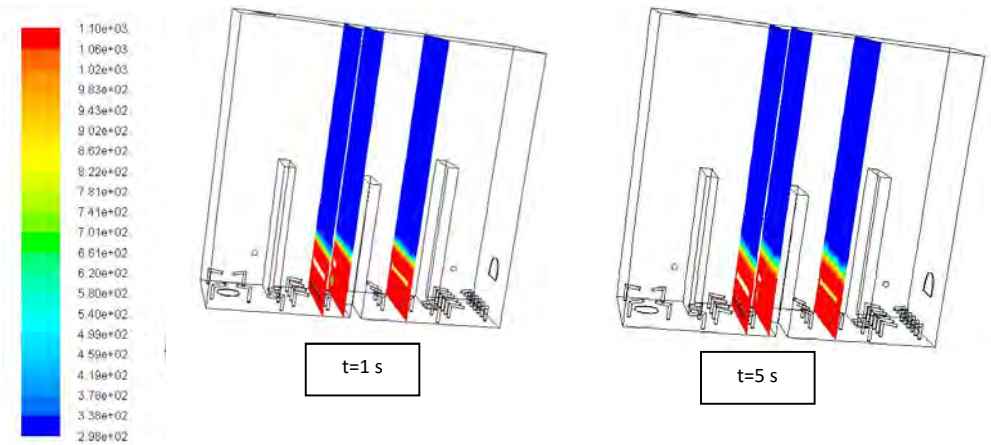

FIGURE 6. Temperature distribution of air (in K)

Figure 3. represents the variation of the instantaneous heat transfer coefficient (HTC) between the bed and the tube. The instantaneous HTC between the immersed tube and the bed has complex nature and cannot be predicted intuitively. The HTC decreases initially, then stabilises, increases to a maxima and shows a sharp decrease. This complex nature arises probably due to the dependence of the HTC on the bubbling phenomena as depicted in figure 4. This is further verified by plotting the velocity vectors of air (figure 4). It is evident that there is a tendency for the air to form vortices near the immersed tube and this tendency strongly influences the heat transfer coefficient between the tube and bed.

4. CONCLUSIONS

This study presents a numerical heat transfer analysis of the proposed ash cooler. The instantaneous heat transfer coefficient, the velocity vectors of solids, the phenomenon of bubbling and local temperature distribution has been presented. The heat transfer coefficient(HTC) varies in the range of 250-350W/m^2K, which is typical for bubbling beds. The results also showcase that heat transfer coefficient is strongly influenced by the phenomenon of bubbling and motion of the air bubbles around the heat transfer tube. This paper concludes that the proposed ash cooler supports high rates of heat transfer as a result of the fluidisation principle and thus is a suitable candidate for replacement of the traditional ash coolers.

REFERENCES

[1] Ravi Inder Singh, Agglomeration in a stripper ash cooler and its possible remedial solutions- A case study*, Journal of Institution of Engineers-Part C*, 2016, DOI: 10.1007/s40032-016-0218.

[2] Bing Zeng, Xiaofeng Lu, Lu Gan, Maolong Shu, Development of a Novel Fluidized Bed Ash Cooler for Circulating Fluidized Bed Boilers: Experimental Study and Application, *Powder Technology*, *212*, 2011, pp. 151–160.

[3] Armstrong, L. M., Gu, S., & Luo, K. H., Study of wall-to-bed heat transfer in a bubbling fluidised bed using the kinetic theory of granular flow. *International Journal of Heat and Mass transfer,2010,53*(21-22), 4949–4959.

[4] T Guo, X F Lu, H Z Liu, Cold Model Experiments and Numerical Simulation on a selective Fluidized Bed Bottom Ash Cooler In A 410t/H CFB Boiler, *Proceedings of 19th International Conference on Fluidized Bed Combustion*, Vienna, Austria, 2006.

[5] Dong, N. H., Armstrong, L. M., Gu, S., & Luo, K. H. ,Effect of tube shape on the hydrodynamics and tube-to-bed heat transfer in fluidized beds. *Applied Thermal Enginnering*,2012, 472–479.

[6] S.V. Thite, S.B Ingole, Modeling of Heat Transfer in Fluidized bed ash cooler, *International Journal of Research in Advent Technology*, Vol.2, No.3, March 2014,pp. *69*-74.

[7] D. Gunn, Transfer of heat or mass to particles in fixed and fluidised beds, Int. J.Heat *Mass Transfer* 21 (1978) 467–476.

[8] Gidaspow,D., Multiphase Flow and Fluidization: Continuum and Kinetic Theory Descriptions, *Academic Press*, San Diego,1994.

Fourth International Conference on Computational Methods for Thermal Problems
THERMACOMP2016, July 6-8, 2016, Georgia Tech, Atlanta, USA
N. Massarotti, P. Nithiarasu and Y. Joshi (Eds.)

CAP1000 in-containment structure temperature analysis on DBA

Xue Shanhu, Ye Cheng, Tian Lin, Wang Minglu
Shanghai Nuclear Engineering Research & Design Institute, Shanghai 200233, xsh@snerdi.com.cn

ABSTRACT

The stress analysis of the steel structure under the condition of the design basis accident (DBA) is an important part of the safety analysis. In this paper, the in-containment structure and typical shape of the CAP1000 structure is summarized, envelope curve of the environment was obtained on comprehensive DBA condition, boundary conditions of the structure were simulated by UCHIDA method on DBA, and the typical structure temperature variance was calculated by ANSYS 13.0 Workbench on the DBA envelope condition.

Key Words: *Steel Structure, Finite Elements, DBA Accident.*

1. INTRODUCTION

In this paper, we study the steel structure includes main equipment support, pipe support and steel platform in containment of CAP1000 nuclear power plant. Under the condition of DBA, the ejection of primary coolant high temperature fluid induces in-containment environment temperature variance and the steel structure stress is changed as the temperature is changed. The stress variance may influence the structure stability. In order to offer the input for stress calculation on DBA condition as well as evaluate the in-containment structure stability, structure temperature is analysed on DBA condition. In this paper, the transient temperature characteristics of the structure are analysed by using ANSYS 13. under a conservative approach.

2. BOUNDARY CONDITION AND MODEL

2.1 Environment temperature

The ejection steam under DBA condition is the main heat source to structure. To be conservative enough, the steam temperature assumes to be the highest temperature in the Double-Ended Hot Leg Guillotine (DEHLG) compartment at first 100 seconds. From 100 seconds to 100000 seconds, the steam temperature assumes equal to Double-Ended Cold Leg Guillotine (DECLG) compartment temperature. This steam temperature input can envelope various DBA conditions.

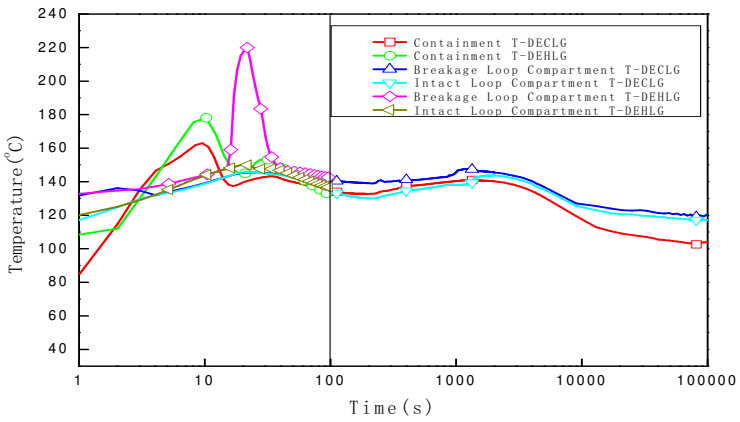

FIGURE 1 Representative environmental temperature curve in DBA

Figure 1 is the representative compartment environmental temperature curve of several DBA conditions calculated by the safety analysis [1][2][3][4]. The figure shows compared to other conditions, the DEHLG broken loop compartment temperature is highest at first 100 seconds. After 100 seconds, the DECLG broken loop compartment temperature is highest, and the environment temperature input is combined as Figure 2 shows.

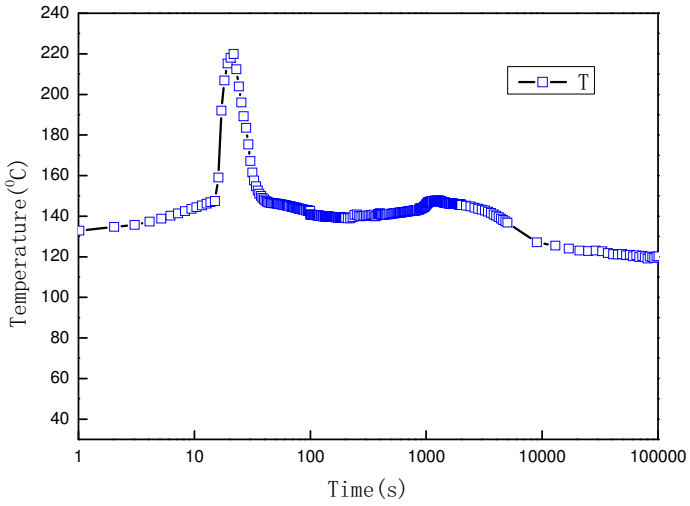

FIGURE 2 Steam temperature input curve

2.2 heat transfer coefficient

During the DBA accident, as an important input in the ANSYS calculation, the heat transfer coefficient between structure and steam is vital. Compared to the single phase heat transfer, the heat transfer coefficient of the phase change is greater. It is conservative to choose condensation heat transfer equation used in Uchida [1] as Equation 1 shows.

$$h(t) = 0.022[\rho_v(t) / \rho_a]^{0.8} \qquad (1)$$

In this equation h is heat transfer coefficient, [Btu/(s · ft^2 · °F)]; ρ_v is steam density in the containment, [lbm/ft^3] and ρ_a is air density in the containment.

Steam density could be fitted as equation 2 shows.

$$\begin{aligned}\rho_v(t) = {} & 0.000000000142708\times t_s^{\,5} - 0.000000118485452\times t_s^{\,4} \\ & + 0.000039268402289\times t_s^{\,3} - 0.006490848943293\times t_s^{\,2} \\ & + 0.535191643192682\times t_s - 17.6088077587746\end{aligned} \qquad (2)$$

Equation 3 quickly converts metric and imperial.

$$h(t)_{\mathrm{W/(mm^2\cdot °C)}} = h(t)_{\mathrm{Btu/(s\cdot ft^2\cdot F)}} \times 5.678264 / 100000 \qquad (3)$$

2.3 Simplify steel structure

CAP1000 steel structure in containment is complex and variety. In this paper, pipe hanger, main equipment support and steel platform were summarized as representative structure. The steel used in pipe hanger and main equipment support can be classified into sheet, rod, pipe and profile. The steel used in the steel platform is always the sheet.

2.3.1 Pipe hanger and main equipment support

Table 1 shows the key parameter, size, model and mesh of representative steel used in pipe hanger and main equipment support.

TABLE 1 Simplify model of pipe hanger and main equipment support

Type	Key Parameter	Size
Sheet	Thickness	3×20×40mm
Rod	Diameter	Φ6×22mm
Pipe	Thickness	Φ32×5×60mm
Profile steel	Thickness	4.5×36×36mm

2.3.2 Steel platform

The shape of steel platform was analyzed in various compartments. The thickness of the steel is the key factor which influences heat transfer. According to the analyzed results, the steel platform is simplified as 5.5×9×45mm.

2.4 Calculation Set

The ANSYS [5][6] calculation input is listed:

- Material properties: The structure material is carbon steel or alloy steel. Carbon steel Q345 is chosen as material properties input as higher thermal diffusion coefficient.
- mesh：The smallest unit size is 1mm;
- Initial temperature: Initial temperature is 50℃；
- Calculation step: From 0 to 100 seconds, time step is 1 seconds; From 100 to 2000 seconds, time step is 19s; From 2000 to 100000 seconds, time step is 980 seconds;
- Boundary conditions: Third-boundary conditions. Every faces of structure transfers heat with environment.
- Calculation time: As the highest temperature peak is observed before 100 seconds and 10000 seconds and after 10000 seconds the temperature between structure and steam is minimal. Set the total calculation time 100000 seconds.

3. CALCULATION RESULTS

3.1 Pipe hanger and main equipment support

3.1.1 Sheet

Figure 3 indicates the sheet temperature is uniform after 100 seconds. At 15 to 40 seconds, steam temperature reaches a peak but has little impact on structure temperature as the time is short. The structure temperature rises along with the steam ejection after DBA accident and reaches peak temperature 136℃ at about 3960 seconds. As the accident progressed to 6076s, structure began to transfer heat to environment and finally both structure and environment reaches the same temperature.

For the bar, pipe, profile steel and even steel platform, the calculation results shown the same phenomenon.

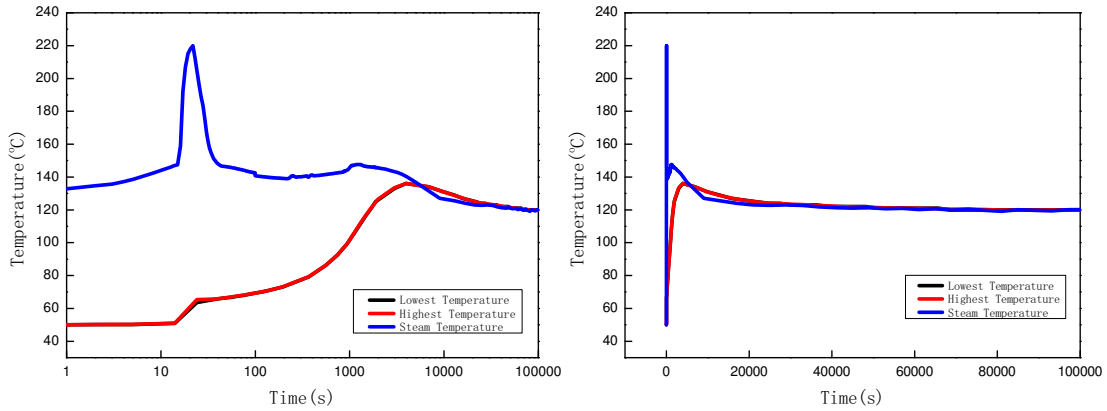

FIGURE 3 Temperature variance of sheet

4. CONCLUSIONS

In this paper, the analysis bases follow conservation:

- Highest temperature in the compartment was chosen in DBA accident.
- Minimized size structure was chosen.
- The Uchida condenser heat transfer model was chosen to calculate heat transfer between structure and environment.
- The structure with heat source is not included.

The main conclusions are:

- Although there is a highest temperature 218.0℃ at the first 100 seconds in the Double-Ended Hot Leg Guillotine accident, it doesn't influence the structure temperature directly; the condensing temperature of the accident is the leading factor.
- In the DBA accident, the highest temperature of steel structure is 136.0℃ and 131.7℃ for the steel platform.
- In this paper, in-containment structure temperature was analyzed only in the DBA accident. The structure temperature in the serious accident needs further study.

REFERENCES

[1] WANG Guodong, Zhang Di, CAP1000 Containment Long Term Pressure and Temperature Evaluation, CAP-GX-GL-015, Rev. 0, 2010

[2] Ye Cheng, Zheng Mingguang, Wang Yong. WGOTHIC Analysis on AP1000 Passive Containment Cooling Water[J]. Atomic Energy Science and Technology, 2013, (12): 2225-2230

[3] Ye Cheng, Zheng Mingguang, Wang Yong. Effect of AP1000 Steel Containment Thickness on Heat Transfer Performance [J]. Atomic Energy Science and Technology, 2014, (3): 457-461

[4] Gao Jianfeng, Ye Cheng. Analysis and Calculation of Containment Passive Cooling Ability[J]. Atomic Energy Science and Technology, 2014, (12): 2274-2279

[5] Ansys Workbench Help. 13.0

[6] Yang Shiming, Tao Wenquan. Heat Transfer[M]. Beijing: Higher Education Press, 1998.

PARALLEL SESSION

ENERGY CONVERSION

Fourth International Conference on Computational Methods for Thermal Problems
THERMACOMP2016, July 6-8, 2016, Georgia Tech, Atlanta, USA
N. Massarotti, P. Nithiarasu and Y. Joshi (Eds.)

BIOMASS SMALL SCALE BATCH GASIFIER: AN EXPERIMENTAL AND NUMERICAL ANALYSIS

Stefano Cordiner, Alessandro Manni*, Vincenzo Mulone, Vittorio Rocco
Dpt of Industrial Engineering, University of Rome Tor Vergata, Via Del Politecnico 1 ,00133 Roma

*corresponding author: alessandro.manni@uniroma2.it

ABSTRACT

The thermochemical gasification process is one of the key intermediate processes to flexibly generate electric/thermal power. In this paper, experimental results of a small externally heated biomass batch-gasification constant volume bomb are presented. The aim of the work is the production of data useful to calibrate CFD-DEM models for more design-oriented applications, by varying temperature and feedstock characteristics such as biomass sample mass and characteristic sizing. A 3D numerical model representing the experiment is also presented here, whose results are compared with the gathered experimental data for validation purposes.

Key Words: *biomass, gasification, pyrolysis, CFD.*

1. INTRODUCTION

The deployment of renewable energy technologies is necessary to increase the energy independence of all the regions in the world, along with related economic and environmental benefits. In this scenario, biomass has come up as a major alternative source, presenting wide availability and limited environmental impact if compared to fossil fuels. Most biomass fuels have low energy density in comparison with fossil fuels, and such that handling, storage and transportation get expensive. Thus, to maximize the biomass yield, it is necessary to improve its transport and handling characterstics. A possible method may foresee the conversion of the solid biomass into liquid or gaseous fuels, via the gasification or pyrolysis. In the last decades, in the provided context, mathematical models for biomass conversion, have proved to be useful tools to describe the gasification process. This representation of the process in modelling terms, helps in gaining knowledge about the importance of the operating parameters affecting the gasifier performance. However, the design process is very challenging, especially to maintain high performance by varying feedstock characteristics (Moisture Content, sizing, Heating Value, etc) and gasifier technological features. Thus, detailed information gathered from smaller scale experiments, as shown in other available studies [1,2], are valuable to that aim. In literature the focus has been mainly devoted to pyrolysis batch experiments, showing details about thermal response, transport phenomena and syngas yield [2]. Other approaches have been used to estimate the yield, such as kinetic/dynamic models [3-4] and neural network applications [5-6] allowing, in some cases, to give better accuracy at the expense of greater higher complexity. The aim of this paper is to show the implementation of a CFD-DEM (Computational Fluid Dynamics, Discrete Element Method) based numerical model for more complex applications or design scale up. The first step, here described, consists of the experimental analysis as well as a slow pyrolysis process simulation, of a common biomass fuel (woody pellet), in order to test the basic capabilities of the systems.

2. EXPERIMENTAL SETUP AND TEST PROTOCOL

The experimental test bench consists of an indirectly heated batch reactor operating at quasi-isobaric pressure (in the atmospheric range). The reactor (Fig 1) is inserted into a cylindrical furnace, capable of reaching temperatures up to 1000 °C. Control and acquisition connections are

plugged through the open side of the furnace. The biomass sample is contained in a vessel (bomb): the produced syngas can continuously recirculate with a pump to both have mixing in the gas phase, and control the air fuel ratio. The temperature is monitored by a set of thermocouples placed in the reactor and in the external circuit to avoid any occurrence of condensation processes. The produced syngas is sampled and analysed with Gas-Chromatography (GC) techniques to measure composition and yield as functions of the main operating parameters.

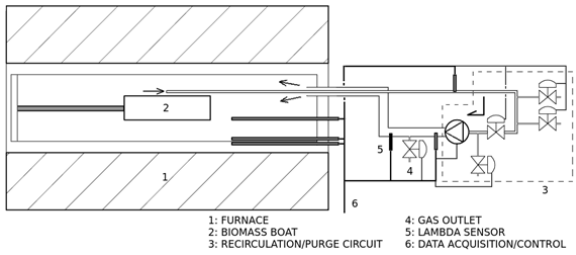

FIGURE 1. Schematic of the experimental test bench

The pyrolysis process has been carried out by filling the reactor with woody biomass (pellets), by washing it with N2, and performing several runs with a selected range of operating conditions. In particular, tests were carried out with different sample amounts (20 and 40g), and different sizing (e.g. whole pellet or ground pellet).A constant temperature ramp has been defined and prescribed to fully heat the sample in about two hours with a corresponding internal heating rate of 8.5 [°C/min] . The produced syngas has been sampled without gas recirculation ,and analysed with the GC, with 100 °C steps, starting from 400° C, up to 900 ° C. All the experiments have been done at quasi-atmospheric pressure and at 900°C peak temperature. Sawdust and pellet have been characterized by means of ultimate (with a VARIO MACRO cube) and proximate (measuring moisture, light gas and ash content with a LECO TGA 701) analyses that have been used for the CFD model setup .

3. NUMERICAL MODEL DESCRIPTION AND MAIN ASSUMPTIONS

The fluid dynamic equation system, as well as the submodels, have been implemented into OpenFOAM [7]. To simulate that system, the coalChemistryFoam (OF 2.1) solver has been used, and modified by adding a DEM capability. The computational grid, as highlighted in Figure 4, takes into account the whole bomb, excluding the recirculating zone. This simplification, according to the extremely low Reynolds number registered in the bomb, allows for a consistent reduction of the total number of computational cells. The domain has been divided into 80k cells, with a grid size of approximately 2.5mm. Cells are mostly hexahedral in shape (98%), giving limited problems in terms of numerical diffusivity [8]. A sensitivity analysis, with a progressive size decrease in the order of 50%, has also been carried out, also in terms of parcel representation, to double check for the obtainment of grid independent results. The numerical simulation of the pyrolysis process, has been carried out under the following main assumptions:

- The gas/bed interaction has been considered through a coupled DEM model.
- The radiation in the energy equation is taken into account through the P1 model, while convective heat transfer with the Ranz-Marshall correlation [9]
- The evaporation process has been treated via a simplified model by Baumgarten [10]. A simple Arrhenius equation has been instead used to represent the volatilization of CH4 ,CO ,H2,CO2 formation, while the TAR fraction has been modeled as C16H34 to have an accurate as possible representation of the average molecular weight.
- The contact forces have been described by the Voigt model which is essentially a simple mass-spring-damper model.

A comparison with an experimentally measured temperature value (with measurement uncertainties in the order of ±1K), gathered over the biomass sample holder, and the syngas production, has been done to prove the overall accuracy of the model. The single pellet element has been considered as a spherical particle with a diameter of 7 mm. Their composition, in terms of liquid gaseous and solid components, has been calibrated via experimental results, while the kinetic parameters have been assumed in line with literature available values. In the proposed case, a 30g sample has been assumed.

4. EXPERIMENTAL AND NUMERICAL RESULTS

The biomass is heated up from the top, via an increasing radiation heat transfer given by the walls and assuring the biomass drying-up (at about 100°C). The bed height presents a decreasing profile over time due to the correspondent mass loss (Fig 2) accurately representing the thermal degradation process. It is also worth noting that the particle diameter is consistently reduced over time. The volatile release starts at about 200°C, with a slope decrease at about 700°C. Experimental and numerical results, in terms of molar concentration are given in Fig 3: a good agreement may be observed between experimental and numerical results by varying operating temperature, especially in terms of average yield over the temperature domain. Results are also affected by a simplified description of the C16H34 phase change kinetics, that has an impact on the gaseous species molar concentration. In Fig 4 the temperature plots are reported respectively at the beginning of the simulation, at 400°C and 800°C: the importance of heat transfer is evident, as the particle temperature is always lower than the ambient. This is also due to the slow kinetics of the considered pyrolysis process.

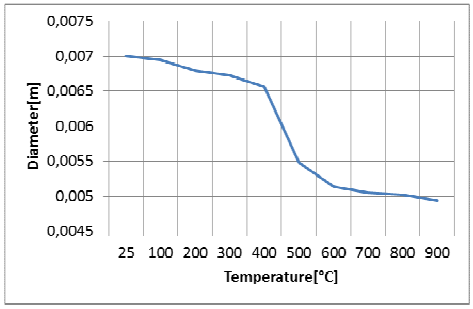

FIGURE 2. Numerical biomass consumption profile as a function of temperature.

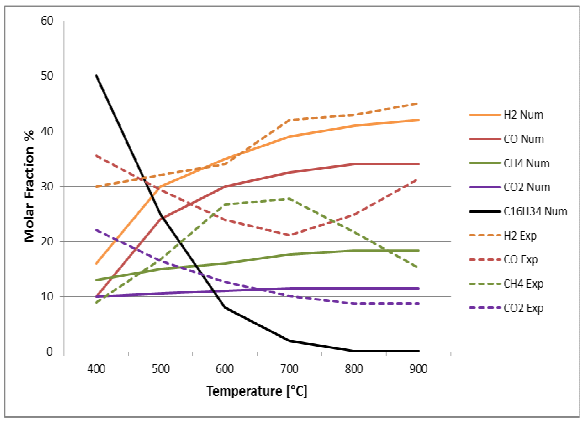

FIGURE 3. Experimental-numerical gaseous species molar concentration as functions of temperature, and numerical TAR (C16H34) concentration.

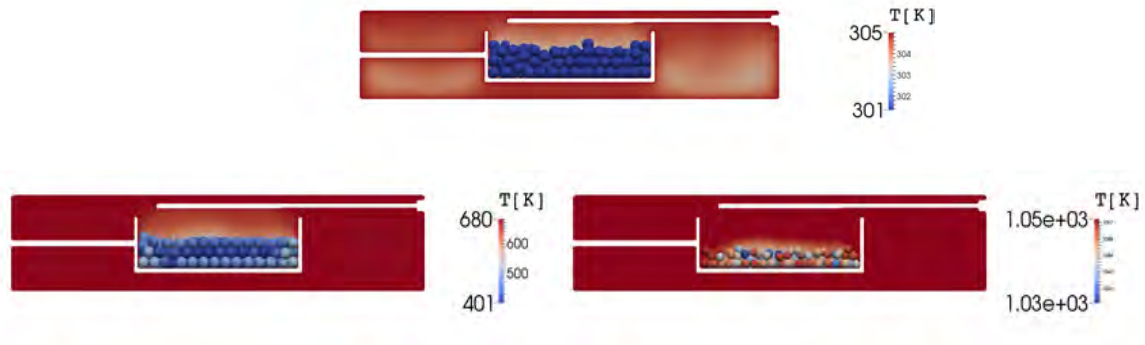

FIGURE 4. Numerical temperature plots at ambient temperature (top), 400°C (left) and 800°C (right).

4. CONCLUSIONS

An experimental procedure and the application of a 3D model to test a small scale batch constant pressure pyroliser/gasifier has been presented in this paper. The CFD model is capable of carefully representing the 3D evolution of the biomass thermochemical consumption through slow pyrolysis. The model is furthermore capable of tracking the main sub-steps of bed evolution, as well as predicting the syngas concentration evolution over time and by varying temperature. The 3D prediction of temperature profiles and syngas yield concentrations would allow to use the CFD tool to scale-up results to a full size system for design purposes.

REFERENCES

[1] Chen G, Andries J, Luo Z, Spliethoff H. Biomass pyrolysis/gasification for gas production: the overall investigation of parametric effects. Energy Conv. Manag. 2003;44:1875–84

[2] P. Baggio, M. Baratieri,L. Fiori,M. Grigiante, D. Avi, P. Tosi, Experimental and modeling analysis of a batch gasification/pyrolysis reactor .Energy Conv. Manag. 50 (2009) 1426–1435

[3] Babu BV, Sheth PN. Modeling and simulation of reduction zone of downdraft biomass gasifier: effect of char reactivity factor. Energy Convers Manage 2006;47:2602–11.

[4] Gøbel B, Henriksen U, Jensen TK, Qvale B, Houbak N. The development of a computer model for a fixed gasifier and its use for optimization and control.BioresourTechnol 2007;98:2043–52.

[5] Guo B, Li D, Cheng C, Lü Z, Shen Y. Simulation of biomass gasification with a hybrid neural network. BioresourTechnol 2001;76:77–83

[6] Mikulandrića R., Lončara D, et al. Artificial neural network modelling approach for a biomass gasification process in fixed bed gasifiers. Energy Conv. and Manag. 2014;87:1210–1223

[7] http://www.openfoam.org/

[8] T.J.Chung, Computational Fluid Dynamics, Cambridge University Press,2010

[9] Cordiner, Stefano, et al. "Biomass furnace study via 3D numerical modeling." International Journal of Numerical Methods for Heat & Fluid Flow 26.2 (2016).

[10] Baumgarten C, Mixture Formation in Internal Combustion Engines. Heat and mass transfer, Springer 2006

Fourth International Conference on Computational Methods for Thermal Problems
THERMACOMP2016, July6-8, 2016, Georgia Tech, Atlanta, USA
N. Massarotti, P. Nithiarasu and Y. Joshi(Eds.)

A ONE-DIMENSIONAL STEADY MODEL FOR DOWNDRAFT BIOMASS GASIFIERS

M. Costa, M. La Villetta, N. Massarotti
CNR - Istituto Motori, Viale Marconi, 4, 80125, Naples, Italy, m.costa@im.cnr.it
Dipartimento di Ingegneria, Università degli Studi di Napoli "Parthenope", Centro Direzionale, Isola C4, 80143 Napoli, Italy. maurizio.lavilletta@uniparthenope.it
Dipartimento di Ingegneria, Università degli Studi di Napoli "Parthenope", Centro Direzionale, Isola C4, 80143 Napoli, Italy. massarotti@uniparthenope.it

D. Piazzullo, V. Rocco
University of Tor Vergata,Via del Politecnico 1, 00133 Rome, Italy, daniele.piazzullo@students.uniroma2.eu
CNR - Istituto Motori, Viale Marconi, 4, 80125, Naples, Italy,v.rocco@im.cnr.it

ABSTRACT

A one-dimensional stationary model of biomass gasification in a fixed bed downdraft gasifier is presented in this paper. The model is based on the mass and energy conservation equations and accounts for the energy exchange between the solid and gaseous phases and the heat transfer by radiation between the solid and gaseous species and the reactor walls. The downdraft gasifier is discretized as a sequence of layers where the following typical sub-processes take place: biomass drying (on the top of the reactor), pyrolysis (in the center), oxidation of char and tar cracking (on the bottom of the reactor). Nine species are considered as participating the gaseous reactions: O_2, N_2, H_2O, CO_2, H_2, CO, CH_4, H_2S, TAR. The model is solved by dividing the system of differential-algebraic equations into two sub-systems: one made of differential equations, solved through algorithms suitable for the solution of stiff problems, one made of non-linear algebraic equations solved through the Newton-Raphson algorithm. The model is suitable of being used as a tool to study the influence of process parameters, such as biomass type, moisture content, gasifier geometry, composition and inlet temperature of the gasifying agent, biomass particle diameter.

Key Words: *Gasification, Differential-Algebraic Equations, Kinetic Model.*

1. INTRODUCTION

Mathematical models are a useful tool in representing engineering systems whose operation is affected by a relevant number of parameters. The description of the biomass gasification process in mathematical terms helps in gaining an insight in the whole process, hence in guaranteeing a high quality of the released syngas. According to ref. [1], simulation models of biomass gasifiers can be classified in the following categories: thermo-chemical equilibrium models, kinetic models, phenomenological models and artificial neural networks. The inadequacy of the equilibrium model to correlate the reactor design parameters and the raw material residence time and interaction with the gasifying agent with the final product gas composition can be overwhelmed by developing proper phenomenological models. These are based on the solution of the balance equation of mass, momentum and energy over at least one direction within the reactor (generally along its axis), where chemical kinetics is also described as a function of the local value of temperature.

2. MATHEMATICAL MODEL OF DOWNDRAFT GASIFIER

In this article, according to the approach followed in ref.[2], the gasification process in a downdraft gasifier is modeled separating the overall process into sub-models of pyrolysis, oxidation and reduction zones, by means of one-dimensional (along the reactor axis) and steady differential mass and energy balance for the solid and gas phases. The momentum equation is not solved, hence the gasifier is isobaric and the velocity of both the phases is assumed as being constant. The model applies the conservative equations to a differential volume ΔV, whose diameter is equal to the reactor diameter D and having height Δz along the gasifier, as shown in Figure 1. Radial gradients are not considered as the residence time of the solids in the bed is assumed being long. Turbulence is not treated formally in the slowly moving bed with low gas velocities, but is accounted for implicitly through the used correlations for the actual heat/mass transfer coefficients. The fed particles are considered spherical and having the same average size; the porosity of the bed is assumed constant along the gasifier. The main processes include moisture:(M) evaporation by a 1st order kinetic equation; devolatilization of dry wood ($Wdaf_{SS}$) described by one step global reaction; homogeneous and heterogeneous reactions (involving char, oxygen, steam, carbon monoxide, carbon dioxide, methane and hydrogen); combustion of volatile species as tars. The partial bed density for ash (A) is assumed constant throughout the reactor; heat and mass transfer across the bed by convection and heat transfer between solid-gas, solid-wall and gas-wallare considered. The solid phase is characterized by the partial bed densities ρ_i ($kg/m^3_{\text{bed volume}}$) for i = $Wdaf_{SS}$, M, C and A, by the solid velocity u_S (m/s) and temperature T_S (K). Similarly, the gas phase is characterized by the partial bed densities ρ_j($kg/m^3_{\text{gas volume}}$) for j = O_2, N_2, H_2O, CO_2, CO, H_2, CH_4, H_2S, Tar (C_mH_n), gas velocity u_G (m/s) and temperature T_G (K). The volatiles are assumed to behave as ideal gases.
The equations of the model are:

Mass conservation of the solid-phase species

$$\text{Wood Daf}_{SS} \qquad \frac{\partial(u_S\rho_{wood})}{\partial z} = -R_{dev} \tag{1}$$

$$\text{Moisture} \qquad \frac{\partial(u_S\rho_M)}{\partial z} = -R_{dry} \tag{2}$$

$$\text{Char} \qquad \frac{\partial(u_S\rho_C)}{\partial z} = \alpha_c \frac{M_C}{M_{woo\,d}} R_{dev} - M_C \sum_{p=1}^{N_{SR}} R_{Sp} \tag{3}$$

$$\text{Ash} \qquad \frac{\partial(u_S\rho_A)}{\partial z} = 0 \tag{4}$$

Mass conservation of the gas-phase species

$$\frac{\partial(\varepsilon\, u_G\rho_j)}{\partial z} = M_j \sum_{l=1}^{N_{GR}} \upsilon_{jl} R_{Gl} \qquad (5-14)$$

Energy balances for the solid and gas phases

$$\sum_{i=1}^{NSS} \frac{\partial(u_S\rho_i\, H_{Si})}{\partial z} = -Q_{SG} - Q_{SW} + (-\Delta H_{dry})R_{dry} + \sum_{p=1}^{N_{SR}} (-\Delta H_{R_{Sp}}) R_{Sp} \tag{15}$$

$$\text{where } H_{Si} = cp_{Si}(T_S - 298.15) \qquad i = \text{Wood Daf}_{SS}, \text{Moisture, Char, Ash}$$

$$\sum_{j=1}^{NGS} \varepsilon \frac{\partial(u_G\rho_j\, H_{Gj})}{\partial z} = +Q_{SG} - Q_{GW} + \sum_{l=1}^{N_{GR}} (-\Delta H_{R_{Gl}}) R_{Gl} \tag{16}$$

$$\text{where } H_{Gj} = cp_{Gj}(T_j - 298.15) \qquad j = O_2, N_2, H_2O, CO, CO_2, H_2, CH_4, H_2S, C_mH_n$$

$$Q_{SW} = \frac{4h_{SW}}{D}(T_S - T_{wall}) \quad Q_{GW} = \frac{4h_{GW}}{D}(T_g - T_{wall}) \quad Q_{SG} = h_{SG}\, A_{SG}\, (T_S - T_G) \quad A_{SG} = \frac{6(1-\varepsilon)}{d_p}$$

Ideal gas law

$$\sum_{j=1}^{NGS} \frac{\rho_j}{M_j} = \frac{P}{R\, T_G} \tag{17}$$

Constant solid velocity

$$u_S = u_{S,in} \tag{18}$$

Details about the reactions rate and other used parameters can be find in refs.[2] and [3]. Regarding the used mathematical approach, the model is solved in Matlab by dividing the system of differential-algebraic equations in two sub-systems: one made of differential equations, solved through algorithms suitable for the solution of stiff problems (ODE15s – Gear's method), that is able to change the integration step when the gradient of variables sharply increases, one made of non-linear algebraic equations solved through the Newton-Raphson algorithm (see Figure 1 on the left).

3. RESULTS

The main results of the developed one-dimensional (1D) model are presented on the right of Figure 1. Entering the gasifier, the treated biomass initially heats-up and loses its moisture. After this process, the temperature increases rapidly and activates the mechanisms of pyrolysis in the temperature range 300 - 650 °C. Subsequently, after 800°C, gasification and combustion in both the homogeneous and heterogeneous phases occur. This allows the gaseous species in the reactor to reach a peak temperature of about 1200K. After the peak, the temperature decreases because there is nothing else to burn, in fact only ash is present. Regarding the mass fraction of the species, the mass fraction of water decreases and, as a consequence, the mass fraction of the organic matter increases. The mass fraction of the water vapor increases in the drying and pyrolysis zone. Indeed, the organic material content begins to decrease and simultaneously its composition is being modified under the production of permanent and condensable gases (as water and tar). The pyrolysis step also leads to an increase in the char content and inorganic matter. After pyrolysis, it is required that the temperature increases before the oxidation of char begins. The constant segment associated with the mass fraction of char, corresponds to the distance required for the critical temperature of oxidation to be reached. Then the consumption of char begins, and hence, the temperature strongly increases because of oxidation combustion reaction which is then followed by gasification with carbon dioxide. Indeed, when the char begins to decrease, all the oxygen decreases to zero because the gasification reaction of char with O_2 takes place and carbon dioxide is generated. The carbon dioxide also decreases because of the gasification reaction of char with CO_2. At the end of the reduction stage, when the temperature falls below specific levels, all chemical reactions are frozen, except the water–gas shift reaction, which slightly favors the formation of CO_2in the place of CO. Of course, the comparison of the present model results with other works in the degradation zone of char, regarding the increase or decrease of chemical species, may be carried out only accounting for possible inclusion of faster or slower chosen reaction kinetics.

4. CONCLUSIONS

A stationary1D model of wood biomass gasification is developed. The model considers the main processes that are relevant for the thermo-chemical transformation of biomass into syngas that can be used as a fuel in reciprocating internal combustion engines. The gasification model allows evaluating the effect of the operational parameters as size of wood, proximate and ultimate analysis,

heating value, equivalence ratio, moisture content, gasifier geometry, composition and inlet temperature of the gasifying agent on the gasification process.

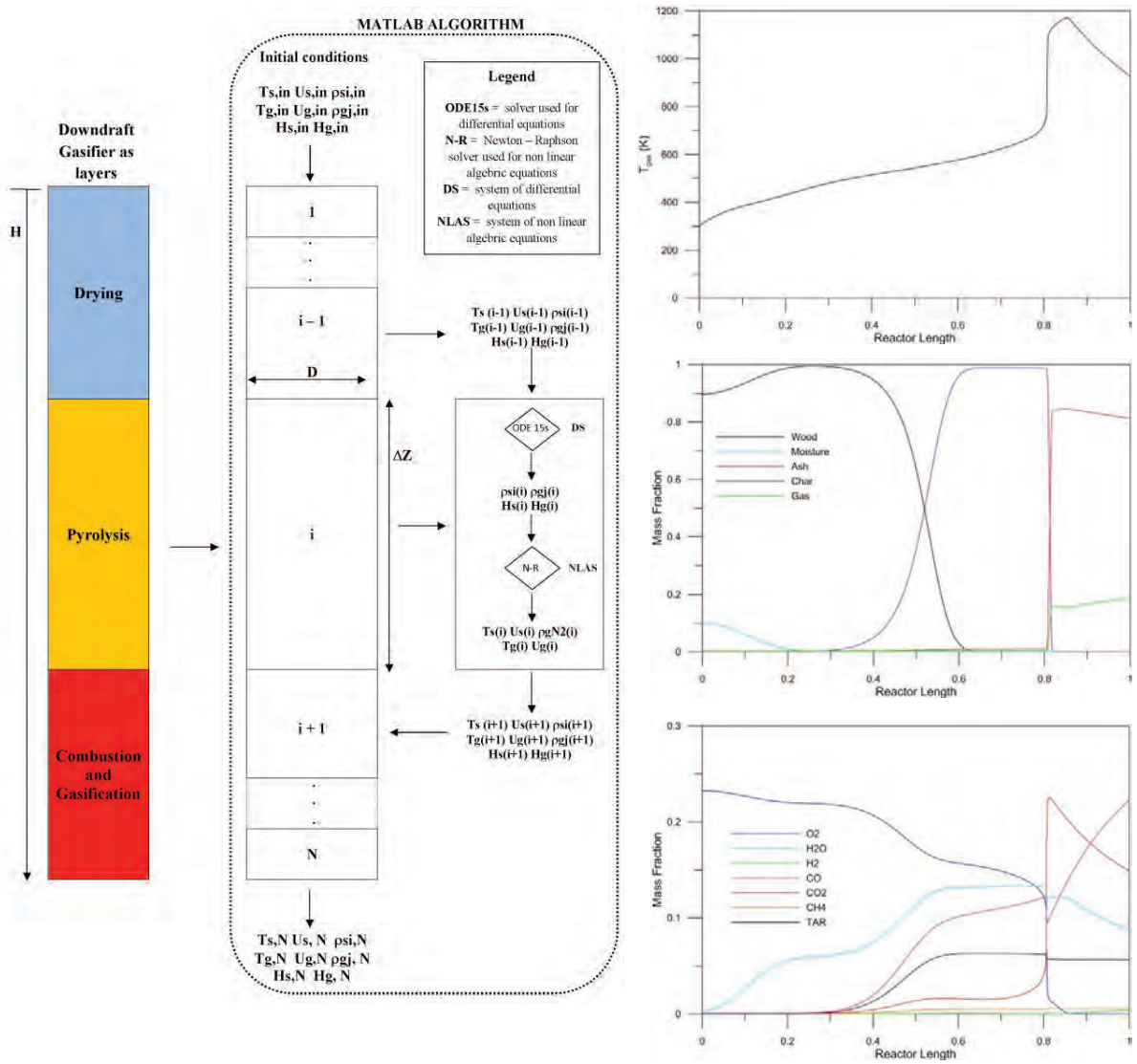

FIGURE 1. Mathematical approach used for the reactor 1D schematization (left) and model results obtained in terms of temperature, mass fraction of solid and gaseous species (right) along the reactor.

REFERENCES

[1] M. Costa, M. La Villetta, N. Massarotti, Optimal Tuning of a Thermo-Chemical Equilibrium Model for Downdraft Biomass Gasifiers, *Chemical Engineering Transactions*, 37,343-348, 2015.

[2] R. Tartarelli, M. Seggiani, Analisi e modellazione numerica del processo di gassificazione del carbone in reattori updraft, *Report RdS 27, ENEA,* 2010.

[3] B. Teislev, Simulation of the biomass updraft gasifier, *MEK-ET-2006-02*, 2006.

Fourth International Conference on Computational Methods for Thermal Problems
THERMACOMP2016, July 6-8, 2016, Georgia Tech, Atlanta, USA
N. Massarotti, P. Nithiarasu and Y. Joshi (Eds.)

Energy piles: a new procedure for effective numerical prediction of thermal performance

Paola Iodice[1], Pasquale Marotta[2], Nicola Massarotti[2], Alessandro Mauro[1,2]
[1]Università Telematica Pegaso, Piazza Trieste e Trento n. 48, 80132 Napoli, Italy,
paola.iodice@unipegaso.it, alessandro.mauro@unipegaso.it

[2]Dipartimento di Ingegneria, Università degli Studi di Napoli "Parthenope", Centro Direzionale, Isola C4, Napoli, Italy, massarotti@uniparthenope.it, alessandro.mauro@uniparthenope.it

ABSTRACT

Energy piles operate as ground coupled heat exchangers and represent an effective solution to increase energy efficiency of heat pumps. The authors propose a numerical procedure to define a correlation among a number of parameters, taken into account for the design and operation of energy piles systems. The procedure is based on the finite element numerical modeling approach and on the Response Surfaces Method (RSM) and Radial Basis Functions (RBF). The numerical model is able to simulate the three-dimensional heat transfer of energy piles and the surrounding ground, and the one-dimensional heat and fluid flow in the probe. The RSM-RBF allow to define a correlation among the main parameters, on the basis of the numerical results obtained by the numerical simulations. The use of the proposed procedure allows to estimate instantaneously the performance of energy piles for all the possible combinations of design/operating parameters.

Key Words: *Heat transfer, Numerical modeling, Energy piles performance.*

1. INTRODUCTION

Geothermal energy piles are an alternative energy source for heating and cooling needs, using the ground as a renewable energy source. Foundation piles of a building can be used as part of the heat transfer system acting, at the same time, as structural elements and as heat exchangers, avoiding additional drilling costs related to traditional geothermal probes.

The performance of energy piles systems depend on a number of design and operating parameters, such as diameter of the probe and of the pile, properties of the employed materials, flow rate and temperature of the working fluid and probe configurations (U-tubes, Double U-tubes, Triple U-tubes, spiral coil).

The authors propose a numerical procedure to define a correlation among a number of parameters, taken into account for the design and operation of energy piles systems. This procedure is based on the use of a simplified and efficient numerical model [1], able to simulate the three-dimensional heat transfer of energy piles and the surrounding ground, and the one-dimensional heat and fluid flow in the probe, to study the behaviour of energy piles and to evaluate their performance for some combinations of the main parameters. Then, the authors employ the RSM and RBF to obtain a correlation among the operating/design and performance parameters.

2. THE NUMERICAL MODEL

Three dimensional conduction heat transfer in soil and concrete has been simulated. The heat and mass transfer model for the fluid and at the interface between the probe and the pile has been simplified: due to the low value of ratio between probe length and diameter, a one dimensional model has been used. Forced convection is considered for the fluid flowing in the probe. The governing equations are:

Conservation of energy in soil and pile

$$\rho_s c_s \frac{\partial T}{\partial t} - \nabla\left(k_s \nabla T\right) = 0 \tag{1}$$

Continuity

$$\frac{\partial\left(A\rho\right)}{\partial t} + \frac{\partial\left(A\rho u\right)}{\partial z} = 0 \tag{2}$$

Momentum Conservation

$$\frac{\partial\left(\rho u\right)}{\partial t} = -\frac{\partial p}{\partial z} - f_d \frac{\rho}{2D_h} u\,|u| \tag{3}$$

Conservation of energy in the fluid

$$\frac{\partial\left(\rho_f A c_f T\right)}{\partial t} + \frac{\partial\left(\rho_f A c_f u T\right)}{\partial z} = \frac{\partial}{\partial z}\left(A k_f \frac{\partial T}{\partial z}\right) + f_d \frac{\rho}{2D_h} |u|^3 + Q_{wall} \tag{4}$$

where ρ_s, c_s and k_s are the solid (soil or pile) density, specific heat capacity and thermal conductivity, respectively, A represents the surface area of the probe, ρ_f is the fluid density, c_f is the fluid specific heat capacity at constant pressure, k_f is the fluid thermal conductivity. The friction factor, f_d, depends on both Reynolds number and ratio between thickness and hydraulic diameter of the probe, as defined in Prandtl and von Karman model [2]. Q_{wall} represents the thermal power per unit of probe's length exchanged through the probe's walls.

As concerns boundary conditions, the temperature of horizontal bottom surface has been assumed to be constant during the simulations, equal to the soil temperature at a depth of 35 m. For the lateral surfaces of the soil, a temperature variation with depth and time has been considered, according to ref. [3]. Concerning the fluid flowing in the probe, the following conditions have been adopted: atmospheric pressure at the inlet and outlet sections of the probe, inlet velocity and temperature, convection dominated heat transfer at outlet of the probe. All the details are available in ref. [1].

3. THE PROPOSED PROCEDURE

The authors propose a new procedure, consisting in three steps, to define a correlation among the main parameters used for the design and operation of energy piles systems.

In the first step, the authors employ the simplified and efficient numerical model described above, to study the behaviour of energy piles and to evaluate their performance for some combinations of input parameters. The numerical simulations allow to find the parameters that have a significant influence on the performance of energy piles. In particular, the authors have considered the following design and operating parameters: the volumetric flow rate of water flowing in the probe, the thermal conductivity and density of the concrete, the diameter of pile and probe, and the probe's configuration. The performance parameter evaluated as output of the numerical simulations is the thermal power per unit of probe's length. The design, operating and performance parameters related to this first step represent the reference database.

The second step of the proposed procedure consists in the application of the RSM-RBF [4, 5], using as input data the reference database. This method allows to define a correlation among the design/operating parameters and the performance parameter, interpolating the values of the reference database available from the previous step. Three different algorithms for the construction of the correlation have been used, in order to find the one which better fit the available data: RSM with Gaussian Processes (a powerful regression model based on mean and covariance functions); Kriging method (based on a covariance function, named as variogram); RBF with the

multiquadratic basis function (a powerful tool for multivariate scattered data interpolation). The correlations obtained by using the above algorithms can be used to estimate instantaneously the performance of energy piles for all the possible combinations of design/operating parameters.

The third step consists in the evaluation of the reliability of the three correlations, derived in the previous step by using the three algorithms, by comparing the obtained results for combinations of design/operating parameters different from those of the reference database with those obtained by using the numerical model for the same input parameters.

4. RESULTS

The results are obtained for an energy pile with a double U-shaped tube in cooling mode operation, concerning the following operating/design/performance parameters: (operating) volumetric flow rate of water entering the probe, V_{in}; (design) thermal conductivity, k_{cls}, and density, ρ_{cls}, of the concrete; pile diameter, D_p, probe diameter, D_s; (performance) thermal power per unit of probe's length, Q/L_S. The results reported in the following tables show that the RBF method with multiquadratic basis function allows to obtain the best correlation. In fact, the values of Q/L_S estimated by using this method, for combinations of design/operating parameters different from the reference database, report an error smaller than 5% with respect to the corresponding values obtained by means of numerical simulations.

						CORRELATION	SIMULATION	
	D_p	**D_s**	**V_{in}**	**k_{cls}**	**ρ_{cls}**	**Q/L_s**	**Q/L_s**	**error**
	[cm]	[mm]	[m^3/h]	[W/(mK)]	[kg/m^3]	[W/m]	[W/m]	%
1	95	22	0,66	1,90	2100	44,18	43,50	1,54
2	88	27	1,10	1,50	1900	42,45	41,40	2,47
3	67	38	0,71	1,70	2200	46,28	46,84	1,21
4	55	35	0,50	2,10	2400	45,52	47,67	4,72
5	75	30	0,70	1,90	2100	46,29	47,51	2,64
6	81	40	0,80	2,00	1800	50,86	52,19	2,62
7	99	23	0,48	1,75	2200	43,21	42,07	2,64
8°	62	29	0,63	1,95	2400	43,50	47,45	9,08
9	52	36	0,49	2,10	2000	40,88	42,69	4,43

TABLE 1. Results of the RSM with Gaussian Processes.

						CORRELATION	SIMULATION	
	D_p	**D_s**	**V_{in}**	**k_{cls}**	**ρ_{cls}**	**Q/L_s**	**Q/L_s**	**error**
	[cm]	[mm]	[m^3/h]	[W/(mK)]	[kg/m^3]	[W/m]	[W/m]	%
1	95	22	0,66	1,90	2100	43,22	43,50	0,65
2	88	27	1,10	1,50	1900	43,27	41,40	4,32
3	67	38	0,71	1,70	2200	45,47	46,84	3,01
4	55	35	0,50	2,10	2400	45,70	47,67	4,31
5	75	30	0,70	1,90	2100	45,79	47,51	3,76
6	81	40	0,80	2,00	1800	46,24	52,19	12,87
7	99	23	0,48	1,75	2200	44,29	42,07	5,01
8	62	29	0,63	1,95	2400	44,69	47,45	6,18
9	52	36	0,49	2,10	2000	42,31	42,69	0,90

TABLE 2. Results of the Kriging method.

						CORRELATION	SIMULATION	
	D_p	D_s	V_{in}	k_{cls}	ρ_{cls}	Q/L_s	Q/L_s	**error**
	[cm]	[mm]	[m^3/h]	[W/(mK)]	[kg/m^3]	[W/m]	[W/m]	%
1	95	22	0,66	1,90	2100	44,96	43,50	3,25
2	88	27	1,10	1,50	1900	42,81	41,40	3,29
3	67	38	0,71	1,70	2200	47,22	46,84	0,80
4	55	35	0,50	2,10	2400	46,43	47,67	2,67
5	75	30	0,70	1,90	2100	48,13	47,51	1,29
6	81	40	0,80	2,00	1800	50,88	52,19	2,57
7	99	23	0,48	1,75	2200	42,91	42,07	1,96
8	62	29	0,63	1,95	2400	46,05	47,45	3,04
9	52	36	0,49	2,10	2000	40,72	42,69	4,84

TABLE 3. Results of the RBF with multiquadratic basis function.

5. CONCLUSIONS

The authors have developed a new procedure able to define a correlation among the main design, operating and performance parameters of energy piles systems. The procedure is based on a finite element numerical model and on RSM-RBF. The derived correlation allows to estimate instantaneously the performance of energy piles for all the possible combinations of the design and operating parameters taken into account.

Three different correlations, obtained by using three different interpolating algorithms (RSM, Kriging, RBF), have been derived. Their effectiveness have been evaluated by comparing the results with those obtained by using the finite element numerical model developed by the authors. The RBF method with multiquadratic basic function has shown the best performance, with a maximum error on the performance parameter (thermal power per unit of probe's length) smaller than 5% with respect to the corresponding values obtained by means of numerical simulations.

REFERENCES

[1] A. Carotenuto, S. Di Fraia, N. Massarotti, A. Mauro, D. Sainas, L. Vanoli. Parametric analysis of vertical energy piles simulated by using an efficient finite element model. *ASME-ATI-UIT 2015 Conference on Thermal Energy Systems: Production, Storage, Utilization and the Environment*, 17 – 20 May, 2015, Napoli, Italy.

[2] M. Dobrnjac, Determination of Friction Coefficient in Transition Flow Region for Waterworks and Pipelines Calculation, Annals of Faculty Engineering Hunedoara, *International Journal of Engineering* X(3), 137-142, 2012.

[3] H. Brandl, Energy foundations and other thermo-active ground structures, *Geotechnique* 56(2), 81-122, 2006.

[4] A.I. Khuri, J.A. Cornell, *Response Surfaces, Design and Analyses*, 2nd edition, Marcel Dekker, New York, 1996.

[5] M. D. Buhmann, *Radial Basis Functions, Theory and Implementations*, Cambridge University Press, Cambridge, 2004.